



**PHYSICAL CHEMISTRY 2018**

14<sup>th</sup> International Conference  
on Fundamental and Applied Aspects of  
Physical Chemistry

Proceedings  
Volume I

**September 24-28, 2018**  
**Belgrade, Serbia**





**PHYSICAL CHEMISTRY 2018**

14<sup>th</sup> International Conference  
on Fundamental and Applied Aspects of  
Physical Chemistry

Proceedings  
Volume I

**September 24-28, 2018**  
**Belgrade, Serbia**

**ISBN** 978-86-82475-36-1

**Title:** Physical Chemistry 2018 (Proceedings)

**Editors:** Željko Čupić and Slobodan Anić

**Published by:** Society of Physical Chemists of Serbia, Studentski Trg 12-16,  
11158, Belgrade, Serbia

**Publisher:** Society of Physical Chemists of Serbia

**For Publisher:** S. Anić, President of Society of Physical Chemists of Serbia

**Printed by:** "Jovan", <Printing and Publishing Company, 200 Copies

**Number of pages:** 550+6, Format B5, printing finished in September 2018

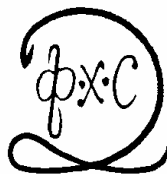
Text and Layout: "Jovan"

Neither this book nor any part may be reproduced or transmitted in any form or by any means, including photocopying, or by any information storage and retrieval system, without permission in writing from the publisher.

200 - *Copy printing*

## CONTENT

<i>Volume I</i>	
<i>Organizer</i>	IV
<i>Comittes</i>	V
<i>Sponsors</i>	VI
<i>Plenary Lecture</i>	1
<i>Chemical Thermodynamics</i>	57
<i>Spectroscopy, Molecular Structure, Physical Chemistry of Plasma</i>	71
<i>Kinetics, Catalysis</i>	157
<i>Nonlinear Dynamics, Oscillatory Reactions, Chaos</i>	253
<i>Electrochemistry</i>	361
<i>Biophysical Chemistry, EPR investigations of biosystems,</i>	419
<i>Photochemistry, Radiation Chemistry</i>	



# **PHYSICAL CHEMISTRY 2018**

*14<sup>th</sup> International Conference on  
Fundamental and Applied Aspects of  
Physical Chemistry*

*Organized by*

*The Society of Physical Chemists of  
Serbia*

*in co-operation with*

*Institute of Catalysis Bulgarian Academy of Sciences*

*and*

*Boriskov Institute of Catalysis Siberian Branch of  
Russian Academy of Sciences*

*and*

*University of Belgrade, Serbia:*

*Faculty of Physical Chemistry*

*Institute of Chemistry, Technology and Metallurgy*

*Vinča Institute of Nuclear Sciences*

*Faculty of Pharmacy*

*Institute of General and Physical Chemistry, Belgrade, Serbia*

## Organizing Committee

**Chairman:** S. Anić (Serbia)

**Vice-chairmans:** M. Gabrovska (Bulgaria)  
A. A. Vedyagin (Russia)  
S. N. Blagojević (Serbia)

**Members:** N. Cvjetičanin (Serbia), S. M. Blagojević (Serbia), M. Daković (Serbia), J. Dimitrić-Marković (Serbia), T. Grozdić (Serbia), Lj. Ignjatović (Serbia), D. Jovanović (Serbia), J. Jovanović (Serbia), M. Kuzmanović (Serbia), D. Marković (Serbia), B. Milosavljević (USA), M. Mojović (Serbia), N. Ostrovski (Serbia), N. Pejić (Serbia), M. Petković (Serbia), A. Popović-Bjelić (Serbia), B. Simonović (Serbia), D. Stanisavljev (Serbia), M. Stanković (Serbia), Z. Šaponjić (Serbia), B. Šljukić (Serbia), G. Tasić (Serbia), S. Veličković (Serbia), N. Vukelić (Serbia)

## Scientific Committee

**Chairman:** Ž. Čupić (Serbia)  
**Vice-chairmans:** V. Bukhtiyarov (Russia)  
S. Todorova (Bulgaria)  
B. Adnađević (Serbia)

**Members:** S. Anić (Serbia), A. Antić-Jovanović (Serbia), D. J. Biswas (India), R. Cervellati (Italy), G. Ćirić-Marjanović (Serbia), V. Dondur (Serbia), S. D. Furrow (USA), A. Goldbeter (Belgium), R. Jerala (Slovenia), M. Jeremić (Serbia), A. Jovović (Serbia), Y. Kalvachev (Bulgaria), E. Kiš (Serbia), Lj. Kolar-Anić (Serbia), U. Kortz (Germany), T. Kowalska (Poljska), V. Kuntić (Serbia), G. Lente (Hungary), Z. Marković (Serbia), S. Mentus (Serbia), K. Novaković (UK), B. Novakovski (Poljska), S. Otto (Netherlands), V. Parmon (Russia), R. Pascal (USA), M. Perić (Serbia), M. Plavšić (Serbia), J. Savović (Serbia), G. Schmitz (Belgium), I. Schreiber (Czech), L. Schreiberova (Czech), H. W. Siesler (Germany), E. M. Barbosa Souto (Portugal), N. Stepanov (Russia), E. Szabó (Slovakia), R. Tomovska (Spain), Á. Tóth (Hungary), M. Trtica (Serbia), V. Vasić (Serbia), D. Veselinović (Serbia), D. Vučković (Canada), V. Vukojević (Sweden), P. Walde (Switzerland)

## Local Executive Committee

**Chairman:** S.N. Blagojević  
**Vice-chairmans:** A. Ivanović-Šašić  
A. Stanojević

**Members:** M. Ajduković, I. N. Bujanja, A. Dobrota, J. Dostanić, D. Dimić, A. Ignjatović, S. Jovanović, Z. Jovanović, A. Jović, N. Jović-Jovičić, D. Lončarević, M. Kragović, J. Krstić, S. Maćešić, J. Maksimović, S. Marinović, V. Marković, D. Milenković, M. Milovanović, T. Mudrinić, B. Nedić, M. Pagnacco, A. Pavićević, N. Potkonjak, D. Ranković, M. Ristić, B. Stanković, K. Stevanović, M. Stević, A. Stoiljković

## SPONSORS

Ministry of Education, Science and Technological Development  
University of Belgrade, Belgrade  
Institute of General and Physical Chemistry, Belgrade  
Analysis d.o.o.  
Institut Mol d.o.o.

*PL-Plenary lecture*



## EMERGENT PROPERTIES OF VESICLES

P. Walde

*ETH Zürich, Department of Materials, Vladimir-Prelog-Weg 5,  
CH-8093 Zürich, Switzerland (peter.walde@mat.ethz.ch)*

### ABSTRACT

Micelles and vesicles formed from amphiphiles in aqueous solution have properties which emerge from the assembly of the amphiphiles. Compared to micelles with their hydrophobic interior, vesicles have an aqueous internal volume which is separated from the bulk aqueous solution by a semi-permeable membrane formed by the amphiphiles. Since this compartment property is one of the key features of all biological cells, vesicular structures may have played important roles as protocellular precursor systems of the first cells at the origin of life. In terms of applications, vesicles from amphiphilic lipids (liposomes) are investigated for pharmaceutical applications, e.g. as drug delivery systems. Less investigated are vesicles as additives for promoting chemical reactions in aqueous media. In this case, the soft and dynamic vesicle membrane provides a reaction environment which differs from the bulk aqueous solution and with this may alter reaction kinetics and reaction pathways.

### MICELLES AND VESICLES

Amphiphiles are a fascinating class of molecules since they combine in one and the same chemical structure hydrophilic (water-soluble) as well as hydrophobic (water-insoluble) parts. Typical and well-known low molar mass amphiphiles are surfactants (“surface-active agents”) like SDS (sodium dodecylsulfate), AOT (sodium bis(2-ethylhexyl)sulfosuccinate), DODAB (dioctadecyldimethylammonium bromide), or phospholipids like POPC (1-palmitoyl-2-oleoyl-*sn*-glycero-3-phosphocholine) (Figure 1), just to mention four of the hundreds of different synthetic or naturally occurring amphiphiles known today.

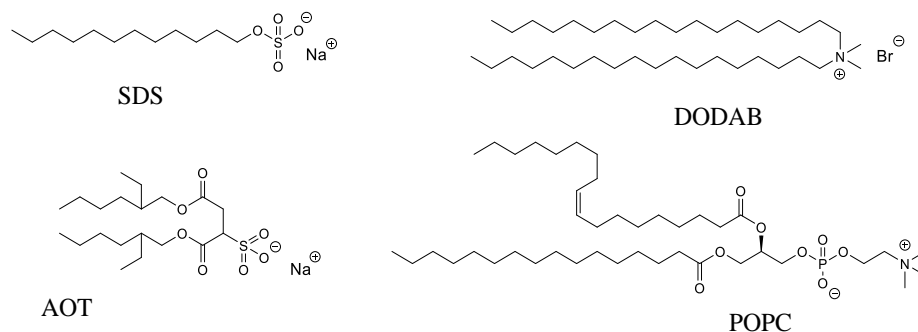


**Figure 1.** Structures of the amphiphiles SDS, AOT, DODAB and POPC.

If amphiphiles are brought into contact with water under conditions at which the hydrophobic parts of the amphiphiles do not adhere to each other very strongly, the water molecules hydrate the hydrophilic parts and the amphiphiles self-organize into dynamic polymolecular assemblies. This is the case at temperatures above the melting temperature of low molar mass amphiphiles, or at temperatures above the glass transition temperature in the case of polymeric amphiphiles (amphiphilic block copolymers). The best known aqueous polymolecular assembly systems are micellar solutions, vesicle dispersions (Figure 2), or cubic phases [1,2]. In the case of vesicle dispersions, the average size of the vesicles as well as their lamellarity can be controlled to some extent by different means, *i.e.*, by the way the vesicle dispersions are prepared or how they are treated after initial formation (so-called “guided assembly”) [3-5]. This allows for a tuning of the vesicle size from about 30 nm to more than 100  $\mu\text{m}$ . In any case, all types of vesicles exist due to a self-closure of layered, sheet-like arrangements of amphiphiles. Vesicles can be seen as “dispersed lamellar phase”. In contrast to micellar solutions and cubic phases, vesicle dispersions obtained through guided assembly processes are only kinetically stable and not thermodynamically. The size of vesicles may change upon storage with time. Such vesicle instabilities caused by vesicle fusions depend on the amphiphile used, on the composition of the aqueous solution, and how the vesicle dispersion is prepared. Despite this “drawback”, vesicles are useful polymolecular aggregates for many applications.

If more than one type of amphiphiles is used, the assembly behavior can be very complex. Other, non-classical aggregates may form as well, for example bicelles (“bilayered micelles”, *i.e.*, disk-like aggregates) or cubosomes (dispersed particles consisting of a cubic phase). The latter ones are again only kinetically stable and not thermodynamically. Moreover,

different types of aggregates may coexist in one and the same aqueous solution.

One common feature of all types of polymolecular assemblies is that they represent soft, dispersed, interface-rich systems which can be useful for many industrial applications and in basic research. The physico-chemical properties of these aggregates emerge from molecular assembly, as the properties of the aggregates are not present in the individual molecules [6,7].

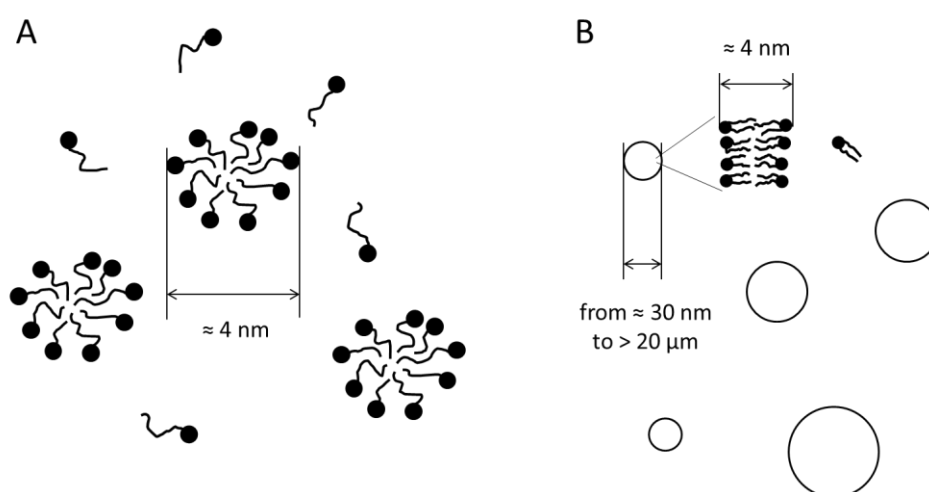


**Figure 2.** Schematic illustration of the difference between conventional micelles formed from low molar mass amphiphiles like SDS (A) and lipid vesicles formed from POPC (B). Both drawings represent cross-sections of dynamic spherical objects. The interior cores of micelles and the interior part of the vesicle membrane are hydrophobic, while the internal pool of a vesicle is an aqueous volume. Vesicles are obtained through a guided assembly. An SDS micelle consists of about 60 SDS molecules. A 100 nm unilamellar POPC vesicle is built from about  $8.1 \times 10^4$  POPC molecules and has an internal volume of about  $4.16 \times 10^{-19}$  L (= 0.4 aL).

In addition to drug delivery applications of vesicles formed from amphiphilic lipids (“liposomes”), vesicle systems are investigated, for example, (i) in studies of the structure and function of membrane proteins, (ii) as model systems of “protocells”, the hypothetical precursor structures of the first cells at the origin of life, (iii) as cell-mimicking compartments for the preparation of synthetic cell-like systems, and (iv) for promoting and guiding reactions towards the formation of desired products. These

possibilities are listed in Figure 3. There are opportunities for “controlling” chemical reactions in vesicle systems which have not been explored yet.

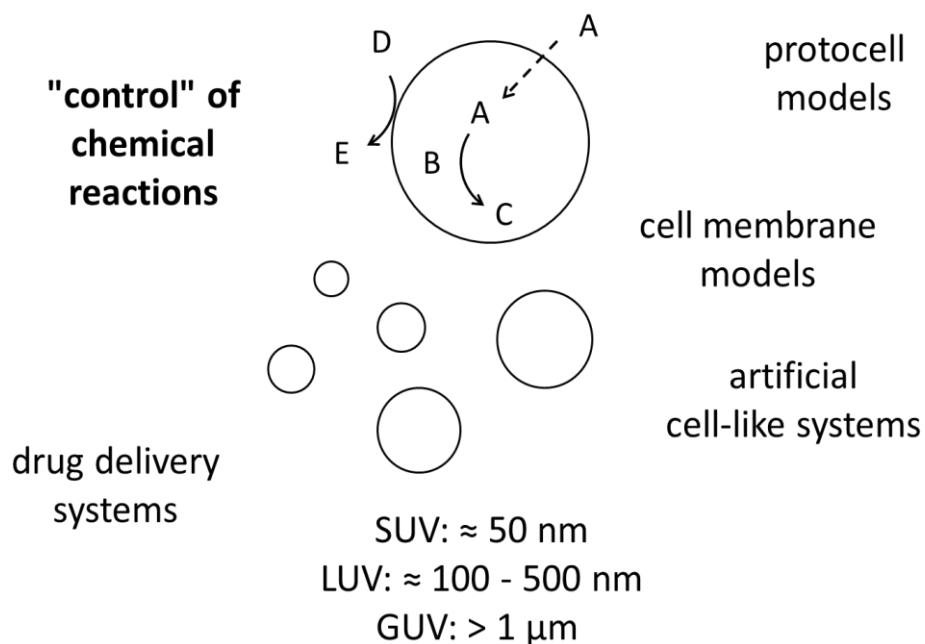


**Figure 3.** Possible applications of vesicle systems. SUV, small (sonicated) unilamellar vesicles; LUV, large unilamellar vesicles; GUV, giant unilamellar vesicles [5]. In the top vesicle, two types of hypothetical reactions are illustrated. One is a reaction taking place between A and B to yield C *inside* the aqueous pool of the vesicles, whereby A must diffuse from the external bulk aqueous solution into the vesicle’s interior. The other reaction is assumed to take place on the surface of the vesicle, whereby D is converted into E. The reaction kinetics and the outcome of the two confined reactions are influenced by the presence of the vesicles.

## REACTIONS IN VESICLE SYSTEMS

### An enzymatic reaction occurring inside the aqueous pool of vesicles

Water soluble enzyme molecules which are entrapped in the internal aqueous pool of vesicles may be protected from interaction and reaction with molecules present in the external bulk aqueous phase (due to the permeability barrier provided by the vesicle membrane). This has been demonstrated in the case of  $\alpha$ -chymotrypsin and POPC LUVs [8]. The entrapped enzyme only catalyzes the hydrolysis of those externally added



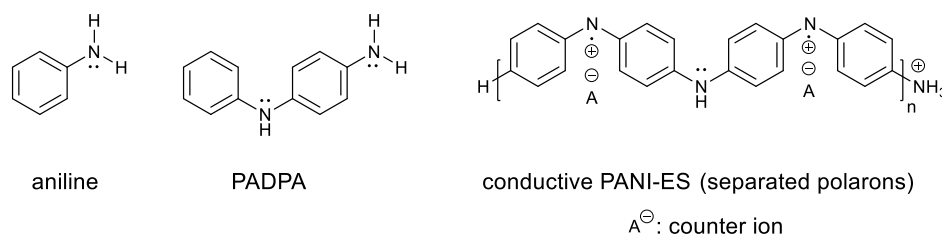


**Figure 5.** Structures of aniline, PADPA and one of the polaron forms of PANI-ES. By using AOT vesicles as “templates”, the counter ion is AOT.

## CONCLUSION

The formation of vesicles (or other polymolecular aggregates) in an aqueous solution transforms this homogeneous solution into a system of dispersed, soft interface-rich entities which is characterized by properties that are very different from the properties of the aqueous solution. Some of these emergent properties allow, for example, for promoting and guiding chemical reactions due to the reactions taking place within the vesicle membrane. Alternatively, the compartment nature of vesicles is attractive for the development of simple models systems of biological cells and protocells.

## Acknowledgements

The fruitful collaborations with Prof. Gordana Ćirić-Marjanović and her team at the University of Belgrade - Faculty of Physical Chemistry, Dr. Boris Rakvin at the Ruđer Bošković Institute in Zagreb, and the group of Prof. Ryszard Ostaszewski at the Polish Academy of Sciences in Warsaw are highly appreciated.

## REFERENCES

- [1] D. F. Evans, H. Wennerström, *The Colloidal Domain. Where Physics, Chemistry, Biology, and Technology Meet*, 2nd edn., Wiley-VCH, New York, 1999.
- [2] O. G. Mouritsen, *Life – as a Matter of Fat: The Emerging Science of Lipidomics*, Springer-Verlag Berlin Heidelberg, 2011.
- [3] V. P. Torchilin, V. Weissig (eds.), *Liposomes – A Practical Approach*, 2<sup>nd</sup> ed., Oxford University Press, 2003.
- [4] P. Walde, in: *Encyclopedia of Nanoscience and Nanotechnology* (ed. Nalwa, H. S.), vol. 9, APS, Valencia, CA, 2004, pp. 43-79.
- [5] P. Walde, K. Cosentino, H. Engel, P. Stano, *ChemBioChem*, 2010, **11**, 848-865.
- [6] P. L. Luisi, *Found. Chem.*, 2002, **4**, 183-200.

- [7] P. Walde, H. Umakoshi, P. Stano, F. Mavelli, *Chem. Commun.*, 2014, **50**, 10177-10197.
- [8] P. Walde, B. Marzetta, *Biotechnol. Bioeng.*, 1998, **57**, 216-219.
- [9] M. Yoshimoto, J. Yamada, M. Baba, P. Walde, *ChemBioChem*, 2016, **17**, 1221-1224.
- [10] D. Paprocki, D. Koszelewski, P. Walde, R. Ostaszewski, *RSC Adv.*, 2015, **5**, 102828-102835.
- [11] K. Junker, G. Zandomenighi, Z. Guo, R. Kissner, T. Ishikawa, J. Kohlbrecher, P. Walde, *RSC Adv.*, 2012, **2**, 6478-6495.
- [12] K. Junker, R. Kissner, B. Rakvin, Z. Guo, M. Willeke, S. Busato, T. Weber, P. Walde, *Enzyme Microb. Technol.*, 2014, **55**, 72-84.
- [13] S. Luginbühl, L. Bertschi, M. Willeke, L. D. Schuler, P. Walde, *Langmuir*, 2016, **32**, 9765-9779.
- [14] S. Luginbühl, M. Milojević-Rakić, K. Junker, D. Bajuk-Bogdanović, I. Pašti, R. Kissner, G. Ćirić-Marjanović, P. Walde, *Synth. Met.*, 2017, **226**, 89-103.

## GREEN SYNTHESIS OF ZEOLITES FROM FLY ASH AND THEIR APPLICATION FOR ENVIRONMENTAL PROTECTION

B. Barbov <sup>1</sup> and Yu. Kalvachev <sup>2</sup>

<sup>1</sup> *Institute of Mineralogy and Crystallography, Bulgarian Academy of Sciences, Acad. G. Bonchev St., Bl. 107, 1113 Sofia, Bulgaria.*

<sup>2</sup> *Institute of Catalysis, Bulgarian Academy of Sciences, Acad. G. Bonchev St., Bl. 11, 1113 Sofia, Bulgaria. (kalvachev@ic.bas.bg)*

### ABSTRACT

Coal combusting power plants are simultaneously among the main emitters of carbon dioxide and the main generator of solid by-products, such as fly ash (FA). An attempt to find a common solution for these environmental problems is reported. Zeolites analcime and faujasite (X) have been successfully synthesized by interaction of FA, originating from lignite coal at Maritsa Iztok 2 thermal power plant with sodium hydroxide, followed by hydrothermal treatment. NaX zeolite crystallisation started later by decreasing NaOH amount. In order to optimise synthesis process a seed-assisted procedure was introduced. In this way, zeolitisation may increase cost-effectiveness and eco-efficiency. Synthesized zeolites were used in environmental protection processes – zeolite X in CO<sub>2</sub> adsorption and analcime in purification of phenol contaminated water. Determination of adsorption capacity towards CO<sub>2</sub> was measured to be 60 mg g<sup>-1</sup> and the adsorption-desorption equilibrium was reached after one hour. The adsorption capacity towards phenol was measured to be 14 mg per gram adsorbent.

### INTRODUCTION

Coal-fired thermal power plants (TPP) are a major source of fly ash (FA). Depending on the type of source and composition of the combustion coal, solid by-product components may vary significantly, but all types of FA include large amounts of silica (amorphous and crystalline) and alumina, both of which are constituent parts of many coal bedrocks. The areas where the production waste from the TPPs is deposited are huge terrains. FA is a fine powder captured from flue gas streams by dust collecting systems prior to their release into the atmosphere. FA is generally stored in landfills. Discharges of the ash create environmental risks due to increased acid content and infiltration of heavy metals and radioactive elements in the soil. Toxic components in FA depend on the specific structure of the

deposit and they may include a variety of the elements found in negligible quantities. Many approaches to the use of FA have been developed, given their composition and degree of crystallinity. Part of deposited ash is used in the construction of roads and buildings, in the form of gypsum, gypsum board, cement, and concrete, in the ceramic industry, and other building mixes. Zeolite synthesis is another solution to utilise FA [2,3]. Zeolite production from FA results in a good ingredient with higher added value compared to ash usage as a cement additive [4–6]. In recent years, many studies have also been accomplished on zeolite synthesis from other alternative sources of  $\text{SiO}_2$  and  $\text{Al}_2\text{O}_3$  because the production of synthetic zeolites from pure silica and alumina sources is quite expensive. For alternative sources of silicon and aluminum, industrial waste or geothermal materials rich in Si and Al [7–14] may be used, as well as FA, which is largely composed of silicon and aluminum units. So naturally, one of the approaches to use FA is their zeolitisation. Zeolites synthesized from fly ash have many applications, including ion exchangers, molecular sieves, and adsorbents, similar to the zeolites obtained by conventional methods.

It has been found that different zeolite structures can be synthesized from the same ash but under different crystallisation conditions, analcime, NaX, and NaY zeolites being of utmost importance. One of them, namely NaX zeolite, which is an analogue to the natural faujasite, has a great ecological application. This zeolite, characterised by a highly developed specific surface area and numerous pores ranging in size from 5.0 to 7.5 Å, facilitates adsorption of 3.2-Å carbon dioxide molecules. Primarily, NaX zeolite is used as a catalyst in biodiesel production and  $\text{CO}_2$  adsorption. Greenhouse gas emissions are reaching alarming rates and they cause global climate change. These gases, such as methane, ozone, and carbon dioxide, are being produced in a natural way, but they also appear as a result of human activities. Fossil fuels still comprise more than 80 % of the total energy resources worldwide and they are the largest source of  $\text{CO}_2$  emissions. This fact makes fossil fuel burning power plants the most logical targets for  $\text{CO}_2$  reductions [15].

The aim of the present work is to be synthesized zeolites analcime and NaX from fly ash obtained after the combustion of lignite coal at Maritsa Iztok 2 TPP and to evaluate the carbon dioxide sorption capacity of zeolite NaX by using the thermogravimetric method. The capacity of the FA-X sample is compared with that of the zeolite X, obtained from pure gel. The present study explores also the adsorptive removal of phenol by zeolite analcime by investigating the effect of initial phenol concentration and contact time.

## EXPERIMENTAL

### *Sample preparation*

Ash residues, containing 52.66 mass % of SiO<sub>2</sub> and 23.37 mass % of Al<sub>2</sub>O<sub>3</sub>, were subjected to a dual stage fusion-hydrothermal transformation. Coal ash and NaOH mixture at a ratio of 1:2 was sintered at 550 °C, and after dilution with water under continuous stirring for 16 hours, the reaction mixture was charged into an autoclave for hydrothermal reaction. The crystallization process was performed under static conditions for a period of several days at room temperature. The obtained solid substance was carefully washed with distilled water and then dried at 105°C for an hour.

Analcime samples were synthesized by using the follow recipe : 1 g NaOH; 0.7 g FA; 0.3 g SiO<sub>2</sub> and 10 g H<sub>2</sub>O are mixed and aged. The experiment was performed in a stainless steel autoclave. After the completion of the reaction at 180 °C, the product was cooled to room temperature, filtered and washed with distilled water. The product was dried at 120 °C for 8 h. The studies were carried out by varying the reaction time (12, 24, 48, 72 and 96 h). Aging was done for 24 and 72 h.

### *CO<sub>2</sub> adsorption*

Carbon dioxide adsorption on FA-X zeolite was studied using the same thermal apparatus following the procedure: (i) The zeolite samples were heated from room temperature to 320 °C in Ar flow (30 ml min<sup>-1</sup> flow rate) at heating rate of 5 °C min<sup>-1</sup>; (ii) after that the system was cooled down to room temperature and stabilized in Ar atmosphere (30 ml min<sup>-1</sup> flow) for 15 minutes and (iii) the adsorption of CO<sub>2</sub> was carried out isothermally in a flow of CO<sub>2</sub> (30 ml min<sup>-1</sup>) in the course of 70-80 min. The initial sample weight for the Na-X was 19.0 mg while for the FA-X was 12.0 mg.

### *Phenol adsorption*

The adsorption studies were conducted in polypropylene containers. A measured amount (0.2 g) of the synthesized analcime or commercial ZSM-5 was added to a measured amount (20 ml) of aqueous solution of phenol of different initial concentrations (50–400 ppm). The concentrations of the adsorbents were monitored with time: initially rapidly (5, 10, 15, 30 min) and subsequently slowly (1, 2 and 5 h) until equilibrium was reached. In each case, 1 ml of the solution was withdrawn. The concentrations were determined using an ultraviolet– visible spectrometer (Lambda 25, PerkinElmer) at 268.4 nm absorbance.

## RESULTS AND DISCUSSION

Table 1 provides data on the crystal- lisation time of zeolite X obtained from fly ash without seed and with 1, 2, and 5% seed, respectively, at a

different NaOH/FA ratio. The NaOH/FA ratios used were 1.2/1, 1.0/1, 0.8/1, and 0.6/1 (Table 1). Higher amounts of NaOH caused NaX zeolite crystallisation to start much earlier. X-ray powder patterns indicate that the best results were obtained when the amount of sodium hydroxide was higher with NaOH/FA ratio of 1.2/1 or 1.0/1. Such a result

**Table1.** The crystallization time of zeolite NaX synthesized from fly ash in the presence of 1, 2 or 5 % seed at room temperature depending from used ratios of NaOH/FA

NaOH/FA	No seeds	1 % seed	2 % seed	5 % seed
1.2/1	25 days	21 days	21 days	21 days
1	29 days	29 days	29 days	21 days
0.8/1	-	37 days	37 days	24 days
0.6/1	-	-	43 days	37 days

could be expected because in this case sodium hydroxide brings about larger amounts of soluble silicates and aluminates from the silica and alumina phases, respectively, present in the fly ash. The latter phases increase their mobility to become able to form zeolite nuclei around which crystal growth takes place to build a zeolite structure. On using a lower amount of sodium hydroxide, however, NaX zeolite synthesis was not successful. X-ray powder patterns of the resulting products synthesised at a NaOH/FA ratio of 1/1 show that a crystalline phase emerged around the 29<sup>th</sup> day after crystallisation at room temperature (Fig. 1) and a high crystalline product of this zeolite was only reached by the 45<sup>th</sup> day of synthesis. On employing a NaOH/FA ratio of 1.2/1 in the studies, the crystallisation of NaX zeolite began about 25 days after synthesis onset.

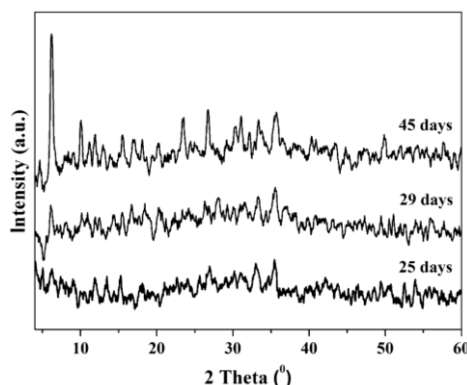


**Figure 1.** X-ray powder patterns of zeolite NaX synthesized without seeds from fly ash at room temperature and ratio of NaOH/FA=1/1.

To reduce crystallisation time and direct synthesis to the desired zeolite structure, a seed-assisted synthesis of NaX zeolite from fly ash was applied by means of 1, 2 or 5 wt.% crystalline NaX zeolite. The weight percentage was calculated regarding the total amount of silica and alumina in the fly ash. NaX zeolite crystallisation at a NaOH/FA ratio of 1.2/1 started earlier on using 1, 2, and 5% seed. Comparing seed-assisted with seed-free NaX zeolite synthesis, crystallisation with the latter started later for the same NaOH/FA ratio. By applying 1, 2 or 5% by weight of crystalline seed crystals, zeolite crystallisation started 21 days after synthesis onset at room temperature.

At ratio NaOH/FA = 1.2/1 the synthesis of zeolite X is the most sensitive to the presence of even small amounts of seed. Upon addition of 1 % seed, the crystallization time decreases to 21 days, whereas without seed, crystallization begins after 25<sup>th</sup> day. Using 5 wt % seed leads to a product with a higher degree of crystallinity. When the NaOH/FA ratio is 1/1 and the crystallization takes place in the presence of 1 or 2 % seed, zeolite NaX begins to crystallize before the 29<sup>th</sup> day. By using a higher amount of seed (5 %), crystallization of zeolite NaX begins earlier than when 1 or 2 % crystal seed are used. In the X-ray powder patterns of the synthesized products, it is observed that zeolite NaX begins to crystallize before the 21<sup>st</sup> day of the synthesis. From these results, it can be concluded that the use of a larger amount of crystal seed favors a significant decrease in crystallization time.

### *CO<sub>2</sub> adsorption*

The TG-DTA profiles of CO<sub>2</sub> adsorption on FA-X sample are represented in Fig.2. The preliminary dehydration reaches up to 14.0 mass % and the restore volume amounted to 5.0 mass %. The main part of the sorption is occurring during the first ten minutes and the peak in DTA curve is sharp. The measured adsorption capacity of the FA zeolite towards CO<sub>2</sub> is 60 mg g<sup>-1</sup> and this value is comparable to the adsorption capacity values of zeolites, obtained from fly ash and impregnated with amine solutions [20]. Nevertheless, this amount of CO<sub>2</sub> is remarkable for zeolite synthesized from fly ash and it can provide a promising solution for lowering of the CO<sub>2</sub> emissions from power plants.

The sample composition of FA zeolite has been studied by an integral energy-dispersive X-ray (EDX) analysis and has been found to consist of 17.21 mass % Na<sub>2</sub>O, 35.55 mass % SiO<sub>2</sub>, 22.11 mass % Al<sub>2</sub>O<sub>3</sub>, and other components from the raw material, such as 16.01 mass % Fe<sub>2</sub>O<sub>3</sub>, 7.39 mass % CaO and 1.73 mass % MgO, which corresponds to a deficit of Na<sub>2</sub>O and an excess in SiO<sub>2</sub> against Al<sub>2</sub>O<sub>3</sub>. Na content is known to effect the uptake of adsorbed CO<sub>2</sub> at equivalent pressures because the Na cation possesses a higher electric field than a proton for example. Additionally, CO<sub>2</sub> has large polarizability together with an electric quadrupole moment. Therefore CO<sub>2</sub> is more prone to perform ion-quadrupole interactions with Na cations located within the extra-framework, and thus, the higher the content of Na cations the higher CO<sub>2</sub> capacity results at equilibrium pressures. Vice versa, the lower the Na cations content results in the lower CO<sub>2</sub> capacity, which is the case of the FA-X sample. Both parameters, lower level of crystallinity and lower sodium cations content lead to lower CO<sub>2</sub> capacity of the FA-X sample, compared with samples synthesized from pure chemicals [16].

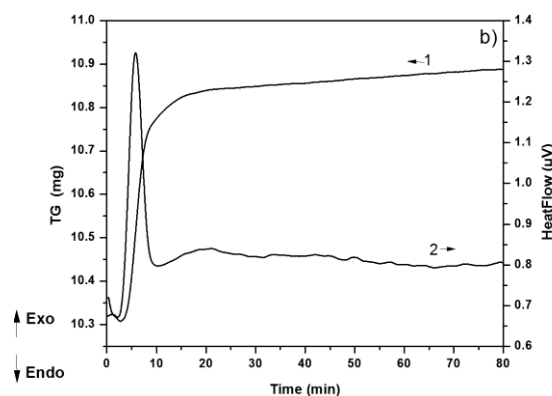


**Figure 2.** Adsorption of CO<sub>2</sub> at 22°C on FA-X zeolite

### *Phenol adsorption*

By using of hydrothermal treatment, zeolite analcime has been synthesized from FA. The analcime was tested in adsorption of phenol from aqueous solution. The maximum amount of phenol ultimately adsorbed from water on analcime was 14 mg/g. Thus, local raw materials could be used to prepare an adsorbent with a good and favourable adsorptive capacity.

### **CONCLUSION**

Zeolite X was successfully synthesised from fly ash produced by combustion of lignite coal at Maritsa Iztok 2 TPP using a two-stage process: fusion with sodium hydroxide followed by hydrothermal treatment at room temperature. Added seed directed synthesis to the desired zeolite structure (mono-phase zeolite X), and reduced both synthesis time and used sodium hydroxide amount upon melting. In this way, the process of zeolitisation is economically cost-effective and better eco-efficient. Using the thermogravimetric method the adsorption capacity of carbon dioxide on the investigated zeolite samples is estimated at 22°C. The CO<sub>2</sub> adsorption capacity of zeolite X synthesized from fly ash is measured to be of the order of 60 mg g<sup>-1</sup>. This value is valuable for by-product zeolites in view of removal of wastes by their utilization. Zeolite analcime synthesized from FA shows good and favourable adsorptive capacity towards phenol.

### ***Acknowledgement***

The authors acknowledge financial support by the Bulgarian National Science Fund (Contract No. DN 19/5).

### **REFERENCES**

- [1] A. M. Cardoso, A. Paprocki, L. S. Ferret, C. M. N. Azevedo, M. Pires, *Fuel*, **139**, 59 (2015).
- [2] Z. T. Yao, X. S. Ji, P. K. Sarker, J. H. Tang, L. Q. Ge, M. S. Xia, Y. Q. Xi, *Earth Sci. Rev.*, **141**, 105 (2015).
- [3] A. A. Ramezaniapour, *Cement Replacement Materials - Properties, Durability, Sustainability*, Springer, 2014.
- [4] N. Murayama, H. Yamamoto, J. Shibata, *J. Chem. Technol. Biotechnol.*, **77**, 280 (2002).
- [5] X. Querol, N. Moreno, J. C. Uman, A. Alastuey, E. Hernaández, A. López-Soler, F. Plana, *Int. J. Coal Geol.*, **50**, 413 (2002).
- [6] X. Querol, F. Plana, A. Alastuey, A. Lopez-Soler, *Fuel*, **76**, 793 (1997).
- [7] S. N. Azizi, S. Ghasemi, S. Kaviani, *Biosens. Bioelectron.*, **62**, 1 (2014).

- [8] T.Wajima, K. Kuzawa, H. Ishimoto, O. Tamada, T. Nishiyama, *Am. Mineral.*, **89**, 1694 (2004).
- [9] C. Belviso, F. Cavalcante, A. Lettino, S. Fiore, *Appl. Clay Sci.*, **80–81**, 162 (2013).
- [10] N. M. Musyoka, R. Missengue, M. Kuisakana, L. F. Petrik, *Appl. Clay Sci.*, **97–98**, 182, (2014).
- [11] A. Baccouche, E. Srasra, M. E. I. Maaoui, *Appl. Clay Sci.*, **13**, 255 (1998).
- [12] G. E. Christidis, H. Papantoni, *Open Mineral. J.*, **2**, 1 (2008).
- [13] D. Hoellen, D. Klammer, I. Letofsky-Papst, M. Dietzel, *Mater. Sci. Eng. B: Solid-state Mater. Adv. Technol.*, **2**, 523 (2012).
- [14] S. K. Masoudian, S. Sadighi, A. Abbasi, *Bull. Chem. React. Eng. Catal.*, **8**, 54 (2013).
- [15] B. P. Spigarelli, S. Kawatra, *J. CO<sub>2</sub> Utilization*, **1**, 69-87 (2013).
- [16] Yu. Kalvachev, D. Zgureva, S. Boycheva, B. Barbov, N. Petrova, *J. Therm. Anal. Calor.*, **124** (1), 101-106 (2016).

## POLYOXOMETALATES FOR APPLICATIONS IN CATALYSIS AND ENERGY

U. Kortz

*Jacobs University, Department of Life Sciences and Chemistry, Campus Ring 1, 28759 Bremen, Germany, [u.kortz@jacobs-university.de](mailto:u.kortz@jacobs-university.de)*

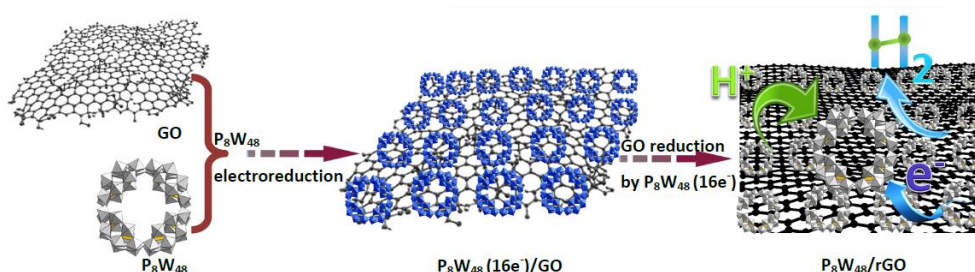
### ABSTRACT

Polyoxometalates (POMs) are discrete metal-oxides and their large structural and compositional versatility gives rise to potential applications in different fields such as catalysis, electrochemistry, magnetism, material science, and medicine.[1]

We have prepared the high-valent manganese-containing polyanion  $[\text{Mn}^{\text{III}}_3\text{Mn}^{\text{IV}}\text{O}_3(\text{CH}_3\text{COO})_3(\text{SiW}_9\text{O}_{34})]^{6-}$ . The tetranuclear manganese-oxo core of the latter species shows a close structural analogy to the active site of photosystem II, and is also active in catalytic water oxidization. Evidence for its photosynthetic properties when combined with  $[\text{Ru}(\text{bpy})_3]^{2+}$  and  $\text{S}_2\text{O}_8^{2-}$  is obtained by nanosecond laser flash photolysis.[2]00

The 20-Cu<sup>II</sup>-containing 48-tungsto-8-phosphate  $[\text{Cu}_{20}\text{Cl}(\text{OH})_{24}(\text{H}_2\text{O})_{12}(\text{P}_8\text{W}_{48}\text{O}_{184})]^{25-}$  and the organo-ruthenium-containing heteropoly-20-tungstates  $[\text{X}_2\text{W}_{20}\text{O}_{70}(\text{Ru-arene})_2]^{10-}$  (X = Sb, Bi) are heterogeneous catalysts supported on SBA-15 for the solvent-free aerobic oxidation of saturated hydrocarbons and aromatics.[3]

We have also prepared a highly active and inexpensive electrocatalyst for the hydrogen evolution reaction (HER) by immobilizing the cyclic  $[\text{H}_7\text{P}_8\text{W}_{48}\text{O}_{184}]^{33-}$  ( $\text{P}_8\text{W}_{48}$ ) on reduced graphene oxide (rGO) sheets. The novel  $\text{P}_8\text{W}_{48}/\text{rGO}$  nanoassembly features excellent HER electrocatalytic performance as evidenced by the sustained production of  $\text{H}_2$  with a faradaic yield of ca. 100%. [4]



**REFERENCES**

- [1](a) Pope, M. T.; Kortz, U. *Polyoxometalates, in Encyclopedia of Inorganic and Bioinorganic Chemistry*, Wiley, Hoboken, **2012**. (b) Izarova, N. V.; Pope, M. T.; Kortz, U. *Angew. Chem. Int. Ed.* **2012**, *51*, 9492-9510.
- [2](Al-Oweini, R.; Sartorel, A.; Bassil, B. S.; Natali, M.; Berardi, S.; Scandola, F.; Kortz, U.; Bonchio, M. *Angew. Chem. Int. Ed.* **2014**, *53*, 11182-11185.
- [3](Chen, L.; Hu, J.; Mal, S. S.; Kortz, U.; Jaensch, H.; Mathys, G.; Richards, R. M. *Chem. Eur. J.* **2009**, *15*, 7490-7497.
- [4](Liu, R.; Zhang, G.; Cao, H.; Zhang, S.; Xie, Y.; Haider, A.; Kortz, U.; Chen, B.; Dalal, N. S.; Zhao, Y.; Zhi, L.; Wu, C.; Yan, L.; Su, Z.; Keita, B. *Energy Environ. Sci.* **2016**, *9*, 1012-1023

## KINETICS, THERMODYNAMICS AND THE DRIVING FORCE FOR LIFE AND ITS ORIGIN

R. Pasca

*CNRS – University of Montpellier – ENSCM, Montpellier, France.  
(robert.pascal@umontpellier.fr)*

### ABSTRACT

Any scientific approach undertaken to account for the origin of life should explain how the exceedingly low probability of the spontaneous assembly of the first life form could be achieved without violating the Second Law. A local decrease in entropy can be compensated by the overall dissipation produced by an open system working in a far from equilibrium regime but thermodynamics cannot help in identifying a precise pathway. Self-organization will be analyzed as the result of the kinetic behavior of self-replicating entities and to the possibility of taking advantage of selection at early stages of self-organization. The requirement that the overall reproduction cycle proceeds irreversible way will be used to semi-quantitatively determine a favorable set of requirements favorable to the origin of life. This approach supports the views that the driving force for self-organization is of kinetic rather than thermodynamic nature and lies in the *persistence* of self-reproducing entities.

## SELFORGANIZATION OF NONLINEAR NONEQUILIBRIUM REACTION SYSTEMS

Lj. Kolar-Anić

*University of Belgrade, Faculty of Physical Chemistry, Studentski trg 12,  
11000 Belgrade, Serbia. (ljiljana.kolar.anic@ffh.bg.ac.rs)*

### ABSTRACT

From the first controlled experimental investigation of the self-organization structures that can appear in non-linear reaction system under far-from-equilibrium conditions, the question arises as to the frequency of such phenomena? The aim of this paper is to point out if the selforganization of a nonlinear nonequilibrium reaction system is an exotic or a common phenomenon that requires serious scientific investigations in a frame of Nonlinear dynamics, using all physico-chemical methods on disposal for these examinations from experimental to theoretical ones.

### INTRODUCTION

When found under far-from-equilibrium conditions, some complex dynamical systems can be self-organized in the ways that are not characteristic for the equilibrium state. Thus, "It is shown that non-equilibrium may become a source of order and that irreversible processes may lead to a new type of dynamic states of matter called *dissipative structures*." [1] The term "dissipative structures" was created by the Nobel laureate Ilya Prigogine to describe the phenomenon of self-organization, which under far-from-equilibrium conditions can give rise to spatio-temporal structures that are fundamentally different from the equilibrium ones. [2].

The self-organization phenomena that arise under non-equilibrium conditions, which are now main subject of Nonlinear dynamics, can be found in almost all natural and social dynamical systems. However, their underlying mechanisms remained unclear until systematic investigations began in the 20<sup>th</sup> century, following the discovery of experimental systems where nonequilibrium states and spatio-temporal dissipative structures could be obtained under controlled conditions [1-16]. We shall focus here on the self-organization phenomena in chemical, physico-chemical and biochemical (biological) reaction systems, or briefly, *reaction systems*. In the following, the answers on several questions will be discussed:

1. **How these new dynamic states of the reaction systems look like?**  
(Examples)
2. **How these strange phenomena can be explained?**
3. **In which reaction systems and under which conditions these dynamic structures can be expected?**
4. **Is selforganization of a nonlinear nonequilibrium reaction system an exotic or a common phenomenon?**

### 1. HOW THESE NEW DYNAMIC STATES OF THE REACTION SYSTEMS LOOK LIKE?

For a very long time the scientists had opinion that the change in concentration during the course of a chemical reaction is necessarily monotonic, as shown in Fig. 1.

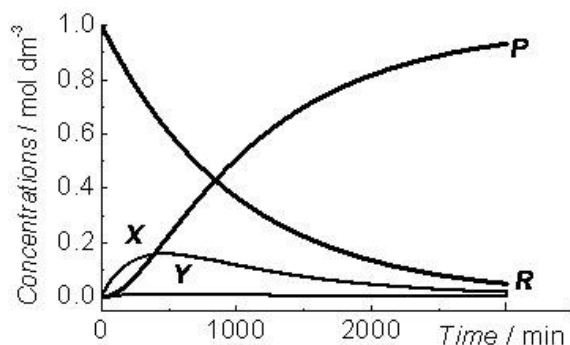


**Figure 1.** Monotonic evolution of the concentration of reactive species in a complex chemical reaction that proceeds *via* series of successive reaction steps such as:  $R \rightarrow X \rightarrow Y \rightarrow P$ .

However, in the early 1920-ties, W. C. Bray noticed a non-monotonic, cascade-like, production of gaseous oxygen during the reaction of hydrogen peroxide decomposition into oxygen and water in an acidic solution of iodate ions (reaction D), (Fig. 2.) [16].



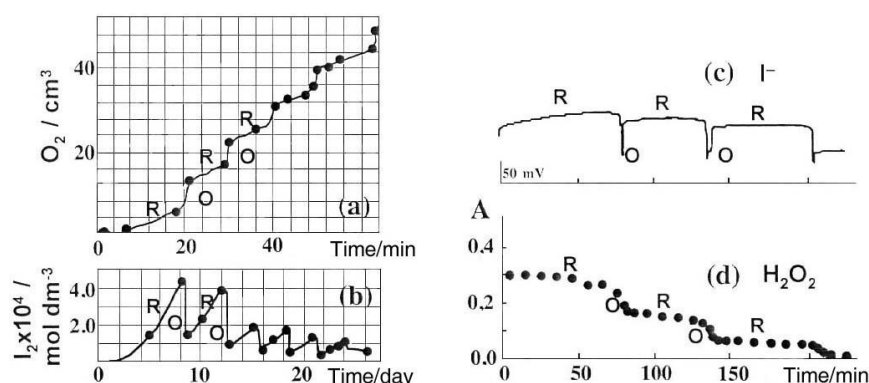


**Figure 2.** Non-monotonic evolution of reactive species in the Bray-Liebafsky (BL) reaction. (a) Step-wise production of gaseous oxygen evolved in cubic centimetre. [16] (b) Oscillatory evolution of iodine concentration. [16] (c) Oscillating potential of iodide ion-sensitive electrode, reflecting changes in iodide concentration. [18] (d) Step-wise decrease in the absorbance of hydrogen peroxide titanyloxalate complex, reflecting changes in the concentration of hydrogen peroxide. [18] Letters R and D denote regions where reduction (R) and oxidation (O) pathways dominate.

This reaction is today known as the Bray-Liebafsky (BL) oscillatory reaction. It proceeds *via* a number of intermediates, such as  $I^-$ ,  $I_2$ ,  $HIO$ ,  $I_2O$  and  $HIO_2$  [16 - 18]. By monitoring the concentration of any intermediate, it was established that it increases and decreases periodically, in accordance with periodic changes of the rate of hydrogen peroxide decomposition. This is illustrated by iodine and iodide oscillations in Fig. 2. b and c, respectively. Because of the periodic oscillatory changes in the concentration of intermediates, this reaction, and all reactions exhibiting the same type of dynamic behaviour obtained the name oscillatory or oscillating chemical reactions, or, even, chemical oscillators.

Independently from the investigations described above, B. P. Belousov has revealed in the middle of the 20<sup>th</sup> century another oscillating chemical reaction during studying the catalytic oxidation of citric acid by bromate ions in an acidic medium [8]. In more common variant of this reaction citric acid is replaced with malonic acid (MA) and cerium sulphate as a catalyst is replaced with ferroin (1,10-ferroin-Fe(II)). The overall chemical reaction of malonic acid decomposition in the presence of bromate ions in an acidic aqueous medium can be represented by the following stoichiometric relation:

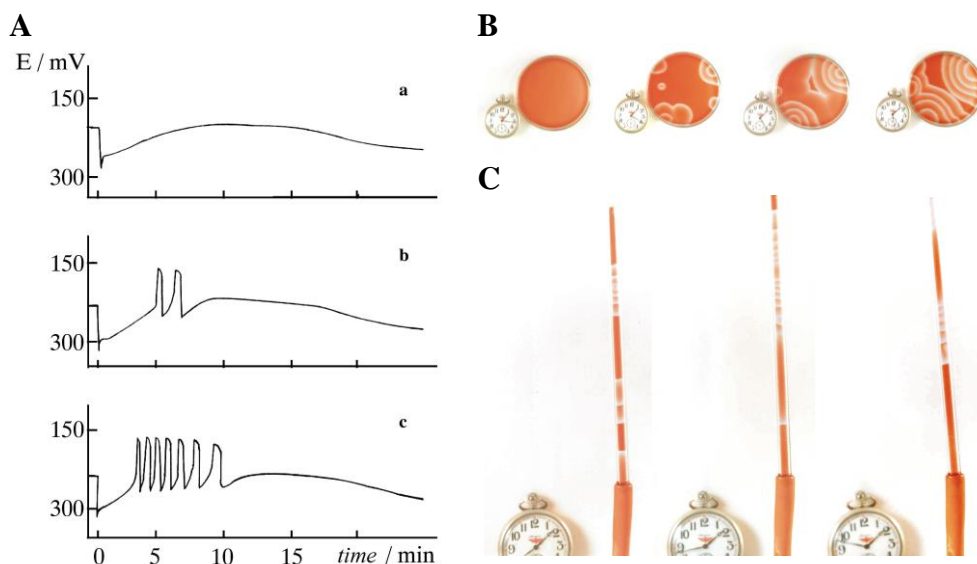
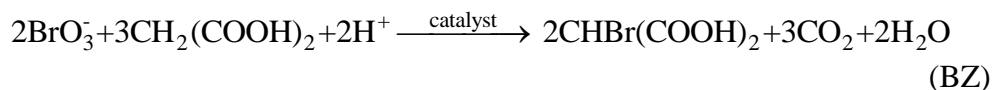


**Figure 3. A.** Changes in the potential of the  $\text{Br}^-$  ion sensitive electrode during the course of the BZ reaction for different initial MA concentrations (in  $\text{mol dm}^{-3}$ ) **(a)**  $9.00 \times 10^{-3}$ , **(b)**  $1.20 \times 10^{-2}$ , **(c)**  $1.60 \times 10^{-2}$ .  $T = 318.2 \text{ K}$ . [19] **B.** Travelling waves in the BZ reaction in a thin layer, whose thickness (about 1 mm) is much smaller than the area of the Petri dish (about  $60 \text{ cm}^2$ ) mimicking the behaviour in a two-dimensional (2D) system. **C.** Travelling waves in a narrow column of liquid (internal diameter of about 4 mm), which is much smaller than the column length (about 20 cm), mimicking the behaviour in a one-dimensional (1D) system. [13]

Similarly as in the BL reaction, a number of intermediates are being formed in the BZ reaction. And, like in the BL reaction, changes in the concentration of  $\text{Br}^-$  ions can be monitored using  $\text{Br}^-$  ion sensitive electrode (Fig. 3 A.). If cerium sulphate is replaced with ferroin, periodic changes in the concentration of intermediates in the BZ reaction become more visually pronounced, the colour of the reaction solution changes periodically from blue to red.

Alternating colour change is consequence of alternating dominance of the red  $\text{Fe(II)}$ , and the blue  $\text{Fe(III)}$  iron complex with ferroin. These visually distinct features helped the discovery of another phenomenon, the

so-called travelling waves in a thin layer, where coupling between molecular diffusion and chemical interactions leads to a radial diffusion of reactive species. When a part of BZ reaction solution is removed to form thin layer in a Petri dish, in the initially homogeneously coloured solution, the reaction centres will start to appear. There the colour of the solution will start to change. From these reaction centres, the chemical reaction will propagate radially and equally coloured rings will appear, signifying that at these locations the BZ reaction progress is in the same phase (Fig. 3 B). The possibility to have more than one reactive centre is leading to yet another phenomenon – chemical interference of travelling waves. If, however, the reaction is conducted in a thin column (1D), movement of the wave front along the column will be visible (Fig. 3. C).

Even though spatio-temporally arranged dissipative structures, as the ones described above, can be observed in a narrow range of the parameter space, numerous chemical, physicochemical and biochemical oscillating processes had been discovered later. One such example is the decomposition of nitrous oxide ( $\text{N}_2\text{O}$ ), to nitrogen ( $\text{N}_2$ ) and oxygen ( $\text{O}_2$ ), catalyzed by the zeolite Cu-ZSM-5 in an open (flow) reactor, where nitrous oxide is carried into the reactor using a stream of helium ( $\text{He}$ ) [20]. Using specific detectors, oscillatory evolution of the non decomposed  $\text{N}_2\text{O}$  and the products of  $\text{N}_2\text{O}$  decomposition, such as:  $\text{NO}$ ,  $\text{N}_2$  and  $\text{O}_2$ , were observed.

Approximately at the same time similar behaviour has been found in biochemical and biological systems (See refs. in [13] and [21]). Thus, rhythmic changes in the action potential were observed in neuronal cells [22, 23], oscillations in the concentration of intermediates were found during glycolysis [24, 25], bioelectric potential oscillations in the cytoplasm of fresh water algae *Nitella mucronata* (Fig. 4) and delayed fluorescence in maize leaves were also obtained [26-28].

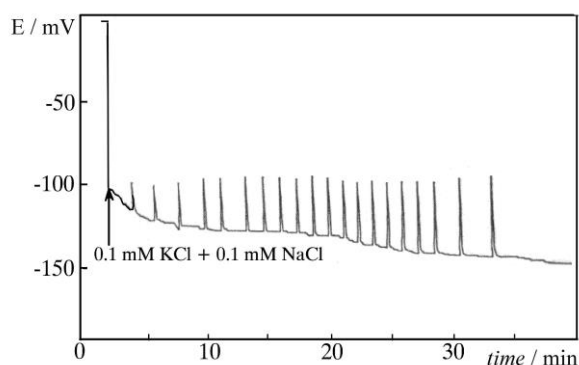
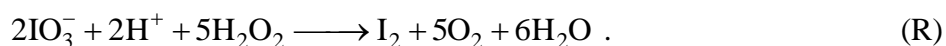


**Figure 4.** Bioelectric potential (E) oscillations in the cytoplasm of live cells of fresh water algae *Nitella mucronata* recorded using an Ag/Cl microelectrode positioned in the cytoplasm with respect to a reference microelectrode placed in the surrounding KCl/NaCl solution. [28]

Generally, in the living organisms the oscillatory dynamic states can be caused by internal self-organized phenomena but also by external periodic changes of, for example, temperature, light (circadian rhythm) or seasonal changes. These changes in environmental conditions initiate corresponding changes in the dynamics of many processes in living organisms, who adapt to them.

## 2. HOW THESE STRANGE PHENOMENA CAN BE EXPLAINED?

The first try to explain the step-wise time evolution of reactants and products (external species) and oscillatory evolution of internal species, gave Bray in the already mentioned publication related to the hydrogen peroxide decomposition in the presence of iodate and hydrogen ions [16, 17]. He said that this decomposition is the result of two complex pathways in which hydrogen peroxide acts either as a reducing (R) or an oxidizing (O) agent:



The sum of reactions (R) and (O) gives reaction (D). When the rates of these two pathways are equal, monotonous decomposition of hydrogen peroxide is observed, experimentally. In other case, when, under defined external conditions, the pathways (R) and (O) alternately dominate one over another, the cascading consumption of hydrogen peroxide and an oscillatory evolution of the intermediates is found (Fig. 2). However, reactions (R) and (O) are obviously net reactions of these two pathways and, moreover, the oscillatory dynamics of the iodine concentration cannot be obtained by numerical simulation of the overall process simply based on them.

On the other side, in 1910, Lotka proposed the mathematical model to give the explanation of the oscillatory evolution of predator-prey interactions in an ecological system. [29] However, his model, now known as Lotka-Volterra model [29-30, 14] exhibits always oscillatory behaviour and although based on mass action kinetics; it had to be improved for application to any real chemical reaction system. Nevertheless, although looks simply, it was hard job.

The improved models such as Brusselator in 1968 [31], Oregonator in 1972 [32] and others, better simulated dynamics of oscillatory reactions, but in all of them the key reaction was chemically unreal direct autocatalytic

**Table 1.** A model of the Bray-Liebafsky reaction

Reactions	no.
$\text{IO}_3^- + \text{I}^- + 2\text{H}^+ \rightleftharpoons \text{HIO} + \text{HIO}_2$	(R1), (R-1)
$\text{HIO}_2 + \text{I}^- + \text{H}^+ \longrightarrow \text{I}_2\text{O} + \text{H}_2\text{O}$	(R2)
$\text{I}_2\text{O} + \text{H}_2\text{O} \rightleftharpoons 2\text{HIO}$	(R3), (R-3)
$\text{HIO} + \text{I}^- + \text{H}^+ \rightleftharpoons \text{I}_2 + \text{H}_2\text{O}$	(R4), (R-4)
$\text{HIO} + \text{H}_2\text{O}_2 \longrightarrow \text{I}^- + \text{H}^+ + \text{O}_2 + \text{H}_2\text{O}$	(R5)
$\text{I}_2\text{O} + \text{H}_2\text{O}_2 \longrightarrow \text{HIO} + \text{HIO}_2$	(R6)
$\text{IO}_3^- + \text{H}^+ + \text{H}_2\text{O}_2 \longrightarrow \text{HIO}_2 + \text{O}_2 + \text{H}_2\text{O}$	(R7)

step or strange stoichiometric factor. Finally in 1983, replacing the autocatalytic step by an autocatalytic loop in the model for BL reaction, Schmitz offered the first model of an oscillatory chemical reaction with chemically acceptable reaction steps. [33] This model for the Bray-Liebafsky reaction could successfully simulate regular oscillations, but for mixed mode oscillations and chaos at least one new reaction step had to be added [34]. Thus, different dynamic states found in the BL reaction could be explained by the model given in Table 1.

Obviously, in this model there are five intermediate species ( $\text{I}^-$ , HIO,  $\text{HIO}_2$ ,  $\text{I}_2\text{O}$  and  $\text{I}_2$ ). By different combinations of several reaction steps of this model the above mentioned reaction routes proposed by Bray (R) and (O) could be obtained, and explained. In fact, it was first successful description of any oscillatory reaction.

### 3. IN WHICH REACTION SYSTEMS AND UNDER WHICH CONDITIONS THESE DYNAMIC STRUCTURES CAN BE EXPECTED?

The above mentioned dynamic structures can be found in *nonlinear reaction systems* with *feedback* when they are *far from equilibrium*, that is, in nonlinear nonequilibrium reaction systems with feedback. [1]

*Let us see how many reaction systems are nonlinear?* If the time evolution of one reaction can be described by the following linear differential equation

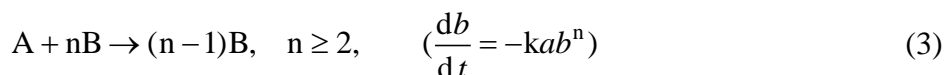
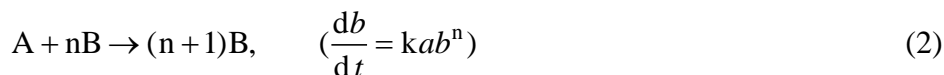
$$\frac{da}{dt} = -ka \quad (1)$$

where  $a$  and  $k$  denote the concentration of species A in time  $t$  and the rate constant of considered reaction, this reaction is linear. In other words, linear

reactions are only first order reactions of the form:  $A \rightarrow P$ ,  $A \rightleftharpoons P$ ,  $A \rightarrow X \rightarrow P$ , etc. All others are nonlinear, [1-6, 13, 35] including the pseudo-first order reactions, although their time-evolution can be described by Eq.(1). [37, 38] Even more, some complex reaction systems, that can be described by the pseudo-first order kinetics, can be in the oscillatory dynamic state. [37, 38]

In addition, almost all reaction systems are complex. At least, they consist of several simple reactions.

*Next, what is feedback?* In the reaction systems the feedback is the phenomenon in which the product of a reaction affects the rate of its own formation in a positive or negative direction (autocatalysis and autoinhibition). In general case, the autocatalysis and autoinhibition with respect to concentration of species B can be described by the equations (2) and (3), respectively



where  $b$  is the concentration of species B in time  $t$ ,  $n$  is the stoichiometric coefficient, and the minus sign in the last case denotes the disappearing of species B.

The feedback is an essential part of complex selforganization phenomena that occurs in nonlinear systems when they are in a state far from thermodynamic equilibrium. [1-6, 13, 36] Normally, for oscillatory dynamics, some additional restrictions would be satisfied. System which can oscillate is not always in the oscillatory state.

#### **4. IS SELFORGANIZATION OF NONLINEAR NONEQUILIBRIUM REAKCION SYSTEM AN EXOTIC OR A COMMON PHENOMENON?**

We have just seen that almost all reaction systems are complex and thus nonlinear. Moreover, many of them, but particularly biological ones, posses feedback. Actually, the key of the life is in the feedback. More precisely, the key of the life is in the surviving, but surviving is based on feedback as a necessary component of adaptation. The feedback always produce nonlinear dynamical behaviour of the reaction system.

Moreover, numerous heterogeneous catalytic systems may be locally selforganized with oscillations and traveling waves, while bulk measurements detect only smooth catalytic behaviour as a consequence of averaging over the complex surface distribution of active centres. [39,40]

Hence, the selforganization of nonlinear nonequilibrium reaction system is a common phenomenon that requires serious scientific investigations in a frame of Nonlinear dynamics, using all methods on disposal for these examinations from experimental to theoretical ones. From this point of view, all experimental physico-chemical methods, together with theoretical approach based on Statistical mechanics, Chemical kinetics, Stoichiometric network analysis (SNA) and Bifurcation analysis including sophisticated numerical investigations necessary for examination of chemical and biochemical reaction networks are inevitable methods to explain obtained phenomena in these reaction systems.

In future, the behaviour of the reaction system in equilibrium will be considered only as the limit case of its behaviour under nonequilibrium condition.

### ***Acknowledgement***

This work is result of long collaboration between many scientists working together on the same project. Some of them are authors of the references below. Unfortunately, all of them can not be presented here due to limitations in space. This work was partially supported by the Ministry of Education, Science and Technological Development of the Republic of Serbia, Grants no. 172015.

### **REFERENCES**

- [1] I. Prigogine, Time, structure and fluctuations, Nobel lecture in chemistry, 1977; Science, 201 (1978) 777-785.
- [2] G. Nicolis, I. Prigogine, Self-organization in Non-equilibrium Systems, J. Wiley, New-York, 1977.
- [3] P. Gray, S. K. Scott, Chemical Oscillations and Instabilities, Clarendon Press, Oxford, 1990.
- [4] S.K. Scott, Chemical Chaos, Clarendon Press, Oxford, 1991.
- [5] G. Nicolis, Introductions to Nonlinear Science, Cambridge University Press, Cambridge, 1995.
- [6] I. R. Epstein, J. A. Pojman, An Introduction to Nonlinear Chemical Dynamics. Oscillations, Waves, Patterns, and Chaos, Oxford University Press, Oxford, 1998.
- [7] G. M. Frank (Ed.), Kolebatel'nye processy v biologicheskikh sistemah, Nauka, Moskva, 1974.
- [8] (a) B. P. A. Belousov, Sbornik Referatov po Radiatsionnoi Meditsine, Medigz, Moskow, 1958, 145; (b) A. M. Zhabotinskii, Koncentrationnyye avtokolebanya, Nauka, Moskva, 1974.

- [9] C. Vidal, A. Pacault (Eds.), *Non-Equilibrium Dynamics in Chemical Systems*, Springer-Verlag, Berlin, 1985.
- [10] R. J. Field, M. Burger (Eds.), *Oscillation and Traveling Waves in Chemical Systems*, J. Wiley, New York, 1985.
- [11] P. Gray, G. Nicolis, P. Borckmans, S. K. Scott (Eds.), *Spatial Inhomogeneities and Transient Behavior in Chemical Kinetics*, Manchester University Press, Manchester, 1990.
- [12] O. R. Kols, G. V. Maksimov, Č. N. Radenović, *Biofizika ritmicheskovo vzbuzhdenya*, ULB, Moskva, 1993.
- [13] Lj. Kolar-Anić, Ž. Čupić, V. Vukojević, S. Anić, *Dynamic of Nonlinear processes*, University of Belgrade, Belgrade, 2011. (*in Serbian*)
- [14] Lj. Kolar-Anić, S. Anić, Ž. Čupić, A. Ivanović-Šašić, N. Pejić, S. Blagojević, V. Vukojević, Chapter 23 *Oscillating Reactions*, in *Encyclopedia of Physical Organic Chemistry*, 6 Vol. Set, Z. Wang (Ed), U. Wille, E. Juaristi (Ass Eds), Vol. 2, Part 2 *Organic Reactions and Mechanisms*, p.p. 1127-1222.
- [15] H. Bénard, *Rev. Gén. Sciences Pure Appl.*, 1900, 11, 1261-1271, 1309-1328,
- [16] W. C. Bray, *J. Am. Chem. Soc.* 1921, 43, 1262-1267.
- [17] W. C. Bray, H. A. Liebhafsky, *J. Am. Chem. Soc.* 1931, 53, 38-44.
- [18] J. Ćirić, S. Anić, Ž. Čupić, Lj. Kolar-Anić, *Science of Sintering* 2000, 32 187-195.
- [19] S. Blagojević, N. Pejić, S. Anić, Lj. Kolar-Anić, *J. Serb. Chem. Soc.* 2000, 65, 709-713.
- [20] T. Ochs, T. Turek, *Chemical Engineering Science*, 1999, 54, 4513-4520.
- [21] A. Goldbeter, *Biochemical Oscillations and Cellular Rhythms*, Cambridge University Press, Cambridge, 1996.
- [22] A. L. Hodgkin, A. F. Huxley, *J. Physiol. (Lond.)*, 1952, 117, 500-544.
- [23] L. N. M. Duysens, J. Amesz, *Biochim. Biophys. Acta*, 1957, 24, 19.
- [24] F. Huxley, *Acad. Sci.*, 1959, 81, 221-248.
- [25] Gosh, A, Chance, B, *Oscillations of Glycolic Intermediates in Yeast Cells*, *Biochem. Biophys. Res.* 16 (1964) 174-181.
- [26] Č. Radenović, L. N. Vorobjev, *Biološki glasnik*, 1967, 20, 133-142.
- [27] Č. Radenović, M. Penčić, *Physiologia Plantarum*, 1970, 23, 697-703.
- [28] Č. Radenović, *Bioelektrične pojave biljnih sistema*, Nolit, Beograd, 1974.
- [29] (a) A. J. Lotka, *J. Phys. Chem.*, 1910, 14, 271-274; (b) A. J. Lotka, *Proc. Natl. Acad. Sci. U.S.A.*, 1920, 6, 410-415; (c) Lotka, A. J., *J. Am. Chem. Soc.* 42 (1920) 1595-1599;
- [30] V. Volterra, *Nature*, 1926, 118, 558-560.

- [31] I. Prigogine, R. Lefever, *J. Chem. Phys.*, 1968, 48, 1695-1700.
- [32](a) R. J. Field, E. Körös, R. M. Noyes, *J. Am. Chem. Soc.*, 1972, 94, 8649-8664; (b) R. J. Field, R. M. Noyes, *J. Chem. Phys.*, 1974, 60, 1877-1884.
- [33](a) G. Schmitz, Stationarite et reactions periodique, *Thesis*, Universite Libre de Bruxelles, Bruxelles, 1983; (b) G. Schmitz, *J. Chim. Phys.*, 1987, 84, 957-965.
- [34](a) Lj. Kolar-Anić, Đ. Mišljenović, S. Anić, G. Nicolis, *React. Kinet. Catal. Lett.*, 1995, 54, 35-41; (b) Lj. Kolar-Anić, Ž. Čupić, G. Schmitz, S. Anić, *Chem. Eng. Sci.* 2010, 65, 3718–3728.
- [35] Lj. Kolar-Anić, Ž. Čupić, in: *Nonlinear dynamics*, K. (Stevanović) Hedrih and Ž. Mijajlović (Eds.), Serbian Society of Mechanics, Belgrade, 2013, pp 67-88.
- [36](a) Ž. Čupić, Modelling of the mechanism of the oscillatory catalytic processes, with application on the reaction of hydrogen peroxide decomposition, Thesis, University of Belgrade, Belgrade 1998. (in Serbo-Croatian) (b) G. Schmitz, Lj. Kolar-Anić, S. Anić, Ž. Čupić, The Illustration of Multistability, *J. Chem. Educ.* 77 (2000) 1502-1505.
- [37] S. Anić, Lj. Kolar-Anić, *Ber. Bunsenges. Phys. Chem.*, 1986, 90, 539-542.
- [38] S. Anić, Lj. Kolar-Anić, *J. Chem. Soc. Faraday Trans. I*, 1988, 84, 3413-3421, and references therein.
- [39] V. D. Belyev, M. M. Slinko, M. G. Slinko, *Proc, VI Intern. Congr. on catalysis. L.*, 1976, pp. 758-762.
- [40] Z. Kurtanjek, M. Sheintuch, D. Luss, *Journal of Catalysis*, 1980, 66, 11-27.

## CAN WE SYNTHESIZE LIFE IN THE LAB? HOW CHEMISTRY MAY BECOME BIOLOGY

S. Otto

*Centre for Systems Chemistry, Stratingh Institute, University of Groningen  
Nijenborgh 4, 9747 AG, Groningen, the Netherlands.  
s.otto@rug.nl*

### ABSTRACT

How the immense complexity of living organisms has arisen is one of the most intriguing questions in contemporary science. We have started to explore experimentally how organization and function can emerge from complex molecular networks in aqueous solution [1]. We focus on networks of molecules that can interconvert, to give mixtures that can change their composition in response to external or internal stimuli. Molecular recognition between molecules in such mixtures leads to their mutual stabilization, which drives the synthesis of more of the privileged structures (Figure 1). As the assembly process drives the synthesis of the very molecules that assemble, the resulting materials can be considered to be self-synthesizing. Intriguingly, in this process the assembling molecules are replicating themselves, where replication is driven by self-recognition of these molecules in the dynamic network [2]. The selection rules that dictate which (if any) replicator will emerge from such networks are starting to become clear [3]. We have observed that factors such as mechanical energy [2] and the nature of the environment [4] can determine which replicator wins the competition for building blocks. We have also witnessed spontaneous differentiation (a process akin to speciation as it occurs in biology) in a system made from a mixture of two building blocks [5]. When such systems are operated under far-from-equilibrium flow conditions adaptation of the replicators to a changing environment can occur. Replicators that are able to catalyze reactions other than their own formation have also been obtained, representing a first step towards metabolism. Thus, the prospect of Darwinian evolution of purely synthetic molecules is tantalizingly close and the prospect of synthesizing life de-novo is becoming increasingly realistic.

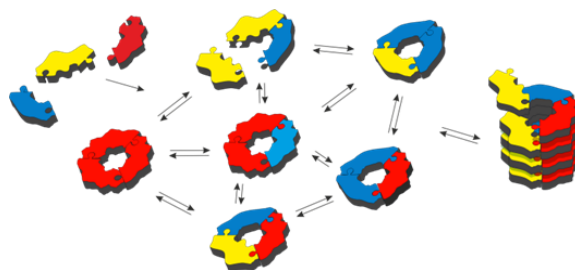


**Figure 1** . Molecular recognition between molecules in a dynamic molecular network can lead to self-synthesizing materials, build up from self-replicating molecules.

#### REFERENCES

- [1] Li, J.; Nowak, P.; Otto, S. *J. Am. Chem. Soc.* **2013**, 135, 25, 9222-9239. [2] Carnall, J. M. A.; Waudby, C. A.; Belenguer, A. M.; Stuart, M. C. A.; Peyralans, J. J.-P.; Otto, S. *Science* **2010**, 327, 1502-1506. [3] Malakoutikhah, M.; Peyralans, J.J-P.; Colomb-Delsuc, M.; Fanlo-Virgos, H.; Stuart, M. C. A.; Otto, S. *J. Am. Chem. Soc.* **2013**, 135, 49, 18406-18417. [4] Leonetti, G. Otto, S. *J. Am. Chem. Soc.* **2015**, 137, 2067-2072. [5] J. W. Sadownik, E. Mattia, P. Nowak, S. Otto, *Nature Chem.* **2016**, 8, 264-269.

## CHEMICAL KINETIC MODELS OF NANOPARTICLE FORMATION: NUCLEATION AND GROWTH

G. Lente

*University of Pécs, Institute of Chemistry, Department of General and Physical Chemistry, Ifjúság útja 6., H-7624 Pécs, Hungary.  
(lente@gamma.ttk.pte.hu)*

### ABSTRACT

A general class of chemical kinetic models of nanoparticle formation is introduced. The models contain slow nucleation steps, in which two or more monomeric units come together to form a seed, and rapid growth steps, in which a seed grows by the addition of a single monomeric unit. Several different possible rate equations are tested for both processes. A mathematical method is developed to solve the simultaneous ordinary differential equations arising from the models analytically or semi-analytically. The final formulas are suitable for comparison with experimental measurements.

### INTRODUCTION

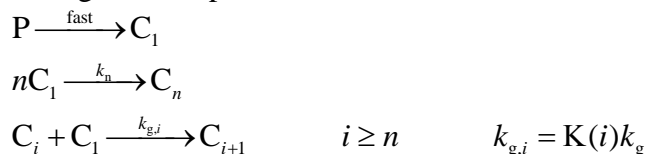
Nanoparticles are widely used and studied in today's chemistry, especially in the field of catalysis. Recently, most of the research focus has been given to metal (mostly noble metals) or semiconductor (oxide or sulfide) nanoparticles, which usually contain a few hundred or a few thousand atoms. This size means that the number of particles on the overall surface is not negligible compared to the number of those inside the particles, which results in unique properties that do not resemble those of macroscopic phases or individual particles, either.

From the point of view of applications, controlling the average size and the size distribution of nanoparticles is a key aspect during synthesis. As nanoparticles are generally thermodynamically unstable relative to the bulk solid state, the size is primarily governed by kinetic factors. Therefore, a rational, designed synthesis method must be based on a suitable kinetic model. Such kinetic models are not very often described and analyzed in the literature, there are only few examples of detailed studies in this field [1-4].

This work introduces a general class of kinetic models based on nucleation and seed growth processes. The first step toward a uniform mathematical handling of the ordinary differential equations arising from this model will be presented.

## RESULTS AND DISCUSSION

Herein a class of nucleation-growth models is introduced based on some literature precedents of less general scope [1-4]. The model consists of the following three steps:



In the first step, a precursor (P) is rapidly transformed into the nanoparticle monomer ( $C_1$ ). The second step is nucleation:  $n$  identical monomers form a single seed that is already capable of growth. This particle growth can only occur through the addition of a single monomer unit to a nanoparticle as given in step 3. The transformation of the precursor into the monomeric unit is only present in the model because this is required by many actual chemical systems: its rate is fast so that it does not influence the overall kinetics. The nucleation step is characterized by  $k_n$ , which is an  $n$ th order rate constant. The growth step actually means a large number of closely related reactions. They all have a second order rate constants, the value of which may be dependent on the size of the nanoparticle.  $K(i)$  is a kernel function that gives how the growth rate constant is related to the size ( $i$ ).

This call of models actually a highly generalized form of earlier models. Rempel et al [1] analyzed a case in which all the reactions were reversible,  $k_n = k_g$  was valid (meaning that nucleation was not any different from particle growth) and the Kernel function was  $K(i) = i^{2/3}$  (this choice is rationalized by the argument that the particle growth rate constant is proportional to the surface of the nanoparticle rather than the mass). Further specific cases were published by Rivallin et al and McKoy et al [2-4].<sup>2-4</sup> In this, The kernel function  $K(i) = i$  was used (the reactivity of a particle is directly proportional to its mass) a continuous distribution of possible particle sizes was assumed rather than a discrete one and aggregation (the reaction of large particles with each other) was also allowed.

The simultaneous ordinary differential equations describing the time evolution of the concentrations takes the following form:

$$\begin{aligned} \frac{d[C_1]}{dt} &= -nk_n[C_1]^n - \sum_{j=n}^{\infty} K(j)k_g[C_1][C_j] \\ \frac{d[C_n]}{dt} &= k_n[C_1]^n - K(n)k_g[C_1][C_n] \\ \frac{d[C_i]}{dt} &= K(i-1)k_g[C_1][C_{i-1}] - K(i)k_g[C_1][C_i] \quad i \geq n+1 \end{aligned}$$

To simplify the formulas, scaled variables [5] are introduced, which are also dimensionless:

$$c_i = \frac{[C_i]}{[P]_0} \quad \tau = k_g [P]_0 t \quad \alpha = \frac{k_n}{k_g}$$

The  $c_i$  quantities are scaled concentrations,  $[P]_0$  is the initial concentration of the precursor,  $\tau$  is the scaled time, whereas  $\alpha$  is the ratio of the nucleation and particle growth rate constants. Using these new variables, the original set of differential equations can be transformed into a somewhat simpler one with dimensionless quantities only:

$$\begin{aligned} \frac{dc_1}{d\tau} &= -n\alpha c_1^n - \sum_{j=n}^{\infty} K(j) c_1 c_j \\ \frac{dc_n}{d\tau} &= \alpha c_1^n - K(n) c_1 c_n \\ \frac{dc_i}{d\tau} &= K(i-1) c_1 c_{i-1} - K(i) c_1 c_i \quad i \geq n+1 \end{aligned} \quad (1)$$

The final goal of the derivation presented here is not to find each  $c_i$ , but to give the average nanoparticle size as a function of time and the final distribution (the one at  $\tau = \infty$ ). It will be assumed here that the particles are roughly spherical, so their radii are proportional to the cube root of the number of monomeric units in them with  $r_0$  as the reference size of the monomeric unit. There are different averages that can be calculated for this population of nanoparticles. The number-average size can be defined by the following formula:

$$r_N = r_0 \frac{\sum_{i=1}^{\infty} i^{1/3} c_i}{\sum_{i=1}^{\infty} c_i}$$

A mass-average size ( $r_M$ ) is defined like this:

$$r_M = r_0 \frac{\sum_{i=1}^{\infty} i^{4/3} c_i}{\sum_{i=1}^{\infty} i c_i}$$

Theoretically, the method dynamic light scattering (DLS) gives a quantity that is called the Z-average size ( $r_Z$ ) of the particles and can be defined as follows:

$$r_Z = r_0 \frac{\sum_{i=1}^{\infty} i^2 c_i}{\sum_{i=1}^{\infty} i^{5/3} c_i}$$

Finally, the average for which the simplest analytical formulas can be derived could be called the cube-root number-average ( $r_C$ ):

$$r_C = r_0 \sqrt[3]{\frac{\sum_{i=1}^{\infty} i c_i}{\sum_{i=1}^{\infty} c_i}}$$

It can be shown that  $r_N \leq r_C \leq r_M \leq r_Z$  holds for the same population of nanoparticles.

The  $q$ th moment of the  $c_i$  variables is defined as:

$$\mu_q = \sum_{i=1}^{\infty} i^q c_i$$

It should be emphasized that  $q$  can be any real number, its values are not limited to positive integers. All of the average sizes defined earlier can be calculated from the moments. In particular,  $r_C$  can be obtained from the ratio of the first and zeroth moments as follows:

$$r_C = r_0 \sqrt[3]{\frac{\mu_1}{\mu_0}}$$

In this work, several different possibilities were considered for the Kernel function. In addition to those already mentioned, which were  $K(i) = i^{2/3}$  and  $K(i) = I$ , the Kernel functions  $K(i) = i^{1/3}$  (growth rate proportional to the linear size) and  $K(i) = 1$  (growth rate independent of the particle size) make good chemical sense.

An equation for the first moment can be obtained by first multiplying each part of Equation (1) by  $i$  and then adding them:

$$\begin{aligned} \frac{dc_1}{d\tau} + 2 \frac{dc_2}{d\tau} + \sum_{i=3}^{\infty} i \frac{dc_i}{d\tau} = \\ -nac_1^2 - \sum_{j=n}^{\infty} K(j)c_1c_j + nac_1^2 - 2K(n)c_1c_2 + \sum_{i=n}^{\infty} iK(i-1)c_1c_{i-1} - \sum_{i=n}^{\infty} iK(i)c_1c_j \end{aligned}$$

After inspecting the indices in this form, it is recognized that on the left hand side, the derivative of the first moment appears, whereas the term cancel each other on the right hand side, so that the final equation is simply:

$$\frac{d\mu_1}{d\tau} = 0$$

This equation simply reflects mass conservation chemically. As the concentrations were scaled by  $[P]_0$ , this time independent value of  $\mu_1$  will simply be 1.

The key question to obtaining an analytical solution (or a good approximation) for the time dependence of  $c_1$  is to express the infinite sum in the first part of Equation (1) somehow. This is particularly easy for the kernel function  $K(i) = i$ , for which:

$$\sum_{j=n}^{\infty} K(j)c_j = \sum_{j=n}^{\infty} jc_j = \mu_1 - c_1 = 1 - c_1$$

Similarly, for the Kernel function  $K(i) = 1$ :

$$\sum_{j=n}^{\infty} K(j)c_j = \sum_{j=n}^{\infty} c_j = \mu_0 - c_1$$

For the kernel function  $K(i) = i$ , this results in a single separable ordinary differential equations that can be solved for  $c_1$ :

$$\frac{dc_1}{d\tau} = -n\alpha c_1^n - c_1(1 - c_1)$$

The most straightforward case here is  $n = 2$ , for which the equation takes the following particular form:

$$\frac{dc_1}{d\tau} = (1 - 2\alpha)c_1^2 - c_1$$

The general solution of this equation is available in the literature [5]:

$$c_1 = \frac{1}{2\alpha e^\tau + 1 - 2\alpha}$$

Further considerations in this system with  $n = 2$  and Kernel function  $K(i) = i$  yield a straightforward way to calculate  $\mu_0$ :

$$\frac{d\mu_0}{d\tau} = \frac{1 - \alpha}{(2\alpha e^\tau + 1 - 2\alpha)^2} - \frac{1}{2\alpha e^\tau + 1 - 2\alpha}$$

This differential equation can simply solved by integration because  $\mu_0$  does not appear on the right hand side:

$$\mu_0 = \frac{\alpha}{2\alpha - 1} + \frac{1 - \alpha}{(1 - 2\alpha)(2\alpha e^\tau + 1 - 2\alpha)} + \frac{\alpha}{(1 - 2\alpha)^2} \left[ \tau - \ln(2\alpha e^\tau + 1 - 2\alpha) \right]$$

Therefore, the time dependence of the cube-root number-average particle size ( $r_C$ ) b given now as the cube root of the ration of  $\mu_1$  and  $\mu_0$  multiplied

by the reference size ( $r_0$ ). Some further, reasonable simplifications yield the following formula:

$$r_C = r_0 \sqrt[3]{\frac{1}{\frac{1}{2\alpha} e^{-\tau} + \alpha \left( \ln \frac{1}{2\alpha} - 1 \right)}}$$

Writing the original parameters instead of the scaled ones provides the following time dependence.

$$r_C = r_0 \sqrt[3]{\frac{1}{\frac{k_g}{2k_n} e^{-k_g [P]_0 t} + \frac{k_n}{k_g} \left( \ln \frac{k_g}{2k_n} - 1 \right)}}$$

For the case of Kernel function  $K(i) = 1$ , Equation (1) can be reduced to a pair of coupled ordinary differential equation for the dependent variables  $c_1$  and  $\mu_0$ :

$$\frac{d\mu_0}{d\tau} = -\alpha(n-1)c_1^n - c_1(\mu_0 - c_1)$$

$$\frac{dc_1}{d\tau} = -n\alpha c_1^n - c_1(\mu_0 - c_1)$$

A useful analytical approximation for the solution of these equations is given as:

$$\mu_0 \cong c_1 - n\alpha + \sqrt{n^2\alpha^2 - 2\alpha c_1 + 2\alpha}$$

$$c_1 \cong \frac{1}{2}(n^2\alpha + 2) - \frac{1}{2}(n^2\alpha + 2) \tanh^2 \left( \frac{\sqrt{\alpha(n^2\alpha + 2)}(C^* - t)}{2} \right)$$

$C^*$  is an integration constant here, the value of which can be calculated from the fact that  $c_1 = 1$  at  $\tau = 0$  (initial conditions).

In general, predicting the size distribution of the nanoparticles is mathematically more demanding. Experience thus far sows that a useful trick is not to look for the time dependence of the  $c_1$  functions directly, but to use  $c_1$  as an alternative independent variable. In this case, Equation (1) is transformed to the following form:

$$\frac{dc_n}{dc_1} = \frac{K(n)c_1c_n - \alpha c_1^n}{nac_1^n + \sum_{j=n}^{\infty} K(j)c_1c_j}$$

$$\frac{dc_i}{dc_1} = \frac{K(i)c_1c_i - K(i-1)c_1c_{i-1}}{nac_1^n + \sum_{j=n}^{\infty} K(j)c_1c_j} \quad i \geq n+1$$

Although this seems like a much more demanding differential equation at first sight, in fact some of the  $c_1$  terms will cancel in the denominator and numerator. Another advantage of this formulation is that when the final distribution is sought, it is enough to consider the limit at  $c_1 \rightarrow 0$  (which is the final state) instead of  $\tau \rightarrow \infty$ .

### CONCLUSION

In summary, this contribution provides a general framework for handling the nucleation-growth type kinetic models of nanoparticle formation. It is shown that obtaining analytical formulas to describe the average particle size in such models is sometimes possible and reasonable approximations can also be used to derive useful formulas.

### REFERENCES

- [1] J. Y. Rempel, M. G. Bawendi, K. F. Jensen, *J. Am. Chem. Soc.*, 2009, **131**, 4479-4489.
- [2] B. J. McCoy, G. Madras, *J. Coll. Interf. Sci.*, 1998, **201**, 200-209.
- [3] B. J. McCoy, *Chem. Eng. Sci.*, 2002, **57**, 2279-2285.
- [4] M. Rivallin, M. Benmami, A. Kanaev, A. Gaunand. Sol-Gel Reactor with Rapid Micromixing. *Trans. IChemE A Chem. Eng. Res. Des.*, 2005, **83(A1)**, 67-74.
- [5] G. Lente, *Deterministic Kinetics in Chemistry and Systems Biology*, Springer New York, 2015.

## OUTLOOK OF METASTABLE Pd-Rh ALLOYS USAGE IN THE CATALYTIC POLLUTION CONTROL SYSTEMS

A.A. Vedyagin<sup>1,2</sup>

<sup>1</sup>*Boreskov Institute of Catalysis SB RAS, pr. Ac. Lavrentieva 5,  
630090 Novosibirsk, Russian Federation. (vedyagin@catalysis.ru)*

<sup>2</sup>*National Research Tomsk Polytechnic University, Lenin Av. 30,  
634050 Tomsk, Russian Federation.*

### ABSTRACT

Among the partly miscible metals, palladium and rhodium attract a special interest due to their efficient application in three-way catalysis. In the present report, the main factors affecting the catalytic stability and activity of the bimetallic Pd-Rh/Al<sub>2</sub>O<sub>3</sub> catalysts will be presented and discussed.

### INTRODUCTION

Since the total amount of engine vehicles grows year by year, development of novel catalytic pollution control systems with improved efficiency becomes more and more attractive. As it is well known, emissions of the gasoline engines contain nitrogen oxides, unburnt hydrocarbons and carbon monoxide. In this case, the pollution control system is mainly represented by a catalytic brick made of cordierite with honeycomb structure and coated with catalytically active composition consisting of secondary support (Al<sub>2</sub>O<sub>3</sub>, CeO<sub>2</sub>, ZrO<sub>2</sub>, etc.) and supported precious metals (Pt, Pd, Rh). These catalysts are known as three-way catalysts (TWC), since they provide simultaneous oxidation of CO and hydrocarbons along with reduction of NO<sub>x</sub> [1-5].

On the other hand, high-temperature deactivation of TWCs remains to be one of the most significant problems. The mechanism of deactivation differs for the active metals used. Thus, palladium undergoes the surface migration and agglomeration [6]. Contrary, rhodium is worldly-wise in the bulk diffusion into the support in the form of Rh<sup>3+</sup> ions [7-9]. In order to solve the deactivation problem, a novel approach considering the use of bimetallic alloys was proposed. The situation with the bimetallic Pd-Rh catalysts is complicated so far as, in accordance with the phase diagram, these metals are partly miscible and the most area of the diagram is represented by non-miscibility [10].

In the present work, the advantages of the bimetallic Pd-Rh/Al<sub>2</sub>O<sub>3</sub> catalysts in comparison with the reference monometallic systems were studied in detail. A special attention was paid to the peculiarities of the decomposition of the Pd-Rh-containing coordination compounds. The effects of the metal ratio, the metal-metal and metal-support interactions were elucidated as well.

## EXPERIMENTAL

The bimetallic Pd-Rh/Al<sub>2</sub>O<sub>3</sub> catalysts were synthesized by an incipient wetness impregnation of  $\gamma$ -Al<sub>2</sub>O<sub>3</sub> (Sasol, 205 m<sup>2</sup>/g) with aqueous solution of Pd(NH<sub>3</sub>)<sub>4</sub>][<sub>3</sub>[Rh(NO<sub>2</sub>)<sub>6</sub>]<sub>2</sub>. Then, the sample was dried at 120 °C. The final loading of metals in all cases was 0.2 wt.%. Monometallic Pd/Al<sub>2</sub>O<sub>3</sub> and Rh/Al<sub>2</sub>O<sub>3</sub> reference samples were prepared analogously using the aqueous solution of [Pd(NH<sub>3</sub>)<sub>4</sub>](NO<sub>3</sub>)<sub>2</sub> or Na<sub>3</sub>[Rh(NO<sub>2</sub>)<sub>6</sub>].

Thermogravimetric (TG) measurements were performed using a thermomicrobalance TG 209 F1 Iris® (Netzsch). X-ray diffraction analysis (XRD) was performed on a DRON-SEIFERT RM4 diffractometer using Cu K $\alpha$  radiation ( $k = 0.15418$  nm) with a graphite monochromator at the diffracted beam. The microstructure and composition of the samples were analyzed by scanning electron microscopy (SEM) with energy dispersive X-ray analysis (EDX) using a JSM-5100LV microscope (JEOL, Japan). High-resolution transmission electron microscopy (TEM) images were obtained with a JEOL JEM-2100F (200 kV) microscope equipped with an EDAX X-ray energy dispersive spectrometer. Electron paramagnetic resonance (EPR) spectroscopy with spin probes (1,3,5-trinitrobenzene, TNB) was applied to characterize the donor sites of the supports and catalysts. UV-vis diffuse reflectance spectra were recorded between 200 and 800 nm using a UV-vis spectrometer UV-VIS 2501 PC (Shimadzu) with IRS-250A diffusion reflection attachment. Photoluminescence (PL) experiments were carried out under atmospheric conditions at 290 K using a Cary Eclipse (Varian) spectrofluorimeter. The samples were additionally characterized by the ethane hydrogenolysis as a testing reaction, which rate depends linearly on the specific surface area of metals in the reduced state.

The catalytic performance and thermal stability of the samples was studied as described elsewhere [11-14].

## RESULTS AND DISCUSSION

The presence of donor sites on the support' surface is liable for stabilization of Pd<sup>2+</sup> species in the case of low-loaded Pd/Al<sub>2</sub>O<sub>3</sub> catalysts (0.125-0.5 wt.%) [11]. The amount of these sites in the case of  $\gamma$ -Al<sub>2</sub>O<sub>3</sub> is estimated to

be near  $(1-2) \times 10^{19}$  sites per gram that corresponds to less than 1% of a monolayer. It is also rather obvious that the appearance of such sites is caused by the presence of coordinately unsaturated structures on the surface. Since there is no unambiguous information in the literature regarding the structure of such sites so far, it seems reasonable to expect them to be present on a high-indexed faces of nanocrystals or on the edges and tops located between them. On the other hand, chemisorbed water chemisorbed on the support's surface appears to play an important role influencing the conditions for the stabilization of the active sites in the Pd/Al<sub>2</sub>O<sub>3</sub> catalysts and their catalytic performance [12]. Hydroxyl groups are seemed to participate in tailoring Pd<sup>2+</sup> ions to be the part of their coordination sphere, thus having a great impact on the catalytic properties.

As it was already mentioned, bimetallic Pd-Rh/ $\gamma$ -Al<sub>2</sub>O<sub>3</sub> catalysts, in their turn, attract a great attention due to their enhanced stability and resistance towards high temperature deactivation (surface migration and agglomeration of palladium, and bulk diffusion of rhodium) [13-18]. Palladium and rhodium are partly miscible metals, and preparation of their solid solution is quite complicated. In our research, we have used [Pd(NH<sub>3</sub>)<sub>4</sub>]<sub>3</sub>[Rh(NO<sub>2</sub>)<sub>6</sub>]<sub>2</sub> coordination compound as a precursor containing both metals. Formation of the solid solutions was confirmed by XRD analysis in all cases [13]. It was found that both the temperature and the atmosphere of precursor's decomposition affect significantly the composition of the alloyed nanoparticles being formed. The oxidative thermolysis of the precursor leads to the formation of the bimetallic alloyed Pd-Rh/ $\gamma$ -Al<sub>2</sub>O<sub>3</sub> catalysts with appropriate activity and excellent stability.

Another important factor affecting both the activity and the stability of the Pd-Rh/ $\gamma$ -Al<sub>2</sub>O<sub>3</sub> catalysts is a metal ratio, so far as it influences significantly the strength of metals interaction [14]. In the case of the Pd:Rh(3:2) sample, when the interaction is the strongest, no noticeable agglomeration of palladium particles or diffusion of rhodium ions into alumina bulk were observed. Such catalysts are characterized with excellent catalytic characteristics even after high temperature aging. Nitrogen oxide participates in the reactions of CO and hydrocarbons oxidation more intensively. Oppositely, the Pd:Rh(7:3) and Pd:Rh(4:1) catalysts catalyzed the reactions via different route. The stability of these samples, especially after aging at 1000 °C, was quite worse, and both agglomeration of Pd and diffusion of Rh were found to take place.

And finally, an extremely important factor which should be noted is the phase transformation of the support [17, 18]. According to the results of a prompt thermal aging, samples based on  $\gamma$ -Al<sub>2</sub>O<sub>3</sub> exhibited lower catalytic

activity and stability. Nevertheless, it was revealed that with the use of  $\gamma$ - $\text{Al}_2\text{O}_3$  the phase transformations of support in the high-temperature region (above 800 °C) are not crucial in terms of deactivation of bimetallic Pd-Rh catalysts. Characterization of the samples after aging at 1000 °C under PTA conditions and on air by set of methods (EPR spin probe, UV-Vis and PL spectroscopies) revealed that mutual Pd-Rh anchoring (metal-metal interaction) and active species stabilization on the donor sites of alumina (metal-support interaction) are the key factors determining the long-term activity and stability of Pd-Rh/alumina catalysts with excellent resistance to a high temperature deactivation. Strong interaction of the active species with donor sites of the support as well as mutual anchoring of the metals provides good stability along with appropriate activity of the samples. Thus, Rh was found to diffuse into bulk of  $\delta$ - $\text{Al}_2\text{O}_3$  during the thermal aging procedure (1000 °C) in all the cases including bimetallic samples. Structural and phase non-uniformity of this support causes concentrating of Rh near the interphase boundaries of  $\delta$ - $\text{Al}_2\text{O}_3$  and  $\theta$ - $\text{Al}_2\text{O}_3$  phases. Moreover, intensified sintering of palladium particles was found to take place on  $\delta$ -alumina.

## CONCLUSION

In general, the obtained results can be considered as an indication of the possibility to create stable and highly active three-way catalysts containing rather low concentrations of the supported Pd and Ph. An important role in the formation of the active sites of such catalysts is played by intrinsic sites of the support, allowing one to stabilize the isolated  $\text{Pd}^{2+}$  species. Strong metal-metal (Pd-Rh) interaction in the case of metal ratio 3:2 permits to prevent deactivation processes and stabilize the activity of the catalysts.

## *Acknowledgement*

The study was financially supported by the Ministry of Education and Science of the Russian Federation within the framework of subsidizing agreement of October 23, 2017 (No. 14.581.21.0028, unique agreement identifier RFMEFI58117X0028) of the Federal Target Program “Research and development in priority directions of the progress of the scientific and technological complex of Russia for the years 2014–2020.”

## REFERENCES

- [1] M. V. Twigg, *Appl. Catal. B-Environ.*, 2006, 70, 2–15.
- [2] R.M. Heck, R.J. Farrauto, *Appl. Catal. A-Gen.*, 2001, 221, 443–457.
- [3] S.H. Oh, G.B. Fisher, J.E. Carpenter, D.W. Goodman, *J. Catal.*, 1986, 100, 360-376.

- [4] K.C. Taylor, *Catal. Rev. Sci. Eng.*, 1993, 35, 457-481.
- [5] M. Shelef, G.W. Graham, *Catal. Rev. Sci. Eng.*, 1994, 36, 433-457.
- [6] A.A. Vedyagin, A.M. Volodin, V.O. Stoyanovskii, I.V. Mishakov, D.A. Medvedev, A.S. Noskov, *Appl. Catal. B-Environ.*, 2011, 103, 397-403.
- [7] V.O. Stoyanovskii, A.A. Vedyagin, G.I. Aleshina, A.M. Volodin, A.S. Noskov, *Appl. Catal. B-Environ.*, 2009, 90, 141-146.
- [8] V.O. Stoyanovskii, A.A. Vedyagin, A.M. Volodin, R.M. Kenzhin, Y.V. Shubin, P.E. Plyusnin, I.V. Mishakov, *Catal. Commun.*, 2017, 97, 18–22.
- [9] E.A. Alikin, A.A. Vedyagin, *Top. Catal.*, 2016, 59, 1033-1038.
- [10] Y.V. Shubin, P.E. Plyusnin, S.V. Korenev, *J. Alloy. Compd.*, 2015, 622, 1055-1060.
- [11] A.A. Vedyagin, A.M. Volodin, R.M. Kenzhin, V.O. Stoyanovskii, V.A. Rogov, D.A. Medvedev, I.V. Mishakov, *J. Therm. Anal. Calorim.*, 2017, 130, 1865-1874.
- [12] A.A. Vedyagin, A.M. Volodin, R.M. Kenzhin, V.O. Stoyanovskii, V.A. Rogov, V.V. Kriventsov, I.V. Mishakov, *Catal. Today*, 2018, 307, 102-110.
- [13] A.A. Vedyagin, P.E. Plyusnin, A.A. Rybinskaya, Y.V. Shubin, I.V. Mishakov, S.V. Korenev, *Mater. Research Bull.*, 2018, 102, 196-202.
- [14] A.A. Vedyagin, V.O. Stoyanovskii, P.E. Plyusnin, Y.V. Shubin, E.M. Slavinskaya, I.V. Mishakov, *J. Alloys Compd.*, 2018, 749, 155-162.
- [15] A.A. Vedyagin, M.S. Gavrillov, A.M. Volodin, V.O. Stoyanovskii, E.M. Slavinskaya, I.V. Mishakov, Y.V. Shubin, *Top. Catal.*, 2013, 56, 1008-1014.
- [16] A.A. Vedyagin, A.M. Volodin, V.O. Stoyanovskii, R.M. Kenzhin, E.M. Slavinskaya, I.V. Mishakov, P.E. Plyusnin, Y.V. Shubin, *Catal. Today*, 2014, 238, 80-86.
- [17] A.A. Vedyagin, A.M. Volodin, V.O. Stoyanovskii, R.M. Kenzhin, P.E. Plyusnin, Y.V. Shubin, I.V. Mishakov, *Top. Catal.*, 2017, 60, 152-161.
- [18] A.A. Vedyagin, A.M. Volodin, R.M. Kenzhin, V.O. Stoyanovskii, Y.V. Shubin, P.E. Plyusnin, I.V. Mishakov, *Catal. Today*, 2017, 293–294, 73-81.

## COILED-COIL PROTEIN ORIGAMI – A NEW DESIGNED TYPE OF PROTEIN FOLDS

R. Jerala

Department of synthetic biology and immunology, National institute of chemistry, Ljubljana, Slovenia

### ABSTRACT

Proteins are the most advanced nanostructures, defined by the linear sequence of amino acids that can fold into complex tertiary structures. Sequence- structure relationship of natural proteins is however highly complex and difficult to predict. We devised a new modular type of protein fold design, inspired by DNA nanostructures. Here the folding problem was bypassed by designing de novo coiled-coil protein origami (CCPO) folds based on the well-understood specificity of coiled-coil dimers and used them as modules to guide the polypeptide chain between vertices of the selected polyhedral cage. The principle was first demonstrated by the construction of a nanoscale protein tetrahedral cage from a single polypeptide chain composed of 12 coiled-coil forming segments<sup>1</sup>. In this assembly 6 edges of the polyhedron are defined by orthogonal coiled-coil dimers. Introduction of supercharged CC building modules<sup>2</sup> and protein origami computational design platform CoCoPOD enabled design of protein origami cages that are able to self-assemble in vivo. Complexity of protein origami structures as extended to more than 700 residue proteins with tetrahedral, four-sided pyramid and triangular prism that fold efficiently, with kinetics and stability comparable to globular proteins<sup>3</sup>. In vivo folding of protein origami opens prospects for new applications of this new type of designed nanostructures.

### REFERENCES

- [1] Gradišar H, Božič S, Doles T, Vengust D, Hafner-Bratkovič I, Mertelj A, Webb B, Šali A, Klavžar S, Jerala R. (2013) *Nat Chem Biol*. 6:362-6.
- [2] Drobnak I, Gradišar H, Ljubetič A, Merljak E, Jerala, R. (2017) Modulation of Coiled-Coil Dimer Stability through Surface Residues while Preserving Pairing Specificity. *J.Am.Chem.Soc.* 139: 8229-8236.
- [3] Ljubetič, A., Lapenta, F., Gradišar, H., Drobnak, I., Aupič, J., Strmšek, Ž., Lainšček, D., Hafner-Bratkovič, I., Majerle, A., Krivec, N., Benčina, M., Pisanski, T., Čirković Veličković, T., Round, A., Carazo, J.M., Melero, R. and Jerala, R., (2017) Design of in vivo self-assembling coiled-coil protein origami. *Nat Biotech*, 35:1094-1101.

## POSTPONED MONITORING OF ENVIRONMENTAL POLLUTION CAUSED BY NATO BOMBING OF SERBIA IN 1999

A. Jovović<sup>1</sup>, J. Raičević<sup>2</sup> and Z. Vukmirović<sup>3</sup>

<sup>1</sup>*University of Belgrade-Faculty of Mechanical Engineering,*

<sup>2</sup>*ret. in Nuclear Facilities of Serbia*

<sup>3</sup>*ret. in the Institute of Physics, University of Belgrade*

[ajovovic@mas.bg.ac.rs](mailto:ajovovic@mas.bg.ac.rs)

### ABSTRACT

During the NATO bombing during spring 1999, more than seventy industrial plants and installations and more than thousand military and urban buildings have been destroyed or damaged, causing significant environmental pollution, primarily as a result of huge pollutant emissions released into the environment, producing high concentration level of pollutants in the air and surface water during episodes and a considerable long-term soil and groundwater contamination in the processes of their deposition. The fires in the oil refineries and oil storage in some cases lasted for many days and created clouds of pollution over wide areas, including the toxic and carcinogenic matter. In addition to other weapons, NATO used the ammunition with depleted uranium (DU).

Estimates of the relevant international organizations have indicated the presence of high levels of soil contamination, primarily by hydrocarbons, PCBs, heavy metals and dioxins in *hot spots* as Pancevo, Kragujevac, Bor, Novi Sad, and Baric, Kraljevo, Nis, Belgrade-new town, Obrenovac, Prahovo and Pristina indicated by the independent experts, stressing out a necessity for remediation activities to be carried out. In 2000, based on the reports mentioned, EU and the UNEP have developed a detailed feasibility study, defining 27 land clean-up and soil remediation projects for sites that had been deemed the most polluted.

The results of many analysis are applicable not only to Kosovo but also to other areas targeted during the conflict. Among the others, more thorough review is required of the health effects of medium- and long-term exposure to DU. Under suitable meteorological conditions, these chemicals could be transported over long distances. The NATO bombing therefore has a wider regional impacts.

However, further work would be needed to determine state of nation and environment after almost twenty years in order to protect populated areas where the high health risk was expected during war and in the post-war period. As an example, for contaminated locations, appropriate available and efficient remediation activities aimed to minimize human exposure and further environmental pollution should be proposed and accompanied by development of related feasibility study. These remediation activities have to be followed by appropriate monitoring. This work deals with the short evaluation of contribution of the further research and monitoring of contaminated sites to further environmental protection and epidemiological studies twenty years after the bombing.

## PHYSICOCHEMICAL ASPECTS OF MAGNETIC RESONANCE MICROSCOPY: INFLUENCE OF TEMPERATURE ON THE IMAGE CONTRAST

S. Macura and P.K. Mishra

*Department of Biochemistry and Molecular Biology, Mayo Clinic,  
Rochester, Minnesota, 55905, USA*

### ABSTRACT

Magnetic resonance microscopy (MRM) is typically performed at room temperature on selected materials or fixed tissue using water protons as the principal source of the signal. In this paper we analyse theoretically and demonstrate experimentally the influence of temperature on the contrast in spin-echo images. Strong gradients used to generate high resolution images affect effective transversal relaxation time,  $T_{2eff}$  making it dependent on the water diffusion coefficient as well. By judicious choice of temperature one can enhance contrast in the region of interest.

### INTRODUCTION

Most effective application of nuclear magnetic resonance imaging (MRI) is in studies of biological systems in vivo but providing images of fresh or fixed tissue specimens in non-invasive way are also very useful. With smaller specimens it is easy to achieve submillimeter resolution per pixel – hence high resolution MRI is also known as magnetic resonance microscopy (MRM). To enhance sensitivity and resolution, the MRM method requires higher  $B_0$  fields and higher field gradients. Although basic properties of the specimens (spin density, rotational and translational diffusion rates) are independent of the field strength, principal magnetic resonance properties such as longitudinal and transverse relaxation times ( $T_1$ ,  $T_2$ ), in addition to the physicochemical state of the specimen, depend on both static magnetic field and magnetic field gradients. This dependence is neither direct nor linear, and therefore the properties of high field, high resolution images hardly can be predicted from the experiments at lower fields and lower resolution.

There is enough experimental evidence that in biological specimens  $T_1$  increases with the static magnetic field strength and  $T_2$  decreases with both, the static field and field gradient strength. Both changes in relaxation times degrade the image quality, so real MRM images are somewhat poorer than expected at higher magnetic field and gradient strengths.

The influence of temperature on MR signal has already been studied [1]. The authors calculated the temperature coefficient of the signal in the gradient and spin-echo experiments and have found that the signal can either increase or decrease with temperature, depending on the choice of the imaging parameters. This is generally true. Here we focus on the temperature dependence of the images in the spin-echo sequences in the fixed tissue. Because of limited temperature range and tissue variability it is easy to set up a general model which allows qualitative analysis of the image properties at various temperatures.

In this work we analyze, theoretically and experimentally, whether the MRM of biological specimen could be improved by variable temperature scans.

## **THEORY**

In heterogeneous systems such as tissue, physicochemical properties of water exhibit a wide distribution (melting point, viscosity, diffusion) which directly affects related MR properties. Usually such distribution is described as an average of properties of several different water phases. For example, in all models for proton relaxation in tissue it is assumed that there are several proton pools, with fast exchange among themselves. Main differences among the models are the origin of the phases and the principal mechanisms of averaging among them [2-5]. For example the EMOR model [5] (exchange-mediated orientational randomization) assumes that majority of protons are in the water-like phase whose properties are moderated by protons in the 'polymer' phase via 'intermediate' phase. In majority of imaging experiments the echo selects the longest lived fraction of the tissue water thus the observed tissue water could be regarded as ordinary water that is perturbed by the macromolecular environment.

It is then reasonable to assume that the temperature dependence of relevant MR parameters of tissue water, (macroscopic magnetization  $M_0$ , longitudinal relaxation time  $T_1$ , transverse relaxation time  $T_2$ , water diffusion coefficient  $D$ , and chemical exchange rate  $k_{ex}$ ) is similar to ordinary water. In neat water, the dynamic is controlled by the network of hydrogen bonds which results in activation energies about 20 kJ/mol [6]. In other systems (tissue, gel, lamellar phases etc.) the activation energy could be somewhat different, [6, 7] but general pattern remains the same. The observable water protons are in the extreme narrowing regime (liquid water at ambient conditions) so relaxation rates are proportional to respective correlation times[8]

$$\frac{1}{T_1} = K_1 \tau_{c,1} \quad (1)$$

and

$$\frac{1}{T_2} = K_1 \tau_{c,1} + K_2 \tau_{c,2} \quad (2)$$

Here  $T_1$  and  $T_2$  are longitudinal and transversal relaxation times, respectively, and  $K_1$  and  $K_2$  are constants that encompass all temperature independent parameters;  $\tau_{c,1}$  is rotational correlation time and  $\tau_{c,2}$  correlation time for other processes that could affect  $T_2$ , e.g., chemical exchange or the translational diffusion through the magnetic susceptibility gradients. Experimentally, in most tissues it is found that  $T_1 \gg T_2$ , thus,  $K_1 \tau_{c,1} \ll K_2 \tau_{c,2}$ .

The influence of magnetic field gradients on the effective relaxation rate is well known [9-11] and well documented and tested in biological tissue [12, 13]. Briefly, longitudinal magnetization is unaffected by the field gradient while the transverse exhibit accelerated effective relaxation due to additional dephasing that is caused by the diffusion of spins in the field gradient:

$$\frac{1}{T_{2,eff}} = \frac{1}{T_2} + \frac{1}{T_{2,Diffusion}} \quad (3)$$

Here  $T_{2,eff}$  is observed relaxation time,  $T_2$  intrinsic relaxation time from eq. (2) and  $T_{2,Diffusion}$  the diffusion contribution, given by [9, 10, 13]

$$\frac{1}{T_{2,Diffusion}} = D \sum_j K_{G_j} G_j^2 \quad (4)$$

$D$  is diffusion coefficient, and summation runs over all events during which gradient  $G_j$  is on. Constants  $K_{G_j}$  take into account the details of the sequence (timing, spin echo or gradient echo, echo order, flip angles etc.). Sequences designed to enhance or eliminate diffusion effects most often have one dominant contribution, and, Eq (4) usually has only one term with well-defined  $K_{G_j}$  constant. However, imaging sequences could comprise several gradients (read dephase and rephrase gradients, encoding gradients etc.) each contributing appreciably to the diffusion enhanced relaxation.

While relaxation rates in extreme narrowing regime are proportional to the correlation time, the diffusion coefficient  $D$  is inversely proportional to

the diffusion correlation time,  $\tau_D$  as expressed by the Einstein-Smoluchowski relation [14]

$$D = \frac{K_D}{\tau_D} \quad (5)$$

where  $K_D$  is time independent constant (proportional to the mean square displacement). In liquids, the dependence of any correlation time  $\tau_x$  on temperature  $T$  can be expressed via the Arrhenius type relation

$$\frac{1}{\tau_x} = \frac{1}{\tau_{x0}} \exp\left(-\frac{E_{a,x}}{RT}\right) \quad (6)$$

where  $E_{a,x}$  is activation energy of respective activated process (rotation, translation, chemical exchange)  $R$  molar gas constant and  $\tau_{x0}$  the scaling constant. Combining Eqs. (2) -(6) we find a general expression for the temperature dependence of effective transverse relaxation rate

$$\frac{1}{T_{2,eff}} = K_1 \tau_{c0,1} \exp\left(+\frac{E_{a,1}}{RT}\right) + K_2 \tau_{c0,2} \exp\left(+\frac{E_{a,2}}{RT}\right) + \sum_j K_{G_j} G_j^2 \frac{K_D}{\tau_{D0}} \exp\left(-\frac{E_{a,D}}{RT}\right) \quad (7)$$

where  $E_{a,1}$  represents activation energy for molecular rotation,  $E_{a,2}$ , is activation energy for other processes that contribute to intrinsic transverse relaxation rate, and  $E_{a,D}$  is activation energy for translational motion (diffusion).

Temperature range in which tissue relaxation could be studied is relatively narrow compared to the absolute temperature (50 K vs. 300 K) and first two terms describing intrinsic relaxation rate could be merged into one with new effective activation energy  $E_a$ . Also, summation over different gradients in the second term could be replaced by a single effective gradient  $G_{eff}$  and Eq. (7) becomes

$$\frac{1}{T_{2,eff}} = K_a \exp\left(+\frac{E_a}{RT}\right) + K_{G,D} G_{eff}^2 \exp\left(-\frac{E_{a,D}}{RT}\right) \quad (8)$$

where  $K_a$  and  $K_{G,D}$  are scaling constants. It is important to note different signs in the exponential terms. Therefore, the change of temperature affects all correlation times in a similar manner (decrease of temperature prolongs correlation times), but it changes relaxation rates and diffusion coefficient in the opposite directions (decrease of temperature decreases the diffusion coefficient and increases relaxation rates). Also,  $D$  and  $T_1$  may have very

similar activation energies, because they are governed by closely related processes (translational and rotational diffusion) whereas the  $T_2$  activation energy may be quite different if other processes (besides rotational motion) prevail (e.g., chemical exchange).

For practical reasons in MRM it is more common to deal with relaxation times than with relaxation rates. Full lines in Figure 1 show dependences of  $T_{2,eff}$  on temperature plots according to Eq. (8) for few indicated cases. With lowering temperatures and lowering effective gradients (curves from bottom to top within the group), the contribution of the diffusion in the field gradient becomes increasingly smaller compared to intrinsic transverse relaxation thus  $T_{2,eff}$  continuously grow (top two lines in Fig. 1C). On the higher temperatures and with increasing gradients strengths (lines top to bottom within the group), relaxation caused by the diffusion in the gradient becomes dominant and  $T_{2,eff}$  decreases with temperature (Fig. 1B above 0 °C). The maximum is reached when

$$E_a f_a = G_{eff}^2 E_{a,D} f_D \quad (9)$$

where  $f_a$  and  $G_{eff}^2 f_D$  represent fractional contributions of intrinsic and diffusion induced relaxation rates, respectively. Besides relative magnitudes of activation energies, the position of the  $T_{2,eff}$  maximum depends on the effective gradient strength: the stronger the gradient (the higher the resolution), the lower the temperature of the maximum, Fig.1.

Therefore, the temperature dependence of the MR image is mediated by several processes, whose contribution is weighted by the imaging parameters. For example, in human imaging where resolution is typically order of millimeters, gradients are comparably small and the influence of diffusion in normal sequences is negligibly small. However, in MRM with resolution of a few tens of microns, the influence of gradients may be the major source of transverse relaxation.

## EXPERIMENTAL

A H<sub>2</sub>O:D<sub>2</sub>O (20:80) phantom was scanned in a 5mm NMR tube to minimize local gradients. The zebrafish was anesthetized using 0.02% tricaine, and fixed in 4% paraformaldehyde in phosphate buffered saline. Experiments were done on the 7 Tesla (formalin fixed zebrafish specimen) and 16.4 Tesla (H<sub>2</sub>O:D<sub>2</sub>O phantom) NMR spectrometers (Bruker, BioSpin, Billerica MA) at a series of temperatures in the range 5 °C to 45 °C. The sample temperature was maintained by a stream of conditioned air. Two-

dimensional (2D) spin-echo sequence was used in all experiments with the slice thickness 1 mm and variable in-plane resolution from 25  $\mu\text{m}/\text{pixel}$  to 1000  $\mu\text{m}/\text{pixel}$  (specified at respective curves in Fig. 1). At selected temperature/resolution a series of images with variable echo time is generated and processed by image sequence analysis module within ParaVision 5.1 software (Bruker, BioSpin, Billerica, MA) generating  $T_{2,eff}$  for selected region of interest (brain and swim bladder).

## RESULTS AND DISCUSSION

We used water diluted by D<sub>2</sub>O to emphasize the influence of diffusion on the  $T_{2,eff}$ . The dilution reduces dipole-dipole interaction among water proton significantly prolonging relaxation times [7]. As Fig. 1A shows, with

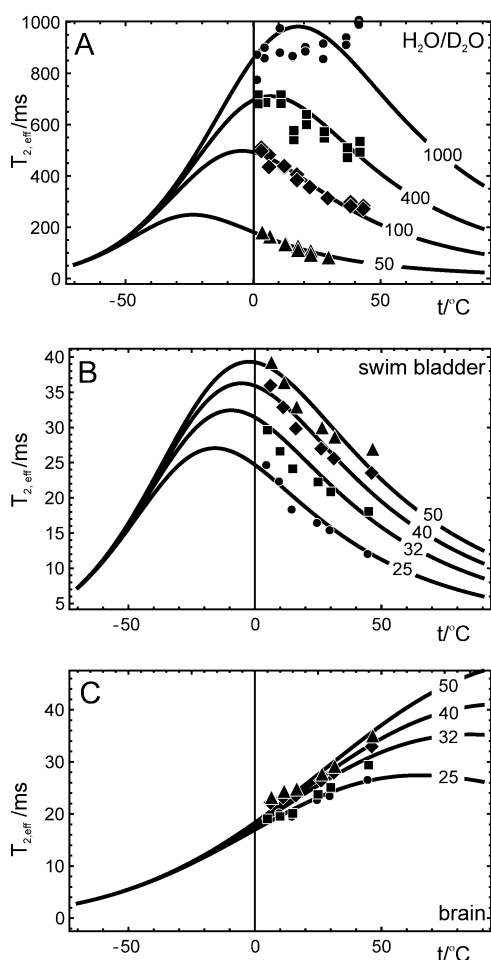


**Figure 1.** The dependence of effective relaxation time  $T_{2,eff}$  on temperature (in  $^{\circ}\text{C}$ ). Full lines - Eq.(8), symbols – experimental points (2D spin-echo), with resolution in  $\mu\text{m}/\text{pixel}$  indicated on respective lines **A)** The  $\text{H}_2\text{O}:\text{D}_2\text{O}$  (20:80) phantom at 16.4 T. Diluted water is used to prolong  $T_2$  and make the  $T_{2,eff}$  dependence on the experimental gradients more obvious. **B)** The swim bladder of fixed zebrafish at 7 T. It is filled mostly with the fixative (formalin in water) thus the pattern is similar to water. **C)** Brain of fixed zebrafish specimen. Diffusion coefficient of water in the zebrafish brain tissue is order of magnitude slower than in neat water thus the maxima are shifted toward higher temperatures.

minimal resolution of 1000  $\mu\text{m}/\text{pixel}$  (and minimal gradients)  $T_{2,\text{eff}}$  in diluted water phantom is close to 1 s. With such a long relaxation time the water diffusion even in a very weak gradients contributes significantly to  $1/T_{2,\text{eff}}$ . In the temperature range of interest increasing resolution from 1000  $\mu\text{m}/\text{pixel}$  to 50  $\mu\text{m}/\text{pixel}$  shortens  $T_{2,\text{eff}}$  approximately fivefold, Fig. 1A.

To investigate effects in tissue we used fixed zebrafish. Zebrafish is very popular model in biomedical research and here is very useful as within the same specimen one can test properties of several tissue types. We have chosen swim bladder and brain as two extremes since we found that the diffusion of water in swim bladder is close to free water and in brain almost order of magnitude slower (data not shown). Indeed, as Fig.1 B shows, the swim bladder temperature dependence of  $T_{2,\text{eff}}$  follows the dependence of water, Fig. 1A. The obvious difference is order of magnitude shorter  $T_{2,\text{eff}}$  in swim bladder, which results in a somewhat attenuated dependence on the resolution and shift of the maxima toward lower temperatures. In contrast to that, the brain  $T_{2,\text{eff}}$  dependence on temperature is less affected by the resolution because water diffusion in the brain is much slower.

Figure 2 shows parametric  $T_{2,\text{eff}}$  image of the zebrafish specimen recorded at different temperatures. Because different organs have slightly different temperature dependence of  $T_{2,\text{eff}}$ , generally, the image contrast is affected by temperature in in unpredictable way.

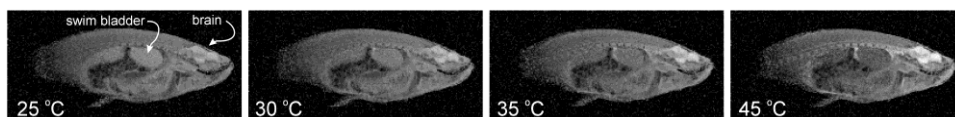


**Figure 2.**  $T_{2,\text{eff}}$  parametric images, of fixed zebrafish specimen at different temperatures. Slice thickness 1 mm and in-plane resolution 32  $\mu\text{m}/\text{pixel}$ . One can notice the progressive increase of brightness in the brain and the decrease in the swim bladder with temperature increase.

## CONCLUSION

Contrary to MRI in high resolution, a MRM contrast depends also on the scanning temperature. Temperature therefore could be used as an additional parameter for contrast optimization in MRM.

## REFERENCES

- [1] D.H. Gultekin, J.C. Gore, J Magn Reson, 172 (2005) 133-141.
- [2] R.G. Bryant, D.A. Mendelson, C.C. Lester, Mag Res Med, 21 (1991) 117-126.
- [3] S.H. Koenig, R.D. Brown III, Mag Reson Med, 30 (1993) 685-695.

- 
- [4] F.V. Chávez, B. Halle, *Mag Res Med*, 56 (2006) 73-81.
- [5] B. Halle, *Mag Res Med*, 56 (2006) 60-72.
- [6] D. Eisenberg, W. Kauzmann, *The Structure and Properties of Water*, Oxford, 2005.
- [7] A. Abragam, *The Principles of Nuclear Magnetism*, first ed., Oxford University Press, Oxford, 1961.
- [8] R.K. Harris, *Nuclear Magnetic Resonance Spectroscopy: A Physicochemical View*, J. Wiley, Somerset, NJ, USA, 1986.
- [9] H.Y. Carr, E.M. Purcell, *Phys Rev*, 94 (1954) 630.
- [10] R. Kaiser, E. Bartholdi, R.R. Ernst, *J Chem Phys*, 60 (1974) 2966-2979.
- [11] H.C. Torrey, *Physical Review*, 104 (1956) 563.
- [12] R.J. Kurland, F.Q.H. Ngo, *Mag Res Med*, 3 (1986) 425-431.
- [13] S. Michaeli, M. Garwood, X.-H. Zhu, L. DelaBarre, P. Andersen, G. Adriany, H. Merkle, K. Ugurbil, W. Chen, *Mag Res Med*, 47 (2002) 629-633.
- [14] J. Phillibert, *Diffusion Fundamentals*, 2 (2005) 1 - 10.

## ***A – Chemical Thermodynamics***



## GUAIACYL MOIETY AS A FREE RADICAL SCAVENGER: THERMODYNAMIC APPROACH

A. Amić<sup>1</sup>, Z. Marković<sup>2</sup> and D. Amić<sup>3</sup>

<sup>1</sup>Department of Chemistry, Josip Juraj Strossmayer University of Osijek,  
Cara Hadrijana 8a, 31000 Osijek, Croatia. (aamic@kemija.unios.hr)

<sup>2</sup>Department of Chemical-Technological Sciences, State University of Novi  
Pazar, Vuka Karadžića bb, 36000 Novi Pazar, Serbia.

<sup>3</sup>Faculty of Agriculture, Josip Juraj Strossmayer University of Osijek,  
Vladimira Preloga 1, 31000 Osijek, Croatia.

### ABSTRACT

The role of guaiacyl moiety of *trans*-ferulic acid (*trans*-FA), *syn*-dihydroferulic acid (*syn*-DHFA) and 3,5-dihydroxy-4-methoxybenzyl alcohol (DHMBA) in double hydrogen atom transfer (dHAT), double sequential proton loss electron transfer (dSPLET) and double electron transfer-proton transfer (dET-PT) mechanisms was investigated. Obtained results reveal that the contribution of guaiacyl moiety in free radical inactivation should not be neglected, as was the case previously.

### INTRODUCTION

Metabolic processes in human body produce free radicals which are essential for normal cell function. However, excessive amounts of free radicals cause oxidative stress, which leads to damage of the cell macromolecules and to the onset of diseases such as cancer and cardiovascular disorders. Eating habits, based on vegetables and fruits, ameliorate human health and longevity, which is mostly ascribed to polyphenolic compounds ubiquitously present in such diet. Polyphenolic compounds are natural antioxidants capable to effectively scavenge free radicals. Such activity is mainly ascribed to phenolic OH group(s), notably to the two vicinal OH groups, i.e., catechol moiety. Despite the fact that the contribution of guaiacyl moiety (vicinal OH and OCH<sub>3</sub> group) in free radical scavenging has been already experimentally [1] and theoretically recognized [2], underlying mechanisms are not fully understood. *trans*-Ferulic acid (*trans*-FA) and *syn*-dihydroferulic acid (*syn*-DHFA) can be found in plant kingdom, and are colon catabolites of various polyphenolic compounds [3]. 3,5-Dihydroxy-4-methoxybenzyl alcohol (DHMBA) is isolated from both plant and animal sources [4]. For these compounds, only a single (1H<sup>+</sup>/1e<sup>-</sup>) free radical inactivation processes were investigated so far. They all contain guaiacyl moiety (Fig. 1) and we here investigated possible

double ( $2\text{H}^+/2\text{e}^-$ ) free radical scavenging mechanisms: double hydrogen atom transfer (dHAT), double sequential proton loss electron transfer (dSPLET) and double electron transfer-proton transfer (dET-PT).

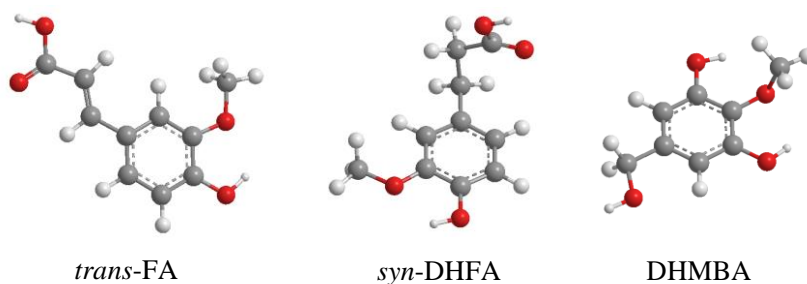


**Figure 1.** The most stable structures of the studied compounds

## METHODS

Geometry optimizations and frequency calculations for *trans*-FA, *syn*-DHFA and DHMBA, as well as for all species involved in studied antiradical mechanisms were performed at SMD/M06-2X/6-311++G(d,p) level of theory using the Gaussian 09 program package. Bond dissociation enthalpies (BDEs) related to dHAT mechanism were evaluated from enthalpies of corresponding species calculated in pentyl ethanoate as a solvent. Proton affinities (PAs) and electron transfer enthalpies (ETEs) related to dSPLET mechanism, and ionization potentials (IPs) and proton dissociation enthalpies (PDEs) related to dET-PT mechanism were evaluated from enthalpies of corresponding species calculated in water as a solvent.

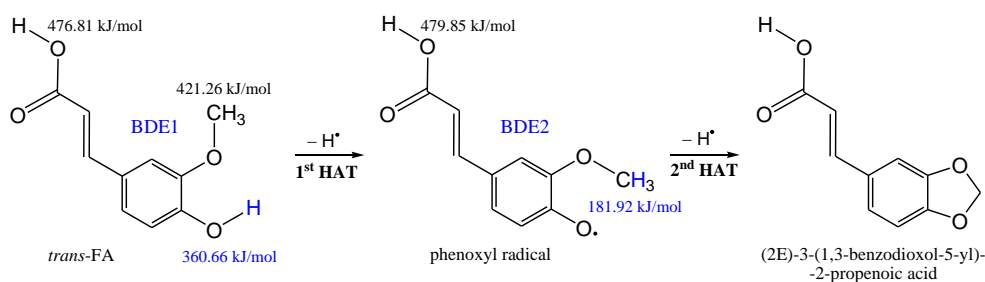
## RESULTS AND DISCUSSION

### dHAT mechanism

Homolytic cleavage of phenolic O–H bond is the first step of the dHAT mechanism. Second step is H-atom abstraction from methoxy group of phenoxyl radical due to a huge decrease of corresponding BDE<sub>2</sub> value (Table 1). Moreover, in the case of DHMBA the second step is not related to another phenolic OH group, but also to H-atom abstraction from vicinal methoxy group. This results in cyclization of all investigated compounds, i.e., formation of 1,3-benzodioxole core as illustrated for *trans*-FA in Fig. 2.

**Table 1:** SMD/M06-2X/6-311++G(d,p) calculated enthalpies (in kJ/mol) related to dHAT mechanism in pentyl ethanoate

	BDE1 (OH)	BDE2 (OCH <sub>3</sub> )	BDE2 (OH)
<i>trans</i> -FA	360.66	181.92	—
<i>syn</i> -DHFA	357.56	183.09	—
DHMBBA	358.08	182.02	353.30

**Figure 2.** dHAT mechanism of *trans*-FA in pentyl ethanoate

**dSPLET mechanism** - Generally, mechanisms where heterolytic bond cleavage occurs are favoured in polar (water) environment.

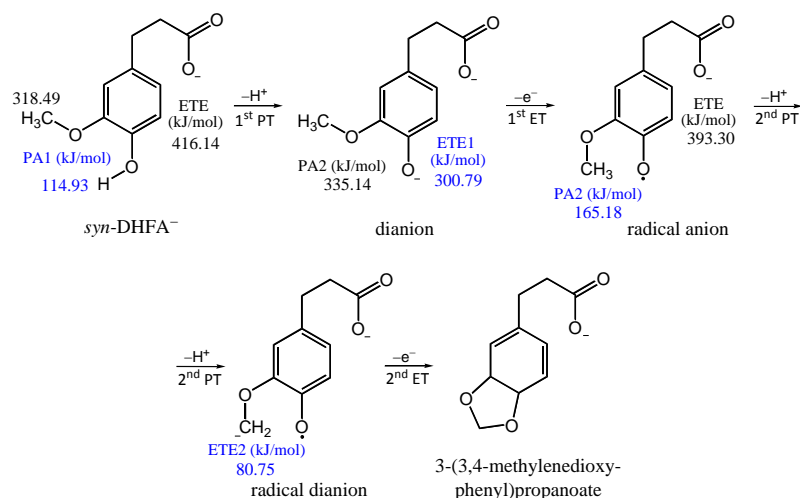
**Figure 3.** dSPLET mechanism of *syn*-DHFA in water

Figure 3 summarized results obtained for dSPLET mechanism by which *syn*-DHFA inactivates free radicals. Because at physiological pH of 7.4 *syn*-DHFA mainly exists in anionic form, all calculations were performed for its carboxylate anion.

Data presented in Table 1 indicate that the driving force for cyclization of all investigated compounds *via* dHAT mechanism is decreased BDE2 value (nearly a half of BDE1). In the case of dSPLET mechanism, driving force for cyclization is an even more reduced ETE2 value (Table 2).

**Table 2:** SMD/M06-2X/6-311++G(d,p) calculated enthalpies (in kJ/mol) related to dSPLET mechanism in water. Active site is given in parenthesis.

	PA1	PA2	PA3	ETE1	ETE2
<i>trans</i> -FA	102.31 (OH)	151.87 (OCH <sub>3</sub> )	–	335.72 (O <sup>–</sup> )	93.92 (OCH <sub>2</sub> <sup>–</sup> )
<i>syn</i> -DHFA	114.93 (OH)	165.18 (OCH <sub>3</sub> )	–	300.79 (O <sup>–</sup> )	80.75 (OCH <sub>2</sub> <sup>–</sup> )
DHMBA	101.31 (OH)	127.28 (OH)	178.87 (OCH <sub>3</sub> )	297.79 (O <sup>–</sup> )	73.02 (OCH <sub>2</sub> <sup>–</sup> )

**dET-PT mechanism** - Because the first step of this mechanism (IP1) is much more energy demanding than the first step of dSPLET mechanism (PA1), dET-PT mechanism is not relevant for investigated compounds in water. Namely, for *trans*-FA, *syn*-DHFA and DHMBA, IP1 values (440.20 kJ/mol, 425.18 kJ/mol and 454.89 kJ/mol, respectively) are much higher than the corresponding PA1 values (Table 2).

## CONCLUSION

The results obtained here indicate that guaiacyl moiety of *trans*-FA, *syn*-DHFA and DHMBA has potential to scavenge free radicals *via* double free radical scavenging mechanisms (dHAT and dSPLET). The main conclusion we would draw here is that the contribution of guaiacyl moiety to free radical inactivation should be taken into account for any compound possessing this moiety, what was mainly ignored earlier.

## REFERENCES

- [1] W. Brand-Williams, M. E. Cuvelier, C. Berset, *Lebensm.-Wiss. u.-Technol.*, 1995, **28**, 25-30.
- [2] N. Nenadis, M. P. Sigalas, *J. Phys. Chem. A*, 2008, **112**, 12196-12202.
- [3] A. Amić, Z. Marković, E. Klein, J. M. Dimitrić Marković, D. Milenković, *Food Chem.*, 2018, **246**, 481-489.
- [4] Y. Villuendas-Rey, J. R. Alvarez-Idaboy, A. Galano, *J. Chem. Inf. Model.*, 2015, **55**, 2552-2561.

## THERMODYNAMIC PROPERTIES OF BIOLOGICALLY ACTIVE SUBSTANCES

A.V. Knyazev<sup>1</sup>, A.S. Shipilova<sup>1</sup>, E.V. Gusarova<sup>1</sup>, S.S. Knyazeva<sup>1</sup>,  
A.A. Amosov<sup>1</sup> and V.N. Emel'yanenko<sup>2</sup>

<sup>1</sup>*Chemistry Department, Lobachevsky State University of Nizhni Novgorod  
Gagarin Av. 23/2, 603950, Nizhni Novgorod, Russia  
(knyazevav@gmail.com)*

<sup>2</sup>*Department of Physical Chemistry, University of Rostock, Dr-Lorenz-Weg  
1, D-18059 Rostock, Germany*

### ABSTRACT

The temperature dependences of heat capacity of the B<sub>2</sub>, B<sub>3</sub>, B<sub>8</sub>, B<sub>9</sub>, B<sub>11</sub>, B<sub>12</sub>, methylprednisolone and methylprednisolone aceponate have been measured for the first time in the range from 5 to 350 K by precision adiabatic vacuum calorimetry. The experimental data were used to calculate standard thermodynamic functions for the range from 0 to 350 K. Enthalpies of combustion of the B<sub>2</sub>, B<sub>8</sub>, B<sub>9</sub>, B<sub>11</sub>, B<sub>12</sub>, methylprednisolone, methylprednisolone aceponate, prednisolone and hydrocortisone acetate were measured for the first time using high-precision combustion calorimeter. The standard molar enthalpies of formation in the crystalline state at 298.15 K were derived from the combustion experiments. Using combination of the adiabatic and combustion calorimetry results the thermodynamic functions of formation of the test substances at T = 298.15 K and P = 0.1 MPa have been calculated.

### INTRODUCTION

A special group of organic compounds are biologically active substances. With their help, the processes of metabolism, growth and development of living organisms are carried out and regulated. Violation of the balance of BAS in the cells and tissues of the body leads to metabolic disorders and the development of pathologies. Vitamins and hormones are the most important useful biologically active substances.

The goals of this work include calorimetric determination of the standard thermodynamic functions of the riboflavin, nicotinic acid, myo-inositol, folic acid dihydrate, acetylcarnitine, cyanocobalamin, methylprednisolone, methylprednisolone aceponate (MPA), prednisolone and hydrocortisone acetate with the purpose of describing biochemical and industrial processes with its participation.

## EXPERIMENTAL

Vitamins and hormones were purchased from Fluka. For phases identification, an X-ray diffraction patterns of the tested substances were recorded on a Shimadzu X-ray diffractometer XRD-6000 in the  $2\theta$  range from  $5^\circ$  to  $60^\circ$ . The X-ray data and certificates led us to conclude that the samples studied were an individual crystalline compounds.

To measure the heat capacity of the studied substances in the range from 5 to 350 K a BKT-3.0 automatic precision adiabatic vacuum calorimeter with discrete heating was used. The calorimeter design and the operation procedure were described earlier [1]. An isoperibol bomb calorimeter described previously [2] was used for the measurements of energies of combustion of the test substances. For complete combustion of samples we used paraffin and benzoic acid as an auxiliary substance.

## RESULTS AND DISCUSSION

The heat capacities measurements of the B<sub>2</sub>, B<sub>3</sub>, B<sub>8</sub>, B<sub>9</sub>, B<sub>11</sub>, B<sub>12</sub>, methylprednisolone and methylprednisolone aceponate (MPA) were carried out between 5 and 350 K. The experimental points of the heat capacities were fitted by means of the least-squares method and polynomial equations of versus temperature have been obtained.

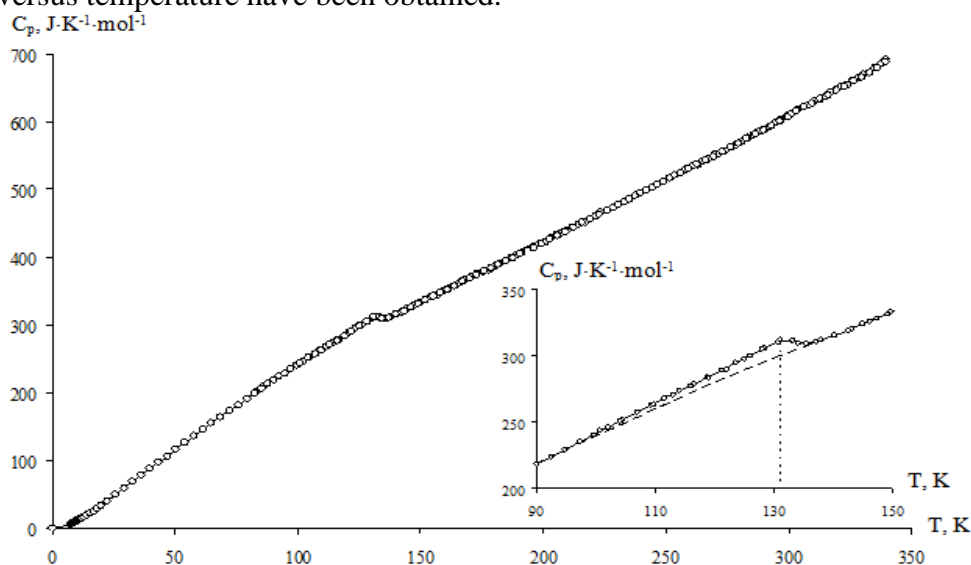


**Figure 1.** Temperature dependence of heat capacity of methylprednisolone aceponate.

The heat capacity for all substances except MPA gradually increases with rising temperature and does not show any peculiarities. The heat capacity curve of the MPA exhibits a bending in the range from 102 to 140 K (Fig. 1). The transition temperature interval was determined graphically on the heat

capacity curve. Using the method of single crystal X-ray diffraction, it was established that the phase transition at  $T = 131$  K is accompanied by an ordering of MPA molecules along the crystallographic direction [010]. In this case, the orientation of the methyl groups C54, C27 and C81 is chaotic, and the translational symmetry disappears. The standard enthalpy of phase transition is  $\Delta_{tr}H^\circ = 220 \pm 2$  J mol<sup>-1</sup>.

The experimental data were used to calculate standard thermodynamic functions, namely the heat capacity, enthalpy  $H^\circ(T) - H^\circ(0)$ , entropy  $S^\circ(T) - S^\circ(0)$  and Gibbs energy  $G^\circ(T) - H^\circ(0)$ , for the range from 0 to 350 K. The standard entropies of formation  $\Delta_f S^\circ$  of the compounds under study at 298.15 K were calculated from the absolute entropy of the compounds and the corresponding simple substances.

**Table 1.** Thermodynamic characteristics of formation of biologically active substances.

Compound	$-\Delta_f H^\circ(298)$ (kJ/mol)	$-\Delta_f S^\circ(298)$ (J/(mol·K))	$-\Delta_f G^\circ(298)$ (kJ/mol)
Riboflavin	$1432 \pm 13$	$1961 \pm 3$	$847 \pm 14$
Nicotinic acid	$344.9 \pm 0.9$ [3]	$503 \pm 3$	$195 \pm 2$
Myo-inositol	$1329.3 \pm 2.3$	$1232.5 \pm 3.5$	$962 \pm 3$
Folic acid dihydrate	$1821.0 \pm 5.7$	$2515.5 \pm 9.5$	$1071 \pm 6$
Acetylcarnitine	$756.2 \pm 2.5$	$1182.5 \pm 3.5$	$403.5 \pm 3$
Cyanocobalamin	$5017 \pm 15$	$7281 \pm 5$	$2846 \pm 15$
Methylprednisolone	$1045.8 \pm 7.3$	$2141 \pm 11$	$407 \pm 8$
Methylprednisolone aceponate	$1465.3 \pm 9.8$	$2592.9 \pm 13.7$	$692 \pm 10$
Prednisolone	$1020.6 \pm 7.6$	-	-
Hydrocortisone acetate	$1307.0 \pm 11.6$	-	-

The energy of combustion of the B<sub>2</sub>, B<sub>8</sub>, B<sub>9</sub>, B<sub>11</sub>, B<sub>12</sub>, methylprednisolone, MPA, prednisolone and hydrocortisone acetate were measured in a calorimeter with a static bomb and an isothermal shield at 298.15 K. They were used to obtain the standard molar enthalpy of combustion  $\Delta_c H^\circ$  and the standard molar enthalpies of formation  $\Delta_f H^\circ$  (1) of the test compounds in the crystalline state.

$$\Delta_f H^\circ(T, C_a H_b O_c, cr) = a \cdot \Delta_f H^\circ(T, CO_2, g) + b/2 \cdot \Delta_f H^\circ(T, H_2O, l) - \Delta_c H^\circ(T) \quad (1)$$

Received values of standard enthalpies and entropies of formation were used to calculate the standard Gibbs function of formation  $\Delta_f G^\circ$  at 298 K by Gibbs–Helmholtz equation. All standard thermodynamic formation functions of the test compounds are collected in Table 1.

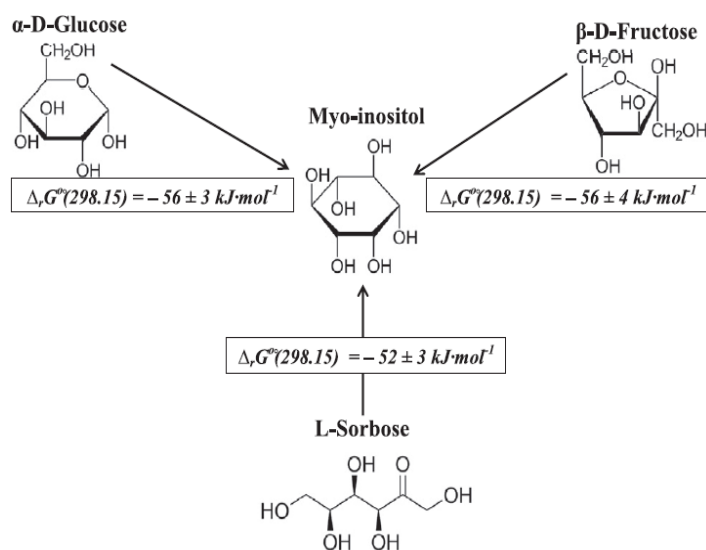


**Figure 2.** Scheme of myo-inositol synthesis. The standard thermodynamic functions can be used for optimization of methods of synthesis, as well as for validation of theoretical and empirical methods for prediction of thermodynamic properties. As an example, we analysed the reactions of myo-inositol synthesis from carbohydrates (Fig. 2). It turns out that the reactions are thermodynamically allowed regardless of natural carbohydrate structure; therefore this is one of the most probable ways of synthesis of this vitamin-like compound in living organisms.

## CONCLUSION

The general aim of these investigations was to report the results of the thermodynamic study of B vitamins and steroid hormones. The heat capacities of studied substance are measured over a wide temperature range from, the thermodynamic functions were calculated. Thermochemical parameters of formation are determined by combining the data obtained by using combustion calorimetry and heat capacity measurements.

## Acknowledgement

The work was performed with the financial support of the Russian Foundation of Basic Research (Project Number 16-03-00288).

## REFERENCES

- [1] A.V. Knyazev, V.N. Emel'yanenko, A.S. Shipilova, E.V. Gusarova, M.I. Lelet, S.S. Knyazeva, *J. Chem. Thermodynamics*, 2018, 116, 76–84.
- [2] A.V. Knyazev, V.N. Emel'yanenko, N.N. Smirnova, A.S. Shipilova, A.V. Markin, E.V. Gusarova, S.S. Knyazeva, S.P. Verevkin, *J. Chem. Thermodynamics*, 2016, 103, 244–248.
- [3] J. Bickerton, G. Pilcher, *J. Chem. Thermodyn.*, 1984, 16, 373-378.

## INFLUENCE OF NICKEL TO THE COPPER-SULPHIDE INTERACTION: 3D COMPUTER MODEL OF THE Ni-Cu-NiS-Cu<sub>2</sub>S SUBSYSTEM T-x-y DIAGRAM

V. Lutsyk<sup>1,2</sup>, V. Vorob'eva<sup>1</sup> and A. Zelenaya<sup>1</sup>

<sup>1</sup>*Institute of Physical Materials Science,  
Sakhyanova St. 6, 670047 Ulan-Ude, Russia (vluts@ipms.bscnet.ru)*  
<sup>2</sup>*Buryat State University, Smolina St. 24a, 670000 Ulan-Ude, Russia*

### ABSTRACT

The three-dimensional computer model of the Ni-Cu-NiS-Cu<sub>2</sub>S subsystem T-x-y diagram is represented. It is shown that the liquid immiscibility in the subsystem Cu-Cu<sub>2</sub>S is transformed in the ternary system with Ni into the small region of immiscibility inside the Cu<sub>2</sub>S liquidus field.

### INTRODUCTION

The investigation of the Ni-Cu-S system is executed within the framework of the project<sup>1</sup>, directed toward a comprehensive study of the 5-component Fe-Ni-Co-Cu-S system and all forming it ternary and quaternary systems. The study includes the experimental investigation of primary crystallization processes and, as a result, design of liquidus and solidus (hyper)surfaces with subsequent assembling of 3-dimensional (3D) and 4-dimensional (4D) computer models of T-x-y and T-x-y-z diagrams. (The program Phase Diagrams Designer is used for these purposes [1-5]).

All ten binary systems are well studied and reference books data of their state diagrams can be confidently used [6, 7].

Design of T-x-y diagram 3D model is fulfilled into several steps [8]: 1) the scheme of uni- and invariant states (UIS) in the table form (Table 1); 2) UIS-scheme in the 3D form as the templates of ruled surfaces and planes, corresponding to the complexes of invariant transformations; 3) the construction of T-x-y prototype, including liquidus, solidus, solvus, etc); 4) input of experimental values of concentrations and temperatures of the base points and the correction of the curvature of unruled surfaces to transfer the prototype into the real system phase diagram 3D model.

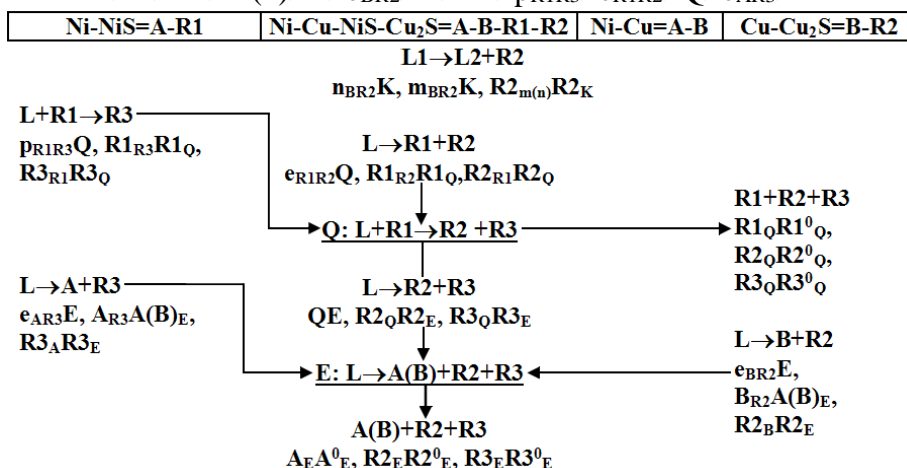
---

<sup>1</sup> Russian Foundation for Basic Research, the project 17-08-00875-a "Assembling of computer 4D models of T-x-y-z diagrams, forming the quinary Fe-Ni-Cu-Co-S system, for the modernization of technological processes of nickel, cobalt and copper production"



$L1 \rightarrow L2 + Cu_2S$ . Therefore the basic experimental work was directed on the determination of type and dimension of the liquid immiscibility region. In contrast to the systems with iron [1] and cobalt [10], the univariant monotectic transformation occurs in the case with nickel. The region of immiscibility is small, and the cupola of immiscibility is located in the liquidus field of the copper sulfide. The remaining part of the T-x-y diagram is simple and includes invariant reactions Q (724°C):  $L + NiS \rightarrow Cu_2S + Ni_3S_2$  and E (585°C):  $L \rightarrow Ni + Cu_2S + Ni_3S_2$ .

**Table 1.** Scheme of uni- and invariant states of the subsystem Ni-Cu-NiS-Cu<sub>2</sub>S=A-B-R1-R2 (Figure 1),  $k > A > R2 > m(n) > B > e_{BR2} > K > R1 > p_{R1R3} > e_{R1R2} > Q > e_{AR3} > E^*$



\* Ni=A, Cu=B, NiS=R1, Cu<sub>2</sub>S=R2, Ni<sub>3</sub>S<sub>2</sub>=R3

### 3D COMPUTER MODEL

Earlier the reference book of computer models of T-x-y and T-x-y-z diagrams of the basic topological types has been created. It includes more than 200 3D models of T-x-y and 7 4D models of T-x-y-z diagrams. Each computer model is the prototype of corresponding topological type phase diagram [11]. In the case with the Ni-Cu-S T-x-y diagram the construction of its 3D model included the templates of the system with the binary incongruently melting compound and the system with the univariant monotectic immiscibility. The 3D model has been constructed on the base of experimental liquidus and solidus surfaces [9] and it consists of the immiscibility cupola, 4 liquidus, 4 solidus, 10 solvus surfaces, 18 ruled surfaces and 2 planes or complexes, corresponding to reactions Q и E (the lower border of the model is the temperature 575°C) (Figure 1).

## RESULTS AND DISCUSSION

The 3D computer model of the Ni-Cu-NiS-Cu<sub>2</sub>S subsystem T-x-y diagram is designed on the base of the experimental liquidus and solidus surfaces x-y projections. It consists of 45 surfaces and 22 phase regions and makes it possible to visualize all its surfaces and phase regions, to construct any isopleths and isothermal sections, to understand the crystallization processes and to calculate the mass balances of the coexisting phases.

## CONCLUSION

The representation of the experimental-calculation results in the form of the 3D model is most preferable both as the accessibility of data and their using for understanding of crystallization processes.

### *Acknowledgements*

This work has been performed under the program of fundamental research SB RAS (project 0336-2016-0006) and was partially supported by the Russian Foundation for Basic Research (project 17-08-00875).

## REFERENCES

- [1] V. I. Lutsyk, V. P. Vorob'eva and A. M. Zyryanov, *Metal. & Mater. Eng. Cong. of South-East Europe*, Belgrade, Serbia, 2015, 125-129.
- [2] V. I. Lutsyk and V. P. Vorob'eva, *13<sup>th</sup> Intern. Conf. on Fundamental and Applied Aspects of Phys. Chem.*, Belgrade, Serbia, 2016, **2**, 779-782.
- [3] V. I. Lutsyk and V. P. Vorob'eva, *49<sup>th</sup> Intern. October Conf. on Mining and Metallurgy*, Bor, Serbia, 2017, 436-439.
- [4] M. D. Parfenova, V. P. Vorob'eva and V. I. Lutsyk, *4<sup>th</sup> Intern. Student Conf. on Technical Sciences*, Bor, Serbia, 2017, 16.
- [5] V. I. Lutsyk and V. P. Vorob'eva, *Rus. J. Phys. Chem.*, 2017, **91**, 2593-2599.
- [6] *Binary Alloy Phase Diagrams*. Editor-in-Chief Thaddeus B. Massalski. American Society for Metals, 1986, V. 1; V. 2.
- [7] *State Diagrams of Binary Metal Systems*, V. 2 / Editor-in-Chief N. P. Lyakishev, Moscow, Mashinostroyenie, 1997 (In Russian).
- [8] V. I. Lutsyk and V. P. Vorob'eva, *Therm. Anal. Calorim.*, 2010, **101**, 25-31.
- [9] R. V. Starykh, S. I. Sineva and S. B. Zakhryapin, *Rus. Metallurgy (Metally)*. 2010. 448-455.
- [10] M. O. Ilatovskaya, R. V. Starykh and S. I. Sinyova, *Metal. & Mater. Trans. B*, 2014, **45B**, 1757-1768.
- [11] V. I. Lutsyk, V. P. Vorob'eva and A. E. Zelenaya, [Solid State Phenomena](#), 2015, **230**, 51-54.

***B – Spectroscopy, Molecular Structure,  
Physical Chemistry of Plasma***



## **HAND-HELD RAMAN, MID-INFRARED AND NEAR-INFRARED SPECTROMETERS: STATE-OF-THE-ART INSTRUMENTATION AND NOVEL APPLICATIONS**

H. W. Siesler

*University of Duisburg-Essen, Department of Chemistry, Schützenbahn 70,  
D 45117 Essen, Germany (hw.siesler@uni-due.de)*

### **ABSTRACT**

Recently, miniaturization of Raman, mid-infrared (MIR) and near-infrared (NIR) spectrometers has made substantial progress and marketing companies predict this segment of instrumentation a significant growth rate within the next few years. This increase will be based on a wider adoption of spectrometers for in-the-field testing, on-site measurements and every-day-life consumer applications. The reduction in size, however, must not lead to compromises in measurement performance and the handheld instrumentation will only have a real impact on quality control if Raman, MIR and NIR spectra of comparable quality to laboratory spectrometers can be obtained. The communication will shortly cover the building principles of typical instruments and will then discuss their applications to selected analytical problems in order to demonstrate the advancement in this field of research.

### **INTRODUCTION**

Miniaturization of vibrational spectrometers has started approximately two decades ago, but only within the last few years **real hand-held** Raman, MIR and NIR scanning spectrometers have become commercially available. While the majority of Raman and MIR spectrometers are still in the >1kg range the reduction of weight for NIR spectrometers has advanced down to the 100 g level. Furthermore, while Raman and MIR hand-held spectrometers are still in the price range of several ten thousand US\$ miniaturized NIR systems have recently reached the <1000 US\$ level.

The present communication will separately discuss instrumental features of novel hand-held Raman, MIR and NIR spectrometers before the results of selected qualitative and quantitative case studies ranging from pharmaceutical to polymer analysis via environmental and geological investigations to food authentication and food scanning will be presented and evaluated in terms of their suitability for on-site and in-the-field measurements.

Finally, the important issue of spectra format transfer will be described so that calibration models (PLS, PCA) developed with the spectra of high-end

laboratory spectrometers can be further utilized with spectra measured in the format of a hand-held spectrometer by applying a novel transfer algorithm. Thus, the necessity to prepare completely new calibration samples and the effort required to develop calibration models when changing hardware platforms is minimized.

### INSTRUMENTATION

While presently only two hand-held FT-IR spectrometers that can be operated in the ATR (attenuated total reflection), external reflection and diffuse reflection modes are available on the market, a broad range of miniaturized Raman systems with different excitation sources and specific operational features is offered. In Figs. 1 and 2 the FT-IR and selected Raman spectrometers, respectively, are shown.

**a****b**

**Figure 1.** Two miniaturized FT-IR spectrometers presently available on the market (a: Agilent 4300 hand-held FT-IR; b: Thermo Fisher Scientific hand-held FT-IR).

**a****b****c****d****e**

**Figure 2.** Hand-held Raman spectrometers based on different excitation sources and operational features (a: Thermo Fisher Scientific, b: RIGAKU Raman Technologies, c: Bruker Optik, d: Metrohm, e: B&W TEK).

Contrary to Raman and MIR spectroscopy miniaturization has been much further driven for NIR spectrometers. The recent progress in miniaturization that has taken advantage of new micro-technologies such as MEMS (Micro-

Electro-Mechanical Systems), MOEMS (Micro-Opto-Electro-Mechanical Systems), micro-mirror arrays or LVFs (Linear Variable Filters) has led to a drastic reduction of spectrometer-size (the weight of the spectrometers discussed in this communication varies between 100 – 200 g) while allowing good performance due to the high-precision implementation of important elements in the final device. High-volume manufacturability will further reduce costs and thereby contribute to a broader dissemination of such instruments for every-day-life applications. In what follows the specific instrumental features of the four hand-held NIR spectrometers used for the presented work will be shortly outlined.

Based on the type of detector, the hand-held NIR spectrometers can be classified in the two categories of array-detector and single-detector instruments. Probably the first commercial, real hand-held NIR spectro-meter (VIAVI MicroNIR 1700 (formerly JDSU), Santa Rosa, CA, USA) has an array detector that covers the wavelength range from 908 - 1676 nm and uses an LVF as monochromator. It has so far been used for a multiplicity of applications ranging from authentication of seafood and determination of food nutrients to the analysis of hydrocarbon contaminants in soil and authentication and quantitative determination of pharmaceutical drugs. However, compared to an array detector the price for a single detector is much lower and in an attempt to further reduce the hardware costs, new developments focused on systems with single detectors. Thus, the DLP NIRscan Nano EVM (Dallas, TX, USA), for example, is based on Texas Instruments's digital micromirror device (DMD<sup>TM</sup>) in combination with a grating and a single-element detector and covers the wavelength range from 900 - 1701 nm. Very recently a MEMS-based FT-NIR instrument, that contains a single-chip Michelson interferometer with a monolithic opto-electro-mechanical structure, has been introduced by Si-Ware Systems (Cairo, Egypt). Contrary to most of the other handheld spectrometers this instrument can scan Fourier-Transform NIR spectra over the extended range from 1298 - 2606 nm. Finally, Spectral Engines (Helsinki, Finland) developed miniaturized NIR spectrometers that are based on a tunable Fabry-Perot interferometer. In order to cover the NIR wavelength region 1350 - 2450 nm, however, the purchase of four spectrometers is required. For the present communication the NR 2.0-W type with a wavelength range of 1550 – 1950 nm was used.

The schematic principles of the monochromator designs of the described NIR spectrometers are summarized in Fig. 3.

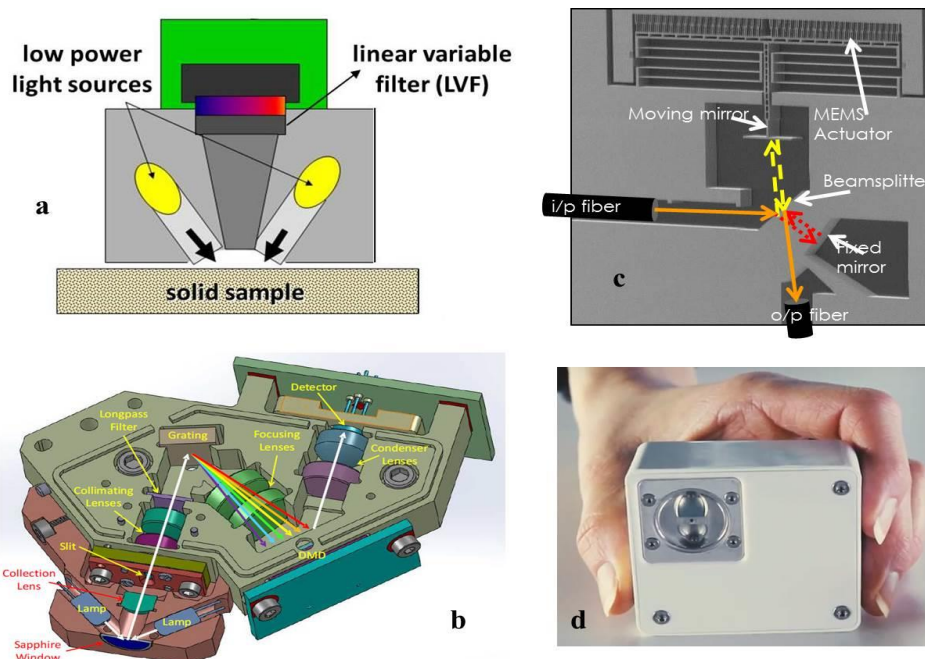


**Figure 3.** Hand-held NIR spectrometers based on different monochromator principles (a: VIAVI MicroNIR 1700, linear variable filter; b: DLP NIRscan Nano EVM with Texas Instruments's digital micromirror device (DMD™); c: Si-Ware Systems, MEMS-based FT-NIR spectrometer; d: Spectral Engines NIR spectrometer with tunable Fabry-Perot interferometer).

## APPLICATIONS

To demonstrate the potential of handheld vibrational spectrometers only a few application examples will be presented here. Thus, Raman spectroscopy has proved primarily valuable for the characterization of inorganic materials. In Fig. 4 the non-invasive discrimination of the different crystal forms of  $\text{TiO}_2$  (rutile and anatase) through a glass vial is demonstrated.

In another feasibility study the change of the ionic structure of sulfuric acid as a function of concentration has been demonstrated by Raman spectra recorded with a hand-held instrument (RIGAKU Raman Technologies). The spectra measured of 96% (concentrated), 80% and 20% sulfuric acid through amber glass are shown in Fig. 5. These differences in ionization are an important issue regarding toxicity for the use of diluted sulfuric acid in cleaning operations of aluminum surfaces.

The application of hand-held FT-IR spectroscopy in the ATR mode is recommended primarily for organic materials that provide good contact with

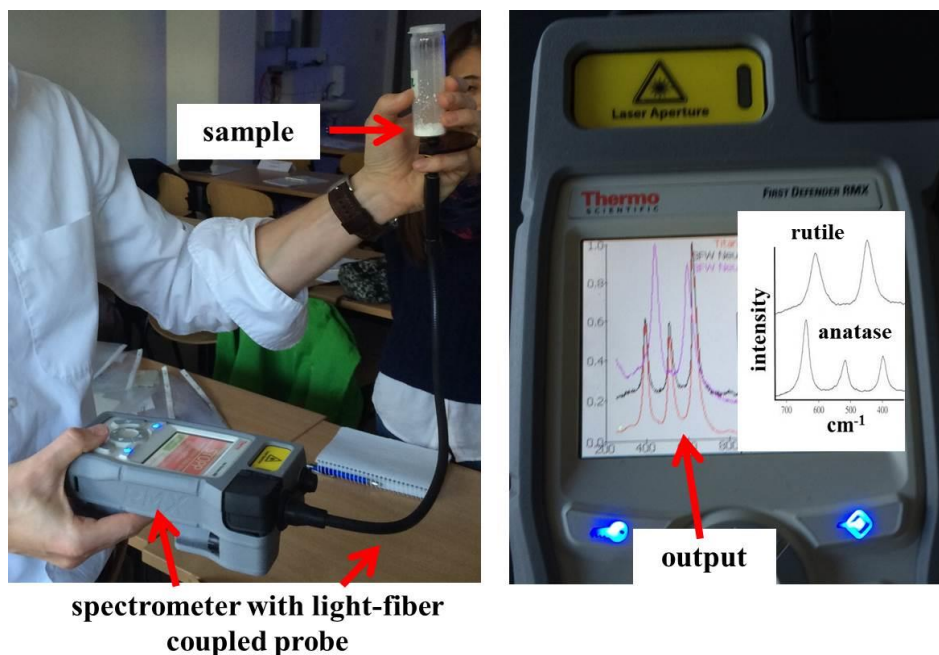


**Figure 4.** Discrimination of rutile and anatase by hand-held Raman spectroscopy (Thermo Fisher Scientific, 785 nm excitation).

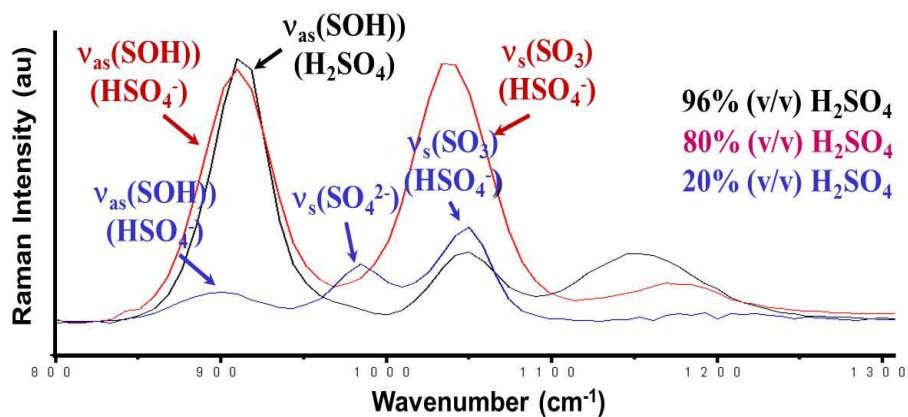


**Figure 5.** Raman spectra of sulfuric acid at different concentration levels measured with the hand-held instrument of RIGAKU Raman Technologies (1064 nm excitation).

the diamond reflection element. Despite its rather difficult sample handling an interesting practical application was the analysis of bitumen. For road construction work bitumen is modified with different polymers in order to adjust the rheological and adhesional properties (polymer modified bitumen, PmB). The rapid quantitative analysis of this admixture is an important quality control issue and the question that arises is whether handheld FT-IR/ATR spectroscopy is applicable for this purpose and could at the end of the day be used for “on-the-road“ analysis. In an extensive feasibility study this issue was addressed by developing calibration models based on the FT-IR/ATR spectra (Fig. 6) of bitumen samples modified by different admixtures of polypropylene/maleicanhydride and successfully predicting test samples that were not contained in the calibration model.

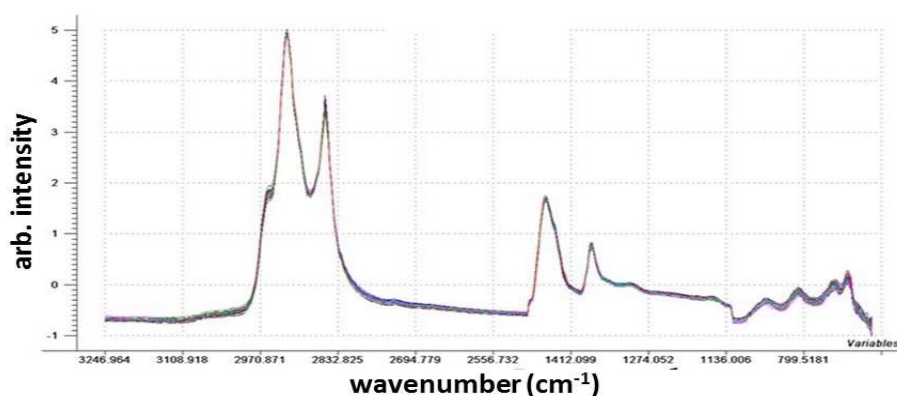


**Figure 6.** Calibration spectra of polymer-modified (PPMA) bitumen samples measured with a hand-held FT-IR spectrometer (Thermo Fisher Scientific, 60 scans,  $4\text{ cm}^{-1}$  spectral resolution) after wavenumber selection ( $3250\text{--}2500\text{ cm}^{-1}$ ,  $1490\text{--}1130\text{ cm}^{-1}$ ,  $930\text{--}680\text{ cm}^{-1}$ ) and SNV transformation.

Due to the advanced level of miniaturization by far the most flexible technique for on-site and in-the-field measurements is NIR spectroscopy and two examples shall demonstrate its potential for every-day-life use. In the first case hand-held NIR spectroscopy was used for the authentication of a silk carpet. In cooperation with an expert who provided the relevant test materials, carpets that had been knotted from mercerized wool and genuine silk, respectively, were readily discriminated based on rapid visual inspection of their NIR spectra only (Fig. 7). Mercerization of wool lends the final product a gloss that could be exploited by an untrustworthy businessman to sell such a carpet as a silk product for an unrealistic prize to a credulous customer.

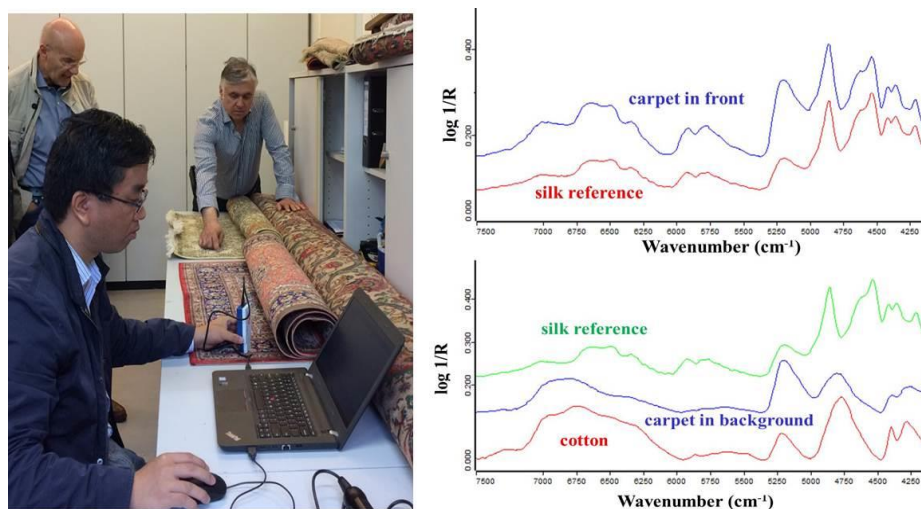


**Figure 7.** Discrimination of a genuine silk carpet (front) from a carpet woven from mercerized cotton (background) by hand-held NIR spectroscopy (the measurements were performed with a Si-Ware Systems FT-NIR spectrometer).

Finally, an application example from food science is outlined in some detail. Thus, it has been demonstrated that in the future handheld NIR spectroscopy may be utilized to rapidly determine nutritional parameters of every-day-life food. At this point, however, a word of caution is necessary: contrary to the approach of direct-to-consumer companies that advertise their “food scanners” with “cloud evaluation of big data” and – in my opinion - unrealistic claims, predictions with an acceptable accuracy can only be achieved if calibrations based on reliable spectral data are developed.

As a starting project in this complex field of research the analysis of the nutritional parameters of pasta/sauce mixtures have been chosen. For this purpose more than 700 plates containing five different combinations of a certain pasta/sauce-type blend (ranging from 0% to 100% sauce addition) were investigated. Each pasta/sauce mixture was prepared “ready-to-eat” on a plate and NIR spectra were recorded in five different positions (to compensate inevitable heterogeneities) with a hand-held NIR spectrometer (Fig. 8). Prior to the development of the calibration models the five spectra were averaged, pretreated by extended multiplicative scatter correction (EMSC) and based on the known nutritional parameters of the utilized pastas and sauce ingredients calibration models were developed for energy, fat, protein, carbohydrates, sugar and fibers.

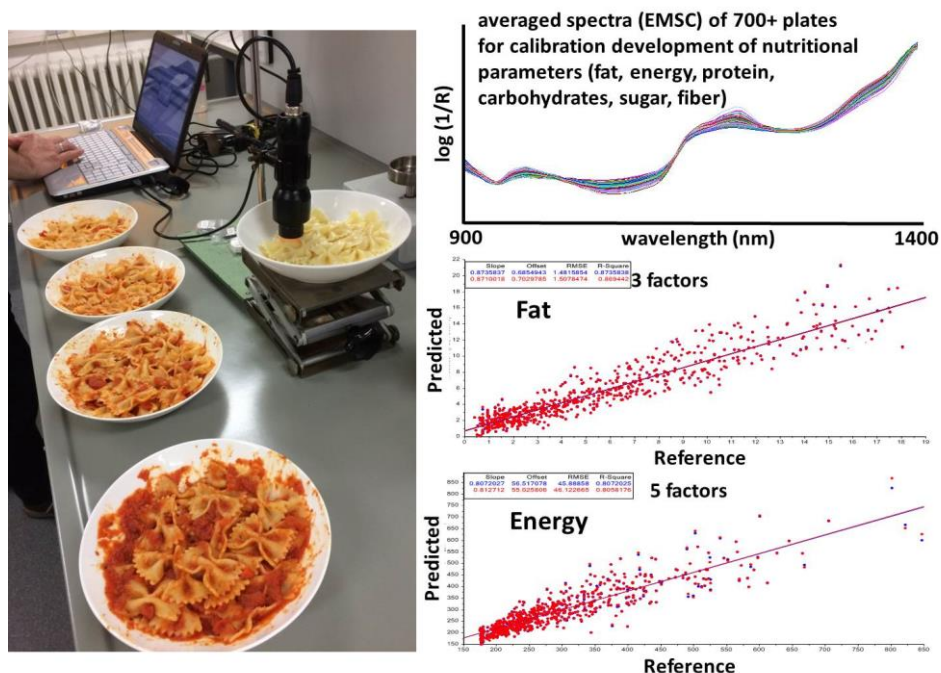


**Figure 8.** NIR spectra acquisition (VIAVI MicroNIR 1700) of pasta/sauce mixtures and exemplary calibration models for fat and energy.

Contrary to what some of the above mentioned direct-to-consumer companies claim, acceptable calibrations could – at best - be achieved for fat, energy and protein only. Due to the similar structural characteristics of carbohydrates, sugar and fibers no reliable calibrations were obtained for these parameters.

## CONCLUSIONS

State-of-the-art hand-held Raman, MIR and NIR spectrometers showed good performance for a multiplicity of case studies.

Generally, hand-held instruments have launched vibrational spectroscopy into a new era of on-site analysis.

New instrumental developments will further promote the use of hand-held spectrometers by a non-expert user community.

---

**DEVELOPMENT OF A CONTINUOUSLY TUNABLE  
MID-INFRARED SOURCE AND ITS APPLICATION IN  
LASER ASSISTED AERODYNAMIC ISOTOPE  
SEPARATION**

D. J. Biswas

*Bhabha Atomic Research Centre, Laser & Plasma Technology Division,  
Mumbai. (dhruba8biswas@gmail.com)*

**ABSTRACT**

The increased enrichment factor when conventional aerodynamic separation process is combined with selective laser excitation has, of late, led to a resurgence of interest in molecular laser isotope separation process. As a single step of vibrational excitation of the appropriate isotopic species by an Infrared laser suffices here, the requirement on the intensity of the laser is much less stringent as compared to the other two extensively researched laser based processes viz., AVLIS and MLIS. Besides presenting a brief overview of molecular laser isotope separation in general and the laser assisted aerodynamic process in particular, this talk will also dwell on our work pertaining to the development of a continuously tunable coherent mid infrared source and its application in isotope selective absorption studies in a molecular jet, an essential precursor before moving on to the separation experiments.

## EARLY STAGE DIAGNOSIS OF TUMORS AND DISEASES BY NANOSPECTROSCOPY

A. Cricenti and M. Luce

*Istituto di Struttura della Materia (ISM-CNR), via del Fosso del Cavaliere  
100, Rome, 00133, Italy. (antonio.cricenti@ism.cnr.it)*

### ABSTRACT

Carcinomas are complex biochemical systems and in the past their diagnosis was based on morphological differences between malignant cells and their benign counterpart. Recently the paradigm has changed and great interest is focused now on the biochemical profile of tumours in view of the availability of new drugs that specifically target neoplastic cells. This new paradigm requires biochemical analysis of each tumour in order to establish the correct personalized oncological “target therapy”. Understanding the mechanism of molecular alterations of a specific tumour is a critical issue to prognosticate its behaviour and to predict the response to personalized therapy.

Raman spectroscopy (RS) is a non-invasive optical label-free tool increasingly used to get molecular fingerprints of biological tissues. It is able to provide bioanalytical information on any molecule with high specificity. Technological advances over the last decade have created a new and faster Raman imaging microscope instrument, providing morphological tissue investigation of large areas, coupled with point-by-point spectral analysis of biochemical composition. This option is important not only for discrimination between healthy and pathological tissues, but especially for pre-cancerous tissue state earlier detection and understanding. Raman mapping of biological tissues have shown that the microscope can operate at a few micron resolution, in order to distinguish between healthy and malignant tissues [1].

The potential of IR spectroscopy to characterise cancerous tissues has long been recognised and studies of various cancers by many groups have established that regions of malignant tissue can be easily identified on the basis of its IR spectrum. Early diagnosis of cancer requires an instrument providing specific chemical images at sub-cellular level and the development of diagnostic imaging. A SNOM meets these requirements provided that it can be coupled with an appropriate infrared light source, that can be based on Free Electron Laser, femtosecond laser or quantum cascade laser [2].

We present Raman and Infrared Scanning Near-field Optical Microscopy (SNOM) in their spectroscopic mode, that is related to the local chemical composition and, thus, to the biological properties of the sample, for tissue

imaging and early cancer diagnostics. Applications in the case of Oesophagous [3] and Cervical Cancer [4] as well as in the progression of Amyotrophic Lateral Sclerosis (ALS) will be presented.

#### **REFERENCES**

- [1] M. Çulha *Bioanalysis*, 2015, 7, 2813-2824.
- [2] A. Cricenti, M. Luce, N. H. Tolk, G. Margaritondo, *Nanosci. Nanotechnol. Lett.*, 2011, 3, 913-921.
- [3] A. D. Smith et al., *Applied Physics Letters*, 2013, 102, 053701.
- [4] D. E. Halliwell et al., *Scientific Reports*, 2016, 6, 29494.

## LIMITATIONS OF BARRIER HEIGHT BENCHMARKS

E.N.Brothers

*Department of Chemistry, Texas A&M University at Qatar, Doha, Qatar*  
[ed.brothers@qatar.tamu.edu](mailto:ed.brothers@qatar.tamu.edu)

### ABSTRACT

The efficacy of a density functional can only be determined via benchmarking, i.e. applying the density functional to the prediction of a chemical property of interest. One critical property is barrier heights, as correct prediction of reaction barriers means accurate modelling of chemical kinetics. This benchmarking typically done at frozen geometries, meaning a geometry developed at a single high level of theory, for a variety of reasons, including computational efficiency, and this has been shown to be an excellent approximation for functionals that perform well for modeling transition states. Put another way functionals with small errors in barrier heights typically have small errors in transition state geometries, so fixed geometries are adequate for functional error ranking at the low error end of the scale. However, for functionals with larger errors, this is a poor approximation, and it is shown here that for certain functionals the errors either increase dramatically or the transition state modeling fails completely if full geometry optimization is performed, i.e. the poor functionals are actually worse than the benchmarking studies indicate. We also show, using energy surfaces, that for some reactions commonly used in benchmarking sets, the barrier disappears with some functionals, making numerical values for error inappropriate.

## OPTICAL EMISSION STUDY OF CARBON PLASMA INDUCED BY TEA CO<sub>2</sub> LASER

M.M. Kuzmanović<sup>1</sup>, D.P. Ranković<sup>1</sup>, J.J. Savović<sup>2</sup>, M.D. Momčilović<sup>2</sup>, J. Ciganović<sup>2</sup> and M. Trtica<sup>2</sup>

<sup>1</sup> *University of Belgrade, Faculty of Physical Chemistry, Studentski Trg 12-16, 11000 Belgrade, Serbia. (miroslav@ffh.bg.ac.rs)*

<sup>2</sup> *University of Belgrade, INN Vinca, Mike Petrovića Alasa 12-14, 11001 Belgrade, Serbia.*

### ABSTRACT

Optical emission spectroscopy studies of plasmas induced in air at atmospheric pressure by a Transversely Excited Atmospheric (TEA) CO<sub>2</sub> laser beam on a graphite target are reported. Atomic and single charged ionic lines, with good signal to noise ratio, were observed, as well as C<sub>2</sub> ( $d^3\Pi_g - a^3\Pi_u$ ) Swan and CN ( $B^2\Sigma^+ - X^2\Sigma^+$ ) violet molecular bands system. Analytical applicability of the obtained emission spectra has been considered. Stark profiles and intensity ratios of ionic to atomic lines of carbon were used to estimate the electron number density and ionization temperature. The rotational and vibrational temperatures of C<sub>2</sub> and CN molecules were determined by comparing the measured and simulated spectra.

### INTRODUCTION

Laser induced breakdown spectroscopy (LIBS) is a sample preparation-free measurements technique, favorable for rapid and sensitive analysis of most elements in the periodic table. Interaction of a pulsed nanosecond laser beam with a solid target results in local overheating and ablation of the sample. If the laser fluence is sufficiently high, a hot and dense plasma will be created. Plasma emission spectra are a “spectral signature” of the elements present in a sample which provides information on the chemical composition of the target material. A special advantage of LIBS is an excellent sensitivity even for light elements, and minimal destructiveness of the samples during the analysis.

Besides fundamental interests, applications of laser-induced plasma from a graphite target attract much attention, especially for LIBS, pulsed laser deposition of diamond layers, and synthesis of the carbon nanoparticles. Atomic and molecular emission can give an important insight into the synthesis mechanism and lead to process optimization. Particularly, C<sub>2</sub> and CN spectral bands could be of interest for the detection of the organic

compounds in the atmosphere or the analysis of targeted material, e.g. potentially dangerous agents (pollutants and explosives) [1]. These species can exist at relatively high temperatures, and have very high emission intensities [2].

The analysis of molecular spectral emission is a useful diagnostic method for determining the translational temperature [3]. This method is less experimentally demanding than high resolution spectroscopy needed for measurement of Doppler line profiles. Studies of molecular emission spectra from laser-induced plasma led to the development of new analytical method for rapid isotopic analysis of the samples, Laser Ablation Molecular Isotopic Spectrometry (LAMIS) [4]. LAMIS is based on the fact that molecular isotopologues formed in laser ablation plasma have isotopic spectral shifts that are considerably larger than those in atomic spectra, and therefore the former can be measured with a general purpose spectrometer at atmospheric pressure.

The most frequently used lasers for LIBS are solid-state lasers Nd:YAG and ruby, and excimer gas lasers. However, CO<sub>2</sub> lasers can be very useful for LIBS [5-10] with some unique advantages, like eyesight safety, efficiency, and transparency “window” in the air atmosphere. The aim of the present work was to check the applicability of the carbon plasma generated by a low energy TEA CO<sub>2</sub> pulsed laser, for spectrochemical analysis and plasma diagnostics.

## EXPERIMENTAL

A compact miniature nanosecond IR gas laser device, developed at the Vinca Institute [11], was used to generate the plasma by irradiation of a graphite sample. The laser emit dominantly on one wavelength in the IR region (10.571  $\mu\text{m}$ ) with a low pulse energy (up to 160 mJ), and a repetition rate up to 2 Hz. A laser beam cross section of 0.015  $\text{cm}^2$  provides a maximal fluence and peak intensity of 11.4  $\text{J}/\text{cm}^2$  and 40  $\text{MW}/\text{cm}^2$ , respectively. The initial peak of the laser pulse contains approximately 35 % of the total energy, with the full width at half maximum (FWHM) of 100 ns. The working gas mixture of laser was CO<sub>2</sub>/N<sub>2</sub>/He in vol. ratio of 2 : 2 : 9 respectively.

The created plasma was bright white colored, and expanded up to approximately 10 mm from the target surface. By an achromatic lens, an image (1:1 magnification) of the plasma was projected on the entrance slit of a 2 m Czerny–Turner spectrometer equipped with a reflective diffraction grating. Typical dispersion and FWHM of the instrumental profile were 7 nm/mm and 0.025 nm. Plasma emission spectra were detected by a back thinned Apogee Alta F1007 CCD camera with enhanced spectral sensitivity up to 200 nm, with low dark current signal provided by Peltier coolers. The

CCD chip active area consists of 1024x122 pixels (pixel dimension 12x12  $\mu\text{m}$ ). For the present spectrograph settings, a detector captures wavelength range of about 8.5 nm.

Laser produced plasmas are transient in nature, the characteristic plasma parameters (line and continuum intensities, temperature, particle densities) evolve both in the space and time. In order to enhance the signal to background ratio, time-gated detection is generally used. An alternative approach is application of Time Integrated Space Resolved Laser Induced Plasma Spectroscopy (TISR-LIPS) [12], which has been successfully applied for the investigation of plasmas induced by IR lasers [8-9]. Instead of time resolved detection, time integrated emission signal is recorded at different positions from the target. In this work, TISR-LIPS technique was applied. A spatial resolution was obtained by changing the observed plasma position.

## RESULTS AND DISCUSSION

The character of the emitted spectrum of the created plasma strongly depends on the laser beam focusing conditions. For a laser beam focused onto the surface of a target or behind the target, the emission spectrum of the created plasma contains atom and single charged-ion lines of carbon (C I and C II) and trace element impurities (Ca I, Ca II, Ti I, Ti II, V I, V II, Cu I, Cu II, Si I, Si II). Part of the registered lines and molecular bands are shown in Fig. 1. Lines of the elements with higher ionization energy appeared at high fluences, e.g. calcium lines were recorded at 4.3 J/cm<sup>2</sup>, while carbon lines only at energies higher than 130 mJ (9.3 J/cm<sup>2</sup>).

The obtained spectral lines of metals are narrow, with excellent signal to noise ratio, giving the opportunity for quantitative elemental analysis with a very low limit of detection (LOD). Even when a target was high purity graphite, the obtained spectra could be used for the determination of very low concentrations of Ca impurity (Fig. 1a). For instance, a rough estimate gives LOD lower than 20 ppm for calcium.

Intense and well-resolved molecular bands of C<sub>2</sub> (Swan system) and CN (violet system) were also recorded at pulse energy of 50 mJ or higher. Both of band systems have a good signal to background ratio for  $\Delta v = -1, 0$  and  $+1$  band sequences. On the other hand, at rather high fluences, the detected nonmetal lines were very weak and usually wide, with unfavorable LOD values. Because of that, C<sub>2</sub> and CN bands are found to be more appropriate for the carbon analysis in the solid samples, and also nitrogen analysis in the controlled gas atmosphere. In comparison with the carbon lines, the integral band intensity can give more than one order of magnitude lower LODs.

In general, LIBS is characterized by high shot-to-shot fluctuations of line intensities, thus, the use of internal standard method is always desirable for

improvement of the precision and accuracy. Due to its high intensity and presence in different spectral regions, C<sub>2</sub> and CN bands detected in plasmas of carbon based samples are suitable as an internal standard for the analysis of metal traces. The intensity ratio of analytic line and appropriate band is less dependent on fluctuation of plasma properties and ablation rates.

When the laser beam was focused in front of the target, an air breakdown could be registered. The obtained plasma was hotter, optically thicker, with higher electron number density compared to previously described case. The plasma contained less amounts of the ablated material, and the spectrum was rich in intensive and wide lines, most of the single-charged N, O and C ions. Such plasma is not suitable for spectrochemical analysis; still it can be of interest for other applications, like the remote LIBS monitoring of air pollution.

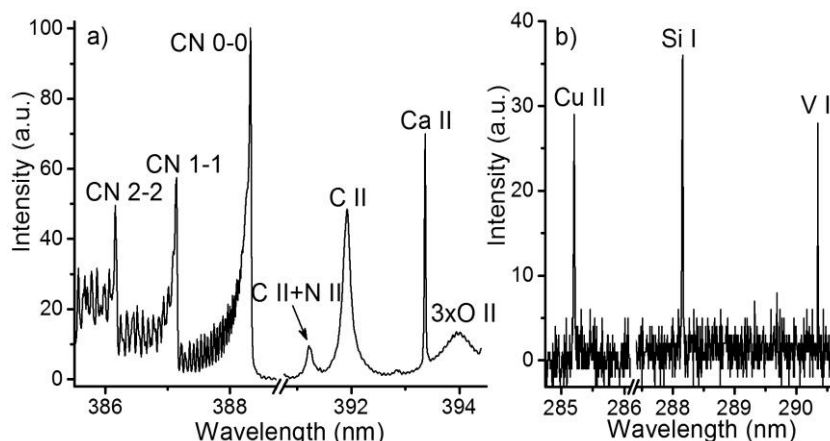


**Figure 1.** Time-integrated LIBS spectra obtained on the graphite sample at the laser pulse energy of 130 mJ. Spectra were taken at 1 mm from the target surface.

The persistent atomic carbon line C I 247.8 nm, and its adjacent single ionized lines C II 250.9 nm, and C II 251.2 nm, are very suitable for diagnostic of the hotter plasma zones in which they appear. Carbon atomic 247.8 nm line has a measurable Stark broadened profile, even at moderate spectral resolution: for electron number density of  $10^{16} \text{ cm}^{-3}$ , and a temperature of 10000 K, its FWHM is 0.0361 nm [13]. An example of the obtained carbon line profiles is given in Fig. 2, together with Hg 253.6 nm line profile obtained from pencil lamp, whose width is very close to the instrumental width. The measured profile is asymmetric toward higher wavelengths, as is typical for the quadratic Stark broadening of the atomic lines. The estimated electron

number density of  $5 \cdot 10^{17} \text{ cm}^{-3}$  confirms the assumption that induced plasma is very dense.

The appearance of carbon ionic lines in the vicinity of 247.8 nm atomic line gives the opportunity for measurement of intensity ratio of the ionic to atomic spectral lines, and evaluation of ionization temperature of the plasma. The spectral closeness of carbon lines enabled simultaneous measurements of line intensities without the need for spectral calibration. The ionization temperature (usually close to the electron temperature) was estimated from the known value of the electron number density and the measured integral intensities of ionic ( $I''$ ) and atomic lines ( $I'$ ), using the following equation [14]:

$$\frac{I''}{I'} = 4.83 \cdot 10^{15} \frac{g'' A'' \lambda' \sqrt{T^3}}{g' A' \lambda'' n_e} e^{-\frac{(E''_{exc} + E_{ion} - \Delta E_{\infty} - E'_{exc}) \cdot 11605}{T}}$$

The approximate ionization temperature was 18000 K. As it can be expected, carbon lines are emitted from the hottest plasma zones.

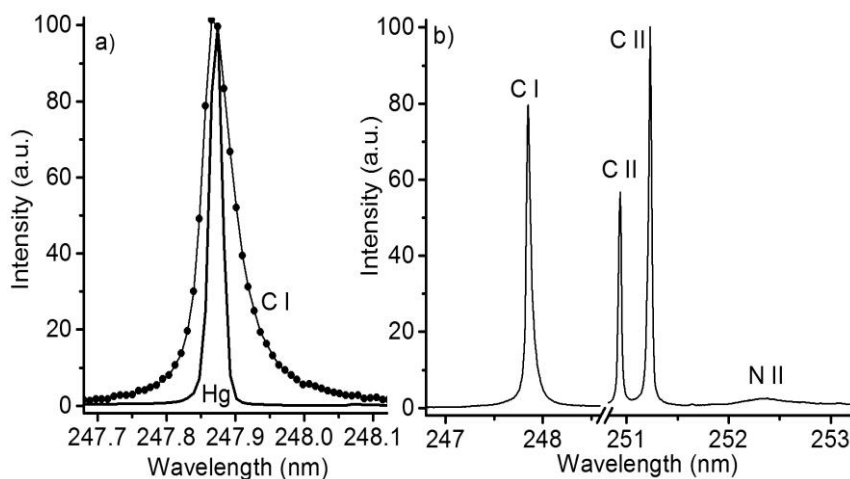


**Figure 2.** a) Line profile of C I 247.8 nm and Hg 253.6 nm line; b) Spectrum of C I 247.8 nm, C II 250.9 nm and C II 251.2 nm spectral lines.

Spectral bands of molecules are very useful for plasma diagnostic because its shape strongly depends on temperature. For the plasmas containing appreciable amount of carbon, CN and C<sub>2</sub> spectral bands can serve for determination of the gas temperature, i.e. heavy particle temperature [3]. The best results are obtained in case the spectral resolution is high enough to provide separation of P and R band components. In that case, the base line of the spectrum can be set precisely, spectral line profiles can be appropriately deconvoluted, and the fine elements of the band contour can be used for the precise assessment of temperature.

Part of the high resolution spectrum of (0-0) and (1-1) bands of the C<sub>2</sub> Swan system is shown in Fig. 3. Spectral intensities are normalized to the intensity values of R branches: their intensities stay constant in relation to the intensity of (0-0) band head.

It is evident from the Fig. 3.a that the normalized spectral intensities of R branch are almost independent of temperature, while the intensities of P branch quickly increase with the temperature [15]. In order to take advantage of this fact, the line profile should be experimentally determined with an accuracy better than 10%. To avoid possible problems with temperature overestimation due to self-absorption (which has a large impact on (0-0) band), it is better to estimate the temperature by fitting the line intensities of P and R branches. In fact, the best way is to use the less intensive part of P components for comparison, because it is obvious from Fig. 3b that these elements also suffer from self-absorption, although to a lesser extent than (0-0) band head. The other reason to avoid scaling of spectra by the band head is its asymmetry, which complicates elimination of a pixelation problem and determination of the true height of the head peak.

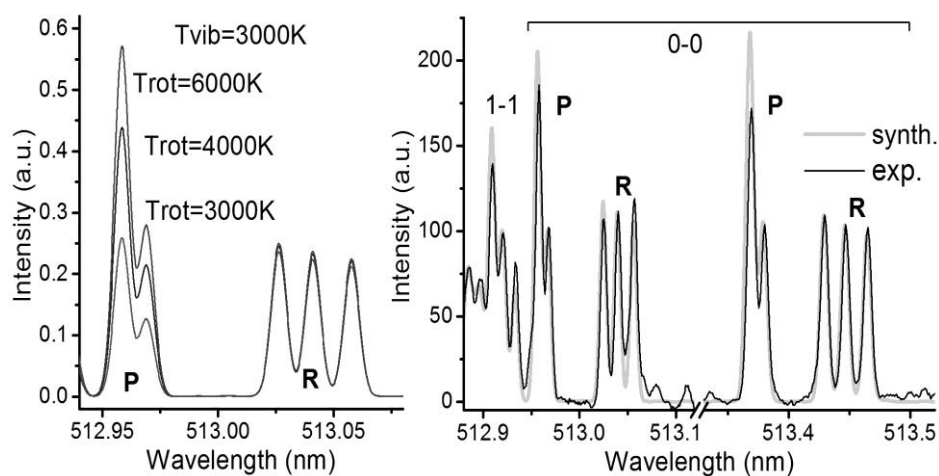


**Figure 3.** Part of synthetic (a), and experimental (b) spectrum of the (0-0) C<sub>2</sub> Swan system. Line profile was Gaussian, with FWHM = 0.0078 nm.

The best agreement between the experimental and synthetic spectrum was obtained for a rotational temperature of 4400 K. The intensity ratio of (1-1) band head and lines of R branches of (0-0) band head is not very sensitive and reliable for determination of vibrational temperature. Anyway, rough estimation gave a vibrational temperature of 3200 K.

The applicability of  $\Delta v = +1$  sequence of CN violet system for determination of the vibrational temperature is demonstrated in Fig. 4. Bands

of this sequence are much less intense than (0-0) band, thus less affected by self-absorption. Despite a favorable circumstance that 3 band heads are situated in a narrow spectral interval (less than 1 nm), the rotational structure of the sequence is not appropriate for estimation of temperature [16].

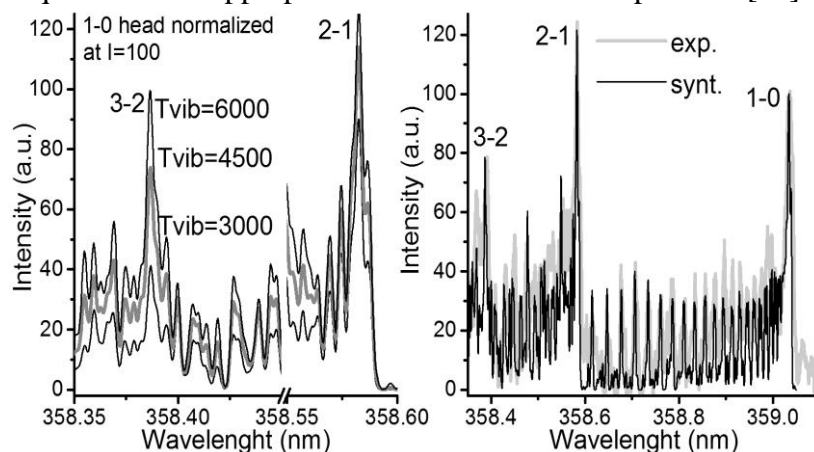


**Figure 4.** Part of synthetic (a) and experimental spectrum (b) of  $\Delta v=+1$  sequence of the CN red system.

The change of relative intensities of band heads allowed relatively precise determination of the vibrational temperature, with the acceptable low impact of the uncertainty of  $T_{rot}$ . By comparison of the experimental and synthetic spectrum (Fig. 4), the vibrational temperature of 4800 K was estimated.

## CONCLUSION

The TISR-LIPS method was used to detect spectral emission of the carbon plasma created by the TEA  $\text{CO}_2$  low energy laser with prolonged pulse duration. The obtained spectra are suitable for direct high sensitivity spectrochemical analysis.

Stark profile of carbon line and the intensity ratio of ionic and atomic lines were used to estimate electron number density and ionization temperature. The obtained values,  $3 \cdot 10^{17} \text{ cm}^{-3}$  and 19000 K, correspond to the hottest plasma zones.

An applicability of  $\text{C}_2$  and CN spectral bands for determination of the rotational and vibrational temperature was discussed in details. By comparing the measured and simulated band spectra temperatures in the range 3200-4400 K, relevant for the cooler parts of plasma, were obtained.

## Acknowledgement

This research was supported by the Ministry of Education, Science and Technological Development of the Republic of Serbia, through the project:

Effects of laser radiation on novel materials in their synthesis, modifications, and analysis (project no. 172019).

### REFERENCES

- [1] J.L. Gottfried, F.C. De Lucia, C.A. Munson, and A.W. Miziolek, *Appl. Spectrosc.*, 2008, 62, 353.
- [2] A. De Giacomo and J. Hermann, *J. Phys. D. Appl. Phys.*, 2017, 50, 183002.
- [3] S. Pellerin, K. Musiol, O. Motret, B. Pokrzywka, and J. Chapelle, *J. Phys. D. Appl. Phys.*, 1996, 29, 2850.
- [4] A.A. Bol'shakov, X. Mao, J. Jain, D.L. McIntyre, and R.E. Russo, *Spectrochim. Acta - Part B At. Spectrosc.*, 2015, 113, 106.
- [5] A.F. Gibson, T.P. Hughes, and C.L.M. Ireland, *J. Phys. D. Appl. Phys.*, 1971, 4, 1527.
- [6] N. Idris, K. Kagawa, F. Sakan, K. Tsuyuki, and S. Miura, *Appl. Spectrosc.*, 2007, 61, 1344.
- [7] J.J. Camacho, L. Díaz, M. Santos, D. Reyman and J.M.L. Poyato, *J. Phys. D: Appl. Phys.*, 2008, 41, 105201.
- [8] M. Momcilovic, M. Kuzmanovic, D. Rankovic, J. Ciganovic, M. Stoiljkovic, J. Savovic, and M. Trtica, *Appl. Spectrosc.*, 2015, 69, 419.
- [9] J. Savovic, M. Stoiljkovic, M. Kuzmanovic, M. Momcilovic, J. Ciganovic, D. Rankovic, S. Zivkovic, and M. Trtica, *Spectrochim. Acta - Part B At. Spectrosc.*, 2016, 118, 127.
- [10] M. Kuzmanovic, M. Momcilovic, J. Ciganovic, D. Rankovic, J. Savovic, D. Milovanovic, M. Stoiljkovic, M.S. Pavlovic, and M. Trtica, *Phys. Scr.*, 2014, T162, 014011.
- [11] M.S. Trtica, B.M. Gakovic, B.B. Radak, and S.S. Miljanic, *Proc. SPIE*, 2002, 4747, 44.
- [12] M.A. Khater, P. van Kampen, J.T. Costello, J.-P. Mosnier, and E.T. Kennedy, *J. Phys. D. Appl. Phys.*, 2000, 33, 2252.
- [13] H.R. Griem, *Spectral Line Broadening by Plasmas*, Academic Press, New York, 1974.
- [14] A.M. Keszler and L. Nemes, *J. Mol. Struct.*, 2004, 211, 695.
- [15] C.M. Western, *J. Quant. Spectrosc. Radiat. Transf.*, 2017, 186, 221.
- [16] J. Luque and D.R. Crosley, *SRI Int. Rep. MP*, 1999, 99, 9.

## EXPERIMENTAL AND THEORETICAL VIBRATIONAL STUDY OF 3-(1-(2-MERCAPTOETHYLAMINO)ETHYLIDENE)-CHROMAN-2,4-DION

E. H. Avdović<sup>1\*</sup>, A. Amić<sup>2</sup>, D. Milenković<sup>3</sup>, V. V. Jevtić<sup>1</sup> and S. R. Trifunović<sup>1</sup>

<sup>1</sup>*University of Kragujevac, Faculty of Science, Department of Chemistry, Radoja Domanovića 12, 34000 Kragujevac, Serbia.*

*([edina.avdovic@pmf.kg.ac.rs](mailto:edina.avdovic@pmf.kg.ac.rs))*

<sup>2</sup>*Department of Biology, The Josip Juraj Strossmayer University, Cara Hadrijana 8a, HR-31000 Osijek, Croatia.*

<sup>3</sup>*Bioengineering Research and Development Center, Prvoslava Stojanovića 6, 34000 Kragujevac, Serbia.*

### ABSTRACT

The infrared (IR) spectroscopy was used in the vibrational spectroscopic analysis of 3-(1-(2-mercaptoethylamino)ethylidene)-chroman-2,4-dion (**L1**) in the range 4000 to 400 cm<sup>-1</sup>, respectively. A combined experimental and theoretical study on vibrational spectra of investigated molecule was employed. Density functional theory was used to assign the peaks in the experimentally obtained vibrational spectrum by the B3LYP-D3BJ functional in combination with the 6-311+G(d,p) basis set implemented in the Gaussian 09 package. The optimized geometry in gas-phase was used to predict the IR spectra. The vibrational peaks of title molecule were assigned on the basis of the PED (Potential Energy Distribution) analysis using the FCART software. The results of the calculations, which were applied to simulated spectra of **L1**, showed an excellent agreement with the experimental spectra.

### INTRODUCTION

Coumarin and its derivatives represent a large group of heterocyclic compounds. Coumarin (2*H*-chromen-2-one) was first isolated by A. Vogel from Tonka beans as early as 1820. Its structure consist of fused benzene and  $\alpha$ -pyrone rings. Coumarin and its derivatives are widely distributed in plants, such as plants that belonging to *Rutaceae*, *Umbelliferae* (*Apiaceae*), *Compositae* (*Asteraceae*), *Leguminosae*, and *Moraceae* families [1]. No coumarins are distributed only in plants, they are also found in products of the metabolism of microorganisms and animals. [1]. In addition to natural sources, a large number of coumarin derivatives are synthesized in

laboratories [1]. Natural and synthetic coumarin derivatives have diverse biological activities such as antibacterial, anticancer, antioxidant, anti-inflammatory, anticoagulant, antifungal activities [2]. Because of their wide biological activity, these compounds have been found application in medicine and pharmacy. IR and UV spectra confirm presence of important functional groups. These compounds typically exhibit a 6-membered  $\alpha,\beta$ -unsaturated lactonic carbonyl absorption (strong) peak at  $\sim 1725\text{ cm}^{-1}$  in their IR spectra. Sometimes a small variation of this peak's position and intensity is due to the presence of different substituents on the coumarin nucleus. Coumarins absorb ultraviolet light at  $\sim 320\text{ nm}$  ( $\log \epsilon \sim 4$ ) [1] due to the  $\alpha, \beta$ -unsaturated- $\delta$ -lactonic carbonyl.

## EXPERIMENTAL

**DFT calculations** - The geometry optimization of **L1** (Fig.1) was performed by using B3LYP functional [3] with empirical D3BJ dispersion corrections [4] and 6-311+G (d, p) basis set as implemented in the Gaussian 09 package [5]. The frequency analysis was performed to determine the nature of the stationary points: equilibrium geometries have no imaginary vibrations. The calculated wavenumbers were scaled with scaling factor of 0.9670 in order to get better match between calculated and experimental wavenumber values. The scaling factor was determined by means of the least squares method, The vibrational modes were assigned on the basis of PED analysis [6] using the FCART version 7.0 software [7].

## RESULTS AND DISCUSSION

**Conformational analysis** - From the optimized molecular structure of the investigated molecule, it is found that torsion angle,  $\tau$ , defined by the C2–C3–C1'–N1 atoms is  $178^\circ$ . The investigated molecule is a planar with the facilitated electron delocalization between the coumarin moiety and side alkyl chain.

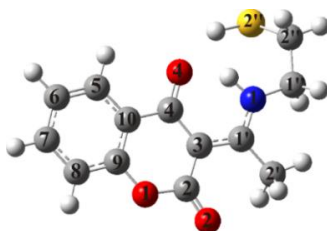


**Figure 1.** The optimized structure and numbering of **L1**

## IR spectra analysis

The comparison of experimental and theoretical IR spectrum is given in Figure 2.

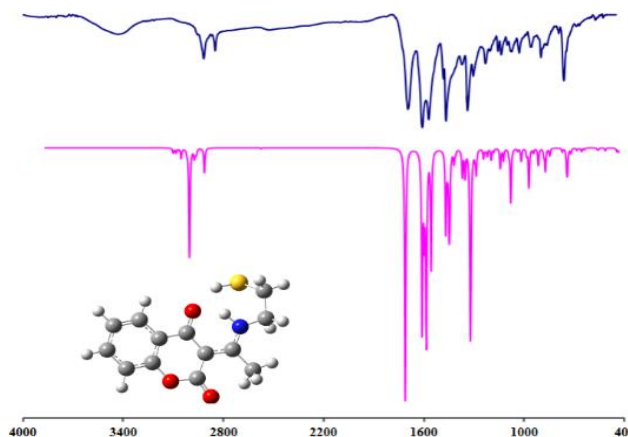


**Figure 2.** Experimental and theoretical IR spectrum of **L1**

The most distinct bands in the IR spectrum of **L1**, appearing in the high frequency region ( $4000\text{--}2000\text{ cm}^{-1}$ ), are assigned to different modes of N–H, C–H and S–H vibrations. This region is dominated by very massive and intense band. Taking into account the structure of **L1**, the intense band positioned at  $3431\text{ cm}^{-1}$  could be taken as possible absorption for (N1–H---O4=C4) hydrogen bond. The high frequency region is also characteristic to C–H ((methyl and methylen) stretching ( $2917$  and  $2849\text{ cm}^{-1}$ )) and S–H (stretching ( $2527\text{ cm}^{-1}$ )) modes.

The majority of the intense bands of IR spectra of **L1**, are to be found in the  $1800\text{--}1500\text{ cm}^{-1}$  wavenumber region (Fig. 2). The low frequency region involves combination of the C=O stretching (very strong intensity band at  $1697$ ) and C–C stretching (two strong intensity bands at  $1610$  and  $1571\text{ cm}^{-1}$ ). The bands between  $1500$  and  $1000\text{ cm}^{-1}$  mostly involve stretching (C–C (ring), C–O, N–C) and bending (H–C–H, H–C–C, H–C–C (ring), H–C–O and H–O–C) vibrations. These bands are of medium to strong intensity. Bands appearing below  $1000\text{ cm}^{-1}$ , medium to low intensity, are assigned to stretchings (C–N and C–C (acyclic parts of molecule)), bending (C–C–C, H–C–C, and H–O–C) modes of benzene, pyron and acyclic parts of the molecule and also to the combination of the various in plane (H–C–C–C, H–C–C–H, H–N–C–C), out of plane (O–C–C–C) (acyclic parts of the molecule) torsion modes.

The obtained results show that there is a linear dependence between the experimental and the calculated wavenumbers. The quality of this linear correlation is evaluated by means of three descriptors: the correlation

coefficient (R), average absolute error (AAE), and average relative error (ARE). The R value for the IR is 0.999. The AAE and ARE values for the IR spectrum are  $4.27 \text{ cm}^{-1}$  and 0.4%. All three descriptors demonstrate that B3LYP-D3BJ provide very good agreement between the experimental and simulated vibrational spectra, indicating correct mode assignments (Fig. 2).

## CONCLUSION

The results of the applied B3LYP-D3BJ/6-311+G(d,p) density functional method in determination of the spectroscopic and electronic features of **L1** point to a planar molecule, characterized by facilitated electron delocalization between the the coumarin moiety and side alkyl chain. Spectral assignments, done on the basis of a best-fit comparison between the experimentally obtained and theoretically calculated IR spectra, match quite well, indicating DFT calculations as a very accurate source of normal mode assignments.

## Acknowledgement

This work was partially supported by the Ministry for Science of the Republic of Serbia (Grants no. 172015, 174028 and 172016).

## REFERENCES

- [1] Talapatra S. K., and Talapatra B., (2015), Chemistry of Plant Natural Products, Berlin Heidelberg, Germany, Springer-Verlag Berlin Heidelberg
- [2] O'Kennedy R, Thornes RD (eds) (1997) Coumarins – Biology, Applications and Mode of Action, John Wiley & Sons Ltd., Chichester
- [3] A.D. Becke, Phys. Rev. A. 1988, 38, 3098–3100
- [4] S. Grimme, S. Ehrlich, L. Goerigk, J. Comput. Chem. 2011, 32, 1456–1465.
- [5] M. J. Frisch, G. W. Trucks, H. B. Schlegel, et al. Gaussian 09, Revision C.01, Gaussian, Inc., Wallingford, CT, USA. 2010.
- [6] R.A. Munos, Y.N. Panchenko, G.S. Koptev, N.F. Stepanov, J. Appl. Spectrosc. 1970, 12, 428–429.
- [7] C.R. Legler, N.R. Brown, R.A. Dunbar, M.D. Harness, K. Nguyen, O. Oyewole, W.B. Collier, Spectrochim. Acta Part A 2015, 145, 15-24.

## 3D MOLECULAR PHARMACOPHORE DETERMINATION OF PI3K- $\alpha$ KINASE INHIBITORS

Ž. Gagić<sup>1</sup>, M. Jovanović<sup>2</sup>, D. Agbaba<sup>2</sup> and K. Nikolić<sup>2</sup>

<sup>1</sup> *Department of Pharmaceutical chemistry, Faculty of Medicine, University of Banja Luka, Save Mrkalja 14, Banja Luka, Bosnia and Herzegovina.*

<sup>2</sup> *Department of Pharmaceutical chemistry, Faculty of Pharmacy, University of Belgrade, Vojvode Stepe 450, Belgrade, Serbia.*

*(katarina.nikolic@pharmacy.bg.ac.rs)*

### ABSTRACT

PI3K- $\alpha$ , as an enzyme with increased activity in many types of cancer, represents important target for research of new cytostatic agents. 3D-QSAR study was applied on 92 PI3K- $\alpha$  inhibitors in order to determine molecular pharmacophore structure. Obtained validation parameters ( $R^2=0.84$ ;  $Q^2=0.67$ ,  $R^2_{pred}=0.681$ ) indicate on reliability and good predictive potential of the 3D-QSAR model. Pharmacophore analysis showed that following structural characteristic have the greatest impact on activity of PI3K- $\alpha$  inhibitors: presence of hydrogen bond donor and hydrogen bond acceptor at a distance of 18-18.4Å or 12-12.4Å, presence of hydrophobic domain and hydrogen bond donor at a distance of 15.2-15.6Å, presence of steric hot spot and hydrogen bond donor at a distance of 1.6-2Å and presence of hydrogen bond acceptor and steric hot spot at a distance of 14.4-14.8Å. These findings provide guidelines for future design of new PI3K- $\alpha$  inhibitors with enhanced activity.

### INTRODUCTION

Phosphatidylinositide 3-kinases (PI3Ks) are a family of lipid kinases that phosphorylate inositol phospholipids at the position 3 of inositol to give phosphatidylinositol 3,4,5-trisophosphate (PIP3). PIP3 leads to binding of PI3P binding proteins to plextrin homologous domains of cell membrane, including AKT serine/threonine kinase (protein kinase B or PKB) and 3-phosphatidylinositol-dependent kinase-1 protein (PDK1). AKT, when bound to the cell membrane, becomes active and phosphorylates several target molecules involved in cell survival, cycle, growth, motility and metabolism[1].

PI3Ks are grouped into three classes, I, II and III, based on their structural characteristics and specificity for substrates. Class I is further divided into IA and IB. Class IA is a set of heterodimeric lipid kinases consisting of a p110

catalytic subunit and a p85 subunit that regulates receptor binding, activation and localization of PI3K enzymes. Mutations of one of the genes encoding primarily p110 $\alpha$  subunit (PI3KCA) can be found in many types of human cancers, including brain, breast, colon, liver, stomach and ovarian cancers.

The aim of this research was to perform 3D-QSAR (3D-Quantitative Structure-Activity Relationship) study in order to define pharmacophore structure of the selective PI3K- $\alpha$  inhibitors that can be further used for design of new, more potent inhibitors.

### EXPERIMENTAL

Experimentally determined  $K_i$  values of 92 PI3K- $\alpha$  inhibitors were collected from ChEMBL database (<https://www.ebi.ac.uk/chembl/>) and expressed as p $K_i$  ( $-\log K_i$ ) [2-5]. Wide range of inhibitory activities (p $K_i$ : 4.5-10.5) was covered, which enabled the formation of a robust 3D-QSAR model with a broad applicability domain. For each compound were checked dominant forms at pH=7.4 in MarvinView 17.28 program. Energy minimization of molecular structures was performed with PM3 semi-empirical and then *ab initio* Hartree-Fock/3-21G method using Gaussian 98W program included in Chem3D Ultra 7.0 software package.

3D-QSAR model was created in Pentacle 1.07 using the GRIND (GRid-Independent) descriptors, derived from molecular interaction fields- MIFs. To calculate these descriptors program uses 4 chemical probes which simulate the interaction of the ligand with the active site of receptor: DRY probe represents a hydrophobic interaction, O probe (carbonyl oxygen) describes the hydrogen bond acceptor, N1 (amide nitrogen) represents the donor of the hydrogen bond, and the TIP probe describes the steric hot spot. The most important regions that represent favorable interactions between probe and ligand are extracted using ALMOND algorithm based on two criteria: the intensity of the field and the distance between the selected probes. For field encoding, the CLACC (Consistently Large Auto and Cross Correlation) methodology was used. 3D-QSAR model was formed using PLS (Partial Least Square) regression.

### RESULTS AND DISCUSSION

Dataset of 92 molecules is divided into a training set (62 molecules) and a test set (30 molecules). Using the training set, a PLS (Partial Least Squares) regression model was created with 2 latent variables and internal validation parameters:  $R^2=0.84$ ;  $Q^2=0.67$ ; SDEP=0.442. For an acceptable QSAR model value of  $R^2$  (coefficient of determination, measures how well the regression line actually fits the data) should be greater than 0.6 and value of  $Q^2$  (cross-validated coefficient of determination) should be greater than 0.5. The test set

was used for external validation and the following parameters were obtained:  $R^2_{\text{pred}}=0.681$ ;  $\text{SDEP}=0.567$ ;  $r^2_{\text{m}}=0.594$ ;  $\overline{r^2_{\text{m}}}=0.594$ ;  $\Delta r^2_{\text{m}}=0.0004$ . These values indicate on the good reliability of the prediction of the created 3D-QSAR model that was further used to analyze 3D pharmacophore structure of PI3K inhibitors.

The variables with the highest positive effect on activity are depicted on 3D structure of the most active compound from dataset (Fig. 1). Var 647 and 632 (O-N1) are formed between nitrogen from triazole as the acceptor of hydrogen bond and nitrogen from the amide functional group as the donor of hydrogen bond; Var 382 (DRY-O) is formed between 1,2,4-triazole as a hydrophobic group and nitrogen amide as a donor of a hydrogen bond; Var 692 (O-TIP) is formed between nitrogen from the amide functional group and hydrogen related to this nitrogen (steric hot spot); Var 810 (N1-TIP) is formed between oxygen as the acceptor of hydrogen bond and the isopropyl ring as a steric hot spot.

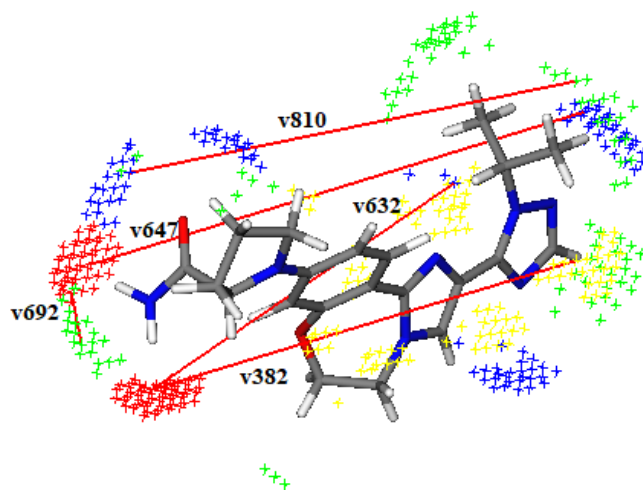


**Figure 1.** 3D structure of the most active compound from data set ( $\text{pK}_i=9.873$ ) with favorable variables depicted in red lines

The variables with the highest negative effect on activity are depicted on 3D structure of the least active compound from dataset (Fig. 2). Var 268 and 270 (TIP-TIP) are formed between oxygen from the amide and methyl group as steric hot spots; Var 724 (O-TIP) is formed between the nitrogen from the amide (hydrogen bond donor) and hydrogen from a pyrimidine (steric hot spot); Var 703 (O-TIP) is formed between the nitrogen from the amide (hydrogen bond donor) and oxygen from the amide (steric hot spot); Var 468

(DRY-N1) is formed between oxygen from the amide as a hydrogen bond acceptor and pyrimidine as a hydrophobic structure.

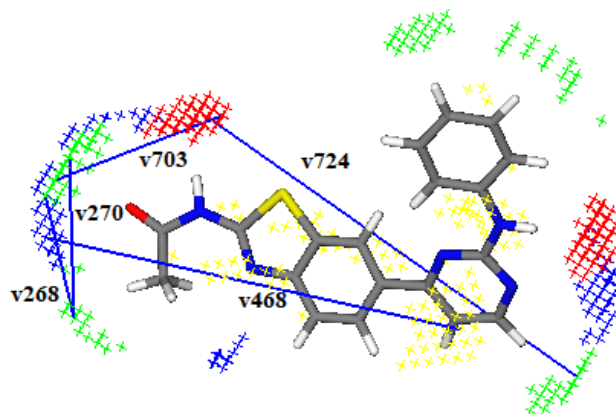


**Figure 2.** 3D structure of the least active compound from data set (pKi=6.970) with unfavorable variables depicted in blue lines

## CONCLUSION

Created 3D-QSAR model can reliably be used for PI3K activity prediction of new compounds within the applicability domain. The most important structural characteristics that have positive and negative impact on activity were identified and will be used for design of new PI3K inhibitors.

## Acknowledgement

This work was supported by the Ministry of Education, Science and Technological Development of the Republic of Serbia (Grant # 172033).

## REFERENCES

- [1] C. Huang, D. Mandelker, S. B. Gabelli, L. M. Amzel, *Cell Cycle*, 2008, 7(9), 1151-1156.
- [2] T. P. Heffron et al, *Journal of Medicinal Chemistry*, 2016, 59, 985-1002.
- [3] T. P. Heffron et al, *ACS Medicinal Chemistry Letters*, 2016, 7, 351-356.
- [4] N. D. D'Angelo et al, *Journal of Medicinal Chemistry*, 2011, 54(6), 1789-1811.
- [5] P. N. Collier et al, *Journal of Medicinal Chemistry*, 2014, 58, 517-521.

## A 3D-QSAR STUDY ON A SET OF MAPK1 INHIBITORS

D. Ruzić, A. Cebzan and K. Nikolić

*University of Belgrade, Department of Pharmaceutical Chemistry, Faculty of Pharmacy, Vojvode Stepe 450, 11000 Belgrade, Serbia.  
(knikolic@pharmacy.bg.ac.rs)*

### ABSTRACT

Three different classes of mitogen-activated protein kinase 1 (*MAPK1*) inhibitors (derivatives of pyrimidine-pyridone, acetamidothiazole and pyrazolyl-pyrrole) were used to perform three-dimensional Quantitative Structure-Activity Relationship (*3D-QSAR*) study. The number of 92 *MAPK1* inhibitors, split into training and test sets, was extracted from ChEMBL database, with their enzymatic inhibitory constants determined on human *MAPK1*. The statistically significant *3D-QSAR* models were further validated. The *3D-QSAR* model with the best statistical and validation parameters was further used to define main structural determinant for efficient inhibition of *MAPK1* enzyme.

### INTRODUCTION

Today, 42 kinase inhibitors [1] have been FDA approved. Mitogen-activated protein kinase 1 (*MAPK1*) presents serine-threonine kinase which is included in *Ras/Raf/MEK/MAPK* signaling pathway [2]. Cancer cells found in pancreas, colon, lungs, ovaries and kidneys may have overexpressed *MAPK1* level [3], which makes this enzyme as an attractive molecular target for the development of novel *MAPK1* inhibitors. So far, there are no registered *MAPK1* inhibitors, thus any new drug design strategy in this field is kindly welcomed. This communication deals with the developing *3D-QSAR* model and consequently analysis of GRIND variables related to developed model.

### EXPERIMENTAL

Diverse 92 compounds with experimentally determined enzymatic inhibitory constants  $K_i$  against human *MAPK1* isoform were downloaded from ChEMBL database (<https://www.ebi.ac.uk/chembl/>). The data set is composed of three different classes of compounds (derivatives of pyrimidine-pyridone, acetamidothiazole and pyrazolyl-pyrrole), with the  $pK_i$  range 4.86-10. The dominant forms at the physiological  $pH=7.4$  were determined by use of Marvin Sketch software, version 5.5.1.0 [4]. The conformations of the

molecules were generated by Chem3D Ultra 7.0 software (Hartree-Fock 3-21G method) [5].

Pentacle Software 1.07 [6] derived the GRIND descriptors for prepared compounds. The software uses four different molecular probes (*DRY* - hydrophobic, *TIP* - molecular shape, *NI* – hydrogen bond accepting (HBA) and *O* – hydrogen bond donating (HBD) interactions), imitating the most important interactions between the examined compounds and the amino acids residues inside the receptor binding cavity. The GRIND descriptors are derived between two probes on a certain distance, thereby correlated with the *pKi* values of the modelled compounds, by using Partial Least Squares (PLS) regression.

In order to develop 3D-QSAR model, the total number of compounds was divided into two data sets – training (composed of 62 compounds) and test set (30 compounds). The training set compounds were chosen according to the Principal Component Analysis (PCA), regarding the principle that the test set compounds remained adjacent at least one of the training set compound. The total number of GRIND variables was reduced by Fractional Factorial Design, whereas the most significant were retained and used for structure-activity relationship description. The validity of the developed 3D-QSAR model was evaluated through calculation of internal and external validation parameters [7].

## RESULTS AND DISCUSSION

The results of the developed 3D-QSAR model are presented in **Table 1**.

**Table 1.** Validation parameters for the developed 3D-QSAR model

Parameter	Internal validation		
	$R^2$	$Q_{\text{Loo}}^2$	RMSEE
	0.900	0.780	0.479
Criteria	> 0.7	> 0.5	

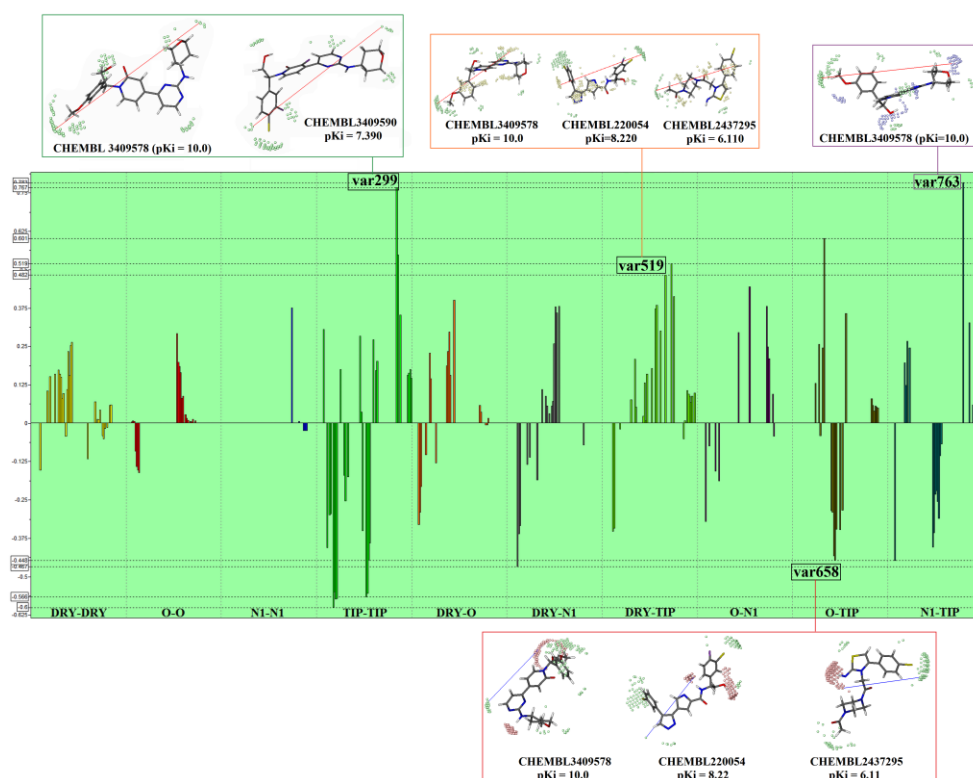
  

Parameter	External validation							
	$R^2_{\text{pred}}$	$R^2_{\text{obs/pred}}$	RMSEP	$r_m^2$	$r_m'^2$	$\Delta r_m^2$	$\overline{r_m^2}$	$k$
	0,677	0.900	0,871	0,625	0,499	0,126	0,562	0,988
Criteria	> 0.6		$\leq 2\text{RMSEP}$	> 0.5	> 0.5	< 0.2	> 0.5	$0.85 \leq k \leq 1.15$

$R^2$  - coefficient of determination,  $Q_{\text{Loo}}^2$  - Leave-One-Out Cross-Validated squared correlation coefficient, RMSEE - Root Mean Square Error of Estimation, RMSEP - Root Mean Square Error of Prediction,  $r_m^2$  metrics ( $r_m^2$ ,  $r_m'^2$ ,  $\overline{r_m^2}$  and  $\Delta r_m^2$ )

The 3D-QSAR model developed by using standard chemometric approaches (PCA and PLS regression) defined valid, three-component

(LV=3) model (the validity and accuracy are presented in **Table 1**). The most significant GRIND variables correlating with the MAPK1 inhibitory activity of the modelled compounds belong to classes of **TIP-TIP**, **DRY-TIP**, **O-TIP** and **N1-TIP** GRIND descriptors (**Figure 1**).



**Figure 1.** PLS coefficient plot presented for MAPK1 3D-QSAR model along with most significant GRIND variables (upper corner, positively correlating var299, var519 and var763 with  $pK_i$  and below – negatively correlating var658 with  $pK_i$ )

**TIP-TIP** var299 has the largest positive influence on the  $pK_i$  only in the highly potent MAPK1 inhibitors, such as pyrimidine-pyridones ( $pK_i = 7.39 - 10.0$ ). It implies that the molecular shape of these inhibitors is complementary to the binding pocket of MAPK1. This variable possesses discriminative property between pyrimidine-pyridones and two other classes of examined MAPK1 inhibitors. GRIND variable 519 (**DRY-TIP**) illustrates the importance of hydrophobic interactions of tetrahydropyran moiety in the MAPK1 inhibitors, as it is consistently pronounced in all the compounds with the same type of ring.

The GRIND variable **N1-TIP** (var763) is presented between steric spot interacting with distal methoxy group attached to pyrimidine-pyridone scaffold and oxygen (HBA group) from tetrahydropyran ring interacting with **N1** probe. This variable is presented on a distance of 24.4-24.8 Å and uniquely existing in pyrimidine-pyridone derivatives.

Finally, the most prominent variable with negative influence on *pKi* value is **O-TIP** var658. It is positioned between steric spots described around heterocyclic ring and **O** probe interacting with amide hydrogen in pyrazolyl-pyrroles. This variable has the largest values in moderate and less potent MAPK1 inhibitors (*pKi* < 7.460), comparing to the most potent pyrimidine-pyridone derivatives, indicating that 13.6-14 Å is not optimal distance between HBD group and distal heterocycle for efficient MAPK1 inhibitions.

## CONCLUSION

The GRIND analysis within developed MAPK1 3D-QSAR model revealed structural motifs which are important for potency against MAPK1. The validity of the model was confirmed by internal and external validation. The most significant variables (var299, var519, var763 and var658) were successfully applied to define the differences in biological activity of pyrimidine-pyridone, acetamidothiazole and pyrazolyl-pyrrole derivatives, as MAPK1 inhibitors.

## Acknowledgement

This work was supported by the Ministry of Education, Science and Technological Development (Grant no. 172033).

## REFERENCES

- [1] <https://www.fda.gov/downloads/drugs/guidancecomplianceregulatoryinformation/lawsactsandrules/ucm602233.pdf>
- [2] W. Kolch, Nature Reviews Molecular Cell Biology, 2005, 6(11), 827-837.
- [3] Ren, Li, et al. Journal of medicinal chemistry, 2015, 58.4, 1976-1991.
- [4] Chem3D Ultra7.0, Cambridge Soft Corporation, 100 Cambridge Park Dr, Cambridge, USA, 2001, <http://www.cambridgesoft.com/>
- [5] Gaussian 98 (Revision A.7) Frisch MJ et al. Gaussian, Inc. Pittsburgh PA, 1998.
- [6] Pentacle, Version 1.0.7, Molecular Discovery Ltd., Perugia, Italy; 2009.
- [7] A. Golbraikh, A. Tropsha. J Mol Graphics Modell, Beware of q2! 2002, 20(4); 269-276.

## 3D-QSAR STUDY OF PYRAZOLO[3,4-d]PYRIMIDINES AND 1,3,4-THIADIAZOLES AS BCR-ABL1 INHIBITORS

N. Đoković, A. Rajković and K. Nikolić

*University of Belgrade, Faculty of Pharmacy, Department of Pharmaceutical Chemistry,  
Vojvode Stepe 450, 11000 Belgrade, Serbia. ([knikolic@pharmacy.bg.ac.rs](mailto:knikolic@pharmacy.bg.ac.rs))*

### ABSTRACT

The treatment of chronic myeloid leukemia (CML) was revolutionized by introducing Bcr-Abl1 inhibitors to the extent that today it could be considered as manageable chronic disease. Although, ATP-competitive Bcr-Abl1 inhibitors set the milestone for treatment of CML, resistance on therapy in significant number of patients still remains major challenge.

3D quantitative structure-activity relationship (3D-QSAR) model of selected Bcr-Abl1 inhibitors was built in order to gain insight into structural requirements for inhibitory activity. The 3D-QSAR model with best validation parameters was selected for further study and design of novel inhibitors.

### INTRODUCTION

Reciprocal translocation between chromosomes 9 and 22, known as Philadelphia chromosome, results in the expression of constitutively activated fused Bcr-Abl1 protein kinase which has the central role in the pathogenesis of chronic myeloid leukemia (CML). Owing to ATP competitive Bcr-Abl1 inhibitors, CML could be considered as chronic disease today. However, development of resistance on therapy with known drugs, especially in the advanced phases of CML, is the major driving force for development of novel inhibitors [1].

During more than 20 years of quest for effective and safe Bcr-Abl1 inhibitors, pyrazolo[3,4-d]pyrimidine and 1,3,4-thiadiazole scaffolds, as privileged fragments in medicinal chemistry and bioisosteres of nucleobases, emerged as some of the most promising fragments for the development of novel generations of inhibitors. Recent reports revealed potential of these compounds in overcoming resistance, even achieving additional allosteric binding sites which could have further positive implications in therapy of resistant patients [2].

The aim of the current study was to generate three dimensional quantitative structure activity relationship (3D-QSAR) model based on alignment-

independent GRIND descriptors calculated for selected pyrazolo[3,4-d]pyrimidine and 1,3,4-thiadiazole Bcr-Abl1 inhibitors in order to identify 3D structural features important for the interaction and to set additional guidance for design of novel Bcr-Abl1 inhibitors.

## EXPERIMENTAL

Activities expressed as  $pK_i$  and structures of Bcr-Abl1 inhibitors have been obtained from ChEMBL database (<https://www.ebi.ac.uk/chembl/>). Total of 107 inhibitors with pyrazolo[3,4-d]pyrimidine and 1,3,4-thiadiazole scaffolds (Figure 1) tested with the same biological assay were extracted for further analysis. Major microspecies at physiological pH were obtained with Marvin

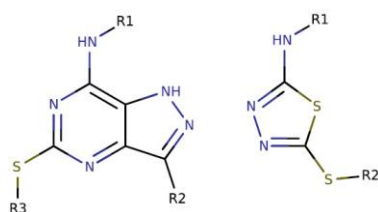


**Figure 1.** Representation of structures in data set. R1 and R2 represent phenyl containing groups while R3 is aliphatic group.

Suite [3]. The Gaussian 98 [4] software with Hartree-Fock/3-21G basis set was applied for geometry optimization. Pentacle software [5] was used for further processing of structures and 3D-QSAR model building and validation.

Pentacle generates molecular interaction fields (MIFs) for each optimized ligand using four GRID-based fields calculating interaction energies between ligands and probes: DRY-hydrophobic reactions, N1-hydrogen bond acceptors, O-hydrogen bond donors and TIP-steric hot spots within molecule. The interaction energies at each grid point called

node are the sum of Lennard-Jones energy, hydrogen bond, and electrostatic interactions. ALMOND algorithm was used to extract the most relevant MIF regions. Encoding of extracted MIFs into alignment independent GRIND (GRid-Independent) descriptors was performed by means of CLACC algorithm. Principal component analysis (PCA) was used for inspection of structural variance of initial data set. After dividing data set into test and training set and fractional factorial design with enhanced replacement method (FFD) for selection of representative GRIND variables from initial pool of descriptors, partial last square regression (PLS) was used for model generation. Internal validation of developed model was evaluated using coefficient of determination ( $R^2$ ), leave-one-out cross-validated coefficient of determination ( $Q^2$ ), root mean square error of estimation (RMSEE). External validation was performed calculating coefficient of determination for test set ( $R^2_{pred}$ ), root mean square error of prediction (RMSEP) and  $r^2_m$  metric parameters.

## RESULTS AND DISCUSSION

Structural variance of initial data set was examined with PCA performed on whole set of GRIND variables. Based on PCA score vectors, outliers were detected and eliminated from initial data set. Remained total of 90 compounds were randomly divided into test and training set. Partial least square regression (PLS) was used for 3D-QSAR model building. Four latent variables (LVs) were selected as optimum number of PLS components for the model interpretation. Validation parameters obtained by leave-one-out cross validation and external validation with test set, indicated excellent quality and justify usage of 4LV 3D-QSAR model in further design of novel Bcr-Abl1 inhibitors (Table 1).

**Table 1.** Validation parameters for selected 3D-QSAR model (4LV).

$R^2$	$Q^2$	RMSEE	$R^2_{pred}$	RMSEP	$\bar{r}^2_m$	$r^2_m$	$\Delta r^2_m$
0.920	0.700	0.240	0.672	0.210	<0,2	>0,5	

4LV PLS coefficients plot (Figure 2A) indicate GRIND variables: var 246 (-TIP-TIP/8,4-8,8Å), var 263(+TIP-TIP/16,2-15,6Å), var 315 (+DRY-O/6-6,4Å), var 401 (+DRY-N1/10,4-10,8Å), var 640 (+O-TIP/16-16,4Å) and var 687 (-N1-TIP/4,8-5,2Å) as the most important for the activity.

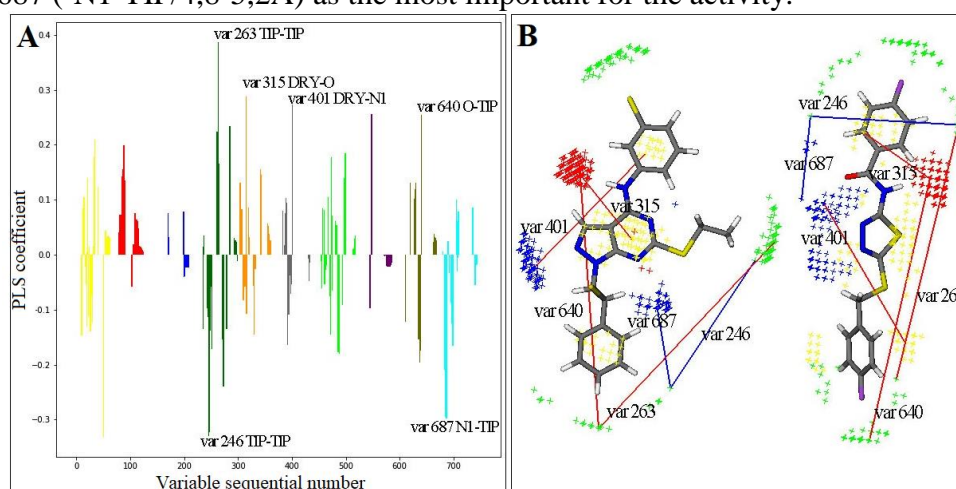


**Figure 2.** **A** 4LV PLS coefficients plot for obtained model with the most significant variables labeled. **B** Pyrazolo[3,4-d]pyrimidine (left) and 1,3,4-thiadiazole (right) derivatives with selected GRIND variables (GRID based fields: TIP-green, DRY-yellow, O-red, N1-blue).

Var 246 (-TIP-TIP) and var 263 (+TIP-TIP) are describing the distance between two steric hot spots that has negative and positive impact on activity, respectively. These variables are related to optimal substitution of phenyl

moieties in both groups of inhibitors. In the group of pyrazolo[3,4-d]pyrimidines, these variables strongly support substitution in  $-p$  position of phenethyl group with voluminous substituents, while in the group of 1,3,4-thiadiazole describe the optimal distance between two opposite sides of molecules indicating that changing the length of linkers will have negative impact on activity. Var 315 (+DRY-O), var 401 (+DRY-N1), var 640 (+O-TIP) and var 687 (-N1-TIP) clearly indicates importance of hydrogen bond donors and acceptors in central scaffold and their optimal distance from steric and hydrophobic hot spots (Figure 2B).

According to developed 3D-QSAR models, we suggest that a more potent inhibitor against Bcr-Abl1 might be obtained by (i) increasing hydrogen bonding strength in central scaffold; (ii) optimal substitution of phenyl groups which increases hydrophobicity of favorable region and maintains optimal distance between described steric hot spots (iii) preserving optimal lengths of linkers in 1,3,4-thiadiazole and by introducing bulky substituent into  $-p$  position of phenethyl group of pyrazolo[3,4-d]pyrimidines.

## CONCLUSION

In summary, an alignment-independent QSAR study was performed on a set of pyrazolo[3,4-d]pyrimidine and 1,3,4-thiadiazole derivatives with Bcr-Abl1 inhibitor activity. Model with good statistic was developed and structural properties important for activity were described. The 3D-QSAR model could be further used for design of novel series of Bcr-Abl1 inhibitors.

## Acknowledgement

This work was supported by the Ministry of Education, Science and Technological Development of the Republic of Serbia (Grants no. 172033).

## REFERENCES

- [1] E. Weisberg, P.W. Manley, et al. Nature Reviews Cancer volume, 2007, 7, 345–356.
- [2] M. Radi, E. Crespan, et al. ChemMedChem, 2010 Aug 2, 5(8):1226-31
- [3] MarvinSketch, version 6.2.2, calculation module developed by ChemAxon, <https://chemaxon.com/products/marvin>, 2018.
- [4] M.J. Frish, G.W. Trucks, et al. Gaussian 98, Revision A. 9, Gaussian Inc. Pittsburgh, PA, 1998.
- [5] M. Pastor, G. Cruciani, et al. J Med Chem, 2000, 43(17):3233-2343.

## CHARACTERISATION OF CURCUMIN-PECTIN CONJUGATES BY UV-VIS SPECTROSCOPY

O. Kovacević, S. Zlatanović, B. Kovačević, S. Ostojić and S. Gorjanović

*University of Belgrade, Institute of General and Physical Chemistry,  
Studentski trg 12-16, P.O. Box 45, 11158 Belgrade 118, Serbia  
(snezana.zlatanovic@gmail.com)*

### ABSTRACT

Water solutions of the curcumin-pectin conjugates (1: 400, 1: 200, 1: 100 and 1: 50 w/w) were prepared and characterized by ultraviolet–visible spectra. Maximum of absorption was between 440 and 447 nm. Position of the maximum was related to curcumin-pectin ratio. Significant bathochromic shift relative to the absorption of curcumin at 427 nm in the ethanolic solution was noticed. A strong absorption at 280 nm, noticed in the spectra of both pectin and curcumin-pectin conjugates, is related to the presence of proteins associated with pectin, not to formation of conjugates. In contrast to low solubility and stability of curcumin in aqueous solutions, curcumin-pectin conjugates whose formation was clearly shown by UV-Vis spectroscopy, is soluble and relatively stable in water.

### INTRODUCTION

Curcumin is a mixture of three major curcuminoids: curcumin (1,7-Bis-(4-hydroxy-3-methoxyphenyl)-1,6-heptadiene-3,5-dione), demethoxy- and bis-demethoxycurcumin [1,2]. Curcumin absorbance at 262 nm has been attributed to substituted phenolic groups. Characteristic absorption in the area of 300-500 nm, with a maximum at about 430 nm, has been found dependent on the difference in the proportion of curcuminoids, the solvent and pH of the solution [1-3]. Curcumin has been recognized as a possible active component in the treatment of many severe diseases. However, curcumin has low water stability and bioavailability [1-4]. In order to achieve better solubility and increase bioavailability the binding of curcumin to different matrices was investigated. Feng Bai et al. (2017) reported that the formation of the curcumin-pectin conjugate was confirmed by the absorption at 280 nm and 420 nm [4].

In this study curcumin-pectin conjugates in water are formed using slightly modified procedure applied to obtain curcumin-cellulose conjugate [5]. Changes in the UV-Vis spectra of curcumin related to the formation of the conjugate are noticed. Specific absorption of curcumin, with maximum

absorption at about 430 nm, was used to determine its content in the solution [3,6]. Absorption at 280 nm was used to determine pectin content in the absence of specific pectin absorption. This absorption probably originates from a proteins associated with pectin [7].

## EXPERIMENTAL

Curcumin (Fluka), pectin from apple (Sigma) and ethanol (MosLab, Belgrade) were used. All water solutions were prepared using distilled water.

Curcumin-pectin conjugates were made according to procedure applied previously for the formation of curcumin-cellulose conjugates, with water and ethyl alcohol [5]. The weight ratio of the curcumin to the pectin was Q1 = 1: 400, Q2 = 1: 200, Q3 = 1: 100 and Q4 = 1: 50. The gel phase was dried in laboratory dryer.

Absorption spectra were recorded using Thermo, type Evolution 600, UV-Vis at the interval of 220-800 nm, with bandwidth of 2.0 nm, scan speed of 60 nm/min, data interval of 0.2 nm, and with Helma quartz cuvette of 1 cm.

## RESULTS AND DISCUSSION

UV-Vis absorption spectra of pectin in aqueous solution (1.9 g/L) is given in Fig. 1. Considering the structure of the pectin (polysaccharides composed primarily of D- galactopyranosyluronic acids [4,8] the absorption at 280 nm is unexpected. It probably originated from associated proteins [7]. In the absence of specific absorption A<sub>280</sub> is used to follow changes in pectin

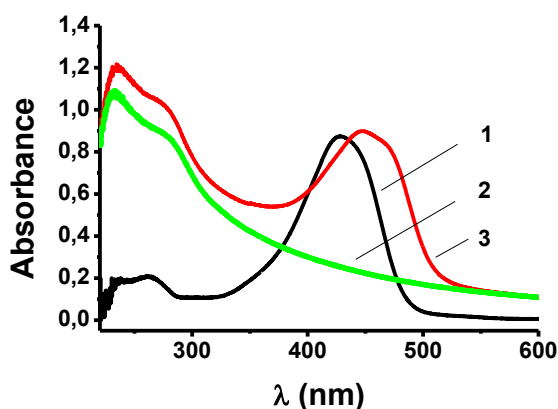


**Figure 1.** UV-Vis absorption spectra of 1) curcumin, in ethanol solution 2) pectin, and 3) pectin-curcumin conjugate in water.

content. The correlation with pectine content is linear up to 4 g/L in water, according to the equation:  $ABS = 0.08748 + 0.41362 \times C$ , where ABS = Absorbance, and C is content given in g/L.

UV-Vis spectrum of water solution of 1.9 g/l of conjugate (Q1) is given in Fig.1 along with the spectrum of 0.005 g/L curcumin in ethanol. Absorption maximum at 427 nm was found specific for this compound in ethanol solution [3,6].

UV-Vis spectrum of water solution of 1.9 g/l of conjugate (Q1) is given in Fig.1 along with the spectrum of 0.005 g/L curcumin in ethanol. Absorption maximum at 427 nm was found

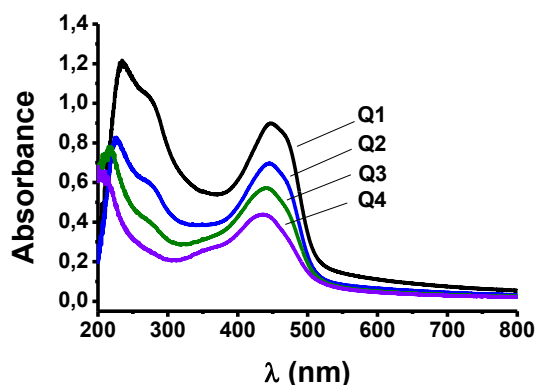


**Figure 2.** UV-Vis absorption spectra of curcumin-pectin conjugate in water (curcumin pectin ratio: Q1=1:400, Q2=1:200, Q3=1:100 and Q4=1:50)

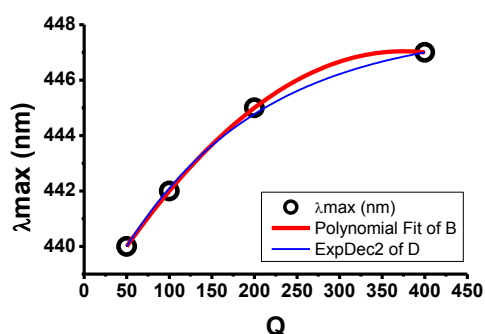


**Figure 3.** Dependence of the adsorption maximum position of curcumin-pectin conjugates in water on curcumin:pectin ratio Q

UV-Vis spectra of conjugate with the content ranged from 0.25 to 2 g/L (Q1 - Q4) are shown in Fig. 2. The solubility of curcumin in water is very low and in the neutral and alkaline environment it decays immediately after dissolution [1,9]. Therefore, there is no spectrum of curcumin in the water solution. The maximum absorption of the formed curcumin-pectin conjugates has been found in the range of 440 to 447 nm, depending on the weight ratio of curcumin to pectin, are shown in Figure 3. Compared to the maximum absorption of curcumin in ethanolic solution curcumin – pectin conjugates in water solution have bathochromic shift.

## CONCLUSION

According to UV-Vis spectra curcumin-pectin conjugates are soluble in aqueous solutions compared to curcumin which is very poorly soluble. Absorption maxima of conjugates dissolved in water are positioned at 440-447 nm. Existence of bathochromic shifts compared to a maximum of curcumin dissolved in ethanol (427 nm) is observed. This suggests that curcumin-pectin conjugates formation may cause an increased delocalization in the conjugated pi-bonding curcumin system. Increased content of pectin in the formation of the conjugate causes a bathochromic shift, probably as the result of new curcumin-pectin bonds. The strong absorption at 280 nm observed in the spectrum of formed conjugates is also present in the spectrum

of untreated pectin. It probably originates from associated proteins and can not be an indicator of the formation of curcumin-pectin conjugates.

### ***Acknowledgement***

This work was partially supported by the Ministry of Education, Science and Technological Development of the Republic of Serbia, under the Project No TR-31055 and TR 31093.

### **REFERENCES**

- [1] M. Heger, R. F. van Golen, M. Broekgaarden, and M. C. Michel, *Pharmacological Reviews*, 2014, **66**, 222–307.
- [2] L. Shen, H.-F. Ji, *Spectrochimica Acta Part A*, 2007, **67**, 619–623.
- [3] A. Rohman, *International Food Research Journal*, 2012, **19(1)**, 19-27.
- [4] F. Bai, J. Diao, Y. Wang, S. Sun, H. Zhang, Y. Liu, Y. Wang, and J. Cao, *Journal of Agricultural and Food Chemistry*, 2017, **65**, 6840–6847.
- [5] B. Li, S. Konecke, L. A. Wegiel, L. S. Taylor, K. J. Edgar, *Carbohydrate Polymers*, 2013, **98**, 1108–1116.
- [6] O. Kovačević, S. Zlatanović, B. Kovačević and S. Gorjanović, 13<sup>th</sup> International Conference of Fundamental and Applied Aspects of Physical Chemistry- PHYSICAL CHEMISTRY 2016, Belgrade, Serbia, Proceedings, 2016, **I**, 167-170.
- [7] S. Christiaens, D. Uwibambe, M. Uyttebroek, B. Van Droogenbroeck, A. M. Van Loey, M. E. Hendrickx, *LWT - Food Science and Technology*, 2015, **61**, 275-282.
- [8] D. W. Dixon, *Electronic Theses and Dissertations*, East Tennessee State University, 2008, Paper 1910. <http://dc.etsu.edu/etd/1910>
- [9] O. Kovačević, S. Zlatanović, B. Kovačević and S. Gorjanović, 13<sup>th</sup> International Conference of Fundamental and Applied Aspects of Physical Chemistry- PHYSICAL CHEMISTRY 2016, Belgrade, Serbia, Proceedings, 2016, **I**, 171-174.

## SYNTHESIS AND CRYSTALLOGRAPHIC STRUCTURE OF NOVEL COUMARIN DERIVATIVE WITH DOPAMINE

D. Dimić<sup>1</sup>, E. Avdović<sup>2</sup>, S. Trifunović<sup>2</sup>, I. Potočňák<sup>3</sup>, J. Dimitrić Marković<sup>1</sup> and Z. Marković<sup>4</sup>

<sup>1</sup>*University of Belgrade, Faculty of Physical Chemistry, Studentski trg 12-16, 11000 Belgrade, Republic of Serbia. (ddimic@ffh.bg.ac.rs)*

<sup>2</sup>*University of Kragujevac, Faculty of Science, Department of Chemistry, Radoja Domanovića 12, 34000 Kragujevac, Republic of Serbia*

<sup>3</sup>*Institute of Chemistry, P. J. Šafárik University in Košice, Moyzesova 11, 04154 Košice, Slovak Republic*

<sup>4</sup>*Department of Chemical-Technological Sciences, State University of Novi Pazar, Vuka Karadžića bb, 36300 Novi Pazar, Republic of Serbia*

### ABSTRACT

Novel derivate of coumarin with dopamine, neurotransmitter, was synthesized. The experimental conditions are described. The crystal structure was obtained and solved. Based on this structure, the quantum-chemical methods were used in order to find the most suitable functional for the theoretical analysis. The difference in experimental and theoretical bond lengths and angles showed that M06-2X should be used for future analysis of interaction and structure description of synthesized compound.

### INTRODUCTION

Coumarin (2H-1-benzopyran-2-one) and its derivative are common structural elements of natural products found in higher plants. They have important biological functions, including signaling and hormonal role, as well as defense functions against herbivores and microorganisms. Many of its derivatives have antibacterial, antifungal, anticoagulant, anti-HIV, antioxidant and cytotoxic activities. Synthetic structural modifications of coumarin have given compounds that act as anticoagulants, drugs for treatment of neurological disorders, molecular photonic devices, coumarin dyes and light-emitting materials.

In this contribution the synthesis and crystallographic structure of novel coumarin derivative with dopamine is described. The experiments were carried out because similar derivatives of coumarin with aminophenols showed good antitumor and antimicrobial activity, and this compound has two hydroxy groups attached to aromatic ring, which is an important

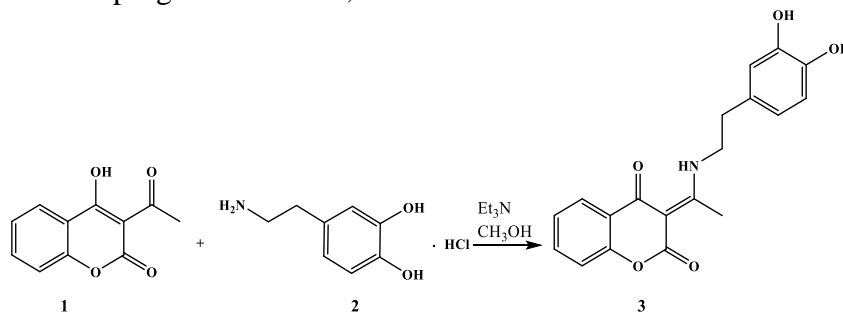
structural element for biological activity. This structure was later optimized with several common functionals, and based on the difference in experimental and theoretical bond lengths and angles, the most suitable method for the theoretical analysis determined.

### EXPERIMENTAL/THEORETICAL METHODS

The starting compound, 3-acetyl-4-hydroxy coumarin was synthesized as described in reference [2]. Dopamine hydrochloride, methanol, toluene, acetone and 96% ethanol were purchased from Sigma Aldrich (Munich, Germany).

The general procedure for the synthesis of 3-(1-((3,4-dihydroxyphenethyl)amino)ethylidene)-chroman-2,4-dione (**3**) is described in the following paragraph. The reaction mixture of 3-acetyl-4-hydroxy-coumarin **1** (0.41 g, 0.002 mol) with (0.002 mol) dopamine hydrochloride **2** and (0.002 mol) triethylamine in methanol (50 mL) was refluxed for 3 h. The overall reaction is given in Scheme 1. Progress of reactions was monitored by TLC (toluene : acetone = 7 : 3). When the reaction was completed the mixture was cooled to room temperature. The obtained white crystals were filtered, air-dried and recrystallized from methanol. The structural analysis, including NMR, IR and elemental microanalysis, proved that the desired compound was obtained.

The data collection for crystallographic structure was performed on the Oxford Diffraction Xcalibur2 diffractometer equipped with Sapphire2 CCD detector with graphite-monochromatized MoK $\alpha$  radiation (wavelength 0.71073 Å). Crysalis CCD was used for data collection while Crysalis RED was used for the cell refinement, data reduction and absorption correction. The structure was solved by SHELXT and subsequent Fourier series using SHELXL, implemented in WinGX program suit. The anisotropic displacement parameters were refined for all non-hydrogen atoms. The analysis of bond distances, angles and non-bonding interactions was performed in programs SHELX, PLATON and DIAMOND.



**Scheme 1.** Synthesis of coumarin derivative.

The optimization of structure was carried out in the Gaussian program package [3]. In order to obtain the most suitable functional, that describes well the bond lengths and angles, several of the common functionals were used: B3LYP, B3LYP-D3, B3PW91, M062-2X and M05-2X in conjunction with 6-311++G(d,p) basis set. These functionals were chosen because of their various qualities. The optimization was performed without any geometrical constraints and changes in original structure. The absence of imaginary frequencies proved that the local minima was found.

## RESULTS AND DISCUSSION

The obtained crystallographic structure is given in Figure 1.

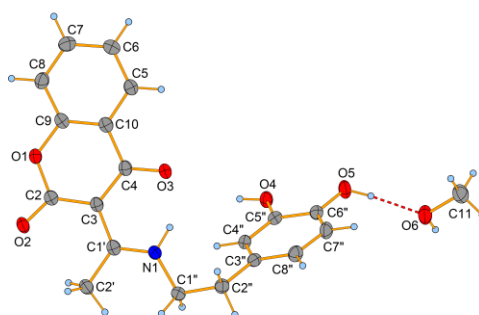


**Figure 1.** The crystallographic structure of synthesized molecule.

The structure consists of bicyclic coumarin fragment, aliphatic chain and aromatic ring with two hydroxy groups. There is also a hydrogen bond formed between N1 and O3, but it is longer than in the previously obtained compound with aminophenols, due to the lower rigidity of structure (longer aliphatic chain). Due to the presence of several electronegative atoms, oxygens in positions 1-5, it is assumed that in crystal structure there are several hydrogen bonds formed with different molecules. The structures with different functionals were optimized starting from the crystallographic structure. The parameters used for the evaluation of performance of functionals were: mean absolute error (MAE) and correlation coefficient (R) separately for bond lengths and angles. The values for these parameters are given in Table 1.

Whenever parameters of the optimized structure are compared to the experimental, it should be noted that the optimization was performed for the isolated molecule in vacuum. Therefore not all of the intramolecular bonds and interactions were taken into considerations and deviations in values are possible.

**Table 1.** Parameters for the comparison of various functionals

	Functional	M062-2X	M05-2X	B3LYP	B3LYP-D3	B3PW91
Bond length	MEA	0.007	0.007	0.008	0.008	0.007
	R	0.991	0.992	0.992	0.991	0.991
Angles	MEA	0.622	0.868	0.698	0.777	0.715
	R	0.970	0.932	0.957	0.944	0.953

As it can be seen in Table 1, all of the functionals describe well the experimental structure. The MEA values for functional are around 0.007 Å. When correlation coefficients are compared the values are almost the same, with M05-2X and B3LYP having higher values for 0.001. Therefore bond lengths are not reliable parameter. The lowest values for MEA for angles are for M06-2X and B3LYP, with the highest R values. Based on these results it can be concluded that M06-2X is the most reliable functional, in conjunction with 6-311++G(d,p) basis set, for the description of structure of synthesized coumarin derivative.

## CONCLUSION

In this contribution we report the synthesis and crystallographic structure of coumarin derivative with dopamine. The compound was prepared under mild conditions. In order to find the most suitable methodology for the further theoretical analysis of structural properties, reactivity and possible interactions, several common functionals were investigated. The structure was optimized from crystallographic structure. The mean average error and correlation coefficient between experimental and theoretical bond lengths and angles were used as the parameters for comparison. Based on these criteria, it was concluded that all of the functionals describe well obtained structure, but M062-2X gives the best reproduction of experimental data.

## Acknowledgement

Authors acknowledge the Ministry of Education, Science and Technological Development of the Republic of Serbia for the financial support through projects No. 172040, 172015, 172016 and 174028.

## REFERENCES

- [1] E. Avdović, D. Milenković, J. Dimitrić Marković, et al. *Spectrochim. Acta A*, 2018, 195, 31-40.
- [2] S. Sukdolak, N. Vuković, S. Solujić, N. Manojlović, L. Krstić, J. *Heterocycl. Chem.*, 2004, 41, 593-596
- [3] M.J. Frisch, G. W. Trucks, H. B. Schlegel, et al. *Gaussian 09*, Revision C. 01, Gaussian Inc. Wallingford, CT. USA, 2010.

## ASSOCIATIVE DETACHMENT (AD) PATHS FOR H AND $C_nN^-$ ( $n=1,3,5$ ) IN THE GAS-PHASE

S. V. Jerosimić<sup>1</sup>, F. A. Gianturco<sup>2</sup> and R. Wester<sup>2</sup>

<sup>1</sup> Faculty of Physical Chemistry, University of Belgrade, Studentski trg 12-16, PAC 105305, 11158 Belgrade, Serbia ([stanka@ffh.bg.ac.rs](mailto:stanka@ffh.bg.ac.rs))

<sup>2</sup> Institut für Ionenphysik und Angewandte Physik, Universität Innsbruck, Technikerstraße 25, 6020 Innsbruck, Austria.

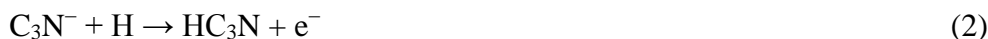
### ABSTRACT

The dynamical paths leading to Associative Detachment (AD) in the low-temperature regions of the Dark Molecular Clouds (DMC) in the ISM, or in cold trap laboratory experiments, are investigated with quantum chemical methods. The potential energy curves for  $H+CN^-$  (and  $H+C_3N^-$ ,  $H+C_5N^-$ ) are obtained for different directions of the H partner approaching the  $C_nN^-$  within the framework of the Born-Oppenheimer approximation. We found that the AD energetics at low temperature becomes favorable only along a selected range of approaching directions: e.g. there is a favorable path of forming HCN at low temperatures, while that of forming its HNC isomer is found to be energetically forbidden.

### INTRODUCTION

$C_{2n-1}N^-$  ( $CN^-$ ,  $C_3N^-$ ,  $C_5N^-$ ) species were detected in interstellar and circumstellar space by combining astronomical observations, laboratory experiments, and high quality *ab initio* calculations [1-3]. Also, the neutrals HCN, HNC,  $HC_3N$ , and  $HC_5N$  were also confirmed for many times in a variety of astrophysical environments (see e.g. ref. [4,5]).

By calculating the stretching potential curves, when H atom is removing from the linear  $C_nN^-$  fragment, we can perhaps find the way for the formation of the  $C_nN^-$  anions. In the other direction, the associative detachment reaction (AD reaction) where colliding partners are H and  $C_nN^-$  can give rise to the neutral  $HC_nN$  molecule plus electron, and we want to examine if this path is possible. This reaction would link  $C_nN^-$  and  $HC_nN$ . The scheme of the possible Associative Detachment processes are:



We will investigate the interaction of the  $\text{CN}^-$  molecular anion with the hydrogen atom in both directions, in order to investigate the possible paths for forming both the HCN or HNC molecules. On the other hand, because of the larger stability of  $\text{HC}_3\text{N}$  or  $\text{HC}_5\text{N}$  neutrals in respect to the  $\text{C}_3\text{NH}$  or  $\text{C}_5\text{NH}$ , we shall analyze only the (2)nd and (3)rd scheme. The later ones show very similar path to the first one of obtaining HCN neutral molecule, therefore in this short paper we shall present the results only for obtaining HCN species. However, conclusions will be drawn for each of the presented reactions. We shall carry out accurate quantum structure calculations, which will allow us to argue the importance of these reactions on the selective abundances of the investigated partners.

### DETAILS OF QUANTUM CALCULATIONS

The geometries of the HCN/HNC system, and of  $\text{CN}^-$  interacting with the approaching H atom, are described by using Jacobi coordinates to present the paths of the incoming atom H towards  $\text{CN}^-$  from different angles (see Fig. 1). The  $R$  coordinate is the distance of H to the center of mass of the  $^{12}\text{C}$  and  $^{14}\text{N}$ , depending on the angle  $\theta$ .

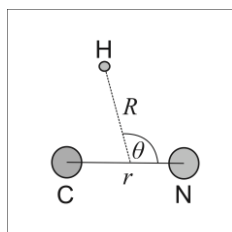


**Figure 1.** Jacobi coordinates of triatomic molecular complex of the present study. The hydrogen atom moves along the  $R$  coordinate taken from the center of mass of the CN system, while the  $\theta$  coordinate varies from the linear HCN ( $\theta=180^\circ$ ) to the linear HNC ( $\theta=0^\circ$ ) complexes.

The potential energy surface (PES) describes the energetics for the interaction of the  $\text{CN}^-$  anion in its ground state ( $X^1\Sigma^+$ ) with the atom H, leading to a neutral HCN plus the outgoing continuous electron. Electronic energies for the lowest-lying adiabatic states of H-CN and H-CN $^-$  systems were calculated by using the state-averaged (SA) full-valence complete active space self-consistent field (CASSCF) reference function for the subsequent internally contracted multi-reference configuration interaction calculations with single and double excitations (MRCISD) [6,7], corrected with perturbative Davidson correction [MRCISD(+Q)]. One-electron space was described by using the doubly-augmented polarized valence correlation

consistent 5-zeta basis set (d-aug-cc-pV5Z) [8]. In the present study, the full valence space consists of 10 electrons in 9 valence orbitals without correlation of the core electrons. Calculations were carried out using MOLPRO 2012.1 software package [9,10].

## RESULTS AND DISCUSSION

The  $^2A'$  ( $^2\Sigma^+$  at linearity) state of  $\text{HCN}^-$  system is the electronic state that correlates with the ground  $\text{H}(^2S)$  and the ground  $\text{CN}^- (^1\Sigma^+)$  asymptotic states; therefore, the asymptote in our figures (as  $R \rightarrow \infty$ ) corresponds to  $\text{H}+\text{CN}^-$ , while the asymptote for the neutral  $^1\Sigma^+$  corresponds to the ground  $\text{H}+\text{CN}$ . The van der Waals complexes for the  $\text{H}\cdots\text{CN}^-$  are formed near the  $R = 2.85 \text{ \AA}$  and over a specific range of angular approaches (near  $180^\circ$ ), but are not stable. For the specific examples of Figure 2, we see that the reference asymptotic energy (point A) is well above the well regions for  $0^\circ$  and  $180^\circ$ , however there is a huge barrier at about  $0^\circ$  indicating that forming the HNC would not be possible at low temperatures. On the other hand, approaches along the  $90^\circ$  PECs would not bring the partners into the region of the AD process because of the endothermicity of the reaction.

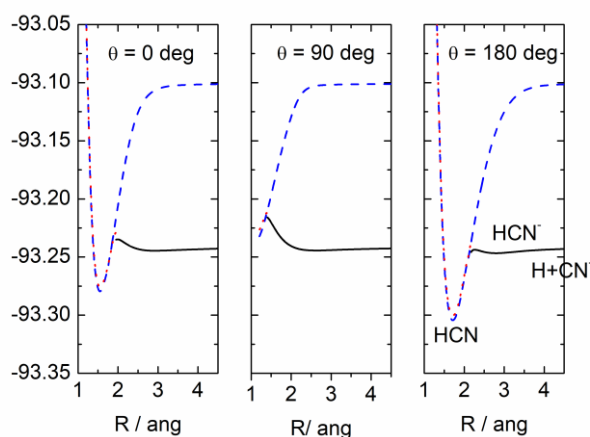


**Figure 2.** PECs for  $\theta=0^\circ$ ,  $90^\circ$ , and  $180^\circ$  along the  $R$  coordinate, at the fixed CN distance of  $1.1817 \text{ \AA}$ . The anionic, stretched  $\text{H}--\text{CN}^-$  system is shown by solid lines, while the attractive branch of the neutral HCN curve is given by the dashed lines. The autodetaching region is given by dots. Energy is in a.u.

## CONCLUSION

The calculations show that the H and CN<sup>-</sup> reach a distance of approach where the anionic complex H...CN<sup>-</sup> becomes metastable and a neutral triatomic molecule HCN plus a continuum electron is the energetically favored species. We have found a specific angular region (between 120° and 0°) for the approaching H and CN<sup>-</sup> which strongly prevents, in the low-temperature, the interacting partners from reaching the AD region. While HCN can be formed even at low temperatures via the AD reaction mechanism, the HNC formation would be prevented at low temperatures by an energy barrier in the environment of the Molecular Clouds where CN<sup>-</sup> has been observed. Additionally, the paths for forming HC<sub>3</sub>N and HC<sub>5</sub>N neutrals by AD reactions are also energetically possible.

## Acknowledgement

This work was supported by the Project ON-172040 by the Ministry of Education, Science and Technological Development of the Republic of Serbia. F.A.G. and R.W. thank the FWF, Austrian Science Fund (FWF) for supporting the present research through the Project P27047-N20.

## REFERENCES

- [1] P. Thaddeus, C. Gottlieb, H. Gupta, S. Brünken, M. McCarthy, M. Agúndez, M. Guélin and J. Cernicharo, *Astrophys. J.* 2008, 677, 1132.
- [2] P. Botschwina, R. Oswald, *J. Chem. Phys.*, 2008, 129, 044305.
- [3] M. Agúndez, J. Cernicharo, M. Guélin, C. Kahane, E. Roueff, J. Kłos, F. Aoi, F. Lique, N. Marcelino, J. Goicoechea, M. G. Garcia, C. A. Gottlieb, M. C. McCarthy, P. Thaddeus, *Astron. Astrophys.*, 2010, 517, L2.
- [4] H. Liszt, R. Lucas, *Astron. Astrophys.*, 2001, 370, 576.
- [5] P. Hily-Blant, M. Walmsley, G. Pineau des Forêts, D. Flower, *Astron. Astrophys.*, 2010, 513, A41.
- [6] H.-J. Werner and P. J. Knowles, *J. Chem. Phys.*, 1988, 89, 5803.
- [7] K. R. Shamasundar, G. Knizia, H.-J. Werner, *J. Chem. Phys.*, 2011, 135, 054101.
- [8] D. E. Woon and T. H. Dunning, *J. Chem. Phys.*, 1994, 100, 2975.
- [9] H.-J. Werner, P. J. Knowles, G. Knizia, F. R. Manby, M. Schütz and others, MOLPRO, Version 2012.1, a package of ab initio programs, 2012, see <http://www.molpro.net>.
- [10] H.-J. Werner, P. J. Knowles, G. Knizia, F. R. Manby, M. Schütz, *WIREs Comput. Mol. Sci.*

## ANTIRADICAL ACTIVITY OF SELECTED TRIAZOLE COMPOUNDS

Z. Marković<sup>1</sup>, J. Đorović<sup>2</sup>, D. Milenković<sup>2</sup>, S. Jeremić<sup>1</sup>, Lj. Joksović<sup>3</sup> and A. Amić<sup>4</sup>

<sup>1</sup> *State University of Novi Pazar, Department of Chemical-Tehnological Science, Vuka Karadžića bb, 36300 Novi Pazar, Serbia  
34000 Kragujevac, Serbia. (e-mail: zmarkovic@kg.ac.rs)*

<sup>2</sup> *Bioengineering Research and Development Center, Prvoslava Stojanovića 6, 34000 Kragujevac, Serbia.*

<sup>3</sup> *Faculty of Science, University of Kragujevac, Radoja Domanovića 12, 34000 Kragujevac, Serbia.*

<sup>4</sup> *Department of Chemistry, Josip Juraj Strossmayer University, Cara Hadrijana 8a, 31000 Osijek, Croatia.*

### ABSTRACT

In the present study the B3LYP-D3/6-311G++(d,p) model is used to evaluate radical scavenging potency of selected triazole. Reaction enthalpies related to the scavenging mechanisms of the investigated species were calculated in methanol and benzene. Sequential proton loss electron transfer is a preferred reaction pathway in benzene. There is competition between that mechanism and hydrogen atom transfer in methanol.

### INTRODUCTION

For the last several decades, 1,2,4-triazole-3-thiones have gained considerable importance due to their biological properties. This 5-membered heterocyclic ring has been incorporated into a number of pharmacologically interesting compounds with anticonvulsant [1], antidepressant [2], anti-inflammatory [3], antibacterial [4], antifungal [5], and anticancer activities [6]. In the field of potential industrial applications, 1,2,4-triazole-3-thiones have demonstrated promising corrosion inhibition of copper, and mild steel [7]. In this paper, we evaluated the possibility of inactivation of three free radicals with one 1,2,4-triazole-3-thione from our previous paper (**4a** – Figure 1) [8]. Free radical species that are used are: methoxy radical, methylperoxy radical and dichloromethylperoxy radical. It is well known that values of reaction enthalpies can significantly contribute to understanding of examined reaction mechanisms: hence reaction enthalpies that describe H-atom abstraction mechanisms are calculated and discussed. Reaction with a free radical (RO<sup>•</sup>) can follow several antioxidant mechanisms: hydrogen atom

transfer (HAT, Eq. (1)), single electron transfer followed by proton transfer (SET-PT, Eqs. (2) and (3)), and sequential proton loss electron transfer (SPLET, Eqs. (4) and (5)).

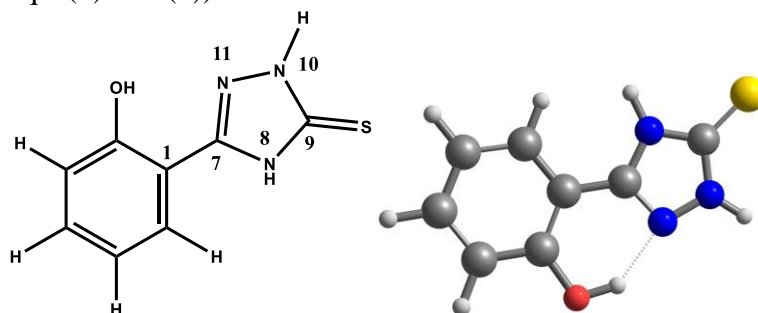
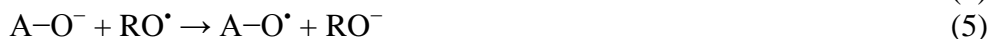
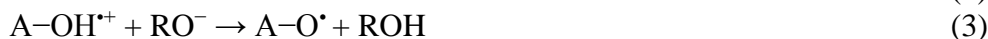


**Figure 1.** Structure of investigated compound 4a



The reaction of examined compound with particular free radical is thermodynamically favourable if it is exothermic:

$$\Delta_r H = [H(\text{products}) - H(\text{reactants})] < 0 \quad (6)$$

In radical inactivation, HAT mechanism (Eq. 1) is characterized by H-atom transfer from the investigated compound to the free radical ( $\text{RO}^\bullet$ ):

$$\Delta_r H_{\text{BDE}} = [H(\text{A-O}^\bullet) + H(\text{ROH})] - [H(\text{A-OH}) + H(\text{RO}^\bullet)] \quad (7)$$

The SET-PT mechanism is described with Eqs. 2 and 3. The first step is determined by  $\Delta_r H_{\text{IP}}$  and the second one by  $\Delta_r H_{\text{PDE}}$ , Eqs. 8 and 9:

$$\Delta_r H_{\text{IP}} = [H(\text{A-OH}^{+\bullet}) + H(\text{RO}^-)] - [H(\text{A-OH}) + H(\text{RO}^\bullet)] \quad (8)$$

$$\Delta_r H_{\text{PDE}} = [H(\text{A-O}^\bullet) + H(\text{ROH})] - [H(\text{A-OH}^{+\bullet}) + H(\text{RO}^-)] \quad (9)$$

The reaction enthalpies of  $\Delta_r H_{\text{PA}}$  and  $\Delta_r H_{\text{ETE}}$  are related to the SPLET mechanism (Eqs. 4 and 5), and are calculated using Eqs. 10 and 11:

$$\Delta_r H_{\text{PA}} = [H(\text{A-O}^-) + H(\text{ROH})] - [H(\text{A-OH}) + H(\text{RO}^-)] \quad (10)$$

$$\Delta_r H_{\text{ETE}} = [H(\text{A-O}^\bullet) + H(\text{RO}^-)] - [H(\text{A-O}^-) + H(\text{RO}^\bullet)] \quad (11)$$

## EXPERIMENTAL

Equilibrium geometries of investigated compounds and corresponding radicals, radical cations, and anions were fully optimized at the B3LYP-D3/6-311G++(d,p) level of theory. Vibrational frequencies were computed: no imaginary frequencies were obtained. The SMD solvation model was applied

to approximate the influence of methanol and benzene as solvents, i.e. to mimic polar and non-polar solvents.

## RESULTS AND DISCUSSION

Scavenging mechanisms are highly influenced by the electronic properties of the scavenged free radical species [9]. Preferred mechanism can be assumed from the  $\Delta_r H_{\text{BDE}}$ ,  $\Delta_r H_{\text{IP}}$ , and  $\Delta_r H_{\text{PA}}$  values. More negative values indicate thermodynamically more favourable mechanisms.

**Table 1:** Calculated reaction enthalpies ( $\text{kJ mol}^{-1}$ ) for reactions of the inspected triazole (**4a**) with selected radicals in methanol and benzene

	HAT	SET-PT		SPLET		HAT	SET-PT	SPLET		
	$\Delta_r H_{\text{BD}}$ E	$\Delta_r H_{\text{I}}$ P	$\Delta_r H_{\text{PD}}$ E	$\Delta_r H_{\text{P}}$ A	$\Delta_r H_{\text{ET}}$ E	$\Delta_r H_{\text{BD}}$ E	$\Delta_r H_{\text{I}}$ P	$\Delta_r H_{\text{PD}}$ E	$\Delta_r H_{\text{P}}$ A	$\Delta_r H_{\text{ET}}$ E
	Methanol					Benzene				
4a – N10 + $\text{CH}_3\text{O}\cdot$	-75	103	-177	-79	4	-64	355	-418	-163	99
4a – N8 + $\text{CH}_3\text{O}\cdot$	-65		-168	-88	23	-62		-416	-180	119
4a –O6 + $\text{CH}_3\text{O}\cdot$	-61		-164	-62	1	-37		-392	-121	84
4a – N10 + $\text{CH}_3\text{OO}\cdot$	1	134	-133	-35	36	13	396	-383	-128	140
4a – N8 + $\text{CH}_3\text{OO}\cdot$	10		-124	-44	54	15		-381	-145	160
4a –O6 + $\text{CH}_3\text{OO}\cdot$	14		-120	-18	32	39		-357	-86	125
4a – N10 + $\text{CHCl}_2\text{O}\cdot$	-28	60	-88	10	-39	-10	271	-281	-25	15
4a – N8 + $\text{CHCl}_2\text{O}\cdot$	-19		-78	2	-20	-8		-279	-43	35
4a –O6 + $\text{CHCl}_2\text{OO}\cdot$	-15		-74	28	-42	16		-254	17	0

It should be emphasized that positive values of  $\Delta_r H_{\text{IP}}$  indicate SET-PT as not-operative mechanistic pathway for radical neutralization of all three examined radicals in both solvents (Table 1). Results obtained in methanol indicate competition between HAT and SPLET mechanisms in the case of methoxy radical. Negative values of  $\Delta_r H_{\text{PA}}$  reveal that methylperoxy radical will probably be inactivated *via* SPLET mechanism. Regarding

dichloromethylperoxy radical,  $\Delta_r H_{\text{BDE}}$  values indicate HAT as favorable mechanism of antioxidant action in methanol. On the other hand, results achieved in benzene undoubtedly indicate SPLET as dominant antioxidant mechanism for inactivation of all examined radicals.

## CONCLUSION

Antioxidant activity of compound **4a** was examined by analysing the reaction enthalpies of three antioxidant mechanisms with three different radicals. Based on obtained results it can be concluded that HAT and SPLET mechanisms are possible reaction pathways in polar solvents, such as methanol. Regarding non-polar solvent, such as benzene, SPLET mechanism is prevailing reaction path in the case of applied radicals.

## Acknowledgement

This work was partially supported by the Ministry of Science and Technological Development of the Republic of Serbia (Grant nos 172016 and 174028).

## REFERENCES

- [1] T. Plech, B. Kapron, J. J. Luszczki, A. Paneth, A. Siwek, M. Kolaczowski, M. Zolnierok, G. Nowak, *Eur. J. Med. Chem.* 2014, **86**, 690–699.
- [2] J. M. Kane, M. W. Dudley, S. M. Sorensen, F. P. Miller, *J. Med. Chem.* 1988, **31**, 1253–1258.
- [3] E. Palaska, G. Sahin, P. Kelicen, N. T. Durlu, G. Altinok, *Farmaco*, 2002, **57**, 101–107.
- [4] I. R. Ezabadi, C. Camoutsis, P. Zoumpoulakis, A. Geronikaki, M. Soković, J. Glamočilija, A. Ćirić, *Bioorg. Med. Chem.* 2008, **16**, 1150–1161.
- [5] J. E. Parker, A. G. Warillow, H. J. Cools, C. M. Martel, W. D. Nes, B. A. Fraaije, J. A. Lucas, D. E. Kelly, S. L. Kelly, *Appl. Environ. Microbiol.* 2011, **77**, 1460–1465.
- [6] A. T. Mavrova, D. Wesselinova, Y. A. Tsenov, P. Denkova, *Eur. J. Med. Chem.* 2009, **44**, 63–69.
- [7] M. S. Kumar, S. Loganathan, A. Kumar, A. Sreekanth, *Ind. Eng. Chem. Res.* 2012, **51**, 5408–5418.
- [8] N. Ivanović, L. Jovanović, Z. Marković, V. Marković, M. D. Joksović, D. Milenković, P. T. Djurdjević, A. Ćirić, L. Joksović, *ChemistrySelect* 2016, **1**, 3870.
- [9] J. Xie and K. M. Schaich, *J. Agric. Food Chem.*, 2014, **62**, 4251–4260.

## REACTIVITY OF CHLOROGENIC ACID TOWARD HYDROXYL RADICAL RELATIVE TO TROLOX IN BENZENE

J. Tošović and S. Marković

*University of Kragujevac, Faculty of Science,  
12 Radoja Domanovića, 34000 Kragujevac, Serbia.  
(jelena.tosovic@pmf.kg.ac.rs)*

### ABSTRACT

The quantum mechanics-based test for overall free-radical scavenging activity was applied for the investigation of antioxidative capacity of chlorogenic acid (**5CQA**) relative to trolox (**Tx**) as a reference compound. Hydrogen atom transfer (HAT), radical adduct formation (RAF), electron transfer (ET) and proton loss (PL) reactions of **5CQA** and **Tx** with HO• radical in benzene were examined. For this purpose the M06-2X/6-311++G(d,p) theoretical model in combination with the CPCM solvation model was employed. Both compounds can react with HO• via HAT and RAF mechanisms. **5CQA** is more reactive toward HO• than **Tx**.

### INTRODUCTION

A wide range of experimental assays (chemical and biological) have been used to evaluate antioxidative capacity of compounds. Recently, a computational protocol has been proposed for estimating antioxidative capacity [1]. This approach offers possibility to determine the relative antioxidative activity using **Tx** as a reference antioxidant by examining all possible antioxidative pathways of both compounds, and calculating their rate constants.

This work is an extension of our efforts aimed at elucidation of antioxidative properties of **5CQA** [2–5]. The goal of the work is to determine relative antioxidative capacity of **5CQA** toward HO• using **Tx** as a reference in nonpolar benzene. The HO• radical was selected because it is produced during Fenton and Haber-Weiss reactions in organism, and represents one of the most potent radicals of biological importance.

### EXPERIMENTAL

All antioxidative pathways of **5CQA** and **Tx** (Figure 1) with the HO• radical were investigated using the M06-2X/6-311++G(d,p) theoretical model in combination with the CPCM solvation model. All calculations were

performed using the Gaussian 09 program package [6]. The following reactions were considered:



where Phenolic stands for **5CQA** and **Tx**. Accordingly, Phenolic<sup>•</sup>, (Phenolic-R)<sup>•</sup>, Phenolic<sup>-</sup>, and Phenolic<sup>+•</sup> represent the free radical, radical adduct, anion, and radical cation issued from the corresponding phenolic compound, respectively.

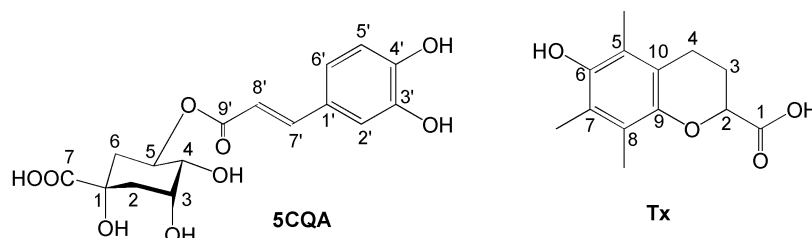


**Figure 1.** Structure of chlorogenic acid (**5CQA**) and trolox (**Tx**).

## RESULTS AND DISCUSSION

The reactions (1) – (4) were first subjected to thermodynamic examination with an aim to select exergonic reaction pathways for further analysis. The results are presented in Table 1. As expected for nonpolar solvents, both compounds show pronouncedly positive  $\Delta_r G$  values for the loss of carboxylic proton [Eq. (3)], and for the transfer of electron to  $\text{HO}^\bullet$  [Eq. (4)]. These results show that neither **5CQA** nor **Tx** undergo the SPLET and SET-PT mechanisms in nonpolar media.

All exergonic reaction pathways were subjected to kinetic investigation, aimed at revealing the transition states and calculating the corresponding rate constants using the Eckart formula:

$$k = \sigma \gamma(T) \frac{k_B T}{h} \exp\left(-\frac{\Delta G_a^\ddagger}{RT}\right) \quad (5)$$

where  $k_B$ ,  $h$ ,  $R$ ,  $\sigma$ ,  $\gamma(T)$ , and  $\Delta G_a^\ddagger$  stand for the Boltzmann, Planck, and universal gas constants, reaction path degeneracy, transmission coefficient, and Gibbs activation energy. The  $k_{\text{overall}}$  values were obtained as the sums of the corresponding  $k$  values. The  $r^T$  (antioxidative activity of **5CQA** relative to **Tx**) value was calculated by dividing  $k_{\text{overall}}$  for **5CQA** with  $k_{\text{overall}}$  for **Tx**. The branching ratio  $\Gamma$  (percent contribution of an antioxidative pathway  $i$  to

the overall reaction of **5CQA**) was calculated by dividing  $k(i)$  with  $k_{\text{overall}}$ , and multiplying with 100. The results are collected in Table 2.

**Table 1.** Gibbs energies  $\Delta_r G$  (kJ mol<sup>-1</sup>) of the reactions (1) – (4) for chlorogenic acid (**5CQA**) and trolox (**Tx**) in benzene.

Mechanism	Position	<b>5CQA</b>	Position	<b>Tx</b>
HAT	3'	-150.7	6	-167.2
	4'	-160.5		
RAF	1'	-18.2	1	25.7
	2'	-53.0		
	3'	-37.9		
	4'	-77.3		
	5'	-33.7		
	6'	-55.6		
	7'	-81.8		
	8'	-101.8		
	9'	24.6		
PL	1	339.4	1	374.1
ET	/	339.4	/	260.1

**Table 2.** Gibbs activation energies  $\Delta G_a^\ddagger$  (kJ mol<sup>-1</sup>), rate constants  $k$  (M<sup>-1</sup> s<sup>-1</sup>), and branching ratios  $\Gamma$  (%) for the investigated reactions.

Compound Mechanism	<b>5CQA</b>				<b>Tx</b>		
		$\Delta G_a^\ddagger$	$k$	$\Gamma$		$\Delta G_a^\ddagger$	$k$
HAT	3'	41.5	1.61×10 <sup>7</sup>	0.7	6	25.3	6.49×10 <sup>6</sup>
	4'	45.5	4.54×10 <sup>6</sup>	0.2			
RAF	1'	52.7	1.21×10 <sup>5</sup>	~0.0	5	18.5	1.33×10 <sup>7</sup>
	2'	36.8	2.89×10 <sup>7</sup>	4.6			
	3'	40.3	1.55×10 <sup>7</sup>	1.4			
	4'	26.5	8.44×10 <sup>7</sup>	65.7			
	5'	36.9	3.73×10 <sup>7</sup>	2.9			
	6'	36.6	6.82×10 <sup>7</sup>	15.3			
	7'	39.9	1.94×10 <sup>7</sup>	2.2			
	8'	25.4	5.82×10 <sup>7</sup>	7.0			
<b><math>k_{\text{overall}}</math></b>			3.33×10 <sup>8</sup>				1.31×10 <sup>8</sup>

In nonpolar benzene the two antioxidants undergo both HAT and RAF pathways with HO<sup>•</sup>. As for the reactions of both phenolics, the RAF pathways are generally faster. The fastest pathways of **5CQA** and **Tx** are RAFs in the

positions 4' and 6, respectively, where transition states are stabilized with hydrogen bonds between approaching HO• and phenolic groups. Attractive interactions in the HAT reaction paths slow down the formation of water and its leaving the reaction system. Thus, addition of HO• to the double bond of **5CQA** is thermodynamically most favorable (Table 1), however, the greatest  $\Gamma$  value for the reaction of **5CQA** with HO• comes from the RAF pathway in the 4' position (Table 2).

**5CQA** is more reactive towards HO• than **Tx** ( $r^T = 2.5$ ). Larger reactivity of **5CQA** is mainly a consequence of very fast RAF pathways. In comparison to **Tx**, **5CQA** has more suitable positions for addition of HO•.

## CONCLUSION

Antioxidative activity of **5CQA** toward the HO• radical relative to **Tx** was evaluated. In nonpolar benzene both compounds undergo HAT and RAF pathways, where **5CQA** is more reactive towards HO• than **Tx** ( $r^T > 1$ ). A logical next step of our investigation is to determine  $r^T$  of **5CQA** in aqueous solution where extremely complex reactions are expected.

## Acknowledgement

This work was partially supported by the Ministry of Education, Science and Technological Development of Serbia (Grant no. 172016).

## REFERENCES

- [1] A. Galano, J. R. Alvarez-Idaboy, 2013, *J. Comput. Chem.* **34**, 2430–2445.
- [2] S. Marković, J. Tošović, 2016, *Food Chem.* **210**, 585–592
- [3] J. Tošović, S. Marković, 2016, *Croat. Chem. Acta* **89**, 535–541.
- [4] J. Tošović, S. Marković, J. M. Dimitrić Marković JM, M. Mojović, D. Milenković, 2017, *Food Chem.* **237**, 390–398.
- [5] J. Tošović, S. Marković, 2018, *Theor. Chem. Acc.* **137**, 76.
- [6] Gaussian 09, Revision D.01. Wallingford: Gaussian, Inc., 2013.

## SYNTHESIS, STRUCTURAL CHARACTERIZATION, SPECTROSCOPIC PROPERTIES, AND THEORETICAL INVESTIGATIONS OF ACETOXY SIDEROL

Z. Özer<sup>1</sup>, T.Kılıç<sup>2</sup>, S. Çarıkçı<sup>3</sup> and A. Azizoğlu<sup>3</sup>

<sup>1</sup>*Balikesir University, Altnoluk Vocational School, Medicinal and Aromatical Plants Program, 10870, Edremit, Balıkesir, Turkey.  
(zuleyhaozer@balikesir.edu.tr)*

<sup>2</sup>*Balıkesir University, Necatibey Education Faculty, Department of Science Educations, 10100, Balıkesir, Turkey.*

<sup>3</sup>*Balıkesir University, Faculty of Sciences and Arts, Department of Chemistry, Campus of Çağış, 10145- Balıkesir, Turkey.*

### ABSTRACT

In the present study, acetoxy siderol was synthesized starting from siderol isolated from endemic *Sideritis* species, then its chemical structure was determined by using various spectroscopic methods (FT-IR, <sup>1</sup>H-NMR, and <sup>13</sup>C-NMR). The geometrical parameters and vibrational frequencies of acetoxy siderol in the ground state have been calculated using the Density Functional Theory (DFT) and Hartree-Fock (HF) methods with the 6-31G(d) basis set. The calculated vibrational frequencies have been compared with that of obtained experimental IR spectrum.

### INTRODUCTION

Medical plants are biologically active and used in the treatment of various diseases among the population since ancient times. Most of the plants belonging to Lamiaceae (Labiatae) family, which contain 224 genera and about 7,200 species, have been used as folk medicines treatment of various diseases since ancient times, as well as used in medicine, food industry, cosmetics and perfumery. *Sideritis* L. belongs to the family of Lamiaceae (Labiatae), which is one of the most common and diverse plants in the world, comprising over 150 species [1,2]. The chemical components found in *Sideritis* genus include terpenes, flavonoids, iridoids, coumarins, lignanes and sterols, among others. Diterpenes and flavonoids occur in almost every species and are the main compounds responsible for the observed in vivo and in vitro pharmacological activities [2,3].

Computational chemistry which is a developing subdivision of theoretical chemistry is tried to explain unknowns about chemistry and especially organic chemistry. A useful feature of computational chemistry is calculated

molecular structures which can not experimentally identified. The first rule in predicting important physical and chemical properties in chemical and biological systems is the use of various computational techniques. DFT is a method used to study the electronic structure of atoms and molecules [4,5].

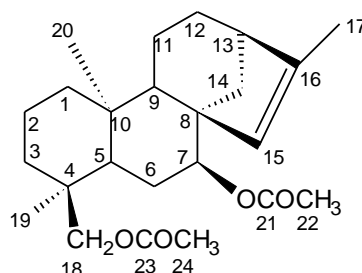


**Figure 1.** Structure and atom numbering scheme of acetoxy siderol.

### EXPERIMENTAL

Siderol having the *ent*-kaurene skeleton can be isolated from different species of *Sideritis* such as *S. akmanii*, *S. argyrea*, *S. condensata*, *S. congesta*, *S. dichotoma*, *S. erythrantha*, *S. huber-morathii*, *S. libanotica*, *S. perfoliata*, *S. sipylea*, *S. stricta*, *S. brevibracteata* and *S. trojana* [6,7]. Acetoxy siderol were synthesized from siderol using acetic anhydride. Infrared spectrum was obtained using a PerkinElmer Spectrum Version 10.02.00. The molecular structure of acetoxy siderol in the ground state (in vacuo) was optimized using Density Functional Theory (DFT) and Hartree-Fock (HF) with the 6-31G(d) basis set. All of the calculations reported in this study have been performed using the Gaussian 09 code [8].

### RESULTS AND DISCUSSION

The molecular geometry (bond lengths, bond angles, and dihedral angles) of the acetoxy siderol has been optimized at the DFT and HF methods. C4-C5, C6-C7 and C13-C14 are 1.551, 1.536 and 1.538 Å for PM3/ZDO method, 1.569, 1.532 and 1.537 Å for B3LYP/6-31G(d) method, 1.562, 1.525 and 1.529 Å for HF/6-31G(d) method and 1.566, 1.530 and 1.535 Å for X3LYP/6-31G(d) method which are in good agreement with a similar molecular structure [4]. Moreover, the optimized O=C<sub>21</sub> and O=C<sub>23</sub> carbonyl group bond lengths obtained 1.213 and 1.212 Å for PM3/ZDO, 1.207 and 1.205 Å for B3LYP/6-31G(d), 1.185 and 1.182 Å for HF/6-31G(d) and 1.208 and 1.204 Å for X3LYP/6-31G(d).

**Table 1.** Selected experimental and theoretical vibrational wavenumbers of acetoxy siderol.

Exp. (cm <sup>-1</sup> )	PM3/ZDO	B3LYP/ 6-31G(d)	HF/6-31G(d)	X3LYP/6-31G(d)	Approximate description
	1107	1223	1073	1049	<b>C18 twisting</b>
	1311	1409	1562	1415	<b>C7-H wagging</b>
1558	1350	1442	1567	1443	<b>CH<sub>3</sub> (C17) wagging</b>
1439	1351, 1356	1422	1559	1422	<b>CH<sub>3</sub> (C24) wagging</b>
1478		1420	1558	1423	<b>CH<sub>3</sub> (C22) wagging</b>
	1376	1539	1680	1541	<b>CH<sub>2</sub> (C18) scissoring</b>
1550	1387, 1389	1508, 1516	1624, 1633	1509, 1518	<b>CH<sub>3</sub> (C17) scissoring</b>
		1504	1622	1505	
	1394	1519	1633	1519	<b>CH<sub>3</sub> (C22) scissoring</b>
	1396	1498	1616	1498	
	1396	1516	1631	1517	<b>CH<sub>3</sub> (C24) scissoring</b>
1656	1866	1720	1877	1724	<b>C=C symmetrical stretching</b>
1707	1983	1846	2022	1839	<b>C=O (C21) symmetrical stretching</b>
1748	1992	1861	2045	1867	<b>C=O (C23) symmetrical stretching</b>
	2820, 2822	3088	3285, 3283	3094, 3089	<b>C7-H symmetrical stretching</b>
	2878	3078	3291	3089	<b>CH<sub>2</sub> (C18) asymmetrical stretching</b>
	2901	3090	3270	3101	<b>CH<sub>2</sub> (C6) asymmetrical stretching</b>
	2952	3093	3278	3109	<b>CH<sub>2</sub> (C3) asymmetrical stretching</b>
2940	2960	3036, 3059		3040	<b>C-H symmetrical stretching</b>
	2962	3028, 3032	3219	3032	<b>CH<sub>2</sub> (C18) symmetrical stretching</b>
	2963	3048	3231	3062	<b>CH<sub>2</sub> (C6) symmetrical stretching</b>
	2991	3047	3213	3052	<b>CH<sub>2</sub> (C14) symmetrical stretching</b>
	3055, 3081	3125	3288, 3340	3131, 3184	<b>CH<sub>3</sub> (C22) asymmetrical stretching</b>
	3061, 3083	3123	3293, 3345	3137	<b>CH<sub>3</sub> (C24) asymmetrical stretching</b>
	3160	3063	3225	3069	<b>CH<sub>3</sub> (C22) symmetrical stretching</b>
	3165	3064	3229	3072, 3186	<b>CH<sub>3</sub> (C24) symmetrical stretching</b>

We have calculated the theoretical spectra of acetoxy siderol using PM3, HF, B3LYP and X3LYP levels with 6-31G(d) basis set. Theoretical and experimental results of title compound are shown in Table 1. The vibrational analysis of acetoxy siderol is performed on the basis of the characteristic vibrations of methyl groups, OAc groups and C=C group. The symmetric

C=C stretching frequencies observed at  $1656\text{ cm}^{-1}$  are theoretically predicted at between  $1720\text{ cm}^{-1}$  and  $1877\text{ cm}^{-1}$ . The OAc vibrations are observed to  $1707$  and  $1748\text{ cm}^{-1}$  in experimental IR spektrum. This bands calculated  $1829\text{-}2022$  and  $1867\text{-}2045\text{ cm}^{-1}$  (C21 and C23 respectively). Methyl vibrations are generally occur in the range  $(2900\text{-}3000)\text{ cm}^{-1}$ . The bands observed in the range  $(3063\text{-}3186)\text{ cm}^{-1}$  using DFT are assigned to symmetrical and asymmetrical stretchching methyl groups. The correlation values are found to be  $0.8785$ ;  $0.9775$ ;  $0.9028$  and  $0.9781$  for PM3, B3LYP, HF and X3LYP with the 6- 31G(d) basis set, respectively. So that X3LYP level with 6-31G(d) basis set is the best method.

### CONCLUSION

In this study, we have calculated the geometric parameters and vibrational frequencies of acetoxy siderol by using HF and DFT (B3LYP and X3LYP) methods with 6-31G(d) basis set. The theoretical vibrational analysis of acotoxy siderol has also been performed for the first time. The calculated vibrational frequencies have been compared with that obtained from the experimental IR spectrum. As a result, experimental fundamentals are found to have slightly a better correlation for X3LYP level with 6-31G(d) basis set than others.

### Acknowledgement

This work was partially supported by University of Balıkesir-BAP (Grant no. 2017/159).

### REFERENCES

- [1] I. Aslan, T. Kılıç, A.C. Gören, G. Topçu, *Industrial Crops and Products*, 2006, 23, 171-176.
- [2] E. González-Burgos, M.E. Carretero, M.P. Gómez-Serranillos, *Journal of Ethnopharmacology*, 2011, 135, 209-225.
- [3] A. Güvenç, Y. Okada, E. Küpeli Akkol, H. Duman, T. Okuyama, I. Çalış, *Food Chemistry*, 2010, 118, 686-692.
- [4] A. Azizoglu, Z. Özer, T. Kilic, *Collect. Czech. Chem. Comm.*, 2011, 76, 95-114.
- [5] T. Wang, X. Wang, *Spectrochimica Acta Part A: Molecular and Biomolecular Spectroscopy*, 2015, 135, 568-575.
- [6] Z.O. Sagir, S. Carikci, T. Kilic, A.C. Goren, *International Journal of Food Properties*, 2017, 20, 2994-3005.
- [7] B.M. Fraga, *Phytochemistry*, 2012, 76, 7-24.
- [8] Gaussian 09. Revision A02, Gaussian, Inc., Pittsburgh.

## PRELIMINARY INVESTIGATION OF THE PLASMA INDUCED ON POTTERY SAMPLE BY TEA CO<sub>2</sub> LASER

D.P. Ranković<sup>1</sup>, M.M. Kuzmanović<sup>1</sup>, J.J. Savović<sup>2</sup>, S. Živković<sup>2</sup>, M. Stoiljković<sup>2</sup> and M. Trtica<sup>2</sup>

<sup>1</sup> *University of Belgrade, Faculty for Physical Chemistry, Studentski Trg 12-16, 11000 Belgrade, Serbia. (miroslav@ffh.bg.ac.rs)*

<sup>2</sup> *University of Belgrade, INN "Vinča", Mike Petrovića Alasa 12-14, 11001 Belgrade, Serbia.*

### ABSTRACT

Laser-induced breakdown spectroscopy (LIBS) was applied for elemental analysis of Serbian medieval pottery artifact. A compact, low energy, Transversely Atmospheric Excited carbon dioxide (TEA CO<sub>2</sub>) laser was used to induce plasma on unglazed side of the pottery sample. The collected spectra contained spectral lines of atoms and ions of the sample constituents (e.g. Fe, Al, Ti, Ca, V) with good signal to noise ratio, suitable for the spectrochemical analysis.

### INTRODUCTION

The chemical analysis of ceramic archaeological samples provides relevant information about their historical and geographic origin. The electrical non-conductivity and aluminosilicate base of the pottery samples make chemical analysis more difficult and reduce choice of available analytical techniques. An additional request for valuable archaeological artefacts is minimization of the amount of sample required to perform analysis. The minor damaging of samples during laser irradiation makes LIBS preferable method for trace element analysis of pottery [1]. In comparison with frequently used XRF method, LIBS has better sensitivity, allow surface chemical analysis and surface mapping (by beam focusing) and does not suffer from problem with determination of the light elements. Similar to other techniques dealing with solid samples, LIBS has limited precision.

One of the advantages of the nanosecond infrared TEA CO<sub>2</sub> laser compared to commonly used lasers for LIBS, like Nd:YAG lasers, is less sample damage. Because of lower photon energy, longer pulse duration, and strong effect of plasma shielding during laser-plasma interaction, ablation of the material is reduced. The aim of the present work was investigation of the analytical applicability of TEA CO<sub>2</sub> laser for LIBS analysis of unglazed parts

of the pottery samples. The sample was a Serbian medieval pottery artefact found in the Kalemegdan Fortress in Belgrade.

### **EXPERIMENTAL**

Plasma was induced using a miniature TEA CO<sub>2</sub> laser, with a wavelength of 10.6 μm and pulse energy up to 160 mJ [2]. The laser pulse had a gain-switched spike (35% of the pulse energy) followed by slowly decaying tail: the full width at half maximum of spike is approximately 100 ns, while the tail last for about 2 μs. A simplified time-integrated space-resolved (TISR) spectroscopy was applied for acquisition of emission spectra. Spatially selected slice of the plasma plume was projected onto the slit of the Carl Zeiss PGS 2 monochromator, equipped with an Apogee Alta F1007 CCD camera.

The sample was rotated with 0.5 rpm using a step motor. LIBS spectra of unglazed side of the medieval pottery sample were recorded in air at atmospheric pressure by averaging at least 30 shots. The same experimental setup has already been successfully applied for the analysis of aluminosilicate samples (basalt rock) [3,4].

### **RESULTS AND DISCUSSION**

The plasma formed by the interaction of laser pulses with a pottery sample was white, with non-spherical plume elongated to about 10 mm from the target surface.

When the laser beam was focused on the target or behind it, narrow and intensive lines of elements contained in the sample dominate the spectrum. Upon focusing of the laser radiation in front of the target, denser and hotter plasma was created, and strong and wide lines of air constituents (N, O) appeared in the spectrum. Such plasma is not convenient for the spectrochemical analysis. Typical LIBS spectra of pottery sample obtained under different focusing conditions are presented in Fig. 1. In both cases, the spectrum was taken from a plasma zone at a distance of 1 mm above the sample surface.

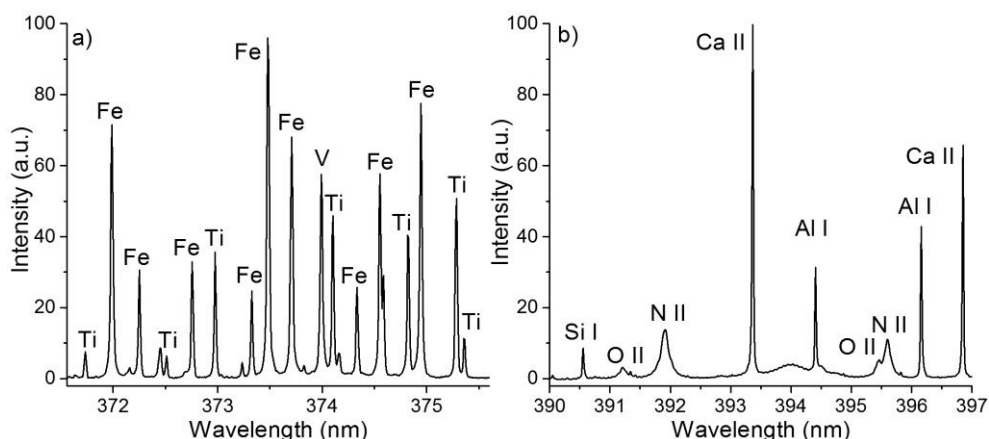


**Figure 1.** An example of time integrated LIBS spectrum of pottery sample, a) Laser focused on the target surface; b) Laser focused in front of the target surface.

From the measured line intensities and background fluctuation, signal to noise ratios (SNR) were calculated for several focal distances. The highest SNR values, both for atomic and ionic lines of iron, were obtained when laser radiation was focused on the target surface. Because the accurate sample composition was unavailable, limit of detection (LOD) was roughly estimated from the typical average composition of the pottery. For Al, Fe and Ca the obtained LODs were of the order of 0.01%, while for Ti and V of the order of 10 ppm. It may be expected that careful optimization of the excitation conditions will result in lower levels of LODs for metal elements.

In Fig. 2, Boltzmann plots of integral intensities of selected atomic iron and titanium spectral lines are shown. From the slope of the fitted graphs the temperature was estimated to be  $(6800 \pm 900)$  K and  $(13300 \pm 800)$  K. Relatively high error was presumably caused by uncertainties in transition probabilities of available spectral lines. The difference in temperatures obtained using atomic and ionic lines point to the fact that atomic and ionic lines are emitted from different plasma zones: the atomic lines from the colder periphery of the plasma, and ionic lines from hotter plasma core (characterized by high ionization degree).

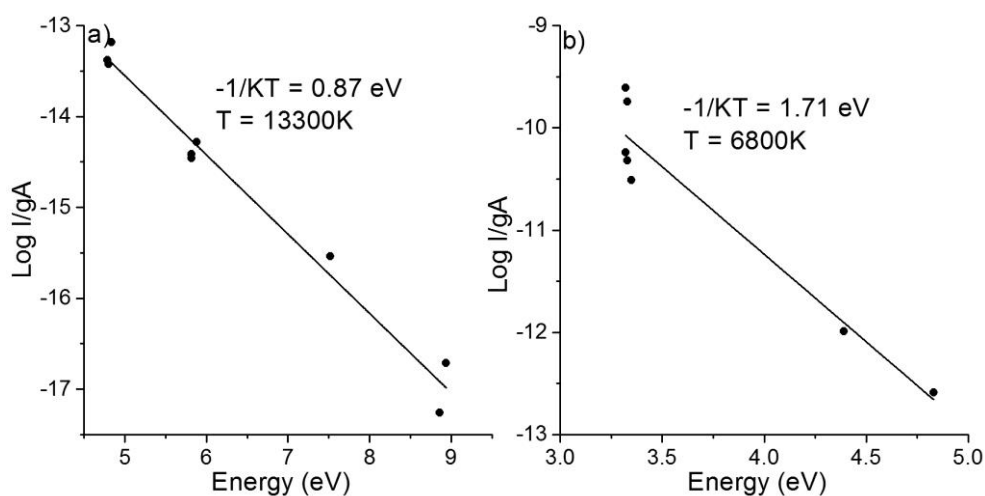


**Figure 2.** Boltzmann plot utilizing the appropriate set of: a) Fe II lines, and b) Ti I lines. The spectral line intensities were taken from part of plasma at a distance of 0.5 mm (Fe II) and 1 mm (Ti I) from the sample surface.

## CONCLUSION

The TISR-LIPS method, based on TEA CO<sub>2</sub> laser, was applied to assess its applicability for the semi quantitative elemental analysis of metal content in unglazed archaeological pottery sample. The recorded narrow and intensive spectral lines of Fe, Ti, Al, Ca and V, with good signal to background ratio, indicated promising spectrochemical properties, including the detectability sufficient for the trace element analysis.

## Acknowledgement

This research was supported by the Ministry of Education, Science and Technological Development of the Republic of Serbia through the project no. 172019.

## REFERENCES

- [1] K. Kuzuya, M. Murakami and N. Maruyama, *Spectrochim. Acta - Part B At. Spectrosc.*, 2003, 58, 957.
- [2] M.S. Trtica, B.M. Gakovic, B.B. Radak, and S.S. Miljanic, *Proc. SPIE*, 2002, 4747, 44.
- [3] J. Savovic, M. Momcilovic, S. Zivkovic, A. Stancalie, M. Trtica, and M. Kuzmanovic, *J. Chem.*, 2017, 2017, 9p.
- [4] J. Savovic, M. Stoiljkovic, M. Kuzmanovic, M. Momcilovic, J. Ciganovic, D. Rankovic, S. Zivkovic, and M. Trtica, *Spectrochim. Acta - Part B At. Spectrosc.*, 2016, 118, 127.

## CHEMILUMINESCENCE OF ACRIDINIUM DERIVATIVES WITH HYDROGEN PEROXIDE IN ALKALINE MEDIA

B. Zadykowicz

*University of Gdansk, Faculty of Chemistry, Laboratory of Luminescence  
Research, Wita Stwosza 63, 80-308 Gdansk, Poland.  
(beata.zadykowicz@ug.edu.pl)*

### ABSTRACT

Density functional theory calculations were performed to investigate the detailed mechanism of the oxidation of 9-substituted-10-methylacridinium cations involved in acridinium esters by hydrogen peroxide in alkaline media. Three general pathways were drawn, which are termed the ‘light path’ (chemiluminogenic) and two ‘dark paths’ (non-chemiluminogenic): hydrolytic and ‘pseudobase’. The thermodynamic data obtained theoretically is well comparable to the experimental findings, as chromatographic and mass spectroscopy analyses.

### INTRODUCTION

Acridinium derivatives are readily oxidized with hydrogen peroxide, persulfates, and other oxidants in alkaline media leading to chemiluminescence (CL). This feature of acridinium salts has prompted their use as chemiluminescent indicators or chemiluminogenic fragments of labels in clinical, pharmaceutical, chemical and biochemical as well as in environmental and food analysis [1,2]. The 10-substituted acridinium cations have been the subject of many investigations, both of a cognitive and utilitarian nature. The reason for this was that they can serve as CL indicators or fragments of labels in extremely sensitive quantitative determinations (limits of detection at the level of  $10^{-19}$  mole of analyte or below) of a wide range of entities of biological importance such as antigens, antibodies, nucleic acids, hormones, food additives hydrogen peroxide and others [1,2].

Taking into account the chemiluminogenic properties of acridinium salts and their practical importance, an understanding of the processes giving rise to the emission of light seems to be indispensable. The mechanism of chemiluminogenic oxidation of some of 10 alkylated acridinium cations with hydrogen peroxide in alkaline media has been discussed by several authors [1–3] and examined in our group in detail for the acridinium esters using the quantum-chemistry methods [4–6]. The mechanism of the mentioned multi-

staged process is thought to proceed by the initial attack of the hydroxyperoxide anion at the acridinium nucleus. When the reaction proceeds in the alkaline environment, the product of the reaction is electronically excited 9-acridinones, which is light-emitting species. Chromatographic analyses of post-CL reaction mixtures revealed that adequate 10-methyl-9-acridinone, phenol, and 10-methylacridinium-9-carboxylic acid derivatives make the final products after CL completion of acridinium esters [7]. However, the above mentioned chromatographic and other standard approaches (electronic spectroscopy – UV-Vis and fluorescence emission) revealed only stable products of the reaction, but did not shed light on the intermediate forms (chemically unstable and short-living) and thus only in a fragmentary way explained the mechanism of chemical transformations of the light-generating acridinium salts. An efficient transformation of acridinium salts to the electronically excited molecules, as well as a limitation of the dark processes (hydrolysis and non-CL reactions), are important issues for the rational design of new acridine-based chemiluminogens of potential utility. The quantum-chemistry methods can be a helpful tool for understanding processes leading to chemiluminescence.

### EXPERIMENTAL

All calculations were performed applying the Density Functional Theory (DFT), using the B3LYP functional and the 6-31G(d,p) basis sets using the Gaussian09 program package. The unconstrained geometry optimizations for stationary points (minima) on the potential energy surface of investigated compounds were carried out in an aqueous solution, employing the polarizable continuum model (PCM) of water in order to account for the effect of a polar environment. The validity of the geometry optimizations was confirmed in the subsequent Hessian calculations (second derivatives of the energy vs. atomic coordinates) followed by normal mode analyses. The enthalpies and Gibbs free energies of formation of gaseous entities were obtained by applying the basic rules of thermodynamics.

### RESULTS AND DISCUSSION

The mechanism of the oxidation process of acridinium salts is thought to proceed by the initial attack of the hydroxyperoxide anion at the carbon atom in position 9 of the acridinium nucleus, following by an immediate reaction of such formed adduct with hydroxide anion (essentially with no kinetic barrier) to form a cyclic intermediate (the peroxy-type of ion) or – after elimination of respective aryloxy anion – a highly energetic acridan spirodioxetanone cyclic intermediate. The above entities may spontaneously decompose with the generation of electronically excited molecules of 10-

methyl-9-acridinones and aryl carbonate anions or carbon dioxide – depending on subtle differences in the structure of the chemiluminogenic substrate. The computations have shown that the reaction pathway involving the formation of dioxethanone as intermediate and the elimination of  $\text{CO}_2$ , is not the most probable means by which light is generated. Such processes need to overcome quite high activation barriers (14–18 kcal/mol in aqueous phase for the various substituted at the benzene moiety 9-(phenoxycarbonyl)acridinium cations [4,5]). The results of our studies [4–6] suggest that light-emitting molecules of 10-methyl-9-acridinone are formed as a result of the elimination of the phenyl carbonate anion, from the cyclic intermediate that is formed after the initial addition of  $\text{OOH}^-$  to the 10-methylacridinium cation and the subsequent abstraction of a proton by  $\text{OH}^-$ . The predicted barriers for the latter process are moderate (2–8 kcal/mol in aqueous phase for the various substituted at the benzene moiety 9-(phenoxycarbonyl)acridinium cations [4,5]), which means that elimination of phenyl carbonate anions and the formation of electronically excited 10-methyl-9-acridinone molecules is achieved under the experimental conditions applied.

However, in an alkaline environment and in the absence of hydrogen peroxide, acridinium esters hydrolyze more or less rapidly with the formation of 10-methylacridinium-9-carboxylate anions; simultaneously with the alkaline hydrolysis some other dark processes occur, indicated by the formation of the so-called ‘pseudo-base’ and finally – 10-methyl-9-acridinone in the ground electronic state. The formation of ‘pseudo-base’ initiates non-chemiluminescent pathways of acridinium cations depletion. According to our predictions, the energy predicting the reaction of 9-(phenoxycarbonyl)acridinium cations to 10-methyl-9-acridinone is too small to electronically excite the above product. The activation barrier for the latter process is higher than that generated light emission (more than 25 kcal/mol in aqueous phase [4,5]).

## CONCLUSION

By applying computational methods, we have proposed a number of possible steps concerning the transformations of acridinium esters in an aqueous alkaline environments with the participation of ions such as  $\text{OH}^-$  and  $\text{OOH}^-$ , which may compete for the electron-deficient acridinium C(9) atom in the initial steps of the acridinium ester transformations. In general, three concurrent reaction pathways have been distinguished. Pathway ‘one’ comprises the ‘light way’ of acridinium esters oxidation, involving ca. 2% percent of the reaction energy released upon the transformation regards to experimentally obtained values of quantum yields. The other two general

pathways are considered as ‘dark’ – making concurrent reaction channels to the above-discussed ‘light way’. The latter two pathways denote a ‘pseudo-base way’ – ending with the formation of 10-methyl-9-acridiones in an electronic ground state and a ‘hydrolytic way’ – ending with the formation of 10-methylacridine-9-carboxylic acid in the ground electronic state. According to the quantum chemistry calculations, the thermodynamic data obtained theoretically is, in general, well comparable to the experimental findings [7].

#### *Acknowledgement*

The calculations were done on computers of the Wrocław Centre for Networking and Supercomputing (grant no. 215).

#### **REFERENCES**

- [1] F. McCapra, *Pure Appl. Chem.*, 1970, **24**, 611 – 629.
- [2] I. Weeks, I. Beheshti, F. McCapra, A.K. Campbell, J.S. Woodhead, *Clin. Chem.*, 1983, **29**, 1474 – 1479.
- [3] J. Rak, P. Skurski, J. Błażejowski, *J. Org. Chem.*, 1999, **64**, 3002 – 3008.
- [4] K. Krzymiński, A. Ożóg, P. Malecha, A.D. Roshal, A. Wróblewska, B. Zadykowicz, J. Błażejowski, *J. Org. Chem.*, 2011, **76**, 1072 – 1085.
- [5] B. Zadykowicz, J. Czechowska, A. Ożóg, A. Renkevich, K. Krzymiński, *Org. Biomol. Chem.*, 2016, **14**, 652 – 668.
- [6] J. Czechowska, A. Kawecka, A. Romanowska, M. Marczak, P. Wityk, K. Krzymiński, B. Zadykowicz, *J. Luminescence*, 2017, **187**, 102 – 112.
- [7] K. Krzymiński, A.D. Roshal, B. Zadykowicz, A. Białk-Bielińska, A. Sieradzan, *J. Phys. Chem. A*, 2010, **114**, 10550 – 10562.

## MOLECULAR MODELING AS A MODERN DIAGNOSTIC TOOL FOR DISEASES

M.Pieńkos, A.Romanowska and B.Zadykowicz

*University of Gdansk, Faculty of Chemistry, Laboratory of Luminescence  
Research, Wita Stwosza 63, 80-308 Gdansk, Poland  
mail: milena.pienkos@phdstud.ug.edu.pl*

### ABSTRACT

The paper outlined investigation on the mechanism of chemiluminescence of 10-methylacridinium derivatives. The process leading to the electronically excited product (light pathway) and dark pathways – hydrolysis and process leading to non-excited product. The results of the study show that computers can be a helpful tool in the design of new chemiluminogenes based on acridine, used in immunoassay analysis.

### INTRODUCTION

Modern molecular diagnostic tools, including immunological ones, allow you to diagnose the causes of infectious and cancerous diseases and to properly control their treatment. The search for luminescent systems with the highest possible light emission yield, high solution stability and moderate light decay rate is a priority for luminescent applications in this area. Chemiluminescence is an extremely interesting phenomenon of the light generation that occurs as a result of the return of a molecule from an electronically excited state to a ground state [1–2]. Electronically excited molecules appear as a result of some chemical reactions, especially oxidation reactions [1]. Efficient chemiluminogens are *N*-substituted acridine derivatives that have been used in immunological diagnostics as luminogen fragments of chemiluminescent labels. Developing a diagnostic tool is very expensive and requires many hours spent in the lab, which mostly turns out to be a failure. Molecular modeling allows to significantly shorten the time and reduce costs of researching new diagnostic instruments. The computational studies enable the prediction of properties and behavior and thus to pre-eliminate undesirable qualities [4-5].

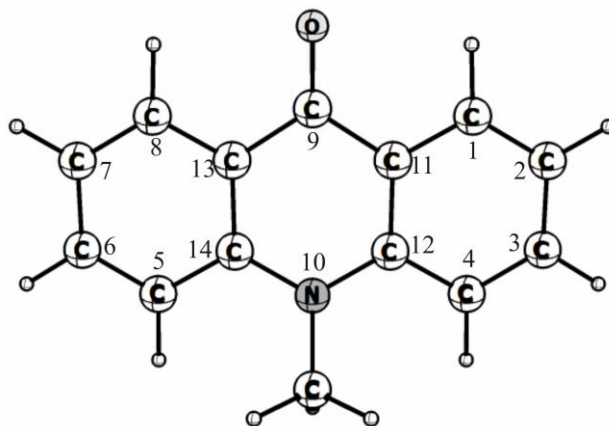


**Figure 1. Structure of 10-methyl-9-acridinone**

### EXPERIMENTAL

Unconstrained geometry optimizations of isolated molecules were carried out, at the DFT level of theory and TDDFT to determine excited states. All calculations were conducted using the popular Becke's three-parameter hybrid functional B3LYP and the 6-31G\*\* basis set, with the Gaussian09 program package. After completion of each optimization, the Hessian (second derivatives of the energy as a function of the nuclear coordinates) was calculated and checked for positive definiteness to assess whether the structures were true minima. The solvent (water) effect with included in the DFT calculations at the level of the Polarizable Continuum Model (PCM) was used to mimic water environment (UAHF radii were used to obtain the molecular cavity).

The enthalpies ( $\Delta_{r,298}H^\circ$ ) and Gibbs' free energies ( $\Delta_{r,298}G^\circ$ ) of the reactions, as well as the enthalpies ( $\Delta_{a,298}H^\circ$ ) and Gibbs' free energies ( $\Delta_{a,298}G^\circ$ ) of activation, were calculated by following the basic rules of thermodynamics. The rate constants ( ${}_{298}k^\circ$ ) for the gaseous phase reactions were obtained by applying the equation:

$${}_{298}k^\circ = \frac{RT}{Nh} \exp[-\Delta_{a,298}G^\circ / (RT)]$$

Using the transition state theory was obtained the reaction completion time ( ${}_{298}\tau_{99}$ ) from the formula:

$${}_{298}\tau_{99} = \ln 100 / {}_{298}k^\circ$$

where  $R$ ,  $T$ ,  $N$ , and  $h$  denote the gas constant, temperature (298.15 K), Avogadro number, and Planck's constant, respectively.

## RESULTS AND DISCUSSION

According to the Frontier Orbital Theory, the Lowest Unoccupied Molecular Orbital (LUMO) distribution of an electrophilic species determines the molecular center sensitive to nucleophilic attack. Another factor important for the generation of chemiluminescence is that  $\text{H}_2\text{O}_2$  reacts spontaneously with OH yielding  $\text{OOH}^-$  [5]. Taking into account mentioned the proposed and studied mechanism of chemiluminescence reaction is proceed by the initial nucleophilic attack of the hydroxyperoxide ion at C(9) of the acridinium nucleus. The  $p_z$  LUMO coefficients at the endocyclic C(9) are ca. 10 times higher than other near atoms.

The main pathway of the chemiluminescence reaction (“light pathway”) leads to formation of the electronically excited product – 10-methyl-9-acridinone. The energy released in the reaction preceding the formation of the mentioned molecule exceeds the necessary value, which is  $88.2 \text{ kcal mol}^{-1}$ , to cause the electronically excited product.

The computational studies present two concurrent pathways (“dark pathway”), which do not lead to the formation of electronically excited product: the first is the hydrolysis of the 10-methylacridinium molecule and the second one is the formation of so-called “pseudobase” and the products its transformation. Unfortunately, the presence of dark pathways may adversely affect the chemiluminescence quantum yields, so it is important to be able to eliminate such processes.

## CONCLUSION

A chemiluminogen can be any molecule capable to efficiently converting electrons to excited states, thereby allowing a chemiluminometric determination of the concentration of the examined macromolecules. Taking into account mentioned above, it is extremely important to know the mechanism of reaction leading to the generation of light by chemiluminogens. Using the computational methods we can be studied the reactions, their products, and properties of the molecules.

### *Acknowledgement*

This study was financed from the Research of Young Scientists grant no. 538-8220-B776-17. The calculations were done on computers of the Wroclaw Centre for Networking and Supercomputing (grant no. 215).

**REFERENCES**

- [1] J. Czechowska, A. Kawecka, A. Romanowska, M. Marczak, P. Wityk, K. Krzyński, B. Zadykiewicz, *J. Luminescence*, 2017, 187, 102-112.
- [2] G. Zomer, J.F.C. Stavenuiter, *Anal. Chim. Acta*, 1989, 227, 11-19.
- [3] A. Natrajan, D. Wen, *Org. Biomol. Chem.*, 2015, 13, 2622-2633.
- [4] A. Roda, P. Pasini, M. Guardigli, M. Baraldini, M. Musiani, M. Mirasoli, *J. Fresenius Anal. Chem.*, 2000, 366, 752-759.
- [5] B. Zadykiewicz, J. Czechowska, A. Ożóg, A. Renkevich, K. Krzyński, *Org. Biomol. Chem.*, 2016, 14, 652-668.

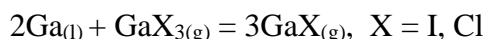
## HIGH-TEMPERATURE VAPOR-PHASE SPECTROPHOTOMETRIC ANALYSIS OF THE Ga-Cl AND Ga-I SYSTEMS

A.V. Kosyakov, A. Y. Zavrazhnov and S.S. Berezin

*Voronezh State University, Universitetskaya sq, 1, 394006, Voronezh,  
Russia. (lavchukb@mail.ru)*

### ABSTRACT

High-temperature spectroscopy was used to study the UV-absorption spectra in Ga – Cl and Ga – I systems. Characteristic peaks of absorption of the corresponding molecular forms in the gas phase were identified. The extinction coefficients of gallium monohalides have been calculated. The temperature dependences of the equilibrium constants for heterophase reactions type as



were found.

### INTRODUCTION

The heterogeneous equilibria of inorganic solid phases with gallium halide vapor can be widely used for the CVT-synthesis of the promising (mainly semiconductive) compounds and also for phase diagrams studying with the use of auxiliary components. [1-3].

The vapor phase in the Ga-Cl and Ga-I systems consists of the following species: GaX, GaX<sub>3</sub>, Ga<sub>2</sub>X<sub>4</sub> and Ga<sub>2</sub>X<sub>6</sub> [4], [5]. It is also known that the first (GaI) and the second (GaI<sub>3</sub>) species predominate in a vapor usually.

For the Ga – Cl and Ga – I systems the following reversible reactions could be written:



Using the characteristic absorption peaks in the vapor it is possible to relate the intensities of the absorption bands to the concentrations of the corresponding species. This makes it possible to obtain the temperature dependences of the equilibrium constants in the systems under consideration by the *optical-vapor-pressure* method. This method has several advantages

over the classical vapor pressure methods for the vapor phase composition studying.

The tasks of this paper was to develop an efficient and simple method that allows one to quantify the vapor composition at different temperatures in the Ga-Cl and Ga-I systems, and to calculate the temperature dependences of the equilibrium constants, first of all – for the main reactions (1) and (4).

## EXPERIMENTAL

In the present work the absorption of gallium halides vapor has been investigated in UV-region. Taking into account the data of [4] and [6], the characteristic absorption peaks of various species have been identified. Thus GaI manifests itself by the wide band near  $\lambda = 310$  nm and by a spectral comb in the wavelength range from 384 to 398 nm (Fig. 1); GaCl – by a complex strong band in the spectral range 248 – 258 nm (Fig. 2) and by a spectral comb in the wavelength range from 321 to 345 nm. Gallium triiodide is characterized by an absorption peak near 220 nm. (Fig. 1).

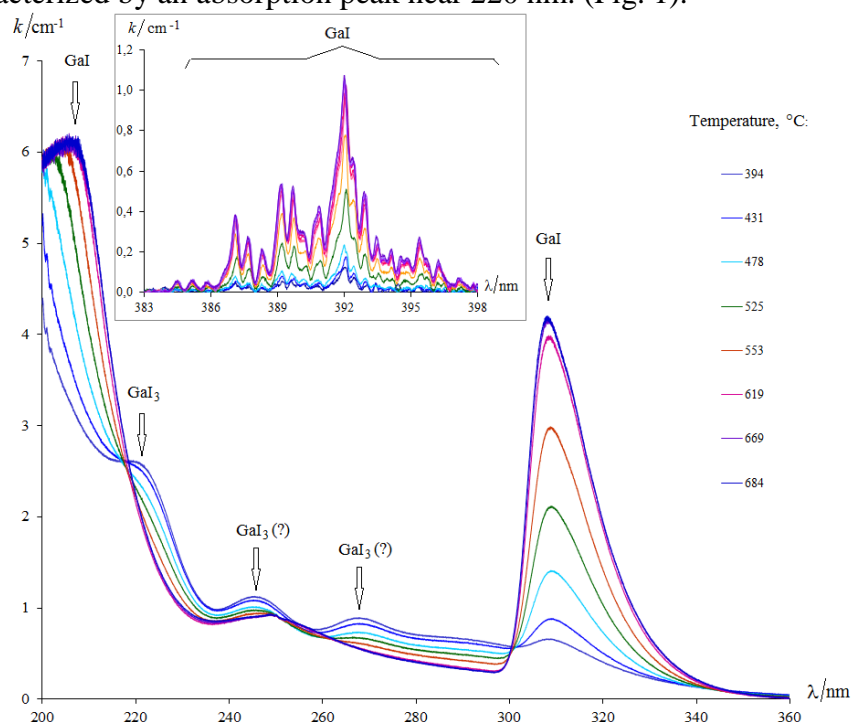


**Figure 1.** The absorption spectra of gallium iodides vapor (unsaturated vapor) in its equilibrium with metallic gallium at different temperatures.  $k$  is the absorption coefficient. The total concentration of iodides in equilibrium is  $0.273 \text{ mol/m}^3$  per atomic iodine.

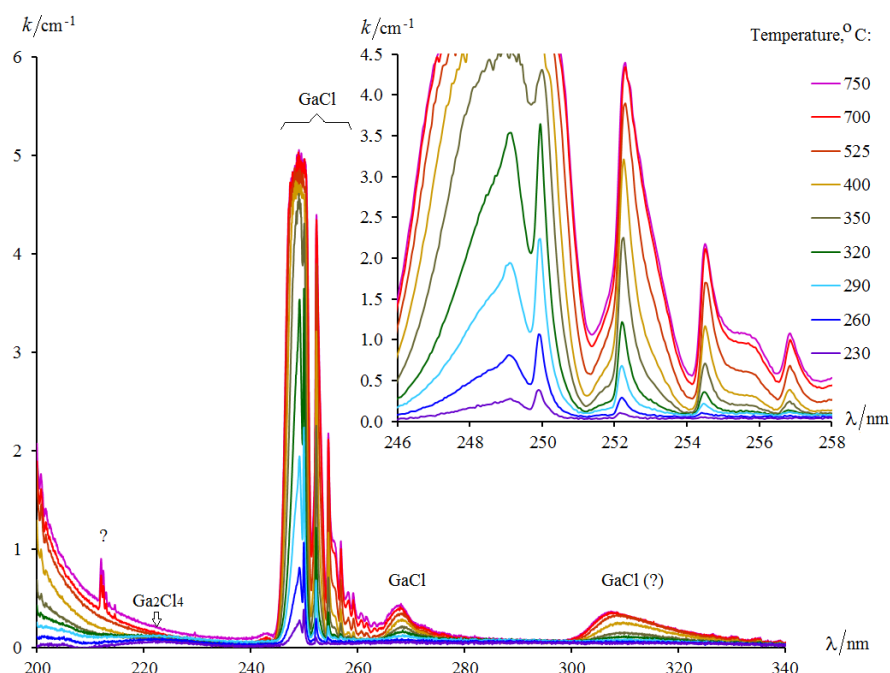


**Figure 2.** The absorption spectra of gallium chlorides vapor (unsaturated vapor) in its equilibrium with metallic gallium at different temperatures. The total concentration of chlorides in equilibrium is  $4.6 \cdot 10^{-3} \text{ mol/m}^3$  per atomic chloride.

To scan the spectra, a monochromator MDR-41 is used, combined with the cylindrical furnace. The equilibrium vapor is investigated in a closed quartz optical cuvette ( $10 \times 10 \times 30 \text{ mm}$ ). During the experiment this cuvette is placed into the furnace, which has two little windows for light passing. This equipment allows one to obtain absorption spectra in the wavelength range from 200 to 800 nm at the temperatures up to 800 °C in a 0.01 increment nm. The possibility for governing the *in situ*-experiments (without the quenching procedures) is a distinctive feature of this work.

The obtained complex spectra were decomposed into the separate Gaussian bands through the *OriginPro* Program.

Almost complete transformation of all gaseous species into monohalides (GaCl and GaI) offers the opportunity to find the extinction coefficients for these molecules. Along with the known extinction coefficients for some other species it allows one to calculate the partial vapor pressures at different temperatures and to find the temperature dependences of the equilibrium constants.

## RESULTS AND DISCUSSION

It should be noted that we were able to fix the concentrations of GaCl molecules in a vapor starting from  $1,3 \cdot 10^{-4} \text{ mol} \cdot \text{m}^{-3}$ , which corresponds to pressures of  $p_{\text{GaCl}}$  from  $5 \cdot 10^{-6} \text{ bar}$ . Thus, in this static vapor-pressure method, the lower limit of measured pressures is significantly extended to the area of mass spectrometric studies.

As a result of a series of experiments the temperature dependence of equilibrium constant for the reaction (1) – both for chlorides and iodides – were found. For the reaction (1), the temperature dependence obtained is:  $\ln(K_p) = -27183/T + 28,268$  for equilibrium with chlorides and  $\ln(K_p) = -26251/T + 27,93$  for iodides.

The obtained data correlate well with the results of [6] and [7]. In the present work we have also investigated the equilibria where the condensed phase – the pure gallium – was substituted for some gallium-content binary phases. Such experiments made it possible to use the equilibria type as (1) in order to find information on the chemical potential of gallium in these phases.

### *Acknowledgement*

This work was partially supported by the Russian Foundation for Basic Research (Grant no. 18-33-00900).

## REFERENCES

- [1] D. Siche, R. Zwierz. *Crystal Research and Technology*. 2018.
- [2] C.E. Morosanu. *The Films since and technology*, 1990. – V. 7, P 61 – 74.
- [3] D. Turchen, Eu. Goncharov, V. Zlomanov *J. Phase Equilibrium - 2001*, V. 22, No 4, P. 482-490.
- [4] Y. Kuniya. *Journal of Crystal Growth*. – 1975, – No. 28, P. 385-391
- [5] Y. Kuniya, T. Chino. *Denki Kagaku. Technical Paper*, Tokyo, Japan. – 1972. – V. 40, No. 12, P. 858-864.
- [6] Y. Kuniya, Y. Tanizawa, M. Hosaka. *Denki Kagaku. Technical Paper*, Tokyo, Japan. – 1973. – V. 41, N. 2. – P. 108 – 111.
- [7] V.N. Kulyukin, E.S. Petrov. *News of the Siberian Branch of the USSR Academy of Sciences. A series of chemical sciences*, – 1970. – №7, V. 3, P. 69-76.

## STRUCTURAL CHARACTERIZATION OF BINUCLEAR PLATINUM(II) COMPLEX ADUCTS WITH DNA AND ANTITUMOR ACTIVITY

G. V. Janjić<sup>1</sup>, B. Konovalov<sup>2</sup>, M. D. Živković<sup>3</sup>, J. Z. Milovanović<sup>4</sup>, D. B. Djordjević<sup>4</sup>, A. N. Arsenijević<sup>4</sup>, I. Vasić<sup>3</sup>, A. Franich<sup>2</sup>, S. Rajković<sup>2</sup> and M. I. Djuran<sup>5</sup>

<sup>1</sup> *Institute of Chemistry, Technology and Metallurgy, University of Belgrade, Njegoševa 12, 11000 Belgrade, Serbia. (janjic\_goran@chem.bg.ac.rs)*

<sup>2</sup> *Faculty of Science, Department of Chemistry, University of Kragujevac, R. Domanovića 12, 34000 Kragujevac, Serbia.*

<sup>3</sup> *Faculty of Medical Sciences, University of Kragujevac, Svetozara Markovića 69, 34000 Kragujevac, Serbia.*

<sup>4</sup> *Center for Molecular Medicine and Stem Cell Research, Faculty of Medical Sciences, University of Kragujevac, Svetozara Markovića 69, 34000 Kragujevac, Serbia.*

<sup>5</sup> *Serbian Academy of Sciences and Arts, Knez Mihailova 35, 11000 Belgrade, Serbia.*

### ABSTRACT

The synthesis and structural characterization of seven binuclear platinum(II) complexes, with general formula  $[\{Pt(L)Cl\}_2(\mu-1,5-nphe)](ClO_4)_2$  (1,5-nphe is 1,5-naphthyridine), were reported. Molecular docking study was performed to evaluate the potential binding sites and binding modes of aqua derivatives of synthesized platinum(II) complexes, at double stranded DNA. Results showed that *groove spanning* and *backbone tracking* are the most stable binding modes. The cytotoxic activity of these complexes was evaluated and it showed that all investigated complexes have almost no cytotoxic effects on 4T1 (murine mammary carcinoma) and very low cytotoxicity toward LLC1 (murine lung cancer).

### INTRODUCTION

Platinum-based drugs have been widely applied as classical chemotherapeutic agents [1, 2], especially cisplatin whose the anticancer activity is based on its intrastrand covalent binding to DNA [3]. Because of the negative side effects during the treatment (such as nephrotoxicity, ototoxicity, cardiotoxicity, neurotoxicity, vomiting, resistance, etc.) new classes of platinum complexes with improved antitumor properties were designed [4]. Polynuclear platinum complexes represent a novel class of promising antitumor agents with

potential clinical significance [5]. It was shown that some binuclear Pt(II) complexes with distinctly different DNA-binding mechanisms may exhibit unique biological activity in comparison with clinically used mononuclear complexes [6].

## EXPERIMENTAL

Binuclear platinum(II) complexes Pt1-Pt7, with general formula  $[\{\text{Pt}(\text{L})\text{Cl}\}_2(\mu\text{-}1,5\text{-nphe})](\text{ClO}_4)_2$ , were prepared from the corresponding mononuclear  $[\text{Pt}(\text{L})\text{Cl}_2]$  complexes (L is  $2\text{NH}_3$  (Pt1), en (Pt2), 1,2-pn (Pt3), dach (Pt4), 1,3-pd (Pt5), 2,2-diMe-1,3-pd (Pt6), or 1,3-pnd (Pt7)).

The binding interaction of Pt1-Pt7 complexes with DNA was studied by UV-Vis and fluorescence spectroscopy.

The molecular docking study was performed on optimized structures of hydrolyzed binuclear Pt(II) complexes and double stranded DNA, extracted from Protein Data Bank and used as a target for the examined complexes (Figure 1).

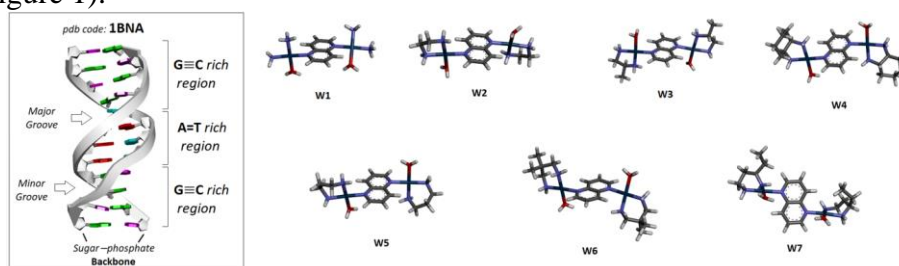


**Figure 1.** The structure of DNA (pdb code-1BNA) and optimized structures of aqua derivatives (W1-W7:  $[\{\text{Pt}(\text{L})(\text{H}_2\text{O})\}_2(\mu\text{-}1,5\text{-nphe})]^{4+}$ ) of the corresponding chloride complexes (Pt1-Pt7:  $[\{\text{Pt}(\text{L})(\text{Cl})\}_2(\mu\text{-}1,5\text{-nphe})]^{2+}$ ).

*In vitro* cytotoxic activity of these complexes was evaluated against murine colon carcinoma (CT26), murine mammary carcinoma (4T1) and murine lung cancer (LLC1) cell lines [7].

## RESULTS AND DISCUSSION

Molecular docking study found a new binding motif (Figure 2), slightly different than conventional "intercalation" and "groove binding" mode, which is called phosphate clamp motif including a *backbone tracking* and *groove-spanning* mode (main binding mode of the examined complexes). It has been shown that the *groove-spanning* mode displays slightly greater influence on the tertiary structure of DNA, which results in condensation of DNA [8]. As a consequence of condensation, intercalated ethidium bromide is displaced

from DNA double helix to the solution, that we registered by a quenching of its fluorescence.

The absorption intensity of binuclear complexes was slightly decreased after the addition of CT-DNA. There were no changes in the absorption wavelength maximum at 317 nm, indicating the presence of electrostatic interactions between the positively charged metal complexes (charge = +4) and negatively charged DNA backbone. This is in accordance with the results obtained from the molecular docking study, which showed that the electrostatic interactions have a greater contribution in total binding energy than hydrogen bonding (Table 1).

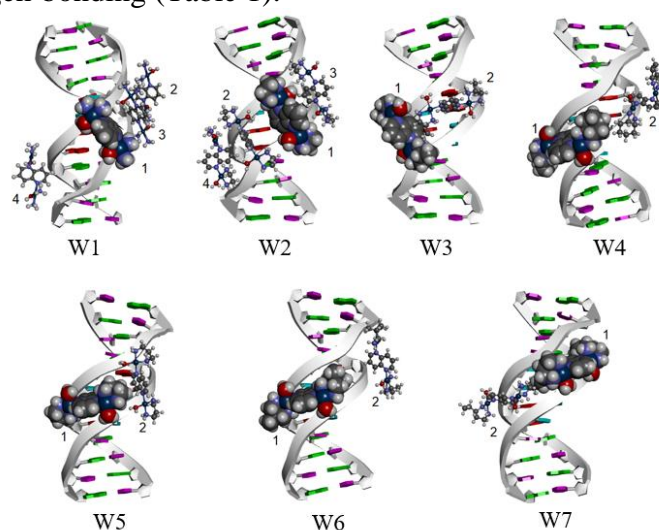


**Figure 2.** The binding modes of hydrolyzed binuclear platinum(II) complexes (W1-W7) to DNA, as assessed by molecular docking.

**Table 1.** The binding energies (in kcal/mol) and results of energy decomposition analysis for the most stable binding modes of hydrolyzed binuclear Pt(II) complexes (W1-W7) to DNA, as assessed by molecular docking.

Model system	DNA + W1	DNA + W2	DNA + W3	DNA + W4	DNA + W5	DNA + W6	DNA + W7
Total energy	-8.60	-10.63	-9.14	-9.33	-9.38	-10.27	-9.47
vdW + H-bond + desolvation energy	-2.44	-2.52	-2.55	-3.28	-3.46	-3.91	-4.77
Electrostatic energy	-8.35	-9.21	-7.70	-7.15	-7.03	-7.46	-6.35

Analysis of IC<sub>50</sub> values indicates that all investigated complexes have almost no cytotoxic effects on 4T1 and very low cytotoxicity toward LLC1 cell lines. Complexes Pt1 and Pt2 have significant cytotoxic activity toward CT26 cells, comparable with cisplatin.

### CONCLUSION

This study reveals that the groove-spanning binding mode of new binuclear Pt(II) complexes to DNA, is the result of a large positive charge of metal complexes and rigid structure of 1,5-naphthyridine bridging ligand, and gives the additional insight into the structure–function paradigm of platinum antitumor compounds.

### *Acknowledgement*

This work was supported by the Ministry of Education, Science and Technological Development of the Republic of Serbia (Projects no. OI 172023, 172036, 172016, 175069 and 175103) and Faculty of Medical Sciences (grant MP 2014/02).

### REFERENCES

- [1] C. Johnstone, K. Suntharalingam, S. J. Lippard, *Chemical Reviews*, 2016, 116, 3436–3486.
- [2] N. J. Wheate, S. Walker, G.E. Craig, R. Oun, *Dalton Transactions*, 2010, 39, 8113–8127.
- [3] J. Reedijk, *Chemical Reviews*, 1999, 99, 2499–2510.
- [4] J. Reedijk, *Proceedings of the National Academy of Sciences of the United States of America* 2003, 100, 3611-3616.
- [5] N. Farrell, S. Spinelli, *Royal Society of Chemistry: London*, 1999, 124-134.
- [6] C. Manzotti, G. Pratesi, E. Menta, R. Di Domenico, E. Cavalletti, H. H. Fiebig, L.R. Kelland, N. Farrell, D. Polizzi, R. Supino, G. Pezzoni, F. Zunino *Clin, Cancer Research*, 2000, 6, 2626-2634.
- [7] T. Mosmann, *Journal of Immunological Methods*, 1983, 16, 55-63.
- [8] A. Prisecaru, Z. Molphy, R. G. Kipping, E. J. Peterson, Y. Qu, A. Kellett, N. P. Farrell, *Nucleic Acids Research*, 2014, 42, 13474–13487.

## HYDROGEN BOND ABILITY OF COORDINATED OXYGEN ATOMS OF GLYCOLATE LIGAND

G. V. Janjić<sup>1</sup>, M. Sarvan<sup>2</sup>, I. Đorđević<sup>1</sup>, D. Sredojević<sup>3</sup> and M. Petković Benazzouz<sup>2</sup>

<sup>1</sup> *Institute of Chemistry, Technology and Metallurgy, University of Belgrade, Njegoševa 12, 11000 Belgrade, Serbia. (janjic\_goran@chem.bg.ac.rs)*

<sup>2</sup> *Faculty of Physics, University of Belgrade, Studentski trg 12-16, Belgrade, Serbia.*

<sup>3</sup> *Vinča Institute of Nuclear Sciences, University of Belgrade, P.O. Box 522, Belgrade, Serbia.*

### ABSTRACT

The hydrogen bond abilities of coordinated oxygen atom of glycolate ligand (hydroxyacetates) were investigated based on crystallographic data and quantum-chemical calculations. The analysis of crystal structures from Cambridge Structural Database was used to obtain valuable crystallographic data on geometry of hydrogen bonds involving the coordinated oxygen atom of glycolate ligand. Quantum-chemical calculations on the water/Pt(II)-glycolate complex model systems have shown how the nature of ligands and charge of metal complexes influence the strength of hydrogen bonding.

### INTRODUCTION

Non-covalent interaction is believed to play a vital role in stabilizing various complex chemical species. The understanding and characterization of varieties of non-covalent interactions have become one of the major interests of computational chemistry [1].

Previous studies on donor ability of water molecules showed that hydrogen bonds of coordinated water are remarkably stronger than the hydrogen bonds of two non-coordinated water molecules (-4.84 kcal/mol), even if the aqua complex is neutral [2]. A recent study has shown that the acceptor ability of metal ion from metal complex to hydrogen bonding is strongly dependent on the charge of metal ion and complexes, as well as, on the nature of metal ion and ligands [3].

### METHODS

The crystal structures from Cambridge Structural Database (CSD) were screened for intermolecular hydrogen bonds of coordinated oxygen atoms of glycolate ligands (*glyc*). A contact was considered as a hydrogen bond if the

distance between the hydrogen atom and the coordinated carboxyl oxygen atom of glycolate ligand was less than 3.5 Å, and hydrogen bond angle ( $\alpha$  or R–H $\cdots$ O angle) was larger than 110°.

The strengths of hydrogen bonds between the water molecule and glycolate complex of Pt(II) were calculated at MP2/aug-cc-pVDZ level. For metal ions the augmented standard cc-pVDZ basis sets with pseudopotentials (aug-cc-pVDZ-PP) was used. The geometry of all glycolate Pt(II) complexes and the water molecule were separately optimized and obtained geometries were used for single point energy calculations.

## RESULTS AND DISCUSSION

The crystal structures from CSD (23 structures), in which the coordinated carboxyl oxygen atom acts as an acceptor in hydrogen bonding were analysed (64 hydrogen bonds). The extracted complexes were neutral and the majority of them have +2 charged metal ions (~70% of complexes). The distribution of  $d$  values showed the maximum in the range from 2.6 to 2.8 Å, and bond angle values ( $\alpha$  angle) were mainly in the range from 110° to 130° (Figure 1). These geometrical parameters show that the glycolate oxygen atom tends to form simultaneous interactions with surrounding chemical species in crystal structures.

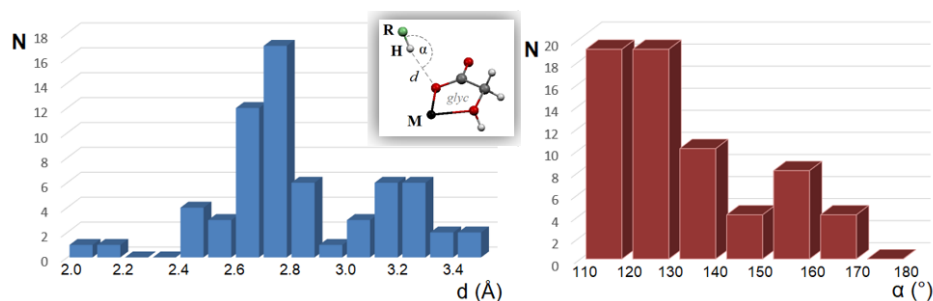


**Figure 1.** The distribution of  $d$  distance and  $\alpha$  angle values for hydrogen bonds in which coordinated carboxyl oxygen atom of glycolate ligand acts as an acceptor of hydrogen bonding.

The intermolecular OH/O-M and ML-OH/O hydrogen bonds between a water molecule and glycolate complex of platinum were studied using quantum chemical calculations. The main purpose was to examine the influence of the charge of a metal complex and the nature of R ligands on the strength of the mentioned bonds. The obtained results indicate that some of the complexes can form very strong hydrogen interactions. The geometries of the model systems are shown in Figure 2.

We studied hydrogen bonds of neutral, positive and negative  $[\text{Pt}(\text{glyc})\text{R}_1\text{R}_2]$  complexes, with different types of  $\text{R}_1$  and  $\text{R}_2$  ligands:  $\pi$ -acceptor ( $\text{CN}^-$  and  $\text{CO}$ ) and electron-donor ligands ( $\text{NH}_2^-$  and  $\text{NH}_3$ ). The interaction energies were calculated, and the most stable geometries of all the investigated systems are presented in Table 1.

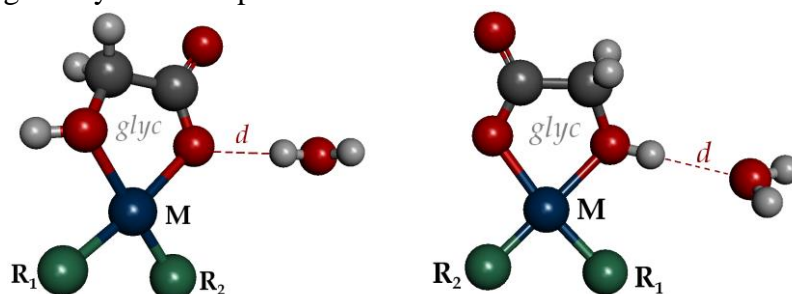


**Figure 2.** The models of water/metal-complex systems used for calculations of OH/O-M (left) and ML-OH/O hydrogen bonds (right).

**Table 1.** Structures, geometries (in Å) and energies (kcal/mol) for OH/O-M and ML-OH/O hydrogen bonds.

Model system	$q^*$	$\text{R}_1^\#$	$\text{R}_2$	OH/O-M		ML-OH/O	
				$d$	energy	$d$	energy
$[\text{Pt}(\text{glyc})(\text{CO})_2]^+\cdots\text{HOH}$	+1	CO	CO	2.2	-0.12	1.6	-23.81
$[\text{Pt}(\text{glyc})(\text{CN})_2]^- \cdots \text{HOH}$	-1	$\text{CN}^-$	$\text{CN}^-$	2.1	-6.36	1.7	-7.25
$[\text{Pt}(\text{glyc})(\text{CN})(\text{CO})] \cdots \text{HOH}$	0	CO	$\text{CN}^-$	2.1	-3.58	1.7	-12.20
$[\text{Pt}(\text{glyc})(\text{NH}_3)_2]^+ \cdots \text{HOH}$	+1	$\text{NH}_3$	$\text{NH}_3$	2.1	-1.59	1.7	-15.65
$[\text{Pt}(\text{glyc})(\text{NH}_2)_2]^- \cdots \text{HOH}$	-1	$\text{NH}_2^-$	$\text{NH}_2^-$	2.0	-8.93	1.9	-1.66
$[\text{Pt}(\text{glyc})(\text{NH}_2)(\text{NH}_3)] \cdots \text{HOH}$	0	$\text{NH}_3$	$\text{NH}_2^-$	1.9	-5.40	1.8	-8.59

\* $q$  = the charge of metal complex

#  $\text{R}_1$  = ligand in *trans* position to carboxyl oxygen atom.

The results of calculations show that metal complexes with  $\pi$ -acceptor ligands ( $\text{CN}^-$  and  $\text{CO}$ ) at  $\text{R}_1$  and  $\text{R}_2$  position have a lower acceptor and greater donor capacity for hydrogen bonding. Furthermore, the total charge of Pt complexes has a significant influence on the strength of the hydrogen bonds: positively charged complexes have significantly pronounced donor capabilities compared to the corresponding negatively charged complexes (with the same type of ligands) which have significantly higher acceptor capabilities.

In all model systems, except in  $[\text{Pt}(\text{glyc})(\text{NH}_2)_2]^- \cdots \text{HOH}$  system, the metal complex builds stronger ML-OH/O bonds than OH/O-M hydrogen bonds.

**CONCLUSION**

On the basis of the computational chemistry results presented here, it can be claimed that the strength of OH/O-ML and ML-OH/O hydrogen bonds between platinum complexes and the water molecule depends strongly on the nature of the ligands R. The charge of the platinum complex also has a strong influence on the strength of OH/O-ML and ML-OH/O hydrogen bonds.

***Acknowledgement***

This work was supported by the Ministry for Science of the Republic of Serbia (Project no. OI 172023, 171035 and 172035).

**REFERENCES**

- [1] Y. Marechal, *The Hydrogen Bond and the Water Molecule, The Physics and Chemistry of Water, Aqueous and Bio-Media*, Elsevier Science, 2006, page count: 332.
- [2] J. M. Andrić, G. V. Janjić, D. B. Ninković, S. D. Zarić, *Physical Chemistry Chemical Physics*, 2012, 14, 10896-10898.
- [3] G. V. Janjić, M. D. Milosavljević, D. Ž. Veljković, S. D. Zarić, *Physical Chemistry Chemical Physics*, 2017, 19, 8657-8660.

## *C – Kinetics, Catalysis*



## IN-SITU STUDY OF THE OXYGEN-INDUCED TRANSFORMATION OF PYROCHLORE $\text{Ce}_2\text{Zr}_2\text{O}_{7+x}$ TO THE $\kappa\text{-Ce}_2\text{Zr}_2\text{O}_8$ PHASE

I. Djerdj<sup>1</sup>, S. Urban<sup>2</sup>, P. Dolcet<sup>3</sup>, L. Chen<sup>4</sup>, M. Möller<sup>2</sup>, O. Khalid<sup>2</sup>, H. Camuka<sup>2</sup>, R. Ellinghaus<sup>2</sup>, C. Li<sup>2</sup>, S. Gross<sup>3</sup>, P. J. Klar<sup>4</sup>, B. Smarsly<sup>2</sup> and H. Over<sup>2</sup>

<sup>1</sup>*Department of Chemistry, Josip Juraj Strossmayer University of Osijek, Cara Hadrijana 8/A, 31000 Osijek, Croatia. (igor.djerdj@kemija.unios.hr)*

<sup>2</sup>*Physikalisch-Chemisches Institut, Justus-Liebig-Universität, Heinrich-Buff-Ring 17, 35392 Giessen, Germany.*

<sup>3</sup>*Dipartimento di Scienze Chimiche, Università degli Studi di Padova via Francesco Marzolo, 1, I-35131 Padova, Italy.*

<sup>4</sup>*I. Physikalisches Institut, Justus Liebig University, Heinrich-Buff-Ring 16, 35392 Giessen, Germany.*

### ABSTRACT

The temporary storage of oxygen in a solid catalyst is imperative for many important industrial oxidation reactions in the gas phase, for instance the post-treatment of automotive exhaust gas. A peculiar mixed Ce-Zr (1:1) oxide, the ordered  $\kappa\text{-Ce}_2\text{Zr}_2\text{O}_8$  phase, is a promising catalytic material exhibiting an extraordinarily high oxygen storage capacity (OSC) and high thermal and chemical stability. We elucidate the temperature-dependent transformation between the pyrochlore  $\text{pyr-Ce}_2\text{Zr}_2\text{O}_{7.3}$  and  $\kappa\text{-Ce}_2\text{Zr}_2\text{O}_8$  phase upon oxygen uptake by in-situ X-ray diffraction, X-ray absorption and *in-situ* Raman spectroscopy, providing insights into the electronic and structural changes on the atomic level, which are at the heart of the extraordinarily high OSC. We demonstrate that the  $\text{Ce}^{3+}$  concentration can be followed during transformation *in-situ* by Raman spectroscopy of the electronic spin flip in the f-shell of  $\text{Ce}^{3+}$ . The catalytic activity of the  $\kappa\text{-Ce}_2\text{Zr}_2\text{O}_8$  phase has been investigated without an additional active component such as Pt: While the high OSC of the kappa phase is beneficial for the oxidation of CO, the oxidation of HCl turns out to be not affected by the high OSC. [1]

### Acknowledgement

We express special thanks to BMBF for funding the related research project entitled: “Neuartige Materialien mit Funktion: Eigenschaften, Struktur und Anwendungen”.

**REFERENCES**

- [1] Sven Urban, **Igor Djerdj**, Paolo Dolcet, Limei Chen, Maren Moeller, Omeir Khalid, Hava Camuka, Rudiger Ellinghaus, Chenwei Li, Silvia Gross, Peter J. Klar, Bernd Smarsly, and Herbert Over, *Chem. Mater.*, **29** (2017) 9218–9226.

## PHOTOCATALYTIC HYDROGEN PRODUCTION OVER NICKEL MODIFIED TITANIA CATALYSTS

D. Lončarević<sup>1</sup>, J. Dostanić<sup>1</sup>, J. Papan<sup>2</sup> and J. Nedeljković<sup>2</sup>

<sup>1</sup> *University of Belgrade, Institute of Chemistry, Technology and Metallurgy, Njegoševa 12, 11000 Belgrade, Serbia.*

*([dloncarevic@nanosys.ihm.bg.ac.rs](mailto:dloncarevic@nanosys.ihm.bg.ac.rs))*

<sup>2</sup> *University of Belgrade, Institute of Nuclear Sciences Vinča, P.O. Box 522, Serbia.*

### ABSTRACT

The photocatalytic production of hydrogen over nickel modified titania catalysts were investigated in the presence of sacrificing agent (isopropanol) under simulated sunlight. Titanate nanotubes (NTs) were prepared by hydrothermal method from commercial Aeroxide TiO<sub>2</sub>-P25 powder. Series of nickel modified titania photocatalysts were prepared by deposition of nickel ions using either carbonate or hydroxide precipitation agents and consequent reduction by H<sub>2</sub> at different temperatures. Several techniques, including TPR, XRD, DR-UV/Vis and N<sub>2</sub> physisorption were employed to examine synthesized photocatalysts. The photocatalyst prepared by reduction at 500 °C from hydroxide precursor exhibited the highest photocatalytic activity with maximum H<sub>2</sub> production rate of 1042 μmol h<sup>-1</sup> g<sup>-1</sup>.

### INTRODUCTION

Energy demand is constantly increasing due to increased industrialization and population growth. In addition, rising levels of pollution, global warming problem and increased fossil fuels consumption are encouraging scientists to find alternative renewable and sustainable sources of energy. Interest in using hydrogen as alternative fuel substitute is constantly increasing. Current hydrogen generation techniques suffer from a reliance on fossil fuel sources and significant costs. The use of solar energy for hydrogen production is a promising solution to overcome these issues [1]. Since the pioneer work of Fujishima and Honda, the photocatalytic water splitting reaction using semiconducting materials has received much attention. TiO<sub>2</sub> has been considered as superior photocatalyst, owing to its low cost, photostability, chemical inertness, nontoxicity, adequate position of conduction and valence bands, *etc.* Nevertheless, high electron-hole recombination rate and large bandgap (3.2 eV) limits its practical application for light-induced H<sub>2</sub> evolution and stipulate the need for initial catalyst modification [2, 3].

Application of co-catalyst such as Ag, Au, Pt, Rh [4] was found to effectively suppresses electron-hole recombination in small band gap semiconductors. However, high cost and low natural abundance of noble metals motivated the researchers to find alternative substitutes. In the recent years low-cost transition metals or metal oxides were found to be applied as promising co-catalysts for light-induced hydrogen generation.

In this study the low cost Ni modified TiO<sub>2</sub> was examined for photocatalytic hydrogen production. The special emphasis was focused on determining the influence of precipitation agent and reduction temperature on photocatalytic hydrogen production. The results were used to clarify the relationship between structural and textural properties of synthesized catalysts and their activity.

### EXPERIMENTAL

Titanate nanotubes were prepared by hydrothermal method described by Kasuga et al. [5]. Briefly, 4 g of TiO<sub>2</sub> powder (Aeroxide-P25) was dispersed in 250 ml of 10M NaOH aqueous solution. After stirring for 40 min in ultrasonicated bath, the suspension was transferred to Teflon-lined stainless steel autoclave. The temperature in autoclave was increased at a ramp of 1.5 °C/min until 150 °C and held at this value for 24 h. The resulting sodium titanate precipitation was separated by filtration. Hydrogen titanates were obtained by ion exchange reaction using 0.1M HCl. The obtained titanate nanotubes are labeled as NTs. Titanate nanotubes calcined at 500 °C are labeled as NTs-500.

Ni/TiO<sub>2</sub> catalysts with 1wt% Ni were synthesized by deposition-precipitation method. The first series of catalysts was prepared using NaOH as precipitating agent by following procedure: nickel(II) nitrate hexahydrate and glycerol (1:2.8 molar ratio) were added to distilled water to form an aqueous nickel(II)-glycerol complex. NTs were then added to this solution. The precipitate of Ni complex was achieved by dropwise addition 0.5 M NaOH, until a pH of 12 was reached. The suspension was stirred for another 1 h, filtered by vacuum filtration and the resultant light green powder precursors were dried overnight at 70 °C. The second series of the catalysts were prepared using Na<sub>2</sub>CO<sub>3</sub> as precipitating agent. First, NTs were added to nickel(II) nitrate hexahydrate suspension. The precipitate of Ni complex was achieved by dropwise addition of 1M Na<sub>2</sub>CO<sub>3</sub> until a pH of 12 was reached. After stirring for 1h and vacuum filtration, the resultant light green powder precursors were dried overnight at 70 °C. Both series of catalysts were finally obtained by reduction of precursors under H<sub>2</sub>/Ar flow (5%, 20 ml/min) at different temperatures (400, 500 or 650) °C. The catalysts prepared using

NaOH were labeled as Ni/TiO<sub>2</sub>-x, while catalysts prepared using Na<sub>2</sub>CO<sub>3</sub> were labeled as Ni-C/TiO<sub>2</sub>-x, where x signifies the reduction temperature.

Temperature-programmed reduction (TPR) was carried out using Thermo Scientific 1100 TPDRO apparatus, equipped with a thermal conductivity detector (TCD). To obtain reduced catalysts, the samples were heated at desired temperature (400, 500 or 650) °C for 2h (heating rate, 10 °C/min) under 5% H<sub>2</sub>/Ar gas flow of 20 ml/min. The TCD signal for H<sub>2</sub> was calibrated by pulse calibration. Nitrogen adsorption-desorption isotherms were determined on Sorptomatic 1990 Thermo Finnigan automatic system. Specific surface area of the samples ( $S_{\text{BET}}$ ) was calculated from the nitrogen adsorption isotherms according to the Brunauer, Emmett and Teller method. Structural analysis was performed using X-ray diffraction measurements on Rigaku Smart Lab diffractometer. DR UV-Vis spectra were recorded on Thermo Electron Nicolet Evolution 500.

The photocatalytic tests were performed in photocatalytic reactor (Ace Glass), equipped with standard reaction flask, quartz immersion well and 16 watt low pressure mercury lamp, whose emission spectrum simulates solar radiation. The cooling of reaction mixture was performed using circulation thermostat (JULABO F25). The photocatalyst (125 mg) was suspended in isopropanol-water mixture (250 ml, iPrOH 1 % v/v in water) and transfer to reaction vessel. Before irradiation, the catalyst suspension was degassed for 60 min in Ar flow. After the lamp was switch on, the effluent gases were analyzed to quantify H<sub>2</sub> production by gas chromatography (Perkin Elmer F33 GC) using a TCD.

## RESULTS AND DISCUSSION

The quantity of reduced nickel was determined from total hydrogen consumption during TPR on predetermined temperature (Table 1). The results show that the quantity of reduced nickel increases with the increase of calcination temperature. The nominal nickel amount was found to be smaller than the actual for samples Ni/TiO<sub>2</sub>-400 and Ni-C/TiO<sub>2</sub>-400 due to incomplete reduction of Ni ions at 400 °C.

**Table 1.** Summarized characterization and photocatalytic activity of synthesized catalysts

Sample	Characterization			Activity	
	H <sub>2</sub> consumed <sup>a</sup>	Ni content <sup>b</sup>	Specific surface area	H <sub>2</sub> production rate	Specific H <sub>2</sub> production rate <sup>c</sup>
	[ $\mu\text{mol g}^{-1}$ ]	[%]	[ $\text{m}^2 \text{g}^{-1}$ ]	[ $\mu\text{mol g}^{-1} \text{h}^{-1}$ ]	[ $\mu\text{mol h}^{-1} \text{m}^2$ ]
Ni/TiO <sub>2</sub> -400	40	0.2	198	402	2
Ni/TiO <sub>2</sub> -500	170	1.0	53	1042	20
Ni/TiO <sub>2</sub> -650	281	1.6	24	139	6
Ni-C/TiO <sub>2</sub> -400	18	0.1	187	487	3
Ni-C/TiO <sub>2</sub> -500	145	0.9	34	229	7

<sup>a</sup> The quantity of hydrogen consumed during reduction of catalyst,

<sup>b</sup> The quantity of reduced nickel determined from total H<sub>2</sub> consumption,

<sup>c</sup> H<sub>2</sub> production rate normalized per catalyst specific surface area.

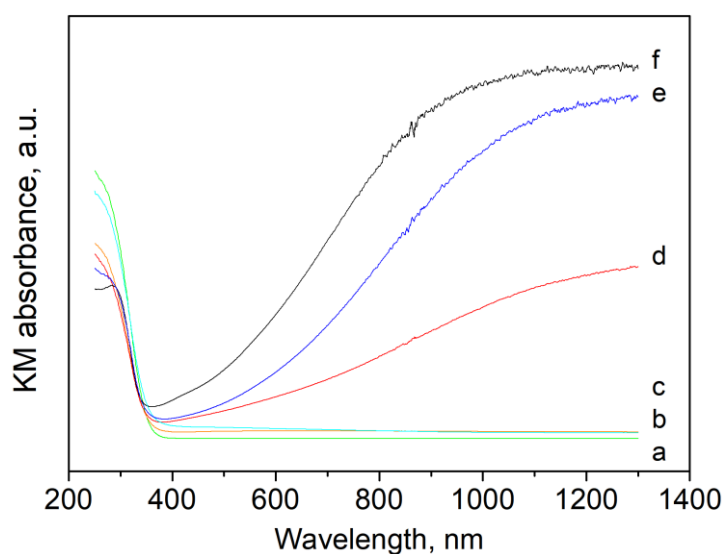


**Figure 1.** Kubelka-Munk transformation of DRS UV/Vis spectra: a) NTs, b) Ni/TiO<sub>2</sub>-400, c) Ni-C/TiO<sub>2</sub>-400, d) Ni/TiO<sub>2</sub>-500, e) Ni-C/TiO<sub>2</sub>-500, f) Ni/TiO<sub>2</sub>-650.

The obtained results indicate that the increase of reduction temperature led to the decrease in specific surface area, due to loss of the nanotubular morphology. In addition, for catalysts prepared at the same temperature, those originating from hydroxide have larger specific surface area compared to those originating from carbonate.

In Fig. 1 Kubelka-Munk transformation of DR UV-Vis spectra of NTs and prepared catalysts are presented. All samples show steep rise of absorption below 400 nm, which can be assigned to titanate nanotube or TiO<sub>2</sub> crystallites. Additional absorption band in visible and near IR region can be assigned to metallic Ni. The intensity of this peak increases with the nominal Ni loading.

XRD patterns of the prepared catalysts are shown in Fig. 2. The catalysts reduced at 400 °C, have a structure of hydrogen titanate, indicating that this temperature was not sufficiently high to induce nucleation of TiO<sub>2</sub> phases. According to the XRD data, NTs starts to transform to beta and anatase crystalline phases at temperatures  $\geq 500$  °C. Beta TiO<sub>2</sub> appears as the main crystalline phase, with increased crystalline size in the sample calcined at 650 °C.

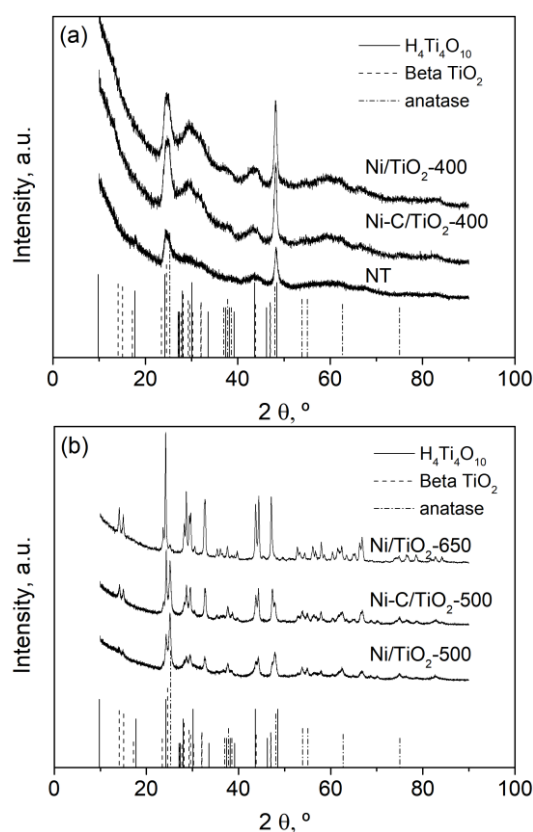


**Figure 2.** XRD patterns of: a) NTs; Ni/TiO<sub>2</sub>-400; Ni-C/TiO<sub>2</sub>-400, b) Ni/TiO<sub>2</sub>-500; Ni-C/TiO<sub>2</sub>-500; Ni/TiO<sub>2</sub>-650.

Photocatalytic activity of prepared Ni modified catalysts was evaluated for H<sub>2</sub> production in isopropanol-water mixture under simulated sunlight irradiation. Fig. 3 shows plots of H<sub>2</sub> production versus time for NTs and prepared catalysts. The results clearly indicate that NTs exhibited low activity for H<sub>2</sub> production, probably due to rapid electron-hole recombination. The addition of metallic nickel significantly improved activity of catalyst, due to increase of active sites for H<sub>2</sub> evolution, reduction of electron-hole recombination and higher solar light-harvesting efficiency.

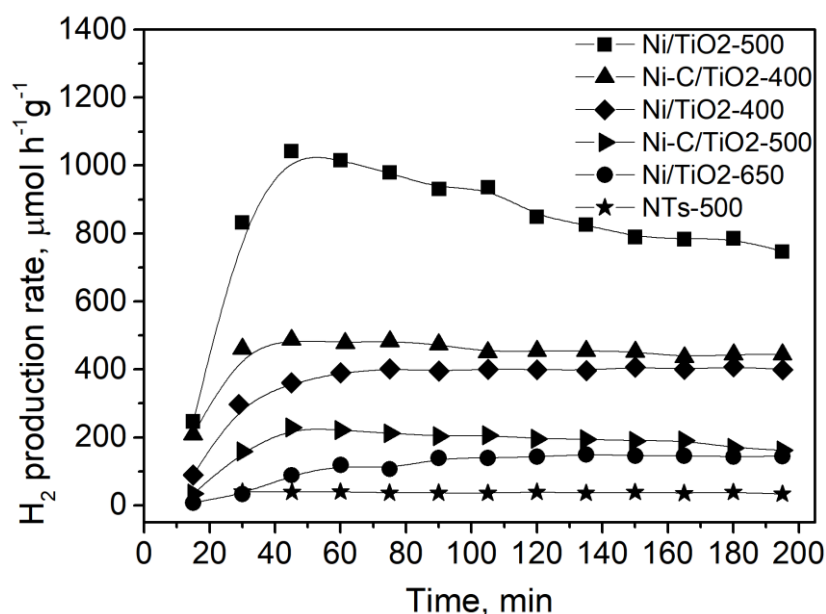


**Figure 3.** Plots of H<sub>2</sub> production rate versus time for NTs-500 and Ni modified catalysts.

Increase of reduction temperature from 400 °C to 500 °C led to higher yield of metallic nickel and transformation of NTs to anatase and beta crystal phases, resulting in improved activity of Ni/TiO<sub>2</sub>-500 sample. This sample exhibited the highest activity among all tested catalysts, with maximum H<sub>2</sub> production rate of 1042 μmol g<sup>-1</sup> h<sup>-1</sup>. Further increase in temperature led to decrease in activity, which is most-likely consequence of larger crystalline size, i.e. consequent loss of specific surface area, as well as partial transformation of anatase to beta crystalline phase.

The results also indicate that catalyst prepared at 500 °C using hydroxide as a precursor exhibited noticeably higher activity compared to its carbonate counterpart. The increased surface area of Ni/TiO<sub>2</sub>-500 catalyst could only be

partially responsible for the obtained increased activity, since the specific H<sub>2</sub> production rate normalized per catalyst specific surface area is still larger within Ni/TiO<sub>2</sub>-500 catalyst (Table 1). Although at this point we are not able to fully explain the obtained results, the further research will be directed toward this issue. On the other hand, we didn't find significant differences in the activity of catalysts prepared at 400 °C. The activity of Ni/TiO<sub>2</sub>-400 was smaller compared to Ni-C/TiO<sub>2</sub>-400 catalyst. The catalyst Ni/TiO<sub>2</sub>-400 show an induction period prior its activity get close to the activity of Ni-C/TiO<sub>2</sub>-400. This induction period can be correlated to photocatalytic reduction of NiO to metallic Ni. On the contrary, the photoreduction of Ni ions to metallic nickel during photocatalytic test could not be achieved in the case of Ni-C/TiO<sub>2</sub>-400 catalyst. Using carbonate precipitating agent, nickel is precipitated as nickel titanate or nickel hydroxide carbonate and the additional photoreduction to metallic nickel is disabled.

## CONCLUSION

The obtained results in this study indicate that the addition of metallic nickel significantly improves hydrogen production rate. Among all modified catalysts, the catalyst prepared at 500 °C by reduction of hydroxide precursor exhibited the highest activity (H<sub>2</sub> production rate was found to be 1042 μmol g<sup>-1</sup> h<sup>-1</sup>) due to the highest loading of metallic nickel and existence of anatase and beta crystal phases. The reducibility of nickel ions originating from carbonate precursor is lower compared to hydroxide precursor due to incorporation of nickel ions into the titanate structure. The results demonstrate that proper choice of synthetic parameters (type of precursor, reduction temperature, *etc.*) can significantly improve photocatalytic performance of the Ni modified TiO<sub>2</sub> catalysts, and consequently increase the efficiency of water splitting reaction.

## Acknowledgement

This work was partially supported by the Ministry of Education, Science and Technological Development of the Republic of Serbia (Grants no. III 45001).

## REFERENCES

- [1] T. Jafari, E. Moharreri, A.S. Amin, R. Miao, W. Song, S. L. Suib, Photocatalytic Water Splitting-The Untamed Dream: A Review of Recent Advances, *Molecules*, 2016, 21(7), 900-929.
- [2] S. Pany, K.M Parida, *Physical Chemistry Chemical Physics*, 2015, 17, 8070-8077.

- 
- [3] J. Fang, L. Xu, Z.Y. Zhang, Y.P. Yuan, S.W. Cao, Z. Wang, L.S. Yin, Y.S. Liao, C. Xue, *ACS Applied Materials & Interfaces*, 2013, 5, 8088-8092.
- [4] J. Jin, C. Wang, X.-N. Ren, S.-Z. Huang, M. Wu, L.-H. Chen, *Nano Energy*, 2017, 38, 118-126
- [5] T. Kasuga, M. Hiramatsu, A. Hoson, T. Sekino, K. Niihara, *Langmuir* 1998, 14, 3160–3163.

## CATALYSIS OF SOLID STATE REACTIONS

E. Kiss and S. Panić

*University of Novi Sad, Faculty of Technology, bul. Cara Lazara 1, 21000  
Novi Sad, Serbia*

### ABSTRACT

This paper presents a number of representative catalytic solid state reactions. Today these reactions are present in all areas of chemistry. The number of newly discovered catalytic solid state reactions is growing rapidly, because these reactions are economically and ecologically justified.

### INTRODUCTION

Chemists have started relatively late to deal with reactions in solid states. Some of the modern scholars believe that the Aristotle's teaching has significantly contributed to this: "No reactions occur in the absence of solvent." (No Coopora nisi Fluida) [1]. Aristotle did not recognize the possibility that qualitative changes can occur even in solid substances. Solid state reactions can occur in organic as well as in inorganic substances. At the turn of third millennium, Kaupp reported over 500 solid state reactions, where the yield was 100%, meaning that the amount of contaminants was practically zero [2, 3]. Kaupp *et al.* [2] classified organic solid state reactions into 25 groups, and only one group is devoted to catalyzed solid state organic reactions. Solid state reactions in modern chemistry are used for economic and environmental reasons. As the concentration of reagents is maximized, the reaction rate is relatively high. If it is needed, the missing energy for the reaction can be compensated easily by microwaves or ultrasound. Solid state reactions are governed by three consecutive steps, by phase rebuilding, phase transformations and crystal disintegration [2]. It is important to stress out that the diffusion rate of the reaction participants in solid phase is far below the diffusion rate in liquids or gases. Solid state reactions could be accelerated and directed towards the desired products by appropriate catalysts. The aim of this paper is to indicate precisely, based on representative examples, the wide possibility of catalyst application in the field of solid state reactions.

## **CATALYSIS OF SOLID STATE ORGANIC REACTIONS**

The investigation of solid state organic reactions started with peptide synthesis (Robert Bruce Merrifield, Nobel Prize in Chemistry, 1984). Merrifield applied amino acids to solid resins [4]. Although the used resin has not shown catalytic effect, it is easy to imagine that in the case when somebody applies the catalytic active support, the conditions encounter with the requirements for catalytic solid state reactions.

### ***Suzuki coupling reaction***

Biaryls and their homologues form a significant class of conjugated polyaromatic compounds. Polyaryls have been widely used in the production of liquid crystals, laser paints and conductive polymers. In addition, biaryls and their higher homologues play an important role in the construction of physiologically important molecules in certain drugs and agrochemicals [5]. Basu *et al.* [6] developed an efficient method for cross-linking polyhaloaromatic compounds with arylboric acid on KF/alumina support, in the presence of palladium catalyst. The necessary energy was provided by an appropriate microwave oven.

### ***Selective synthesis of 1,2-disubstituted benzimidazoles***

Functionalized benzimidazoles are a major class of nitrogen-containing heterocyclic compounds. They have a major role in the pharmaceutical industry due to their antiulcerative effect, and can also be used as antihypertensives. Benzimidazoles counteract the effects of histamine which may cause allergy. Selective synthesis of 1,2-disubstituted benzimidazoles starts with the corresponding diamine compound, which reacts with the aliphatic aldehyde in the presence of sulfate catalyst, supported on silica gel. The reaction proceeds smoothly even at room temperature [7].

### ***Transfer hydrogenation of the nitroarenes with palladium catalyst***

Hydrogenation of nitroarenes has an important industrial significance. Formic acid is often used as a hydrogen donor. Basu *et al.* [8] performed the reduction of the nitro group with 2 mol% Pd(OAc)<sub>2</sub> catalyst, Amberlite resin formiate (ARF) supporting aminomethyl polystyrene and a small amount of N,N-dimethylformamide (DMF, N,N-Dimethylformamide) at 100-120°C for 6-14 hours.

***C-C Cross-coupling reactions***

In modern organic chemistry, the use of palladium catalyst for different synthesis is very widespread. C-C cross-reactivity products have been recognized as very important drugs and bioactive materials [9]. Heck (Richard F. Heck), Suzuki (Akira Suzuki) and Negishi (Ei-ichi Negishi) received the Nobel Prize in Chemistry in 2010, “for palladium-catalyzed cross coupling in organic synthesis”.

***Solid state enzyme catalysis***

Solid phase enzyme catalysis is also present in industrial processes. Enzymes are fixed (immobilized) on solid-phase organic or inorganic supports at a suitable pH under dry conditions. Immobilized enzymes can work at higher temperatures compared to their working temperatures in a liquid medium [10]. After the reaction, the product can be easily removed from the system, as the enzyme retains in the fixed position on the support.

***Solvent-free phase transfer catalysis***

Phase transfer catalysis (PTC) promotes the diffusion of the reactant from one phase to another during the reaction. PTC is characteristic for anionic reactions where a small amount of phase transfer agent is used (tetraalkylammonium salts, crown ethers). The solvent-free process provides the maximum concentration of the reactant. The phase transfer agent as an electrophilic material simultaneously fills the role of the reactant and the organic material [11, 12]. The solvent-free PTC consists of the three characteristic steps: *i*) transferring the reactive anion from the solid phase to the organic phase; *ii*) transferring the anion product from the organic phase to the solid phase; *iii*) equilibrium (partitioning) of the reactant and product anion between the organic and the solid phase [13]. These reactions are, in most of the cases, impracticable in solvents. Solvent-free PTC is often used in pharmaceutical chemistry and biochemistry [14], polymer chemistry [15], and liquid crystal chemistry [16].

***Catalysis of solid state rocket propellants***

Solid rocket propellants are composites. These composites consist of a mixture of solid oxidant granules (perchlorates) in polymeric binders and flakes or powders of energy compounds. The burn rate modifiers, i.e. catalysts (iron oxide, copper oxide) are also present in these composites [17]. Ammonium perchlorate,  $\text{NH}_4\text{ClO}_4$  is an interesting rocket propellant, because it can be used simultaneously as an energy source and as a strong oxidizing agent [18].

## CATALYSIS OF SOLID STATE INORGANIC REACTIONS

### *Catalysis of solid state reactions in alumina and silica ceramics*

The role of catalysts in the aluminum and silicate ceramics is not fully clarified. It is well known that *d*-elements can be effectively used in the chemical reactions. In the vicinity of suitable transition metals, geometric distortion of molecules and ions can be observed due to the interactions of electric field with the crystal field of reactants [19, 20]. This phenomenon is known as Jahn-Teller effect. The Jahn-Teller effect is also registered in minerals [21]. This phenomenon was studied in the systems of gibbsite, boehmite and  $\gamma$ -Al<sub>2</sub>O<sub>3</sub> in the presence of copper, zinc and magnesium oxide [22]. The results, obtained by diffuse reflectance spectroscopy, confirmed the theoretical expectations. The accelerated polymorphic transformations of alumina were detected only in copper oxide systems (equimolecular CuO/Al<sub>2</sub>O<sub>3</sub>, 900°C, 10h, air) [22]. Beside copper oxide, similar experiments were further expanded with iron and manganese oxide catalysts. Boehmite and kaolinite samples were prepared with previously mentioned transition metal oxide catalysts. Jahn-Teller effect was detected in every sample, by diffuse reflectance spectroscopy [23, 24]. Accelerated phase transformations of unstable alumina, as well as the accelerated mullite formation in kaolinite samples were registered. At the same time, accelerated sintering of alumina and kaolinite was observed [25].

Ozawa *et al.* [26] have very interesting observations regarding the accelerated transformation of  $\gamma$ -Al<sub>2</sub>O<sub>3</sub>. Without additives,  $\gamma$ -Al<sub>2</sub>O<sub>3</sub> transforms into  $\alpha$ -Al<sub>2</sub>O<sub>3</sub> at 1050°C [26]. When the changes were studied in the presence of copper oxide, a new “Cu-modified Al<sub>2</sub>O<sub>3</sub>” phase was registered at temperature of 800°C. This new copper modified alumina phase exists in the temperature range of 830-950°C and transforms directly into  $\alpha$ -Al<sub>2</sub>O<sub>3</sub> at 950°C. The expected transition  $\theta$ -form of alumina was not developed. The formation of copper spinel, CuAl<sub>2</sub>O<sub>4</sub> was registered above 950°C. CuO further precipitated at 1100°C from the copper spinel [26]. The mechanism of this catalytic reaction has three important moments. During the heat treatment in the presence of copper ions, the intermediate “Cu-modified Al<sub>2</sub>O<sub>3</sub>” form was registered. Also, the way of polymorphic transformation of alumina is altered. The formation of  $\theta$ -Al<sub>2</sub>O<sub>3</sub> lags behind, and  $\alpha$ -Al<sub>2</sub>O<sub>3</sub> forms directly. The CuO catalyst can be separated from the intermediate. Taking into account the mechanism of this reaction, the previously mentioned changes can be indicated as solid state catalytic ones.

### *Synthesis of artificial diamonds with transition metal catalysts*

The synthesis of artificial diamonds can be carried out catalytically, but also without catalysts (detonation nanodiamond). There are two catalytic methods

for diamond synthesis: high pressure and high temperature, HPHT and chemical vapor deposition, CVD [27]. It should be emphasized that none of these methods is a real solid state catalytic method. In the case of HPHT method, during the synthesis the catalyst (metal-solvent-catalyst) is in the liquid state, in which the solid reactants/graphite dissolve. In the case of CVD method, a gaseous phase occurs. In the HPHT process (5GPa, 1500°C), graphite is dissolved in the melted transition metal catalyst, and the less soluble diamond crystals are separated from the mixture [28]. According to Gou's explanation, the empty  $3d$  orbital of the transition metals and the free  $2p$  electron of the coal/graphite ( $\pi$ -electrons) weakly interact. The result of this interaction is the transformation of the hexagonal crystalline plates of the graphite into tetragonal form of diamond. General Electric applies FeNiCr, De Beers process applies FeCo and FeNi catalysts. Russians use NiMn, and Chinese NiMnCo catalysts [28]. In the CVD process, iron [29], nickel [30] or other metals [31] are sublimed to the walls of the closed silica tube (quartz), at high temperatures (800°C), while the required carbon atoms are cut off from the hydrocarbon molecules (methane, acetylene). The carbon atoms condense on the metal catalyst surface followed by their transformation into diamond crystals.

***Solid phase catalyzed dimerization and trimerization of fullerene***

The monomer fullerene can be activated in high speed vibration mill for 30 minutes (high speed vibration milling, HSVM) in the presence of a KCN or NaCN catalyst. The extent of dimerization is 30%. Similar yields can be achieved with alkali metal catalysts. Magnesium and aluminum also have a similar activity [32].

***Catalytic solid state degradation of perchlorates and potassium dichromate***

In the sixties of the last century Solymosi *et al.* [33, 34] dealt with solid phase catalytic degradation of perchlorates, chlorates and similar salts. At that time, under the leadership of Z. Szabó [35], catalytic solid state reactions were systematically investigated in Hungary. Copper oxide significantly accelerates the thermal decomposition of ammonium-perchlorate and lowers its explosion temperature. In Serbia, catalytic solid state reactions have been studied mainly in the context of catalyst synthesis and catalyst ageing. Significant part of these investigations was published by Paula Putanov and her coworkers. Within the scope of these investigations, solid state degradation of potassium dichromate was carried out [36]. Potassium dichromate decomposes over 900°C [37]. In the presence of copper, manganese and iron ions, potassium dichromate decomposes with considerable rate even at 800°C [36].

### ***Catalytic solid state reactions in metallurgy***

Y. K. Rao noted [38] that catalysts have not been used in metallurgy in terms of the expected opportunities. However, there are options for the application of the catalytic methods in the field of metallurgy. Rao reduced ZnO with carbon black at 1020°C for 6 hours. However, the reduction was completed within a few minutes when 1.7 wt% Li<sub>2</sub>O catalyst has been added to the reaction mixture. Similar results were obtained with the Na<sub>2</sub>CO<sub>3</sub> catalyst. Tanaka and Lund [39] observed that Na<sub>2</sub>CO<sub>3</sub> and K<sub>2</sub>CO<sub>3</sub> catalyze iron-graphite alloy formation, by generating a carburising gas atmosphere. Like K<sub>2</sub>CO<sub>3</sub>, tungsten and molybdenum have a similar catalytic effect on the formation of iron-carbon alloys [40].

### **CONCLUSION**

Today the catalyzed solid state reactions are present in all branches of chemistry and chemical technologies. They are especially present in the field of synthesis of pharmaceutical and biological products, polymers, agrochemicals, liquid crystals, etc. Catalyzed solid state reactions have significant importance in the field of environmental protection, and they are also justified in economic terms. At the 5<sup>th</sup> International Conference of the Society of Physical Chemists of Serbia, one section lecture “Accelerated polymorphous transformations and solid state reaction” was dedicated to the catalytic solid state reactions [36].

### ***Acknowledgement***

Financial support of Serbian Ministry of Education, Science and Technological Development [grant number 172059] is highly appreciated.

### **REFERENCES**

- [1] F. Toda, *Accounts Chem. Res.*, 1995, **28**, 480-486.
- [2] G. Kaupp, J. Schmeyers, J. Borg, *Chemosphere*, 2001, **43**, 55-61.
- [3] G. Kaupp in: *Topics in Current Chemistry*, Vol.254, F. Toda (Ed.), Springer-Verlag, Berlin, Heidelberg, 2005.
- [4] R. B. Merifield, *J. Am. Chem. Soc.*, 1963, **85**, 2149-2154.
- [5] B. Basu, S. Paul, *J. Catalysts (Hindawi)*, 2013, **2013**, 1-20.
- [6] B. Basu, P. Das, M. M. H. Bhuiyan, S. Jha, *Tetrahedron Lett.*, 2003, **44**, 3817-3820.
- [7] S. Paul, B. Basu, *Tetrahedron Lett.*, 2012, **53**, 4130-4133.
- [8] B. Basu, P. Das, S. Das, *Mol. Divers.*, 2005, **9**, 259-262.
- [9] L. Yin, J. Liebscher, *Chem. Rev.*, 2007, **107**, 133-173.
- [10] E. Guibé-Jampel, G. Rousseau, *Tetrahedron Lett.*, 1987, **28**, 3563-3564.

- [11]M. Kidwai, *Pure Appl. Chem.*, 2001, **73**, 147-151.
- [12]A. Loupy, *Topics Curr. Chem.*, 1999, **206**, 153-207.
- [13]C. M. Starks et al., *Phase-Transfer Catalysis*, Chapman & Hall, Inc., 1994.
- [14]K. O. Yerdelen, *Int. J. Pharm. Sci. Res.*, 2012, **3**, 126-129.
- [15]P. Keller, *Macromolecules*, 1987, **20**, 462-464.
- [16]H. Strzelecka, C. Jallabert, M. Veber, J. Malthete, *Mol. Cryst. Liq. Cryst. Incorpor. Nonlinear Optics*, 1988, **156**, 347-353.
- [17]World Heritage Encyclopedia, *Rocket Propellant*, World eBook. Id: WHEN 0030873089.
- [18]S. Chaturvedi, P. N. Dave, *J. Exp. Nanosci.*, 2012, **7**, 205-231.
- [19]N. B. Hannay, *Treatise on Solid State Chemistry*, Vol.1. Plenum Press, New York, London, 1975.
- [20]R. B. Heslop, K. Jones, *Inorganic Chemistry. A Guide to Advanced Study*, Elsevier, Amsterdam, 1980.
- [21]J. B. Goodenough, *Ann. Rev. Mater. Sci.*, 1998, **28**, 1-27.
- [22]E. E. Kiš, G. A. Lomić, G. C. Bošković, R. P. Marinković-Nedučin, *React. Kinet. Catal. L.*, 1998, **63**, 323-328.
- [23]E. E. Kiss, P. S. Putanov, *React. Kinet. Catal. L.*, 2002, **75**, 39-45.
- [24]J. S. Kiurski, D. Ž. Obadović, E. E. Kiš, R. P. Marinković-Nedučin, *React. Kinet. Catal. L.*, 2005, **84**, 359-366.
- [25]E. E. Kiss, P. S. Putanov, *React. Kinet. Catal. L.*, 2003, **79**, 325-331.
- [26]M. Ozawa, *Appl. Catal. B.-Environ.*, 1996, **8**, 123-140.
- [27]U. F. S. D'Haenens-Johansson, K. S. Moe, P. Johnson, S. Y. Wong, R. Lu, W. Wang, *Gems Gemol.*, 2014, **50**, 30-45.
- [28]J. C. Sung, J. Lin, *Diamond Nanotechnology: Synthesis and Applications*, Pan Stanford Publishing Pte. Ltd., Singapore, 2009.
- [29]Y. Shimada, N. Mutsukura, Y. Machi, *Japan. J. Appl. Phys.*, 1992, **31**, Part 1, Iss. 6B, 1958-1963.
- [30]K. Zare, M. A. Malkeshi, *J. Nanostruct. Chem.*, 2013, **3**, 1-5.
- [31]S. Matsumoto, Y. Sato, M. Kamo, N. Setaka, *Japan. J. Appl. Phys.*, 1982, **21**, L183-L185.
- [32]K. Komatsu in *Organic Solid State Reactions*, Vol.254, F. Toda (Ed.), Springer-Verlag, Berlin, Heidelberg, 2005.
- [33]F. Solymosi, L. Révész, *ZAAC*, 1963, **322**, 86-100.
- [34]F. Solymosi, E. Krix, *J. Catal.*, 1962, **1**, 468-480.
- [35]P. Tétényi, K. Lázár, Z. Paál, L. Simándi, *Magyar Tudomány*, 2002, **12**, 1548-1556.
- [36]E. E. Kiš, *Proc. 5<sup>th</sup> Int. Conf. Fund. Appl. Phys. Chem.*, S. Ribnikar, S. Anić (Eds), Society of Physical Chemists of Serbia, Belgrade, 2000.

- [37]H. Römpp, Vegyészeti Lexikon, 2. kötet, Műszaki Könyvkiadó, Budapest, 1960.
- [38]Y. K. Rao, JOM, 1983, **35**, 46-50.
- [39]Y. Tanaka, J. A. Lund, Powder Metall., 1988, **31**, 45-51.
- [40]J. Jin, T. Hong, J. Wu, J. Mater. Sci. Chem. Eng., 2017, **5**, 77-86.

## HIERARCHY OF SLOW RELAXATIONS IN CATALYST DYNAMICS

N. Ostrovskii<sup>1</sup> and V. Parmon<sup>2</sup>

<sup>1</sup>*Euro Gas, Sencanski put 75, 24000 Subotica, Serbia*

*(n-ostr@yandex.ru)*

<sup>2</sup>*Boriskov Institute of Catalysis, Novosibirsk, Russia*

### ABSTRACT

The analysis of nature and special features of slow relaxations in the catalytic reactions is presented. It is emphasized that they are subdivided into reversible transient regimes (structural or phase transformations in the catalyst) and irreversible transients (poisoning, deactivation, aging).

The generalized structure of the models of catalytic reaction with slow relaxation of catalyst properties is proposed. Several concrete examples of the transient regimes are presented that are caused by transformations in the catalyst, and by phenomena of catalyst deactivation.

### INTRODUCTION

In the case of catalytic reaction, the dynamic behavior is that, in which the reaction rate  $r = f(C_i, T, \Theta_j)$  changes with the time. Here  $C_i, T, \Theta_j$  – are phase coordinates of the system:

$$\frac{dr}{dt} = F \left( \frac{dC_i}{dt}, \frac{dT}{dt}, \frac{d\Theta_j}{dt} \right) \quad (1)$$

where  $C_i$  – concentration,  $T$  – temperature,  $\Theta_j$  – intermediate complex on the catalyst surface (coverage).

By catalyst dynamics we will understand the transient regimes, caused by changes in the active centers of the catalyst, i.e.  $d\Theta_j/dt$ , while catalytic reaction remains quasi-stationary.

This means that the transient mode of such catalyst dynamics (relaxation) occurs much slower than the reaction rate [1, 2], providing the application of the catalyst in practice. Otherwise, the catalyst would change (or deactivate) at the reaction rate, i.e. within a few seconds.

From the description point of view, such systems are divided into two subsystems with “rapid” and “slow” variables, to which two scales of

characteristic times correspond [2]. Such a splitting of variables into rapid and slow serves as a basis of quasi-steady-state principle in chemical kinetics [3].

For the slow relaxation in the catalyst itself, the segregation is also possible based on characteristic times. They are divided into the processes of catalyst reconstruction (in adsorbed layer and in the catalyst bulk) [2], and into the processes of catalyst deactivation (poisoning, coking, et al.) [4].

It is also necessary to distinguish the reversible and irreversible transient regimes.

Reversible relaxations include the phenomena of adjustment of the intermediate complexes in adsorbed layer  $[\bar{\theta}]_1 \rightarrow [\bar{\theta}]_2$  under changed concentrations  $[\bar{C}]_1 \rightarrow [\bar{C}]_2$  or temperature  $[\bar{T}]_1 \rightarrow [\bar{T}]_2$ . In this case the intermediates will restore their original state  $[\bar{\theta}]_1 \leftarrow [\bar{\theta}]_2$  after recovering of reagents composition  $[\bar{C}]_1 \leftarrow [\bar{C}]_2$  and/or temperature  $[\bar{T}]_1 \leftarrow [\bar{T}]_2$ .

If this phenomenon occurs very rapidly (compared with the reaction rate) that it becomes inseparable from the reaction kinetics itself. Sometimes it is called “Nonstationary kinetics”. The most complicated case is the regime of self-oscillations of the reaction rate, to which a large number of works is devoted. This area has long ago become independent and we will not concern it here.

But if the rate of relaxation is lower than the reaction rate (so that this becomes noticeable in the experiment), then real transient regime appears. Boreskov [1] has named this phenomenon as “the Action of the Reaction Medium on the Catalyst” - ARMC.

Irreversible relaxations include the processes in which the return of state  $[\bar{\theta}]_1$  does not occur after recovering previous condition ( $C$  and  $T$ ). They include the phenomena of poisoning, reconstruction of the catalyst surface (or phase transformations), the deactivation by coke, etc.

Examples of transient regimes of both types (reversible and irreversible) will be considered below, and the corresponding equations will be also presented. Particular attention will be given to the quasi-stationary characteristics of regimes, i.e., to the initial and final (steady) states of these transient regimes.

### TYPES OF SLOW TRANSIENT REGIMES

Besides entire variety of the reasons for the “catalyst dynamics”, there are only several types of slow transient regimes, which are differentiated by the character of a change in the reaction rate with time (Fig. 1):

- A reversible increase or reduction in the rate from the initial level  $r_o$  to the level of the new steady value  $r_a$  - (catalyst adapting);

- An irreversible decrease of the reaction rate from  $r_o$  or  $r_a$  to the level of quasi-steady value  $r_s$  - (catalyst deactivation);
- A reversible adapting of the rate  $r_a$  with the simultaneous irreversible decrease to the level  $r_s$  - (adapting and deactivation of the catalyst).

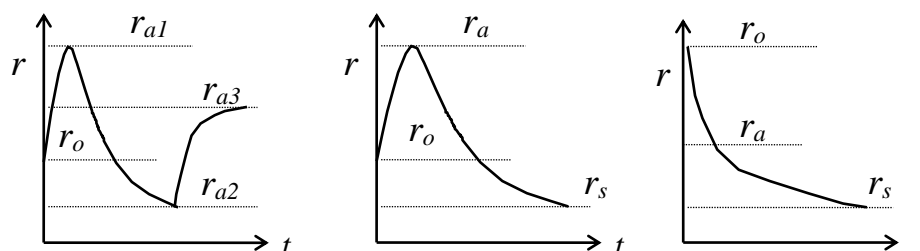


**Figure 1.** Types of slow transient regimes of catalytic reaction.

Since the rates of transient processes are substantially lower than the reaction rate, then the reaction must be considered as the quasi-stationary with respect to relaxations listed above.

For this reason, the structure of mathematical model of the reaction dynamics becomes “universal”, and it covers all types of transient regimes.

In the case of a single reaction, which occurs in a gradientless or plug-flow reactor, the model can be written as follows:

$$C_i - C_{io} = \tau v_i r, \quad r(t) = r_o \psi a, \quad r_o = f(\bar{C}_i, T), \quad (2)$$

$$\frac{dC_i}{d\tau} = v_i r, \quad \frac{d\psi}{dt} = \varphi_c(\bar{C}_i, T), \quad \frac{da}{dt} = \varphi_d(\bar{C}_i, T, a) \quad (3)$$

where  $C_i$  – concentration,  $T$  – temperature,  $v_i$  – stoichiometric coefficient,  $\tau$  – contact time,  $\psi$  – function of a catalyst surface state,  $a = r / r_o$  – relative activity of the catalyst.

At universal structure of the model (2, 3), the features of reaction kinetics expresses the function  $f(C_i, T)$ , whereas the types of transient regimes reflect functions  $\varphi_c(C_i, T)$  and  $\varphi_d(C_i, T, a)$ .

### ARMC – The Action of Reaction Medium on the Catalyst

Term ARMC was introduced by Boreskov still in the 40's. Reaction rate in this case is expressed by the product of two functions [1, 5]:

$$r = k f(C_i, \Theta_i) \psi(C_i) \quad (4)$$

It was established, that for the reaction of butylenes oxidative dehydrogenation over oxide Fe-Sb catalyst [5]:

$$f(C_i, \Theta_i) = k' C_{C4H8}, \quad \psi(C_i) = k'' (C_{O2}/C_{C4H8})^{0.5} \quad (5)$$

Equation (4, 5) describes some steady modes of the reaction, but at the same time, does not describe the transient regimes.

The duration of the transient regimes (1–2 of hour) is caused not only by reconstruction in the adsorbed layer, but also in the bulk of catalyst. For describing of this reaction dynamics, the differential equations of type (3) should be derived on the basis of assumed mechanism [6]:

$$\text{Oxidation of the reduced active centers:} \quad r_{ox} = k_o \sqrt{C_o} \Theta_r$$

$$\text{Reduction of the oxidized active centers:} \quad r_{rd} = k_r C_A \Theta_o$$

"Curing" of the reduced vacancies due to

$$\text{oxygen ions from the depth of crystallites:} \quad r_{sh} = k_s \sigma_s \Theta_r$$

$$\frac{d\psi}{dt} = \frac{d\Theta_o}{dt} = (k_s \sigma_s + k_o \sqrt{C_o}) \Theta_r - k_r C_A \Theta_o \quad (6)$$

$$\frac{\partial \sigma}{\partial t} = \frac{D}{L^2} \frac{\partial^2 \sigma}{\partial \xi^2}, \quad \xi = 1: \quad \frac{d\sigma}{d\xi} = -\frac{L^2}{D} k_s \sigma_s \Theta_r \quad (7)$$

where  $r_i$  – reaction rate,  $k_i$  – reaction rate constant,  $C_i$  – concentration,

$\Theta_o, \Theta_r$  – fractions of oxidated and reduced active centers,

$\sigma, \sigma_s$  – oxidation degree of the catalyst in the depth and on the surface of crystallites,  $L$  – size of crystallite,  $D$  – diffusion coefficient of oxygen ions in oxide,  $\xi$  – dimensionless coordinate of crystallite.

Long time relaxations are caused by slow diffusion of ions  $O^-$  in solid oxide. For example, in  $Fe_3O_4$  the diffusion coefficient  $D = 10^{-19} \div 10^{-18} \text{ cm}^2/\text{s}$ .

For the estimation of quasi-stationary rate of the reaction we should determine the value of  $\psi = \Theta_o$  at  $\delta\psi/dt = 0$ .

Since  $\Theta_r = 1 - \Theta_o/\gamma$ , where  $\gamma = 1 / (1 + b_o \sqrt{C_o})$ , then from (6) we obtain:

$$\psi_{qs} = \left( \gamma + k_r C_A / k_o \sqrt{C_o} \right)^{-1}. \quad (8)$$

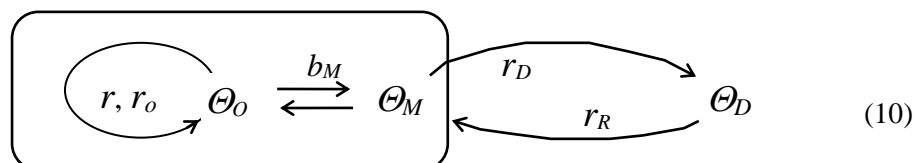
## CATALYST DEACTIVATION

In respect to deactivation, an important is the correction of the principle of quasi-steady state, introduced by Semenov. It consists in the fact that in quasi-stationary regime, the condition of Franck-Kamenetsky ( $\delta\Theta_j/dt = 0$ ) is not satisfied for the part of intermediate products ( $\Theta_D$ ).

In catalysis,  $\Theta_D$  is a portion of the active centers "switched off" from the reaction, i.e., deactivated. Therefore, in quasi-steady state:

$$\frac{d\Theta_j}{dt} = 0, \quad \frac{d\Theta_D}{dt} \neq 0, \quad \sum \Theta_j = 1 - \Theta_D \quad (9)$$

Let us consider, as an example, the cyclohexane dehydrogenation into benzene  $C_6H_{12} = C_6H_6 + 3H_2$  on the catalyst Pt/Al<sub>2</sub>O<sub>3</sub>. The mechanism of reaction and deactivation is presented in the form of graph [4]:



Side stage of methylcyclopentane formation on the surface  $\Theta_M$  and its hydrogenations does not enter into catalytic cycle, but it is the key stage for coke formation with the rate  $r_D = k_d P_M \Theta_M$ . Hydrogen provides self-regeneration of catalyst with the rate  $r_R = k_r P_H \Theta_D$ .

According to (9),  $\Theta_M = \Theta_M^0 (1 - \Theta_D)$ , when the rates of deactivation and self-regeneration become equal  $k_d P_M \Theta_M = k_r P_H \Theta_D$ , the activity ( $a = 1 - \Theta_D$ ) stops change and takes the value of stationary activity  $a_s$ .

Then model takes the form [4]:

$$r = r_o a, \quad r_o = \frac{k P_C}{1 + b_B P_B} \left( 1 - \frac{P_B P_H^3}{K_P P_C} \right), \quad -\frac{da}{dt} = k_d b_M \frac{P_M^2}{P_H} \frac{a - a_s}{1 - a_s} \quad (11)$$

where  $P_B, P_C, P_H, P_M$  – partial pressure of benzene, cyclohexane, hydrogen and methylcyclopentane,  $b_i$  – adsorption coefficient,  $a_s$  – stationary activity.

Similar equations are applicable in all cases of catalyst deactivation, accompanied by self-regeneration phenomena. They include almost all processes realized in the surplus of hydrogen, for example hydrogenation, hydrotreating, isomerization, naphtha reforming, and also oxidative dehydrogenation, etc.

## COMPLEX REGIMES

In many processes are present both ARMC and deactivation.

**Example 1.** Let us consider the reactions of alkynes hydrogenation, which are impurities in olefins C<sub>2</sub>–C<sub>4</sub>, and are the poisons of the catalysts in olefins polymerization. Process includes the period “running-in” (0.5–2.0 of hour) in which activity of catalyst (Pd, Pd-Ag, Pd-Au) grows. Majority of authors suppose that this is caused by formation of oligomeric structures, which form the active centers of hydrogenation. Simultaneously, oligomeric structures are the precursors of “of green oil”, which deactivates the catalyst.

The crucial influence on these processes exerts hydrogen, which contributes to develop the active centers of optimal structure, and also is reduced the rate of “green oil” formation. The influence of hydrogen on the state of active centers is reversible, therefore it corresponds to determination of “the action of reaction medium on the catalyst”  $\psi(t)$ . This can be represented by the competitive stages, which reduce to the equation:

$$\frac{d\psi}{dt} = k_f C_H (1-\psi) - k_g C_A \psi \quad (12)$$

As for catalyst deactivation in these processes, it is the typical coking, accompanied by self-regeneration of the catalyst with hydrogen:

$$\frac{da}{dt} = -k_d C_A \frac{a-a_s}{1-a_s}, \quad a = a_s + (1-a_s) \exp(-k_d C_A t) \quad (13)$$

Summary influence of both phenomena (ARMC and deactivation) in this process is represented on Fig. 2, in the form of conversion X:

$$X(t) = \tau \frac{r_o}{C_{A0}} \psi(t) a(t), \quad r_o = k \sqrt{C_A} C_H \quad (14)$$

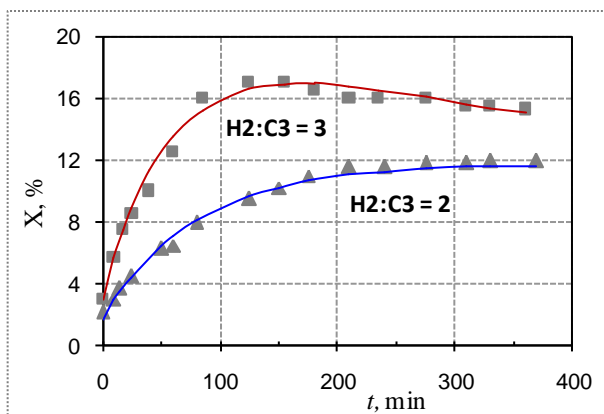


**Figure 2.**  
Dynamics of methylacetylene conversion over Pd/C.  
Points - exper. from [7].  
Lines - calcul. by eq. (14).  
T = 25 °C, H<sub>2</sub>:C<sub>3</sub>H<sub>4</sub> = 3; 2.

**Example 2.** Let us consider now the reaction of propylene polymerization on Ziegler-Natta catalyst TiCl<sub>4</sub>/MgCl<sub>2</sub>, with co-catalyst AlEt<sub>3</sub>, in heptane as solvent. The olefin polymerization reactions are characterized by the fact that they occur entirely in the nonstationary, transient regimes. The catalyst of polymerization is consumed in the process, since it remains inside polymer.

All characteristics of reaction change in the time:

- polymer particle continuously grows "like pomegranate fruit";
- the way of monomer to the catalyst surface always increases, and the regime of reaction changes from the diffusion to the kinetic;
- active centers are continuously generated and continuously deactivated.

The following model reflects all listed special features [8]:

$$\text{Propylene in gas phase } (P_m): \quad \frac{dP_m}{dt} = W \frac{RT}{MV_G} - \beta (C_m^* - C_m) RT \frac{V_L}{V_G} \quad (15)$$

$$\text{Propylene in liquid phase } (C_m): \quad \frac{dC_m}{dt} = \beta (C_m^* - C_m) - R_P, \quad (16)$$

$$\text{Reaction rate } (R_P): \quad R_P = k_P G_c C_m \psi a, \quad \psi = \frac{b_A C_A + b_H C_H}{(1 + b_A C_A + b_H C_H)^2} \quad (17)$$

$$\text{Activity } (a): \quad \frac{da}{dt} = k_a C_A C_m a_i - k_d C_m x_p a + k_s C_A (1 - a), \quad (18)$$

$W$  – weight flow rate of propylene;  $G_c$  – weigh of the catalyst;  $V_G$ ,  $V_L$  – volume of gas and liquid in the reactor;  $\beta$  – coefficient of interphase mass transfer;  $k_P$  – rate constant of polymerization;  $C_A$ ,  $C_H$  – concentration of co-catalyst and hydrogen in a liquid;  $k_a$ ,  $k_d$ ,  $k_s$  – rate constants of activation, deactivation and self-regeneration of active centers.

In experiments, the rate of propylene consumption is measured at the entrance of reactor. Usually, this is interpreted as a reaction rate.

The comparison of experiments with the catalyst and without it, and their interpreting using model (15-18), shows that the total rate of process coincides with the reaction rate only in steady state.

Depending on the initial conditions, the reaction rate can be lower or higher than the measured rate of monomer consumption.

This clearly illustrates Fig. 3, where the typical regime of the process (Fig. 3a) is compared with regime where preliminary saturation of heptane by propylene is used (Fig. 3b).

Let us note in conclusion that in the polymerization the characteristic times of transient regimes are comparable with the total reaction time (1-3 hour), that make transient regimes important also for practical purposes.

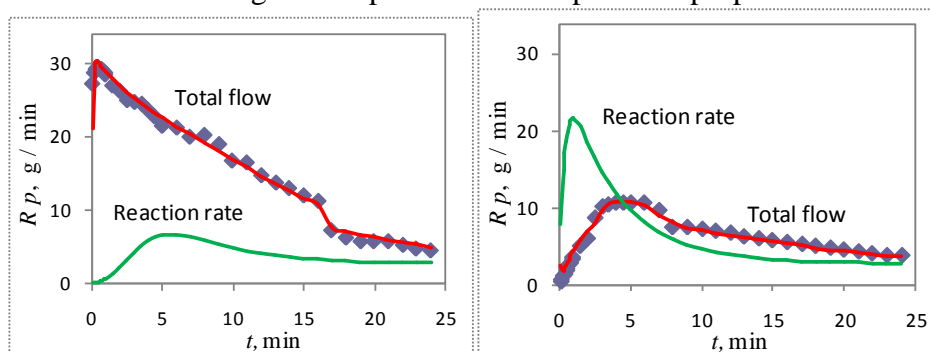


**Figure 3a,b.** Dynamics of propylene polymerization [8].

Points – experiment. Lines – calculation by model (15-18).

a) -  $C_m(t=0) = 0$ ; b) -  $C_m(t=0) = C_m^*$ .

## CONCLUSIONS

Transient regimes (relaxations) in catalytic reactions are usually slow if are caused by reconstruction of structure and phase composition of the catalyst, or by phenomena of catalyst deactivation.

During slow relaxations, the reaction occurs in quasi-stationary condition. Therefore, the model of process can be divided according to characteristic times: time of reaction; of reversible relaxations; of irreversible changes.

The total reaction rate, in this case, can be represented as a product of three functions (or functional): the function of kinetics and of mass balance; the function of reversible relaxation; the function of catalyst deactivation.

Transient regimes (even slow) are considerably more informative, than stationary, for understanding of the mechanism, and features of the process.

## REFERENCES

- [1] G.K. Boreskov – Heterogeneous catalysis. Moscow, Nauka, 1986.
- [2] V.N. Parmon – Thermodynamics of Non-Equilibrium Processes for Chemists with a Particular Application to Catalysis. Elsevier. 2010.
- [3] D.A. Frank-Kamenetsky – Zhurn. Fiz. Khim. 1940, **14**, 695-700. (in Russian).
- [4] N.M. Ostrovskii – Catalyst Deactivation Kinetics. Moscow, Nauka, 2001.
- [5] G.K. Boreskov – Kinetika i Kataliz, 1980, **21**, 5-16. (in Russian).
- [6] N.M. Ostrovskii, S.I. Reshetnikov – Chem. Eng. J., 2005, **107**, 141-146.
- [7] R. Marshall, G. Webb, S.D. Jackson, D. Lennon – J. Mol. Catal. A: Chem., 2005, **226**, 227-230.
- [8] N.M. Ostrovskii, L. Fekete – Polyolefins Journal, 2015, **2**, 89-97.

## NANOSTRUCTURED ORGANIC-INORGANIC HYBRID SMECTITE BASED COMPOSITES

N. Jović-Jovičić, Z. Mojović, M. Ajduković, P. Banković, T. Mudrinić,  
S. Marinović and A. Milutinović-Nikolić

*University of Belgrade–Institute of Chemistry, Technology and Metallurgy,  
National Institute,  
Center for Catalysis and Chemical Engineering,  
Njegoševa 12, 11000 Belgrade, Republic of Serbia.  
(natasha@nanosys.ihm.bg.ac.rs)*

### ABSTRACT

This paper represents a survey of the investigation conducted in the Center for Catalysis and Chemical Engineering of the Institute of Chemistry, Technology and Metallurgy, Belgrade, during last decade regarding nanostructured organic-inorganic hybrid smectite based composites and their application as adsorbents and modifiers of glassy carbon electrode.

### INTRODUCTION

Nanostructured organic-inorganic hybrid smectite based composites (HC) are among the most promising contemporary materials for various applications. HC obtained by interaction of quaternary alkyl ammonium cations (QAAC), organic anions and biopolymer chitosan were investigated as adsorbents of pertechnetate, anionic textile dyes, of phenol and its nitro derivatives and nicotine. Comparison of bare glassy carbon electrode (GCE) and GCE modified with different HC was performed [1-24].

### EXPERIMENTAL

The first step in synthesis of nanostructured organic-inorganic hybrid smectite based composites (HC) is preparation of Na<sup>+</sup>-enriched homoinic smectite (Na-S) as a precursor material. The Na-S was obtained by replacing of naturally present exchangeable cations in the interlamellar space of smectite with solely Na<sup>+</sup> [2, 25]. The HC were synthesized by intercalation of selected (bio) organic cations into smectite structure. Intercalation was performed with quaternary alkylammonium cations (QAAC) with different smectite/QAAC ratios and different QAAC. The intercalation with biopolymers i.e. chitosan was also performed in order to test green alternative to QAAC.

The QAAC used for synthesis of HC were: hexadecyltrimethylammonium (HDTMA), dodecyltrimethylammonium (DDTMA), tetramethylammonium (TMA) and benzyltrimethylammonium (BTMA) cations. The QAAC/smectite ratios were defined as multiples of cation exchange capacities (CEC) of smectite in the range from 0.2 to 2.0. The samples were denoted according to QAAC and multiples of CEC i.e. 1.0 TMA-S. The HC were obtained by intercalation of QAAC into the interlamellar space of smectite. The arrangement of the intercalated QAAC depended on the length of intercalated alkyl cation chains and the amount of the intercalated cations forming monomolecular layer, lateral bimolecular layer, pseudo-trimolecular layer and paraffin type of layer [12, 26, 27]. The HC with organic anion dodecyl sulfate was obtained by interaction with acidic smectite surface, developed by acid modification and denoted as DS-S<sub>A</sub> [22].

The bio-polymer used for synthesis of HC was high molar mass chitosan (deacetylated chitin or poly(D-glucoseamine), av.  $M_w = 342500 \text{ g mol}^{-1}$ ). Chitosan/smectite HC had chitosan intercalation in mono- and bi-layer arrangement. Synthesis was performed using chitosan solution of pH=4.9 that enabled presence of ammonium groups in chitosan structure, and preserved the smectite structure [20, 28, 29]. The samples were denoted according to chitosan layer formation as Cml-S and Cbl-S for monolayer and bi-layer formation in smectite structure, respectively.

Chemical composition of starting smectites was obtained by ICP-OES, while composition of organic phase (C, H and N) in HC samples was determined by elemental analysis [12, 20]. The intercalation of organics into smectite structure was monitored by X-ray diffraction (XRD). The FTIR was used to confirm the electrostatic interaction of positively charged organic species with negatively charged sites of smectite [12, 20]. The point of zero charge was used to estimate the surface acidity of the synthesized HC [5, 12, 21]. Textural properties were determined by low temperature N<sub>2</sub> physisorption in order to correlate porous structure with the adsorptive and electrochemical properties [2, 3, 6, 7, 10, 16]. The morphology of HC was analyzed by SEM [5, 17]. The process of adsorption was monitored using UV-Vis spectrophotometry and inductively coupled plasma (ICP). The electrochemical behavior of GCE modified with HC was analyzed using cyclic voltammetry, multisweep cyclic voltammetry and square wave voltammetry.

## RESULTS AND DISCUSSION

### Adsorption study

The review of comprehensive adsorption investigations is summarized in Table 1. The amount of adsorbed dye (AO10, AY99 and RB5) at equilibrium time ( $q_e$ ) increased with: (i) increase of QAAC/CEC ratio, and (ii) number of C-atoms present in applied QAAC. Generally, it could be assumed that adsorption of textile azo dyes strongly depends on arrangement of intercalated organic cation in smectite interlamellar space. The organic cations were incorporated in smectite structure in different layered structures. Monolayer, bi-layer, pseudo-trilayer and paraffin type of arrangements were found in 0.2 HDTMA-S, 0.5-HDTMA-S, 1.0-HDTMA-S and 2.0 HDTMA-S, respectively. The adsorption mechanism of acid azo dyes on samples with amount of QAAC  $\leq$  CEC was mainly through different organic interactions. Adsorption of azo dyes on hybrid nanocomposites with QAAC  $>$  CEC is governed by additional electrostatic interaction i.e. via attraction of  $-\text{SO}_3^-$  groups of dyes with ammonium groups [12, 29]. The amount of adsorbed dyes at equilibrium time was the highest for AY99 and the lowest for AO10. It was found [12] that developed surface area was less significant for the adsorptive properties of QAAC-smectite nanocomposites toward organic contaminants than arrangement of organic phase in composite. The highest adsorption efficiency toward investigated dyes showed 2.0 HDTMA-S, although this sample possessed the least pronounced textural properties [12].

Jović-Jovičić et al. [2, 3, 5, 12] showed that there is no competition between acid dyes (AO10, AY99 and RB5) and  $\text{Pb}^{2+}$  in simultaneous adsorption from bi-component solutions. Moreover, the adsorptions of dye molecule or  $\text{Pb}^{2+}$  become the new adsorption sites, enhancing adsorption from their bi-component solutions [2, 5, 12].

The 0.5 HDTMA-S and 1.0 HDTMA-S were tested as multifunctional adsorbent for three-component solution of dyes (AO10, AY99 and RB5), three-component solution of toxic metallic cation ( $\text{Pb}^{2+}$ ,  $\text{Ni}^{2+}$  and  $\text{Cd}^{2+}$ ) as well as their hexa-component solution. Both samples showed the highest adsorption affinity toward AY99 among dyes and  $\text{Ni}^{2+}$  among cations. The 1.0 HDTMA-S was found to be more efficient multifunctional adsorbent of hexa-component solution, showing synergistic effect in simultaneous adsorption of textile azo dyes and metal cations [14].

Among QAAC-smectite nanocomposites the 1.0 TMA-S was found to be the most efficient toward nicotine adsorption. In this sample intercalated  $\text{TMA}^+$  cations formed pillar-like arrangement within smectite interlamellar space that led to developed textural structure and enhanced specific surface

**Table 1.** The review of adsorption studies on smectite nanocomposites

Adsorbate	Adsorbent	$q_e$ [mg g <sup>-1</sup> ]	Ref
AO10	0.2 HDTMA-S	2.2	2
	0.5 HDTMA-S	5.4	2
	1.0 HDTMA-S	22.8	2
	2.0 HDTMA-S	100.0	2
	2.0 DDTMA-S	12.3	2
	2.0 TMA-S	2.5	2
	Cml-S	21.9	21
AY99	0.2 HDTMA-S	18.3	3
	0.5 HDTMA-S	103.5	3
	1.0 HDTMA-S	142.3	3
	2.0 HDTMA-S	253.7	3,4
	2.0 DDTMA-S	88.9	3
	2.0 TMA-S	21.4	3
	Cml-S	121.8	21
RB5	0.2 HDTMA-S	2.7	12
	0.5 HDTMA-S	11.9	12
	1.0 HDTMA-S	54.7	12
	2.0 HDTMA-S	193.6	12
	2.0 DDTMA-S	39.5	12
	2.0 TMA-S	1.0	12
	Cdl-S	166.7	15
	Cml-S	87.1	21
Nicotine	1.0 TMA-S	58.4	23
Pb <sup>2+</sup>	0.2 HDTMA-S	51.3	2
	0.5 HDTMA-S	45.0	2
	1.0 HDTMA-S	43.4	2
	2.0 HDTMA-S	31.9	2
	2.0 DDTMA-S	60.4	12
	2.0 TMA-S	63.3	12
AO10, Pb <sup>2+</sup>	0.2 HDTMA-S	1.8, 50.1	2
	0.5 HDTMA-S	10.9; 44.2	2
	1.0 HDTMA-S	36.2; 36.8	2
	2.0 HDTMA-S	99.3; 29.5	2
AY99, Pb <sup>2+</sup>	0.2 HDTMA-S	30.7; 50.6	3
	0.5 HDTMA-S	90.1; 40.0	3
	1.0 HDTMA-S	219.2; 21.7	3
	2.0 HDTMA-S	243.6; 22.7	3
	2.0 DDTMA-S	195.7; 47.9	3
	2.0 TMA-S	30.7; 67.0	3
RB5, Pb <sup>2+</sup>	0.2 HDTMA-S	8.0; 63.0	12
	0.5 HDTMA-S	22.0; 40.3	12
	1.0 HDTMA-S	66.4; 21.1	12
	2.0 HDTMA-S	168.3; 10.5	12
	2.0 DDTMA-S	55.5; 42.1	12
	2.0 TMA-S	3.7; 63.8	12
AO10, AY99, RB5	0.5 HDTMA-S	8.3; 68.1; 3.9	14
	1.0 HDTMA-S	19.1; 138.3; 25.0	14
Ni <sup>2+</sup> , Cd <sup>2+</sup> , Pb <sup>2+</sup>	0.5 HDTMA-S	41.1; 27.0; 56.0	14
	1.0 HDTMA-S	18.2; 18.0; 39.4	14
AO10, AY99, RB5 Ni <sup>2+</sup> , Cd <sup>2+</sup> , Pb <sup>2+</sup>	1.0 HDTMA-S	19.0; 151.2; 57.2	14
	1.0 HDTMA-S	7.6; 7.9; 31.1	14
phenol	2.0 HDTMA-S	172.0	19
2-nitrophenol	2.0 HDTMA-S	500.4	19
3-nitrophenol	2.0 HDTMA-S	476.8	19
4-nitrophenol	2.0 HDTMA-S	597.7	19
<sup>99</sup> Tc(VII)	1.0, 1.5 and 2.0 HDTMA-S	523; 1295 and 1295 MBq g <sup>-1</sup>	13

area that favored nicotine adsorption [23].

The Cml-S with monolayer arrangement of chitosan showed adsorption affinity toward investigated dyes in the following order: AY99 > RB5 > AO10. It was found that adsorption was most efficient in acidic medium, probably due to electrostatic attraction between protonated active sites of Cml-S with anionic groups of dyes [21]. The adsorption of RB5 was also studied on Cdl-S, the bionanocomposite with intercalated bilayered arrangement of chitosan chains. The additional cationic sites ( $-\text{NH}_3^+$ ) present in bilayer structure, could be the reason for almost two times higher amount of adsorbed RB5 on Cdl-S than on Cml-S [15, 21].

The removal of radioactive  $^{99}\text{TcO}_4^-$  from aqueous solution at room temperature was investigated on HDTMA-S adsorbents with different HDTMA<sup>+</sup> cation loading. The samples with HDTMA/S value > 1 were able to adsorb significant amount of  $^{99}\text{TcO}_4^-$  [13].

The adsorption of phenol and its nitro derivatives was investigated on 2.0 HDTMA-S. Among investigated phenols the 4-nitrophenol (NP) had the highest adsorption capacity ( $q_e=597.7 \text{ mg g}^{-1}$ ) [19].

For all investigated adsorption systems, the adsorption kinetics followed pseudo-second order kinetics model, while adsorption isotherms were best described by Langmuire isotherm [1, 13, 19, 21].

### Electrocatalysis

The electrochemical performance of glassy carbon electrode (GCE) modified with different HC was tested.

The phenol electrooxidation showed similar behavior on 0.2 HDTMA-S, 0.2 DDTMA-S and 0.2 TMA-S, with the highest electrochemical response with 0.2 TMA-S. The major difference was found between Tafel slopes, indicating different types of adsorption [6].

Phenol determination was performed on series of HDTMA-S based electrodes in acidic and alkaline solutions. It was proved that HDTMA/S ratio plays the key role in phenol oxidation [7, 9]. Sensitivity of phenol oxidation was improved with increasing of HDTMA<sup>+</sup> loading, while deactivation was observed only in electrode with 0.2 HDTMA-S [7]. It was also confirmed that presence of HDTMA<sup>+</sup> in electrode materials allowed the analyte preconcentration and prevent phenol polymerizations on electrode surface [9].

The electrooxidation of 4-nitrophenol was investigated using electrodes based on three series of HC: (i) TMA-S composites with different TMA/S ratios in range from 0.2 – 2.0 [10]; (ii) series of different QAAC (HDTMA<sup>+</sup>, DDTMA<sup>+</sup>, TMA<sup>+</sup>) with constant QAAC/S ratio of 0.2 [10] and (iii) series with aromatic BTMA<sup>+</sup> cation with 0.2-2.0 BTMA<sup>+</sup>/S ratios [8, 16].

The results showed that current density of anodic peak at 1.2 V assigned to 4-NP oxidation depended on type and amount of QAAC loading. The electrode contained 0.2 TMA-S showed the highest signal for 4-NP oxidation, with detection limit of  $1 \cdot 10^{-6} \text{ mol dm}^{-3}$  [10].

The electrooxidation of 4-NP using electrodes based on BTMA-S showed that increasing of BTMA<sup>+</sup> loading lead to the increase of electrochemical activity and stability [8, 16]. The linear dependence of current density of 4-NP concentration was observed for electrode with 2.0 BTMA-S [8].

The Cbl-S was used for glassy carbon electrode modification and used for detection of phenol and its nitro derivatives from acidic and alkaline solutions [20]. In acidic solution the investigated electrode proved to be applicable for the simultaneous detection of phenol, 2-NP and 4-NP, although with high rate of passivation. On the other hand, in the alkaline solution the rate of passivation was very low, but all three analytes could not be detected simultaneously [20].

GCE modified with DS-S<sub>A</sub> was used for electrooxidation of nicotine [25] and testing of electrochemical behavior of immobilized hemoglobin in alkaline solution [22]. The intensity of the nicotine oxidation peak was lower on the GCE-DS-S<sub>A</sub> than on the bare GCE, and the onset and peak potentials were significantly shifted towards less positive values. The nicotine peak intensity increased gradually with the increase of the accumulation time improving the sensitivity of GCE-DS-S<sub>A</sub> [25].

Investigation of immobilized hemoglobin (Hgb) on GCE-DS-S<sub>A</sub> revealed that presence of DS resulted in partial oxidation/denaturation of Hgb as well as formation of hemichrome. In alkaline medium, two reduction peaks were observed ascribed to reduction of Fe(III)/Fe(II) heme pair and highly reduced HgbFe(I). The peaks current were enhanced in presence of H<sub>2</sub>O<sub>2</sub> in alkaline solution, and linear response to concentration was observed [22].

## CONCLUSION

The variety of different nanostructured organic-inorganic hybrid smectite based composites (HC) was synthesized. Their chemical and phase composition together with morphological and textural properties was determined. The most important feature that influenced HC adsorptive and electrochemical properties was the arrangement of (bio) organic phase within inorganic aluminosilicate structure. HC with high amounts of intercalated quaternary alkyl ammonium cations (QAAC) showed superior adsorptive potential toward pertechnetate and anionic textile dyes. HC obtained with chitosan although with somewhat lower adsorption capacity represent green alternative to HC with QAAC. Glassy carbon electrode modified with

different HC improved electrochemical response toward phenol, its nitro derivatives and nicotine.

### ***Acknowledgement***

This work was supported by the Ministry of Education, Science and Technological Development of the Republic of Serbia (III 45001).

### **REFERENCES**

- [1] N. Jović-Jovičić, A. Milutinović-Nikolić, I. Gržetić, D. Jovanović, *Chem. Eng. Technol.*, 2008, 31, 567–574.
- [2] N. Jović-Jovičić, A. Milutinović-Nikolić, P. Banković, Z. Mojović, M. Žunić, I. Gržetić, D. Jovanović, *Appl. Clay Sci.*, 2010, 47, 452–456.
- [3] N. Jović-Jovičić, A. Milutinović-Nikolić, P. Banković, B. Dojčinović, B. Nedić, I. Gržetić, D. Jovanović, *Acta Phys. Pol. A*, 2010, 117, 849-854.
- [4] M. Žunić, A. Milutinović-Nikolić, N. Jović-Jovičić, P. Banković, Z. Mojović, D. Manojlović, D. M. Jovanović, *Hem. Ind.*, 2010, 64, 193-199.
- [5] N. Jović-Jovičić, Ph.D. thesis, University of Belgrade – Faculty of Chemistry, 2010.
- [6] Z. Mojović, N. Jović-Jovičić, P. Banković, M. Žunić, A. Abu Rabi-Stanković, A. Milutinović-Nikolić, D. Jovanović, *Appl. Clay Sci.*, 2011, 53, 331–335.
- [7] Z. Mojović, N. Jović-Jovičić, A. Milutinović-Nikolić, P. Banković, A. Abu Rabi-Stanković, D. Jovanović, *J. Haz. Mater.*, 2011, 194, 178-184.
- [8] A. Abu Rabi-Stanković, A. Milutinović-Nikolić, N. Jović-Jovičić, P. Banković, M. Žunić, Z. Mojović, D. Jovanović, *Clays Clay Miner.*, 2012, 60, 291–299.
- [9] Z. Mojović, N. Jović-Jovičić, A. Milutinović-Nikolić, P. Banković, A. Abu Rabi – Stanković, D. Jovanović, *Env. Prog. Sus. Energy*, 2013, 32, 1124–1128.
- [10] A. Abu Rabi-Stankovic, Z. Mojovic, A. Milutinović-Nikolić, N. Jović-Jovičić, P. Banković, M. Žunić, D. Jovanović, *Appl. Clay Sci.*, 2013, 77-78, 61-67.
- [11] M. Žunić, N. Jović-Jovičić, A. Milutinović-Nikolić, P. Banković, Z. Mojović, A. Ivanović-Šašić, D. Jovanović, *Russian J. Phys. Chem. A*, 2013, 87, 2260–2263.
- [12] N. Jović-Jovičić, A. Milutinović-Nikolić, M. Žunić, Z. Mojović, P. Banković, I. Gržetić, D. Jovanović, *J. Contam. Hydrol.*, 2013, 150, 1-11.
- [13] A. Milutinović-Nikolić, D. Maksin, N. Jović-Jovičić, M. Mirković, D. Stanković, Z. Mojović, P. Banković, *Appl. Clay Sci.*, 2014, 95, 294-302.

- [14] N. Jović-Jovičić, A. Milutinović-Nikolić, M. Žunić, Z. Mojović, P. Banković, B. Dojčinović, A. Ivanović-Šašić, D. Jovanović, J. Serb. Chem. Soc., 2014, 79, 253–263.
- [15] M. Žunić, A. Milutinović-Nikolić, D. Stanković, D. Manojlović, N. Jović-Jovičić, P. Banković, Z. Mojović, D. Jovanović, Appl. Surf. Sci., 2014, 313, 440–448.
- [16] U. Andjelković, A. Milutinović-Nikolić, N. Jović-Jovičić, P. Banković, T. Bajt, Z. Mojović, Z. Vujčić, D. Jovanović, Food Chem., 2015, 168, 262–269.
- [17] P. Banković, A. Ivanović-Šašić, Z. Mojović, N. Jović-Jovičić, M. Žunić, A. Milutinović-Nikolić, D. Jovanović, Modified Clays in Environmental Protection, in Proceedings of the III Advanced, Ceramics and Applications Conference, Springer Inter. Pub. AG & Atlantis Press, Paris, France, 2015, 221–240.
- [18] S. Marinović, M. Ajduković, N. Jović-Jovičić, P. Banković, Z. Mojović, A. Milutinović-Nikolić, D. Jovanović, Sci. Sint., 2016, 48, 167–176.
- [19] N. Jović-Jovičić, Z. Mojović, M. Darder, P. Aranda, E. Ruiz-Hitzky, P. Banković, D. Jovanović, A. Milutinović-Nikolić, Appl. Clay Sci., 2016, 124–125, 62–68.
- [20] N. Jović-Jovičić, P. Banković, Z. Mojović, B. Nedić-Vasiljević, S. Marinović, T. Mudrinić, A. Milutinović-Nikolić, Sci. Sint., 2017, 49, 419–429.
- [21] N. Jović-Jovičić, Z. Mojović, M. Mojović, P. Banković, M. Ajduković, A. Milutinović-Nikolić, D. Jovanović, Appl. Surf. Sci., 2017, 400, 347–354.
- [22] N. Jović-Jovičić, I. Ilić, S. Marinović, M. Ajduković, T. Mudrinić, Z. Mojović, A. Milutinović-Nikolić, „Tetramethylammonium-smectites as nicotine adsorbents“, Serbian Ceramic Society Conference – ACA VI, September, 18–21, 2017, Belgrade, Serbia pp. 77–78.
- [25] P. Baskaralingam, M. Pulikesi, D. Elango, V. Ramamurthi, S. Sivanesan, J. Hazard. Mater., 2006, 128, 138 – 144.
- [26] G. Lagaly, M. Ogawa, I. Dékány, Handbook of Clay Science, Developments in Clay Science, Elsevier, Amsterdam, 2013.
- [27] H. He, R.L. Frost, T. Bostrom, P. Yuan, L. Duong, D. Yang, Y. Xi, J. T. Kloprogge, Appl. Clay Sci., 2006, 31, 262–271.
- [27] P. Monvisade, P. Siriphannon, Appl. Clay Sci., 2009, 42, 427–431.
- [28] M. Darder, M. Colilla, E. Ruiz-Hitzky, Chem. Mater., 2003, 15, 3774–3780.
- [29] J. Ma, B. Cui, J. Dai, D. Li, J. Hazard. Mater., 2011, 186, 1758–1765.

## SYNTHESIS OF CALCIUM OXIDE BASED CATALYSTS FOR BIODIESEL PRODUCTION

I. Lukić<sup>1\*</sup>, Ž. Kesić<sup>1</sup>, M. Zdujčić<sup>2</sup> and D. Skala<sup>1</sup>

<sup>1</sup> *University of Belgrade, Faculty of Technology and Metallurgy, Karnegijeva 4, 11000 Belgrade, Serbia. (ivanal888@yahoo.co.uk)*

<sup>2</sup> *Institute of Technical Sciences of SASA, KnezMihailova 35, 11000 Belgrade, Serbia.*

### ABSTRACT

In this work, synthesis of several types of calcium oxide based catalysts by mechanochemical treatment and subsequent calcination is presented. Prepared nanocomposite CaO·ZnO, calcium containing perovskites CaTiO<sub>3</sub>, CaMnO<sub>3</sub>, CaZrO<sub>3</sub> and Ca<sub>2</sub>Fe<sub>2</sub>O<sub>5</sub>, a series of CaO·SiO<sub>2</sub> mixed oxides and calcium diglyceroxide (CaDG) were characterized and tested in the methanolysis of sunflower oil under different working conditions: catalyst amount, agitation speed, temperature and methanol to oil molar ratio.

### INTRODUCTION

Biodiesel, a mixture of fatty acid methyl esters (FAME), due to its environmental benefits such as non-toxicity and biodegradability and the fact that it might be synthesized from renewable resources, has gained significant attention as a promising alternative substitute to diesel fuels. Commonly, biodiesel is produced by alcoholysis of different triacylglycerols in the presence of homogeneous or heterogeneous catalysts. Calcium oxide due to the high activity, availability and low cost is one of the most studied heterogeneous catalysts [1]. However, since leaching into the reaction medium was observed for this catalyst, it is important to improve CaO properties by supporting it on different carriers or mixing with other oxides. Mechanochemical synthesis is a simple and waste-free technique for the preparation of different materials, including catalysts.

Milling of CaO and ZnO with water was carried out to obtain calcium zinc hydroxide hydrate (CaZn<sub>2</sub>(OH)<sub>6</sub>·2H<sub>2</sub>O), which was subsequently transformed to CaO·ZnO catalyst by calcination at 700 °C for 3h [2]. Calcium diglyceroxide (Ca(C<sub>3</sub>H<sub>7</sub>O<sub>3</sub>)<sub>2</sub>) was synthesized by mechanochemical treatment of CaO dispersed in glycerol [3]. Calcium-containing perovskites CaTiO<sub>3</sub>, CaMnO<sub>3</sub>, CaZrO<sub>3</sub> and Ca<sub>2</sub>Fe<sub>2</sub>O<sub>5</sub> were synthesized by calcination of mechanochemically treated stoichiometric mixtures of CaCO<sub>3</sub> and either TiO<sub>2</sub>, MnO<sub>2</sub>, ZrO<sub>2</sub> or Fe<sub>2</sub>O<sub>3</sub> powders [4]. Mixtures of CaO and SiO<sub>2</sub> in a molar

ratio in the range of 1 to 3 with addition of water have been mechanochemically treated and calcined to prepare a series of  $\text{CaO}\cdot\text{SiO}_2$  mixed oxides.

## EXPERIMENTAL

Mechanochemical treatment of different starting materials was carried out in the planetary ball mill Fritsch Pulverisette 5, in air atmosphere. The prepared catalysts were characterized by XRD, TGA/DSC, FTIR, SEM/EDX, and base strength using Hammett indicator method. The detailed preparation of catalysts and the used instruments for their characterization are described elsewhere [2-4].

The methanolysis of sunflower was carried out in 300 cm<sup>3</sup> batch autoclave or in a 250 ml three-necked thermostated glass flask with a condenser and magnetic stirrer under different working conditions: catalyst amount, agitation speed, temperature and methanol to oil molar ratio.

## RESULTS AND DISCUSSION

The X-ray diffraction patterns of prepared catalysts are shown in Fig. 1.

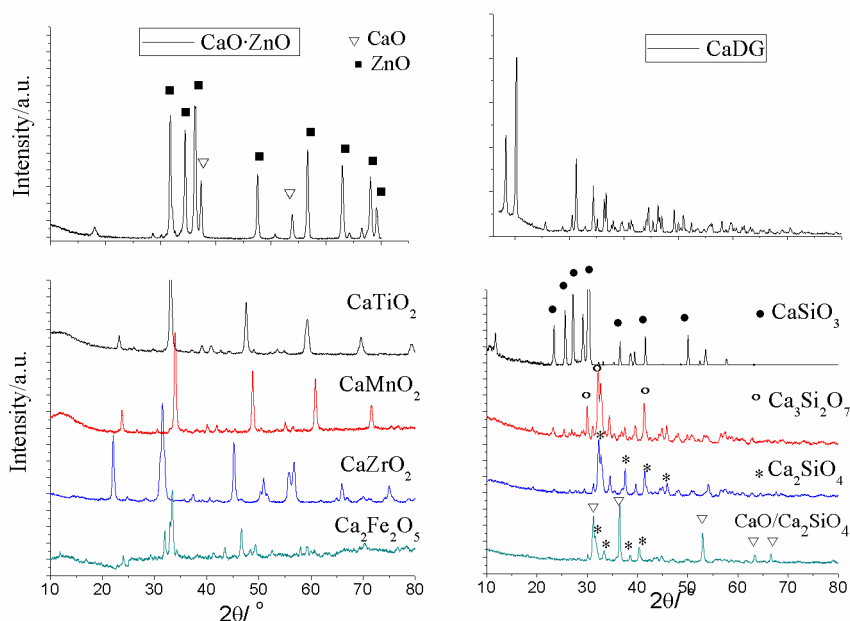


**Figure 1.** XRD patterns of synthesized catalysts

Mechanochemical treatment of  $\text{CaO}$  and  $\text{ZnO}$  powder mixture with water and subsequent calcination led to the formation of fine composite powder composed of  $\text{CaO}$  and  $\text{ZnO}$ . The formation of  $\text{CaDG}$  by mechanochemical

treatment of CaO and glycerol was confirmed with all the peaks well indexed to the calcium diglyceroxide phase  $\text{Ca}(\text{C}_3\text{H}_7\text{O}_3)_2$ . XRD patterns revealed that  $\text{CaTiO}_3$ ,  $\text{CaMnO}_3$ ,  $\text{CaZrO}_3$  and  $\text{Ca}_2\text{Fe}_2\text{O}_5$  perovskites consist dominantly of one phase. Milling of  $\text{CaO} + \text{SiO}_2$  powder mixtures with molar ratio in the range of 1–2 followed by calcination at 900 °C for 48 h, produced single-phase calcium silicate compounds, while starting from the  $3\text{CaO} + \text{SiO}_2$  powder mixture, two phase  $\text{CaO}/\text{Ca}_2\text{SiO}_4$  was obtained.

**Table 1.** Catalytic activity of synthesized catalysts

Catalyst	Starting material and calcination temperature	Basic strength	Reaction conditions <sup>a</sup>	FAME yield, %
$\text{CaO}\cdot\text{ZnO}$	$\text{CaO} + \text{ZnO} + \text{H}_2\text{O}$ $T_{\text{calc}}=700\text{ °C}, 3\text{h}$	$11 < H_- < 18.4$	$T = 60\text{ °C};$ $\text{MR} = 10:1;$ $\text{Cat} = 2\%;$ $t = 4\text{h}$	98.2
$\text{Ca}(\text{C}_3\text{H}_7\text{O}_3)_2$ (CaDG)	$\text{CaO} + \text{Glycerol}$ /	$11 < H_- < 15.0$	$T = 60\text{ °C};$ $\text{MR} = 10:1;$ $\text{Cat} = 0.5\%;$ $t = 2\text{h}$	97.9
$\text{CaTiO}_3$	$\text{CaCO}_3 + \text{TiO}_2$	$6.8 < H_- < 9.3$		0.1
$\text{CaZrO}_3$	$\text{CaCO}_3 + \text{ZrO}_2$	$6.8 < H_- < 9.3$	$T = 60\text{ °C};$	0.0
$\text{CaMnO}_3$	$\text{CaCO}_3 + \text{MnO}_2$	$6.8 < H_- < 9.3$	$\text{MR} = 6:1;$	0.0
$\text{Ca}_2\text{Fe}_2\text{O}_5$	$\text{CaCO}_3 + \text{Fe}_2\text{O}_3$ $T_{\text{calc}}=700\text{ °C}; 24$	$6.8 < H_- < 9.3$	$\text{Cat} = 10\%;$ $t = 10\text{h}$	0.0
<sup>b</sup> $\text{CaO}/\text{CaTiO}_3$	<sup>b</sup> $\text{CaCO}_3 + \text{TiO}_2$ $T_{\text{calc}}=1050\text{ °C}, 2\text{ h}$	<sup>b</sup> $9.3 < H_- < 10$		<sup>b</sup> 98.1
$\text{CaSiO}_3$	$\text{CaO} + \text{SiO}_2$	$H_- < 9.3$	$T = 60\text{ °C};$	0.31
$\text{Ca}_3\text{Si}_2\text{O}_7$	$3\text{CaO} + 2\text{SiO}_2$	$H_- < 9.3$	$\text{MR} = 10:1;$	0.52
$\text{Ca}_2\text{SiO}_4$	$2\text{CaO} + \text{SiO}_2$	$H_- < 9.3$	$\text{Cat} = 2\%;$	0.81
$\text{CaO}/\text{Ca}_2\text{SiO}_4$	$3\text{CaO} + \text{SiO}_2$ $T_{\text{calc}} = 900\text{ °C}, 48\text{h}$	$11 < H_- < 15$	$t = 5\text{h}$	96.03

<sup>a</sup> $T$  = temperature; MR = molar ratio methanol to oil; Cat = catalyst loading;  $t$  = time.

<sup>b</sup>Mixed using agate mortar and pestle (but without subsequent mechanochemical treatment)

The results of catalytic activity of the prepared catalysts in methanolysis of sunflower oil, along with their basic strength ( $H_-$ ), reaction conditions, and preparation procedure are given in Table 1.

The high FAME yields were achieved when CaO·ZnO and CaDG were used as catalysts, as well as two-phase samples containing CaO, while pure perovskites and calcium silicates showed no activity in methanolysis at 60 °C. High catalytic activity of prepared catalysts is related to high basic strength, which is considered as one of the most significant factor that affects the activity of different catalysts for biodiesel production. With the exception of CaDG, which has different structure, in all other cases the high basicity of samples, accompanied with their high catalytic activities, arises from the existence of CaO phase. The perovskites possess different structure compared to the rock salt structure of CaO and from that reason they are not active in transesterification of sunflower oil at lower temperature.

## CONCLUSION

Mechanochemical treatment was successfully used for the synthesis of various CaO based heterogeneous catalysts. Prepared CaO·ZnO and CaDG showed a high catalytic activity in methanolysis of sunflower oil at 60 °C resulting in FAME yield over 96%. Under these conditions, pure perovskites (CaTiO<sub>3</sub>, MnO<sub>3</sub>, CaZrO<sub>3</sub> and Ca<sub>2</sub>Fe<sub>2</sub>O<sub>5</sub>) and pure calcium silicates (CaSiO<sub>3</sub>, Ca<sub>3</sub>Si<sub>2</sub>O<sub>7</sub> and Ca<sub>2</sub>SiO<sub>4</sub>) phases exhibited no catalytic activity, while two-phase samples containing CaO (CaTiO<sub>3</sub>/CaO and Ca<sub>2</sub>SiO<sub>4</sub>/CaO) were active.

## Acknowledgement

This work was financially supported by the Ministry of Education, Science and Technological Development of the Republic of Serbia (III 45001).

## REFERENCES

- [1] Ž. Kesić, I. Lukić, M. Zdujić, Lj. Mojović, D. Skala, *Chemical Industry and Chemical Engineering Quarterly*, 2016, 22, 391–408.
- [2] Ž. Kesić, I. Lukić, D. Brkić, J. Rogan, M. Zdujić, H. Liu, D. Skala, *Applied Catalysis A: General*, 2012, 427–428, 58–65.
- [3] I. Lukić, Ž. Kesić, M. Zdujić, D. Skala, *Fuel*, 2016, 165, 159–165.
- [4] Ž. Kesić, I. Lukić, M. Zdujić, Č. Jovalekić, V. Veljković, D. Skala, *Fuel Processing Technology*, 2016, 143, 162–168.

## GOLD SUPPORTED ON NiAl LAYERED DOUBLE HYDROXIDE CATALYSTS FOR WATER-GAS SHIFT REACTION

M. Gabrovska<sup>1</sup>, T. Tabakova<sup>1</sup>, I. Ivanov<sup>1</sup>, D. Kovacheva<sup>2</sup> and V. Idakiev<sup>1</sup>

<sup>1</sup> *Institute of Catalysis, Bulgarian Academy of Sciences, Acad. G. Bonchev St., Bldg. 11, 1113 Sofia, Bulgaria (margarita.gabrovska@abv.bg)*

<sup>2</sup> *Institute of General and Inorganic Chemistry, Bulgarian Academy of Sciences, Acad. G. Bonchev St., Bldg. 11, 1113 Sofia, Bulgaria*

### ABSTRACT

Two series of catalyst precursors for CO conversion with water vapor (water-gas shift reaction) were synthesized. The first one involves co-precipitated NiAl layered double hydroxides with Ni<sup>2+</sup>/Al<sup>3+</sup> molar ratios of 1.5, 2.5 and 4.0. The second series includes Au deposited over the prepared NiAl layered systems. It was established that the catalytic activity was affected by Ni<sup>2+</sup>/Al<sup>3+</sup> molar ratio as well as in the presence of Au. Probable scheme is proposed about reaction mechanism, comprising redox Ni<sup>2+</sup> ↔ Ni<sup>3+</sup> transition on the catalyst surface and CO activation on Au nanoparticles.

### INTRODUCTION

The conversion of CO by water vapor, named water-gas shift reaction (WGSR, CO + H<sub>2</sub>O ↔ CO<sub>2</sub> + H<sub>2</sub>, ΔH<sub>300°C</sub> = -41.2 kJ/mol) is one of the economic routes traditionally used for CO reduction in the synthesis gas and production of pure hydrogen which is further used for fuel cell applications, ammonia synthesis, and selective hydrogenation processes [1]. It was reported in our earlier papers that the nickel hydroxides [2] and co-precipitated NiAl layered double hydroxides (LDHs), promoted either by addition of magnesium [3] or potassium [4] are active in the WGSR.

NiAl LDHs, also referred to as takovite-like (TKl) compounds, according to the name of mineral takovite, Ni<sub>6</sub>Al<sub>2</sub>(OH)<sub>16</sub>CO<sub>3</sub>·4H<sub>2</sub>O [5] are lamellar nanostructured materials which belong to a large group of natural or synthetic inorganic layered compounds. The structure consists of consequent positively charged brucite-like NiAl hydroxide sheets [Ni<sup>2+</sup><sub>1-x</sub>Al<sup>3+</sup><sub>x</sub>(OH)<sub>2</sub>]<sup>x+</sup> and interlayers [A<sup>n-</sup><sub>x/n</sub>·mH<sub>2</sub>O], containing charge compensating exchangeable anions (A = NO<sub>3</sub><sup>-</sup>, SO<sub>4</sub><sup>2-</sup>, CO<sub>3</sub><sup>2-</sup>, Cl<sup>-</sup>, etc.) and *m* molecules of water. Here, *x* represents the fraction of the Al<sup>3+</sup> ion. The lamellar structure supposes uniform distribution of the octahedrally coordinated Ni<sup>2+</sup> and Al<sup>3+</sup> cations in the hydroxide layer [5, 6].

In recent years, Au-based catalysts have received extended attention since they show very high activity at low temperatures and potential stability in oxidizing atmospheres [7].

The aim of this paper is to describe new data related to the investigation of the NiAl LDHs with different molar ratios as catalyst precursors for WGS. On the base of the mentioned considerations, in the present study, NiAl LDHs are used as supports for Au deposition, aiming to improve the catalyst activity. The role of  $\text{Ni}^{2+}/\text{Al}^{3+}$  molar ratio and the presence of gold on the WGS performance was examined.

## EXPERIMENTAL

The carbonate forms of TKI precursors with  $\text{Ni}^{2+}/\text{Al}^{3+}$  molar ratios of 1.5, 2.5 and 4.0 were obtained by co-precipitation at constant  $\text{pH} = 8$  and temperature of  $80\text{ }^\circ\text{C}$  under vigorous stirring, using ‘*pro analyze*’ purity grade nitrate salts of the corresponding metals,  $\text{Ni}(\text{NO}_3)_2 \cdot 6\text{H}_2\text{O}$  and  $\text{Al}(\text{NO}_3)_3 \cdot 9\text{H}_2\text{O}$ , and  $\text{Na}_2\text{CO}_3$  as precipitating agent. Gold (3 wt. %) was deposited by deposition–precipitation method on a NiAl supports preliminary suspended in water. All synthesized samples were dried at  $80\text{ }^\circ\text{C}$  for 20 h and designated as  $y\text{-NiAl}_z$ , where  $z$  represents  $\text{Ni}^{2+}/\text{Al}^{3+}$  molar ratio and  $y$  denotes Au. The spent catalysts were marked as  $y\text{-NiAl}_z\text{-s}$ . The phase composition of the as-synthesized and spent samples was established by powder X-ray diffraction (PXRD) technique. The data was collected on a Bruker D8 Advance powder diffractometer employing  $\text{CuK}\alpha$  radiation, operating at  $U = 40\text{ kV}$  and  $I = 40\text{ mA}$ . The WGS catalytic activity was measured in a flow reactor at atmospheric pressure by step-wise increase of the reaction temperature under the following conditions:  $0.5\text{ cm}^3$  catalyst bed volume with  $0.63\text{--}0.80\text{ mm}$  pellets, GHSV of  $4000\text{ h}^{-1}$  and reactant gas mixture 3.76 vol. % CO, 25.01 vol. %  $\text{H}_2\text{O}$  and 71.23 vol. % Ar. The detailed analysis after achieved stationary CO conversion (at every  $20\text{ }^\circ\text{C}$  step) at the reactor outlet was performed on an ‘‘URAS-3G’’ (Hartmann and Braun AG) gas analyzer. The catalytic activity was expressed by the degree of CO conversion.

## RESULTS AND DISCUSSION

PXRD patterns of the as-synthesized NiAl samples (Fig. 1A) point to the reflections typical of the takovite-type structure (ICDD-PDF file 00-015-0087) containing carbonate anions in the interlayer space, better organized in  $\text{NiAl}_{2.5}$ . All solids display sharp and symmetrical reflections for (003), (006), (110) and (113) planes and broad and asymmetric for (012), (015), and (018), respectively. The doublet corresponding to the (110) and (113) planes is well resolved for  $\text{NiAl}_{2.5}$  sample, suggesting a better ordering of the cations in the layers [8].

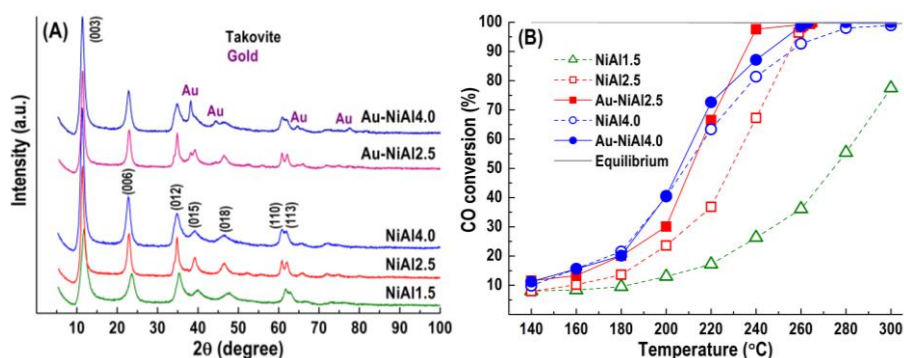


**Figure 1.** PXR patterns (A) and WGS activity (B) of all samples

The change of  $\text{Ni}^{2+}/\text{Al}^{3+}$  molar ratio results in lowering of the peak intensities and broadening of the TKI reflections for NiAl1.5 and NiAl4.0 samples. This finding confirms the statement that single stoichiometric TKI structure can exist only for a narrow range of  $\text{Ni}^{2+}/\text{Al}^{3+} = 2\text{--}3$  [6]. The increase of Ni loading in the NiAl systems induces rising in CO conversion degree (Fig. 1B). It is clearly seen that NiAl1.5 catalyst exhibits relatively low CO removal. PXR analysis of the spent catalysts (Fig. 2) discloses not well crystallized NiO phase (ICDD-PDF file 00-015-0087) with mean size 3.3–3.7 nm, being better formed in NiAl2.5-s. The lines' broadening is a consequence of  $\text{Al}^{3+}$  ions incorporation into the cubic framework of NiO. The deposition of Au on both active NiAl2.5 and NiAl4.0 catalysts prompts appearance of TKI reflections along with additional diffraction lines of Au phase (ICDD-PDF file 00-004-0784), better organized in Au-NiAl4.0 (Fig. 1A). It is visible that the Au presence provokes partial amorphization of the TKI phase. Moreover, the performance of Au-supported catalysts is improved noticeable (Fig. 1B). A more significant difference in the WGS activity is observed in the range 220–260 °C, sharply emphasized by Au-NiAl2.5 catalyst. The promoting role of Au in Au-NiAl2.5 is clearly demonstrated by reaching the equilibrium conversion value of 97.6 % at 240 °C. PXR patterns of spent Au-containing catalysts (Fig. 2) reveal reflections of ill crystallized NiO accompanied by an Au phase. The latter phase is highly dispersed in Au-NiAl2.5-s. A possible explanation of the observed WGS behavior is based on the

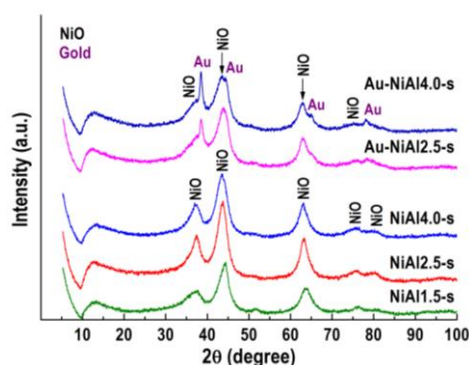


**Figure 2.** PXR patterns of the spent catalysts

supposition that under the influence of the reaction media and temperature TKI structure collapses with formation of poorly organized NiO phase. The presence of a large amount of water vapor causes partial hydroxylation of NiO surface leading to formation of nickel hydroxide phases Ni(OH)<sub>2</sub> and NiOOH, containing Ni<sup>2+</sup> and Ni<sup>3+</sup> ions, respectively. Participation of these phases in redox WGS is associated with occurrence of a reversible redox transition between the active nickel species (Ni<sup>2+</sup> ↔ Ni<sup>3+</sup>) [4]. It is worth noting that the presence of Au is favorable for formation of a specific working composition on the catalyst surface and CO activation.

### CONCLUSION

It can be deduced from results obtained in this study that the WGS activity is strongly affected by the Ni/Al molar ratio and the presence of Au, and is related to the availability of optimal Ni<sup>2+</sup>/Ni<sup>3+</sup> ratio. The effect of supported Au is more significant in catalyst with lower Ni loading (Au-NiAl<sub>2.5</sub>), thus permits obtaining and using of promising and cost-effective catalyst for medium temperature WGS.

### Acknowledgement

The authors T.T., I.I. and V. I. gratefully acknowledge financial support by the Bulgarian Science Fund (Contract ДН 09/5/2016)

### REFERENCES

- [1] F. Tao and Z. Ma, Phys. Chem. Chem. Phys., 2013, 15, 15260-15270.
- [2] A. Andreev, V. Idakiev, K. Kostov, M. Gabrovska, Catal. Lett., 1995, 31, 245-252.
- [3] M. Gabrovska, R. Edreva-Kardjieva, V. Idakiev, B. Kunev, Bulg. Chem. Commun., 2002, 34, 395-404.
- [4] M. Gabrovska, V. Idakiev, K. Tenchev, D. Nikolova, R. Edreva-Kardjieva, D. Crisan, Russ. J. Phys. Chem. A, 2013, 87, 2152-2159.
- [5] D. Bish and G. Brindley, Am. Mineral., 1977, 62, 458-464.
- [6] F. Cavani, F. Trifirò, A. Vaccari, Catal. Today, 1991, 11, 173-301.
- [7] T. R. Reina, M. González Castaño, S. Palma, S. Ivanova, J. A. Odriozola in: Heterogeneous Gold Catalysts and Catalysis, vol. 18, Z. Ma, Sh. Dai (Eds.), Royal Society of Chemistry, Cambridge, 2014.
- [8] P. Benito, F. Labajos, V. Rives, J. Solid State Chem., 2006, 179, 3784-3797.

## SYNTHESIS OF BINARY Ni-Mg-O OXIDE SYSTEM AND STUDY ON ITS BEHAVIOR IN REDUCTION-OXIDATION CYCLES

T. M. Karnaukhov<sup>1,2</sup>, A. A. Vedyagin<sup>1,3</sup>, S. V. Cherepanova<sup>1,2</sup>,  
V. A. Rogov<sup>1,2</sup> and I. V. Mishakov<sup>1,3</sup>

<sup>1</sup>*Boriskov Institute of Catalysis SB RAS, pr. Ac. Lavrentieva 5,  
630090 Novosibirsk, Russian Federation. (timofey941@yandex.ru)*

<sup>2</sup>*National Research Novosibirsk State University, Pirogova str. 1,  
630090 Novosibirsk, Russian Federation.*

<sup>3</sup>*National Research Tomsk Polytechnic University, Lenin Av. 30,  
634050 Tomsk, Russian Federation.*

### ABSTRACT

In the present work, the binary Ni-Mg-O oxide system was prepared by means of a sol-gel technique, which provides high dispersity and uniform distribution of the nickel species within the MgO matrix. It was found that during the preparation procedure, a partial substitution of Mg<sup>2+</sup> ions with Ni<sup>2+</sup> ions resulting in formation of solid solution takes place. Reduction of the as-prepared sample in a temperature-programmed regime with heating up to 700 °C leads to decomposition of the solid solution and formation of dispersed particles of metallic nickel of 7 nm in size finely distributed within the MgO matrix. Subsequent oxidation transforms the Ni<sup>0</sup> into NiO nanoparticles. Starting from the second reduction/oxidation cycle, Ni-Mg-O system shows the reproducible behavior, and thus can be considered as a chemical looping agent.

### INTRODUCTION

Nickel oxide attracts a great attention to be applied as a component of the catalysts, sensors, batteries, etc. [1, 2]. On the other hand, NiO-based systems can be considered as an oxygen storage material. Such materials are able to allot oxygen in a reductive medium and thus can be used in the chemical looping processes [3]. Thereby, the study on the reduction behavior of the NiO-based systems is quite important and actual.

On the other hand, NiO is known to interact strongly with MgO. The values of ionic radius for Ni<sup>2+</sup> and Mg<sup>2+</sup> are practically coincided (0.078 Å), which leads to the formation of solid solutions of substitution. Reduction of such joint phases is complicated if compared with pristine NiO. As an example, addition of 1-2 wt.% MgO to alumina-supported NiO (10 wt.%)

significantly increases the activation energy of the NiO reduction with hydrogen and shifts the reduction temperature range to higher temperatures (on about 400 °C) [4]. An enlargement of the MgO-NiO ratio in the two-component oxide system rises the degree of nickel cations bonding within MgO matrix [5]. All this is reflected in the corresponding reduction profiles: the hydrogen consumption peaks are getting broader and become shifted towards elevated temperatures. The value of the relative reduction degree is also diminished with an increase of the MgO-NiO ratio.

Taking into account all mentioned above, binary Ni-Mg-O system looks very promising to be used as a main chemical looping component. The present work continues the series of research papers devoted to the study of the MgO-based binary systems derived via a sol-gel technique [6].

## EXPERIMENTAL

A two-component Ni-Mg-O oxide system was prepared by means of a sol-gel technique as described elsewhere [7]. The nickel loading was 15 wt.% in regard to NiO. Pure nickel oxide used as a reference sample was obtained by decomposition of nickel (II) nitrate hexahydrate at step-by-step heating up to 500 °C.

The prepared samples were characterized by a low-temperature nitrogen adsorption using ASAP-2400 (Micrometrics, USA) and Digisorb-2600 instruments (Quantochrome, USA). The texture of the Ni-Mg-O samples was studied using a JSM-6460 (Jeol, Japan) scanning electron microscope. Powder X-ray diffraction (XRD) analysis of the samples was performed in an in situ regime under reductive and oxidative atmospheres using a diffractometer D8 (Bruker, Germany). The reduction behavior of the Ni-Mg-O oxide system was studied as described elsewhere [6].

## RESULTS AND DISCUSSION

According to the scanning electron microscopy, the sample is represented by the chaotically adherent agglomerates of the nanocrystalline particles. Low-temperature nitrogen adsorption has shown that an introduction of NiO into MgO matrix diminishes the value of specific surface area from 243 m<sup>2</sup>/g for pure MgO to 154 m<sup>2</sup>/g for the Ni-Mg-O sample. The average pore diameter changes correspondingly from 61 to 189 Å.

Fig. 1A shows the TPR profiles for the binary oxide sample along with a reference sample – bulk NiO prepared via calcination of the same precursor. In the case of bulk NiO, the reduction process goes through one stage with a maximum at 380 °C, which corresponds to a phase transition of NiO to metallic Ni. In contrast, reduction of the binary Ni-Mg-O system, when NiO species are considered to be uniformly distributed within the MgO matrix,

gives more complicated picture. There are three hydrogen uptake peaks which can be assigned to reduction of the surface NiO species having weak interaction with MgO (200–350 °C), reduction of the similar NiO species distributed in the bulk of MgO matrix (370–500 °C), and reduction of strongly bonded nickel species formed due to substitution of  $\text{Mg}^{2+}$  ions with  $\text{Ni}^{2+}$  ions (500–890 °C).

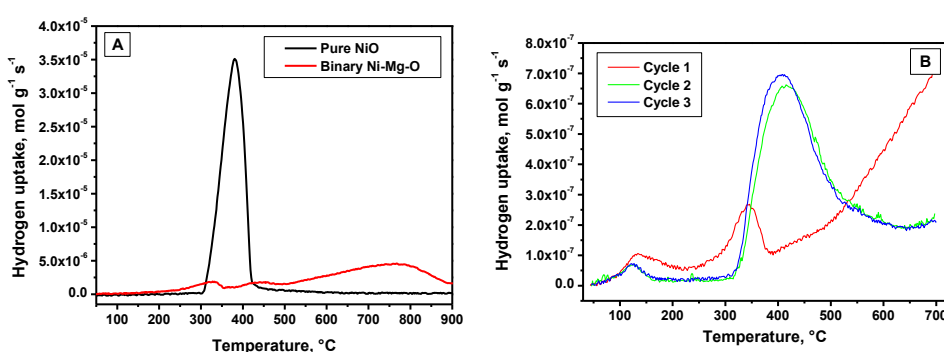


**Figure 1.** TPR profiles for the Ni-Mg-O sample and pure nickel oxide (A), and for Ni-Mg-O sample in consecutive oxidation/reduction cycles (B).

The results of reduction/oxidation cycling are presented in Fig. 1B. The TPR profiles for the first and subsequent cycles are noticeably different. In the first cycle, reduction of the NiO proceeds through three stages described above. Starting from the second cycles, only two hydrogen uptake peaks are well seen. In order to elucidate the possible changes of the phase composition, the sample was studied by an in situ X-ray diffraction analysis.

**Table 1.** Quantitative results of an in situ XRD analysis.

Phase (content)	Initial		Reduced		Oxidized	
	a, Å	$D_{av}$ , nm	a, Å	$D_{av}$ , nm	a, Å	$D_{av}$ , nm
MgO	4.221(1)	7	4.217(1)	12	4.215(1)	13
Ni (10 %)	-	-	3.522(2)	7	-	-

As it follows from the obtained results (Table 1), high temperature treatment leads to an enlargement and crystallization of the MgO particles. The lattice spacing progressively decreases approaching to the reference value for MgO crystals (4.211 Å). The differences in the reduction behavior in the first and consecutive TPR cycles can be explained by the different strength of interaction between NiO and MgO. During the first reduction

cycle nickel species strongly bonded with the MgO matrix undergo reduction at temperatures near 700 °C, which results in formation of metallic Ni of 7 nm in size. The subsequent oxidation of the dispersed metallic particles leads to formation of NiO nanoparticles only.

## CONCLUSION

A sol-gel approach was applied to prepare the binary Ni-Mg-O oxide system. Nickel oxide species were shown to be uniformly distributed within the MgO matrix. Partial substitution of Mg<sup>2+</sup> ions with Ni<sup>2+</sup> ions takes place at the used preparation conditions. All this significantly affects the reducibility of nickel oxide. At least three types of nickel species were found to be present in the binary oxide sample: weakly bonded surface NiO nanoparticles; weakly bonded NiO nanoparticles uniformly distributed within the MgO matrix; strongly bonded nickel species formed via the substitution of Mg<sup>2+</sup> ions with Ni<sup>2+</sup> ions. Heating the Ni-Mg-O sample up to 700 °C in a reducing medium (hydrogen flow) results in decomposition of the NiO-MgO solid solution with formation of metallic Ni nanoparticles of 7 nm distributed in the bulk of MgO. The following oxidation/reduction cycles are reproducible and the main hydrogen uptake takes place within the temperature interval of 350-550 °C.

## Acknowledgement

The present work was performed within Government Order for BIC (Projects no. AAAA-A17-117041710086-6 and AAAA-A17-117041710079-8).

## REFERENCES

- [1] M. Tadic, M. Panjan, D. Markovic, *Mat. Lett.*, 2010, **64**, 2129–2131.
- [2] M. Zare, M. Ketabchi, *J. Therm. Anal. Calorim.*, 2017, **127**, 2113–2123.
- [3] J. Adanez, A. Abad, F. Garcia-Labiano, P. Gayan, L. F. de Diego, *Prog. Energ. Combust. Sci.*, 2012, **38**, 215–282.
- [4] J. T. Richardson, R. M. Scates, M. V. Twigg, *Appl. Catal. A-Gen.*, 2004, **267**, 35–46.
- [5] Y. Wang, X. Yang, Y. Wang, *Int. J. Hydrogen Energ.*, 2016, **41**, 17846–17857.
- [6] T. M. Karnaukhov, A. A. Vedyagin, S. V. Cherepanova, V. A. Rogov, V. O. Stoyanovskii, I. V. Mishakov, *Int. J. Hydrogen Energ.*, 2017, **42**, 30543–30549.
- [7] A. A. Vedyagin, I. V. Mishakov, T. M. Karnaukhov, E. F. Krivoshapkina, E. V. Ilyina, T. A. Maksimova, S. V. Cherepanova, P. V. Krivoshapkin, *J. Sol-Gel Sci. Technol.*, 2017, **82**, 611–619.

## SYNTHESIS OF Ag-MODIFIED ADSORPTIVE-CATALYTIC SYSTEMS BASED ON ZSM-5 AND $\gamma$ -Al<sub>2</sub>O<sub>3</sub> AND THEIR STUDY UNDER “COLD START” CONDITIONS

V. L. Temerev<sup>1</sup>, A. A. Vedyagin<sup>2</sup>, K. N. Iost<sup>1</sup>, L. V. Pirutko<sup>2</sup>,  
E. V. Starokon<sup>2</sup>, Y. V. Shubin<sup>3</sup>, P. E. Plyusnin<sup>3</sup>, S. V. Cherepanova<sup>2</sup>,  
A. M. Volodin<sup>2</sup>, R. M. Kenzhin<sup>2</sup>, V. O. Stoyanovskii<sup>2</sup> and D. A. Shlyapin<sup>1</sup>

<sup>1</sup> *Institute of Hydrocarbons Processing SB RAS, Neftezhavodskaya Str. 54, 644040 Omsk, Russian Federation. (tv1@ihcp.ru)*

<sup>2</sup> *Boreskov Institute of Catalysis SB RAS, pr. Ac. Lavrentieva 5, 630090 Novosibirsk, Russian Federation.*

<sup>3</sup> *Nikolaev Institute of Inorganic Chemistry SB RAS, pr. Ac. Lavrentieva 3, 630090 Novosibirsk, Russian Federation.*

### ABSTRACT

In the present work, adsorptive-catalytic properties of the system based on ZSM-5 zeolite and  $\gamma$ -Al<sub>2</sub>O<sub>3</sub> as a binder were studied. Such system is considered to be used as adsorption trap within vehicle exhaust gas neutralization concept in order to solve so-called “cold start” problem. In aim to study modifying effect of silver on the properties of zeolite, such compositions as Ag/ZSM-5+ $\gamma$ -Al<sub>2</sub>O<sub>3</sub> and HZSM-5+Ag/ $\gamma$ -Al<sub>2</sub>O<sub>3</sub> were prepared. The silver loading was 10 wt.%. The samples were tested in a prompt thermal aging regime. The composition of the reaction mixture was varied to elucidate the effects of CO and hydrocarbons on the state of the active sites.

### INTRODUCTION

Nowadays, the requirements for residual content of contaminants after onboard neutralizing systems become more and more stringent. In these terms, three-way catalysts are quite effective in elimination of the contaminants from the gasoline vehicle exhaust gases. However, the most of the developed catalysts are characterized with light-off temperatures above 200 °C. Since the temperature of exhaust gases and, correspondingly, catalytic brick is significantly lower during the engine start, it faces so-called “cold start” problem [1]. One of the approaches being developed to solve this problem is installation of an additional adsorptive-catalytic block. Usually, the adsorption function in such systems is played by zeolites, which serve as a trap catching the pollutants and keeping them until the temperature of the

gases is enough to implement the catalytic neutralization stage [2]. Then, desorbed molecules go through the catalytic brick where they undergo oxidation.

There is a lot of information reported in the literature concerning the adsorption systems based on the zeolites. Among such systems, silver-modified zeolites attract a special interest [3]. Silver ions  $\text{Ag}^+$  in the modified zeolite are known to form  $\pi$ -complex with unsaturated hydrocarbons, thus making it possible to trap them until high temperatures (200 °C and above) [4].

On the other hand, it is well known that silver-containing systems are active in oxidation of CO and hydrocarbons [5]. At the same time, effects of unsaturated hydrocarbons on the catalytic performance are not well studied.

In the present work, silver was supported on both the alumina and zeolite supports. Studies on adsorption and catalytic performance were carried out in a prompt thermal aging regime [6, 7]. In general, reaction mixture contains such pollutants as hydrocarbons, CO and nitrogen oxide. In order to elucidate the effect of the exact components, hydrocarbons or CO were excluded from the mixture.

## EXPERIMENTAL

The  $\text{Ag/ZSM-5}+\gamma\text{-Al}_2\text{O}_3$  sample was prepared as follows. Silver-modified zeolite was obtained via ion exchange of ZSM-5 ( $\text{SiO}_2/\text{Al}_2\text{O}_3 = 23$ ) in H-form using solution of  $\text{AgNO}_3$  followed by drying at 120 °C for 2 h and calcination at 350 °C for 4 h. Then, the sample was milled in a mortar together with a powder of  $\gamma\text{-Al}_2\text{O}_3$ , tableted and crashed to obtain a fraction of 0.25-0.5 mm in size. The reverse  $\text{HZSM-5}+\text{Ag}/\gamma\text{-Al}_2\text{O}_3$  sample was prepared by an incipient wetness impregnation of the alumina support with aqueous solution of  $\text{AgNO}_3$  followed by drying at 105 °C for 2 h and calcination at 350 °C for 2 h. Then, the resulted powder was mixed with HZSM-5 and granulated as described above.

The prepared samples were characterized by a set of physicochemical methods: X-ray diffraction analysis; a low-temperature nitrogen adsorption; transmission electron microscopy, etc.

Adsorptive-catalytic performance of the samples was examined as described elsewhere [6, 7]. The sample (300 mg) was loaded into the quartz reactor. The reaction gas mixture contains 0.15 vol.% of CO, 0.01 vol.% of hydrocarbons (methane, propylene and toluene), 0.015 vol.% of nitrogen oxide (NO), 14 vol.% of oxygen, and nitrogen as a balance. The gas flow rate was 300 ml/min that corresponds to GHSV of 180000  $\text{h}^{-1}$ . In some experiments, hydrocarbons or CO were excluded from the reaction mixture.

Concentration of the components was monitored by on-line gas analyzers. Each experiment considers 7 heating-cooling cycles with varied values of the final temperature: 1, 2 – up to 320 °C; 3, 4 – up to 600 °C; 5, 6 – up to 800 °C; 7 – up to 400 °C. A temperature ramping rate in all the cases was 10 °C/min.

## RESULTS AND DISCUSSION

As it follows from the results presented in Fig. 1, the Ag/ZSM-5+ $\gamma$ -Al<sub>2</sub>O<sub>3</sub> sample is quite active in CO oxidation without hydrocarbons (curve 3) showing light-off temperature near 250 °C. Its activity does not change noticeably even after heating up to 800 °C. Contrary, addition of hydrocarbons into the reaction gas mixture results in a rapid deactivation of the catalytic sites active in CO oxidation (curves 4 and 5). The reverse HZSM-5+Ag/ $\gamma$ -Al<sub>2</sub>O<sub>3</sub> sample, when silver was deposited on alumina, demonstrates similar catalytic activity regardless to reaction conditions (curves 1 and 2). In this case, heating the catalyst up to 800 °C does not have any negative effects.

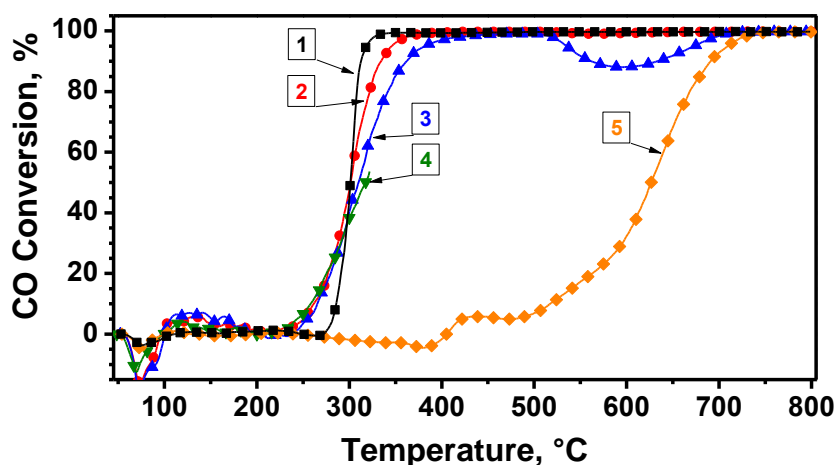


**Figure 1.** Light-off curves of CO conversion in a prompt thermal aging regime: **1** - [HZSM-5+Ag/ $\gamma$ -Al<sub>2</sub>O<sub>3</sub>], 6<sup>th</sup> cycle, complete reaction mixture; **2** - [HZSM-5+Ag/ $\gamma$ -Al<sub>2</sub>O<sub>3</sub>]; 6<sup>th</sup> cycle, without HCs; **3** - [Ag/ZSM-5+ $\gamma$ -Al<sub>2</sub>O<sub>3</sub>], 6<sup>th</sup> cycle, without HCs; **4** and **5** - [Ag/ZSM-5+ $\gamma$ -Al<sub>2</sub>O<sub>3</sub>], 4<sup>th</sup> and 6<sup>th</sup> cycles, complete reaction mixture.

It was already mentioned that ion-exchanged silver (Ag<sup>+</sup>) located within zeolite structure forms  $\pi$ -complex with unsaturated hydrocarbons, thus weakening their intermolecular interactions [4]. All this enhances their reaction ability, including oxidation processes. It is suggested that the

interaction between zeolite and silver ions participating in formation of  $\pi$ -complex with hydrocarbons becomes weaker as well, that facilitates an enlargement of the silver species into particles by coalescence or via Ostwald mechanism.

## CONCLUSION

Thereby, it can be concluded that silver-containing active sites of the zeolites, which are active in oxidation of CO, despite the tolerance towards elevated temperatures, undergo significant transformations in a presence of unsaturated hydrocarbons. The mechanism of their deactivation is not evident, and, most probably, it is connected with an increase in silver species mobility and a breakage of the silver bonding with zeolite during the decomposition of its  $\pi$ -complex with hydrocarbons on the stage of oxidative desorption. The latter was indirectly confirmed by a significant decrease of silver dispersity for the Ag/ZSM-5+ $\gamma$ -Al<sub>2</sub>O<sub>3</sub> samples being in contact with hydrocarbons.

## Acknowledgement

The present work was performed within Government Order for BIC (Project no. AAAA-A17-117041710086-6).

## REFERENCES

- [1] H. Chang, H. Chen, K. Koo, J. Rieck, P. Blakeman, SAE Int. J. Fuels Lubr., 2014, 7(2), 480-488.
- [2] A. Westermann, B. Azambre, G. Fingueneisel, P. Da Costa, F. Can, Appl. Catal. B-Environ., 2014, 158–159, 48-59.
- [3] V. L. Temerev, A. A. Vedyagin, T. N. Afonassenko, K. N. Iost, Y. S. Kotolevich, V. P. Baltakhinov, P. G. Tsyurul'nikov, Reac. Kinet. Mech. Catal., 2016, 119, 629-640.
- [4] X. Liu, J. K. Lampert, D. A. Arendarskii, R. J. Farrauto, Appl. Catal. B-Environ., 2001, 35, 125-136.
- [5] V. Ulrich, B. Moroz, I. Sinev, P. Pyriaev, V. Bukhtiyarov, W. Grünert, Appl. Catal. B-Environ., 2017, 203, 572-581.
- [6] A. A. Vedyagin, A. M. Volodin, V. O. Stoyanovskii, R. M. Kenzhin, P. E. Plyusnin, Y. V. Shubin, I. V. Mishakov, Top. Catal., 2017, 60, 152-161.
- [7] A. A. Vedyagin, A. M. Volodin, R. M. Kenzhin, V. O. Stoyanovskii, Y. V. Shubin, P. E. Plyusnin, I. V. Mishakov, Catal. Today, 2017, 293–294, 73-81.

## EFFECT OF THE CARBON SUPPORT GRAPHITIZATION ON THE THERMAL STABILITY AND ACTIVITY OF THE Ru-Ba-Cs/C CATALYST

K. N. Iost, V. A. Borisov, V. L. Temerev, Yu. V. Surovikin,  
M. V. Trenikhin, A. B. Arbuzov, D. A. Shlyapin and P. G. Tsyrlunikov

*Institute of Hydrocarbons Processing SB RAS, Neftzavodskaya st. 54,  
Omsk 644040, Russian Federation. (iost.k.n@mail.ru)*

### ABSTRACT

Carbon-supported ruthenium catalysts modified with barium and cesium were prepared and studied. In order to minimize the methanation process (hydrogenation of the carbon), carbonaceous composite material Sibunit used as a support in the present work was additionally subjected to the graphitization procedure at 1900 °C. This treatment affects significantly properties of the support decreasing its specific surface area from 320 to 46 m<sup>2</sup>/g. According to the X-ray diffraction data, an increase of both the thickness and the number of graphene layers in the packet (from 11 to 26) takes place. Raman spectroscopy has shown an appearance of the line at 1617 cm<sup>-1</sup>, which testifies towards graphite formation. The dispersity of ruthenium particles was close in both the cases (average particle size of about 10 nm). At the same time, the activity of the sample based on the graphitized support was in 1.6 times lower if compare with initial support, while the thermal stability was better.

### INTRODUCTION

Carbon-supported metal catalysts are widely used in modern chemical industry. Some of these processes deal with a reducing atmosphere. Hydrogen can be fed into the reaction volume initially, like in the case of selective hydrogenation of organic compounds [1] or low-temperature synthesis of ammonia [2, 3]. On the other hand, it can be released as a product of the catalytic process, for example, dehydrogenation of alcohols [4] or ammonia decomposition [5, 6]. The latter is used to produce pure hydrogen for fuel cells.

The synthetic carbon material Sibunit used in the present work is an unique composite that combines both the properties of graphite (mechanical strength, thermal and chemical resistance) and the properties of active coals (high specific surface area, developed pore structure) [7]. Being applied in industrial hydrogenation processes, Sibunit-supported catalysts containing

metals of platinum group are known to be stable in a hydrogen containing medium within the temperature range of 150-350 °C. However, the situation has changed cardinally at the elevated temperatures. Supported particles of platinum metals activate hydrogen, and the latter starts to interact with carbon of the support forming methane. All these change the textural and structural characteristics of Sibunit, facilitate sintering of the metal particles, and finally lead to the catalyst deactivation [8].

There are few approaches how to prevent the undesirable process of methanation, which are reported in the literature [9]. Thus, the intensity of methanation can be reduced by an introduction of modifying elements into the catalyst's composition [2, 10]. Particles of these elements localized near the active sites diminish noticeably the contact area of the platinum metals particles with the carbon support. Another approach is a high-temperature pretreatment of the support in an inert atmosphere [11, 12]. The aim of the present study was to elucidate the effect of graphitization of Sibunit on thermal stability of the Ru-Ba-Cs/C catalyst and its activity in ammonia decomposition reaction.

## EXPERIMENTAL

Carbonaceous composite material Sibunit was used as a support (labeled as C<sub>init</sub>). Graphitization of the support was carried out in a Tamman furnace at 1900 °C in a nitrogen atmosphere for 30 min (labeled as C<sub>1900</sub>). Prior to deposition of ruthenium and modifiers, the supports were dried at 120 °C for 3 h. Catalysts containing 4 wt.% of Ru, 8 wt.% of Ba and 5 wt.% of Cs were prepared by an impregnation of the support as described elsewhere [13]. The thermal stability of the samples in a hydrogen atmosphere was studied in a setup consisting of a U-shaped quartz reactor and a mobile furnace [12]. The amount of the formed methane and the loss of the sample's weight were the target characteristics.

The reaction of ammonia decomposition was studied in a fixed-bed reactor at 500 °C and atmospheric pressure. NH<sub>3</sub> (21 ml/min) was fed into the reactor with a sample (0.1 g). The contact time was 0.37 s. The gas mixture was analyzed using gas chromatograph. From the data obtained, the catalytic activity  $W$ , mol[NH<sub>3</sub>]/(g<sub>Ru</sub>·h) was calculated.

## RESULTS AND DISCUSSION

The procedure of the support graphitization leads to compaction of carbon, ordering of the graphene layers and increase in their number (Table 1). All this results in a noticeable drop of the SSA from 320 to 46 m<sup>2</sup>/g. In the Raman spectrum, the G-band is shifted from 1596 to 1583 cm<sup>-1</sup>, and new line at 1617

$\text{cm}^{-1}$  has appeared (D-band; characteristic of graphite). The intensity of the 2D band has increased indicating a growth of the graphene layers number.

All these changes of the support affect the catalytic properties. Thus, the Ru-Ba-Cs/C<sub>1900</sub> sample was 1.6 times less active in ammonia decomposition at 500 °C comparing with the Ru-Ba-Cs/C<sub>init</sub> sample (Fig. 1). The corresponding values were 5.7 and 9.3 mol[NH<sub>3</sub>]/(g<sub>Ru</sub>·h). It should be noted that in both the case, ruthenium particles of about 10 nm in size are evenly distributed on the surface of the support. Barium is present in the form of large crystals of carbonate, while cesium species were not identified. In terms of thermal stability the Ru-Ba-Cs/C<sub>1900</sub> sample overcomes its concurrent in several times. Comparing these catalysts with monometallic reference samples, the following thermal stability order was obtained: Ru-Ba-Cs/C<sub>1900</sub> > Ru/C<sub>1900</sub> > Ru-Ba-Cs/C<sub>init</sub> >> Ru/C<sub>init</sub>. It is seen that the graphitization procedure has more strong effect on the stability than modification with Ba and Cs.

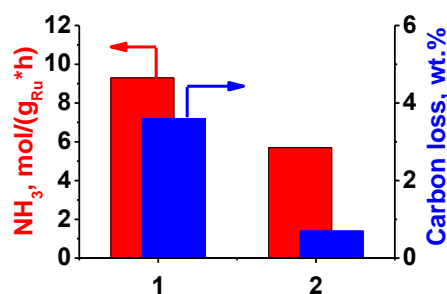


**Figure 1.** Carbon loss and activity in ammonia decomposition for the samples: 1 - Ru-Ba-Cs/C<sub>init</sub>; 2 - Ru-Ba-Cs/C<sub>1900</sub>.

**Table 1.** Specific surface area and structural parameters of the supports\*.

Support	SSA, m <sup>2</sup> /g	d <sub>002</sub> , Å TEM	d <sub>002</sub> , Å XRD	L <sub>c</sub> , Å XRD	N
Sibunit	320	3,65	3,47	34	11
Sibunit-1900	46	3,45	3,45	87	26

\* SSA is the specific surface area determined by the low-temperature nitrogen adsorption in accordance with BET method; d<sub>002</sub> is the average distance between carbon layers; L<sub>c</sub> is the average height of the crystallite in the direction c; N is a number of layers.

## CONCLUSION

Calcination of the carbon support in an inert atmosphere at 1900 °C was shown to lead to its graphitization. According to TEM, XRD and Raman spectroscopy, this procedure crucially changes the properties of the support. Thus, the specific surface area has been sharply decreased in almost 7 times. On the other hand, graphitization of Sibunit has a positive effect on the thermal stability of Ru-Ba-Cs/C<sub>1900</sub> catalyst. In terms of activity in ammonia

decomposition, catalyst based on the graphitized support was worst if compare with the sample of the similar composition but supported on initial Sibunit. Since the dispersity of ruthenium particles is close in both the cases (about 10 nm), the main reason of the difference in activity is believed to be more significant blockage of the Ru active sites by modifiers (Ba, Cs).

### ***Acknowledgement***

The present work was performed within Government Order for IHP SB RAS (Project no. 0364-2016-0003).

### **REFERENCES**

- [1] O. B. Belskaya, R. M. Mironenko, V. P. Talsi, V. A. Rodionov, S. V. Sysolyatin, V. A. Likholobov, *Procedia Engineer.*, 2016, 152, 110–115.
- [2] Z. Kowalczyk, S. Jodzis, W. Raróg, J. Zieliński, J. Pielaszek, *App. Catal. A-Gen.*, 173, 1998, 153–160.
- [3] N. B. Shitova, N. M. Dobrynkin, A. S. Noskov, I. P. Prosvirin, V. I. Bukhtiyarov, D. I. Kochubei, P. G. Tsyruľnikov, D. A. Shlyapin, *Kinet. Catal.*, 2004, 45, 414–421.
- [4] E. V. Shelepova, A. A. Vedyagin, L. Y. Ilina, A. I. Nizovskii, P. G. Tsyruľnikov, *Appl. Surf. Sci.*, 2017, 409, 291–295.
- [5] L. Li, Z. H. Zhu, Z. F. Yan, G. Q. Lu, L. Rintoul, *Appl. Catal. A-Gen.*, 2007, 320, 166–172.
- [6] W. Raróg-Pilecka, D. Szmigiel, Z. Kowalczyk, S. Jodzis, J. Zielinski, *J. Catal.*, 2003, 218, 465–469.
- [7] Y. I. Yermakov, V. F. Surovikin, G. F. Plaksin, *React. Kinet. Catal. Lett.*, 1987, 33, 2, 435-440.
- [8] H. Zeng, T. Hihara, K. Inazu, K.-i Aika, *Catal. Lett.*, 2001, 76, 193-199.
- [9] I. Rossetti, F. Mangiarini, L. Forni, *Appl. Catal. A-Gen.*, 323, 2007, 219–225.
- [10] P. G. Tsyruľnikov, K. N. Iost, N. B. Shitova, V. L. Temerev, *Catal. Ind.*, 2016, 8, 341–347.
- [11] I. Rossetti, N. Pernicone, L. Forni, *Catal. Today*, 2005, 102–103, 219–224.
- [12] K. N. Iost, V. A. Borisov, V. L. Temerev, Y. V. Surovikin, P. E. Pavluchenko, M. V. Trenikhin, A. A. Lupanova, A. B. Arbuzov, D. A. Shlyapin, P. G. Tsyruľnikov, A. A. Vedyagin, *Surf. Interfaces*, 2018, 12, 95-101.
- [13] K. N. Iost, V. L. Temerev, N. S. Smirnova, D. A. Shlyapin, V. A. Borisov, I. V. Muromtsev, M. V. Trenikhin, T. V. Kireeva, A. V. Shilova, P. G. Tsyruľnikov, *Russ. J. Appl. Chem.*, 2017, 90, 887–894.

## WGS ACTIVITY OF GOLD CATALYSTS ON ALUMINA SUPPORTED COPPER-MANGANESE OXIDES WITH DIFFERENT COMPOSITION

T. Tabakova <sup>1</sup>, I. Ivanov <sup>1</sup>, E. Kolentsova <sup>2</sup>, P. Petrova <sup>1</sup>, Y. Karakirova <sup>1</sup>, G. Avdeev <sup>3</sup>, K. Ivanov <sup>2</sup> and V. Idakiev <sup>1</sup>

<sup>1</sup> *Institute of Catalysis, Bulgarian Academy of Sciences, Acad. G. Bonchev str., Bl. 11, 1113 Sofia, Bulgaria. (tabakova@ic.bas.bg)*

<sup>2</sup> *Department of Chemistry, Agricultural University, 12 Mendeleev Blvd. 4000 Plovdiv, Bulgaria.*

<sup>3</sup> *Institute of Physical Chemistry, Bulgarian Academy of Sciences, Acad. G. Bonchev str., Bl. 11, 1113 Sofia, Bulgaria.*

### ABSTRACT

Alumina supported copper manganese oxide samples with different Cu/Mn ratio were prepared by wet impregnation. Deposition-precipitation method was used for synthesis of gold catalysts. The characterization of as-prepared and used in water-gas shift (WGS) reaction samples was performed by XRD, HRTEM, EPR and TPR in order to explain the relationship between structure, reduction behaviour and WGS activity. Higher activity was demonstrated by the sample with higher Cu content, i.e. that with ratio 2:1. Catalytic tests revealed beneficial role of gold addition.

### INTRODUCTION

The sustainable energy future is focused on improving the quality of life by development of highly efficient and more environmentally friendly energy devices. The advancement in fuel cells technology provoked renewed interest in the water-gas shift (WGS) reaction because of its importance in clean hydrogen production. Copper is widely used as the active component in WGS catalysts due to its activity at low temperatures and lower cost in comparison with the noble metals. Recently, the evaluation of catalytic activity demonstrated the superior WGS performance of Cu-Mn spinel oxide catalysts [1]. Due to their good redox property, these mixed oxides play an important role in the activation of water. However, the use of gold catalysts for the WGS opened up exciting possibilities. These catalysts possess some advantageous features like high activity and stability in oxidizing atmosphere. They are non-pyrophoric and can be used without preliminary activation.

The aim of present study was to develop cost-effective and catalytically

efficient formulations based on  $\gamma$ -Al<sub>2</sub>O<sub>3</sub> modified with a superficial fraction of Cu–Mn mixed oxides. The effect of Cu/Mn molar ratio and the role of Au addition on the structural and catalytic properties were examined.

## EXPERIMENTAL

The samples were prepared by the wet impregnation method. Commercial  $\gamma$ -Al<sub>2</sub>O<sub>3</sub> was calcined at 500 °C for 2 h before use. Then, mixed solutions of copper and manganese nitrates with Cu/Mn molar ratio of 2:1 and 1:5 (20 wt. % active phase) were added. The support remained immersed for 12 hours in the salt solutions at 80°C. The samples were dried at 120 °C for 10 h and calcined at 450 °C for 4 h. Gold-containing samples (2 wt. %) were synthesized by deposition-precipitation method at pH 7.0 and temperature 60 °C, washed, dried and calcined at 400 °C within 2 h.

All details about instruments used for samples characterization (XRD, HRTEM, EPR and TPR) and experimental conditions were described elsewhere [2].

WGS activity measurements were carried out in a flow reactor at atmospheric pressure over a temperature range 120 - 260 °C. The following conditions were applied: catalyst bed volume = 0.5 cm<sup>3</sup> (0.63-0.80 mm pellets), gas mixture 4.5 vol. % CO in Ar, space velocity 4000 h<sup>-1</sup>, partial pressure of water vapor = 31.1 kPa [1]. The degree of CO conversion was calculated on the basis of inlet and outlet CO concentration, measured with an Uras 3G (Hartmann&Braun AG) gas analyzer.

## RESULTS AND DISCUSSION

Catalytic activity results revealed the effect of Cu/Mn molar ratio (Fig. 1). Higher activity was demonstrated by the sample with higher Cu content, i.e. that with ratio 2:1. Both gold-containing catalysts were more active than the corresponding Cu-Mn mixed oxides supported on alumina. The highest catalytic activity among the studied catalysts was shown by the gold catalyst on Cu-rich sample, i.e. with Cu/Mn

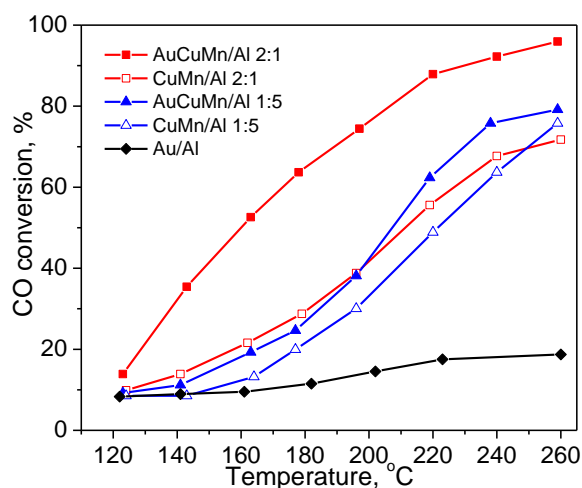
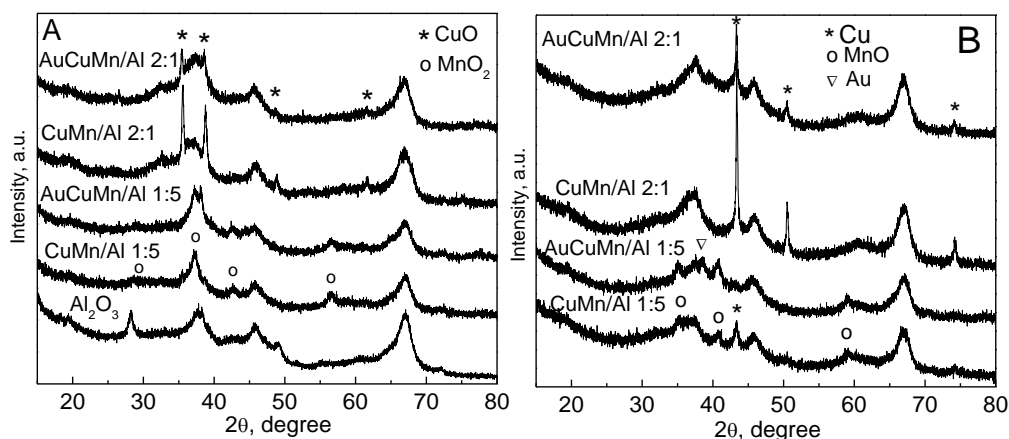


Figure 1. WGS activity of the studied samples

ratio 2:1. The addition of gold enhanced significantly its activity: more than 40 % higher degree of CO conversion was attained at 200 °C. On the contrary, modification with gold of Mn-rich sample caused only slight improvement of activity. The role of Cu-Mn mixed oxide phase on WGS activity of gold catalyst was clearly demonstrated by comparison with behaviour of Al<sub>2</sub>O<sub>3</sub> supported gold catalyst that exhibited very low activity.

In Fig. 2 (A) are shown the X-ray powder diffraction patterns of the fresh samples. The well visible reflections at  $2\theta = 35.6, 38.8, 48.6$  and  $61.8^\circ$  in the



**Figure 2.** Powder XRD patterns of fresh (A) and WGS tested (B) samples.

diffractogram of CuMn/Al 2:1 sample were assigned to the CuO phase. Broad reflections of MnO<sub>2</sub> were registered in the pattern of CuMn/Al 1:5 sample. Additionally, the TG/DTA analysis allowed assuming the presence of a Cu-Mn spinel phase. HRTEM images and SAED patterns were used to identify definitely phase composition. The formation of Cu<sub>1.5</sub>Mn<sub>1.5</sub>O<sub>4</sub> spinel phase was confirmed basing on the measurements of distances among the crystalline lattice fringes. The spacing of these fringes (0.240, 0.140 and 0.293 nm) corresponds to the (2 2 2), (5 3 1) and (2 2 0) planes of Cu<sub>1.5</sub>Mn<sub>1.5</sub>O<sub>4</sub>. The intensity of CuO and MnO<sub>2</sub> reflections significantly decreased after modification with Au. However, diffraction peaks assignable to the presence of crystalline Au were not discernible, evidencing high dispersion of metallic gold particles.

The XRD patterns of the samples after WGS tests (Fig. 2 (B)) indicated that during the reaction the separate phase of CuO in Cu-rich samples was reduced to Cu<sup>0</sup> (peaks at  $2\theta = 43.3, 50.4$  and  $74.1$ ), while MnO<sub>2</sub> in samples with Cu/Mn ratio 1:5 was reduced to MnO (peaks at  $2\theta = 34.9, 40.6$  and  $58.7$ ). It was observed that the presence of gold affected crystallite size of metallic copper. It was calculated to be about 31 nm, while in CuMn/Al 2:1 sample it

is two-fold higher – 62 nm. An important observation is the appearance of weak reflection at  $2\theta = 38.4^\circ$  in the diffractogram of Au/CuMn/Al 1:5, corresponding to metallic gold, while no such peak was detected in Cu-rich catalyst, indicating availability of finely dispersed gold particles.

H<sub>2</sub>-TPR measurements were carried out in order to study the reduction behavior of the samples. The reduction profile of CuMn/Al 2:1 was complex with two components ( $T_{\max}$  at 192 and 259 °C), assigned to the reduction of separate CuO phase and to highly dispersed Cu-Mn spinel phase. The profile of CuMn/Al 1:5 exhibited a peak with well-defined maximum at 293 °C ascribed to reduction of MnO<sub>2</sub> and a broad shoulder in the low-temperature side, related to the reduction of copper species. The addition of gold boosted the reduction of the spinel phase and improved the reducibility of the mixed oxides. The favorable role of gold on reducibility was confirmed by TPR measurements of the samples used in WGSR.

The nature of the active phase species was studied by EPR spectroscopy. The analysis of the spectra of fresh CuMn/Al 2:1 and calculation of the parameters  $g$  and  $A$  showed that Cu (II) is present as a mixture of isolated Cu<sup>2+</sup> ions and aggregates of Cu<sup>2+</sup> ions. The lack of EPR signal characteristic for Mn species revealed that most likely they exist as Mn<sup>4+</sup>. The spectra after WGSR are in good agreement with XRD and TPR data. Traces of Cu<sup>2+</sup> were registered in the spectrum of Au/CuMn/Al 2:1, pointing on the promotional role of gold to facilitate CuO reduction and spinel decomposition.

## CONCLUSION

Novel catalysts with improved efficiency and economic viability for hydrogen production via WGSR were prepared by combination of gold nanoparticles and alumina supported Cu-Mn mixed oxides. The best performance of gold-promoted sample with Cu/Mn ratio 2:1 was related to the favorable effect of Au on CuO reduction during the reaction, thus ensuring the presence of two highly dispersed active metallic phases.

### *Acknowledgement*

The authors affiliated at Institute of Catalysis gratefully acknowledge financial support by the Bulgarian Science Fund (Contract ДН 09/5/2016).

## REFERENCES

- [1] T. Tabakova, V. Idakiev, G. Avgouropoulos, J. Papavasiliou, M. Manzoli, T. Ioannides, *Applied Catalysis A*, 2013, 451, 184-191.
- [2] T. Tabakova, E. Kolentsova, D. Dimitrov, K. Ivanov, M. Manzoli, A. M. Venezia, et al., *Topics in Catalysis*, 2018, 60, 110-122.

## REACTION BETWEEN SULFUR(IV) AND CHLORO-1,4-BENZOQUINONES

V. Kiss<sup>1</sup>, L.J. Csépes-Ruzicska<sup>1</sup>, B.M. Hülvely<sup>1</sup>, P. Tarczali-Sarudi<sup>1</sup>, I. Fábíán<sup>2</sup> and K. Ósz<sup>3</sup>

<sup>1</sup> *University of Debrecen, Department of Physical Chemistry, Egyetem tér 1., Debrecen, H-4032, Hungary.*

<sup>2</sup> *University of Debrecen, Department of Inorganic and Analytical Chemistry,*

*Egyetem tér 1., Debrecen, H-4032, Hungary.*

<sup>3</sup> *University of Pécs, Department of General and Physical Chemistry, Ifjúság útja 6., Pécs, H-7624, Hungary. (oszk@gamma.ttk.pte.hu)*

### ABSTRACT

In this paper, the kinetics of the reaction between 1,4-benzoquinones (R-Q) and Na<sub>2</sub>SO<sub>3</sub> (S(IV)) is presented in aqueous solutions at different pH values, temperatures and reagent concentrations. The stopped-flow technique with spectrophotometric detection was used to measure the kinetic traces at different wavelength values and the kinetic fitting program ZiTA was used to fit a three-step model to the data. Also, a detailed mathematical evaluation of a simplified reaction scheme was carried out under non-flooding conditions showing that our model can be fitted to a double exponential function even when none of the reagents are in large excess. The stoichiometry of the reaction is 1:2 R-Q:S(IV) and, in the case of 2,5-dichloro-1,4-benzoquinone and 2,6-dichloro-1,4-benzoquinone, reductive dehalogenation happens instead of simple reduction to hydroquinone.

### INTRODUCTION

Chlorinated 1,4-benzoquinones are the by-products of water disinfection treatment [1-3]. Although they are present only in low concentrations (ng/L) in pool waters and in drinking waters [4-6], they might have carcinogenic and mutagenic effects. For this reason, dehalogenation of these substances is essential.

Sulfur(IV) in aqueous solution might be a mild and non-toxic reductive agent to carry out these processes.

On the other hand, 1,4-benzoquinones are also formal ketones, so, the reaction between these two reagents can be explained as a ketone-bisulfite addition reaction [7-10].

The investigation of the reaction is even more complex because of the fact that 1,4-benzoquinones in aqueous solutions are photo-sensitive. Their photochemical reaction results in the formation of hydroquinones and hydroxy-quinones [11].

### EXPERIMENTAL

The reaction was investigated using the stopped-flow technique with spectrophotometric detection. The typical time-scale of the reaction was 1-10 s. The photo-sensitivity of the derivatives investigated was also tested in the stopped-flow instrument and also in a diode-array spectrophotometer.

The derivatives used in this study are as follows: 1,4-benzoquinone (Q), 2-chloro-1,4-benzoquinone (Q-Cl), 2,5-dichloro-1,4-benzoquinone (Q-2,5-Cl<sub>2</sub>) and 2,6-dichloro-1,4-benzoquinone (Q-2,6-Cl<sub>2</sub>).

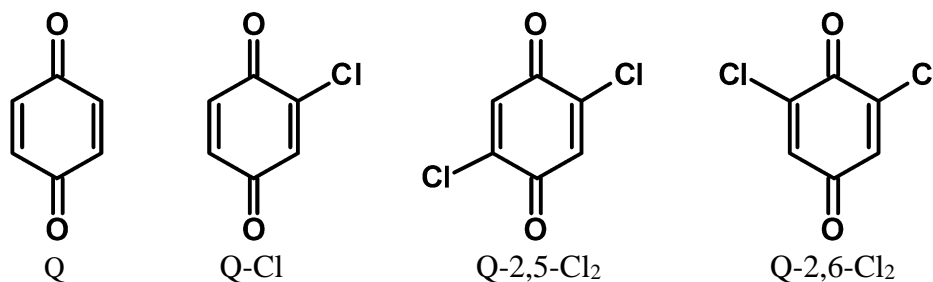


**Figure 1.** Structures of the 1,4-benzoquinone derivatives investigated.

### RESULTS AND DISCUSSION

For all four 1,4-benzoquinones, several kinetic traces in a wide quinone and S(IV) concentration range were measured and fitted to a kinetic model containing a bimolecular addition equilibrium reaction of the two reactants, followed by an unimolecular step forming a second intermediate, and finally a very rapid step between the intermediate and a second molecule of S(IV). The 1:2 stoichiometry was verified using the Job method based on spectrophotometric observations and the products were also identified by measurements with electrospray ionization mass spectrometry (ESI-MS) and a chloride ion selective electrode. The reaction mechanism under most of the concentration conditions can be described by a three-step process presented in Figure 2:

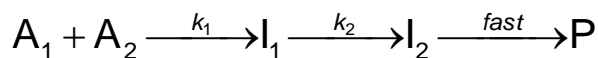


**Figure 2.** Model of the reaction investigated ( $A_1$  and  $A_2$  are R-Q and S(IV)).  
[12]

The reactions between 1,4-benzoquinones and sulfite ion clearly involve intermediates, the existence of which was proved by the fact that the observed absorbance-time traces show a maximum in a wide wavelength region. For such systems, it is expected that a double exponential curve could describe the traces well under flooding conditions. However, we could successfully use the double exponential for all cases, independently of the initial ratio of the reactants (even when this ratio was exactly stoichiometric). This interesting phenomenon was thoroughly investigated using mathematical simulations, and the results of the simulations were used to estimate the rate constants of the kinetic model.

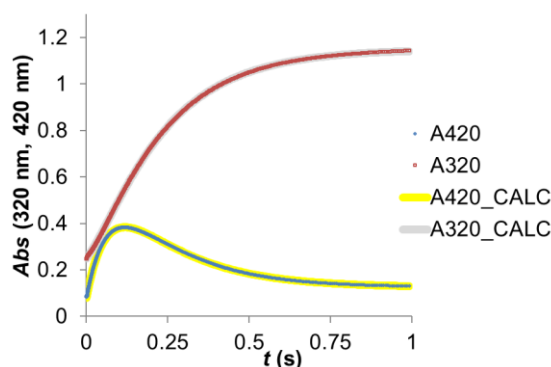


**Figure 3.** Kinetic traces of the reaction between Q-2,5-Cl<sub>2</sub> and S(IV) measured at 420 nm (·) and 320 nm (·), together with the fitted double exponential curves (— and —).  
 $c(\text{Q-2,5-Cl}_2) = 0.50 \text{ mM}$ ,  $c(\text{S(IV)}) = 1.0 \text{ mM}$ ,  $\text{pH} = 4.5$ ,  $T = 293 \text{ K}$ .

## CONCLUSION

Double exponential fitting can be well used to describe the kinetic traces of our ketone-bisulfite addition reaction in a wide concentration range. Rate constants of the kinetic model can be estimated based on the observed rate constants of the double exponential fitting. The pH and temperature dependence of the kinetics of the reaction was in agreement with the usual expectations.

**Acknowledgement**

Hungarian Science Funding Agency OTKA is acknowledged for support under contract no. NK105156.

The authors wish to thank Gábor Lente for helpful discussions.

**REFERENCES**

- [1] F. Qin, Y.-Y. Zhao, Y. Zhao, J.M. Boyd, W. Zhou, X.-F. Li, *Angew. Chemie Int. Ed.*, 2010, 49, 790-792.
- [2] J. Li, B. Moe, S. Vemula, W. Wang, X.-F. Li, *Environ. Sci. Technol.*, 2016, 50, 6744-6752.
- [3] J. Li, W. Wang, H. Zhang, X.C. Le, X.-F. Li, *Toxicol. Sci.*, 2014, 141, 335-343.
- [4] W. Wang, Y. Qian, J. Li, B. Moe, R. Huang, H. Zhang, S.E. Hrudey, X.-F. Li, *Anal. Chem.*, 2014, 86, 4982-4988.
- [5] R. Huang, W. Wang, Y. Qian, J.M. Boyd, Y. Zhao, X.-F. Li, *Anal. Chem.*, 2013, 85, 4520-4529.
- [6] Y. Qian, W. Wang, J.M. Boyd, M. Wu, S.E. Hrudey, X.-F. Li, *UV-Environ. Sci. Technol.*, 2013, 47, 4426-4433.
- [7] H.C. Brown, W.S. Park, B.T. Cho, P.V. Ramachandran, *J. Org. Chem.*, 1987, 52, 5406-5412.
- [8] E.A. Betterton, Y. Erel, M.R. Hoffmann, *Environ. Sci. Technol.*, 1988, 22, 92-99.
- [9] D.P. Kjell, Brian J. Slattery, M.J. Semo, *J. Org. Chem.*, 1999, 64, 5722-5724.
- [10] P.G. Wuts, C.L. Bergh, *Tetrahedron Lett.*, 1986, 27, 3995-3998.
- [11] É. Józsa, V. Kiss, K. Ósz, *J. Photochem. Photobiol. A Chem.*, 2018, 360, 166-173.
- [12] V. Kiss, K. Ósz, *Int. J. Chem. Kinet.*, 2017, 49, 602-610.

## SOLVENT-FREE ALCOHOL ACYLATION BY ACETIC ACID OVER NOVEL LANTHANIDE-GRAFTED CATALYTIC SYSTEM

A. P. Koskin<sup>1</sup> and A. O. Borodin<sup>2,3</sup>

<sup>1</sup>*Boreskov Institute of Catalysis SB RAS, pr. Ac. Lavrentieva 5, 630090 Novosibirsk, Russian Federation. (koskin@catalysis.ru)*

<sup>2</sup>*National Research Novosibirsk State University, Pirogova str. 1, 630090 Novosibirsk, Russian Federation.*

<sup>3</sup>*Nikolaev Institute of Inorganic Chemistry SB RAS, pr. Ac. Lavrentieva 3, 630090 Novosibirsk, Russian Federation.*

### ABSTRACT

Lanthanide triflates ( $\text{Ln}(\text{SO}_3\text{CF}_3)_3$ ;  $\text{Ln}(\text{OTf})_3$ ) are successfully used in a number of homogeneous processes of fine organic synthesis traditionally catalyzed by Lewis acids. In the present study, novel heterogeneous analogue of  $\text{Ln}(\text{OTf})_3$  was prepared. Synthesized  $\text{Ln}^{3+}\text{SFP}/\text{support}$  systems (SFP - sulfonated fluoropolymer;  $\text{Ln} = \text{Sc, La, Pr, Eu, Tm, Yb}$ ) are insoluble in the reaction mixture and able to catalytic recycle. High texture characteristics of the Nf/CNF (Nf - Nafion) samples have also great impact on the catalytic process. Various supported Ln-Nf catalysts were synthesized and tested in the acylation of alcohols with acetic acid.

### INTRODUCTION

Lanthanide perfluoroalkanesulfonate salts are successfully used in a number of homogeneous processes of fine organic synthesis [1]. An important advantage of such salts in comparison with standard Lewis acids is their stability in proton media and ability to recycle the catalyst. A lot of heterogeneous systems with such type of active sites are reported in the literature: (i) lanthanide triflates supported on silica [2]; (ii) lanthanides contained in polystyrene stabilized microemulsions [3]; (iii) lanthanides grafted to sulfonated fluoropolymer (Ln-Nafion) and to acidic resins (Ln-Amberlyst etc.) [4].

This study is considered as a step forward from pure Ln-Nafion to the systems supported on carbon nanofibers (CNF). The use of CNF as support has allowed us to increase availability of sulfonic groups and, thus, to reduce the loading of Nafion (Nf) without any losses in catalytic activity.

## EXPERIMENTAL

SFP/CNF composites were synthesized as described elsewhere [5-6]. Nafion (equal mass 1000 g/mol; ion exchange capacity 1.0 mmol/g) and polymer F4SF (structural analog of Nafion prepared in IMC RAS; 780 g/mol; 1.2 mmol/g) were used as a composite acid phase (SFP). The samples of sulfated carbon materials (SO<sub>3</sub>H-CNF) were obtained by CNF sulfation in the H<sub>2</sub>SO<sub>4</sub>/VOSO<sub>4</sub> mixture at 200 °C [7]. The Ln<sup>3+</sup>-grafted composites were synthesized by soaking of Na-precursor (Na<sup>+</sup> SFP/support (20 wt. % SFP) or Na<sup>+</sup>SO<sub>3</sub>CNF) with excess (1:100 molar ratio) of Ln(OAc)<sub>3</sub> aqueous solution (Ln = Sc, La, Pr, Eu, Tm, Yb). The resulted suspension was filtered and washed by diluted acetic acid (pH~5). Ln cation content (C<sub>Ln</sub>, mmol/g) was defined by AAS-analysis (iCAP-6500). The structure of the synthesized samples was investigated by a set of methods: TEM (JEM-2010), BET (ASAP-2400), SAXS (S3 MICRO) and XPS (SPECS).

In the catalytic experiments, Ln<sup>3+</sup>composite (1 g) was added to stirred mixture of ethanol (99.9%, Acros Organics, 3 M) and acetic acid (99.7%, Aldrich, 6 M) in 45 ml of THF. Acylation of other alcohols was tested similarly. Conversion (X<sub>AcOH</sub>) was detected by a change of mixture pH or by means of <sup>1</sup>H-NMR.

## RESULTS AND DISCUSSION

As known, the reflux procedure (boiling in EtOH/DMSO mixture) is required to obtain the unsupported Ln<sup>3+</sup>SFP samples in order to increase the accessibility of Nafion sulfonates [4]. Contrary, Ln-grafted composites can be prepared by simple mixing of the precursors at a room temperature. The Ln-composites consist of SFP blocks and thin SFP layer over the surface of CNF fibers. The blocks of SFP polymer, in its turn, are represented by microcrystallites which form chaotic system of hydrophilic channels (estimated by SAXS) [6]. Analysis of the Yb<sup>3+</sup>SFP/CNF sample by means of XPS shows the presence of Yb<sup>3+</sup> multiplet peak (180-210 eV; Yb4d) with a binding energy typical for carboxylic Yb<sup>3+</sup>/sulfate Yb<sup>3+</sup> mixture. According to EDX data, the lanthanide ions are evenly distributed within the SFP blocks (Yb(OAc)<sub>1-0</sub>(SO<sub>3</sub><sup>-</sup>)<sub>2-3</sub>) and SFP layer (Yb(OAc)(SO<sub>3</sub><sup>-</sup>)<sub>2</sub>). An insignificant amount of Yb(OAc)<sub>3</sub> particles is located on the uncoated surface of CNF.

In the case of acylation without catalyst (autocatalysis by AcOH), the product yield did not exceed 10% (24 h). The highest initial rates (TOF<sub>in</sub>, Table 1) were shown by the homogeneous catalysts, since no substrate diffusion to Yb-sulfonates is required. In the case of heterogeneous systems, the highest TOF<sub>in</sub> values were found for H<sup>+</sup>-acid samples (CNF-supported H<sup>+</sup>Nf and H<sup>+</sup>F4SF). However, the conversion of EtOH acylation (X<sub>AcOH</sub>, Table 1) was not so high due to the reverse reaction of EtOAc hydrolysis.

$\text{Ln}^{3+}\text{Nf}/\text{CNF}$  systems were more active if compare with  $\text{Ln}^{3+}\text{SO}_3\text{-CNF}$ . The higher acidity of the Nafion sulfonates provides a greater lanthanide cation charge density. In the lanthanide screening test, the following activity row was observed:  $\text{Sc}\sim\text{Yb}>\text{Tm}>\text{Eu}>\text{Pr}>\text{La}$ . As seen, the highest catalytic activity was performed by the Yb- and Sc-containing samples.

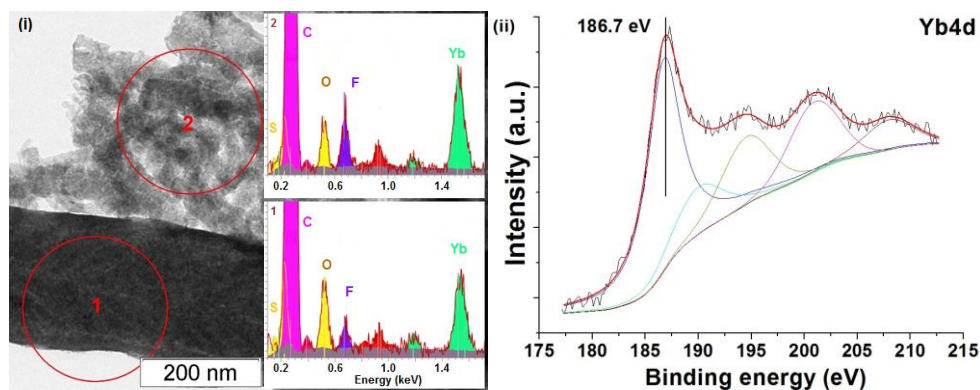


**Figure 1.** (i) - TEM and (ii) - XPS spectra (Yb4d) of a sample  $\text{Yb}^{3+}\text{Nf}/\text{CNF}$ .

**Table 1.** Ethanol acylation by AcOH in a presence of Ln-grafted composite.

Ln-grafted sample	$C_{\text{Ln}}(C_{\text{H}^+})$ (mmol/g)	Ethanol acylation by acetic acid	
		$X_{\text{AcOH}}^*$ (%)	$\text{TOF}_{\text{in}}^{**}$ ( $\text{min}^{-1}$ )
CNF	-	6	-
$\text{Yb}(\text{OAc})_3/\text{CNF}$	0.03	16	-
$\text{Yb}(\text{OTf})_3$	-	99	13.1
HOTf; HOPf (0.011 g)	-	75	24.7
$\text{H}^+\text{Nf}/\text{CNF}$	(0.2)	72	7.6
$\text{H}^+\text{F4SF}/\text{CNF}$	(0.24)	73	9.0
$\text{SO}_3\text{H-CNF}$	(0.3)	67	6.7
$\text{Yb}^{3+}\text{Nf}$ (0.2 g)	0.36	99	7.0
$\text{Yb}^{3+}\text{SO}_3\text{CNF}$	0.14	91	5.3
$\text{Yb}^{3+}\text{Nf}/\text{CNF}$ (20 wt. % Nf)	0.08	99	7.7
$\text{Ln}^{3+}\text{F4SF}/\text{CNF}$ (20 wt. % Nf) (Ln=Sc, La, Pr, Tm, Yb)	0.15	89-99	5.1-8.2

\* Conversion of AcOH at 10 h of acylation reaction

\*\* Values for initial TOF ( $t=10$  min) were calculated as  $\text{TOF}_{\text{in}} = C_{\text{AcOH}}^0 \cdot X_{\text{AcOH}}(t) \cdot V_{\text{reaction\_mixt}} / (C_{\text{Ln}} \cdot m_{\text{cat}} \cdot t)$ . In the case of protic samples TOF<sub>in</sub> was calculated per  $C_{\text{H}^+}$ .

Similar activity rows are inherent for other acid catalytic reactions and may be explained by a decrease of Ln ion radius [8]. According to AAS data, the  $\text{Ln}^{3+}$  cations are not present in the acylation mixture after catalyst separation. The separated catalyst remains the catalytic activity during the recycling. The active sites are seemed to be lanthanide cations grafted to Nafion sulfonates.

The substrates presumably undergo polarization on the Ln cation during the esterification reaction. The yield of ROAc in the acylation of butan-1-ol, butan-2-ol, cyclohexanol, t-butanol and 2-phenyl-ethanol has reached 99, 74, 46, 65 and 99 %, respectively. Lower acylation activity of secondary or tertiary alcohols is believed to be associated with a steric hindrance.

## CONCLUSION

In summary, the preparation method of Ln<sup>3+</sup>SPF/CNF composites was developed. Synthesized systems are insoluble in the reaction mixture and possess high specific surface area. It was found that Ln-composite contains blocks of SFP and thin SFP layer over the surface of CNF fibers. The lanthanide ions are evenly distributed within the polymer structure. The catalytic activity of synthesized Ln-composites was studied in the acylation of alcohols by acetic acid. It was shown that Ln<sup>3+</sup>Nf/CNF systems have a higher catalytic activity if compare with unsupported samples (Ln<sup>3+</sup>Nf) and Ln<sup>3+</sup>SO<sub>3</sub>-CNF. Yb- and Sc-containing systems showed the highest catalytic activity within the studied lanthanides.

## Acknowledgement

This work was performed within Government Order for BIC (Projects no. AAAA-A17-117041710090-3 and AAAA-A17-117041710086-6). The authors are grateful to Y.V. Larychev and A.V. Nartova (SAXS, XPS), A.V. Istchenko (TEM), A.R. Tsygankova (AAS), and R.V. Andreev (<sup>1</sup>H-NMR).

## REFERENCES

- [1] P. G. Steel, J. Chem. Soc., Perkin Trans. 1, 2001, 2727-2751.
- [2] K. N. Tayade, M. Mishra, K. Munusamy, R.S. Somani, Catal. Sci. Technol., 2015, **5**, 2427-2440.
- [3] S. Kobayashi, R. Akiyama, Chem. Commun., 2003, 449-460.
- [4] L. Yu, D. Chen, J. Li, P. G. Wang, J. Org. Chem., 1997, **62**, 3575-3581.
- [5] A. P. Koskin, R. M. Kenzhin, A. A. Vedyagin, I. V. Mishakov, Cat. Comm., 2014, **53**, 83-86.
- [6] A. P. Koskin, Y. V. Larichev, A. I. Lysikov, O. N. Primachenko, S. S. Ivanchev, Kinet. Catal., 2017, **58**, 655-662.
- [7] Y. V. Larichev, A.P. Koskin, Kinet. Catal. 2017, **58**, 663-667.
- [8] T.N. Parac-Vogt, K. Deleersnyder, K. Binnemans, Eur. J. Org. Chem. 2005, 1810-1815.

## CATALYTIC OXIDATION OF TARTRAZINE IN THE PRESENCE OF RADICALS GENERATED FROM POTASSIUM PEROXYMONOSULFATE USING COBALT IMPREGNATED PILLARED MONTMORILLONITE

M. P. Marković<sup>1</sup>, S. Marinović<sup>2</sup>, T. Mudrinić<sup>2</sup>,  
N. Jović-Jovičić<sup>2</sup>, M. Ajduković<sup>2</sup>, A. Milutinović-Nikolić<sup>2</sup> and P. Banković<sup>2</sup>

<sup>1</sup>University of Belgrade, Faculty of Technology and Metallurgy,  
Karnegijeva 4, 11000 Belgrade, Serbia and Serbian Armed Forces

<sup>2</sup>University of Belgrade, Institute of Chemistry, Technology and Metallurgy,  
Center for Catalysis and Chemical Engineering,  
Njegoševa 12, 11000 Belgrade, Serbia. (sanja@nanosys.ihtm.bg.ac.rs)

### ABSTRACT

In this work aluminum pillared clay impregnated with cobalt (CoAP) was tested as catalyst in the degradation of azo-dye tartrazine in the presence of potassium peroxymonosulfate (Oxone®). Aluminum pillared clay was synthesized using  $\leq 74 \mu\text{m}$  fraction of Na-exchanged clay from Wyoming, USA (Na-Wy) using common procedure. The influence of Oxone®/catalyst ratio on catalytic performance was investigated. The cobalt impregnated pillared montmorillonite was found to be promising catalyst for dye decolorization.

### INTRODUCTION

Potassium peroxymonosulfate (Oxone®,  $\text{KHSO}_5 \cdot 0.5\text{KHSO}_4 \cdot 0.5\text{K}_2\text{SO}_4$ ) has increasingly been gaining attention as effective substitute for Fenton's reagent in the catalytic oxidation of water pollutants [1]. Oxone® is commercially available and environmentally-friendly source of  $\text{SO}_4^{\cdot-}$  radicals that have similar or even higher oxidation potential than  $\text{OH}^{\cdot}$ , higher selectivity for unsaturated bonds and aromatic constituents and relatively long half-life comparing with that of  $\text{OH}^{\cdot}$  [2]. Activation of Oxone® is necessary in order to generate  $\text{SO}_4^{\cdot-}$  radicals [3]. Oxone® is the most effectively activated by transition metallic cations, with cobalt showing the best performance [4]. Several studies have proposed homogeneous cobalt ions as a catalyst for decomposition into radicals [5]. The difficulty of recovering cobalt ions for preventing possible subsequent pollutions led to attempts to make the catalyst where cobalt is immobilized onto various supports [3].

In this work cobalt impregnated pillared montmorillonite was used as a catalyst for Oxone® “activation” in catalytic oxidation of tartrazine dye as the water pollutant.

## EXPERIMENTAL

The  $\leq 74 \mu\text{m}$  fraction of clay from Wyoming, USA rich in montmorillonite, was used for pillaring. After Na-exchange (Na-Wy) the sample was modified by pillaring. The process of pillaring was carried out according to a common procedure comprising the following steps: pillaring, rinsing, drying and calcination [6]. The obtained pillared clay was impregnated with cobalt using incipient wetness impregnation method and denoted as CoAP.

Tartrazine degradation by Oxone® without catalyst as well as catalytic tests with Na-Wy and CoAP were conducted. Catalytic tests were performed in a system containing potassium peroxymonosulfate (Oxone®) as the source of peroxy radicals and aqueous solution of tartrazine as model pollutant. The concentration of Oxone® and the mass of the catalyst were varied. Decolorization was monitored using Thermo Scientific, Evolution 220 UV–Visible Spectrophotometer and  $\lambda_{\text{max}}=426 \text{ nm}$ .

## RESULTS AND DISCUSSION

The effects of Oxone® without catalyst, Na-Wy and the catalyst (CoAP) on tartrazine decolorization were monitored for the defined experimental conditions:  $200 \text{ cm}^3$  of  $C_{\text{dye}}=50 \text{ mg dm}^{-3}$  tartrazine solution,  $40 \text{ mg}$  of Oxone®,  $0.1 \text{ g}$  of catalyst,  $50 \text{ }^\circ\text{C}$ ,  $240 \text{ min}$  (Figure 1).

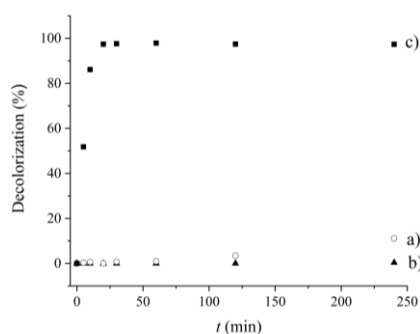


**Figure 1.** Decolorization of tartrazine a) Oxone® (without catalyst), b) Na-Wy, c) CoAP.

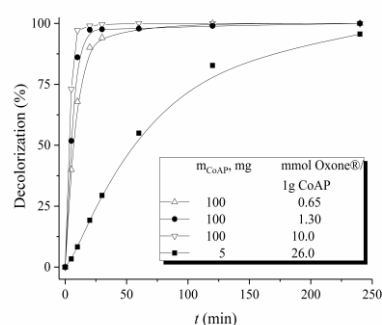


**Figure 2.** Decolorization of tartrazine with different ratios of Oxone® and catalyst.

The decolorization of tartrazine in the presence of the CoAP was almost complete after only 30 minutes (Figure 1) at the peak at  $426 \text{ nm}$  for the investigated conditions. On the other hand, in the reaction system without

catalyst, decolorization occurred, although very slow. After four hours the intensity of the initial color decreased for only 11 %. Reaction occurrence even without catalyst can be explained by the fact that Oxone® degraded tartrazine to some extent, even when there was no  $\text{Co}^{2+}$  to promote the creation of free radicals originating from Oxone®. It was probably due to selfdecomposition of Oxone® which led to formation of species that are able to oxidize although less efficient than radicals. In the case of the presence of Na-Wy in the reaction system decolorization was insignificant, indicating that Na-Wy did not show catalytic activity. Even more, Na-Wy, probably, adsorbed Oxone®, thus hindering the ability of Oxone® to decolorize tartrazine.

It can be observed (Figure 2) that, when the Oxone®/catalyst ratio was 10.0 mmol per 1g of catalyst, the reaction rate was the highest reaching 100% after 30 minutes. The drawback of these reaction conditions was that pH was 2.3 which was too low and resulted in undesirable level of  $\text{Co}^{2+}$  leaching into the reaction mixture. For the Oxone®/catalyst ratio of 26.0 mmol / 1g of catalyst, the rate of decolorization was the lowest because of lower amount of introduced catalyst (5 mg) in comparison with that in the other three investigated systems (100 mg). In this system pH was 3.5 and leaching was insignificant. Namely, it was below  $20 \mu\text{g dm}^{-3}$ .

## CONCLUSION

Clay rich in montmorillonite was modified by means of Na-exchange process (Na-Wy) and subsequently pillared with aluminum. The obtained pillared clay was impregnated with  $\text{Co}^{2+}$  (CoAP). The CoAP was tested as catalyst in tartrazine solution decolorization. The role of catalyst was the activation of radical formation from potassium peroxydisulfate (Oxone®). The comparison of the effects of Oxone® without catalyst, Na-Wy and the catalyst (CoAP) on tartrazine decolorization revealed that after 30 minutes only in the CoAP+Oxone® system total decolorization occurred. The influence of the Oxone®/catalyst ratio on tartrazine solution decolorization was investigated and conditions for negligible impact of homogeneous catalysis were found. The cobalt impregnated pillared montmorillonite was found to be promising catalyst for dye decolorization.

## *Acknowledgement*

This work was supported by the Ministry of Education, Science and Technological Development of the Republic of Serbia (Project III 45001).

**REFERENCES**

- [1] O. Gimeno, J. Rivas, M. Carbajo, T. Borrvalho, World Academy of Science, Engineering and Technology, International Journal of Chemical and Molecular Engineering 2009, 3(9), 481-484. urn:dai:10.1999/1307-6892/1687
- [2] K. Y. A. Lin, Y. C. Chen, C. F. Huang, Separation and Purification Technology, 2016, 170, 173–182.
- [3] K. Y. A. Lin, J. T. Lin, X. Y. Lu, C. Hung, Y. F. Lin, Journal of Colloid and Interface Science, 2017, 505, 728–735.
- [4] K. Y. A. Lin, W. C. Tong, Y. Du, Chemosphere 195 (2018) 272-281.
- [5] G. P. Anipsitakis, E. Stathatos, D. D. Dionysiou, The Journal of Physical Chemistry B 2005, 109(27), 13052-13055.
- [6] P. Banković, A. Milutinović-Nikolić, Z. Mojović, N. Jović-Jovičić, M. Perović, V. Spasojević, D. Jovanović, Microporous&Mesoporous Materials, 2013, 165, 247-256.

## RHODAMINE B PHOTODEGRADATION OVER HYDROTHERMALLY SYNTHESIZED CdIn<sub>2</sub>S<sub>4</sub>

T. Savić, J. Kuljanin –Jakovljević, N. Abazović and M. Čomor

*University of Belgrade, Vinča Institute of Nuclear Sciences, Mike Petrovića  
Alasa 12-14, 11351 Vinča, Belgrade, Serbia (kiki@vin.bg.ac.rs)*

### ABSTRACT

Cubic CdIn<sub>2</sub>S<sub>4</sub> (CIS) is synthesized by simple and low-cost hydrothermal route. The estimated band-gap of synthesized semiconductor is in the visible spectral region and has a value of about 2.55 eV. Photocatalytic performance of obtained powder is probed in photodegradation of Rhodamine B (RhB), under simulated Solar light illumination. It is proposed that RhB photodegradation starts as de-ethylation process thru indirect dye sensitization, while  $\bullet\text{O}_2^-$  radicals are identified as main active species responsible for degradation of de-ethylated intermediates.

### INTRODUCTION

Photocatalytic degradation of environmental pollutants usually implies usage of wide band-gap metal oxides and consequently, costly UV light sources. As a good way to reduce cost of process and widen applicability of method, usage of narrow band-gap metal sulfides that absorb light from visible part of solar spectrum is considered. As binary metal sulfides undergo photocorrosion, their more stable ternary counterparts, members of AB<sub>2</sub>X<sub>4</sub> family, emerged as replacement.

CdIn<sub>2</sub>S<sub>4</sub> is direct band-gap semiconductor with bulk band – gap energy of about 2.1 – 2.7 eV[1], meaning that its absorption threshold is placed in visible part of solar spectrum from about 450 to about 600 nm. However, desired optical characteristics doesn't necessarily mean a good photocatalyst, as photocatalytic performance depends also on crystal structure, particle size, specific surface area and surface charge of particular semiconductor.

Here, simple and low-cost hydrothermal synthesis of CIS is presented. In order to probe photocatalytic performance of synthesized material, organic dye RhB is used as model compound. It is cationic dye with pK<sub>a</sub> value around 4.1 [2] and absorption maximum at 554 nm, and it is widely used in studies of photocatalytic efficiencies of various photocatalysts. However, as degradation of RhB is typically tracked thru lowering of intensity of main maximum, formation of products that can be harmful to environment are often neglected, and common mistake is that de-ethylation of RhB is misinterpreted

as “complete degradation”. In this study, we tried to avoid this mistake and to explain in detail mechanism of CIS-RhB interaction under simulated Solar light illumination.

### EXPERIMENTAL

All chemicals were used as received. Deionized water from Mili Q system was used. CIS was synthesized using hydrothermal treatment. In a Teflon vessel (25 ml volume) 0.0213g cadmium acetate dihydrate (Sigma-Aldrich), 0.0484g indium acetate (Sigma-Aldrich), 0.0500g thioacetamide (Merck) and 8 ml water were added. Dispersion was vigorously stirred for 1h and then autoclaved at 160°C for 4h. The obtained powder was washed three times with water and ethanol (J.T. Baker) in order to discard all rests of unreacted salts (if any). Finally, obtained orange powder was centrifuged and dried at 70° C until a constant weight.

The XRD powder pattern was obtained by using a Philips PW 1050 powder diffractometer with Ni filtered Cu K $\alpha$  radiation ( $\lambda = 1.5418 \text{ \AA}$ ). The average crystallite size (D in nm) was determined from XRD spectra according to the Scherrer equation. UV/vis absorption spectra of aliquots collected during photocatalysis of RhB (Sigma,  $\approx 95\%$ ), as well as reflectance spectra of CIS powder were obtained using an Evolution 600 spectrophotometer (Thermo Scientific).

**Photodegradation procedure:** 10 mg of CIS was added to 40 cm<sup>3</sup> of 10 ppm RhB aqueous solution. Before illumination, the mixture was stirred in the dark for one hour in order to achieve the adsorption-desorption equilibrium. Reaction suspension was constantly bubbled with O<sub>2</sub> and magnetically stirred during irradiation. Suspensions were placed into a vessel which was exposed to simulated Solar light from an Osram Vitalux lamp. The aliquots (1 cm<sup>3</sup>) were taken in 5 min intervals, the CIS powder was removed from the solution using centrifugation.

### RESULTS AND DISCUSSION

XRD pattern of synthesized CIS is presented in Fig 1a. CIS crystallizes in pure cubic spinel structure (JCPDS 27-60) with no peaks related to binary CdS or  $\beta$ -In<sub>2</sub>S<sub>3</sub> or any other impurities. Applying Scherrer equation at (311) peak, it was calculated that average crystal domain size is about 36 nm.

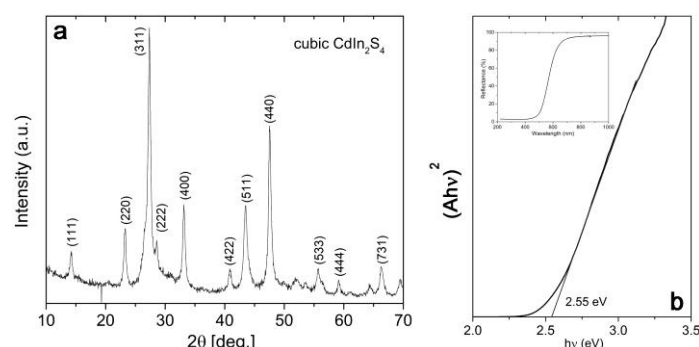


**Figure 1.** a) XRD pattern of synthesized CIS; b) Tauc plot of CIS; insert: reflection spectra

By extrapolation of the linear region of Tauc plot obtained from reflection spectrum (Fig. 1b), it was estimated that band-gap energy of synthesized CIS is about 2.5 eV (~500 nm). Using empirical equations  $E_{CB} = \chi - E_0 - 1/2E_g$  and  $E_{VB} = E_g - E_{CB}$ , where  $\chi$  is the absolute electronegativity,  $E_g$  is the estimated band-gap energy of the semiconductor, while  $E_0$  represents the difference between the normal hydrogen electrode (NHE) and the vacuum, it was calculated that conduction band (CB) edge of CIS is placed at -0.985V, while valence band (VB) edge is at +1.565V vs NHE.

Absorbance spectra of RhB during adsorption and photodegradation on CIS are presented in Fig 2a. More than 50% of initial concentration of RhB is adsorbed on CIS surface through initial equilibration, which is expected since RhB as cationic dye easy interacts with CIS surface rich with sulfur anions. Immediately after illumination, fast degradation starts, and after 30 min there is less than 5% of initial conc. of RhB in reaction solution. However, during degradation process, absorption maximum is gradually blue-shifted, that corresponds to step-by-step de-ethylation of RhB. At the end of illumination period, the main feature of absorption spectrum is peak at 496 nm which originates from completely de-ethylated form of RhB. Still, during illumination period, both characteristic peaks coexist in absorption spectra indicating that processes of de-ethylation of RhB and degradation of de-ethylated intermediates run simultaneously. In order to understand mechanism of RhB-CIS interaction, photodegradation experiments are conducted in presence of chloroform (e- scavenger) (Fig. 2b) and argon (absence of  $O_2$ , i.e.  $\bullet O_2^-$  radicals) (Fig. 2c). Potential of holes in VB of CIS is not high enough to generate  $OH^\bullet$  radicals from water so they are not studied. In the presence of chloroform, overall shape of absorption spectra is mostly preserved indicating that the reaction mechanism is the same. However, in absence of  $\bullet O_2^-$  radicals, process of de-ethylation of RhB is more pronounced

than direct degradation of RhB, indicating that reactive species other than  $\bullet\text{O}_2^-$  radicals, are responsible for de-ethylation process.

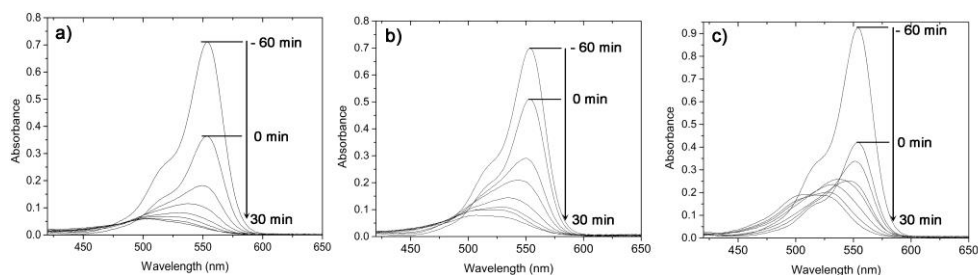


**Figure 2.** UV–vis absorption spectral changes during the photocatalytic degradation of RhB a) without scavenger b) in presence of chloroform c) in presence of argon

Upon illumination, due to intermolecular  $\pi\text{-}\pi^*$  transitions, photogenerated electron is transferred to excited state of the dye [1], placed at - 1.1V (vs. NHE). Due to favourable potential of CB edge of CIS, and fact that RhB is adsorbed on CIS surface, this electron is easily injected to CB of CIS (indirect dye sensitization) [3], and from there to  $\text{O}_2$  adsorbed on surface, forming  $\bullet\text{O}_2^-$  radicals, active species responsible for degradation of de-ethylated intermediates.

## CONCLUSION

Hydrothermally synthesized CIS powder is probed as photocatalyst in photodegradation of RhB. More than 95% of RhB is degraded in just 30 min of simulated Solar light illumination, proving that CIS can be used as very efficient photocatalyst for cationic dyes.  $\bullet\text{O}_2^-$  radicals are identified as main reactive species in process of photodegradation of de-ethylated intermediates.

## Acknowledgement

Financial support for this study was granted by the Ministry of Education, Science and Technological Development of the Republic of Serbia (Project III45020).

## REFERENCE

- [1] Q.Zhou, Z. Zheng, Y. Zhang, S. Kang, X. Li, J. Mu, Mat. Lett. 2014, 124, 61–63
- [2] T. Liu, L. Wang, X. Lu, J. Fan, X. Cai, B. Gao, R. Miao, J. Wang, Y. Lv, RSC Adv. 2017, 7, 12292-12300
- [3] S. Liu, K. Yin, W. Ren, B. Cheng, J. Yu, J. Mater. Chem. 2012, 22, 17759-17767.

## HPLC-DAD STUDY OF CATECHOL AUTOXIDATION IN THE PRESENCE OF Mg(II) AND Ca(II) IONS

G. M. Nikolić<sup>1</sup> and S. C. Živanović<sup>2</sup>

<sup>1</sup> *Department of Chemistry, Faculty of Medicine, University of Niš, Bulevar dr Zorana Đinđića 81, 18000 Niš, Serbia. (goranhem@yahoo.com)*

<sup>2</sup> *Research Center for Biomedicine, Faculty of Medicine, University of Niš, Bulevar dr Zorana Đinđića 81, 18000 Niš, Serbia.*

### ABSTRACT

High performance liquid chromatography with diode-array detection (HPLC-DAD) was applied to study the influence of Mg(II) and Ca(II) ions on catechol autoxidation in weakly alkaline aqueous solution. Both Mg(II) and Ca(II) ions greatly enhanced autoxidation rate of catechol at pH 8.4. However, Mg(II) ions had stronger influence in the initial phase of autoxidation and Ca(II) ions displayed stronger influence at the later phase of reaction. Based on the DAD UV-Vis spectra of two autoxidation products obtained from catechol in either absence or presence of metal ions we concluded that they have quinoid structures. Catechol autoxidation in the presence of both Mg(II) and Ca(II) ions leads to the formation of some products not obtained in the absence of these ions.

### INTRODUCTION

Catechol (1,2-benzenediol) moiety is an integral part of many plant polyphenols and drugs and due to its ease of oxidation and autoxidation it may be regarded responsible to the great extent for their biological activities [1,2]. Oxidation and autoxidation of catechol(s) was also recently considered in the design of wet adhesive materials [3].

The most important factors influencing catechol(s) autoxidation are pH value [3,4] and presence of metal ions [5-9]. Increase of pH value greatly enhances catechol autoxidation rate [3] and so does the presence of transition metal ions at very low (catalytic) concentrations [5]. On the other hand, earth alkaline ions, like Mg(II) and Ca(II), exert this effect at much higher concentrations [7,8] but their influence may be very important due to their ubiquitous presence in the environment and all living organisms.

Most studies of catechol autoxidation were concerned with reaction kinetics and little attention has been paid to the nature of reaction products. For that reason we decided to apply high performance liquid chromatography

with diode-array detection (HPLC-DAD) to study the influence of Mg(II) and Ca(II) ions on catechol autoxidation in weakly alkaline aqueous solution.

### EXPERIMENTAL

All the chemicals used in this study were of analytical (p.a.) grade except acetonitrile which was HPLC grade. Catechol (Merck, Germany) was used without additional purification since its purity was proved to be satisfactory by HPLC. Solutions of catechol ( $0.5 \text{ mmol dm}^{-3}$ ) were prepared just before the use from stock solution ( $10 \text{ mmol dm}^{-3}$  in  $0.1 \text{ mol dm}^{-3}$  HCl obtained by dissolving exactly weighed amount of catechol) by dilution with deionized, air saturated, water. TRIS buffer ( $100 \text{ mmol dm}^{-3}$ , pH 8.4) without metal ions or TRIS-M(II) buffers containing  $0.2 \text{ mol dm}^{-3}$  of  $\text{MgCl}_2$  or  $\text{CaCl}_2$  were used for the experiments. Autoxidation of catechol was initiated by mixing catechol solutions with equal volume of TRIS or TRIS-M(II) buffer.

An Agilent Technologies 1200 Series liquid chromatography system equipped with a diode-array detector (DAD) was employed for HPLC analyses. Separation was achieved by using Purospher STAR RP-18e column ( $150 \times 4.6 \text{ mm}$ ,  $5 \mu\text{m}$ , Merck, Germany) at  $30 \text{ }^\circ\text{C}$ . Gradient elution was employed with 0.1% aqueous trifluoroacetic acid as mobile phase A and acetonitrile as mobile phase B. The sample injection volume was  $10 \mu\text{L}$  and the mobile phase flow rate was  $0.5 \text{ mL/min}$ . The chromatograms were recorded at detection wavelengths of  $220 \text{ nm}$ ,  $275 \text{ nm}$ , and  $320 \text{ nm}$ .

### RESULTS AND DISCUSSION

Chromatograms of reaction mixtures obtained after 90 minutes of catechol autoxidation at pH 8.4 in the absence and presence of Mg(II) and Ca(II) ions are shown in Fig. 1. The most prominent chromatographic peak in all three systems at retention time (RT) of 15.8 minutes belongs to catechol. In the chromatogram of CAT system only two chromatographic peaks of autoxidation products with RT values of 6.25 and 14.1 minutes respectively, are present, while chromatograms of CAT-Mg(II) and CAT-Ca(II) systems, beside these two chromatographic peaks, contain more chromatographic peaks not present in the chromatogram of CAT system. It is evident that catechol peak area is much smaller in CAT-Mg(II) and CAT-Ca(II) systems in comparison to the system where catechol autoxidation was performed in the absence of metal ions (CAT).

The dependence of relative catechol HPLC peak area on autoxidation time is given in Fig. 2. Both Mg(II) and Ca(II) ions greatly enhanced catechol consumption and some differences in their influence may be attributed to the differences in their charge/(ionic radius) ratios [8].

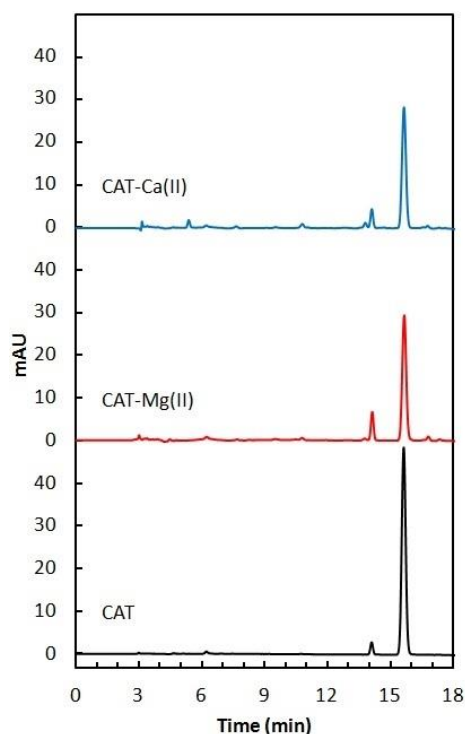


**Figure 1.** Chromatograms of reaction mixtures after 90 minutes of catechol autoxidation (detection at 275 nm).

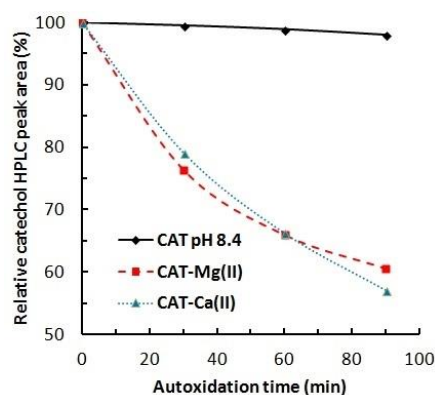


**Figure 2.** Catechol consumption during the autoxidation in various systems.

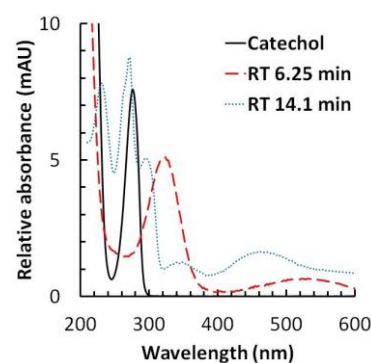


**Figure 3.** DAD UV-Vis spectra of catechol and two common autoxidation products.

DAD UV-Vis spectra of catechol and two compounds present in all three investigated systems (at RT of 6.25 and 14.1 minutes) are shown in Fig. 3. Increased absorbance of these two autoxidation products above 400 nm is a consequence of further electron delocalization which may be indicative for the formation of quinoid compounds during catechol autoxidation [7].

## CONCLUSION

HPLC-DAD study of catechol autoxidation at pH 8.4 revealed that presence of both Mg(II) and Ca(II) ions greatly enhanced the autoxidation rate with Mg(II) ions having stronger influence in the initial phase of autoxidation and Ca(II) ions displaying stronger influence at the later phase of reaction. DAD UV-Vis spectra of two common autoxidation products obtained from catechol

in either absence or presence of metal ions indicated the formation of quinoid structures. Catechol autoxidation in the presence of both Mg(II) and Ca(II) ions leads to the formation of some products not obtained in the absence of these ions.

### ***Acknowledgement***

This work was partially supported by the Ministry for Science and Technological Development of the Republic of Serbia (Grant no. 172044).

### **REFERENCES**

- [1] S. Quideau, D. Deffieux, C. Douat-Casassus, L. Pouységu, *Angewandte Chemie International Edition*, 2011, **50**, 586-621.
- [2] D. P. Yang, H. F. Ji, G. Y. Tang, W. Ren, H. Y. Zhang, *Molecules*, 2007, **12**, 878-884.
- [3] G. P. Maier, C. M. Bernt, A. Butler, *Biomaterials Science*, 2018, **6**, 332-339.
- [4] M. Friedman, H. S. Jürgens, *Journal of Agricultural and Food Chemistry*, 2000, **48**, 2101-2110.
- [5] J. Balla, T. Kiss, R. F. Jameson, *Inorganic Chemistry*, 1992, **31**, 58-62.
- [6] P. García, C. Romero, M. Brenes, A. Garrido, *Journal of Agricultural and Food Chemistry*, 1996, **44**, 2101-2105.
- [7] G. M. Nikolić, P. I. Premović, R. S. Nikolić, *Spectroscopy Letters*, 1998, **31**, 327-333.
- [8] A. V. Lebedev, M. V. Ivanova, A. A. Timoshin, E. K. Ruuge, *ChemPhysChem*, 2007, **8**, 1863-1869.
- [9] E. Nikhili, M. Loonis, S. Mihai, H. El Hajji, O. Dangles, *Food & Function*, 2014, **5**, 1186-1202.

## ENHANCED PHOTO(ELECTRO)CATALYTIC PROPERTIES OF ZnO PARTICLES SYNTHESIZED BY CTAB-ASSISTED MICROWAVE PROCESSING

S. B. Marković<sup>1</sup>, I. Stojković-Simatović<sup>2</sup>, S. Ahmetović<sup>2</sup>, Lj. Veselinović<sup>1</sup>, S. Stojadinović<sup>3</sup>, V. Rac<sup>4</sup>, S.D. Škapin<sup>5</sup> and D. Uskoković<sup>1</sup>

<sup>1</sup>*Institute of Technical Sciences of SASA, Knez Mihailova 35/IV, 11000 Belgrade, Serbia. (smilja.markovic@itn.sanu.ac.rs)*

<sup>2</sup>*University of Belgrade, Faculty of Physical Chemistry, Belgrade, Serbia.*

<sup>3</sup>*University of Belgrade, Faculty of Physics, Belgrade, Serbia.*

<sup>4</sup>*University of Belgrade, Faculty of Agriculture, Belgrade, Serbia.*

<sup>5</sup>*Jožef Stefan Institute, Ljubljana, Slovenia.*

### ABSTRACT

ZnO/CTAB powder was prepared by microwave processing of a precipitate with the aid of cetyltrimethylammonium bromide (CTAB). The effects of CTAB on the crystal structure, morphology, optical and photo(electro)catalytic properties of ZnO particles were studied. The results showed that CTAB did not influence crystal structure or phase purity of ZnO. However, even low concentration of CTAB varies particles morphology; cone-like particles were prepared by processing without CTAB, while a mixture of spheroidal and plate-like ZnO particles were produced when 0.001 M CTAB was used. It was found that synthesized ZnO powders have ~0.10 eV lower band gap energy than bulk ZnO (3.37 eV). A high photocatalytic activity for decolorization of methylene blue water solution was established after 2 h of sunlight irradiation; efficiency was 100 and 67% for ZnO/CTAB and ZnO, respectively. Electrochemical test showed faster oxygen evolution kinetics when ZnO/CTAB was used as anode material. Enhanced photo(electro)catalytic activities of ZnO/CTAB particles are attributed to better absorption of visible light due to both, larger dimensions and surface sensitization by CTAB.

### INTRODUCTION

Heterogeneous photocatalysis is recognized as an effective process for mineralization of a wide variety of organic and biological pollutants from drinking and wastewater [1]. Due to their high photoactivity and chemical inertness, semiconductors such as ZnO, TiO<sub>2</sub>, SnO<sub>2</sub>, etc. can be used to initiate photoreaction. Their application for the degradation of pollutants under direct sunlight irradiation is restricted by a wide band gap (> 3 eV),

allowing the absorption of UV light only. Such disadvantage can be overcome by particles' surface sensitization [1]. In this research, CTAB was used as surfactant to modify ZnO particles' surface; its influence on the optical and photo(electro)catalytic properties of ZnO powder was examined.

## EXPERIMENTAL

ZnO powders were prepared by microwave (MW) processing of a precipitate. The starting materials were ZnCl<sub>2</sub>, NaOH, and CTAB as a surfactant. After the dissolution of zinc chloride and CTAB, an adequate amount of the aqueous solution of NaOH was added dropwise, resulting in a white precipitate. The as-prepared suspension was MW processed for 5 min in a domestic oven (2.45 GHz, 800 W). The powders synthesized without and with surfactant are designated as ZnO and ZnO/CTAB, respectively.

The phase purity and crystal structure were identified by XRD analysis (Philips PW-1050). The data were collected over a  $2\theta$  range 10–70° with a step of 0.05° and a counting time of 5s. The particles morphology was observed by FE-SEM (ULTRA plus, Carl Zeiss). Optical properties were studied by UV-Vis diffuse reflectance (DR) (Thermo Scientific) and photoluminescence (PL) spectroscopy (Horiba Jobin Yvon).

The photocatalytic activity of ZnO particles was studied by the decolorization of methylene blue (MB) dye under direct sunlight irradiation. In each of the experiments 100 mg a powder was mixed with 100 ml of MB (10 ppm). Prior to sunlight irradiation, the suspension was magnetically stirred for 1 h in a dark to establish an adsorption-desorption equilibrium. Stirring was maintained during irradiation, too. At specific time intervals 3 ml of aliquots was withdrawn and centrifuged at 8000 rpm during 5 min. The concentration of MB after photocatalytic decomposition was determined by UV-Vis spectrophotometry (GBC Cintra) in the wavelength range of 450–750 nm. Electrochemical characterization was performed by the linear sweep voltammetry in the three-electrode quartz cell using Gamry PCI4/750. FTO glass coated by ZnO particles was used as the working electrode; Pt foil and saturated calomel electrode (SCE) were used as the counter and the reference electrode, respectively. An aqueous solution of 1 M KCl was used as the electrolyte. The scan rate was 20 mV·s<sup>-1</sup>.

## RESULTS AND DISCUSSION

The XRD patterns of ZnO and ZnO/CTAB particles are shown in **Figure 1(a)**. The patterns indicate wurtzite hexagonal symmetry without other crystal phases or impurities. However, minor differences in the XRD patterns on their reflection ratios, especially on I(100)/I(002)/I(101), implicating the differently oriented crystallites growth. This assumption is confirmed by the

FE–SEM analyses, **Figure 1(b-c)**. ZnO crystallites are organized in cone-shaped particles with the average length of 93 nm, while ZnO/CTAB powder is consisted of spheroidal particles with average diameter of 36 nm; the particles are scatterely organized in thin plate-like agglomerates with average width of 260 nm and thickness of 20 nm.

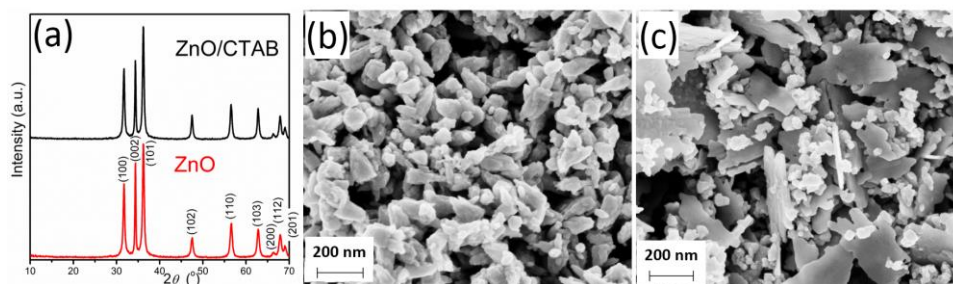


**Figure 1.** (a) XRD patterns, (b-c) FE–SEM images of ZnO and ZnO/CTAB particles, respectively.

The optical properties of processed powders were examined by UV–Vis DR and PL spectroscopy, **Figure 2**. In the visible light region ZnO/CTAB particles revealed ~5% higher absorbance capacity than ZnO particles, **Figure 2(a)**. The direct band gap energies, determined from Tauc plot, are about 3.25 eV with neglected difference. Two emission bands appeared in PL spectra of examined powders, **Figure 2(b)**, at 410 and 620 nm, and can be attributed to surface and deep-level defects, respectively. PL spectra implicate that ZnO/CTAB particles contained larger number of surface defects than ZnO particles, while number of structural defects is reduced.

**Figure 2(c)** shows the efficiency of the photocatalytic degradation of MB dye in the presence of examined powders. ZnO/CTAB shows 100% of efficiency after 2h of direct sunlight irradiation, while the efficiency of ZnO was 67%. The linear sweep voltammograms under dark was shown in **Figure 2(d)**. The oxygen evolution potential values were 1.315 and 1.324 V vs. SCE for ZnO/CTAB and ZnO, respectively. Thus, applying ZnO/CTAB as anode reduces the potential value for oxygen evolution. Besides, the anodic current at 1.35 V vs. SCE was increased when ZnO/CTAB was used as anode, indicating faster oxygen evolution kinetics comparing with ZnO.

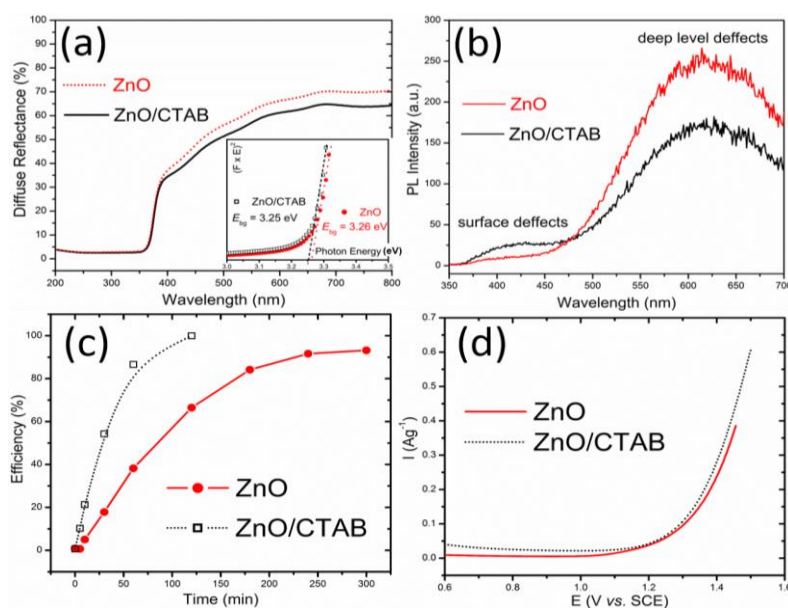


**Figure 2.** (a) UV–Vis DR spectra with inserted Tauc plots, (b) PL spectra of examined powders, (c) photocatalytic efficiency for the degradation of MB in the presence of examined powders, and (d) linear sweep voltammograms.

## CONCLUSION

ZnO/CTAB powder prepared by a microwave processing consists mixture of spheroidal and plate-like particles with distinguished amount of surface defects. The band gap energy of ZnO/CTAB powder is 3.25 eV; in the Vis range it absorbs up to 70% of the incident light intensity. The plate-like particles' morphology combined with surface defects enhanced visible-light absorption and promoted photocatalytic activity under direct sunlight irradiation. Applying of ZnO/CTAB as anode material reduces the potential for oxygen evolution and the oxygen evolution kinetics become faster.

## Acknowledgement

This study was supported by the Ministry of Education, Science and Technological Development of the Republic of Serbia, Grant no III45004.

## REFERENCES

- [1] S. Marković, V. Rajić, A. Stanković, Lj. Veselinović, J. Belošević-Čavor, K. Batalović, N. Abazović, S.D. Škapin D. Uskoković, *Solar Energy*, 2016, 127, 124-135.

## THE EFFECT OF AEROSOL-DEPOSITED ASH COMPONENTS ON A COBALT-BASED FISCHER-TROPSCH CATALYST

Lj. Gavrilović<sup>1</sup>, J. Brandin<sup>2</sup>, A. Holmen<sup>1</sup>, H. J. Venvik<sup>1</sup>, R. Myrstad<sup>3</sup> and E. A. Blekkan<sup>1</sup>

<sup>1</sup>*Norwegian University of Science and Technology, Department of Chemical Engineering, Sem Sælands vei 4, 7491 Trondheim, Norway.  
(ljubisa.gavrilovic@ntnu.no)*

<sup>2</sup>*Linnæus University, Department of Built Environment and Energy Technology, 351 95 Växjö, Sweden.*

<sup>3</sup>*SINTEF Industry, NO-7465 Trondheim, Norway.*

### ABSTRACT

The effect of ash salts on Co-based Fischer-Tropsch catalysts was studied using an aerosol deposition technique. Catalyst characterization did not reveal significant differences in cobalt dispersion, reducibility, surface area, pore size, or pore volume between the unpoisoned sample and the poisoned catalysts. The activity declined with increasing ash concentration. The selectivity towards heavier hydrocarbons (C<sub>5+</sub>) was slightly increased with increasing ash loading, while the CH<sub>4</sub> and CO<sub>2</sub> selectivity was reduced for all the treated samples.

### INTRODUCTION

Biomass to liquid fuels (BTL) via gasification and Fischer-Tropsch synthesis (FTS) is an attractive process for production of liquid fuels (diesel and jet fuel)[1]. The process involves gasification of biomass where synthesis gas (CO + H<sub>2</sub>) is produced. Following cleaning and gas conditioning, the synthesis gas is converted to hydrocarbons *via* the Fischer-Tropsch synthesis. During biomass gasification, the inorganic species are usually converted into bottom ash or fly ash. Imperfections in the cleaning section or poor design can allow the presence of these components in the produced syngas. Deactivation of Co based Fischer-Tropsch (FT) catalyst by alkali species is known from before[2,3]. In previous communications [4,5] we have shown that aerosol deposition of potassium salts lead to deactivation of a Co-based catalyst while it was however difficult to observe any measurable change in the catalyst characteristics following deposition. This implies that the deactivating species is somehow transported to the active sites of the catalyst during pretreatment or reaction. In this communication we aim to investigate

the influence of impurities present in the real feed, by collecting a sample of fly ash from burning charcoal and depositing this ash on a cobalt-based FTS catalyst. The produced ash was expected to contain a realistic mixture of inorganic contaminants, which potentially can reach the FTS catalyst in a BTL plant.

### EXPERIMENTAL

The reference catalyst (20%Co/0,5%Re/ $\gamma$  Al<sub>2</sub>O<sub>3</sub>, for the detailed description of catalyst synthesis see[4]) was poisoned using the aerosol deposition technique[6]. A solution of the ash salt was atomized carried over the catalyst sample. In order to investigate different concentration levels, the deposition time was varied (30, 60 and 300 minutes) with corresponding samples names Ash1, Ash2 and Ash3, respectively. A scanning mobility particle sizer (SMPS; TSI Inc.) was used to physically characterize aerosol particles according to their electrical mobility[6]. This technique provides an estimate of the particle size distribution. Inductively coupled plasma (ICP-MS) was used to determine ppm levels of ash components. Poisoned catalysts were characterized using standard characterization techniques (H<sub>2</sub>-chemisorption, BET, Temperature Programmed Reduction)[2]. Fischer–Tropsch synthesis was carried out in four parallel 10 mm ID steel tube fixed bed reactors at 483 K, 20 bar and H<sub>2</sub>/CO ratio of 2,1. A detailed description can be found elsewhere[5].

### RESULTS AND DISCUSSION

The generated aerosol particles from ash salt have been characterized by SMPS with the mass average diameter around 400 nm. The ash-salt particle size is significantly larger than the average pore-size of the material (approx. 13.3 nm), suggesting deposition on the external surface of the catalyst particles. As it was expected potassium is the dominant element, but there are also significant concentrations of sulfur and chlorine found by ICP-MS.

Key characterization results are as follows: all the poisoned samples showed the same dispersion (approx. 7.5%), surface area (approx. 135 m<sup>2</sup>/g), pore size (approx. 13.3 nm) and pore volume (0.47 cm<sup>3</sup>/g), all close to the values measured for the reference catalyst. All the samples showed almost the same TPR profile previously observed for alumina-supported cobalt catalysts[2]. This is in agreement with the previous work[4] where different pure potassium salts were deposited on the Co based catalyst using the same technique applied here.

**Table 1.** Catalyst activity

Sample	K level (ppm)	STY (s <sup>-1</sup> )	C <sub>5+</sub> (%)	CH <sub>4</sub> (%)	CO <sub>2</sub> (%)
Reference	0	0.046	84.0	7.6	0.21
Ash1	233	0.046	84.5	7.67	0.23
Ash2	520	0.039	84.4	7.51	0.29
Ash3	1677	0.040	85.0	7.37	0.37

Catalyst activity reported as STY (site time yield) together with the selectivities to C<sub>5+</sub>, CH<sub>4</sub> and CO<sub>2</sub> are presented in Table 1. The sample with the shortest exposure to the ash salts (Ash1) showed the same activity as the reference catalyst, while the samples with longer exposure and higher concentrations of ash components showed a small but significant loss in activity. The selectivity towards higher hydrocarbons and CO<sub>2</sub> increases with increasing ash concentration, while the methane selectivity decreased. These selectivity changes are similar to those observed previously using pure potassium salts [2–5]. The combined evidence indicates that also in the case of aerosol deposition of mixed ash salts is there a significant effect on the cobalt FTS catalyst, but the effect is less severe than that observed for pure potassium salts. This could be linked with the physical nature of the particles, the particles are significantly larger than those deposited from pure potassium salts, and the transport of alkali and other species from the external surface to the internal surface of the catalysts is probably more difficult, either because of the physical distance or that the activation and transport of the ash components is slower due to the larger particles.

## CONCLUSION

A cobalt-based FTS catalyst was exposed to solid aerosol particles of typical biomass ash components. The characterization revealed no significant differences in dispersion, reducibility, surface area, pore size or pore volume while the FTS activity was slightly reduced, and the selectivity altered in the same direction as observed with pure potassium salts, indicating that deactivating species somehow is transported to the cobalt active centers responsible for FTS.

## Acknowledgements

Financial support from The Research Council of Norway under contract no. 228741 is gratefully acknowledged.

**REFERENCES**

- [1] E. van Steen, M. Claeys, *Chem. Eng. Technol.* 31, 2008, 655–666.
- [2] C.M. Balonek, A.H. Lillebø, S. Rane, E. Rytter, L.D. Schmidt, A. Holmen, *Catal. Letters*. 138, 2010, 8–13.
- [3] A.H. Lillebø, E. Patanou, J. Yang, E.A. Blekkan, A. Holmen, *Catal. Today*, 2013, 60–66.
- [4] L. Gavrilović, J. Brandin, A. Holmen, H.J. Venvik, R. Myrstad, E.A. Blekkan, *Ind. Eng. Chem. Res.* 57, 2018, 1935–1942.
- [5] L. Gavrilović, J. Brandin, A. Holmen, H.J. Venvik, R. Myrstad, E.A. Blekkan, *Appl. Catal. B Environ.* 230, 2018, 203–209.
- [6] J. Einvall, S. Albertazzi, C. Hulteberg, A. Malik, F. Basile, A.C. Larsson, J. Brandin, M. Sanati, *Energy and Fuels*. 21, 2007, 2481–2488.

## ZnFe-MIXED METAL OXIDES AS EFFICIENT AND PROMISING PHOTOCATALYSTS

M. Hadnadev-Kostić<sup>1</sup>, J. Dostanić<sup>2</sup>, T. Vulić<sup>1</sup> and A. Jokić<sup>1</sup>

<sup>1</sup> *University of Novi Sad, Faculty of Technology, Bul. cara Lazara 1, 21000 Novi Sad, Serbia. (hadnadev@tf.uns.ac.rs)*

<sup>2</sup> *University of Belgrade, Serbian National Institute, Institute of Chemistry, Technology and Metallurgy Belgrade, Department of Catalysis and Chemical Engineering, Njegoševa 12, 11000 Belgrade, Serbia.*

### ABSTRACT

ZnFe photocatalysts have been increasingly investigated in wastewater purification due to the high demands in this field, such as activity, selectivity, toxicity, cost and stability. The presented study is focused on the synthesis and characterization of ZnFe mixed metal oxides, and their application in photocatalytic degradation of organic dye pollutant Rhodamine B (RhB) in aqueous solution under simulated solar light irradiation. The mixed metal oxides were composed of wurzite ZnO phases and after thermal treatment the formation of the spinel-structured ZnFe<sub>2</sub>O<sub>4</sub> phase was observed. It was detected that the photocatalyst with the additional spinel phase exhibited superior photocatalytic activity probably due to better crystallinity leading to broader light absorption.

### INTRODUCTION

Exponential increase of environmental pollution with no systematic solution has become an overwhelming concern in the scientific community [1]. One of major organic pollutants are residual dyes from different industries, and considering their toxicity, unpleasant coloring and non-biodegradation these pollutants are sought to be extremely hazardous to the environment [2]. Therefore effective removal methods present a challenging as well as motivating task that need to be addressed with great precision in order to decrease or completely eliminate environmental problems regarding dye pollutants in wastewater [3]. One of the resourceful candidates in green environmental management has been cited as zinc oxide (ZnO) because of its wide band gap (3.2 eV) in the near-UV spectral region, strong oxidation ability, good photocatalytic property and low cost [2]. Additionally, coupling of ZnO and a semiconductor with a narrow energy band would possess a more enhanced photocatalytic activity that would be a route to the efficient exploitation of the visible light source.

The motivation for this investigation was to develop a simple and inexpensive synthesis method for ZnFe-mixed metal oxides with the desired properties in order to enhance photocatalytic performances in the photodegradation of organic dyes.

### EXPERIMENTAL

Mixed metal oxides were synthesized by the coprecipitation method using  $\text{Zn}(\text{NO}_3)_2 \cdot 6\text{H}_2\text{O}$  and  $\text{Fe}(\text{NO}_3)_3 \cdot 9\text{H}_2\text{O}$  precursors that were added in the base solution (0.67 M  $\text{Na}_2\text{CO}_3$  and 2.25 M  $\text{NaOH}$ ) and vigorously stirred at constant temperature (40°C). The precipitates were aged and then washed with deionized water until pH 7 was reached. The products were dried for 24 h at 100°C (sample denoted as ZnFe-100) and thermally treated for 5 h at 500°C (denoted as ZnAl-500).

X-ray powder diffraction (XRD) analysis was used for the interpretation of the phase composition, conducted by Rigaku MiniFlex 600. Photocatalytic tests were performed in an open cylindrical thermostated Pyrex reaction vessel using ULTRA VITALUX 300 W lamp, which emission spectrum simulates solar light. Before illumination, reaction mixtures (50 mg of catalysts and 100 ml of 10 M RhB solution) were stirred in the dark for 30min to ensure adsorption/desorption equilibrium. The reaction solutions were then stirred under light source and aliquots were analyzed at the defined time intervals using UV-VIS spectrophotometer. The photocatalytic activity was estimated by RhB photodegradation, monitoring the decrease of the RhB concentration in time.

### RESULTS AND DISCUSSION

XRD diffraction peaks of the photocatalysts are presented in **Figure 1(a)**. For sample ZnFe-100 sharp intense diffraction peaks were observed at 31.79°; 34.4°; 36.25°; 47.5°; 56.6°; 62.85° i 67.97° that correspond to (100), (002), (101), (102), (110), (103) i (112) crystalline lattice for the ZnO phase [4].

After thermal treatment at 500°C the formation of additional spinel phase  $\text{ZnFe}_2\text{O}_4$  with the cubic structure was detected at  $0.05^\circ$ ,  $35.36^\circ$ ,  $42.78^\circ$ ,  $52.96^\circ$ ,  $56.78^\circ$  and  $62.2^\circ$  [5]. Thermal treatment provoked the formation of the spinel phase that has been cited as the phase that enhances photocatalytic properties of the photocatalyst.

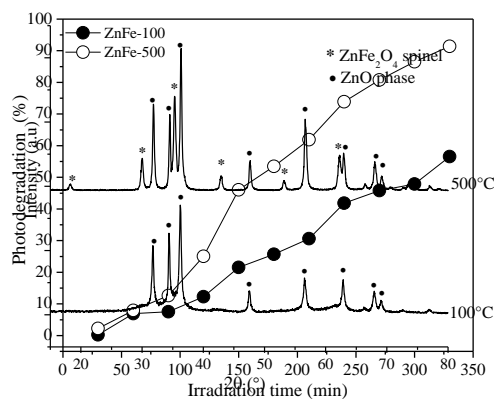


**Figure 1.** (a) XRD patterns of ZnFe-100 and ZnFe-500, (b) RhB photodegradation tests.

The photocatalytic degradation of prepared catalysts is presented in **Figure 1 (b)**. The thermally activated photocatalyst (ZnFe-500) exhibited higher activity compared to ZnFe-100. The enhanced photocatalytic activity could be ascribed to the formation of

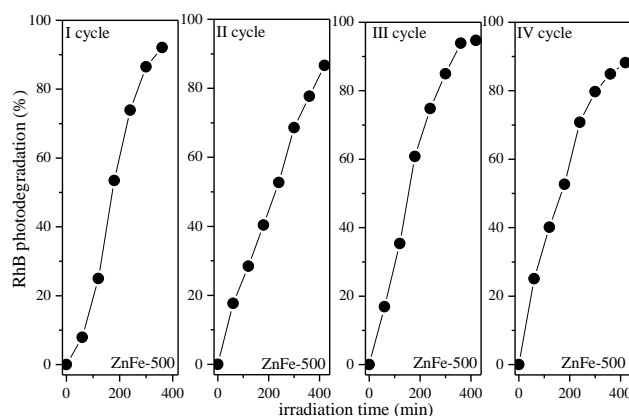


**Figure 2.** Recycling tests of ZnFe-500 for RhB photodegradation under solar irradiation.

additional  $\text{ZnFe}_2\text{O}_4$  spinel phase after thermal treatment. In order to determine the stability of the ZnFe-500, repeated degradation reactions were performed (**Figure 2**). It was observed that the photocatalyst did not display any significant loss of activity after four consecutive reaction cycles indicating excellent stability of the investigated photocatalyst.

## CONCLUSION

The ZnFe-500 catalyst, comprised of wurzite ZnO phases and spinel structured ZnFe<sub>2</sub>O<sub>4</sub>, had better crystallinity and enhanced photocatalytic activity in the RhB photodegradation compared to ZnFe-100. The results showed that the ZnFe<sub>2</sub>O<sub>4</sub> spinel phase conclusively impacts the photocatalytic efficiency due to the synergic coupling effect of ZnO and ZnFe<sub>2</sub>O<sub>4</sub>. Additionally, the photocatalyst did not exhibit any significant loss of activity after four consecutive reaction cycles indicating satisfactory stability.

## Acknowledgement

This work was partially supported by the Ministry for Science of the Republic of Serbia (Grants no. OI 172022 and III45001).

## REFERENCES

- [1] M. Hadnadjev-Kostic, T. Vulic, R. Marinkovic-Neducin, D. Loncarevic, J. Dostanic, S. Markov, Dusan Jovanovic, *Journal of Cleaner Production*, 2017, **164**, 1-18.
- [2] Q Yang, S. Wang, F. Chen, K. Luo, J. Sun, C. Gong, F. Yao, X. Wang, J. Wu, X. Li, D. Wang, G Zeng, *Catalysis Communications*, 2017, **99**, 15-19.
- [3] D. Zhang, *Acta Chimica Slovaca*, 2013, **6**, 1, 141-149.
- [4] P. Geetha Devi, A. Sakthi Velu, *Journal of Theoretical and Applied Physics*, 2016, **10**, 233-240.
- [5] C. G. Anchietta, A. Cancelier, M. A. Mazutti, S. L. Jahn, R. C. Kuhn, A. Gündel, O. Chiavone-Filho, E. L. Foletto, *Materials*, 2014, **7**, 6281-6290.

## PHOTOCATALYTIC HYDROGEN PRODUCTION OVER NICKEL MODIFIED TITANIA CATALYSTS

J. Dostanić and D. Lončarević

*University of Belgrade, Serbian National Institute, Institute of Chemistry,  
Technology and Metallurgy,  
Njegoševa 12, 11000 Belgrade, Serbia.  
([jasmina@nanosys.ihtm.bg.ac.rs](mailto:jasmina@nanosys.ihtm.bg.ac.rs))*

### ABSTRACT

The development of efficient, low cost semiconductor materials for photocatalytic H<sub>2</sub> production from water using sunlight is a main challenge toward a sustainable hydrogen economy. In this study, the photocatalytic H<sub>2</sub> production from aqueous isopropanol solution has been investigated over nickel modified TiO<sub>2</sub> catalysts. Series of catalysts were prepared by deposition-precipitation method under different synthetic conditions (type of precipitating agent, reduction temperature, *etc*). Among all modified catalysts, the catalyst prepared at 400 °C by reduction of carbonate precursor exhibited the highest photocatalytic activity. The results indicate that the proper choice of reduction temperature and precursor type results in improved photocatalytic efficiency of prepared nickel modified catalysts.

### INTRODUCTION

Increased industrialization and population growth has led to increase in global energy consumption. Fossil fuels still dominate world energy supply, leading to high emission of greenhouse gasses. Therefore, it is imperative to develop new and renewable alternative sources of energy to attenuate the negative effects of fossil fuel consumption. Due to its unique properties, hydrogen is considered as an ideal promising alternative to the conventional fossil fuels. Since the seminal paper from Fujishima and Honda in 1972, the production of H<sub>2</sub> by photocatalytic water splitting has been extensively investigated. Photocatalytic water splitting is perspective method since it offers carbon free route with good economical feasibility and potential to achieve high theoretical solar-to-H<sub>2</sub> efficiencies [1].

As known, TiO<sub>2</sub> is the most widely used semiconductor in environmental photocatalytic applications owing to its superior physical and chemical properties. However, pristine TiO<sub>2</sub> shows low efficiencies for H<sub>2</sub> production, and additional modification is necessary for catalyst activity improvement. In the recent years low-cost transition metals or metal oxides have been applied

as a promising alternative to expensive noble metals co-catalysts for light-induced hydrogen generation [2].

In this study, the photocatalytic hydrogen production performance of Ni modified TiO<sub>2</sub> catalysts, which were prepared by deposition-precipitation method, was investigated. The goal of this work is to better understand how variables such as type of precipitating agent and reduction temperature affect the reducibility, nickel dispersion and photocatalytic performance of prepared catalysts.

### EXPERIMENTAL

Nickel modified TiO<sub>2</sub> catalysts with 1wt% Ni were synthesized by deposition-precipitation method. The first series of catalysts (labeled as Ni/P25-x, where x designates reduction temperature) was prepared by following procedure: nickel(II) nitrate hexahydrate and glycerol were added to distilled water, and Evonik Aeroxide TiO<sub>2</sub> P25 was then added to this solution following by dropwise addition 0.5 M NaOH, until a pH of 12 was reached. The suspension was stirred for another 1 h, filtered by vacuum filtration and dried at 70 °C. The second series of the catalysts were prepared using Na<sub>2</sub>CO<sub>3</sub> as a precipitating agent (labeled as Ni-C/P25-x). Both series of catalysts were finally obtained by reduction of precursors under 5% H<sub>2</sub>/Ar flow at 400 °C or 500 °C for 2h (10 °C/min).

Temperature-programmed reduction (TPR) profiles were obtained by passing a flow of 5% H<sub>2</sub>/Ar at a rate of 20 ml/min through the sample (app. 50 mg). The H<sub>2</sub> chemisorption was measured at 45 °C by introducing pulses of H<sub>2</sub> with a volume of 0.353 ml into the argon flow. The pulses were continued until no further uptake of H<sub>2</sub> was measured. The dispersion of nickel was calculated from the H<sub>2</sub> uptake.

The photocatalytic tests were performed in photocatalytic reactor (Ace Glass), equipped with low pressure mercury lamp, whose emission spectrum simulates solar radiation. Before irradiation, the catalyst suspension (125 mg photocatalyst in 250 ml 1vol% isopropanol in water) was degassed for 60 min in Ar flow. After the lamp was switch on, the effluent gases were analyzed to quantify H<sub>2</sub> production by gas chromatography (Perkin Elmer F33 GC) using a TCD.

### RESULTS AND DISCUSSION

The characterization of reducibility of nickel species on catalysts are determined by TPR measurements carried out in the temperature range from 25 °C to 900 °C (Fig. 1a). The TPR profiles of carbonate and hydroxide precursors show a main peak centered at 293 °C and 322 °C respectively, which is assigned to reduction of nickel species. The intensity of the peak is

higher for the carbonate precursor than for hydroxide precursor, indicated higher extent of reduction at lower temperature for carbonate precursor. The occurrence of low intensity peaks at higher reduction temperatures suggests the existence of additional nickel phases or indicates different interactions between nickel ions and support during reduction process.

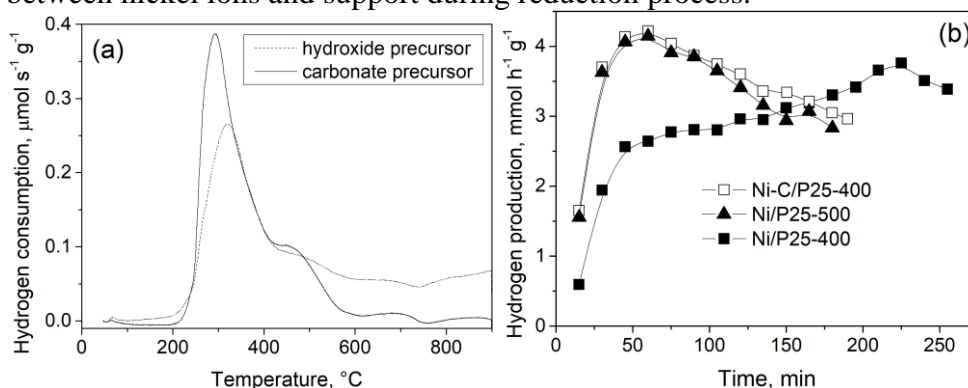


**Figure 1.** a) TPR profiles of carbonate and hydroxide precursors, b) H<sub>2</sub> production rate of prepared catalysts.

The obtained results revealed that nickel dispersion is linked to the type of precipitation agent. The sample obtained from hydroxide precursor show somewhat larger nickel dispersion (3.8 %) compared to its carbonate counterpart (3.2 %).

Photocatalytic H<sub>2</sub>-production activity of the prepared Ni modified catalysts was evaluated under simulated solar light using isopropanol as a sacrificial reagent (Table 1). The results clearly indicate that pristine TiO<sub>2</sub> exhibited low activity for H<sub>2</sub> production, probably due to rapid electron-hole

**Table 1.** H<sub>2</sub>-production activity rate

Sample	H <sub>2</sub> production rate [μmol g <sup>-1</sup> h <sup>-1</sup> ]
TiO <sub>2</sub> P25	200
Ni-C/P25-400	4218
Ni/P25-400	3759
Ni/P25-500	4144

recombination. The addition of metallic nickel exhibits a significant influence on the photocatalytic H<sub>2</sub>-production activity of TiO<sub>2</sub>. The enhanced activity of Ni modified catalysts is caused by suppression of electron-hole recombination, reduction of the overpotential of hydrogen production and

increased production of hydrogen by providing additional active sites for H<sub>2</sub> evolution. Fig. 1b shows plots of H<sub>2</sub> production versus time for prepared catalysts. The catalyst reduced at 500 °C from hydroxide precursor and catalyst reduced at 400 °C from carbonate precursor exhibited similar activity

for light induced H<sub>2</sub> generation. In addition, both catalysts showed higher activity than the catalyst reduced at 400 °C from hydroxide precursor. Reduction from hydroxide precursor at lower temperature yields a catalyst with lower amount of surface nickel, resulting in its lower activity. Fig. 1b revealed that the catalyst Ni/P25-400 showed prolonged period before maximal rate of H<sub>2</sub> production was achieved. This induction period can be correlated to photo reduction of NiO to metallic Ni, leading to formation of an additional amount of reduced nickel species and thus to enhancement of its activity. With the increase in quantity of reduced nickel, activity gets close to the activity of Ni-C/P25-400.

### CONCLUSION

The prepared Ni modified TiO<sub>2</sub> exhibited significantly improved activity toward hydrogen production compared to pristine TiO<sub>2</sub>. The quantity of reduced nickel ions is found to be appreciably enhanced by using sodium carbonate as precipitating agent, yielding its higher activity. Testing the influence of synthetic parameters (type of precursor, reduction temperature, *etc.*) suggests that the carbonate origin catalyst reduced at lower temperature is suitable choice to obtain maximal H<sub>2</sub> production. The use of carbonate precipitating agent allows lower temperatures to be employed in catalyst preparation, thus retaining its specific surface area and anatase structure.

### *Acknowledgement*

This work was partially supported by the Ministry of Education, Science and Technological Development of the Republic of Serbia (Grants no. III 45001).

### REFERENCES

- [1] C.-H. Liao, C.-W. Huang, J.C.S. Wu, *Catalysts*, 2012, **2**, 490-516.
- [2] W.-T. Chen, A. Chan, D. Sun-Waterhouse, T. Moriga, H. Idriss, G.I.N. Waterhouse, *Journal of Catalysis*, 2015, **326**, 43-53.

***D – Nonlinear Dynamics,  
Oscillatory Reactions, Chaos***



## USING STOICHIOMETRIC NETWORK THEORY TO IDENTIFY MECHANISMS OF NONLINEAR REACTIONS

I. Schreiber, F. Muzika, V. Radojković and L. Schreiberová

*University of Chemistry and Technology, Prague, Department of Chemical Engineering, Technická 5, 16628 Praha, Czech Republic.  
(igor.schreiber@vscht.cz)*

### ABSTRACT

We introduce a new method for estimation of unknown kinetic parameters. The method is based on matching experimental data at a saddle-node or an oscillatory instability with stoichiometric constraints of the mechanism formulated by applying stability theory of reaction networks. As an example, we apply the method to find unknown rate coefficients in a basic mass action model for urea-urease reaction displaying bistability. The found kinetic parameters are consistent with experimentally observed bistable dynamics. Our method can be applied to any reaction system with an experimentally observed dynamical instability.

### INTRODUCTION

Stoichiometric network analysis [1] is a method for examining stability of steady states of reaction networks bound by fixed stoichiometric relations among reacting species. Model equations of such systems possess a pseudolinear form enabling the network at steady state to be decomposed into elementary subnetworks, also known as elementary fluxes or extreme currents. The elementary subnetworks can be linearly combined using arbitrarily chosen non-negative coefficients, producing the full network. The role of these coefficients may be seen as to couple the subnetworks or express their contribution to the whole.

In this work, the role of coupling coefficients is explored to understand effects of individual subnetworks on dynamics of the whole network and to estimate unknown kinetic parameters by matching the network with available experimental data. SNA assumes power law dependence of fluxes on concentrations which allows for qualitative description of the system's dynamics in the vicinity of steady state. The elementary subnetworks, or subnetworks that are formed by combining certain elementary subnetworks, are tested for potential instability, which does not require knowledge of rate coefficients and steady state concentrations of participating species. Such instability is inherited by the entire network provided that the coupling of the

unstable subnetwork to the network is significant, or in other words, that the unstable subnetwork is dominant. Given the coupling coefficients of all subnetworks and preserving dominance of the unstable one, the actual instability is ensured when steady state concentrations for certain species occurring in the unstable subnetwork are small relative to concentrations of other species. [1]

Although this result of the SNA proved very useful in understanding the nature of chemical oscillators [2-7], when using a model of a reacting system in terms of component mass balances and kinetic rate expressions, the coupling coefficients and steady state concentrations (convex parameters), cannot be chosen freely. Rather, they must be consistent with (known) rate coefficients and inflow/initial constraints (kinetic parameters).

We are interested in a frequently met situation, where the kinetic parameters (particularly the rate coefficients) are only partly known, and there are experimental data available (inflow constraints, steady state concentrations of some species) indicating an instability of the steady state: either emergence of oscillations via a Hopf bifurcation or a bistable switch to another steady state via saddle-node bifurcation. An instability threshold can be easily found using convex parameters, but transition to relevant kinetic parameters is complicated by redundancy of convex parameters. Therefore SNA can state whether the given model is, in general, capable of exhibiting certain kind of instability, but it cannot precisely relate such predictions to a specific set of kinetic parameters.

Thus a complementary approach is needed, which would provide a relation between convex and kinetic parameters that could be used to estimate values of missing kinetic parameters in order to match the experimentally available data. In our previous work [8,9] we outlined such an approach and applied it to an oscillatory enzyme reaction. In this work briefly introduce the theory and show how it works when applied to a simple mass action model of urease bistable switch. The bistability was observed in continuous stirred tank reactor [10] and in urease loaded alginate beads placed in urea solution with addition of sulfuric acid using cresol red as pH indicator [11].

## THEORY

**Method for estimation of kinetic parameters.** Given that the model is formulated in terms of the stoichiometric network, we need to estimate unknown kinetic parameters necessary for occurrence of a subcritical Hopf bifurcation or a saddle-node bifurcation. To that end we use the stoichiometric network theory [1] and introduce a method of matching experimental results at the condition of emergence of oscillations with the stoichiometric

constraints imposed by the assumed mechanism. The entire reactor-reservoir system can be written as

$$\frac{d\mathbf{x}}{dt} = \mathbf{N}\mathbf{v}(\mathbf{x}), \quad (1)$$

where  $\mathbf{N}$  is the  $(n \times m)$  stoichiometric matrix,  $\mathbf{x} = (x_1, \dots, x_n)$  is the vector of concentrations of  $n$  dynamical species (inert products and buffered/pooled species are not included),  $\mathbf{v} = (v_1, \dots, v_m)$  is the vector of  $m$  reaction rates assumed to follow mass action kinetics.  $\mathbf{N}$  and  $\mathbf{v}$  accommodate all the inflows, outflows and membrane transport terms treated as pseudoreactions of zeroth or first order. For the species occurring in both the reactor and the reservoir there are separate components in  $\mathbf{x}$ . Also, different volumes of both subsystems are reflected in  $\mathbf{N}$ . The rate vector  $\mathbf{v}$  is expressed as  $\mathbf{v} = (k_1 \bar{v}_1, \dots, k_m \bar{v}_m) = \text{diag}(\mathbf{k}) \bar{\mathbf{v}}$ , where the vector  $\mathbf{k}$  includes the rate coefficients and  $\bar{\mathbf{v}}(\mathbf{x})$  is the vector of reduced rates. The set of all rate vectors  $\mathbf{v}_s = \mathbf{v}(\mathbf{x}_s)$  at a stationary state  $\mathbf{x}_s$  satisfies  $\mathbf{N}\mathbf{v}_s = \mathbf{0}$  and thus  $\mathbf{v}_s$  is restricted to the non-negative part of the null space of  $\mathbf{N}$  called the flux cone. According to the stoichiometric network theory<sup>20</sup> the set of all rate vectors  $\mathbf{v}_s$  can be expressed as

$$\mathbf{v}_s = \mathbf{E}\boldsymbol{\alpha}, \quad \boldsymbol{\alpha} = (\alpha_1, \dots, \alpha_f), \quad \alpha_k \geq 0, \quad (2)$$

where the columns of  $\mathbf{E}$  are the (normalized) edges of the flux cone. The edges represent irreducible subnetworks called extreme currents or elementary subnetworks/fluxes. Thus the steady state network  $\mathbf{v}_s$  is obtained as a non-negative linear combination of elementary subnetworks where  $\alpha_k$  represents a contribution of the  $k$ -th subnetwork.

For the purpose of parameter determination the rate coefficient vector  $\mathbf{k}$  and the steady state concentration vector  $\mathbf{x}$  (for convenience we drop the subscript denoting a steady state) can be split to three parts with: (i) fixed values, known or estimated, (ii) unknown values to be determined, and (iii) indeterminate values implied by solving for the unknowns,

$$\mathbf{k} = (\mathbf{k}^{(fv)}, \mathbf{k}^{(uv)}, \mathbf{k}^{(iv)}), \quad \mathbf{x} = (\mathbf{x}^{(fv)}, \mathbf{x}^{(uv)}, \mathbf{x}^{(iv)}). \quad (3)$$

Moreover,  $\mathbf{E}$  and  $\boldsymbol{\alpha}$  can be split into two parts,  $\mathbf{E} = [\mathbf{E}^{(uds)}, \mathbf{E}^{(uv)}]$  and  $\boldsymbol{\alpha} = (\boldsymbol{\alpha}^{(uds)}, \boldsymbol{\alpha}^{(uv)})$ , where  $\boldsymbol{\alpha}^{(uv)}$  corresponds to  $\mathbf{E}^{(uv)}$  and includes unknown

coefficients  $\alpha_k$  to be determined and  $\boldsymbol{\alpha}^{(uds)}$ ,  $\mathbf{E}^{(uds)}$  represent a preselected unstable dominant subnetwork (*uds*). The selection of *uds* is based on stability analysis of the elementary subnetworks [1] and selecting one (or combination of a few) that represent the decisive instability leading to the emergent dynamics observable in experiments, most notably to an oscillatory instability via a Hopf bifurcation. Then  $\boldsymbol{\alpha}^{(uds)}$  is playing the role of a bifurcation parameter that upon variation lets the system to pass through the bifurcation point. We can now formulate the constraint equations for a set of unknowns by selecting certain equations from eq 2 given that we can fix: (i) the entire reaction rate (by fixing both the rate coefficient and the relevant concentrations), (ii) reduced reaction rate (by measuring or estimating the relevant concentrations), (iii) expression derived from the reaction rate which contains a concentration as a linear unknown (by fixing the rate coefficient and all concentrations except that which is a linear unknown).

As a result, we obtain the constraint equations,

$$\begin{bmatrix} 0 & 0 \\ \hat{\mathbf{E}}^{(uv)} & \mathbf{A} & 0 \\ 0 & \mathbf{B} \end{bmatrix} \begin{bmatrix} \boldsymbol{\alpha}^{(uv)} \\ \mathbf{k}^{(uv)} \\ \mathbf{x}^{(uv)} \end{bmatrix} = \begin{bmatrix} \mathbf{v}^{(fv)} \\ 0 \\ 0 \end{bmatrix} - \hat{\mathbf{E}}^{(uds)} \boldsymbol{\alpha}^{(uds)}, \quad (4)$$

where  $\mathbf{v}^{(fv)}$  are the fixed rates based on  $\mathbf{k}^{(fv)}$  and  $\mathbf{x}^{(fv)}$  according to case (i), and matrices  $\mathbf{A}$  and  $\mathbf{B}$  are constructed according to cases (ii) and (iii) respectively. The symbol  $\hat{\mathbf{E}}$  indicates that only rows of  $\mathbf{E}$  relevant to the selected reactions are retained in  $\hat{\mathbf{E}}$ .

Eqs 4 are expected to have more unknowns than equations due to a typically large number of elementary subnetworks. Thus there is a continuum of solutions and we need a clue how to select a suitable one. A reasonable choice is suggested by the relation between the unstable dominant subnetwork and all the other elementary subnetworks. To ensure that the *uds* at the Hopf bifurcation is indeed dominant, we may require that the sum of the contributions of the remaining subnetworks is minimal, i.e.,

$$f(\boldsymbol{\alpha}^{(uv)}, \mathbf{x}^{(uv)}, \mathbf{k}^{(uv)}) = \sum \alpha_k^{(uv)} = \min. \quad (5)$$

This leads to a linear optimization problem where the unknowns are assumed non-negative and subject to constraints in eqs 4 with the objective function in eq 5. Once the unknown values  $\boldsymbol{\alpha}^{(uv)}$ ,  $\mathbf{k}^{(uv)}$  and  $\mathbf{x}^{(uv)}$  are

determined,  $\mathbf{v}_s$  can be found from eq 2 and subsequently  $\mathbf{k}^{(iv)}$  and  $\mathbf{x}^{(iv)}$  evaluated.

## RESULTS AND DISCUSSION

The overall reaction for the urease-catalyzed hydrolysis of urea is



The rate equation is usually given in terms of Michaelis-Menten expression modified to accommodate general effect of pH on enzymes and substrate/product inhibition [10]. When one wishes to apply mass action kinetics to the urea-urease reaction, one has to formulate a detailed model. It is rather straightforward to write detailed steps describing interaction with hydrogen protons (H); here we assume a simple scheme involving urea as substrate (S), the unprotonated form of urease (EH), the protonated form (EH2) and the unprotonated/protonated forms of the enzyme-substrate complex (EHS/EH2S). In addition, rapid protonation equilibria for ammonia and water are used. All other possible reactions (carbon dioxide dissolution, enzyme inhibition) are neglected. Thus the mass action scheme is



We assume a reactor with the enzyme confined to the vessel but open for nonenzyme species, which is formally written as pseudoreactions



Thus there are 18 (pseudo)reactions for 9 dynamical species S,H,OH,NH<sub>3</sub>, NH<sub>4</sub><sup>+</sup>, EH, EHS, EH2 and EH2S. For this reaction scheme the stoichiometric matrix N and the kinetic matrix are easily obtained from the stoichiometric coefficients. In literature [10] we can find the values of the following rate

coefficients of inorganic reactions:  $k_8=10^{11} \text{ M}^{-1}\text{s}^{-1}$ ,  $k_9=10^{-3} \text{ M s}^{-1}$ ,  $k_{10}=4.3 \times 10^{10} \text{ M}^{-1} \text{ s}^{-1}$ ,  $k_{11}=24 \text{ s}^{-1}$ . For the enzyme part, we know the dissociation equilibrium constant  $K_{\text{EH}} = k_4/k_5 = 5 \times 10^{-6} \text{ M}$ . The ratio  $k_6/k_7$  is expected to have similar but not necessarily the same value. Finally, from [10] we chose the inflow/outflow parameters for the switch from a less acidic steady state to more acidic steady state as follows: the flow rate  $k_0 = 0.04 \text{ s}^{-1}$ , the inflow concentration of urea  $S_0 = 5 \text{ mM}$  and the inflow of hydrogen protons  $H_0$  varies in the range  $0.1 - 0.6 \text{ mM}$  depending on whether sulfuric or acetic acid is used. Also, pH at the switch is about 6. Unlike in [10], we assume enzyme confined to the reactor, so the inflow concentration of urease  $U_0 = 1.4 \text{ U/ml} \approx 0.9 \times 10^{-4} \text{ mM}$ , is taken as total enzyme concentration  $E_{\text{tot}} = \text{EH} + \text{EHS} + \text{EH}_2 + \text{EH}_2\text{S}$  in the reactor. This assumption may affect the conditions of the switch somewhat and therefore our results are indicative rather than precisely reflecting measurements in [10].

When applying the outlined method, the first step is to decompose the network into elementary subnetworks (extreme currents) and determine the dominant unstable subnetwork. There are 11 elementary subnetworks and the chosen dominant unstable subnetwork is a combination of two extreme currents (two-face) formed by the reactions R1, R3, R6, R7, R10, the inflows of S and H (R12, R14) and the outflow of  $\text{NH}_4^+$  (R18). This subnetwork becomes unstable if H and EHS are small relative to concentrations of other species.

Next we need to formulate constraint equations (4) based on the known input data indicated above. The unknown rate coefficients are,  $k_1$ - $k_7$ , but the given ratio  $k_4/k_5$  needs to be fulfilled. In addition, apart from H no other steady state concentration is known. The SNA is used as a guide to estimating the distribution of the enzyme into its different forms: since EHS should be small enough at the instability, initially we chose EHS to be ten times smaller than other enzyme species. Later we verified that moderate variation of this enzyme concentration distribution does not affect the results significantly. Steady state concentrations of other species are left unknown apart from H, which is set to  $10^{-6} \text{ M}$  as indicated by the experiments. With this set of input data we obtain a set of 16 constraint equations (4) for 9 unknown coefficients  $\alpha_k$ , six unknown rate coefficients  $k_2$ - $k_7$  and four unknown concentrations S, OH,  $\text{NH}_3$  and  $\text{NH}_4^+$ . This system is solved as a convex optimization problem subject to (5) for a sequence of increasing values of  $\alpha^{(uds)}$  which allows the unstable network to become dominant and imply the saddle-node bifurcation indicating the observed switch. The rate coefficients that were not solved for in Eq. (4) can be calculated subsequently (we call them implied unknowns),

because the solution provides the rate vector  $\mathbf{v}_s$  as well as the reduced rate vector  $\bar{\mathbf{v}}(\mathbf{x})$ .

Upon adjusting the steady state concentration of H to  $H = 5 \times 10^{-6} \text{ M}$  we arrived at the following values of the unknown rate coefficients:  $k_1 = 3.2 \times 10^3 \text{ M}^{-1} \text{ s}^{-1}$ ,  $k_2 = 10^2 \text{ s}^{-1}$ ,  $k_3 = 60.6 \text{ s}^{-1}$ ,  $k_4 = 2 \times 10^9 \text{ M}^{-1} \text{ s}^{-1}$ ,  $k_5 = 10^4 \text{ s}^{-1}$ ,  $k_6 = 5.45 \times 10^7 \text{ M}^{-1} \text{ s}^{-1}$  and  $k_7 = 27.3 \text{ s}^{-1}$  while all other rate coefficients are fixed at their input values. This set of parameters reproduces the switch behavior of the experimental system rather well except that the inflow concentration  $H_0$  is by one order of magnitude less than the experimental value. This is likely to be accounted for by simplicity of the model, which should include other reactions that involve protonation/deprotonation such as the  $\text{CO}_2$  dissolution.

## CONCLUSION

We have used the urea-urease switch reaction to show how certain rate coefficients can be estimated using the outlined method exploiting stoichiometry and stability. The method holds promise for analysis of reaction systems with oscillatory or switch dynamics, where mechanisms are available but kinetic data are scarce and difficult to obtain by established methods of reaction kinetics. If alternative mechanisms are available, the method can help in distinguishing among them and revealing their potential for making reliable predictions. Such systems occur in heterogeneous catalysis with important industrial applications, *in vitro* enzyme reactions as treated here, and oscillatory reactions occurring in living organisms. In particular, applications to biological oscillators are of interest. In this regard, models of biological oscillating systems would need to be formulated in terms of power law kinetics based on (pseudo)elementary steps rather than using rational polynomial functions as is currently prevailing.

## Acknowledgement

This work was supported by the grant 18-24397S from the Czech Science Foundation.

## REFERENCES

- [1] B. L. Clarke, *Advances in Chemical Physics*, 1980, 43, 1–278.
- [2] M. Eiswirth, A. Freund and J. Ross, *Advances in Chemical Physics*, 1991, 80, 127–199.
- [3] M. Eiswirth, J. Bürger, P. Strasser and G. Ertl, *Journal of Physical Chemistry*, 1996, 100, 19118–19123.
- [4] T. Chevalier, I. Schreiber and J. Ross, *Journal of Physical Chemistry*, 1993, 97, 6776–6787.

- 
- [5] I. Schreiber and J. Ross, *Journal of Physical Chemistry A*, 2003, 107, 9846–9859.
- [6] J. Ross, I. Schreiber and M. O. Vlad, *Determination of Complex Reaction Mechanisms*, Oxford University Press, Inc., New York, 2006.
- [7] H. Errami, M. Eiswirth, D. Grigoriev, W. M. Seiler, T. Sturm and A. Weber, *J. Comput. Physics*, 2015, 291, 279–302.
- [8] F. Muzika, R. Jurasek, L. Schreiberova, V. Radojkovic and I. Schreiber, *Journal of Physical Chemistry A*, 2017, 121, 7518–7523.
- [9] V. Radojkovic and I. Schreiber, *Physical Chemistry Chemical Physics*, 2018, 20, 9910–9921.
- [10] G. Hu, J. A. Pojman, S. K. Scott, M. M. Wrobel and A. F. Taylor, *J. Phys. Chem. B*, 2010, 114, 14059–14063.
- [11] F. Muzika, T. Jr. Bánsági, I. Schreiber, L. Schreiberová and A. Taylor, *Chem. Commun.*, 2014, 50, 11107–11109.

## DYNAMIC BEHAVIOUR OF SINGLE AND COUPLED GLYCOLYTIC OSCILLATORS

F. Muzika, L. Schreiberová and I. Schreiber

*University of Chemistry and Technology, Prague, Faculty of Chemical Engineering, Department of Chemical Engineering, Technická 5, 16628 Praha, Czech Republic. (igor.schreiber@vscht.cz).*

### ABSTRACT

Our study is focused on experimental observations of dynamic behaviour of glycolytic oscillatory reaction using yeast extract and glucose solution reaction in a single cell and two coupled cells via reciprocal peristaltic pumping. Dynamic oscillatory behaviour of each cell is measured using UV-vis spectrophotometer, specifically 340nm for NADH and 260nm for adenosine metabolic pool and NAD<sup>+</sup>. We report occurrence of oscillations of NADH, bursting of NADH and bistability connected with depletion of adenosine metabolic pool.

Another part of our study is focused on modelling of ring of twenty coupled cells, using core model of glycolysis proposed by Moran and Goldbeter. Transport rate coefficients are set to be equal. The coexistence of nonuniform stationary states and oscillatory region is shown in solution diagram in a plane of concentration of ADP in the first reactor and inhibition rate coefficient  $\sigma_{inh}$ .

### INTRODUCTION

One of the oldest and the most common biochemical reaction is glycolysis. It is an enzymatic reaction system capable of both autocatalysis and inhibition. It shows multiple dynamic regimes, such as oscillations [1, 2], quenched oscillations [3], glycolytic bursting [4] and stationary regimes including bistability [5]. The bistability has been observed in wild type of *Saccharomyces cerevisiae*[5], where one stationary state is deemed “imbalanced” and yeast cells in such state are unviable. Bistability of glycolysis has been modelled by Mulukutla et al. [6] using glycolytic reaction model. This model has been extended by experimental work with cultivated mammalian cells of recombinant Chinese hamster ovary (CHO)[7].

Glycolytic oscillatory reaction in connection with diffusion forms reaction-diffusion system and it is capable of expressing discrete spatiotemporal patterns [8] described in pioneering work of A. Turing[9]. Patterns defined in A. Turing paper would occur spontaneously due to

condition of higher transport rate coefficient for inhibitor species over activator species. Vastano et al. proposed a hypothetical situation of occurrence of Turing patterns by perturbations in a system with equal transport rate coefficients for both inhibitor and activator species, providing solution diagram [10]. Region of occurrence of Turing patterns also provides possibility of simultaneous occurrence of stationary state and oscillatory regime, this states is called chimera [11].

### EXPERIMENTAL

Yeast extract powder Y1625 was supplied by Sigma Aldrich (France), D-Glucose was supplied by Penta (Czech Republic),  $\text{NaHCO}_3$  was supplied by Penta (Czech Republic),  $\text{Na}_2\text{CO}_3$  was supplied by Penta (Czech Republic), Ethanol UV- grade was supplied by Penta (Czech Republic), ATP disodium salt hydrate was provided by Sigma Aldrich (USA), Apyrase was supplied by Sigma Aldrich (USA). All solutions were prepared using demineralized water with conductivity  $<1\mu\text{Scm}^{-1}$ . pH of D-glucose solution(0.33M) and yeast extract(10g/l) was set at pH=9.2 using carbonate buffer, which increases activity of glycolysis, but due to increased temperature over  $37^\circ\text{C}$ , it was maintained at pH=8.8 . Temperature of both solutions was maintained at  $48^\circ\text{C}$ , ambient temperature was maintained at  $25^\circ\text{C}$ .

NADH is measured using 340nm, adenosine pool (ATP+ADP+AMP) +  $\text{NAD}^+$  are measured at 260nm.

Experimental setup is shown in Fig. 1. Physical cells are represented by quartz cuvettes (volume 4 ml; 2.6ml used), which are coupled by peristaltic pump with reciprocal pumping through capillaries with volume 1.089ml each. Cells 4 and 5 are continuously fed via peristaltic pump 10 with stock solutions 1 and 2, which are preheated and stirred with heater plate 6, while the same pump 10 drains outlets from cells 4 and 5 into a waste tank 3. Both cells 4 and 5 are coupled via reciprocal pumping of reaction solution by peristaltic pump 11. Reaction solutions are measured by UV-vis spectrophotometers 7 and 8. Perturbations are applied via syringes 12. Temperature inside cells is discretely checked by thermometer probes 13.

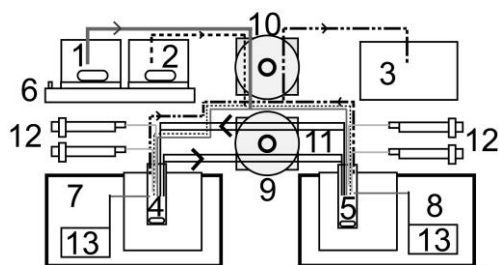


**Figure 1.** Schematic diagram of experimental setup: 1) yeast extract supply solution; 2) D-glucose supply solution; 3) waste solution; 4) 1<sup>st</sup> cuvette - measured, thermostated and stirred; 5) 2<sup>nd</sup> cuvette - measured, thermostated and stirred; 6) heater and stirrer of stock solutions, 7) Agilent 8453 UV-vis

spectrophotometer, 8) Agilent 8454 UV-vis spectrophotometer; 9) peristaltic reciprocal pump for coupling of both cuvettes; 10) peristaltic supply/waste pump; 11) coupling capillaries; 12) perturbations via syringes (Ext.=yeast extract, Glu.=glucose); 13) thermometers.

## MODEL

One cell can be modelled using mass balance equation:

$$\frac{dF}{dt} = F(X, P), \quad (1)$$

where vector  $X=(x_1, \dots, x_m)$  represents concentration of  $m$  independent chemical species, function  $F(X, P)=(F_1(X, P), \dots, F_m(X, P))$  represents overall production consumption of all chemical species and  $P=(P_1, \dots, P_\square)$  is a vector of  $\mu$  parameters. For  $N$  cells coupled via diffusive transport, the dynamic evolution equation is:

$$\frac{dX_i}{dt} = Q_i(X_i, P) = F(X_i, P) + \text{diag}(K_d)(X_{i+1} - 2X_i + X_{i-1}), i = 1, \dots, N. \quad (2)$$

Boundary conditions need to be applied for ring of coupled cells:

$$X_i = X_N. \quad (3)$$

Vector  $K_d=(k_1, \dots, k_m)$  represents vector of transport rate coefficients for each species. For our case, where activator and inhibitor transport rate coefficients are equal throughout the whole ring, we can introduce one transport rate coefficient  $k_d=k_1=k_2=\dots=k_m$ .

Core model of glycolysis [2] for  $N=20$  cells can be modified into reactions and then inserted into Eq.(2):

$$\begin{aligned} F(x_i, P) &= \nu + \sigma_{inh} \frac{y_i^n}{M^n + y_i^n} - \sigma_M \frac{x_i(1 + x_i)(1 + y_i)^2}{L + (1 + x_i)^2(1 + y_i)^2} \\ F(y_i, P) &= \phi \sigma_M \frac{x_i(1 + x_i)(1 + y_i)^2}{L + (1 + x_i)^2(1 + y_i)^2} - k_S y_i - \phi \sigma_{inh} \frac{y_i^n}{M^n + y_i^n} \end{aligned} \quad (4)$$

$$i = 1, 2, 3, \dots, 20,$$

where  $x_i$  represents ATP and  $y_i$  represent ADP in  $i$ -th cell,  $\nu$  is the ATP uptake rate,  $\phi$  is ratio of dissociation constants of ATP to ADP,  $\sigma_M$  is autocatalysis rate coefficient,  $\sigma_{inh}$  is inhibition rate coefficient,  $n$  is Hill coefficient,  $L$  is allosteric constant,  $k_S$  is rate coefficient of degradation of ADP and  $M$  is Michealis constant. Constant parameters are  $\phi=1$ ,  $\nu=1.84$ ,  $n=4$ ,  $L=5 \cdot 10^6$ ,  $M=10$ ,  $k_S=0.06s^{-1}$ , variable parameters are  $\sigma_M$ ,  $k_d$  and  $\sigma_{inh}$ .

## RESULTS AND DISCUSSION

Numerous experiments have been performed. Glycolytic bursting together with special type of oscillation are shown in Fig. 2. The second, third, fourth and sixth perturbation of 1st cell triggers oscillatory irregular behaviour similar to bursting, which can be seen both on NADH levels and adenosine and  $\text{NAD}^+$  levels. The fourth perturbation of 1st cell also triggers regular oscillation with period 450s, which is repeated 6 times. Second perturbation of 2nd cell project itself into one oscillation peak in 1st cell.

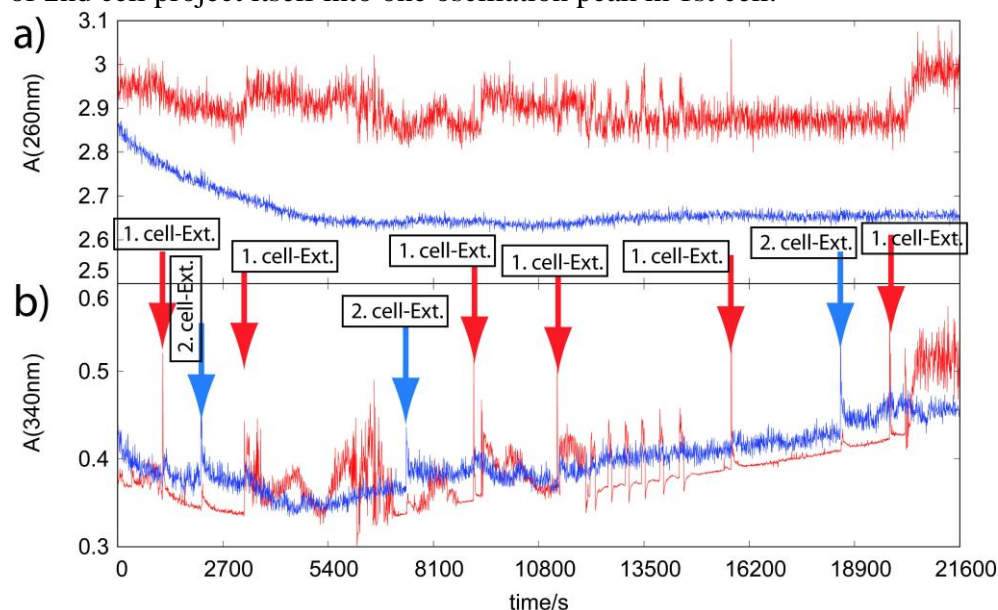


**Figure 2.** Simultaneous recording of absorbance spectra in time of two coupled cells: a) 340nm, b)260nm. Red curve – 1st cell, blue curve - 2nd cell, arrow – perturbation.  $T_1=T_2=40.3^\circ\text{C}$ ,  $\tau_d=112\text{s}$ ,  $\tau_{\text{coupling}}=35.3\text{s}$ .

Glycolytic bursting can be seen also in Fig. 3, where two cells are measured without coupling. Perturbation by ethanol was able to quench glycolytic bursting in this case. Fig. 4 shows two uncoupled cells, where there are oscillations of NADH in 1st cell while adenosine pool (Fig 4a - red curve) remains constant (this is the most observed scenario). In 2nd cell there are adenosine pool (Fig 4a - blue curve) oscillations reflecting itself into NADH levels.

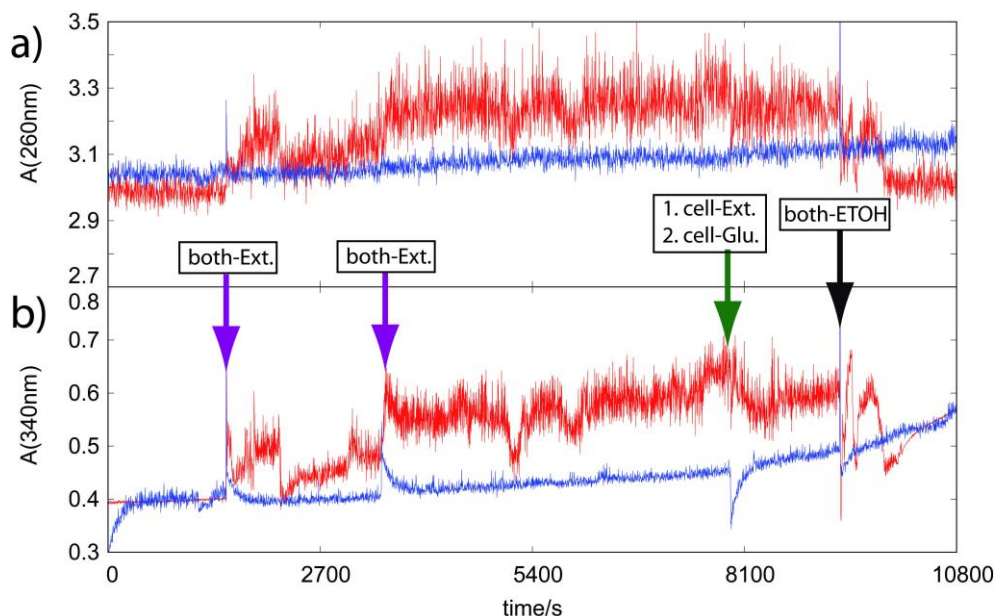


**Figure 3.** Simultaneous recording of absorbance spectra in time of two uncoupled cells: a) 340nm, b)260nm. Red curve – 1st cell, blue curve - 2nd cell, arrow – perturbation.  $T_1=40.3^\circ\text{C}$ ,  $T_2=40.2^\circ\text{C}$ ,  $\tau_d=112\text{s}$ .

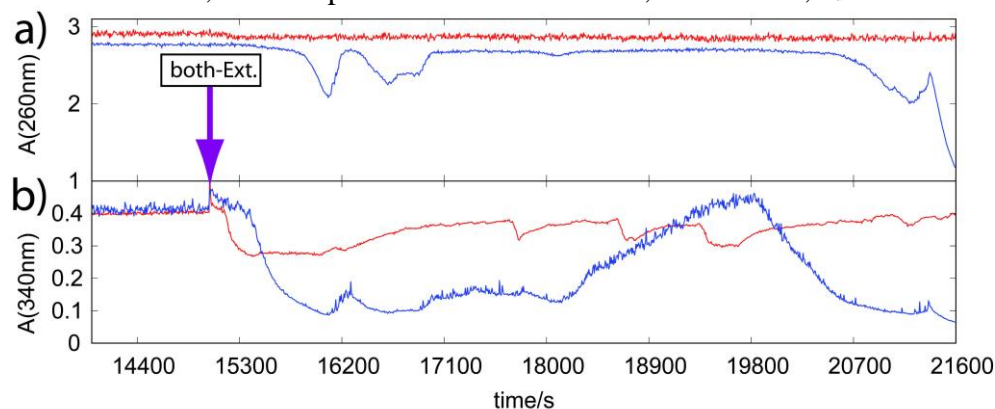


**Figure 4.** Simultaneous recording of absorbance spectra in time of two uncoupled cells: a) 340nm, b)260nm. Red curve – 1st cell, blue curve - 2nd cell, arrow – perturbation.  $T_1=41^\circ\text{C}$ ,  $T_2=41.1^\circ\text{C}$ ,  $\tau_d=112\text{s}$ .

Other experiment with adenosine pool oscillations is shown in Fig. 5. The lowest stationary state of adenosine pool is probably “imbalanced stationary state” described by Van Herden[5] or it can be the effect of spatiotemporal pattern defined by A. Turing. Perturbation of this state led to oscillation with

period 250 s, other perturbation somehow disrupted regularity of the oscillations.

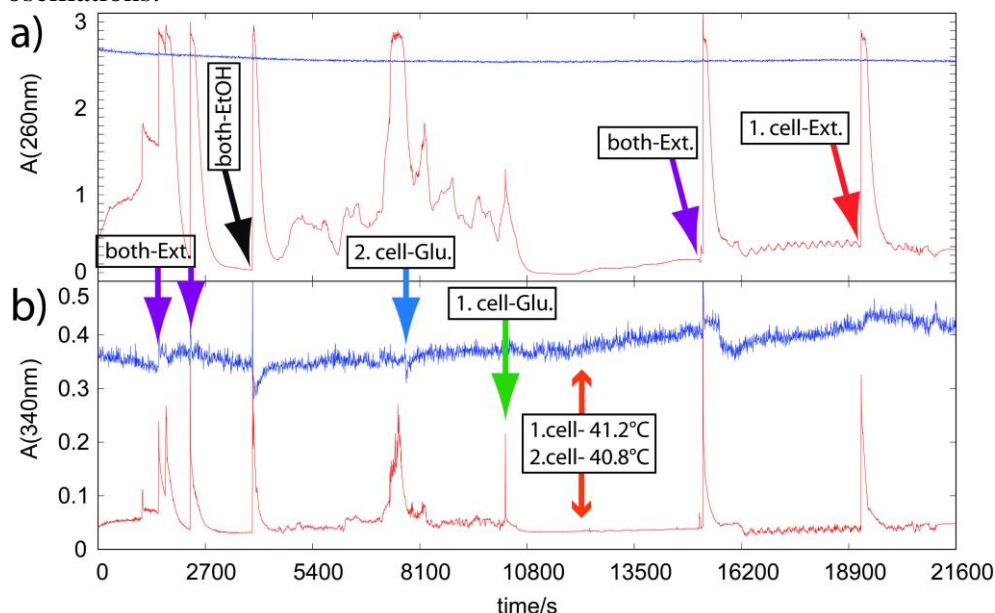


**Figure 5.** Simultaneous recording of absorbance spectra in time of two coupled cells: a) 340nm, b)260nm. Red curve – 1st cell, blue curve - 2nd cell, arrow – perturbation.  $T_1=43.3^\circ\text{C}$  until  $t=11700\text{s}$ ,  $T_2=43.5^\circ\text{C}$  until  $t=11700\text{s}$ ,  $\tau_d=112\text{s}$ ,  $\tau_{\text{coupling}}=35.3\text{s}$ .

Combination of NADH and adenosine pool oscillatory behaviour can be seen in Fig. 6. Both cells start at nonuniform stationary states, then “imbalanced” stationary state is induced by yeast extract perturbation. Perturbation by ethanol switches cells back to starting regime, but performing an oscillation peak. Further perturbations induce nonuniform oscillatory regime, then stationary state and ethanol shifts cells to uniform oscillations for a short period of time. Perturbation by ATP creates nonuniform stationary state and perturbation by 21 units of apyrase switches 2nd cell to high stationary state and set 1st cell to oscillatory regime, this situation can be marked as chimera.

Model results for 20 coupled cells can be seen in a form of solution diagram in Fig.7. The system of spatiotemporal patterns is quite complex showing 11 regions, where nonuniform patterns are secondarily stabilized by a Hopf bifurcations. All patterns are located inside a “tubus” delimited by large oscillations (minima and maxima are marked by black curve).

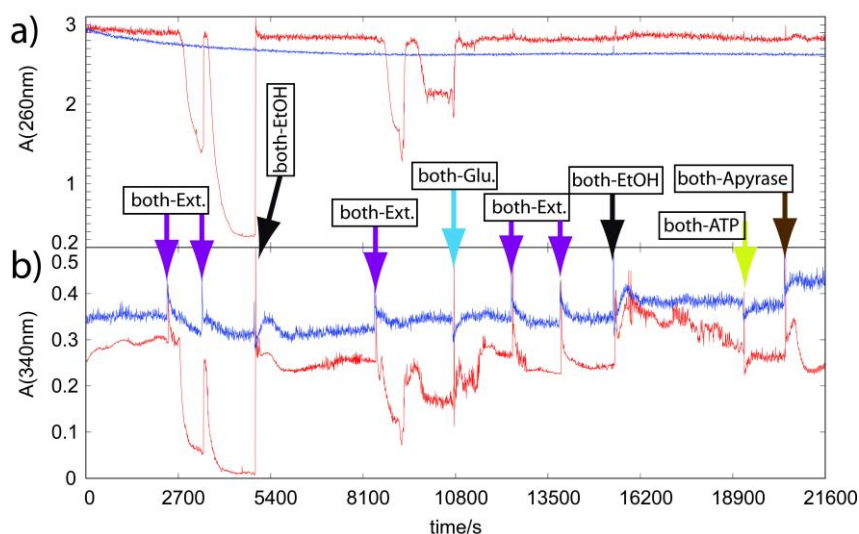


**Figure 6.** Simultaneous recording of absorbance spectra in time of two coupled cells: a) 340nm, b)260nm. Red curve – 1st cell, blue curve - 2nd cell, arrow – perturbation.  $T_1=36.5^\circ\text{C}$ ,  $T_2=37.6^\circ\text{C}$ ,  $\tau_d=112\text{s}$ ,  $\tau_{\text{coupling}}=35.3\text{s}$ .

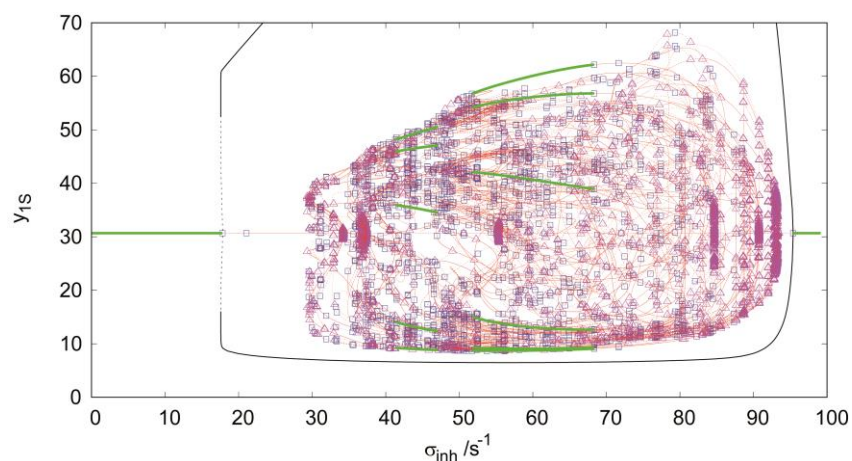


**Figure 7.** Solution diagram of ADP in the first reactor ( $y_{1s}$ ) for  $\sigma_M=100\text{s}^{-1}$ ,  $k_d=0.5\text{s}^{-1}$ . Green curve – stable stationary state, red dashed curve – unstable stationary state, solid black curve – stable minima and maxima of glycolytic oscillations, dashed black curve – unstable minima and maxima of glycolytic oscillations, square – Hopf bifurcation point, triangle – branch point.

## CONCLUSION

Single cell and two cells with reciprocal peristaltic pumping with glycolytic oscillatory reaction using reaction of yeast extract and glucose have been analysed by UV-vis spectrophotometers. By carefully targeted perturbations using yeast extract and ethanol glycolytic bursting can be induced and quenched. It is also possible to induce glycolytic oscillations and imbalanced stationary state. Perturbation by ATP was able to establish nonuniform stationary state and perturbation by apyrase was able to induce chimera state [11].

Model of ring of 20 coupled cells with glycolytic oscillatory reaction has been analysed to model the experimental system of two cells coupled by tubes with peristaltic reciprocal pumping. It shows presence of 11 regions of stable nonuniform patterns for equal transport rate coefficients, therefore nonuniform stationary states can occur in this system after perturbation.

## Acknowledgement

This work was supported by the grant 18-24397S from the Czech Science Foundation.

## REFERENCES

- [1] F. Hynne, S. Danø, P.G.Sørensen, *Biophysical Chemistry*, 2001, 94, 121-163.
- [2] A. Goldbeter, F. Moran, *Biophys. Chem.*, 1984, 20, 149-156.
- [3] K. Nielsen, P.G. Sørensen, F. Hynne, H.G. Busse, *Biophysical Chemistry*, 1998, 72, 49-62.
- [4] R. Bertam, L. Satin, M. Zhang, P. Smolen and A. Sherman, *Biophysical Journal*, 2004, 87, 3074-3087.
- [5] J. H. Van Heerden, M. T. Wortel, F. J. Bruggeman, J.J. Heijnen, Y. J.M. Bollen, R. Planqué, J. Hulshof, T. G. O'Toole, S. A. Wahl, B. Teusink, *Science*, 2014, 343, 1245114-1-9.
- [6] B. C. Mulukutla, A. Yongky, P. Daoutidis, W.S. Hu, *Plos One*, 2014, 9, e98756-1-12.
- [7] B.C. Mulukutla, A. Yongky, S. Grimm, P. Daoutidis, W.S.Hu, *Plos One*, 2016, 10, 0121561-1-20.
- [8] F. Muzika, L. Schreiberová, I. Schreiber, *RKMC* 2016, 118, 99-114.
- [9] A. Turing, *Phil. Trans. R. Soc. Lond. B*, 1952, 237, 37-72.
- [10] J.A. Vastano, J. E. Pearson, W. Horsthemke, H. L. Swinney, *Phys. Lett. A*, 1987, 124, 320-324.
- [11] A. Zakharova, M. Kapeller, E. Schöll, *Phys. Rev. Lett.*, 2014, 112, 154101-1-5.

## KINETICS OF REACTIONS OF IODINE INORGANIC COMPOUNDS IN ACIDIC SOLUTIONS

G. Schmitz<sup>1</sup> and S. D. Furrow<sup>2</sup>

<sup>1</sup>*Université Libre de Bruxelles, Ecole Polytechnique, Av. Franklin Roosevelt, 50, 1050 Brussels, Belgium (gschmite@ulb.ac.be).*

<sup>2</sup>*Penn State Berks College, Pennsylvania State University, Reading, Pennsylvania 19610, United States.*

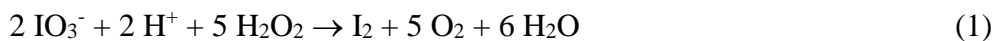
### ABSTRACT

The kinetics of iodine reactions, as part of the mechanism of the oscillating Bray Liebhafsky and Briggs Rauscher reactions, is discussed with emphasis on the role of I<sub>2</sub>O. Preliminary results of a new study of the kinetics of the I(+1) disproportionation using I<sub>2</sub>O as reactant show that this kinetics is more complicated than previously admitted. We have found also that I<sub>2</sub>O is a volatile compound and its possible role in the chemistry of the atmosphere is suggested.

### THE IODINE HOUSE

The main iodine compounds in acidic solutions are shown in the drawing below. There are many reactions between the compounds of these families and we are particularly interested in the reaction of the iodous acid family at level 3 and the hypoiodous acid family at level 1.

The iodine house has also an elevator. Hydrogen peroxide can reduce several compounds in reactions called by Liebhafsky "down reactions" and oxidize other compounds in reactions called by Liebhafsky "up reactions". Especially interesting reactions are the global down reaction (1), the iodate reduction to iodine, and in the global up reaction (2), the oxidation of iodine to iodate.



Normally, the rates of these two reactions tend to become equal giving only the catalysis of the decomposition of hydrogen peroxide. However, there are experimental conditions where the catalytic steady state is unstable giving the oscillations discovered by Bray.

<b>Level 5</b>	$\text{IO}_3^-$	$\text{HIO}_3$	
<b>Level 4</b>	$\text{OIO}^\cdot$		
<b>Level 3</b>	$\text{HOIO}$	$\text{OIO}^-$	
<b>Level 2</b>	$\text{IO}^\cdot$	$\text{I}_2\text{O}_2$	
<b>Level 1</b>	$\text{HOI}$	$\text{I}_2\text{O}$	
<b>Level 0</b>	$\text{I}_2$	$\text{I}_2\text{OH}^-$ $\text{I}^\cdot$	
<b>Level -1</b>	$\text{I}^-$		

### $\text{I}_2\text{O}$ AND THE BRAY-LIEBHAFSKY REACTION

The main features of the mechanism of reaction (1) are fairly well known. It includes at least one down reaction which is (3) according to Liebhafsky [1].



The mechanism of reaction (2) is less simple [2, 3]. A mixture of hydrogen peroxide and iodine can remain unchanged during hours because the direct reaction between hydrogen peroxide and iodine is extremely slow. The hydrolysis of iodine,  $\text{I}_2 + \text{H}_2\text{O} \rightleftharpoons \text{HOI} + \text{I}^- + \text{H}^+$ , is very fast and hydrogen peroxide could reduce HOI and oxidize  $\text{I}^-$ . However, their concentrations in acidic  $\text{I}_2$  solutions are very small and we obtain only a very slow disproportionation of hydrogen peroxide. However, if the  $\text{I}^-$  ions are removed, for example by adding  $\text{Ag}^+$  or  $\text{Hg}^{++}$ , the oxidation of iodine starts immediately and is very fast. By removing the  $\text{I}^-$  ions we have shifted the iodine hydrolysis equilibrium and produced a significant concentration of HOI which is quickly oxidized. During the Bray-Liebhafsky (BL) reaction, the  $\text{I}^-$  ions are removed by iodate and iodous acid. It remains to explain why hydrogen peroxide reduces HOI during reaction (1) and oxidizes it during reaction (2), a problem mentioned but not solved by Liebhafsky. We have proposed [4] that hydrogen

peroxide does not oxidize HOI itself but well its dimer I<sub>2</sub>O according to reactions (4) and (5).



The rate of reduction (3) is proportional to [HOI] while the rate of oxidation (5) is proportional to the square of [HOI] so that the net result is a reduction when [HOI] is small and an oxidation when [HOI] is large. Stanisavljev [5] pointed out that the direct reaction between iodine and hydrogen peroxide has a very high barrier of activation energy, which is true, but the system does not try to go over this barrier, it goes around.

The last version of a model based on the I<sub>2</sub>O assumption explains nearly quantitatively all the experimental observations, including the unusual kinetics of the oxidation of iodine by hydrogen peroxide [2, 3]. However, I<sub>2</sub>O remained an assumption and we had to wait till 2012 to obtain a direct proof of its existence [6].

The main problem remaining is the effect of oxygen. Oxygen can oxidize the iodide ions but the mechanism remains unknown and this reaction is represented in the proposed model by an empirical rate equation. It is most probably a radical mechanism but the last important work devoted to it only highlighted problems, especially memory effects, but did not allow to understand it [7]. It is very frustrating that a reaction that seems simple is still not understood. The oxidation of iodide by oxygen could explain the formation of radicals observed by Stanisavljev *et al* during the BL reaction [8]. It is interesting to note that the concentration in radicals measured by Stanisavljev *et al* is largest during the period where the concentration of iodide rises suddenly in a solution probably supersaturated with oxygen.

### IODOUS ACID REACTIONS

A major advance in the knowledge of the inorganic reactions of iodine was made by Zoltan Noszticzius *et al* in 1983 [9] when they discovered a method for the preparation of I(+3) solutions in concentrated sulfuric acid. This method allowed the study of the kinetics of HOIO reactions in diluted sulfuric acid and, in particular, the rate of the reaction (R3) in Table I discussed hereafter with the kinetics of the HOI disproportionation.

Before this discussion, we must address a theoretical debate. The relation  $K = k_+/k_-$  is often presented as a consequence of the principle of microscopic reversibility. However, reactions in Table I are not elementary reactions and the application of the principle of microscopic reversibility can be doubtful. On the other hand, (R3) is a reversible reaction going in the forward direction

during one period of the BL oscillations and in the reverse direction during the other period. Let us consider a situation where the forward and backward rates are equal:  $k_{+R3} [\text{HOIO}] [\text{HOI}] = k_{-R3} [\text{IO}_3^-][\text{I}^-][\text{H}^+]^2$ . This expression must be identical to the thermodynamic expression of equilibrium  $K_{R3} = [\text{IO}_3^-][\text{I}^-][\text{H}^+]^2 / [\text{HOIO}][\text{HOI}]$  so that  $k_{+R3}/k_{-R3}$  must be equal to  $K_{R3}$ . This is what we called the thermodynamic consistency of reactions mechanisms [10].  $k_{-R3}$  was known and the measurement of  $k_{+R3}$  allowed to estimate  $K_{R3}$  and then the Gibbs energy of formation of HOIO [11]. We must, however, mention briefly two complications. Firstly, the rate constants of ionic reactions depend on the ionic strength and the above calculations imply an estimation of the activity coefficients. Secondly, the rate of the Dushman reaction is given by  $k_{-R3} [\text{IO}_3^-][\text{I}^-][\text{H}^+]^2$  only when the iodide ions concentration is lower than  $10^{-6}$  M, what is the case during the BL reaction. At higher iodide ions concentrations, the Dushman reaction is order two in  $[\text{I}^-]$  and we must consider a more complicated mechanism involving the intermediate  $\text{I}_2\text{O}_2$  [12].

### **I<sub>2</sub>O PREPARATION**

When Zoltan Noszticzius proposed a method to prepare I(+3) solutions by the reactions of  $\text{I}_2$  with  $\text{HIO}_3$  in concentrated sulfuric acid [9], he noted that it is necessary to use large  $[\text{HIO}_3]/[\text{I}_2]$  ratios to avoid the formation of I(+1). Muntean *et al* showed later [6] that the same reaction with smaller  $[\text{HIO}_3]/[\text{I}_2]$  ratios provides a new method to prepare I(+1) solutions and that the obtained I(+1) can be extracted in DCM (dichloromethane). This new method of I(+1) solutions preparation paved the way for new kinetic studies and for a better understanding of the levels 1 and 3 of the iodine house. A study of the reactions between  $\text{I}_2$  with  $\text{HIO}_3$  in concentrated sulfuric acid in a large range of concentrations and  $[\text{HIO}_3]/[\text{I}_2]$  ratios allowed to identify the different reactions and to estimate their equilibrium constants [13]. An important conclusion of this work is that I(+1) is present in concentrated sulfuric acid as  $\text{I}_3^+$ ,  $\text{I}_5^+$  and  $\text{I}_2\text{O}$ , not as  $\text{IHSO}_4$ . The only compound that can be extracted in DCM is  $\text{I}_2\text{O}$  and we have finally a proof of its existence.

### **KINETICS OF THE HOI DISPROPORTIONATION**

The mechanism of the HOI disproportionation has several parts in common with the mechanism of the BL and BR reactions so that a kinetic study of this disproportionation can give information very valuable in constructing models of these oscillating systems. It is generally accepted that the stoichiometry of the disproportionation corresponds to reaction (6) and that it follows a rate law of order two.



$$d[\text{I}_2]/dt = k_{\text{obs}} [\text{HOI}]^2 \quad (7)$$

HOI being unstable, it must be generated in situ from some other reaction. Stanley Furrow has used the fast reaction of  $\text{Ag}^+$  and  $\text{Hg}^{++}$  with  $\text{I}^-$  shifting the hydrolysis equilibrium  $\text{I}_2 + \text{H}_2\text{O} \rightleftharpoons \text{HOI} + \text{I}^- + \text{H}^+$  to the right [14]. He has obtained  $k_{\text{obs}} = 25 \text{ M}^{-1}\text{s}^{-1}$  by three different techniques in  $\text{HClO}_4$  0.025 to 0.10 M and in  $\text{H}_2\text{SO}_4$  0.58 M. This value was confirmed later [15]. Lengyel et al. [16] have produced HOI by hydrolysis of  $\text{ICl}$  and obtained  $k_{\text{obs}} = 22 \text{ M}^{-1}\text{s}^{-1}$  at  $\text{pH} = 1.8$ . Thus, the value of  $k_{\text{obs}}$  seemed well known in acidic solutions. Many authors have also studied the disproportionation in buffered solutions with very discordant results. Urbansky *et al* [17] have reviewed these works and have noted "Such discordance suggests a more complex behavior and offers a compelling reason to further study this system." Although they have obtained important results, this is still true. By extrapolating their values to a buffer concentration equal zero, they have obtained  $k_{\text{obs}} < 2 \text{ M}^{-1}\text{s}^{-1}$ . The difference with the above values cannot be explained by a pH effect and we have undertaken a new kinetic study using the new method of  $\text{I}_2\text{O}$  preparation. The first results reveal unexpected complications. Table I shows the common part of the Dushman and the BL reactions models in a form showing its application to the disproportionation of HOI in non-buffered solutions. When a solution of  $\text{I}_2\text{O}$  in DCM is injected into an aqueous acidic solution, we get very quickly a solution of HOI. Reaction (R1) is fast but its equilibrium constant is very small so that the concentrations of  $\text{I}_2\text{O}$  in aqueous solutions are extremely small which explains why they have never been measured.

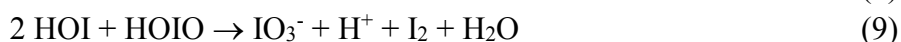
**Table I.** A model of the HOI disproportionation.

(R1)	$2 \text{HOI} \rightleftharpoons \text{I}_2\text{O} + \text{H}_2\text{O}$	1	2
(R2)	$\text{I}_2\text{O} + \text{H}_2\text{O} \rightleftharpoons \text{HOIO} + \text{I}^- + \text{H}^+$	1	2
(R3)	$\text{HOI} + \text{HOIO} \rightleftharpoons \text{IO}_3^- + \text{I}^- + 2 \text{H}^+$	1	0
(R4)	$\text{HOI} + \text{I}^- + \text{H}^+ \rightleftharpoons \text{I}_2 + \text{H}_2\text{O}$	2	2
(R5)	$2 \text{HOIO} \rightarrow \text{IO}_3^- + \text{HOI} + \text{H}^+$	0	1

The last two columns in Table I give the numbers by which the steps of this model must be multiplied to obtain the reaction (6). In terms of the stoichiometric network analysis (SNA) [18, 19], they are two extreme currents giving the same stoichiometry. A previous discussion showed that direct measurements and the application of the thermodynamic consistency of reactions mechanisms allow to estimate all the rate constants independently [2, 3]. The kinetics of the oxidation of iodine by hydrogen peroxide has shown

that the equilibrium of reaction (R1) is reached extremely rapidly and can be disturbed only by large concentrations of peroxide of hydrogen. During the disproportionation of HOI we have  $[I_2O] = K_1 [HOI]^2$  and, if the step (R2) is rate determining,  $r_2 = k_2 K_1 [HOI]^2$ . The experimentally measurable kinetic constant is  $k_{HOI} = k_2 K_1$ . On the other hand,  $k_{obs}$  in relation (7) looks like a kinetic constant but it is not even a constant for different reasons.

- Urbansky et al [17] observed that a significant amount of HOIO is formed at the beginning of the reaction and we confirmed this observation. Reaction (6) must be decomposed into two consecutive reactions (8) and (9).



The first extreme current above gives  $k_{obs} = k_{HOI}$  at the very beginning of the reaction when HOIO is produced and  $k_{obs} = 2 k_{HOI}$  when the reaction (9) becomes important.

- The rate of reaction (R5) is given by the experimental equation  $r_{R5} = k_{R5} [\text{HOIO}]^2 / [\text{H}^+]$  [20]. In very acid solutions, it is much smaller than  $r_{R3}$  and only the first extreme current is obtained. When the acidity decreases  $r_{R5}$  increases quickly and the second extreme current becomes important. Then,  $k_{obs} = k_{HOI}$  during all the disproportionation.
- Reaction (R2) becomes rapidly reversible. It ceases to be the rate determining step and there is no longer a simple kinetic law. The integrated form of the second-order kinetic law seems to be verified only as long as the deviations remain smaller than the experimental errors.
- Acetate buffers, and also other buffers, form complexes with I(+1). The model in Table I needs to be completed but this problem is not solved yet.

Chemical kinetics is full of traps and tricks and the kinetics of the HOI disproportionation is still not well understood. So, we are very audacious when we propose models for much more complicated reactions such as oscillating reactions.

## **I<sub>2</sub>O AND THE ATMOSPHERIC CHEMISTRY**

Experiments performed by one of us (S.F.) have recently shown that I<sub>2</sub>O is a volatile compound. We have seen that I(+1) prepared by reaction of iodate with iodine in concentrated sulfuric acid can be extracted in DCM. Then, the

upper organic layer can be separated and distilled. The dark brown distillate shows an absorption peak at 442 nm and its I<sub>2</sub>O content can be titrated by iodometry. These distillations proved that I<sub>2</sub>O was transferred via the gas phase. Moreover, the gas phase above the distillates shows a peak at 471 nm not present in the DCM spectrum.

HOI is an important intermediate of iodine reactions in the upper troposphere / lower stratosphere, where iodine is extremely O<sub>3</sub> depleting. However, we found only two old works that mention I<sub>2</sub>O [21, 22]. Strangely, recent models include I<sub>2</sub>O<sub>x</sub> with x = 2, 3, 4 but not with x = 1 [23, 24]. I<sub>2</sub>O could be produced by the reaction IO<sup>•</sup> + I<sup>•</sup> + M → IOI + M. It can also be produced in the stratospheric aerosol layer composed of highly concentrated sulfuric acid droplets. Now that a method for obtaining I<sub>2</sub>O in the gas phase is established, it would be interesting to study its reactions.

## CONCLUSION

The kinetics of the non-radical reactions of iodine involved in the mechanism of the BL and BR oscillating reactions begin to be well known and the discovery of a method for the preparation of I<sub>2</sub>O should make it possible to specify the value of the kinetic constants of the I(+1) reactions. On the other hand, radical reactions, not essential for the BL oscillations but well for the BR oscillations, remain poorly known. Even the kinetics of the seemingly simple reaction of iodide oxidation by oxygen remains unknown.

To understand complicated systems, one must start by studying simpler subsystems. A characteristic of basic research is that you never know what it is going to serve. Another characteristic is that it always ends up being useful, sometimes in areas that were not thought of.

## REFERENCES

- [1] H. A. Liebhafsky, *J. Am. Chem. Soc.*, 1932, **54**, 3504
- [2] G. Schmitz, *Phys. Chem. Chem. Phys.* 2010, **12**, 6605.
- [3] G. Schmitz, *Phys. Chem. Chem. Phys.* 2011, **13**, 7102.
- [4] G. Schmitz, *J. Chim. Phys.*, 1987, **84**, 957.
- [5] K. Z. Stevanović, I. N. M. Bubanja, D.R. Stanisavljev, *Chem. Phys. Letters* 2017, **684**, 257.
- [6] N. Muntean, L. B. Thuy, K. Kaly-Kullai, M. Wittmann, Z. Noszticzius, L. Onel, S. D. Furrow, *J. Phys. Chem. A* 2012, **116**, 6630.
- [7] F. D. Aldridge, Ph.D. thesis, University of California, 1966.
- [8] D. R. Stanisavljev, M. C. Milenković, A. D. Popović-Bijelić, M. D. Mojović, *J. Phys. Chem. A* 2013, **117**, 3292.
- [9] Z. Noszticzius, E. Noszticzius, Z. A. Schelly, *J. Phys. Chem.*, 1983, **87**, 510.

- [10]G. Schmitz, *J. Chem. Phys.*, 2000, **112**, 10714.
- [11]G. Schmitz, *Int. J. Chem. Kinet.*, 2008, **40**, 647.
- [12]G. Schmitz, *Phys. Chem. Chem. Phys.* 1999, **1**, 1909.
- [13]G. Schmitz, Z. Noszticzius, G. Hollo, M. Wittmann, S. D. Furrow, *Chem. Phys. Lett.*, 2018, **691**, 44.
- [14]S. D. Furrow, *J. Phys. Chem.* 1987, **91**, 2129.
- [15]G. Schmitz, *Int. J. Chem. Kinet.* 2004, **36**, 480.
- [16]I. Lengyel, J. Li, K. Kustin, I. R. Epstein, *J. Am. Chem. Soc.* 1996, **118**, 3708.
- [17]E. T. Urbansky, B. T. Cooper, D. W. Margerum, *Inorg. Chem.*, 1997, **36**, 1338.
- [18]B. L. Clarke, *Adv. Chem. Phys.* 1980, **43**, 1.
- [19]G. Schmitz, Lj. Kolar-Anić, S. Anić, Ž. D. Čupić, *J. Phys. Chem..A*, 2008, **112**, 13452.
- [20]G. Schmitz, S. D. Furrow, *Int. J. Chem. Kinet.*, 2013, **48**, 525.
- [21]J. L. Jimenez, R. Bahreini, D. R. Cocker III, H. Zhuang, V. Varutbangkul, R. C. Flagan, J. H. Seinfeld, C. D. O'Dowd, T. Hoffmann, *J. Geophys. Res.* 2003, **108**, 4318.
- [22]N. Begović, Z. Marković, S. Anić, Lj. Kolar-Anić, *Environ. Chem. Lett.* 2004, **2**, 65.
- [23]A. Saiz-Lopez, R. P. Fernandez, C. Ordóñez, D. E. Kinnison, J.C. Gómez Martín, J.-F. Lamarque, S. Tilmes, S., *Atmos. Chem. Phys.* 2014, **14**, 13119.
- [24]T. Sherwen, M. J. Evans, L. J. Carpenter, S. J. Andrews, R. T. Lidster, B. Dix, T. K. Koenig, R. Sinreich, *Atmos. Chem. Phys.* 2016, **16**, 12239.

## RECENTLY REVEALED DYNAMIC AND MECHANISTIC ASPECTS OF THE H<sub>2</sub>O<sub>2</sub>-BASED HOMOGENEOUS OSCILLATORY REACTIONS

M. Orlik, A. Wiśniewski, M. Jędrusiak, R. Jurczakowski, M. T. Gorzkowski and K. Pękala

*University of Warsaw, Faculty of Chemistry, ul. Pasteura 1,  
02-093 Warsaw, Poland (morlik@chem.uw.edu.pl)*

### ABSTRACT

We are reviewing our recent studies of temporal and spatiotemporal dynamics, reported for the H<sub>2</sub>O<sub>2</sub> - SCN<sup>-</sup> - OH<sup>-</sup> - Cu<sup>2+</sup> and H<sub>2</sub>O<sub>2</sub> - S<sub>2</sub>O<sub>3</sub><sup>2-</sup> - H<sup>+</sup> - Cu<sup>2+</sup> oscillatory systems. For the former system we elaborated three simplified versions of the original mechanism, including the 3-variable “minimal oscillator”. We explained unique and apparently anomalous potentiometric oscillatory responses of the Pt, Au and other inert electrodes. Furthermore, upon addition of luminol, the spatiotemporal patterns (kinematic waves) were reported in the inhomogeneous temperature field. Analogous conditions applied to the thin-layer H<sub>2</sub>O<sub>2</sub> - S<sub>2</sub>O<sub>3</sub><sup>2-</sup> - H<sup>+</sup> - Cu<sup>2+</sup> system with thymol blue as the pH-indicator caused the progress of the travelling color front of the solution pH, also of kinematic origin. The mechanisms of the formation of those patterns was confirmed by numerical models. These phenomena constitute novel and rather unique examples of instabilities of thermokinetic origin in liquid media.

### INTRODUCTION

Chemical oscillators in which hydrogen peroxide is an oxidant for thiocyanate and thiosulfate ions, were discovered by Orbán et al. [1-3] and since then have been intensively studied. For both the dissipative oxidation of thiocyanate in basic media and the oxidation of thiosulfates in acidic media, the Cu(II)/Cu(I) redox couple was used as a catalyst engaged in the oscillatory instability. In spite of apparent chemical similarity of both systems, the kinetic mechanism of the oscillations is essentially different – for the oxidation of SCN<sup>-</sup> by H<sub>2</sub>O<sub>2</sub>, the oscillations occur at constant (and sufficiently high) pH, while the thiosulfate-H<sub>2</sub>O<sub>2</sub> system is a pH-oscillator, involving engagement of H<sup>+</sup> ions in the feedback steps destabilizing the steady-state. Moreover, the latter system exhibits sustained oscillations only in the flow reactor, while in the batch only a single peak of the Pt electrode potential (as well as the solution pH) develops at an early stage of the process.

Studies of both oscillators published by the year 2007 resulted in the elaboration of their original homogeneous kinetic mechanisms. However, for none of these systems the formation of spatial or spatiotemporal patterns was reported. Our more recent studies were oriented on: (i) simplification of the literature mechanisms towards the “minimal oscillator” reaction scheme, and (ii) creation of the experimental conditions for the formation of spatiotemporal patterns in these systems.

### EXPERIMENTAL

All reagents: Pure for analysis (p.a.) NaSCN (Fluka), p.a. NaOH (Merck, Germany), p.a.  $\text{Na}_2\text{S}_2\text{O}_3 \times 5\text{H}_2\text{O}$  (ChemPur, Poland), p.a. 95 % (w/w)  $\text{H}_2\text{SO}_4$  (ChemPur), p.a.  $\text{CuSO}_4 \times 5\text{H}_2\text{O}$  (ChemPur), p.a. 30%  $\text{H}_2\text{O}_2$  (ChemPur), p.a. luminol (5-amino-2,3-dihydro-1,4-phthalazinedione)  $\text{C}_8\text{H}_7\text{N}_3\text{O}_2$  (Roth, Germany) and thymol blue (POCh, Poland, pure for analysis) were used without further purification. Potentiometric experiments were conducted with different (GC, Au, Pd, Pt) indicator electrodes, with either the  $\text{Ag}|\text{AgSCN}|0.1 \text{ M NaSCN}$  or the  $\text{Ag}|\text{AgCl}|\text{KCl}(\text{sat.})$  reference electrode (separated from the studied solution with an appropriate salt bridge filled with 0.1 M NaSCN or sat. KCl, respectively). For the recording potential-time course a three-channel Hewlett Packard 7090A Measurement Plotting System (USA) was employed.

For the studies of the oscillations both the glass batch reactor ( $V = 25 \text{ cm}^3$ ) and the flow reactor of the same volume were used. The latter reactor was connected to the three-channel peristaltic pump ISMATEC SA MS REGLO (Switzerland), with the stepwise adjustment of the flow rate. The contents of both reactors were homogenized with the use of a magnetic stirrer PM TYPE MM 6 (Poland), and measurements were made at an ambient temperature maintained within the range 292 - 300 K and within the 290 – 320 K range.

Numerical integration of differential equations was performed using the Mathematica ver. 9 software package (© Wolfram Research), with the automatic choice of the integration algorithm involving time step adaptation.

## RESULTS AND DISCUSSION

### 1. Gradual reduction of the 26-variable kinetic mechanism of the $\text{H}_2\text{O}_2\text{-SCN}^- - \text{OH}^- - \text{Cu}^{2+}$ system to the “minimal oscillator”

The first advanced kinetic mechanism of the oscillations and bistability in this system involved 26 intermediate species, engaged in 30 reaction steps [2] and allowed to reproduce both the oscillations and bistability. We undertook the problem of the gradual simplification of the oscillatory course of this mechanism towards the extreme case of the “minimal oscillator”, revealing only those positive and negative feedback loops, which are absolutely essential for the oscillatory instability (see Table 1).

**Table 1.** Construction of the three–variable kinetic mechanism of the Orbán (minimal) oscillator.  $[\text{A}] = 0.075 \text{ M} = \text{const}$ ,  $\text{X} \equiv \text{OS}(\text{O})\text{CN}^-$ ,  $\text{Q} \equiv \text{HO}_2^\bullet$ ,  $\text{R} \equiv \text{HO}_2\text{Cu}(\text{OH})_2^-$ ,  $\text{P}$  = final products. Reprinted from [4] with permission from John Wiley and Sons, Inc. © 2015

Step number	Reaction scheme	Rate constant
I	$\text{A} \rightarrow \text{X}$	$k_1 = 1 \times 10^{-7} \text{ s}^{-1}$
II	$\text{X} \rightarrow m\text{X} + \text{R}$	$k_2 = 6 \times 10^{-3} \text{ s}^{-1}$
III	$\text{R} \rightarrow \text{Q}$	$k_3 = 3 \times 10^{-3} \text{ s}^{-1}$
IV	$\text{X} + \text{Q} \rightarrow \text{P}$	$k_4 = 5 \times 10^3 \text{ M}^{-1}\text{s}^{-1}$

Numerical integration of the autonomous ordinary differential equations corresponding to reactions steps in Table 1 shows the supercritical Hopf bifurcation for the stoichiometric parameter  $m = 1.53$  [4]. For the sake of chemical reliability, also the models, involving 5 and 9 intermediates were elaborated (see below for the application of the 9-variable version).

### 2. Unique potentiometric characteristics of the $\text{H}_2\text{O}_2 - \text{SCN}^- - \text{OH}^- - \text{Cu}^{2+}$ oscillator and its explanation

Potentiometric studies of the dynamics of the  $\text{H}_2\text{O}_2\text{-SCN}^- - \text{OH}^- - \text{Cu}^{2+}$  oscillator (both in batch and the flow reactor) revealed surprising and unique dependence of the phase and amplitude of the oscillations on the chemical nature of apparently inert electrode material (e.g. Au, Pd, and Pt) (Fig. 1).

Explanation of this phenomenon could not be based on the construction of the “minimal oscillator”. This was because the potentiometric response of the inert indicator electrode is essentially a *mixed potential*. It is thus impossible to calculate the contribution from each redox couple, if some of their components are missing in the strongly reduced model. Therefore, we used our nine-variable model, which included, among others, two essential Ox/Red couples:  $[\text{Cu}(\text{OH})_3]^-$

$/[\text{Cu}(\text{OH})_2]^-$  and  $\text{OH}^\bullet/\text{OH}^-$ . Based on this assumption we reproduced the oscillations in the model and proved that independently of the indicator electrode material they are driven by the oscillatory variations of the concentrations of Cu(II) and Cu(I) species [6].

For comparison, one should note that such diverse potentiometric characteristics were not reported for the  $\text{H}_2\text{O}_2 - \text{S}_2\text{O}_3^{2-} - \text{H}^+ - \text{Cu}^{2+}$  oscillator and thus they remain a unique feature of the  $\text{H}_2\text{O}_2 - \text{SCN}^- - \text{OH}^- - \text{Cu}^{2+}$  system.

### 3. Spatiotemporal luminescent patterns in the $\text{H}_2\text{O}_2 - \text{SCN}^- - \text{OH}^- - \text{Cu}^{2+}$ oscillatory system

The search for patterns required a visual indicator – luminol, known from earlier observations of periodic bursts of luminescence [7]. We used a thin-layer reactor being a part of the experimental setup shown in Fig. 2. In the initially homogeneous and quiescent solution with the oscillatory reaction running in the  $\text{H}_2\text{O}_2 - \text{SCN}^- - \text{OH}^- - \text{Cu}^{2+}$  system, in the presence of luminol,

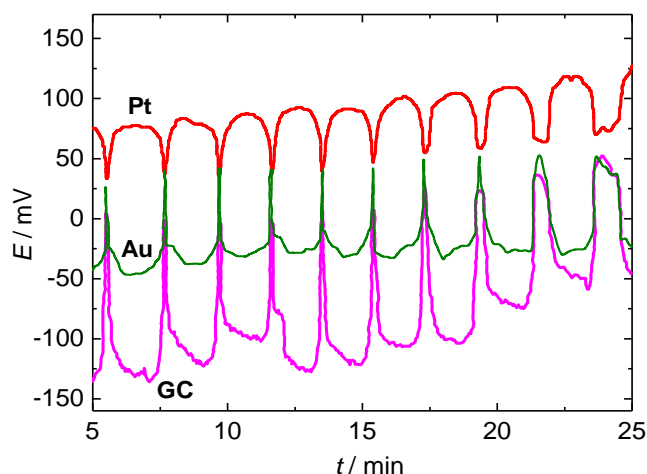


**Figure 1.** Oscillatory variations of the electric potential of various indicator (glassy carbon - GC, Au and Pt) electrodes, for the  $\text{Cu}^{2+}$ -catalyzed oxidation of  $\text{SCN}^-$  with  $\text{H}_2\text{O}_2$ , in a stirred batch reactor. Initial concentrations of reactants (M):  $[\text{H}_2\text{O}_2]_0$ : 0.38;  $[\text{NaSCN}]_0$ : 0.056;  $[\text{NaOH}]_0$ : 0.038;  $[\text{CuSO}_4]_0$ :  $2.46 \times 10^{-4}$ . Temperature: 299.2 K. Reproduced from [5] with permission of Springer

patterns of weak blueish luminescence evolved, only if the distribution of the solution temperature was inhomogeneous. In other words, the externally applied programmed temperature gradient allowed to take control over the formation and the evolution of the traveling luminescent fronts. Technically it was achieved in this way that initially isothermal thin layer of the solution was brought into contact with the non-uniformly preheated transparent cover. For example, Fig. 3 shows that the solution temperature, decreasing from the left to the right edge of the reactor caused the impression of the luminescent front, traveling along the reactor .

Since the speed of the front propagation is much faster than the progress of molecular diffusion but correlates well with the thermal conductivity of water, the reported front is largely a phase (or kinematic) wave. This source of pattern was by us confirmed by the relevant model in which to the slowest step of the 9-variable kinetic mechanism the appropriate activation energy was ascribed, which, through the Arrhenius equation, made the local oscillatory kinetics sensitive to local temperature. It is thus clear that patterns like those shown in Fig. 3 cannot develop in the absence of temperature gradients.

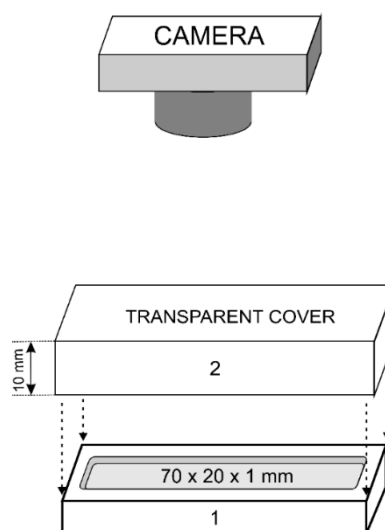


**Figure 2.** Schematic view of the experimental setup with a horizontal thin-layer reactor for monitoring the luminescent chemical waves initiated by temperature gradient: (1) Cuboidal Teflon® block with a 1 mm deep gouge as the reaction space, (2) Transparent Plexiglas® cover as a source of temperature gradient transformed to the adjacent solution in a gouge. In other experiments, instead of Teflon, the graphite block of approximately 5 times larger height and remaining in contact with external water bath (22 °C) was used. Reprinted with permission from [8]. Copyright 2013 American Chemical Society

#### 4. Traveling pH front in the non-oscillatory $\text{H}_2\text{O}_2$ - $\text{S}_2\text{O}_3^{2-}$ - $\text{H}^+$ - $\text{Cu}^{2+}$ system

The pattern formation driven by inhomogeneous temperature field should occur also for other dissipative systems with chemical kinetics appropriately sensitive to temperature, including the  $\text{H}_2\text{O}_2$  -  $\text{S}_2\text{O}_3^{2-}$  -  $\text{H}^+$  -  $\text{Cu}^{2+}$  pH oscillator. However, in the batch reactor (as in Fig. 2) one can expect only a single broad peak of initially low pH (ca. 3-4) which only once and transiently increases to pH ca. 9 (at room temperature), i.e. within the region suitable for application of thymol blue as color indicator. An increase in temperature from 290 to 315 K strongly shortens the duration of the transient, high pH, phase. Therefore, when the solution with the  $\text{H}_2\text{O}_2$  -  $\text{S}_2\text{O}_3^{2-}$  -  $\text{H}^+$  -  $\text{Cu}^{2+}$  system, enriched with thymol blue, was placed in the thin-layer reactor from Fig. 2 and quasi-linear distribution of the solution temperature was imposed, different parts of the solution changed their color from initial yellow to blue and then back to yellow at different times. This produced the impression of the traveling color front, being also a kinematic wave (Fig. 4). Such a thermokinetic mechanism was again confirmed [9] by

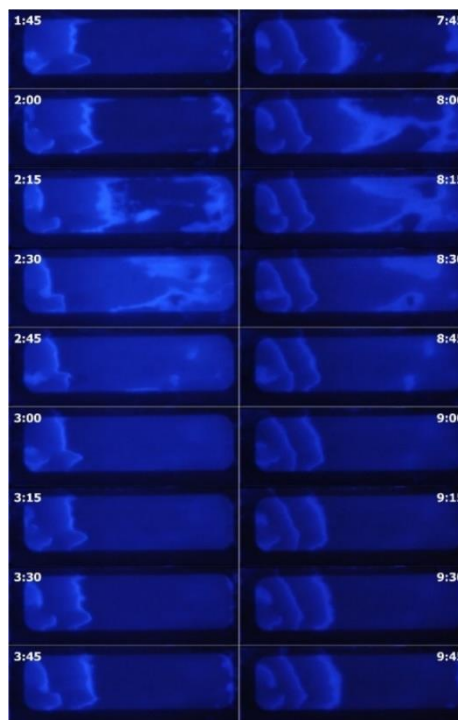


**Figure 3** The programmed birth and spatiotemporal evolution of luminescent waves from the left edge of the thin-layer rectangular Teflon reactor from Fig. 2. The initial composition of the oscillatory system: 0.051 M NaSCN, 0.045 M NaOH, and 0.34 M  $\text{H}_2\text{O}_2$  +  $5.5 \times 10^{-4}$  M luminol. Prior to the experiment  $2.4 \times 10^{-4}$  M  $\text{CuSO}_4$  was added to the sample, the homogeneous solution was transferred to the reactor, covered by transparent Plexiglas block preheated at its left end, and photographs were taken from the top every 15 seconds. See [8] for more details. Reprinted with permission from [8]. Copyright 2013 American Chemical Society.

numerical modeling in which the activation energy was incorporated,

in the form of the Arrhenius dependence, to the respective step of the literature kinetic model of the oscillator [10], extended by us [9].

### CONCLUSION

In spite of earlier extensive experimental and model studies, two  $\text{H}_2\text{O}_2$ -based homogeneous chemical oscillators revealed recently some of their unique dynamic features. In particular, the  $\text{H}_2\text{O}_2$ - $\text{SCN}^-$ - $\text{OH}^-$ - $\text{Cu}^{2+}$  system exhibits, not reported before for any chemical oscillators, differences in the characteristics of the oscillations monitored potentiometrically with different chemically inert electrodes, showing even the opposite phases for the gold and platinum electrode. It proves that one should always use more than one indicator electrode to compare the oscillatory responses. Moreover, it also shows that such characteristics produced by homogenous kinetics cannot be understood without invoking the concepts of interfacial electrochemistry (mixed potential). Various simplified or extended versions of the kinetic mechanisms, including the extreme case

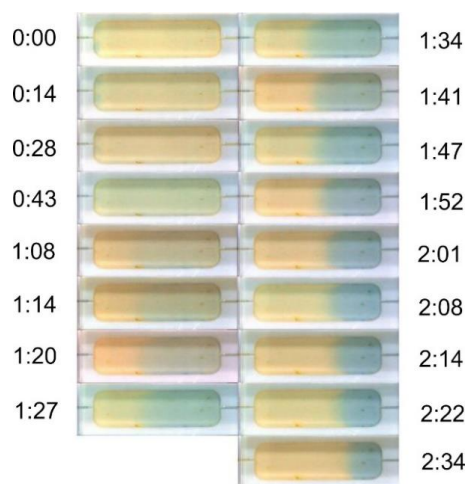


**Figure 4.** Spatiotemporal evolution of a decreased pH front along the thin-layer of the solution in the Teflon reactor from Fig. 2, the left edge of which was preheated in boiling water. With thymol blue as a pH indicator, blue and yellow regions correspond to relatively high (above 9.6) and low (below 8.0) pH, respectively. Subsequent photos were taken approximately every 8 seconds and the time scale is given in [min:sec]. Initial concentrations of reactants: 0.1 M  $\text{H}_2\text{O}_2$ , 0.01 M  $\text{Na}_2\text{S}_2\text{O}_3$ , 0.001 M  $\text{H}_2\text{SO}_4$ ,  $2.5 \times 10^{-6}$  M  $\text{CuSO}_4$  and ca.  $1 \times 10^{-5}$  M thymol blue as an indicator. An initial temperature difference between the opposite ends of the transparent cover was approximately equal to 10 K (i.e. from 310 K to 300 K). See [9] for more details. Reprinted with permission from [9]. Copyright 2016 American Chemical Society

of the “minimal oscillator” help to understand experimental observations. Furthermore, it became understandable that dissipative patterns were not reported before for both  $\text{H}_2\text{O}_2\text{-SCN}^- - \text{OH}^- - \text{Cu}^{2+}$  and  $\text{H}_2\text{O}_2\text{-S}_2\text{O}_3^{2-} - \text{H}^+ - \text{Cu}^{2+}$  systems as they were studied presumably only under isothermal conditions. Imposing non-homogeneous temperature field causes the spatial distribution of the local chemical kinetics, resulting in the formation of the phase (kinematic) waves. The structure-forming effect of the inhomogeneous temperature field is known for the combustion of fuels but was apparently not considered as such factor operating in aqueous solutions subject to relatively minor temperature gradients.

### **Acknowledgement**

This work was partially financed through the research grant N N204 242134 from the Ministry of Science and Higher Education, Poland, for the years 2008 – 2011, for the research project. M. J. acknowledges financial support from the research grant 120000-501/86-DSM-110200, from the Faculty of Chemistry, University of Warsaw.

### **REFERENCES**

- [1] M. Orbán, *J. Am. Chem. Soc.*, 1986, 108, 6893-6898
- [2] Y. Luo, M. Orbán, K. Kustin, I.R. Epstein, *J. Am. Chem. Soc.*, 1989, 111, 4541-4548
- [3] M. Orbán, I. R. Epstein, *J. Am. Chem. Soc.*, 1987, 109, 101-106
- [4] M. Jędrusiak, A. Wiśniewski, M. Orlik, *Int. J. Chem. Kin.*, 2015, 47, 791-802
- [5] K. Pękala, R. Jurczakowski, M. Orlik, *J. Solid State Electrochem.* 2010, 14, 27-34
- [6] A. Wiśniewski, K. Pękala, M. Orlik: *J. Phys. Chem. A*, 2010, 114, 183-190
- [7] S. Sattar, I. R. Epstein, *J. Phys. Chem.*, 1990, 94, 275–277
- [8] A. Wiśniewski, M. T. Gorzkowski, K. Pękala, M. Orlik, *J. Phys. Chem. A*, 2013, 117, 11155 - 11166
- [9] M. Jędrusiak, M. Orlik, *J. Phys. Chem. B*, **120** (2016) 3169-3177
- [10] M. Orbán, K. Kurin-Csörgei, G. Rábai, I. R. Epstein, *Chem. Eng. Sci.*, 2000, 55, 267-273

## EXPANDING THE HORIZONS OF Pd-CATALYSED OSCILLATORY CARBONYLATION REACTIONS: SOLVENT, SUBSTRATE, CATALYST

K .Novaković and A. Isakova

*School of Engineering, Merz Court, Newcastle University, Newcastle-upon-Tyne, UK (katarina.novakovic@ncl.ac.uk)*

### ABSTRACT

On our way to producing all-polymeric self-oscillatory systems, we have expanded the horizons of oscillatory palladium-catalysed oxidative carbonylation reactions by searching for alternative substrates, solvents and even catalysts. In this paper, we demonstrate that pH oscillations of a similar pattern occur both in methanol and ethanol solutions, when using mono- and dialkyne-functionalised benzenes (phenylacetylene and diethynylbenzene, respectively) and when a non-leaching polyacrylate-palladium catalyst is used. The resulting oscillations are highly regular and can be sustained for a long time, suggesting that carbonylation reactions have strong potential for the discovery and development of new oscillatory chemical systems.

### INTRODUCTION

Aiming to produce fully self-oscillatory materials [1], materials that act life-like and are able to carry and dispense their content in a predefined rhythm, we have focused on the oscillatory palladium-catalysed oxidative carbonylation reaction (PCOC) as a driving force. PCOC readily proceeds under mild temperatures (0-40 °C) and atmospheric pressure in batch and can sustain oscillations in pH, redox properties and turbidity over a prolonged period of time (monitored up to a month)[2–6]. We have made a number of advancements in the area of polymeric oscillators within the framework of PCOC. Firstly, we demonstrated polymeric alkyne-terminated polyethylene glycol (PEG) as a viable substrate [7]. Secondly, we studied polymer-bound catalytic species, successfully yielding oscillations under a range of conditions using polymeric dicyclohexylphenylphosphine palladium diacetate [8]. Aiming to aid the ongoing efforts of producing an all-polymer oscillating system, we report here studies employing a new substrate, catalyst and solvents, and showcase their ability to yield sustained oscillatory behavior.

## EXPERIMENTAL

Reactions were performed at approximately 20 °C in a flat-bottom Erlenmeyer flask (100 mL) at constant stirring, while the HEL micronote (or LabVIEW National Instruments, by Jon Howse) system logged pH and temperature within the bulk of the reaction mixture. Prior to the reaction, the pH probe was calibrated at room temperature against NIST-traceable buffer solutions of pH 2, 7 and 10. KI (4.150 g) and palladium diacetate ( $\text{Pd}(\text{OAc})_2$ ) (30 mg) were charged into the flask in their solid state and suspended in 100 mL of solvent (methanol (MeOH), ethanol (EtOH), isopropanol (IPA) or PEG400-OH) by stirring. When polymeric catalyst is used in place of  $\text{Pd}(\text{OAc})_2$ , 200 mg of catalyst is added. In the experimental study employing diethynylbenzene (DEB) as the substrate, 90 mL of MeOH is initially added.

The pH and temperature monitoring started while the KI and catalyst were dissolving and continued throughout the experiment. Stabilisation of pH indicated that the dissolution of KI was complete. Following this, the CO and air purging (15 mL  $\text{min}^{-1}$  each) through the solution commenced. Once the pH value had stabilised following an initial pH drop, substrate was added. Either phenylacetylene (PhAc) (1.38 mL, 12.57 mmol) or diethynylbenzene (DEB) (1.585 g (12.57 mmol) in 10 mL of acetone) was used. A sample of the reaction mixture was taken at the end of the reaction and analysed using GC-MS to determine substrate conversion as well as product content. A Varian Saturn 2200 GC-MS fitted with a VF-5ms column (30 m) was used. The method was as follows: injector temperature 150 °C; helium flow rate 1 mL  $\text{min}^{-1}$ ; oven temperature 100-195 °C over 35 min in 5 steps. Prior to analysis, samples were filtered over silica and then diluted 1:1 with 0.02 M solution of naphthalene in methanol. Naphthalene was used as an internal standard.

## RESULTS AND DISCUSSION

Firstly, we explored four different solvents: MeOH, EtOH, IPA and PEG<sub>400</sub>-OH, while phenylacetylene was used as a substrate and  $\text{Pd}(\text{OAc})_2$  was used as a catalyst. This selection of solvents, which in carbonylation reactions also serve as reactants yielding the formation of esters, covered a range of densities and solubilities of carbon monoxide [9]. As can be noted from Figure 1a), following the initial pH drop oscillations in pH occurred only in the methanol and ethanol reaction systems. The drop of pH during CO purging was associated with the discoloration of the reaction solution, indicating the incorporation of CO into the structure of  $\text{Pd}(\text{OAc})_2$  catalyst. The oscillations in MeOH and EtOH had similar amplitudes (0.40-0.50 for MeOH and 0.45-0.65 for EtOH) and periods (35-45 min for MeOH; and 40-45 min for EtOH), although the induction period in EtOH was longer than in MeOH (275 min

against 79 min). These similarities speak for the comparable affinity of both solvents towards the substrate and CO [7]. End sample GC-MS analysis showed that after 4000 min in both MeOH and EtOH, conversion of substrate was approximately the same (6.6% and 6.7%, respectively), with a similar distribution of products [8] (Figure 2, compounds **1-3** and **4-6**, respectively; Table 1). Only three products were generated as a result of the reaction: Z- and E-isomers of the diester product and a phenylfuranone compound.

At the same time, neither IPA, nor PEG400-OH demonstrated any significant pH changes upon purging with CO. No colour change associated with the incorporation of CO into the structure of the catalyst was observed [8]. While solubility of CO in PEG<sub>400</sub>-OH is anticipated to be low, this should not be the case with IPA [9]. Yet, no substrate conversion was observed by GC-MS, indicating that in these two solvents in the absence of CO insertion into the Pd(OAc)<sub>2</sub> structure, the carbonylation did not occur.

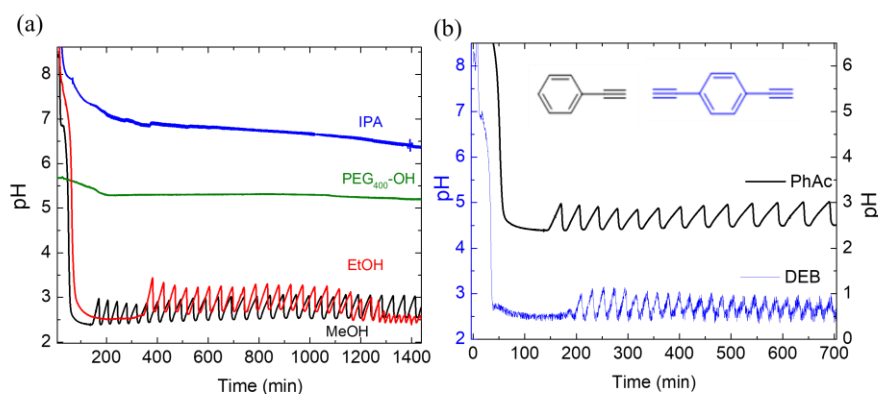


**Figure 1.** (a) pH recorded in the PCOC of phenylacetylene in methanol (black), ethanol (red), isopropanol (blue) and PEG<sub>400</sub>-OH (green line). (b) pH recorded in the Pd(OAc)<sub>2</sub>-catalysed PCOC of phenylacetylene (PhAc, black line) and diethynylbenzene (DEB, blue line).

When phenylacetylene (PhAc) as a mono-functionalised substrate was substituted for diethynylbenzene (DEB) under the same conditions (MeOH as solvent and Pd(OAc)<sub>2</sub> as a catalyst), the pH oscillations, as well as induction period, were similar to those observed in the PhAc substrate system (Figure 1b). The period was shorter for DEB, 19-21 min against 35-45 min for PhAc with the same amplitude of 0.60-0.65 pH units. Importantly, as indicated by GC-MS analysis, in the DEB system, the second alkyne group did not participate in the reaction (Figure 2, compounds **7-9**; Table 1). This might be associated with the electronic effects of the substituents on the benzene ring affecting the reactivity of the second alkyne group, and thus

preventing it from participation in the carbonylation. This example of dialkyne-functionalised molecule and prospective studies where both alkyne groups should remain active in the PCOC reaction, suggests the importance of a spacer between these two functionalities.

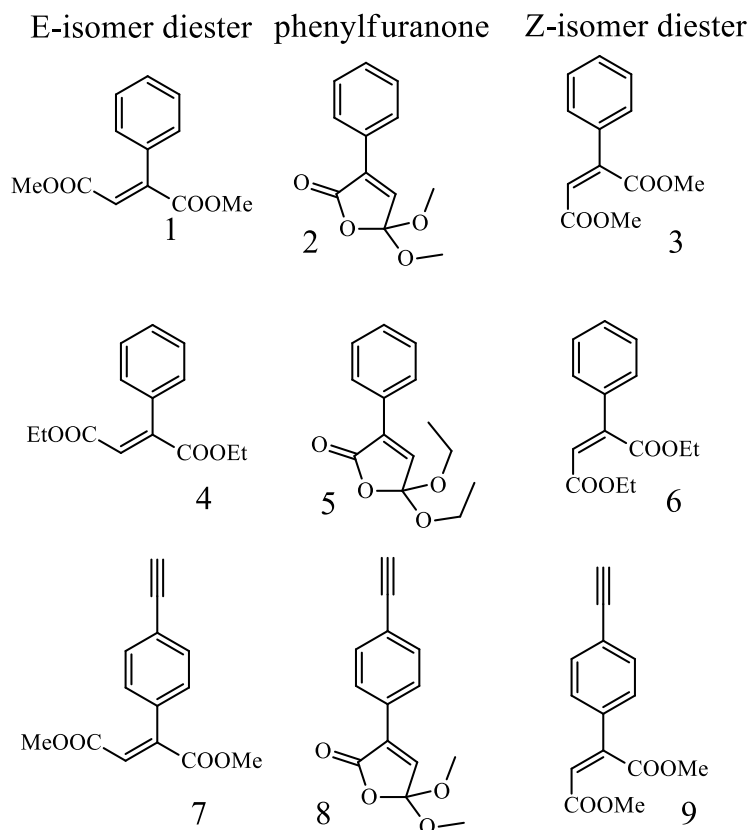


**Figure 2.** Products of the PCOC reaction: **1** dimethyl (2E)- 2- phenyl- 2- butenedioate; **2** 5,5- dimethoxy- 3- phenyl- 2(5H)- furanone; **3** dimethyl (2Z)- 2- phenyl- 2- butenedioate; **4** diethyl (2E)- 2- phenyl- 2- butenedioate; **5** 5,5- diethoxy- 3- phenyl- 2(5H)- furanone; **6** diethyl (2Z)- 2- phenyl- 2- butenedioate; **7** dimethyl (2E)- 2- (4-ethynyl)phenyl- 2- butenedioate; **8** 5,5- dimethoxy- 3- (4-ethynyl)phenyl- 2(5H)- furanone; **9** dimethyl (2Z)- 2- (4-ethynyl)phenyl- 2- butenedioate.

**Table 1.** Product distributions and starting material conversions for various PCOC conditions after 4000 min of the reaction.

	<b>E-isomer, mmol (1, 4, 7)*</b>	<b>Z-isomer, mmol (3, 6, 9)*</b>	<b>phenyl furanone, mmol (2, 5, 7)*</b>	<b>Conversion [%]</b>
<b>PhAc/Pd(OAc)<sub>2</sub>/MeOH</b>	-	0.53	0.30	6.60
<b>PhAc/Pd(OAc)<sub>2</sub>/EtOH</b>	0.036	0.50	0.30	6.70
<b>PhAc/Pd(OAc)<sub>2</sub>/IPA</b>	-	-	-	-
<b>PhAc/Pd(OAc)<sub>2</sub>/PEG<sub>400</sub>-OH</b>	-	-	-	-
<b>DEB/Pd(OAc)<sub>2</sub>/MeOH</b>	0.036	0.51	0.56	8.84
<b>PhAc/polyacrylate-Pd/MeOH</b>	0.040	0.40	0.47	6.95

\* the calculations were based on the assumption of the same detector response for E-isomer diester compounds 1,4,7; phenylfuranone compounds 2,5,8; and Z-isomer diester compounds 3,6,9.

Finally, we substituted the small catalyst molecule Pd(OAc)<sub>2</sub>, with a polymeric polyacrylate-Pd [11] in the same experiments (phenylacetylene (PhAc) as a substrate and MeOH as a solvent) (Figure 3). In polymeric polyacrylate-Pd the molecules of palladium serve as crosslinkers between the polymer chains, and polyacrylate as a counter ion, rather than as a ligand to support palladium [8]. This construct allowed a high loading of palladium to be achieved (16.26% as determined by inductively-coupled plasma optical emission spectrometry, ICP-OES) and zero leaching of palladium from the catalyst (as determined by ICP-OES, after the reaction).

In the polyacrylate-Pd-catalysed system, the pH behaved in a similar way to when small molecule Pd(OAc)<sub>2</sub> was used. An initial pH drop was recorded while the KI/catalyst mixture was purged with CO. A further pH drop was observed after addition of the PhAc substrate. This pH drop then recovered from 5.05 to 5.59 when the pH oscillations started, 206 min after addition of PhAc. The oscillations occurring at this high pH are rarely observed [4,12]. It is worth noting that in the case of polyacrylate-Pd, the recorded oscillations had a period of 18-24 min and a small amplitude of 0.1-0.15 pH units.

After 4000 min, the conversion was 6.95%, very similar to conversion in the Pd(OAc)<sub>2</sub> systems in MeOH and EtOH (Table 1). However, product distribution was different, with almost equal concentrations of compounds 2 and 3, Table 1.

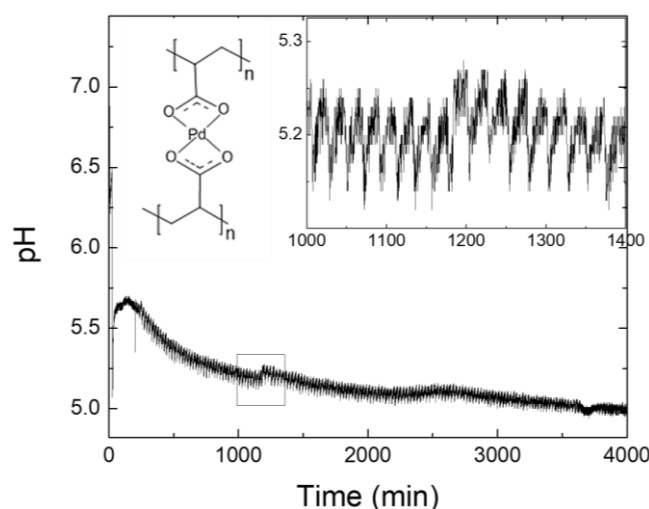


**Figure 3.** pH recorded in PCOC of phenylacetylene (PhAc) in methanol using polyacrylate-Pd catalyst. The structure of the catalyst is shown as an inset.

## CONCLUSION

We have demonstrated the versatility of the PCOC reaction by obtaining oscillations in pH in Pd(OAc)<sub>2</sub>-catalysed carbonylation of phenylacetylene in both ethanol and methanol, solvents with a similar carbon monoxide solubility, whereas no oscillations were observed in isopropanol or PEG400-OH. Furthermore, oscillations had a very similar pattern, period and amplitude. The same oscillatory patterns were demonstrated when dialkyne-functionalised substrate was employed, with only one alkyne group participating in the reaction (as determined by GC-MS). Finally, oscillations were demonstrated, using polymeric polyacrylate-Pd catalyst with zero leaching rates, a promising candidate for future exploration in all-polymeric self-oscillating systems.

## REFERENCES

- [1] A. Isakova, K. Novakovic, *Eur. Polym. J.* 95 (2017) 430–439.
- [2] S.N. Gorodsky, *React. Kinet. Mech. Catal.* 1 (2018.) 93-112.
- [3] K. Novakovic, C. Grosjean, S.K. Scott, A. Whiting, M.J. Willis, A.R. Wright, *Chem. Phys. Lett.* 435 (2007) 142–147.
- [4] J. Parker, K. Novakovic, *ChemPhysChem* 18 (2017) 1981–1986.
- [5] J. Parker, K. Novakovic, *React. Kinet. Mech. Catal.* 118 (2016) 73-85.
- [6] L. Donlon, J. Parker, K. Novakovic, *React. Kinet. Mech. Catal.* 112 (2014) 1-13.
- [7] L. Donlon, K. Novakovic, *Chem. Commun.* 50 (2014) 15506–15508.

- [8] A. Isakova, B. Murdoch, K. Novakovic, *Phys. Chem. Chem. Phys.* 20 (2018) 9281-9288.
- [9] IUPAC, Analytical Chemistry Division Commission on Solubility Data, Solubility Data Series, Vol 43, Carbon Monoxide, <https://srdata.nist.gov/solubility/IUPAC/SDS-43/SDS-43.pdf>
- [10] C. Grosjean, K. Novakovic, S.K. Scott, A. Whiting, M.J. Willis, A.R. Wright, *J. Mol. Catal. A Chem.* 284 (2008) 33–39.
- [11] S.U. Rehman, F.A. Khwaja, A. Ul Haq, M.S. Zafar, *Polym. Degrad. Stab.* 45 (1994) 267–272.
- [12] J. Parker, K. Novakovic, *React. Kinet. Mech. Catal.* 123 (2018) 113–124.

## CATEGORIZING OF SYSTEMS FEATURING CLOCK BEHAVIOUR UNEQUIVOCALLY

A. K. Horváth

*University of Pécs, Institute of Chemistry, Department of Inorganic Chemistry,*

*Ifjúság u. 6., 7624 Pécs, Hungary. (horvatha@gamma.ttk.pte.hu)*

### ABSTRACT

When a product forms instantaneously after a certain time lag in a chemical system, usually this feature is called as a clock reaction. The original Landolt reaction [1] (sulfite-iodine system) is autocatalytic with respect to both hydrogen and iodide ions, where the characteristic color of iodine appears suddenly only if certain stoichiometric requirements are fulfilled. Thus it seems to be straightforward that existence of stoichiometric constraints is a necessary prerequisite to categorize a reaction as a clock reaction. However, when a reaction is strongly autocatalytic with respect to a product it is also evident that formation of a product is somewhat delayed and simultaneously its formation may be so fast after this well-defined time lag that opens a possibility to characterize this reaction a clock reaction as well.[2] The dispute over the term of clock reaction has yet not been settled[3,4] therefore a new approach to classify systems featuring clock behavior is introduced. It is recommended [5] that recently discovered reactions featuring clock behavior can easily be categorized into three groups, substrate-driven clock behavior, autocatalysis-driven clock behavior and crazy-clock behavior. Based on real chemical systems it is shown that these groups are not distinct ones and change of the experimental conditions may easily lead to an interesting situation that classification of a chemical reaction cannot be unequivocal and may even depend on the experimental conditions as well. We shall show unambiguously that in case of the arsenous acid-iodate system depending on the experimental condition the reaction can be classified as a clock reaction (at high pHs), but at low pHs the appearance of iodine is not connected with depletion of arsenous acid hence the system cannot be categorized as a clock reaction.

Consequently, we suggest that categorization based on a phenomenological approach seems to be more appropriate than the easily conceivable so called „mechanistic approach” containing the necessary requirement of a stoichiometric constraint.

The lecture will systematically analyze different reaction systems from the literature exhibiting clock behavior.

### ***Acknowledgement***

This project has been supported by the European Union, co-financed by the European Social Fund Grant no.: EFOP-3.6.1-16-2016-00004 entitled by Comprehensive Development for Implementing Smart Specialization Strategies at the University of Pécs as well as by the Hungarian Research Fund, NKFIH-OTKA Grant no K116591.

### **REFERENCES**

- [1] H. Landolt, Chem. Ber., 1886, 19, 1317.
- [2] R. T. P. Sant'Anna, E. V. Monteiro, J. R. T. Pereira, R. B. Faria, R. B., Plos One, 2013, 8, e83706.
- [3] A. P. Oliveira, R. B. Faria, J. Am. Chem. Soc., 2005, 127, 18022.
- [4] G. Lente, G. Bazsa, I. Fábián, New J. Chem., 2007, 31, 1707.
- [5] A. K. Horváth, I. Nagypál, ChemPhysChem, 2015, 16, 588.

## DECOUPLING THE AUTOCATALYTIC AND THE AUTOINHIBITORY STEPS IN A STOICHIOMETRIC MODEL OF THE HYPOTHALAMIC-PITUITARY-ADRENAL AXIS

Ž. Čupić<sup>1</sup>, V. Vukojević<sup>2</sup>, A. Stanojević<sup>3</sup>, V.M. Marković<sup>3</sup>, S. Maćešić<sup>3</sup> and Lj. Kolar-Anić<sup>1,3</sup>

<sup>1</sup> *University of Belgrade, Institute of Chemistry, Technology and Metallurgy, Department of Catalysis and Chemical Engineering, Njegoševa 12, 11000 Belgrade, Serbia. ([zcupic@ihm.bg.ac.rs](mailto:zcupic@ihm.bg.ac.rs))*

<sup>2</sup> *Karolinska Institute, Department of Clinical Neuroscience, Center for Molecular Medicine CMM L8:01, 17176 Stockholm, Sweden*

<sup>3</sup> *University of Belgrade, Faculty of Physical Chemistry, Studentski trg 12-16, 11000 Belgrade, Serbia.*

### ABSTRACT

Direct autocatalytic and autoinhibitory steps that epitomize the positive and negative feedback actions of the glucocorticoid hormone cortisol on the hypothalamic-pituitary-adrenal axis in a series of stoichiometric network models are uncoupled to include the glucocorticoid receptor (GR) and the mineralocorticoid receptor (MR) as dynamical variables. We demonstrate here that the instability and oscillating potential of the model are maintained while the feedback actions are described by more realistic reaction steps.

### INTRODUCTION

A reaction system can be in the oscillatory dynamic state if it possesses the feedback with respect to at least one of the intermediate species. [1] The simplest two-variable non-linear representation that describes feedback actions and gives rise to oscillatory behavior in a mathematical model of a chemical reaction system is in the form of direct autocatalytic (AC) and autoinhibitory (AI) steps: [2]



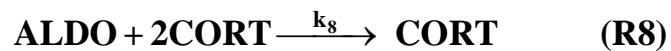
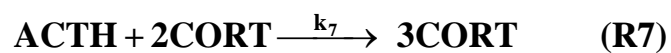
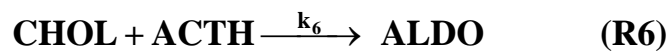
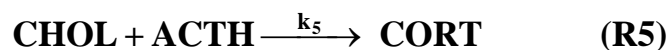
These direct representations of feedback actions must be considered as net reactions encompassing numerous elementary steps, since they do not appear in any real reaction system in the outlined form. However, decoupling of these

direct autocatalytic and autoinhibitory steps is not trivial and the oscillatory dynamics may be lost in this process. [3] In the following, we present a successful decoupling of the direct AC and AI steps in a stoichiometric model of the hypothalamic-pituitary-adrenal (HPA) axis.

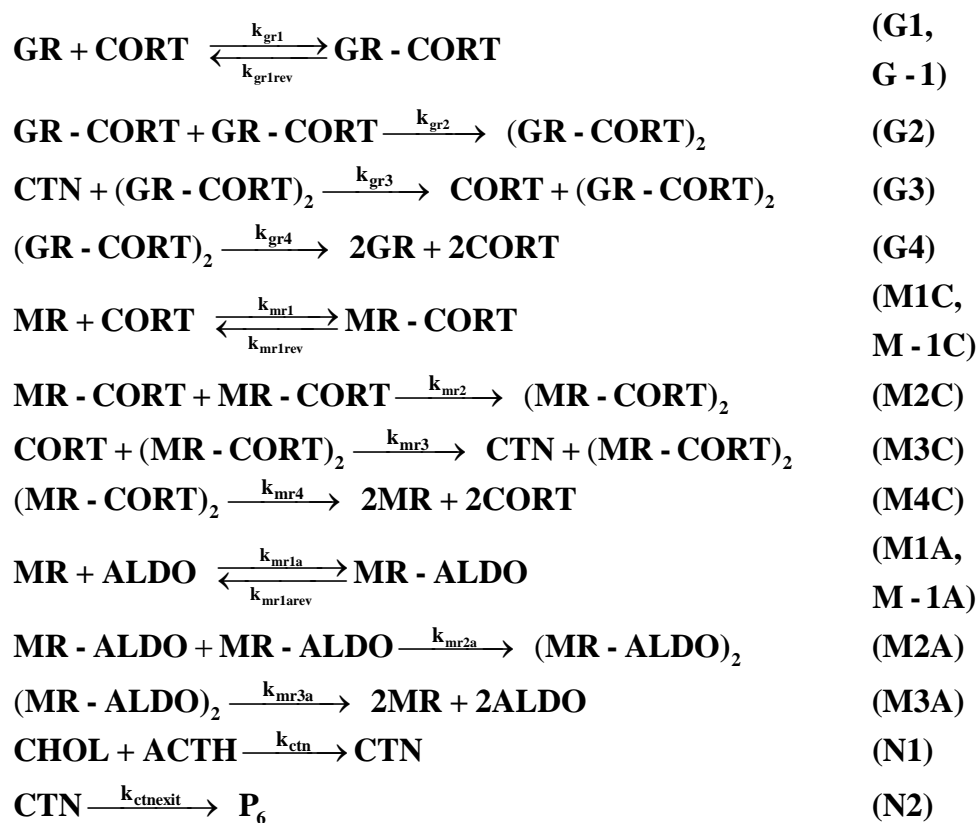
Since the beginning of our work [4], several variants of the model were formulated, recently reviewed in [5], to emulate dynamic features of the HPA axis, which is the main stress responding neuro-endocrine subsystem in mammalian organisms. All of them contain the unique instability core with the direct AC and AI steps presented above. Due to these two steps, ultradian oscillations of the HPA axis were successfully simulated. Moreover, when coupled with a circadian periodic function, double periodicity of the HPA axis is described as well. The circadian periodic function  $D$  modulates inherent ultradian oscillations, imitating the day-night secretory dynamics of the HPA glands.

Modelling the experimentally found positive and negative feedback actions of cortisol on the HPA axis using direct autocatalysis and autoinhibition was an initially necessary oversimplification [4] that allowed us to account for negative feedback of cortisol, which is commonly recognized in the literature as part of the control system of the HPA axis, [6] and its positive feedback actions, for which the underlying mechanism is still being a matter of discussion. [7-9] Both the AC and AI feedback loops are complex regulatory networks that involve glucocorticoid and mineralocorticoid receptor binding with their corresponding ligands.

The aim of the present article is to replace the direct AC and AI steps in the HPA axis model by corresponding loops of more realistic reaction steps, while preserving the potential of the model to accurately emulate ultradian oscillations in blood levels of principal HPA axis hormones. For this purpose, a five-dimensional variant of the model was selected that includes only main HPA axis components: peptide hormones represented by the corticotropin-releasing hormone (CRH) and the adrenocorticotrophic hormone (ACTH), steroid hormones represented by the glucocorticoid hormone cortisol (CORT) and the mineralocorticoid aldosterone (ALDO), and cholesterol (CHOL), the sole precursor of all steroid hormones. [10] The initial model, with direct autocatalytic (R7) and autoinhibitory steps (R8) is shown in Table 1.

**Table 1.** Initial model of the HPA axis dynamics with direct autocatalytic and autoinhibitory steps.**UNCOUPLING THE DIRECT FEEDBACK STEPS**

Instead of the direct reaction steps (R7) and (R8) in the initial model describing neuroendocrine transformations underlying the HPA axis (Table 1), several reaction steps (Table 2) are introduced in the new model to succinctly account for the complex ligand-induced activation of GR and MR.

**Table 2.** Uncoupling of direct autocatalytic and autoinhibitory steps.

Upon entering the cell, cortisol binds to the glucocorticoid receptor (GR) in the cytoplasm forming a ligand-receptor complex (GR-CORT). This process, which is subsequently followed by a series of biochemical interactions that result in GR translocation from the cytoplasm into the cell nucleus, is succinctly represented in the model (Table 2) by the reverse reaction of CORT binding to the GR (G1, G-1). During this intricate process a homodimer (GR-CORT)<sub>2</sub> is being formed, which is represented by (G2) [11-13]. The subsequent cascade of complex process in which CORT autoregulates its own production by facilitating the transformation of cortisone (CTN) to cortisol, a process that is mediated by the enzyme 11β-hydroxysteroid dehydrogenase (11β-HSD) which production is regulated by CORT, is accounted for by the step (G3). [13-16] Finally, the reaction step (G4) represents the multifaceted disintegration of the GR-CORT dimer after it has exerted its physiological effects. [12, 13]

In addition to binding to GR, CORT binds also to MR. This is described in Table 2 by a sequence of reaction steps (M1C-M4C), which is analogous to reaction steps (G1-G4). [17-21]

In contrast to GR which are ubiquitously present in almost all of the cells in the body, MR are found in the heart, brain, epithelial kidney cells, colon, and exocrine glands. When the brain is concerned, GR can be found in hypothalamus and pituitary glands, while most MR in the brain are in the hippocampus. [17-19] It is important to emphasise that as an inactive form of cortisol, cortisone does not bind to MR. Upon entering the cell, cortisol can also bind to MR forming a complex (MR-CORT). This process is represented in the model by the reverse reaction (M1C, M-1C). The process of (MR-CORT)<sub>2</sub> formation is represented by the reaction step (M2C). [20, 21]

Reaction (M3C) describes complex process in which genomic effects of (MR-CORT)<sub>2</sub> facilitate transformation of cortisol to cortisone. 11 $\beta$ -HSD type 2 catalyses conversion of active cortisol to inactive cortisone. [21]

Reaction (M4C) represents the multistep disintegration of dimer (MR-CORT)<sub>2</sub> into MR and cortisol after exerting its physiological effects. [20, 21]

In contrast to CORT which can bind to both GR and MR, ALDO can bind only to MR. [22] In tissues where ALDO exerts its action, 11 $\beta$ -HSD type 2 catalyses conversion of active CORT to inactive CTN. [19, 21] Reaction steps which describe ALDO binding and action at MR are analogous to those of cortisol, as concisely represented by reaction steps (M1A-M3A) in Table 2, where ALDO reversibly binds to MR forming a ligand-receptor complex (MR-ALDO) (represented by the reverse reaction (M1A, M-1A)); complex MR-CORT dimerize forming a dimer (MR-ALDO)<sub>2</sub> (represented by reaction step (M2A)); disintegration of dimer (MR-ALDO)<sub>2</sub> into MR and aldosterone (represented by reaction step (M3A)).

Finally, in analogy with reaction steps (R5) and (R6) in Table 1, reaction step (N1) in Table 2 represents the production of CTN from cholesterol following the activation by ACTH. Reaction (N2) represents elimination of cortisone.

## NUMERICAL SIMULATION

Numerical simulation of the ultradian CORT oscillations using the new model (Table 2) is given in Figure 1.

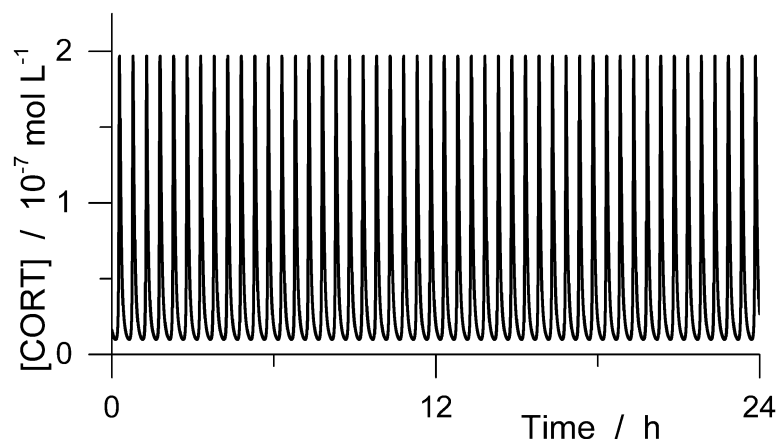


**Figure 1.** Numerical simulation of CORT blood levels using the new model (Table 2), where the direct autocatalytic steps are uncoupled.

Oscillations in Fig. 1 are obtained without changing the rate constants of the remaining reaction steps in the initial model (Table 1). Only the rate constants of the new reactions are selected to ensure oscillating potential of the model. (See Tables 1 and 2)

## CONCLUSION

A simple model of the HPA axis dynamics is further developed to decouple the core of instability in a stoichiometric network model of the HPA axis dynamics. In the newly derived model the direct AC and AI steps are uncoupled and replaced by several more realistic reaction steps that include GR and MR as dynamical variables. Feedback loops were designed to include only highly probable steps that can be justified by known facts of reaction mechanism. Resulting new model is also able to simulate ultradian oscillations in cortisol levels.

## Acknowledgement

This work was partially supported by the Ministry for Science of the Republic of Serbia (Grants 172015 and 45001) and the ERASMUS+ exchange program.

## REFERENCES

- [1] Lj. Kolar-Anić, S. Anić, Ž. Čupić, A. Ivanović-Šašić, N. Pejić, S. Blagojević and V. Vukojević, Chapter 23 Oscillating Reactions, in Encyclopedia of Physical Organic Chemistry, (Eds) Z. Wang, U. Wille,

- E. Juaristi, Vol. 2, Part 2 Organic Reactions and Mechanisms, p.p. 1127-1222, Wiley, New York, 2017.
- [2] S. Maćešić Ž. Čupić, S. Anić, Lj. Kolar-Anić, International Journal of Non-Linear Mechanics, 2015, 73, 25-30.
- [3] G.B. Cook, P. Gray, D.G. Knapp, S.K. Scott, Journal of Physical Chemistry, 1989, 93, 2749–2755.
- [4] S. Jelić, Ž. Čupić, Lj. Kolar-Anić, Mathematical Biosciences, 2005, 197, 173-187.
- [5] A. Stanojević, V.M. Marković, Ž. Čupić, Lj. Kolar-Anić and V. Vukojević, Current opinion in chemical engineering, 2018, 21, 84–95.
- [6] A.E. Calogero, W.T. Gallucci, P.W. Gold, G.P. Chrousos, The Journal of Clinical Investigation, 1988, 82, 767–774
- [7] J.P. Schulkin, P.W. Gold, B.S. McEwen, Psychoneuroendocrinology, 1998, 23, 219–243.
- [8] S. Makino, K. Hashimoto, P.W. Gold, Pharmacology, Biochemistry and Behavior, 2002, 73, 147-158.
- [9] H.L. Fehm, K.H. Voigt, G. Kummer, E.F. Pfeiffer, The Journal of clinical investigation, 1979, 64, 102-108.
- [10] V.M. Marković, Ž. Čupić, S. Maćešić, A. Stanojević, V. Vukojević, Lj. Kolar-Anić, Mathematical Medicine and Biology 2016, 33, 1–28
- [11] C. Kellendonk, P. Gass, O. Kretz, G. Schütz, F. Tronche, Brain research bulletin, 2002, 57, 73-83.
- [12] M.D. Heitzer, I.M. Wolf, E.R. Sanchez, S.F. Witchel, D.B. DeFranco, Reviews in endocrine and metabolic disorders, 2007, 8, 321-330.
- [13] K. Scheschowitsch, J.A. Leite, J. Assrey, Frontiers in endocrinology, 2017, 8, article 16.
- [14] H. Ortsäter, Å. Sjöholm, A. Rafacho, Regulation of glucocorticoid receptor signaling and the diabetogenic effects of glucocorticoid excess. INTECH Open Access Publisher, 2012.
- [15] J.E. Hall. Guyton and Hall textbook of medical physiology - e-Book. Elsevier Health Sciences, 2015.
- [16] S. Whirledge, D.B. DeFranco. Endocrinology, 2017, 159, 46-64.
- [17] E.R. de Kloet, E Vreugdenhil, M.S. Oitzl, M. Joel, Endocrine reviews, 1998, 19, 269-301.
- [18] C. Tsigos, G.P. Chrousos, Journal of psychosomatic research, 2002, 53, 865-71.
- [19] D. Vojnović Milutinović Analiza funkcije i ekspresije glukokortikoidnog receptora kod žena obolelih od sindroma policističnih jajnika. Doctoral thesis, Faculty of Biology, University of Belgrade, Belgrade, 2010.

- [20]F.M. Rogerson, F.E. Brennan, P.J. Fuller, *Molecular and cellular endocrinology*, 2004, 217, 203-212.
- [21]M. Joëls, E.R. de Kloet, *Journal of Endocrinology*. 2017, 234, T49-66.
- [22]M.A. Sacta, Y. Chinenov, I. Rogatsky, *Annual review of physiology*, 2016, 78, 155-80.

## ADAPTING THE BELOUSOV-ZHABOTINSKY REACTION AS A QUANTITATIVE TASK FOR THE 50<sup>th</sup> INTERNATIONAL CHEMISTRY OLYMPIAD

E. Szabo

*Department of Physical and Theoretical Chemistry, Faculty of Natural Sciences, Comenius University in Bratislava, Mlynská dolina, 84215 Bratislava, Slovakia. (erik.szabo@uniba.sk)*

### ABSTRACT

Each year, thousands of motivated students all around the globe compete to represent their country at the International Chemistry Olympiad (IChO). In 2018, practical tasks for IChO were made in Slovakia, and our Preparatory Problems were dedicated to the Belousov-Zhabotinsky reaction. They have combined approaches known previously with new insights, e.g. we have demonstrated that almost complete FKN mechanism follows quite naturally from just a few experiments. Most importantly, in our Preparatory Problems we have maximized showcasing the BZ reaction as a system that can be studied quantitatively.

### INTRODUCTION

IChO is the highest-level competition in chemistry for high-school students, currently involving 82 countries [1]. It is at the top of a hierarchy of national, regional and local competition rounds, driving a large network of dedicated students and teachers with passion for chemistry.

In 2018, the jubilee 50<sup>th</sup> IChO was organized in cooperation of two countries, Slovakia and the Czech Republic, with the slogan *Back to Where It All Began*, because it was in Czechoslovakia, where IChO was founded and held for the first time, in July 1968.

By coincidence, in the same month of 1968, Prague also hosted another international event, one of a few rare occasions that brought together Western scientists with the scientists from the Eastern Bloc. It was at this conference named *Biological and Biochemical Oscillators*, that a young Russian chemist Anatol Zhabotinsky presented to



**50<sup>th</sup> IChO 2018**  
INTERNATIONAL CHEMISTRY OLYMPIAD  
SLOVAKIA & CZECH REPUBLIC

**Figure 1.** Logo.

the audience a remarkable new oscillator, now known as the Belousov-Zhabotinsky (BZ) reaction.

Although discovered much earlier by Belousov, only after Zhabotinsky's careful verifications did the reaction finally attract the worldwide attention that it deserved. For that reason, it is the 1968 conference in Prague that is sometimes cited as the birthplace of nonlinear chemical dynamics [2].

With chemical kinetics being an established topic of IChO tasks in physical chemistry, the 50<sup>th</sup> IChO was a perfect occasion to dedicate our set of Preparatory Problems [3] to promoting the subject of oscillating reactions.

### THE PREPARATORY PROBLEMS

Each task of the competition must be appropriately introduced with a set of Preparatory Problems (PPs) published several months before the competition, especially if the tasks contain concepts and skills considered as Advanced Topics. With respect to dedicating the PPs to the BZ reaction, we set out to incorporate the following themes:

- observing the BZ oscillator in a stirred reactor, as well as formation of spatio-temporal structures on a Petri dish, ideally using recipes as similar as possible
- understanding the core chemistry behind the BZ oscillations, ideally elucidating some of the steps of its mechanism through guided inquiry
- focus on the potential of the BZ reaction as a system that can be studied and evaluated quantitatively

Fortunately, practical restrictions on the PPs are not as severe as those on the competition tasks that must be solved by 320 students simultaneously. PPs are usually exercised on a national level, in boot camps organized by Universities for selected groups of candidates, who can qualify for IChO. Therefore, the part with stirred BZ oscillator, for instance, could be designed for a proper jacketed reactor with a circulation thermostat.

### GUIDED INQUIRY INTO THE BZ REACTION MECHANISM

The mechanism of the BZ reaction is often seen as elaborate, uncovered only through years of research. However, as it turned out, almost entire FKN mechanism can be deduced very naturally from just a few simple experimental observations combined with some basic formal requirements.

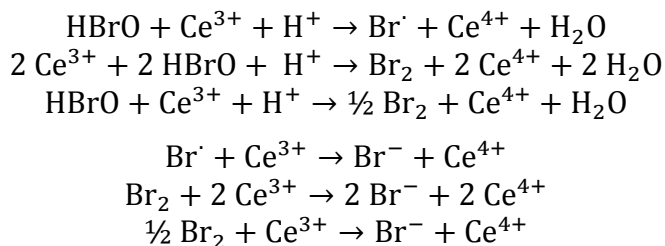
**One-period BZ clock.** Of paramount importance to understanding the BZ oscillations is a clock reaction that results from a simple modification of the BZ recipe. If we combine bromate(V), a metal catalyst, and we replace the organic substrate with some bromide, for some time the metal catalyst will remain in its reduced state, and then transition abruptly to the oxidized state.

Most obviously, this demonstrates that the oxidation of the metal catalyst is inhibited by bromide. More importantly, it also proves, that the catalyst is not oxidized directly by bromate(V), because there is clearly a period, when plenty of bromate(V) is present side by side with the reduced-form catalyst.

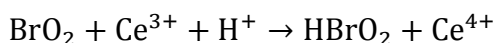
**Formal requirements on the mechanism.** Indeed, in the question which species oxidizes the metal catalyst, the key fact is that a one-electron oxidation must be taking place. Not all bromine-containing species can undergo one-electron reduction.

Bromine is not considered to exist in a  $\text{Br}^{\text{II}}$ , therefore we can rule out that the metal catalyst is oxidized by any  $\text{Br}^{\text{III}}$  species. Still, we are left with three couples of oxidations states that are allowed:  $\text{Br}^{\text{IV}}/\text{Br}^{\text{III}}$ ,  $\text{Br}^{\text{I}}/\text{Br}^{\text{0}}$  and  $\text{Br}^{\text{0}}/\text{Br}^{-\text{I}}$ .

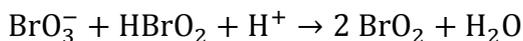
There are multiple ways to disqualify the couples involving  $\text{Br}^{\text{0}}$  based on formal requirements. We can enforce that the only radical allowed in the BZ reaction mechanism is  $\text{BrO}_2$ , or in other words, the only form of  $\text{Br}^{\text{0}}$  must be a  $\text{Br}_2$  molecule. Finally, we point out, that the mechanism should always include oxidized and reduced species in a 1:1 stoichiometry, and integer stoichiometric coefficients for all products. That rules out any oxidation of the metal catalyst (here cerium) by a  $\text{Br}^{\text{I}}/\text{Br}^{\text{0}}$  or a  $\text{Br}^{\text{0}}/\text{Br}^{-\text{I}}$  redox couple:



**Autocatalysis and inhibition.** Overall, we were left with only one option for how the metal catalyst is oxidized – by a  $\text{Br}^{\text{IV}}/\text{Br}^{\text{III}}$  redox couple.



Moreover, there is just one option for how that  $\text{BrO}_2$  can be produced:



These two reactions can be summed in two ways, either by eliminating  $\text{BrO}_2$  or by eliminating  $\text{HBrO}_2$ . Either way, the resulting summed equation will be autocatalytic.

To inhibit this autocatalytic cycle,  $\text{Br}^{-}$  must deplete either  $\text{BrO}_2$  or  $\text{HBrO}_2$ . However, with the above formal requirements in place,  $\text{Br}^{-}$  cannot be oxidized to  $\text{Br}^{\text{0}}$ , and the only option for the inhibition is the following:



**The organic subset.** Based on just a single modification of the BZ reaction into a one-period clock reaction, it was possible to work out the key reactions responsible for the positive and negative feedback loops. With just one more modification the picture may be completed even with the organic subset.

If we combine bromate(V), organic substrate and bromide, but this time we omit the metal catalyst, we will observe the classical synproportionation formation of  $\text{Br}_2$ , followed by its gradual consumption through bromination of the organic substrate. These reactions are probably the easiest to decipher for the students, so we used them as warm-up questions.

This needs to be combined with the insight from the other modification of the reaction – that each transition of the BZ oscillator to the oxidized state represents the point where bromide is consumed. The full circle of the BZ mechanism is closed by asking where the bromide for each cycle comes from.

### EXPLORING SUITABLE CATALYSTS

Among the many practical issues that had to be addressed to present the best BZ recipe for our PPs, a particularly important decision was on the metal catalyst. In the end, we adopted a mixed catalyst, with some ferroin, but mostly cerium. While the ferroin provided attractive color changes, cerium guaranteed reasonable induction periods and periods of oscillation at reasonable color intensities.

Ferroin alone had the disadvantage that at desired color intensity periods of oscillation tended to be rather short and the induction periods too large. Most importantly, in the one-period BZ clock modification, ferroin in its reduced state and bromine yielded a brown suspension that was unattractive, and it obscured what was really happening in the reaction.

**Mn-pyrophosphate-catalyzed BZ reaction.** We also examined whether manganese could be used as the metal catalyst under the right circumstances. Normally, Mn-catalyzed BZ does not provide striking color changes. However, it is known that bromate oxidation of  $\text{Mn}^{2+}$  can be turned into a colorful clock reaction [4] by addition of  $\text{Na}_4\text{P}_2\text{O}_7$ , which yields purple  $\text{Mn}^{\text{III}}$  complex anion,  $[\text{Mn}(\text{H}_2\text{P}_2\text{O}_7)_3]^{3-}$ .

Previously it was thought that in the Mn-catalyzed BZ reaction only a very small fraction of the catalyst transits into the oxidized state [5]. Therefore, to increase our chances of observing the purple  $\text{Mn}^{\text{III}}$  complex, we adapted a BZ recipe that was known to produce some faint, but visible red color of oxidized Mn even without pyrophosphate (Figure 2a).

Surprisingly, when  $\text{Na}_4\text{P}_2\text{O}_7$  was added (Figure 2b), we did not observe the purple color of  $[\text{Mn}(\text{H}_2\text{P}_2\text{O}_7)_3]^{3-}$  only in the oxidized phases. To the contrary, the reaction was purple with the  $\text{Mn}^{\text{III}}$  complex throughout.

Oscillations were still detected, but they were manifested only as hints of color intensification during the oxidized phases.

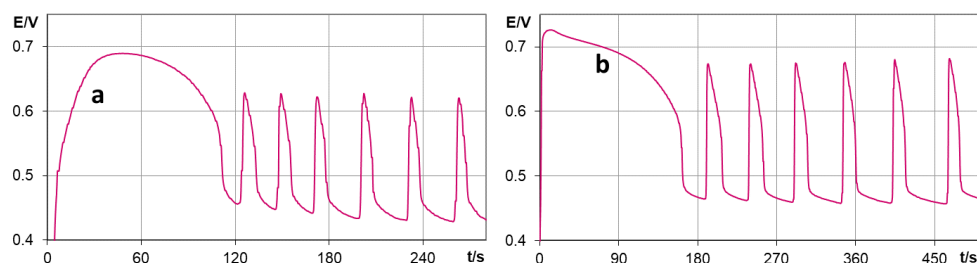


**Figure 2.** The first five periods in Mn-catalyzed BZ reaction as recorded by potentiometric signals from a Pt electrode against a mercurousulfate electrode: a) 1.5 M  $\text{H}_2\text{SO}_4$ , 0.1 M malonic acid, 0.03 M  $\text{MnSO}_4$ , 0.05 M  $\text{NaBrO}_3$ ; b) the same as in a) with added 0.01 M  $\text{Na}_4\text{P}_2\text{O}_7$ .

While this poses interesting questions about the significance of different oxidation states of Mn for the BZ reaction, it did not help us to use Mn in our Preparatory Problems. Mn could not even be used as a mixed catalyst with ferriin – in the Mn-catalyzed BZ reaction, ferriin never leaves its blue state.

### ADAPTING THE BZ REACTION AS A QUANTITATIVE TASK

Although understanding the mechanism of the BZ reaction was an important theme of our PPs, Chemistry Olympiad practical tasks in physical chemistry are unthinkable without a prominent quantitative aspect. In the case of the BZ this may be quite a challenge for several reasons.

In the first place, the BZ reaction is a complex system. Relations between its observable features (induction period, periods of oscillation, etc.) and the controllable parameters are convoluted. It may be difficult to design a measurement that provides direct insight into the reaction. We identified four possibilities to do so:

**Mass balance estimations.** The time it takes to consume all  $\text{Br}^-$  in the modified one-period BZ clock (without the organic substrate) allows us to enumerate the average rate of consumption of  $\text{Br}^-$ . Comparing this to the period of BZ oscillations, we can roughly estimate how much  $\text{Br}^-$  is digested in each cycle. As the  $\text{Br}^-$  is used mainly for bromination of the organic substrate, we can also estimate how much is brominated in each cycle.

**Dependence on the catalyst.** It is instructive to observe the dependence of the periods of BZ oscillations on the concentration of the metal catalyst. The word *catalyst* in this context is often intuitively misinterpreted. The usual expectation is that higher concentrations of the catalyst should yield faster oscillations. That is, indeed, not the case. And even though this evaluation

does not lead to a single number, it can still be graded based on whether the correct data points were obtained.

**Activation energies.** As an island of simplicity in the complex reaction, it is well-known that the temperature dependences of both, the induction period and the periods of oscillation, obey the Arrhenius' law [6]. Finding the activation energies corresponding to these changes is perhaps as close as we can get to the ideal of a Chemistry Olympiad practical task with a BZ system.

Remarkably, in our case with the mixed cerium-ferroin catalyst, it was found that only the  $E_a$  from the induction periods was closer to the value published for Ce-catalyzed oscillations [6]. Even though the concentration of Ce in the system was 20-times larger than that of ferroin, and the periods of oscillation were closer to those observed with Ce alone, the corresponding  $E_a$  was closer to the value published for ferroin-catalyzed BZ reactions [6].

**Wave-front propagation velocity.** It is a well-known phenomenon, that the BZ reaction on a Petri dish forms chemical trigger waves. They propagate through the medium with constant velocity, which reflects quite directly the rate of the underlying autocatalytic step [7]. Finding how the velocity varies with concentrations of bromate(V) or with acidity of the medium can be used to investigate the corresponding rate law.

Using this idea for one of our PPs was a clear decision, as it had already been elaborated into a neat student laboratory experiment by Pojman [8], and we had already had several years of experience with this experiment in our courses of practical physical chemistry.

For the PPs we adapted the ferroin-only version of the experiment for the new recipe using mixed cerium-ferroin catalysis. In the end, the medium on the Petri dish was almost identical to the one used in the stirred BZ reaction, except for the concentration of ferroin, which had to be increased for reasonable visibility.

As a new tweak to the experiment, we found it interesting to point out that the partial reaction orders found experimentally do not always have to agree with theory. Only the order with respect to bromate(V) was supposed to be close to 1, as expected. On the other hand, the concentrations of  $\text{H}_2\text{SO}_4$  were not above 0.5 M, where the order with respect to  $\text{H}_2\text{SO}_4$  is also close to 1. To the contrary, the order was examined at lower concentrations, where it appears to increase significantly, in our case suggesting a 3<sup>rd</sup> order reaction!

## REPRODUCIBILITY

Even though the above list may seem as there are more than enough options of quantitative measurements in the BZ reaction, this was not the only challenge in making it a quantitative task. The BZ reaction is well-known to

be a very sensitive system and its reputation in the regard of predictability and reproducibility is, at best, mixed.

Some issues are broadly recognized, e.g. that contamination even with traces of chloride must be strictly avoided. Other chemical factors have also been reported, e.g. that of common contaminants in malonic acid [9]. In our PPs we also warn specifically about rapid ageing of the  $\text{Ce}^{\text{III}}$  stock solutions, which can also cause significant variations in results.

Many of the factors affecting the reproducibility of measurements with the BZ reaction are, unfortunately, quite often overlooked even in professional literature. The reaction is well-documented to be very sensitive to oxygen [10] and stirring [11]. Yet, it is not uncommon that many papers publish data without any mention of the geometry of the reactor, the stir-bar etc.

To minimize unexpected outcomes, we pointed out repeatedly that results may vary based on stirring rate, reactor geometry etc. The PPs that we designed were, however, tested repeatedly and in our experience, as long as these parameters remained under control, all the measurements were very reproducible.

## CONCLUSION

Designing quantitative tasks based on the BZ reaction while adhering to standards of the Chemistry Olympiad was not a trivial task. However, this unique reaction certainly deserves continued recognition, not only through experiments that have already proved useful in the past, but also through developing new and improved approaches. Hopefully, the number of those, who become intrigued by this extraordinary reaction, will continue to grow, maybe even with new fans found among the participants of the International Chemistry Olympiad.

### *Acknowledgement*

This work was partially supported by the Cultural and Educational Grant Agency of the Ministry of Education, Science, Research and Sport of the Slovak republic (Grant no. KEGA 014UK-4/2018).

**REFERENCES**

- [1] Data from the 50<sup>th</sup> IChO web page, <https://50icho.eu/participation/>
- [2] N. Manz, R. J. Field, K. Kiprijanov, Illustrative Timeline of Boris P. Belousov and Anatol Zabortinsky, Gordon Research Conference on Oscillations and Dynamic Instabilities in Chemical Systems, Stove, 2016.
- [3] E. Szabo, Problems P4 and P5 in: Preparatory Problems: Practical, P. Ménová, M. Putala (Eds.), 2018, published online at the 50<sup>th</sup> IChO web page – <https://50icho.eu/problems/icho-2018-preparatory-problems/>
- [4] R. L. Rich, R. M. Noyes, *J. Chem. Ed.*, 1990, **67**, 606 – 607.
- [5] B. Z. Shakhshiri, *Chemical Demonstrations*, Vol. 2, The University of Wisconsin Press, Madison, 1985, 274 – 275.
- [6] K. Yoshikawa, *Bull. Chem. Soc. Jpn.*, 1982, **55**, 2042 – 2045.
- [7] R. J. Field, R. M. Noyes., *J. Am. Chem. Soc.*, 1974, **96**, 2001 – 2006.
- [8] I. R. Epstein, J. A. Pojman, *An Introduction to Nonlinear Chemical Dynamics*, Oxford University Press, New York, 1998, 356 – 359.
- [9] Z. Noszticzius, W. D. McCormick, H. L. Swinney, *J. Phys. Chem.*, 1987, **91**, 5129 – 5134.
- [10] O. Steinbock, C. T. Hamik, B. Steinbock, *J. Phys. Chem. A*, 2000, **104**, 6411 – 6415.
- [11] M. Menzinger, P. Jankowski, *J. Phys. Chem.*, 1990, **94**, 4123 – 4126.

## REACTION-DIFFUSION FRONTS DRIVEN BY THE AUTOCATALYTIC HYDROGENASE REACTION

D. Horváth<sup>1</sup>, L. Gyevi-Nagy<sup>2</sup>, E. Lantos<sup>2</sup> and Á. Tóth<sup>2</sup>

<sup>1</sup>*University of Szeged, Department of Applied and Environmental  
Chemistry, Rerrich Béla tér 1, H-6720 Szeged, Hungary.  
(horvathd@chem.u-szeged.hu)*

<sup>2</sup>*University of Szeged, Department of Physical Chemistry and Material  
Sciences, Rerrich Béla tér 1, H-6720 Szeged, Hungary.*

### ABSTRACT

Hydrogenase is an enzyme catalyzing the reversible hydrogen oxidation reaction. The reaction is shown to be autocatalytic with one of the enzyme form is being the autocatalyst. We have built a chemically feasible model [1] to describe the spatiotemporal behavior observed experimentally. The existence of two different front types is confirmed by linear stability analysis where the major factor determining the front properties is the ratio of the total concentration of the electron acceptor to that of the enzyme. At low concentration ratio the autocatalysis and the electron acceptor reduction are spatially separated while at higher ratios regular chemical fronts develop. The pH-dependent hydrogen uptake and production profiles are also reproduced numerically in good agreement with the experiments [2].

### REFERENCES

- [1] L. Gyevi-Nagy, E. Lantos, T. Gehér-Herczegh, Á. Tóth, Cs. Bagyinka, D. Horváth, *J. Chem. Phys.*, 2018, 148, 184701.
- [2] G. Bodó, R. M. M. Branca, Á. Tóth, D. Horváth, Cs. Bagyinka, *Biophys. J.*, 2009, 96, 4976-4983.

## ELECTROCOALESCENCE PROCESS IN THE FRAME OF DECOHERENCE THEORY

A.M. Spasic<sup>1</sup>, J.M. Jovanovic<sup>2</sup>, V. Manojlovic<sup>1</sup> and M. Jovanovic<sup>3</sup>

<sup>1</sup>*Institute for Technology of Nuclear and Other Mineral Raw Materials, Dept. of Chem. Engng., 86 F. d'Esperey St., 11000 Belgrade, Serbia,*

<sup>2</sup>*Innovationi Center, Dept. of Met. & Tech., University of Belgrade, 4 Karnegijeva St., 11000 Belgrade, Serbia*

<sup>3</sup>*Dept. of Met. & Tech., University of Belgrade, 4 Karnegijeva St., 11000 Belgrade, Serbia*

### ABSTRACT

Here presented example that will help justifying the idea is coalescence process, and because this event occurs at small separations more appropriate term could be electrocoalescence process (EC). Hence, the EC process, as the subject of rheology or nano-rheology, may be situated on the border between the classical and quantum mechanics. The selected, representative, finely dispersed system (FDS)-double emulsion was taken from the pilot plant for uranium extraction from wet phosphoric acid. The entrained double emulsion was droplet (H<sub>3</sub>PO<sub>4</sub>)-film [synergistic mixture 0.5 M D2EHPA-0.125 M TOPO in dearomatized kerosene (DTK)] structure submerged into the droplet homo-phase. Breaking of the selected double emulsion was performed in the lamellar coalescer. The chosen framework required for the elucidation of processes during demulsification, rupture on an inclined plate and coalescence or EC, is based on electrohydrodynamics (EHD) principles.

### INTRODUCTION

The selected FDS-emulsions and double emulsions, or droplet-film structures immersed in the droplet homo-phase "continuum", including their cycles of the formation, duration, and destruction, studied in this research, are to be considered as close to the open macroscopic quantum system (OMQS), under specified conditions. In general, these three cycles may be related to the existence of a number of various systems, for example, life of biological cells, polymer conformations and stability, DNA, brain, and other macromolecular structures, universe as a giant macroscopic polydispersed system. Also, the process of coalescence and electrocoalescence, as treated in this presentation, will be taken as a kind of electro-mechanical oscillators' or clusters' conformational limit. So, it is convenient to consider the

selected cluster conformation stability and transitions, that may be assumed as similar to the molecular conformations stability and transitions, in the frame of quantum decoherence theory [1-8].

### MODELING DOUBLE EMULSION AS MEMRISTIVE SYSTEM

It was necessary to develop two concepts for easier understanding of the events at liquid-liquid interfaces of the selected double emulsion. The first is a concept of an entity and the corresponding classification of finely dispersed systems; this concept permit consideration of the electron transfer phenomenon beside heat, mass, and momentum transfer phenomena. The second concept is an introduction of an almost forgotten basic electrodynamic element, the memdiode or memristor (M) as the current controlled device, and the corresponding memristive system. This concept is needed because the fundamental electrodynamic elements, the resistor (R), the inductor (L), and the capacitor (C) are not sufficient for a satisfactory explanation of complex phenomena that occur at liquid-liquid interfaces. Now, the electrodynamic elements are: the C and M as electroelastic elements, and the L and R as electroviscous elements. Also, the terms electrical forces and electrical interfacial potential (EIP) were introduced beside the terms mechanical forces and interfacial tension, because at small separations the forces of electrical origin become dominant compared to the forces of mechanical origin [1-4].

### MEMRISTIVE SYSTEM AS OMQS AND ITS DYNAMICS

The selected FDS-double emulsion can be presented as a “sandwich“: droplet  $\text{H}_3\text{PO}_4$ -film DTK-droplet homophase  $\text{H}_3\text{PO}_4$ . Here, the possible idea, related to this system, in a quantum mechanical framework, may be applied; then, the complex composite system is the droplet-film (object S) + the droplet homophase (environment E), that is, (S+E). The interaction Hamiltonian  $\widehat{H}_{S+E} \equiv \widehat{H}_{\text{int}}$  is a two-body observable, coupling the observables of both the system S and environment E. Now, the composite system's Hamiltonian is given by

$$\widehat{H} = \widehat{H}_S \otimes \widehat{I}_E + \widehat{I}_S \otimes \widehat{H}_E + \widehat{H}_{\text{int}} \quad (1)$$

here, the third term present the interaction energy, which is a “two-system” observable changing the states of the system S and environment E [1]. The initial state of the selected OMQS S is  $\widehat{\rho}_S(t=0)$ , and the initial state of the environment E is  $\widehat{\sigma}_E(t=0)$ . Now, by definition, the initial state of the composite system S+E is given by  $\widehat{\rho}_S(t=0) \otimes \widehat{\sigma}_E(t=0)$ . Then considering

the Eq. (1) the unitary evolution operator  $\widehat{U}$  for the composite system, that is, to its unitary dynamics is expressed as

$$\widehat{\rho}_{S+E}(t) = \widehat{U} \widehat{\rho}_S(t=0) \otimes \widehat{\sigma}_E(t=0) \widehat{U}^* \quad (2)$$

Now, according to the general rules of quantum mechanics, the subsystem's state is defined as

$$\widehat{\rho}_S(t) = \text{tr}_E \widehat{\rho}_{S+E}(t) \quad (3)$$

The interaction term from Eq. (1), as the central to the OMQS is given by

$$\widehat{H}_{\text{int}} = \widehat{V}_S \otimes \widehat{I}_E + \widehat{I}_S \otimes \widehat{V}_E \quad (4)$$

two subsystems evolve mutually independently in time, as it is given by

$$\widehat{\rho}_{S+E}(t) = \widehat{\rho}_S(t) \otimes \widehat{\sigma}_E(t) \quad (5)$$

For the nontrivial coupling of the observables of the two subsystems the correlation of states will be given by Eq. (1).

Hence, related to decoherence theory when the initial state of the system S is a "pure" quantum state (an element of the system's Hilbert state space),  $|\psi\rangle_S$  then

$$\widehat{\rho}_S(t=0) = |\psi\rangle_S \langle\psi| \quad (6)$$

and

$$|\psi\rangle_S = \sum_i C_i |\varphi_i\rangle_S \quad (7)$$

Now,

$$\widehat{\rho}_S(t=0) = \sum_{i,j} C_i C_j^* |\varphi_i\rangle_S \langle\varphi_j| \quad (8)$$

with the nonzero off-diagonal ( $i \neq j$ ) terms of  $\widehat{\rho}_S$ . Here, one of the central findings of the decoherence theory is the observation that for certain special states (orthonormalized basis)  $\{|\varphi_i\rangle_S\}$ , the evolution in time effects in the

loss of the off-diagonal terms of  $\widehat{\rho}_S$ ; now, for the off-diagonal terms the limit may be written as

$$\lim_{t \rightarrow \infty} \rho_{Sij}(t) = 0, i \neq j \quad (9)$$

For the short time intervals of the order of  $\tau_D$ , that is, decoherence time.

The matrix presentation of  $\widehat{\rho}_S$  in the basis  $\{|\varphi_i\rangle_S\}$  - "pointer basis" - is of quasi-diagonal form, thus giving rise to the effective superselection rules for the OMQS, which is described by the orthogonal decomposition of the system's Hilbert state given by

$$H_S = \sum_n^{\oplus} H_n \quad (10)$$

Here, the environment influences the loss of coherence in the OMQS's state,  $H$ , for the states belonging to the different subspace  $H_n; \langle \varphi_i | \varphi_j \rangle = 0$ , if  $|\varphi_i\rangle \in H_n, |\varphi_j\rangle \in H_{n'}, n \neq n'$  [1, 2, 6].

### THE PHYSICAL AND PHYLOSOPHICAL CONTENTS

A corresponding constitutive model of liquids was developed and applied to the selected double emulsion. Considering Marangoni instabilities of the first and second order and possible electrical analogues the EC process, in some extent, was elucidated. Hence, both, the qualitative and quantitative physical pictures of the EC process are presented and discussed in the frame of decoherence theory. The EC process is explained as a kind of entangled electro-mechanical oscillators or clusters' conformational limit.

### *Acknowledgment*

Financial support by Ministry of Education and Science, Republic of Serbia, grants: former 142034 and present 34009 and 46010.

### REFERENCES

- [1] A.M. Spasic, *Rheology of Emulsions, electrohydrodynamics principles*, Academic Press, 2018.
- [2] A.M. Spasic et al. CHISA 1987-2018 All Congresses, Prague, CZ.
- [3] A.M. Spasic, J.M. Jovanovic, V. Manojlovic, M. Jovanovic, J. Colloid Interface Sci. 2016; 479 165-172.
- [4] A.M. Spasic, J.M. Jovanovic, M. Jovanovic, Adv. Colloid Interface Sci. 2012; 174 31-49.
- [5] J-P Hsu, A.M. Spasic, *Interfacial Electroviscoelasticity and Electrophoresis*, CRC Press-Taylor & Francis, Boca Raton London New York, 2010.
- [6] M. Dugic, D. Rakovic, M. Plavsic In: A.M. Spasic and J.P. Hsu (Eds.) *Finely Dispersed Particles: Micro-, Nano-, and Atto-Engineering*, CRC Press-Taylor and Francis, Boca Raton London New York, 2006.
- [7] A.M. Spasic, M.P. Lazarevic, M.V. Mitrovic and D.N. Krstic In: Ibid.
- [8] A.M. Spasic In: A.V. Delgado (Ed.) *Interfacial Electrokinetics and Electrophoresis*, Marcel Dekker Inc.: New York, 2002.

## MODELLING OF EXTERNALLY INDUCED CHOLESTEROL PULSES ON HYPOTHALAMIC- PITUITARY-ADRENAL AXIS PERTURBED WITH ETHANOL

M. Anđelković<sup>1</sup>, A. Stanojević<sup>1</sup>, V.M. Marković<sup>1</sup>, Ž. Čupić<sup>2</sup>  
and Lj. Kolar-Anić<sup>1,2</sup>

<sup>1</sup> *University of Belgrade, Faculty of Physical Chemistry, Studentski trg 12-16, 11000 Belgrade, Serbia. (20150011@student.ffh.bg.ac.rs)*

<sup>2</sup> *Institute of Chemistry, Technology and Metallurgy, University of Belgrade, Department of Catalysis and Chemical Engineering, Njegoševa 12, 11000 Belgrade, Serbia*

### ABSTRACT

This study deals with the mathematical modelling of the acute cholesterol and ethanol perturbations of the already proposed stoichiometric network model of the hypothalamic–pituitary–adrenal (HPA) axis. Results of numerical simulations suggest that both ethanol and cholesterol alters the dynamics regulation of HPA axis activity by affecting the amplitudes of hormonal ultradian oscillations. Moreover, different responses of the HPA axis to the cumulative effect of cholesterol and ethanol from the response to the ethanol perturbation only were observed. Results provided insight into dose-dependent response of the HPA axis to ethanol and cholesterol consumption, and new views to further understanding of the mechanisms of the alcohol effects on this neuroendocrine system.

### INTRODUCTION

The hypothalamic–pituitary–adrenal (HPA) axis is a complex neuroendocrine system of direct influences and feedback interactions among hypothalamus, pituitary and adrenal glands. Due to the complex interplay between these feedback mechanisms and the coupling with the circadian clock system, this complex nonlinear system functions under conditions that are far from thermodynamic equilibrium, causing oscillatory temporal evolution of HPA axis hormones concentrations, that exhibit ultradian oscillations (period in the range between 20 and 120 min), that are superimposed on the circadian ones, which fluctuate within the 24h cycle [1].

Ethanol and other psychoactive substances can act as physiological stressors causing activation of HPA axis [2], whereas cholesterol, the precursor of steroid hormones, is a powerful modulator in steroidogenesis,

and thus affects HPA axis dynamics. Even though ethanol is likely to be the longest known substance with psychoactive potential, detailed molecular mechanisms of its action on here studied neuroendocrine system remain only partially understood.

The aim of this study was to investigate cumulative effect of ethanol and cholesterol intake on HPA axis dynamics. The cumulative effect was investigated in order to improve this model of HPA axis activity to more accurately describe realistic conditions of ethanol consumption.

### **MATHEMATICAL MODELLING**

In this study, already developed stoichiometric network model for regulating the role of cholesterol on HPA activity [3], extended by Čupić et al [4] in order to examine the influence of ethanol, was used. The main dynamical variables that participate in the set of differential equations are concentrations of CHOL (cholesterol), CRH (corticotrophin releasing hormone), ACTH (adrenocorticotrophic hormone), CORT (cortisol), ALDO (aldosterone), AcALD (acetaldehyde), EtOH (ethanol), as well as A and B species. Dynamical variable A represents external sources of cholesterol, whereas dynamical variable B represents species that mediate cholesterol elimination from global circulation (for example, high-density lipoproteins (HDL), as well as statins).

The circadian regulation of CRH production, dictated by circadian clock system in the suprachiasmatic nucleus, is simulated by coupling of an extrinsic periodic function, designed to appropriately mimic the asymmetry of the 24-hour rhythm in humans-daily rhythm (with about eight hours of sleep [4]), with equation that describes CRH secretion.

Numerical simulations were performed in MATLAB, using the ODE15s solver routine based on the Gear algorithm for integration of stiff differential equations. All initial parameters were individually adjusted to obtain, by numerical integration, basal hormone levels that are in the physiological range. Solutions of the system of ODEs obtained by numerical integration, give the ultradian dynamics of the HPA axis. In order to simulate acute perturbations with ethanol and cholesterol, numerical integration of the set of ODEs was stopped at a specified time point, and new initial conditions for the subsequent integration were defined. For the new initial conditions, initial concentration of ethanol and concentration of A and B were specified for an indicated amount, whereas the concentrations

of all other species retained the values that they have attained before the numerical integration was stopped. The final results of these simulations, time

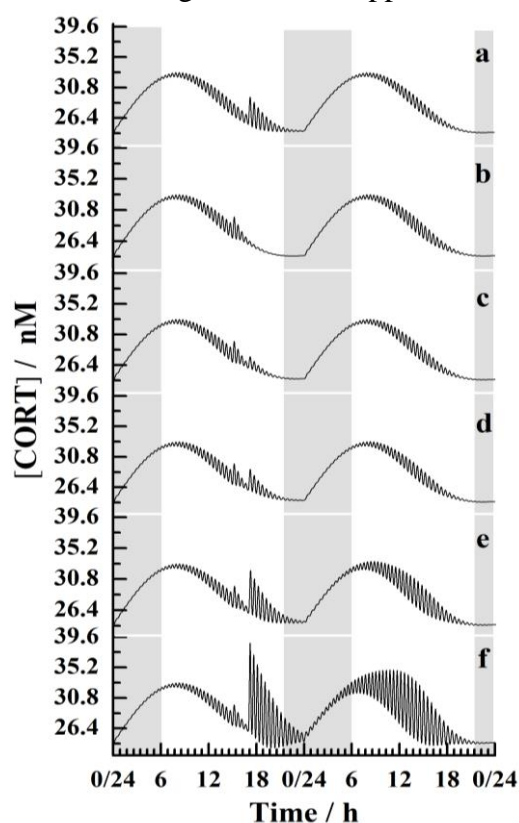


**Figure 1.** Time evolution of cortisol perturbed by: a)  $[\text{EtOH}]_0=10 \text{ mM}$ ; b) cholesterol pulse with  $[\text{A}]_0=3 \text{ mM}$  and  $[\text{B}]_0=0,1 \mu\text{M}$ ; c) cholesterol pulse and  $[\text{EtOH}]_0=5 \text{ mM}$ ; d) cholesterol pulse and  $[\text{EtOH}]_0=10 \text{ mM}$ ; e) cholesterol pulse and  $[\text{EtOH}]_0=20 \text{ mM}$ ; f) cholesterol pulse and  $[\text{EtOH}]_0=40 \text{ mM}$ . In all cases cholesterol pulses were the same and system was perturbed at 3 pm, whereas all perturbations with ethanol were done at 5 pm.

of ethanol annul the effects of lowering the amplitudes of ultradian oscillations by cholesterol (Figs. 1b-1f), and return the system to the dynamics it possessed before perturbation. Results showed that the response of HPA axis is proportional to tested initial concentration of EtOH. Thus, as

evolution of cortisol concentration, in this study were presented as a two-day evolution.

## RESULTS AND DISCUSSION

Perturbation of the studied system with A and B gives rise to cholesterol pulses with asymmetrically distributed concentration profile. The width of the cholesterol pulse, which perturbs the model, was observed to be much wider compared to width of the cortisol ultradian oscillation.

Results indicated that the cumulative effect of cholesterol pulses and ethanol perturbations initiate different changes in cortisol concentrations from ethanol perturbations only. When the system was perturbed with ethanol only (Fig. 1a), amplitudes of ultradian oscillations of cortisol were higher than amplitudes in the system perturbed with the same initial concentration of ethanol but also with cholesterol (Figs. 1a and 1d).

It can be observed that perturbations of the system with all tested initial concentrations

the initial EtOH concentration is getting higher, the more raised the amplitudes of cortisol ultradian oscillations are (Figs. 1c-1f). Ethanol initial concentrations over 20 mM, regardless of the lowering of the amplitudes of cortisol ultradian oscillations by the present cholesterol, can even have an impacts on the cortisol dynamics during the day after the perturbation was conducted (Figs. 1e and 1f).

The time needed for HPA axis to restore its dynamics, for all tested ethanol concentrations showed agreement with the experimental measurements [5].

### CONCLUSION

Response of the HPA system model considered here, to the cumulative effect of cholesterol and ethanol was different from the response to the ethanol perturbations alone. Model showed high dependence on the initial concentration of EtOH. Although high degree of quantitative agreement with the empirical results has been reported in the literature when simulating separately effects of ethanol and cholesterol on the dynamics of this specific model of HPA axis, comparison of the real to the cumulative effect, numerically analyzed here, should be carried out as well.

### Acknowledgement

This work was partially supported by the Ministry for Science of the Republic of Serbia (Grants 172015 and 45001).

### REFERENCES

- [1] Hartmann, A., Veldhuis, J. D., Deuschle, M., Standhardt, H. & Heuser, I. *Neurobiol. Aging*, 1997, **18**, 285–289.
- [2] Waltman, C., Blevins, Jr. L. S., Boyd, G., Wand, G.S. *J. Clin. Endocrinol. Metab.*, 1993, **77** (2): 518-522.
- [3] Stanojević, A., Marković M. V., Čupić, Ž., Vukojević, V., Kolar-Anić, Lj. *Russ. J. Phys. Chem. A*, 2017, **13** (91): 112-119.
- [4] Čupić, Ž., Stanojević, A., Marković M. V., Kolar-Anić, Lj., Terenius, L., Vukojević, V. *Addict. Biol.*, 2016, **22** (6): 1486-1500.
- [5] De Waele, J.P., Gianoulakis, C. *Neuroendocrinology*. 1993, **57** (4): 700-709.

## THE BRAY-LIEBHAFSKY OSCILLATING CHEMICAL REACTION AS A SYSTEM FOR QUININE DETECTION

M. Mažić, I. N. Bubanja<sup>1</sup>, D. Stanisavljev<sup>1</sup> and S. N. Blagojević<sup>2</sup>

<sup>1</sup> Faculty of Physical Chemistry, University of Belgrade, Studentski trg 12-16, Belgrade, Serbia (Corresponding Author: [itana.bubanja@ffh.bg.ac.rs](mailto:itana.bubanja@ffh.bg.ac.rs))

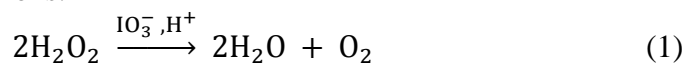
<sup>2</sup>Institute of General and Physical Chemistry, University of Belgrade, Studentski trg 12/V, Belgrade, Serbia

### ABSTRACT

In this study the Bray-Liebhafsky oscillating chemical reaction was used as a detection system for quinine determination. BL reaction was performed under batch reactor conditions under two different experimental procedures. In Procedure I, per one experiment only one concentration of quinine was added at the end of 4<sup>th</sup> oscillation and in Procedure II, per one experiment different concentrations of quinine were successively added. Results show that BL reaction in both performed procedures is sensitive to quinine. Besides, Procedure I does not have cumulative quinine effect and is more suitable for analytical purposes.

### INTRODUCTION

Oscillating chemical reactions are interesting systems for the investigation of their peculiar dynamics with unknown roles of many of the involved intermediates. Over the years, oscillating chemical reactions have become very popular for analytical purposes[1,2] as well. The main idea for analytical application of the chemical oscillators lays in the fact that investigated analyte reacts with reaction components and changes easily observable dynamic properties of the system such as induction period, frequency and amplitude. Namely, addition of analyte may affect amplitude or period of oscillations or even totally quench oscillating evolution. In this paper, we used the oldest known oscillating chemical reaction Bray-Liebhafsky (BL)[3,4] as a detection system for the quinine determination. Also, we compared two different experimental approaches in order to determine which one is more suitable to quinine perturbations. The BL reaction is considered as catalytic decomposition of hydrogen peroxide into water and oxygen in the presence of iodate and hydrogen ions:



Although apparently simple, it has a very complex underlying mechanism which involves numerous non-radical and radical intermediate species.

Quinine is a bitter flavored, white crystal alkaloid, insoluble in water. The oldest and most important application of the quinine is his usage as a medicine to treat malaria caused by *Plasmodium falciparum*. Nowadays thanks to its bitter flavor small amounts of quinine are present in some carbonated drinks and tonic water.

### EXPERIMENTAL

BL reaction was realized in batch reactor conditions. All experiments were performed in a glass vessel wrapped in a water recirculation jacket connected to a thermostat. In all experiments glass vessel was protected from light and for homogenization of the reaction mixture, a magnetic stirring was used at 900 rpm. All used chemicals were pro analysis-grade purity, and their solutions were prepared in deionized water. Quinine solutions were prepared with ethanol since it is insoluble in water. BL reaction was followed by potentiometric method. Reaction dynamics was followed by measuring potential of Pt working electrode versus double-junction Ag/AgCl reference electrode. High resistance voltmeter (PC-Multilab EH4 16-bit ADC) coupled with a personal computer was used to record the potential-time evolution of BL oscillator. In this study, we used two experimental procedures for quinine determination. In both procedures total volume of reaction mixture (52 ml) and the order of reactant solutions addition (25 ml  $\text{KIO}_3$  0.15 M and 25 ml  $\text{H}_2\text{SO}_4$  0.1 M are thermostated to 62 °C, followed by addition of 2 ml of  $\text{H}_2\text{O}_2$  4.89 M) were the same. In Procedure I at the end of 4th oscillation 100  $\mu\text{l}$  of quinine solution was injected into the reaction mixture. The first experiment was performed with the addition of the lowest quinine concentration (in reaction mixture quinine concentration was  $[\text{C}_{20}\text{H}_{24}\text{N}_2\text{O}_2]_0 = 5 \times 10^{-5}$  M). Every next experiment was performed with higher quinine concentration (quinine concentration in reaction mixture were:  $1 \times 10^{-4}$  M;  $2 \times 10^{-4}$  M;  $3 \times 10^{-4}$  M;  $4 \times 10^{-4}$  M;  $5 \times 10^{-4}$  M;  $7 \times 10^{-4}$  M). In Procedure II 100  $\mu\text{l}$  of the different quinine solution concentration were successively added during the same experiment after train of 4 oscillations. Procedure I is designed for the verification of quinine effects on BL reaction as well as their reproductivity. The Procedure II is aimed to investigate cumulative effects of quinine and possibility of shortening calibration procedure.

### RESULTS AND DISCUSSION

Before both experimental procedures pure BL reaction was performed three times to verify reproductivity of basic experiments. Because all quinine solutions were prepared in ethanol one BL experiment was perturbed with 0,7 ml of pure ethanol as well. It was noticed that addition of ethanol does not affect dynamics of BL reaction. Some oscillograms obtained from Procedure

I are given in Figure 1. As it can be seen from Figure 1, concentrations of quinine in reaction mixture of  $3 \times 10^{-4}$  M and  $7 \times 10^{-4}$  M notably prolong period between 4th and 5th oscillation.

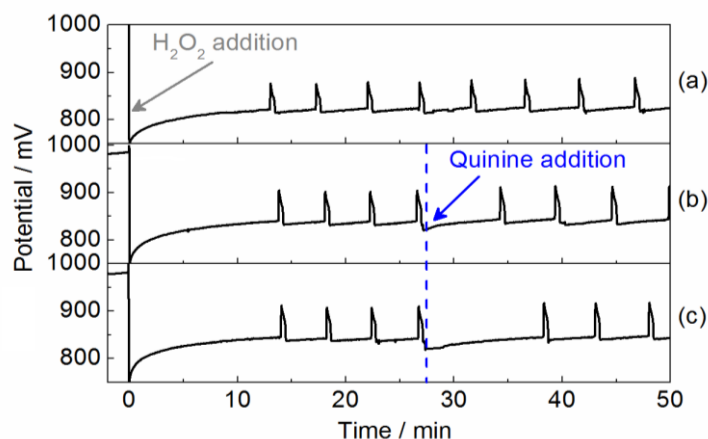


**Figure 1.** Obtained oscillograms in batch BL reaction system without quinine addition (a) and with addition of quinine (b, c). Concentrations of quinine in reaction mixture were:  $3 \times 10^{-4}$  M (b),  $7 \times 10^{-4}$  M (c).

Obtained oscillogram where different concentrations of quinine were successively added into BL system according to Procedure II is shown at Figure 2.

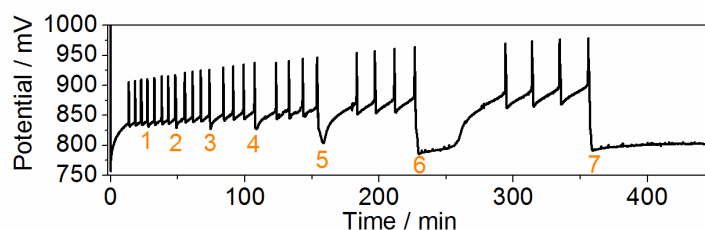


**Figure 2.** Oscillogram of the batch BL system with successive addition of quinine. Places where quinine was added are marked with numbers and concentrations of quinine in reaction mixture from 1 to 7 respectively were:  $5 \times 10^{-5}$  M,  $1 \times 10^{-4}$  M,  $2 \times 10^{-4}$  M,  $3 \times 10^{-4}$  M,  $4 \times 10^{-4}$  M,  $5 \times 10^{-4}$  M and  $7 \times 10^{-4}$  M.

From Figure 2, it is noticeable that higher concentrations of quinine will prolong the period between oscillations. Also, unlike to Procedure I in Procedure II, the highest quinine concentration of  $7 \times 10^{-4}$  M totally quenched the oscillations. At Figure 3, the relative prolongation of the period between oscillations after quinine addition vs quinine concentration in the reaction mixture are shown for both procedures.

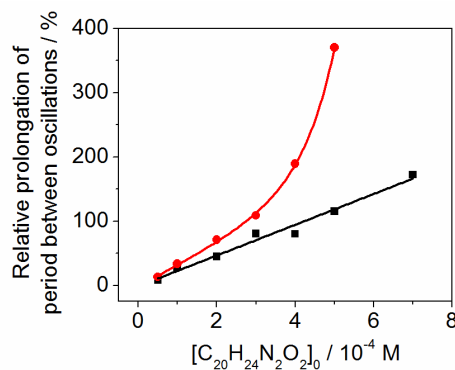


**Figure 3.** Relative prolongation of the period between oscillations after quinine addition dependence of quinine concentration in reaction mixture obtained from Procedure I (squares) and II (circles).

It is clear (Figure 3.) that relative prolongation of period linearly increases as the quinine concentration increases when Procedure I is applied while results obtained from Procedure II indicate the presence of cumulative effect of quinine on the BL dynamics.

## CONCLUSION

Two experimental procedures were compared for determination of quinine using BL reaction as a detection system. Due to the linear calibration curve, Procedure I is more suitable for analytical purposes if concentration of quinine is between  $5 \times 10^{-5}$  M and  $7 \times 10^{-4}$  M in the reaction mixture. Although it is unknown how quinine reacts with BL system investigations of the quinine products, after the reaction, will help to better define specific reactions with BL components. Application of complementary analytical techniques may help to better understand BL reaction mechanism and opens a wide range of future investigations.

## Acknowledgement

This research was financially supported by the Ministry of Education, Science and Technological Development of Republic of Serbia, through Project No. 172015-OI.

## REFERENCES

- [1] J. Maksimović, Lj. Kolar-Anić, S. Anić, D. Ribič, N. Pejić, J. Braz. Chem. Soc., 2011, **22** (1), 38-48.
- [2] N. D. Pejić, S. R. Anić, Lj. Z. Kolar-Anić, Hem. Ind., 2012, **66** (2), 153-164.
- [3] W. C. Bray, J. Am. Chem. Soc., 1921, **43**, 1262-1267.
- [4] W. C. Bray, H. A. Liebafsky, J. Am. Chem. Soc., 1931, **53**, 38-44.

## PROPERTIES OF THE BRIGGS-RAUSCHER REACTION IN DIFFERENT ALCOHOL-WATER MIXTURES

J. Damjanović<sup>1</sup>, J. Maksimović<sup>1</sup>, K. Stevanović<sup>1</sup>, B. Božić<sup>2</sup> and M. C. Pagnacco<sup>1</sup>

<sup>1</sup> *University of Belgrade, Faculty for Physical Chemistry, 11000 Belgrade, Serbia. (maja.milenkovic@ffh.bg.ac.rs)*

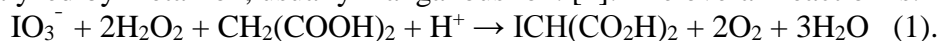
<sup>2</sup> *University of Belgrade, Faculty of Biology, Institute of Physiology and Biochemistry, 11000 Belgrade, Serbia*

### ABSTRACT

In this work, the oscillating Briggs-Rauscher (BR) reaction is carried out in three different water- 20% alcohol mixtures and obtained BR behavior is compared with the same results found in water. All examined alcohols: methanol, propanol, and 2-propanol, caused the appearance of the induction period, as well as the significant reducing of the BR oscillatory region. The obtained BR behavior in the alcohol-water mixture is probably the consequence of new competitive reactions. The possible mechanism of alcohol acting is proposed.

### INTRODUCTION

The Briggs-Rauscher (BR) reaction is an oscillating reaction, in which the acidic oxidation of malonic acid by hydrogen-peroxide and iodate, is catalyzed by metal ion, usually manganous ion. [1]. The overall reaction is:



This reaction (Eq 1) is accomplished by two also complex-component reactions. The first component reaction is:



while the second one is:



The BR reaction is mostly used in the chemical demonstration, due to the visually impressive color changing, when starch is used as an indicator [2].

Cervellati *et al.* [3] reported BR reaction usage as a method to assess antioxidant capacity. In general, the application of this antioxidant assay is limited to water-soluble samples, due to the BR reaction occurred in a water medium. In this work, we report the effects of various alcohol-water mixtures (methanol, propanol, and 2-propanol, 20 vol%) on the behavior of the BR reaction. The goal of this work is to investigate and elucidate some of the ways how alcohol (20 vol%) solvent can influence the course of oscillatory

BR reaction. The influence of solvent reflects extremely complex phenomena involving many different intermolecular interactions, potentially affected oscillatory dynamics. Thus, recognizing some of the ways how water-alcohol mixtures affect the course of BR reaction, it is the important part of the kinetics investigation of oscillatory reactions in general.

### EXPERIMENTAL

In order to investigate solvent effects on BR reaction dynamics, three different solvents methanol, propanol, and 2-propanol are used. The effect of different solvent is investigated in changed volume percentage (100 % water - 0% examined solvent and 80% water - 20% examined solvent). The overall mixing volume is maintained constant at 88 ml (100 %). All chemicals are p.a. grade and deionized water is used. Thus, the 0.8324 g of malonic acid, 0.1268 g MnSO<sub>4</sub>, 0.8024 g of KIO<sub>3</sub> and 0.32 ml of perchloric acid (C<sub>HClO<sub>4</sub></sub>= 9.138 M) were mixed in total volume 88 ml (70.4 ml water and 17.6 ml particular alcohol). The 22 ml of this solution was moved to the reaction vessel, after the temperature and electrochemical potential stabilized, the 3 ml of 30 % hydrogen-peroxide was added, starting the BR reaction. The moment when H<sub>2</sub>O<sub>2</sub> was added to the vessel was taken at the beginning of the reaction. The time evolution of the BR reaction was followed potentiometrically. As working electrode used Pt electrode, while double junction Ag/AgCl electrode, used as a reference electrode. The reaction temperature maintained constant value at 37 °C. The mixing was 900 rpm. All measurements are done in triplicate.

### RESULTS AND DISCUSSION

The BR reaction dynamics obtained in 100% water solution is shown in Figure 1a. The addition of any of the examined alcohols to the BR system caused the appearance of the induction period, as well as the significant reducing of the oscillatory region (Figure 1b, c, and d). Besides, propanol and 2-propanol (although isomers) exhibit actually different behavior in BR system. The obtained BR parameters in different alcohol-water mixtures are summarized in Table 1. Results also show satisfactory reproducibility in three independent experiments (Table 1.). The appearance of induction period in alcohol-water solution can be understood, if we take in consideration the potential reactions between investigated alcohols and BR reaction species. The main candidates, which can produce obtained behavior are radicals existing in BR system, such as HO• and HOO• [4,5]. Since alcohols can easily react with potentially present and high reactive HOO• and HO• radicals [6,7] (Eqs 4-8), accordingly, it can cause the appearance of the induction period, as well as the shortening of the oscillatory region.

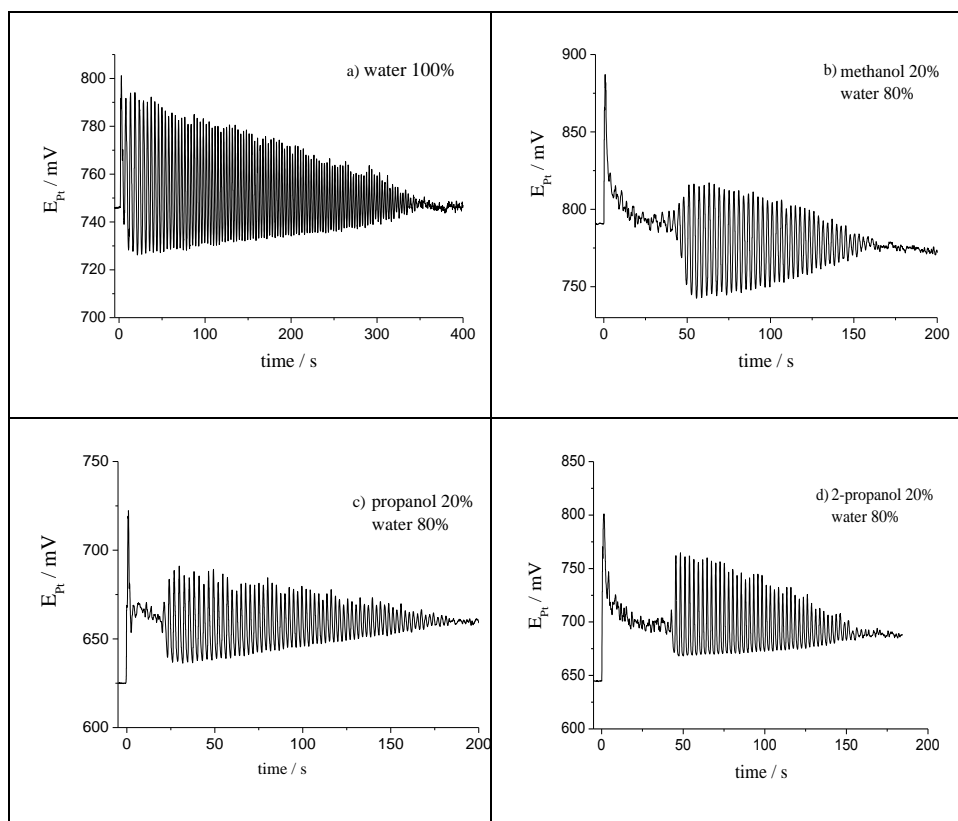
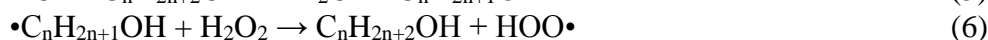
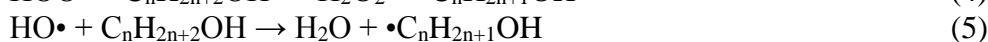
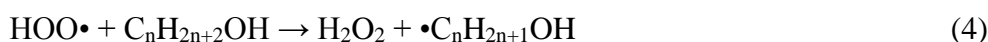


**Figure 1.** Temporal representation of the Pt electrode potential ( $E_{Pt}$ ) of the BR reaction in different alcohol/water solution. Experimental conditions are presented in Experimental part.

**Table 1.** The obtained BR parameters (induction period, oscillatory period and number of oscillations) in different water-alcohol mixtures

solvent	%vol alcohol	%vol water	Exps	Ind. period / s	Osc. period / s	Osc. number
water	0	100	1.	0	338	99
			2.	0	345	103
			3.	0	349	104
methanol	20	80	1.	36	123	43
			2.	42	121	43
			3.	36	129	47
propanol	20	80	1.	22	160	66
			2.	23	155	66
			3.	28	155	66
2-propanol	20	80	1.	42	131	51
			2.	35	140	54
			3.	36	140	55

Thus, obtained BR behavior in alcohol-water mixture seems to be the consequences of new competitive (parallel) reactions (Eqs 4-8), indicating the additional role of alcohol. Namely, reactions between alcohol and HO• and HOO• radicals, can be competitive for elementary BR reactions (in only water-medium) including mentioned radicals. The potential mechanism of alcohol (C<sub>n</sub>H<sub>2n+2</sub>OH) acting could be [6,7]:



The further investigation, in order to connect Briggs-Rauscher reaction parameters obtained in alcohol-water mixtures with particular alcohol properties should be done.

## CONCLUSION

In this work, the BR reaction is carried out in three different water-alcohol mixtures. The obtained BR behavior is compared with the same results obtained in deionized water as a solvent. The addition of all examined alcohols (methanol, propanol, and 2-propanol) to the BR system caused the appearance of the induction period, as well as the significant reduction of the oscillatory region. The obtained BR behavior in the alcohol-water mixture is the probable consequence of new competitive reactions.

## Acknowledgement

This work was partially supported by the Ministry for Science of the Republic of Serbia (Grants no. 172015 and 173052).

## REFERENCES

- [1] T. Briggs, W. Rauscher, J. Chem. Educ., 1973, 50, 496-496.
- [2] S. Furrow, J. Chem. Educ., 2012, 89, 1421-1424.
- [3] R. Cervellati et al. Helvetica Chimica Acta, 2001, 84, 3533-3547
- [4] R. Cervellati et al. Helvetica Chimica Acta, 2004, 87, 133-155.
- [5] D. Stanisavljev et al. J. Phys. Chem. A. 2011, 115, 7955-7958.
- [6] P. Ulanski, C. Sonntag, J. Chem. Soc., Perkin Trans., 1999, 2, 165-168.
- [7] A. Shilpov, G. Shul'pin, Activation and Catalytic Reactions of Saturated Hydrocarbons in the Presence of Metal Complexes, Kluwer Academic Publishing, London, 2000.

## THE INFLUENCE OF POSITIVE FEEDBACK IR COMPENSATION ON OSCILLATING ELECTROCHEMICAL SYSTEM: COPPER - 1M PHOSPHORIC ACID

N. I. Potkonjak,

*Chemical Dynamics Laboratory, Vinca Institute of Nuclear Sciences,  
University of Belgrade,  
Mike Petrovica Alasa 12-14, 11000 Belgrade, Serbia.  
([npotkonjak@vin.bg.ac.rs](mailto:npotkonjak@vin.bg.ac.rs))*

### ABSTRACT

In this study, the influence of the positive feedback IR compensation technique was investigated on the oscillatory behavior of current during the anodic dissolution/passivation of copper in 1 M phosphoric acid. Results are presented to show strong influence of used compensation technique on bifurcation points and number of oscillating events inside oscillatory region.

### INTRODUCTION

Electrochemical cell is a far-from-equilibrium system in which dynamical instabilities can spontaneously arise in the form of temporal current/potential oscillations [1]. Origin of current oscillations is linked to the synchronized action of coupled non-linear processes due to electrode kinetics, chemical reaction, electrical effect and mass transport. In electrochemical oscillatory systems, potential drop across the double layer ( $\phi_{DL}$ ), is consider being an essential variable for oscillatory mechanism of the N-NDR system, the system where the negative differential resistance appears as N-shape polarization curve [1]. The applied potential ( $E$ ) is composed of the  $\phi_{DL}$  and the Ohmic potential drop ( $IR_e$  drop) in the electrolyte [2]. The phenomenon of  $IR_e$  drop is associated to the existence of the electrolyte resistance ( $R_e$ ) and the flow of the electric current ( $I$ ) trough electrolyte. It has been argued by several authors that  $IR_e$  drop plays an important role in arising of the current oscillation phenomenon during the electro-dissolution of metals [2]. The positive feedback IR compensation technique requires that the user enter a value for the electrolyte resistance [2]. It then increases the applied potential by multiplying the chosen resistance value time the cell electric current. In this study, the positive feedback  $IR$  compensation technique was applied to the voltammetric investigation of the oscillating electrochemical system copper/1 M phosphoric acid.

## EXPERIMENTAL

The electrolytic cell consists of the copper disc ( $0.0314 \text{ cm}^2$ ) as a working electrode, the Pt-foil auxiliary electrode and a saturated calomel electrode (SCE) as a reference electrode. The electrolyte solution was 1M phosphoric acid ( $\text{H}_3\text{PO}_4$ ), prepared from  $\text{H}_3\text{PO}_4$  (Merck) and deionized water ( $18 \text{ M}\Omega \text{ cm}^{-1}$ ). Electrochemical experiments were performed using Solartron SI 1286 electrochemical interface, supported with corrosion measurement software (CorrWare®). The scan rate was  $10 \text{ mV s}^{-1}$ . The working electrode was polarized anodically, by means of linear sweep voltammetry, starting from 0 mV vs. SCE. The positive feedback *IR* compensation technique was applied with compensation resistance ( $R_{\text{comp}}$ ) of 0, 10, 20, 30, 40 and 50  $\Omega$ . The temperature of cell was 295 K.

## RESULTS AND DISCUSSION

Anodic *I-E* polarization curves (voltammogram) of Cu electrode immersed in 1 M  $\text{H}_3\text{PO}_4$  have revealed the existence of current oscillations in the certain potential region ( $E_{\text{Oss}}$ ), Fig.1 a). This region was found between two stable steady-state regions (SSS1 and SSS2). Looking from the direction of increasing polarization, the first to appear is SSS1 region in which anodic dissolution of copper is dominant process, the active region. This region is characterized with increase of the electric current with the applied potential. The SSS1 region ends at 0.538 V. Thereupon, the potential region of current oscillations can be observed. First bifurcation (point) potential appears at  $E_{\text{Bif1}} = 0.541 \text{ V}$ . This bifurcation point can be considered as point where the electrochemical system enters into oscillatory state (OsS state). Oscillatory region ends at 0.615 V. The system leaves oscillatory state throughout this bifurcation point. The width of OsS region is  $\Delta E_{\text{Oss}} = 0.074 \text{ V}$ . The electrochemical system enters SSS2 region at 0.625 V. This state is characterized by limiting current, the passive state.

Various values of  $R_{\text{comp}}$ , from 10  $\Omega$  to 50  $\Omega$ , have been used in order to investigate the effect of the positive feedback *IR* compensation technique on characteristic of  $E_{\text{Oss}}$ . Some of recorded voltammograms are presented in Fig. 1 b) and c). It is observed that the potential region of current oscillations is shifted towards more cathodic potentials, with the increasing  $R_{\text{comp}}$ . Tracing the shift of the first bifurcation point linear correlation between the potential of  $E_{\text{Bif1}}$  and the applied  $R_{\text{comp}}$  was found with the correlation coefficient of linearity of  $r = -0.99975$  was found, Fig 2. Furthermore, summation of the value of  $E_{\text{Bif1}}$  and the value of compensated resistance multiplied with the characteristic electric current (the electric current just before bifurcation

point,  $I = 0.0069$  A) give a values which are close to the value of  $E_{\text{Bif}}$  when no compensation techniques was applied, Fig 2 (presented as circles).

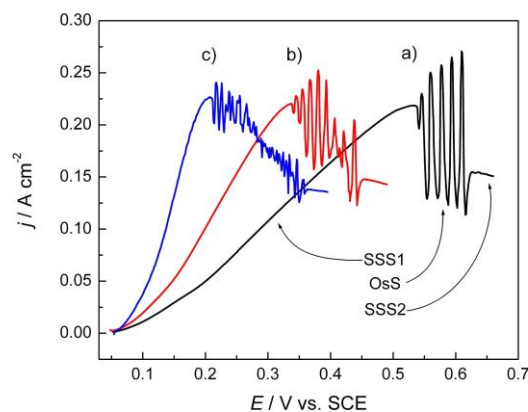


**Figure 1.** Voltammograms of the anodic dissolution of Cu in 1M  $\text{H}_3\text{PO}_4$   
a)  $R_{\text{comp}} = 0 \Omega$ , b)  $R_{\text{comp}} = 30 \Omega$  and c)  $R_{\text{comp}} = 50 \Omega$ .

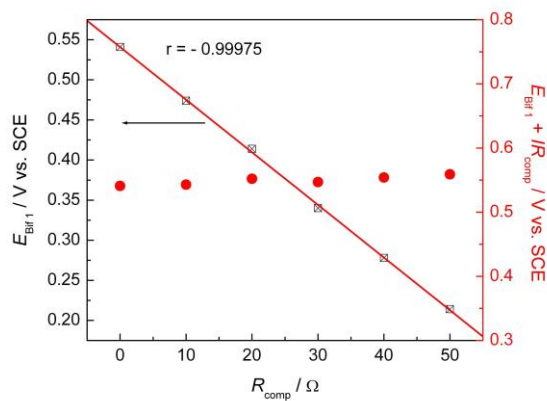


**Figure 2.** Dependence of the first bifurcation point and the sum of the first bifurcation point and  $IR_{\text{comp}}$  value (with the compensated resistance ( $R_{\text{comp}}$ ),  $I$  – the electric current just before bifurcation, 0.0069 A).

As presented in Fig. 1, current oscillations are affected by the use of positive feedback  $IR$  compensation, throughout decrease of the amplitude with increasing of  $R_{\text{comp}}$ . Also the structure of oscillatory region has been affected, current oscillations switch from large amplitude relaxation type

to small amplitude chaotic oscillations. Number of oscillatory events inside oscillatory region increases exponentially with increasing  $R_{\text{comp}}$ , Fig. 3.

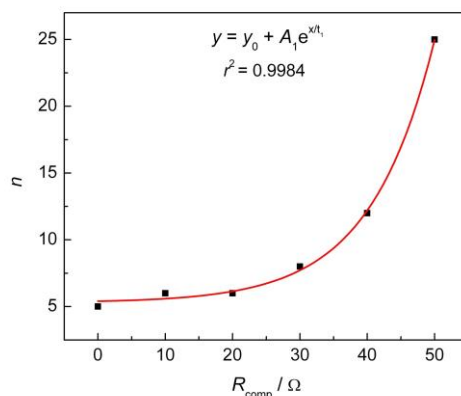


**Figure 3.** Dependence of number of oscillatory events in the potential region of current oscillations with the compensated resistance ( $R_{\text{comp}}$ ).

## CONCLUSION

The positive feedback  $IR$  compensation was applied in voltammetric measurements of anodic dissolution of copper electrode in 1 M phosphoric acid. A strong influence of used compensation technique on current oscillatory characteristics has been observed. However current oscillations were not suppressed by this technique. Some further experiments concerning the application of positive feedback  $IR$  compensation have to be made with great care in order overview its advantages and weaknesses.

## Acknowledgement

This work was supported by the Ministry of Education, Science and Technological Development of Republic of Serbia (Grants no. 172015).

## REFERENCES

- [1] I. Z. Kiss, T. Nagy, V. Gáspár in: Handbook of Solid State Electrochemistry, Vol.2, V. V. Kharton (Eds.), WILEY-VCH Verlag GmbH & Co. KGaA, 2011.
- [2] M. Orlik, Self-Organization in electrochemical systems I: General principles of self-organization. Temporal Instabilities, Springer-Verlag, Berlin, Heidelberg, 2012.

## PH OSCILLATION TYPES IN UREA-UREASE MEMBRANE REACTOR

L. Schreiberová , F. Muzika and I. Schreiber

*University of Chemistry and Technology, Prague, Faculty of Chemical Engineering, Department of Chemical Engineering, Technická 5, 16628 Praha, Czech Republic. (igor.schreiber@vscht.cz)*

### ABSTRACT

This work is focused on experimental study of pH dynamic behaviour of urea-urease enzymatic system in a two-compartment membrane reactor with vertically oriented semipermeable membrane. The first compartment is a continuous stirred tank reactor closed to the atmosphere and the second one is a continuous stirred reservoir, also closed to the atmosphere, coupled with the main reactor via semipermeable membrane, they are both operating under temperature  $\sim 25^{\circ}\text{C}$ . The protonation of the solutions is provided via addition of sulphuric acid into the stock solutions.

We report pH oscillations (volumetric permeation rate coefficients  $k_{\text{H}^+}$  >  $k_{\text{urea}}$  proposed by Bansági et al.) in the membrane reactor closed to the atmosphere with various oscillation periods from 300 s to 11600 s having pH amplitudes from  $\sim 0.1$  pH units up to  $\sim 4$  pH units.

The pH dynamics appears to be both periodic and chaotic.

### INTRODUCTION

The first periodic oscillatory behaviour in the urea-urease reaction was observed by Gnoll [1] using Van Slykes method [2] of measurement of volume of produced ammonia extracted from reaction mixture of hydrolysed urea under buffered pH. The urea-urease reaction can be utilized in its stationary regime as part of the hemodialysis [3], it can also be used as part of electrode for determination of urea in blood serum [4] and its usage was proposed in wastewater recycling system in spaceships [5]. Urease is currently used in medicine to assess the presence of *Helicobacter pylori* in stomach as gastric ulcer effector [6].

The urea-urease enzymatic reaction system is also able to operate in bistable regime and in many dynamic regimes. The bistability was observed in continuous stirred tank reactor [7] and in urease loaded alginate beads placed in urea solution with addition of sulphuric acid using cresol red as pH indicator [8]. The dynamic regimes were observed in a form of travelling pH

waves in gel layer [9] and in a form of pH oscillatory behaviour in continuous stirred tank reactor using addition of sulphuric and acetic acid [7].

### EXPERIMENTAL

Experiments were conducted under 25°C using thermostated system. Our experiments were measured in a membrane reactor system closed to the atmosphere, Fig. 1. The main reactor **1** in the membrane reactor system is fed by urease solution **8** with adjusted pH using peristaltic pump **6**, the solution is stirred at 500rpm using stirring bar and stirrer **5**. The reservoir **2** is fed by urea solution **7** with adjusted pH using peristaltic pump **6**, the solution is stirred at 500rpm using stirring bar and stirrer **5**. Both the main reactor **1** and the reservoir **2** are connected via semipermeable membrane Spectra/Por 7 MWCO:1000 **3**, which is oriented vertically. Urea and H<sup>+</sup> ions are transported through the membrane **3**, thus allowing the reaction of urea-urease to occur. The resulting pH is measured every second by the pH probe **4**, temperature is measured every second by the thermometer probe **10** in the waste tank **9**. Data from pH and temperature measurements are recorded in the pH meter **11**.

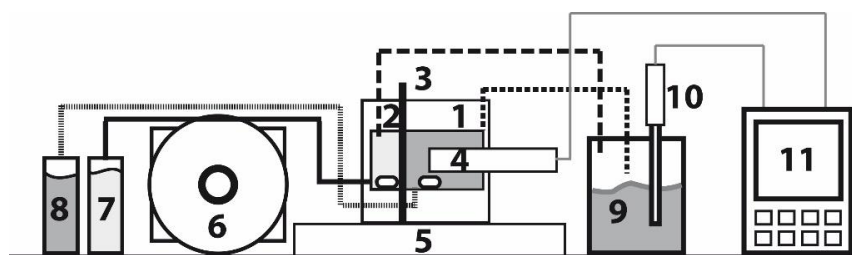


**Figure 1.** Experimental setup of the membrane reactor system closed to the atmosphere. Description: 1) continuous stirred tank reactor – volume 0.64ml - mean residence time  $\tau=96s$ , 2) reservoir – volume 0.8743ml - mean residence time  $\tau_r=546.43s$ , 3) membrane, 4) pH probe, 5) stirrer, 6) peristaltic pump, 7) urea stock solution, 8) urease stock solution, 9) waste tank, 10) thermometer probe, 11) pH meter HI 5222.

Our measurement using UV-vis spectrophotometer Agilent 8454 and pH meter HI 5222 showed the volumetric permeation rate coefficients for urea  $k_{urea}=2.65 \times 10^{-4} s^{-1}$  and for H<sup>+</sup> ions  $k_{H^+}=7.36 \times 10^{-4} s^{-1}$ . The ratio of these coefficients is 2.7, which is near the ratio <3.3, 20> necessary for oscillator behaviour, calculated by Bánsági et al.[10].

### RESULTS AND DISCUSSION

pH oscillatory behaviour in the membrane reactor with vertically oriented membrane are in general quite irregular and may display several parts with their own characteristic periods observed during one experimental run.

Examples of two pairs of mutually similar regimes of pH oscillations representing two distinct dynamical modes are shown in Fig. 2, namely curves A and C with shorter period and small amplitude, and curves B and D showing composite oscillations with several small amplitude oscillations overlaid a large amplitude peak, but with similar periods. When arranged with the increasing concentration of enzyme, the order of the dynamical regimes is ABCD, therefore there is an alternating sequence of simple small-amplitude oscillations and composite oscillations.

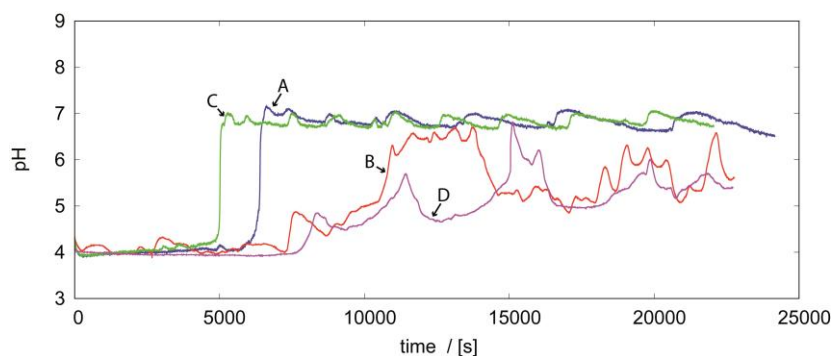


**Figure 2.** Comparison of recordings of pH in reactor in time for increasing concentration of enzyme from  $a_0=4.803$  U/ml to  $a_0=4.838$  U/ml: A –  $a_0=4.803$ U/ml,  $\text{pH}_{\text{urease}_0}=4.261$ ,  $\text{pH}_{\text{urea}_0}=2.875$ ; B -  $a_0=4.820$  U/ml,  $\text{pH}_{\text{urease}_0}=4.2$ ,  $\text{pH}_{\text{urea}_0}=3.03$ , C -  $a_0=4.837$  U/ml,  $\text{pH}_{\text{urease}_0}=4.55$ ,  $\text{pH}_{\text{urea}_0}=2.836$ , D -  $a_0=4.838$  U/ml,  $\text{pH}_{\text{urease}_0}=3.7$ ,  $\text{pH}_{\text{urea}_0}=2.73$ .  $c_{\text{urea}_0}=0.015\text{M}$ ,  $\tau=96\text{s}$ ,  $\tau_r=546.43\text{s}$ .

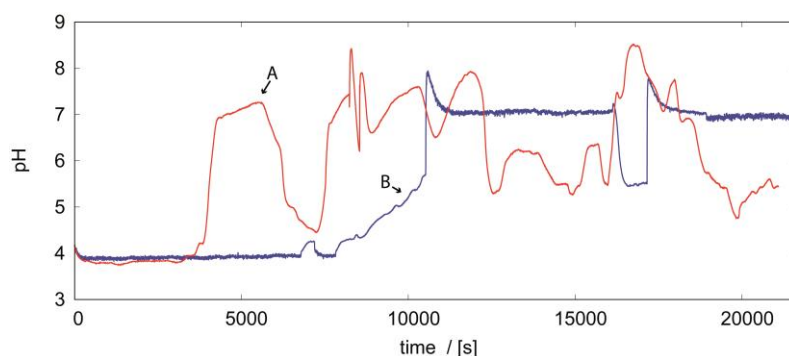


**Figure 3.** Example of recordings of pH in reactor in time showing two distinct regimes of large amplitude pH oscillations: A –  $a_0=4.752$ U/ml,  $\text{pH}_{\text{urease}_0}=4.0$ ,  $\text{pH}_{\text{urea}_0}=2.935$ ; B -  $a_0=5.301$ U/ml,  $\text{pH}_{\text{urease}_0}=3.998$ ,  $\text{pH}_{\text{urea}_0}=2.881$ .  $c_{\text{urea}_0}=0.015\text{M}$ ,  $\tau=96\text{s}$ ,  $\tau_r=546.43\text{s}$ .

The largest recorded amplitude of pH oscillations is ~4 pH units for the case of chaotic pH oscillations, see Fig. 3 curve A, with periods around 3100s, 1700s, 1000s and 300s. The second largest recorded amplitude of pH oscillations ~3 pH units for the case of pH oscillations with specific dynamic mode, but only one oscillation peak, see Fig. 4 curve B.

### CONCLUSION

pH dynamic behaviour in a membrane reactor with vertically oriented membrane for narrow range of concentration of enzyme was measured. Oscillatory region occurs for the concentration of urea 0.015M, pH of urea solution set between  $\text{pH}=\langle 2.73, 3.386 \rangle$ , pH of urease solution set between  $\text{pH}=\langle 3.7, 4.55 \rangle$  and concentration of enzyme between 4 and 6 Units/ml. Periodic pH oscillations were found to have amplitude from 0.1 to 3 pH units and period between 2000s and 6000s. Chaotic pH oscillations were found having amplitude from 0.1 to 4 pH units and period ranging from 300s to 11600s. Following this preliminary report we plan to examine the oscillatory region in more detail.

### Acknowledgement

This work was supported by the grant 18-24397S from the Czech Science Foundation.

### REFERENCES

- [1] T. Groll, Colloid Polym. Sci., 1917, 21, 138-148.
- [2] D. D. Van Slyke and G. E. Cullen, The Journal of Biological Chemistry, 1914, 19, 141-180.
- [3] S.R. Ash, R. G. Barile, J. A. Thornhill, J. D. Sherman and N-H. L. Wang, Trans. Am. Soc. Artif. Intern. Organs., 1980, 26, 111-115.
- [4] M. Mascini and G. G. Gullbault, Analytical Chemistry, 1977, 46, 795-798.
- [5] Schussel L. J. and Atwater J. E., Chemosphere, 30, 1995, 985-994.
- [6] B. E. Dunn and M. G. Grütter, Nature Structural Biology, 2001, 8, 480-482.
- [7] G.Hu, J.A. Pojman, S. K. Scott, M. M. Wrobel and A. F. Taylor, J. Phys. Chem. B, 2010, 114, 14059–14063.
- [8] F. Muzika, T. Jr. Bánsági, I. Schreiber, L. Schreiberová and A. Taylor, Chem. Commun., 2014, 50, 11107-11109.
- [9] M. M. Wrobel, T. Jr. Bánsági, S. K. Scott, A. F. Taylor, Ch. O. Bounds A. Carranzo and J.A. Pojman, Biophysical Journal, 2012, 103, 610–615.
- [10] T. Bánsági Jr. and A. F. Taylor, J. Phys. Chem. B, 2014, 118, 6092-6097.

## GALLIC ACID EFFECT ON THE BRIGGS-RAUSCHER REACTION DYNAMICS

J. P. Maksimović<sup>1</sup>, Ž. D. Čupić<sup>2</sup>, S. R. Anić<sup>1,2</sup>, L. Z. Kolar-Anić<sup>1,2</sup>, E. Greco<sup>3</sup>, R. Cervellati<sup>3</sup> and M.C. Pagnacco<sup>1</sup>

<sup>1</sup>University of Belgrade, Faculty of Physical Chemistry, Studentski trg 12-16, 11158 Belgrade, Serbia. (jelena.maksimovic@ffh.bg.ac.rs)

<sup>2</sup>University of Belgrade, Institute of Chemistry, Technology and Metallurgy, Njegoševa 12, 11000 Belgrade, Serbia

<sup>3</sup>University of Bologna, Department of Chemistry "Giacomo Ciamician", via Selmi 2, 40126 Bologna, Italy

### ABSTRACT

The effect of different concentration of gallic acid (GA) on the oscillatory behavior of the Briggs-Rauscher (BR) reaction is reported. In this work, the sample was injected before the start of oscillations. The main effect is the appearance of an induction time that increases with the concentration of GA added. Other parameters as a number of oscillations and oscillatory period are affected. These latter linearly depend on the concentration and can be used for quantitative GA analytical assay in a GA concentration range  $3.00 \times 10^{-5}$  M –  $4.00 \times 10^{-4}$  M. The perturbation is very different from that previously reported, in which samples of phenolics were added to an active BR mixture, indicating that the mechanism of perturbation largely depends on the injection point.

### INTRODUCTION

It is well known that the Briggs-Rauscher (BR) system (Malonic acid,  $\text{KIO}_3$ ,  $\text{H}_2\text{O}_2$ ,  $\text{Mn}^{2+}$ ,  $\text{H}^+$ ) is a hybrid of two more famous oscillating reactions, the Bray-Liebhafsky (BL) and the Belousov-Zhabotinsky (BZ) reactions [1]. The BR oscillating reaction has been used as a test to measure the relative antioxidant activity of free-radicals scavengers, particularly phenolic compounds [2,3]. In this work, the effects of different concentration of gallic acid on the BR system were investigated. The gallic acid (3,4,5-Trihydroxybenzoic acid, GA) is a well-known antioxidant as well as a free radical scavenger. The GA is present in a variety of plants and fruits. Studies on gallic acid and its derivatives have reported their potential in the treatment of oxidative cell stress that accompany several diseases as diabetes, ischemic heart attack, ulcer and other ailments [4].

## EXPERIMENTAL

The experiments were carried out in a closed well-stirred (with stirring rate,  $\sigma = 900$  rpm) and thermostated (at  $T = (37.0 \pm 0.2)$  °C) batch reactor. Initial concentrations of the reactants were:  $[C_3H_4O_4]_0 = 0.0789$  M,  $[MnSO_4]_0 = 0.0075$  M,  $[HClO_4]_0 = 0.0300$  M,  $[KIO_3]_0 = 0.0752$  M and  $[H_2O_2]_0 = 1.2690$  M. A 100  $\mu$ l aliquot of GA of different concentration was added, yielding an initial concentration of  $[GA]_0 = 3.17 \times 10^{-5}$  M,  $5.07 \times 10^{-5}$  M,  $6.34 \times 10^{-5}$  M,  $1.90 \times 10^{-4}$  M,  $3.17 \times 10^{-4}$  M,  $3.81 \times 10^{-4}$  M,  $4.00 \times 10^{-4}$  M,  $4.12 \times 10^{-4}$  M,  $4.44 \times 10^{-4}$  M and  $6.34 \times 10^{-4}$  M ( $M = \text{mol/dm}^3$ ). All chemicals were of analytical grade and used without further purification. Solutions of GA were prepared in methanol whereas all other reactants were dissolved in deionized water. The total volume of the reaction mixture in all experiments was 25 ml. The reactants were added to the reaction vessel in the following order: 7 ml  $C_3H_4O_4$ , 5 ml  $MnSO_4$ , 5 ml  $HClO_4$ , 5 ml  $KIO_3$ , and when the temperature and potential were stabilized 100  $\mu$ l of GA was added. Three minutes after addition of GA, 3 ml  $H_2O_2$  was added to the reaction vessel. The instant of  $H_2O_2$  addition was taken as the beginning time of the reaction. The time evolution of the BR reaction was followed potentiometrically. A PC-Multilab EH4 16-bit analog-to-digital converter electrochemistry analyzer was directly connected to the reactor through a Pt working electrode and a double junction Ag/AgCl reference electrode and used to record changes in the Pt-electrode potential.

## RESULTS AND DISCUSSION

Traces of potential changes *vs* time are reported in Fig. 1. As can be seen GA concentration from  $3.17 \times 10^{-5}$  M to  $6.34 \times 10^{-4}$  M has a strong influence on the BR oscillatory reaction dynamics: for increasing GA concentration the induction period increases as well. Addition of GA also changes other important parameters of the oscillation train, such as the number and period of oscillations (Figures 1 and 2).

As can be seen from Fig. 2 (a), the induction period is a nonlinear function of GA concentration. On the contrary, in a range of GA concentration from  $3.17 \times 10^{-5}$  M to  $4.00 \cdot 10^{-4}$  M, the period of oscillations (Fig. 2 (b)) and the number of oscillations (Fig. 2 (c)) show a clear linearity. Therefore, on the basis of this dependence, the BR reaction can be used for analytical purposes. The concentration of GA above  $4.44 \times 10^{-4}$  M totally quenched the oscillatory behavior (Fig. 1 (e)).

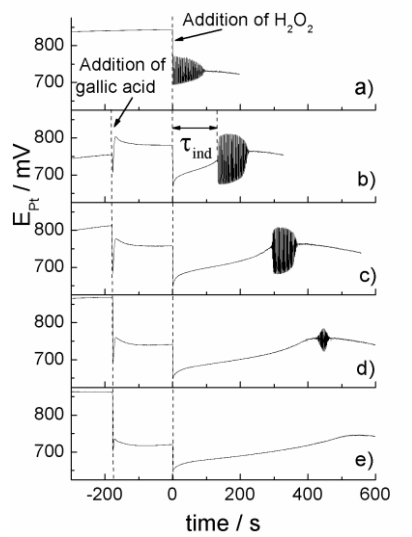


**Figure 1.** Recording of the Pt-electrode potential versus time for Briggs-Rauscher reaction mixture without GA (a) and with following initial concentrations  $[GA]_0 = 5.07 \times 10^{-5}$  M (b),  $1.90 \times 10^{-5}$  M (c),  $4.12 \times 10^{-4}$  M (d),  $6.34 \times 10^{-4}$  M (e).

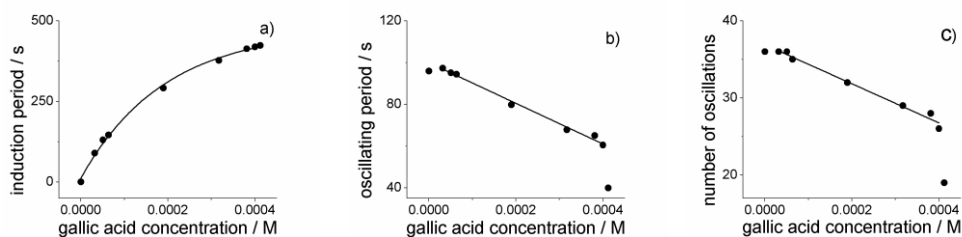


**Figure 2.** Induction period (a), oscillations period (b) and the number of oscillations (c) as a function of GA concentration.

Recently, we investigated caffeic acid (3,4-Dihydroxy-*trans*-cinnamic acid, CA) under the same experimental conditions [5]. The perturbation was similar to that reported here but the CA concentrations that give the same effects were one order of magnitude smaller than those of GA, at  $[CA]_0 > 2 \times 10^{-5}$  M the oscillations were completely quenched. So, it seems that CA (two phenolic OH) is a better antioxidant than GA (three phenolic OH). However, Wright et al. [6] reached the conclusion that the number of phenolic OH groups is largely irrelevant and that it is the strategic placing of such groups that determines the antioxidant activity. They also proposed empirical additivity rules to evaluate the contribution of some groups in a different position to the bond dissociation enthalpy ( $\Delta BDE$ ) of a given OH. Following these rules, we found that the most active OH group for both compound is that in the *p*- position with respect to the acidic group with estimated  $\Delta BDE$  of  $-13.9$  kcal/mol and  $-11.6$  kcal/mol, for CA and GA respectively. These

estimates are in agreement with the experimental results presented here, showing that CA is a better radical scavenger than GA.

In the previously implemented test [2], operating at 25 °C, the addition of antioxidant sample is made after the second or third oscillation. The effect was an immediate quenching of oscillations that resumed after a period called inhibition time. Inhibition time linearly depended on the concentration of the antioxidant added and was used to evaluate the antioxidant activity. The same authors also studied, besides the subtraction of HOO• radicals, the possible parallel reaction of phenolics with reagents and intermediates. They concluded that the main action of the phenolic compounds during inhibition time is quenching of the radicals [3]. The point of addition clearly affects the dynamics of the perturbed BR reaction by phenols. A study of the differences, from the experimental and mechanistic point of view will be the object of further investigation.

## CONCLUSION

Addition of GA before starting the oscillatory evolution in the Briggs-Rauscher oscillating system leads to an induction period that increases with the concentration of GA. Interestingly, this perturbation is very different from that previously studied adding phenolics to an active BR oscillation system. This difference provides the opportunity to deeply investigate the mechanism of a system governed by non-linear dynamics.

## Acknowledgment

This work was supported by the Ministry of Education, Science and Technological Development of Republic of Serbia (Projects No. 172015 and 45001).

## REFERENCES

- [1] R. M. Noyes, *J. Phys. Chem.*, 1990, *94*, 4404-4412.
- [2] R. Cervellati, K. Höner, S. D. Furrow, C. Neddens, S. Costa, *Helv. Chim. Acta*, 2001, *84*(12), 3533-3547.
- [3] R. Cervellati, K. Höner, S. D. Furrow, F. Mazzanti, S. Costa, *Helv. Chim. Acta*, 2004, *87*, 133-155.
- [4] N. Nayeem, A. SMB, H. Salem, S. AHEL-Alfay, *J. App. Pharm.*, 2016, *8*, 1-4.
- [5] J. Maksimović, K. Stevanović, I. Bujanja, Lj. Kolar-Anić, S. Anić, N. Potkonjak, M. Pagnacco, 6<sup>th</sup> International Congress of Serbian Society of Mechanics, Mountain Tara, Serbia, June 19-21, 2017.
- [6] J. S. Wright, E. R. Johnson, G. A. DiLabio GAet., *J. Am. Chem. Soc.*, 2001, *123*, 1173-1183.

## REDUCING MIXING EFFECTS WITH GLASS POWDER IN BRAY-LIEBHAFSKY OSCILLATORY REACTION

K. Stevanović, I. N. Bubanja and D. Stanisavljev

*University of Belgrade, Faculty of Physical Chemistry, Studentskitrg 12-16,  
11000 Belgrade, Serbia. ([kristina@ffh.bg.ac.rs](mailto:kristina@ffh.bg.ac.rs))*

### ABSTRACT

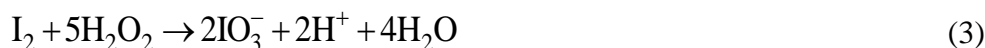
The influence of the mixing and inert glass powder addition on Bray–Liebhafsky (BL) oscillating chemical reaction was investigated. It has been noticed that decrease of the mixing rate has the same influence on the induction period and period per oscillations as an addition of the glass to the reaction mixture. Observed effects indicate that BL mechanism may be influenced by heterogeneous processes coupled with chemical reactions.

### INTRODUCTION

The Bray-Liebhafsky (BL) reaction is an oscillatory system at certain conditions, which represents decomposition of hydrogen peroxide into the water and oxygen in the presence of hydrogen and iodate ions [1, 2]:



Reaction (1) results from two processes, the reduction (2) of iodate to iodine and the oxidation (3) of iodine to iodate, which alternately dominate over each other:



Reactions (2) and (3) are themselves complex and their mechanisms involve several intermediate species, such as  $\text{I}_2$ ,  $\text{I}^-$ ,  $\text{HIO}$  and  $\text{HIO}_2$  [3]. This just confirms complexity of the system, which seems deceptively simple.

Ever since its discovery BL reaction was treated as a homogenous system regardless to the evolving of the gaseous phase from constant oxygen production. There was an attempt to point out the importance of the oxygen in such systems [4], but in most of the investigations the reaction is treated as homogeneous. Formation of the gaseous cavities (bubbles) in the solution indicates that nucleation processes may also take part in a reaction mechanism. Coupling between nucleation phenomena and chemical reactions is not well understood and may be important for a class of chemical oscillators producing gaseous phase.

In our recently published paper [5] we suggested that heterogeneous processes are included in the reaction of the iodine oxidation, the most intriguing part of the BL reaction (3). In mentioned paper it is argued that reaction mechanism may be influenced by physical effects related with formation of critical gaseous cavities. Here we tried to investigate influence of physical effects such as mixing and addition of inert glass powder on BL oscillator.

### EXPERIMENTAL

In this study, BL reaction system was performed in batch reactor. All experiments were carried out in a 50 mL glass vessel wrapped in a water recirculation jacket connected to a thermostat. Working temperature was 62 °C. For initial homogenization of the reaction mixture, a magnetic stirrer was used. Reaction was followed by potentiometric method. The working Pt electrode was connected to a double-junction Ag/AgCl reference electrode. The potential-time evolution of the BL reaction was recorded by an electrochemical device (PC-Multilab EH4 16-bit ADC) coupled with a personal computer. Two types of experiments were performed. In first group only influence of mixing was analyzed, and in second one influence of the glass powder addition at the maximal mixing rate is examined. In second group glass was added in a reactor right before all reactants. Thermostated and protected from light, the reaction vessel was filled with the reactants in the following order: 22 ml of 0.1091 M H<sub>2</sub>SO<sub>4</sub> (Merck, Germany), 22 ml of 0.1636 M KIO<sub>3</sub> (Alfa Aesar, Germany) and when temperature achieved a stable value of T = 62 °C, 6 ml of 3.83 M H<sub>2</sub>O<sub>2</sub> (Merck, Germany) was added. After the induction period, oscillations took place and at the end of 6th oscillation recording was stopped. All used chemicals were pro analysis grade, and their solutions were prepared with deionized water (18 MΩ cm). Glass powder was prepared from grounded laboratory glass and additionally purified with chromosulfuric acid and deionized water. Average size of the glass particles was in range from 0.8 to 10 μm peaked sharply to 1 μm, measured by Mastersizer 2000 (Malvern Instruments).

### RESULTS AND DISCUSSION

Reaction started at the moment when hydrogen peroxide was added to the reaction mixture. Oscillations occurred after passing an induction period. The mean values calculated from three repeated experiments of the potential-time recordings such as induction period ( $\langle\tau_{ind}\rangle$ ), average period per oscillation ( $\langle\tau_{1-6}/5\rangle$ ) and amplitude of oscillations  $\langle A \rangle$  are given in Table 1. All stated errors, at Table 1, represent 95% confidence interval of the mean values from three separate experiments. The same dynamical properties were determined

for experiments with glass addition (at maximal mixing rate) and are shown in Table 2. In this preliminary results only one experiment per mass of added glass was performed without estimated error.

**Table 1.** Average values of induction period,  $\langle\tau_{\text{ind}}\rangle$ , period per oscillation,  $\langle\tau_{1-6/5}\rangle$ , and amplitude,  $\langle A \rangle$ , obtained for different mixing rates.

<b>Experiments without glass powder</b>			
$\sigma$ / rpm	$\langle\tau_{\text{ind}}\rangle$ / s	$\langle\tau_{1-6/5}\rangle$ / s	$\langle A \rangle$ / mV
<b>1100</b>	940±50	180±20	16±3
<b>600</b>	790±20	210±30	55±8
<b>0</b>	610±40	240±20	62±5

**Table 2.** Values of induction period,  $\tau_{\text{ind}}$  period per oscillation,  $\tau_{1-6/5}$  and amplitude,  $A$ , obtained for different glass masses and maximal stirring rate  $\sigma = 1100$  rpm.

<b>Experiments with glass powder</b>			
$m$ / g	$\tau_{\text{ind}}$ / s	$\tau_{1-6/5}$ / s	$A$ / mV
<b>0</b>	940	180	16
<b>0.3386</b>	803	190	50
<b>0.5445</b>	699	210	63
<b>0.9530</b>	626	230	67

Figure 1 (a,b) shows induction period vs mixing rate and induction period vs glass mass dependences respectively. Table 1 underlines stochasticity of the whole process in agreement with previous discussion [5]. The most important result is that even at the highest mixing rate, addition of powdered glass decrease induction period and facilitates oscillatory evolution, i.e. reduces effects of mixing. Although mixing alone changes convection and diffusion of oxygen through interphase surface, inert glass addition should not manifest through the same processes. The ability of fine glass powder to decrease mixing effects indicates that beside convection and diffusion, some other phenomena, common for both influences (glass powder addition and mixing), are involved. Reasonable assumption is that nucleation processes may participate in the reaction mechanism as well. This opens a new point of view on BL reaction modelling, but also on all class of chemical oscillators producing gaseous phase.

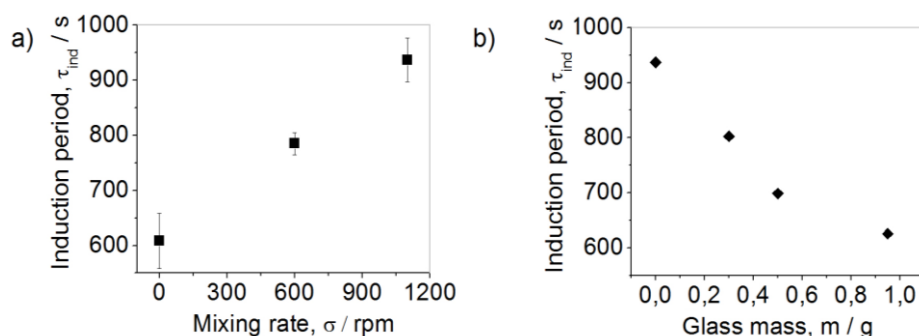


**Figure 1.** a) Induction period/mixing rate and b) induction period/glass mass for  $\sigma = 1100$  rpm dependences.

## CONCLUSION

The influence of the mixing as well as inert glass particles addition on Bray-Liebafsky (BL) oscillating chemical reaction was investigated. Obtained experimental results show that increase of the glass mass, at maximal mixing rate, reduces effects of mixing on the BL reaction dynamic. The ability to produce opposite effects on the BL reaction dynamics by two different physical perturbations strongly supports importance of heterogeneous processes in the whole mechanism which are not of the diffusion and convection types only. Although it opens the possibility of coupling between nucleation processes and chemical reactions, further investigations are necessary for more detailed description of observed phenomena.

## Acknowledgement

This work was partially supported by the Ministry for Science of the Republic of Serbia (Grants no. 172015).

## REFERENCES

- [1] W. C. Bray, *Journal of the American Chemical Society*, 1921, **43**, 1262-2167.
- [2] W. C. Bray, H. A. Liebhafsky, *Journal of the American Chemical Society*, 1931, **53**, 38-44.
- [3] H. A. Liebhafsky, W. C. McGawock, R. J. Reyes, G. M. Roe, L. S. Wu, *Journal of the American Chemical Society*, 1978, **100**, 87-91.
- [4] P. Ševčík, K. Kissimonová, L. Adamčíková, *Journal of Physical Chemistry A*, 2000, **104**, 3958-3963.
- [5] D. R. Stanisavljev, K. Z. Stevanovic, I. N. Bubanja, *Chemical Physics Letters*, 2018, **706**, 120-126.

## PREDICTION OF OSCILLATORY ELECTROCHEMICAL SYSTEM EVOLUTION BY ANALYSIS OF CORRESPONDING ATTRACTOR STRUCTURE

N. I. Potkonjak,

*Chemical Dynamics Laboratory, Vinca Institute of Nuclear Sciences,  
University of Belgrade,  
Mike Petrovica Alasa 12-14, 11000 Belgrade, Serbia.  
(npotkonjak@vin.bg.ac.rs)*

### ABSTRACT

The oscillatory electrochemical system copper/1M trifluoroacetic acid was an object of this investigation. Results are presented to show that two-dimensional projection of the reconstructed attractor can be successfully applied in order to predict the achievable values of the steady-stated variables (observables), even when the system is still in oscillatory state.

### INTRODUCTION

Electrochemical systems can undergo dynamic self-organization in a form of bistability, excitability, oscillations, intermittency and different flavors of chaos [1]. All these temporal dynamical behaviors are associated with interplay between nonlinear reaction dynamics, mass-transport processes and electrical effect [1]. Two-dimensional projection of attractors has been used for the analysis of phase coherence as attractor structure. These attractors can be topologically reconstructed by means of time-delay [2]. Optimal value of the time delay for the state space reconstruction can be estimated by the mutual information (MI) function [3].

### EXPERIMENTAL

All experiments were carried out in a three-electrode electrolytic cell at 295 K, having a copper rod as the working electrode, Pt foil as the counter electrode, and a saturated calomel electrode (SCE) as the reference one. The electrolyte solution was 1M trifluoroacetic acid (TFA). Electrochemical experiments were carried out using a Solartron SI 1286 electrochemical interface. The potentiodynamic experiments were performed using anodic (forward) and cathodic (backward) potential scan starting from 0.0 V up to 0.785 V, at a scan rate 5 mV s<sup>-1</sup>. Potentiostatic experiments were performed at the selected electrode potential starting from 0.620 V and up to 0.700 V

(with step size increase of 10 mV between the experiments). The "optimal" value of the time delay ( $\tau$ ) for the attractor reconstruction was estimated by using the MI function (the software Visual Reconstruction Analysis by Kononov) [4].

## RESULTS AND DISCUSSION

In the Fig.1 are presented segments of the current density-potential ( $j$ - $E$ ) curves of the Cu electrode immersed in 1.0 M TFA and polarized in forward and backward direction. This segment shows the existence of regions of oscillatory behavior of current. As shown, no hysteresis was observed between bifurcation points which characterized transition from stable steady-state (SSS) to oscillatory state (OsS), SSS1  $\rightarrow$  OsS and OsS  $\rightarrow$  SSS1. Both transitions occur at  $E_{\text{BIF1}} \approx 0.569$  V. However, a noticeable hysteresis  $\Delta E_{\text{HOsS} \leftrightarrow \text{SSS2}} = 32$  mV was observed between OsS  $\rightarrow$  SSS2 ( $E_{\text{BIF OsS} \rightarrow \text{SSS2}} = 0.662$  V) and SSS2  $\rightarrow$  OsS ( $E_{\text{BIF SSS2} \rightarrow \text{OsS}} = 0.694$  V) transitions.

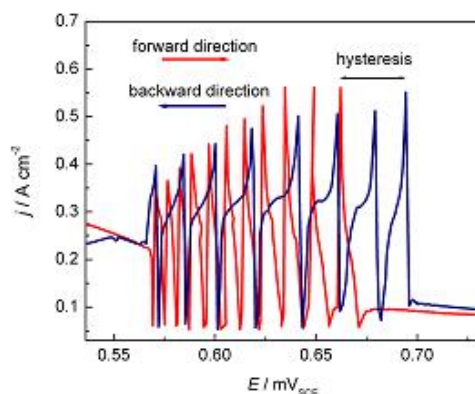


**Figure 1.** Segment of the current density-potential  $j$ - $E$  polarization curves of the anodic dissolution of Cu in 1M TFA showing region of current oscillations.

In order to inspect duality in the region of hysteresis, potentiostatic experiments were performed, starting from 0.620 V and up to the potential where current oscillatory behavior cease to exist and the system reach its stable steady-state (SSS2). In order to reach the transition OsS  $\rightarrow$  SSS2, a series of potentiostatic current density-time ( $j$ - $t$ ) polarization curves have been recorded. The highest applied potential at which oscillatory current behavior emerge was 0.690 V, Fig. 2 (black line). Thereafter, when the applied potential was set at 0.700 V, response of the system implies that SSS2 has been reached, Fig. 2 (red line). Potentiostatic measurements have showed

that the bifurcation point of the OsS  $\leftrightarrow$  SSS2 transition is between 0.690 V and 0.700 V ( $E_{\text{BIF SSS2} \leftrightarrow \text{OsS}}$ ). If compare this result with one obtained by the potentiodynamic measurements, it seem that bifurcation point observed at the SSS2  $\rightarrow$  OsS transition ( $E_{\text{BIF SSS2} \rightarrow \text{OsS}} = 0.694$  V), Fig 1. mach well with findings obtained by potentiostatic measurements

As show in Fig. 2, current oscillatory behavior at 0.690 V suggests that the system periodically switch between two possible values of SSS2. It appears that after sharp increase or decrease (maximum and minimum of oscillations) the system show a tendency to slowly stream toward certain values, but it never reaches them. It would be interesting to see if it is possible to estimate these two values from  $j$ - $t$  polarization curve obtained at 0.690 V.

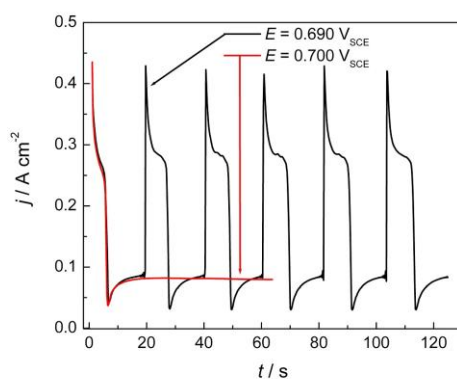


**Figure 2.** Current density-time ( $j$ - $t$ ) polarization curves of the anodic dissolution of Cu in 1M TFA. The applied potentials were: 0.690 V (black curve) and 0.700 V (red curve).

Striving of the system toward certain values of its response was estimated using the two-dimensional attractor projection, reconstructing by using time delayed coordinates. The time delay is  $\tau = 3$  s. Fig. 3 shows the two-dimensional projection was reconstructed by using time series of the current density values ( $j_t$  on  $x$ -axis and  $j_{t+\tau}$  on  $y$ -axis) obtained from the  $j$ - $t$  curve at 0.690 V (Fig. 2). Prediction of possible values of response of the system (the current density) when it enters SSS2 can be estimated from horizontal segments of the attractor projection, Fig 3. Thus, response of the system (current density), when it enters SSS2, will be either  $0.077$  A  $\text{cm}^{-2}$  (lower horizontal line) or  $0.281$  A  $\text{cm}^{-2}$  (upper horizontal line). True value of the system response (current density), when it reached SSS2, was experimentally obtained from  $j$ - $t$  curve at 0.700 V (Fig 2). As shown, this state is characterized with current density of  $0.08$  mA  $\text{cm}^{-2}$ . This experimentally

obtained response of the system in SSS2 is in agreement with one obtained from lower horizontal line of the two-dimensional attractor projection,  $0.077 \text{ mA cm}^{-2}$ .

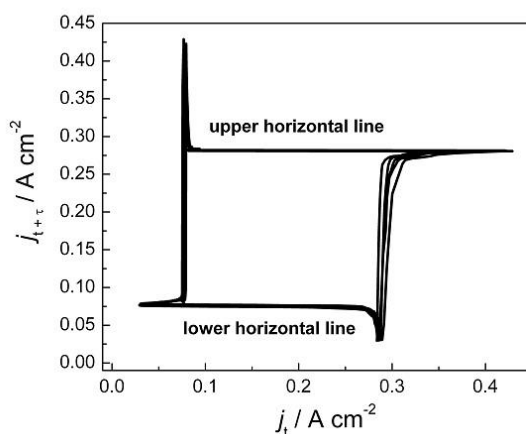


**Figure 3.** Reconstructed attractor using time delay coordinates from  $j-t$  curve at the applied potential 0.690 V. Time delay is  $\tau = 3 \text{ s}$ .

## CONCLUSION

Two-dimensional attractor projection of the oscillatory copper/1M trifluoroacetic acid system response can be successfully applied in order to predict achievable values of the system observables for its stable steady-state that follows oscillatory state. This was confirmed by experimental findings.

## Acknowledgement

This work was supported by the Ministry of Education, Science and Technological Development of Republic of Serbia (Grants no. 172015).

## REFERENCES

- [1] M. Orlik, Self-Organization in electrochemical systems I: General principles of self-organization. Temporal Instabilities, Springer-Verlag, Berlin, Heidelberg, 2012.
- [2] Y. Zou, R.V. Danner, M. Wickramasinghe, I. Z. Kiss, M. Small, Chaos, 2012, 22, 033130.
- [3] A.M. Frase, H.L. Swinney, Physical Review A, 1986, 33, 1134-1140.
- [4] E. Kononov, Visual recurrent analysis (VRA), version 4.9 <http://web.archive.org/web/20070123002807/http://www.myjavaserver.com:80/~nonlinear/vra/vra49.zip>

## STOICHIOMETRIC NETWORK ANALYSIS OF THE MODEL OF OSCILLATORY CARBONYLATION OF PEGA IN OPEN REACTOR

S. Maćešić<sup>1</sup>, Ž. Čupić<sup>2</sup>, K. Novaković<sup>3</sup>, S. Anić<sup>1</sup> and Lj. Kolar-Anić<sup>1</sup>

<sup>1</sup> *University of Belgrade, Faculty of Physical Chemistry, Studentski trg 12-16, 11000 Belgrade, Serbia, e-mail: [stevan.macesic@ffh.bg.ac.rs](mailto:stevan.macesic@ffh.bg.ac.rs)*

<sup>2</sup> *University of Belgrade, Institute of Chemistry, Technology and Metallurgy, Njegoševa 12, 11000 Belgrade, Serbia.*

<sup>3</sup> *Newcastle University, School of Engineering, Merz Court, Newcastle upon Tyne, NE1 7RU, United Kingdom*

### ABSTRACT

The model of palladium-catalysed oscillatory carbonylation of mono-alkyne-terminated poly(ethylene glycol)methyl ether acetylene (PEGA) was adapted to simulate continuous flow stirred tank reactor (CSTR) with substrate and catalyst being flown in and out while intermediary species being only flown out. Stability analysis was then performed using stoichiometric network analysis (SNA). By employing SNA, possible reaction routes in this model were determined together with the types of bifurcations which can occur.

### INTRODUCTION

Oscillatory carbonylation reactions have been subjected to the numerous studies in the past two decades while addition of the polymeric substrate and more recently polymeric catalysts have raised a new research interests and directions.[1,2] Thus, in this paper we applied stoichiometric network analysis (SNA)[3] to the model of palladium-catalysed oscillatory carbonylation of mono-alkyne-terminated poly(ethylene glycol)methyl ether acetylene (PEGA), commonly known as oscillatory carbonylation of PEGA[4] with aim to examine its stability.

### MODEL

In this paper we analyzed the model of PEGA proposed by Donlon and Novakovic[4] adapted for a continuous flow stirred tank reactor (CSTR). The model is presented in Table 1.

This model consists of 14 reactions. Concentrations of CH<sub>3</sub>OH, O<sub>2</sub> and CO are in excess, therefore considered constant and included in the rate constants  $k_i$ . The species H<sub>2</sub>O and PEGP are the products of reactions and consequently they do not appear in the reaction rates.

**Table 1.** Oscillatory carbonylation of PEGA proposed by Donlon and Novaković.[4]

PEGA + PdI <sub>2</sub> + 2 HI + 2CH <sub>3</sub> OH + 2CO → PEGP +Pd + 4 HI	$r_1 = k_1 c_1 c_3^2 c_6$	(R.1)
2 HI + 0.5 O <sub>2</sub> → I <sub>2</sub> + H <sub>2</sub> O	$r_2 = k_2 c_3^2$	(R.2)
Pd + I <sub>2</sub> → PdI <sub>2</sub>	$r_3 = k_3 c_2 c_4$	(R.3)
Pd + I <sub>2</sub> + PdI <sub>2</sub> → 2 PdI <sub>2</sub>	$r_4 = k_4 c_1 c_2 c_4$	(R.4)
PdI <sub>2</sub> + CH <sub>3</sub> OH + CO → IPdR + HI	$r_5 = k_5 c_1$	(R.5)
IPdR + HI → PdI <sub>2</sub> + CH <sub>3</sub> OH + CO → PEGA	$r_6 = k_6 c_3 c_5$	(R.6)
→ PdI <sub>2</sub>	$r_7 = j_0 c_{6,in}$	(R.7)
PEGA →	$r_8 = j_0 c_{1,in}$	(R.8)
PdI <sub>2</sub> →	$r_9 = j_0 c_6$	(R.9)
Pd →	$r_{10} = j_0 c_1$	(R.10)
HI →	$r_{11} = j_0 c_2$	(R.11)
I <sub>2</sub> →	$r_{12} = j_0 c_3$	(R.12)
IPdR →	$r_{13} = j_0 c_4$	(R.13)
	$r_{14} = j_0 c_5$	(R.14)

Concentrations  $c_1$ - $c_6$  represents PdI<sub>2</sub>, Pd, HI, I<sub>2</sub>, IPdR and PEGA respectively,  $j_0$  is specific flow rate while  $k_1$ - $k_6$  are rate constants. There are inflow and outflow of PEGA and PdI<sub>2</sub> and only outflow of Pd, HI, I<sub>2</sub> and IPdR.

### STOICHIOMETRIC NETWORK ANALYSIS

Stoichiometric network analysis (SNA) is very powerful method for stability analysis of multidimensional models of chemical reactions and determination of the types of instabilities which can occur without knowing parameter values. Within this method the reaction rates  $r_{ss,i}$  at the steady state are expressed as linear combination of new parameters, current rates  $j_i$ , using relation  $\mathbf{r}_{ss} = \mathbf{E}\mathbf{j}$  where  $\mathbf{E}$  is matrix of extreme currents and  $\mathbf{j}$  is vector of current rates. Matrix  $\mathbf{E}$  consists of nonnegative elements with each column representing one possible reaction route. In SNA, stability of the steady state can be evaluated using several criteria such as calculation of eigenvalues, calculation of Hurwitz determinants or alpha approximation. The most practical way, especially in the case of complex models with many

intermediate species, is to analyze diagonal minors of the matrix of current rates  $\mathbf{V} = -\mathbf{S}\text{diag}(\mathbf{E}_j)\mathbf{K}^T$ , where  $\mathbf{S}$  is stoichiometric matrix while  $\mathbf{K}$  is matrix of order of reactions and  $^T$  stands for its transpose. The steady state can be unstable if at least one diagonal minor can be negative under certain conditions. Although this is an approximation, this SNA criterion often gives very good results.[5–7]

## RESULTS AND DISCUSSION

Matrices  $\mathbf{S}$ ,  $\mathbf{K}$  and  $\mathbf{E}$  for the model presented in Table 1 are:

$$\mathbf{S} = \begin{bmatrix} -1 & 0 & 1 & 1 & -1 & 1 & 1 & 0 & -1 & 0 & 0 & 0 & 0 & 0 \\ 1 & 0 & -1 & -1 & 0 & 0 & 0 & 0 & 0 & -1 & 0 & 0 & 0 & 0 \\ 2 & -2 & 0 & 0 & 1 & -1 & 0 & 0 & 0 & 0 & -1 & 0 & 0 & 0 \\ 0 & 1 & -1 & -1 & 0 & 0 & 0 & 0 & 0 & 0 & 0 & -1 & 0 & 0 \\ 0 & 0 & 0 & 0 & 1 & -1 & 0 & 0 & 0 & 0 & 0 & 0 & -1 & 0 \\ -1 & 0 & 0 & 0 & 0 & 0 & 0 & 1 & 0 & 0 & 0 & 0 & 0 & -1 \end{bmatrix} \quad (1)$$

$$\mathbf{K} = \begin{bmatrix} 1 & 0 & 0 & 1 & 1 & 0 & 0 & 0 & 1 & 0 & 0 & 0 & 0 & 0 \\ 0 & 0 & 1 & 1 & 0 & 0 & 0 & 0 & 0 & 1 & 0 & 0 & 0 & 0 \\ 2 & 2 & 0 & 0 & 0 & 1 & 0 & 0 & 0 & 0 & 1 & 0 & 0 & 0 \\ 0 & 0 & 1 & 1 & 0 & 0 & 0 & 0 & 0 & 0 & 0 & 1 & 0 & 0 \\ 0 & 0 & 0 & 0 & 0 & 1 & 0 & 0 & 0 & 0 & 0 & 0 & 1 & 0 \\ 1 & 0 & 0 & 0 & 0 & 0 & 0 & 0 & 0 & 0 & 0 & 0 & 0 & 1 \end{bmatrix} \quad (2)$$

$$\mathbf{E}^T = \begin{bmatrix} 0 & 0 & 0 & 0 & 1 & 1 & 0 & 0 & 0 & 0 & 0 & 0 & 0 & 0 \\ 0 & 0 & 0 & 0 & 0 & 0 & 1 & 0 & 1 & 0 & 0 & 0 & 0 & 0 \\ 0 & 0 & 0 & 0 & 1 & 0 & 1 & 0 & 0 & 0 & 1 & 0 & 1 & 0 \\ 0 & 1 & 0 & 0 & 2 & 0 & 2 & 0 & 0 & 0 & 0 & 1 & 2 & 0 \\ 0 & 0 & 0 & 0 & 0 & 0 & 0 & 1 & 0 & 0 & 0 & 0 & 0 & 1 \\ 1 & 1 & 1 & 0 & 0 & 0 & 0 & 1 & 0 & 0 & 0 & 0 & 0 & 0 \\ 1 & 1 & 0 & 1 & 0 & 0 & 0 & 1 & 0 & 0 & 0 & 0 & 0 & 0 \\ 1 & 0 & 0 & 0 & 0 & 0 & 1 & 1 & 0 & 1 & 2 & 0 & 0 & 0 \\ 1 & 1 & 0 & 0 & 0 & 0 & 1 & 1 & 0 & 1 & 0 & 1 & 0 & 0 \end{bmatrix} \begin{matrix} E_1 \\ E_2 \\ E_3 \\ E_4 \\ E_5 \\ E_6 \\ E_7 \\ E_8 \\ E_9 \end{matrix} \quad (3)$$

where rows of matrices  $\mathbf{S}$  and  $\mathbf{K}$  correspond to the following intermediate species: PdI<sub>2</sub>, Pd, HI, I<sub>2</sub>, IPdR, PEGA respectively.

By analyzing diagonal minors of matrix  $\mathbf{V}(\mathbf{j})$  we have detected that there are 40 negative ones. Smallest negative minor is of dimension  $1 \times 1$  and corresponds to the intermediate species HI. The expression for this minor is:

$$\beta_3(\mathbf{j}) = j_1 + j_3 + 4j_4 - 2j_8 \quad (4)$$

This suggests that source of instabilities in the model is autocatalysis of HI. Appearance of negative minor of dimension  $1 \times 1$ , which was not detected when model was analyzed under batch conditions, shows great impact that inflows and outflows of intermediate species can have on the stability of this system. Furthermore, by calculating two largest Hurwitz determinants  $\Delta_5$  and  $\Delta_6$  we found that both of them have negative terms which suggest that model can exhibit Andronov-Hopf and saddle-node bifurcations. Obtained results will facilitate further optimization of the model.

## CONCLUSION

Model of palladium-catalysed oscillatory carbonylation of PEGA in a continuous flow stirred tank reactor was analyzed by using SNA. It was found that autocatalysis of intermediate species HI is the source of instabilities in considered model. It was also determined that model can exhibit Andronov-Hopf and saddle-node bifurcation.

## Acknowledgement

This work was supported by the Ministry of Education, Science and Technological Development of the Republic of Serbia (Grants no. 172015 and 45001) and UK Engineering and Physical Sciences Research Council (EPSRC) grant number EP/N033655/1.

## REFERENCES

- [1] A. Isakova, B. J. Murdoch, K. Novakovic, *Phys. Chem. Chem. Phys.* **2018**, 20, 9281–9288.
- [2] A. Isakova, K. Novakovic, *J. Mater. Chem. B.* **2018**. DOI: 10.1039/C8TB00781K.
- [3] B. L. Clarke, *Cell Biochem. Biophys.* **1988**, 12 (1), 237–253.
- [4] L. Donlon, K. Novakovic, *Chem. Commun. Camb. Engl.* **2014**, 50 (98), 15506–15508.
- [5] S. Maćešić, Ž. Čupić, L. Kolar-Anić, *Hem. Ind.* **2012**, 66 (5), 637–647.
- [6] S. Maćešić, Ž. Čupić, S. Anić, L. Kolar-Anić, *Int. J. Non-Linear Mech.* **2015**, 73, 25–30.
- [7] S. Maćešić, Ž. Čupić, L. Kolar-Anić, *React. Kinet. Mech. Catal.* **2016**, 118 (1), 39–55.

## CONSTRUCTION OF PERIODIC SOLUTION IN THE MODEL OF BRAY-LIEBHAFSKY OSCILLATORY REACTION

S. Maćešić

*University of Belgrade, Faculty of Physical Chemistry, Studentski trg 12-16,  
11000 Belgrade, Serbia, e-mail: [stevan.macesic@ffh.bg.ac.rs](mailto:stevan.macesic@ffh.bg.ac.rs)*

### ABSTRACT

In this paper multi-shooting technique was used to construct periodic solutions of Bray-Liebhafsky oscillatory reaction. The aim was to investigate effects of the initial concentration of hydrogen peroxide  $[H_2O_2]_0$  on the oscillatory dynamics of the considered model. It was determined that  $[H_2O_2]_0$  affects oscillatory dynamics in complex manner, which can be observed from amplitudes and periods of oscillations.

### INTRODUCTION

Oscillatory chemical reactions are complex chemical systems capable to display diverse dynamics such as monotonous dynamics, simple oscillations, mixed-mode oscillation, chaos etc. Regarding the fact that oscillatory behavior is defining feature of these systems, analysis of periodic solutions is the crucial part of the modeling processes. This can be done by performing numerous numerical simulations but much efficient way is to construct periodic solutions of the considered models by using some of existing methods such as finite difference method, shooting and multi-shooting methods or orthogonal collocation method.[1,2] Although effects of the initial concentration of hydrogen peroxide  $[H_2O_2]_0$  on the dynamics of the variant of Bray-Liebhafsky reaction model were investigated[3], methods for construction of periodic solutions haven't been used. Thus in this paper we applied multi-shooting technique to construct periodic solutions in the model of well-known Bray-Liebhafsky reaction.[4,5]

### MODEL

The model of Bray-Liebhafsky reaction M(1-6, 8)[4,5] consists of seven chemical reactions among which three are reversible. There are ten chemical species in the model:  $H_2O_2$ ,  $O_2$ ,  $H^+$ ,  $IO_3^-$ ,  $\Gamma$ ,  $HIO$ ,  $HIO_2$ ,  $I_2$ ,  $I_2O$  and  $H_2O$ . Intermediate species which govern dynamics of the model are ( $\Gamma$ ,  $HIO$ ,  $HIO_2$ ,  $I_2$ ,  $I_2O$ ) while concentrations of  $H^+$  and  $IO_3^-$  are much higher than concentrations of other intermediate species and therefore they are considered

to be constant and their concentrations are incorporated into the values of the appropriate rate constants. Chemical species  $O_2$  and  $H_2O$  are products and therefore they do not affect model dynamics. On the other hand  $H_2O_2$  is reactant which can be considered as a reservoir and whose concentration can also be considered constant. Therefore, dynamics of the model M(1-6, 8) can be obtained by solving following set of differential equations:

$$\begin{aligned} d[I^-] / dt = & -k_1[I^-] + k_{-1}[HIO][HIO_2] - k_2[I^-][HIO_2] \\ & -k_4[I^-][HIO] + k_{-4}[I_2] + k_5[HIO][H_2O_2]_0 \end{aligned} \quad (2)$$

$$\begin{aligned} d[HIO] / dt = & k_1[I^-] - k_{-1}[HIO][HIO_2] + 2k_3[I_2O] - 2k_{-3}[HIO]^2 \\ & -k_4[I^-][HIO] + k_{-4}[I_2] - k_5[HIO][H_2O_2]_0 + k_6[I_2O][H_2O_2]_0 \end{aligned} \quad (3)$$

$$\begin{aligned} d[HIO_2] / dt = & k_1[I^-] - k_{-1}[HIO][HIO_2] - k_2[I^-][HIO_2] \\ & +k_6[I_2O][H_2O_2]_0 + k_8[H_2O_2]_0 \end{aligned} \quad (4)$$

$$d[I_2O] / dt = k_2[I^-][HIO_2] - k_3[I_2O] + k_{-3}[HIO]^2 - k_6[I_2O][H_2O_2]_0 \quad (5)$$

$$d[I_2] / dt = k_4[I^-][HIO] - k_{-4}[I_2] \quad (6)$$

$$k_1 = 1.375 \times 10^2 \text{ min}^{-1} \quad k_{-1} = 7.91 \times 10^7 \text{ M}^{-1} \text{ min}^{-1} \quad k_2 = 4.79 \times 10^{10} \text{ M}^{-1} \text{ min}^{-1}$$

$$k_3 = 5 \times 10^3 \text{ min}^{-1} \quad k_{-3} = 3.15 \times 10^8 \text{ M}^{-1} \text{ min}^{-1} \quad k_4 = 3 \times 10^{11} \text{ M}^{-1} \text{ min}^{-1}$$

$$k_{-4} = 46.97 \text{ min}^{-1} \quad k_5 = 1.487 \times 10^4 \text{ M}^{-1} \text{ min}^{-1} \quad k_6 = 5 \times 10^5 \text{ M}^{-1} \text{ min}^{-1}$$

$$k_8 = 2.2303 \times 10^{-4} \text{ min}^{-1} \quad [H^+] = 9.58 \times 10^{-2} \text{ M} \quad [IO_3^-] = 4.74 \times 10^{-2} \text{ M}$$

## METHODS

Multi-shooting technique is based on converting initial value problem

$$dx / dt = f(x; k) \quad (7)$$

into a two point boundary-value problem ( $x \in R^n$  and  $k \in R^m$ ) and finding solution  $x(t)$  with minimal period  $T$  such that  $x(T) = x(0)$ . [1,2] To facilitate integration independent variable  $t$  is transformed into  $\tau$  using relation  $t = T \times \tau$ , where  $\tau$  goes from 0 to 1 (when  $\tau = 1$  then  $t = T$ ). Now equation (6) becomes

$$dx / d\tau = Tf(x; k) \quad (8)$$

In multiple shooting methods  $\tau$  is partitioned into following grid points

$$0 = \tau_0 < \tau_1 < \tau_2 < \dots < \tau_N = 1 \quad (9)$$

Let denote  $\Delta_i = \tau_{i+1} - \tau_i$  and let  $x^i = x(\tau_i)$  be the unknown solution values at the mesh points and  $\Phi^{\Delta_i}(x^i)$  be solution of equation (7) on interval  $\Delta_i$  and initial condition  $x^i$ , where  $i = 1, 2, \dots, N-1$ . Then, finding unknown  $x^i$  and period  $T$  is done by solving following set of nonlinear equations[1]

$$\Phi^{\Delta_0}(x_0) - x_1 = 0 \quad (10)$$

$$\Phi^{\Delta_1}(x_1) - x_2 = 0 \quad (11)$$

$$\vdots \quad (12)$$

$$\Phi^{\Delta_{N-1}}(x_{N-1}) - x_0 = 0 \quad (13)$$

$$\int_0^1 x^{tr}(\tau) x_{old}(\tau) d\tau = 0 \quad (14)$$

where  $^{tr}$  stands for transpose while  $x_{old}(\tau)$  represents derivatives of previous solution over  $\tau$ . For solving equations (9-13) *Broyden's method* was used.

## RESULTS AND DISCUSSION

In this paper multi-shooting technique was applied for the first time to the model M(1-6, 8) with aim to construct its periodic solutions. Main goal was to investigate effects which initial concentration of hydrogen peroxide  $[H_2O_2]_0$  has on oscillatory dynamics of the considered model. The value  $[H_2O_2]_0$  was varied from  $2.92 \times 10^{-3}$  M to  $5.79 \times 10^{-2}$  M. Both values are in vicinity of Andronov-Hopf bifurcation where transition of the stable steady state to unstable one (in vicinity of  $[H_2O_2]_0 = 2.92 \times 10^{-3}$  M) and *vice versa* (in vicinity of  $[H_2O_2]_0 = 5.79 \times 10^{-2}$  M) occur. For each tested value of  $[H_2O_2]_0$  periodic solutions were successfully calculated together with the values of period  $T$ . Bifurcation diagrams are presented on Figure 1.

As can be seen from Figure 1, effects of  $[H_2O_2]_0$  on the oscillatory dynamics of the model M(1-6, 8) are quite complex. Starting from  $[H_2O_2]_0 = 2.92 \times 10^{-3}$  M, both the amplitudes and period gradually increase with increase of  $[H_2O_2]_0$  until reaching their maximum values after which they start to gradually decrease. It was determined that maximum of amplitudes of oscillations was observed at  $[H_2O_2]_0 = 2.9927 \times 10^{-2}$  M while maximum period was detected at  $[H_2O_2]_0 = 1.1661 \times 10^{-2}$  M. After reaching their maximum, amplitudes and period of oscillations start to gradually decrease until the value of  $[H_2O_2]_0 = 5.79 \times 10^{-2}$  M after which system undergo Andronov-Hopf bifurcation and oscillations disappear.

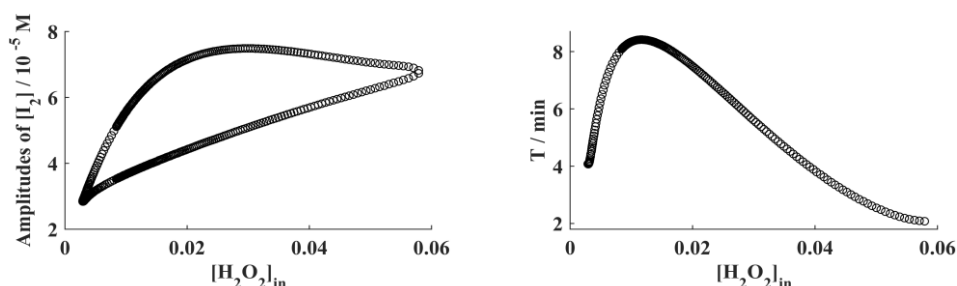


**Figure 1.** a) Minimums and maximums of the oscillations of  $[I_2]$  as a function of  $[H_2O_2]_0$  b) Period of oscillations as a function of  $[H_2O_2]_0$

## CONCLUSION

Multi-shooting technique was successfully applied to the construction of the periodic solutions of the model of Bray-Libehafsky reaction. It was found that initial concentration of hydrogen peroxide  $[H_2O_2]_0$  strongly affects oscillatory dynamics of considered model. Both amplitudes and period of oscillations show gradual increase with the increasing value of  $[H_2O_2]_0$  until they reach their maximums after which they start to decrease. Maximums of the period and amplitudes of oscillation were detected at different values of  $[H_2O_2]_0$

## Acknowledgement

This work was supported by the Ministry of Education, Science and Technological Development of the Republic of Serbia (Grant no. 172015).

## REFERENCES

- [1] Y. A. Kuznetsov, Elements of Applied Bifurcation Theory, Springer-Verlag, New York **1995**.
- [2] A. H. Nayfeh, B. Balachandran, Applied Nonlinear Dynamics: Analytical, Computational, and Experimental Methods, John Wiley & Sons **2008**.
- [3] S. Maćešić, Ž. Čupić, Lj. Kolar-Anić, React. Kinet. Mech. Catal. **2016**, 118 (1), 39–55.
- [4] Lj. Kolar-Anić, D. Misljenović, S. Anić, G. Nicolis, React. Kinet. Catal. Lett. **1995**, 54 (1), 35–41.
- [5] Lj. Kolar-Anić, Ž. Čupić, G. Schmitz, S. Anić, Chem. Eng. Sci. **2010**, 65 (12), 3718–3728.

## OPTIMIZATION OF THE MODEL OF BRAY-LIEBHAFSKY REACTION USING STEADY-STATE CONCENTRATIONS AS PARAMETERS

S. Maćešić

*University of Belgrade, Faculty of Physical Chemistry, Studentski trg 12-16, 11000 Belgrade, Serbia, e-mail: [stevan.macesic@ffh.bg.ac.rs](mailto:stevan.macesic@ffh.bg.ac.rs)*

### ABSTRACT

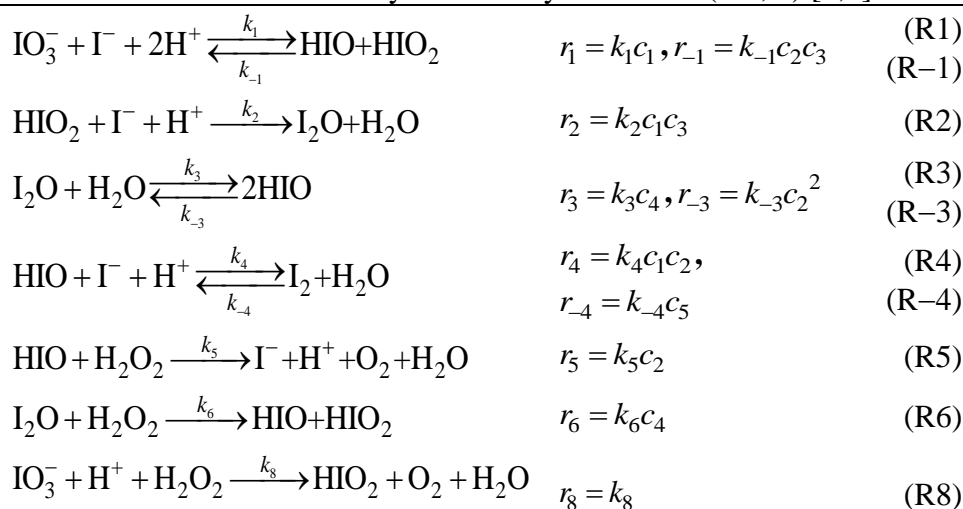
Model of Bray-Liebhafsky reaction was analyzed using stoichiometric network analysis (SNA) with aim to determine optimal steady-state concentrations of the intermediate species to obtain its oscillatory dynamics. Dependence of Andronov-Hopf bifurcation on steady-state concentrations of intermediate species HIO and I<sub>2</sub>O was successfully obtained.

### INTRODUCTION

Oscillatory chemical reactions are complex nonlinear systems well-known for their complex dynamics and equally complex mathematical models. Essential tool in validation and optimization of these models is stability analysis. Stability analysis is usually done by evaluating effects of reaction rate constants on system stability which, depending on the model structure, can affect several or even all concentrations of chemical species present in the model. This can be serious problem when the goal is to obtain certain dynamics in specified concentration range. Solution to stability problem offer *Stoichiometric Network Analysis* (SNA).[1] Thus, in this paper we apply SNA to the model of well-known Bray-Liebhafsky reaction [2] with aim to determine dependence of the Andronov-Hopf bifurcation on the reciprocal steady-state concentrations of HIO and I<sub>2</sub>O.

### MODEL

Model of BL oscillatory reaction, a complex chemical process in which hydrogen peroxide decomposes in the presence of both iodate and hydrogen ions, is given in Table 1. Model M(1-6, 8)[3,4] consists of seven reactions among which three are reverse. There are five intermediates species I<sup>-</sup>, HIO, HIO<sub>2</sub>, I<sub>2</sub>, I<sub>2</sub>O (whose concentrations are denoted by  $c_1$ - $c_5$  respectively in expressions for reaction rates in Table 1) essential for the dynamics, and three external species H<sub>2</sub>O<sub>2</sub>, O<sub>2</sub> and H<sub>2</sub>O whose concentration, together with the concentration of H<sup>+</sup> and IO<sub>3</sub><sup>-</sup>, can be considered constant due to much slower temporal evolution and therefore incorporated in the values of rate constants.

**Table 1.** Model of Bray-Leibhafsky reaction M(1-6, 8) [3,4]

### STOICHIOMETRIC NETWORK ANALYSIS

In SNA the reactions rates at steady-state are given as positive linear combination of new parameters current rates  $j_i$  by using relation  $\mathbf{r}_{ss} = \mathbf{E}\mathbf{j}$ , where  $\mathbf{E}$  is matrix of extreme currents and  $\mathbf{j}$  is vector of current rates. Matrix  $\mathbf{E}$ , whose elements are nonnegative numbers and whose each column represents one possible reaction route, is calculated by solving steady-state equation  $\mathbf{S}\mathbf{r}_{ss} = 0$ , where  $\mathbf{S}$  is stoichiometric matrix consisting of only independent intermediate species. By using new set of parameters  $\mathbf{j}$ , kinetic equations can be written as  $\mathbf{dx}/dt = \text{diag}(\mathbf{h})\mathbf{S}\text{diag}(\mathbf{E}\mathbf{j})\mathbf{x}^{\mathbf{K}}$ , where  $x_i = c_i / c_{i,ss}$  ( $c_{i,ss}$  is steady-state concentration of intermediate species  $i$ ,  $i=1,2,\dots,5$ ),  $h_i = 1 / c_{i,ss}$  represents reciprocal steady-state concentration of species  $i$  while  $\mathbf{K}$  is a matrix of the order of reactions.

Steady state stability evaluation and bifurcation points detection, particularly Andronov-Hopf bifurcation, can be done by analyzing eigenvalues of the Jacobian, although other criteria were also successfully used.[5,6] In SNA notation, Jacobian can be written as  $\mathbf{M}(\mathbf{j}, \mathbf{h}) = \text{diag}(\mathbf{h})\mathbf{S}\text{diag}(\mathbf{E}\mathbf{j})\mathbf{K}^T$ . Usage of parameters  $\mathbf{j}$  and  $\mathbf{h}$  in stability analysis of the steady states allows efficient model optimization in desired concentration range. Matrices  $\mathbf{S}$ ,  $\mathbf{K}$  and  $\mathbf{E}$  for considered model are:

$$\mathbf{S} = \begin{matrix} & R_1 & R_{-1} & R_2 & R_3 & R_{-3} & R_4 & R_{-4} & R_5 & R_6 & R_8 \\ \begin{bmatrix} -1 & 1 & -1 & 0 & 0 & -1 & 1 & 1 & 0 & 0 \\ 1 & -1 & 0 & 2 & -2 & -1 & 1 & -1 & 1 & 0 \\ 1 & -1 & -1 & 0 & 0 & 0 & 0 & 0 & 1 & 1 \\ 0 & 0 & 1 & -1 & 1 & 0 & 0 & 0 & -1 & 0 \\ 0 & 0 & 0 & 0 & 0 & 1 & -1 & 0 & 0 & 0 \end{bmatrix} & \begin{matrix} c_1 \\ c_2 \\ c_3 \\ c_4 \\ c_5 \end{matrix} \end{matrix} \quad (15)$$

$$\mathbf{K} = \begin{matrix} & R_1 & R_{-1} & R_2 & R_3 & R_{-3} & R_4 & R_{-4} & R_5 & R_6 & R_8 \\ \begin{bmatrix} 1 & 0 & 1 & 0 & 0 & 1 & 0 & 0 & 0 & 0 \\ 0 & 1 & 0 & 0 & 2 & 1 & 0 & 1 & 0 & 0 \\ 0 & 1 & 1 & 0 & 0 & 0 & 0 & 0 & 0 & 0 \\ 0 & 0 & 0 & 1 & 0 & 0 & 0 & 0 & 1 & 0 \\ 0 & 0 & 0 & 0 & 0 & 0 & 1 & 0 & 0 & 0 \end{bmatrix} & \begin{matrix} c_1 \\ c_2 \\ c_3 \\ c_4 \\ c_5 \end{matrix} \end{matrix} \quad (16)$$

$$\mathbf{E}^T = \begin{matrix} & R_1 & R_{-1} & R_2 & R_3 & R_{-3} & R_4 & R_{-4} & R_5 & R_6 & R_8 \\ \begin{bmatrix} 1 & 1 & 0 & 0 & 0 & 0 & 0 & 0 & 0 & 0 \\ 0 & 0 & 0 & 1 & 1 & 0 & 0 & 0 & 0 & 0 \\ 0 & 0 & 0 & 0 & 0 & 1 & 1 & 0 & 0 & 0 \\ 0 & 0 & 1 & 0 & 0 & 0 & 0 & 1 & 1 & 0 \\ 0 & 1 & 1 & 0 & 0 & 0 & 0 & 0 & 1 & 1 \end{bmatrix} & \begin{matrix} E_1 \\ E_2 \\ E_3 \\ E_4 \\ E_5 \end{matrix} \end{matrix} \quad (17)$$

## RESULTS

It was found that Andronov-Hopf bifurcation, and therefore oscillatory dynamics (Figure 1a), emerge at  $\mathbf{j} = (1.1894 \times 10^{-4}, 3.2540 \times 10^{-3}, 3.2540 \times 10^{-3}, 3.2540 \times 10^{-3}, 1.1894 \times 10^{-4}) \text{ M s}^{-1}$  and  $\mathbf{h} = (5.1672 \times 10^7, 1.8943 \times 10^6, 3.1384 \times 10^6, 4.9737 \times 10^7, 1.9505 \times 10^4) \text{ M}^{-1}$ , and therefore this was initial point in analysis. To determine how Andronov-Hopf bifurcation depends on the values of  $h_2$  and  $h_4$ , we varied the values of  $h_2$  in range from  $1.8943 \times 10^6 \text{ M}^{-1}$  to  $1 \times 10^7 \text{ M}^{-1}$  and then calculated the value of  $h_4$  for which Andronov-Hopf bifurcation reemerge while keeping the values of all other parameters constant. In this way bifurcation diagram presented on Figure 1b was obtained. Area below the solid line represents stable steady states while area above represents unstable steady states. As can be seen from Figure 1b,  $h_4$  initially decreases very fast with increase of  $h_2$  until the plateau is reached after which the change in  $h_4$  becomes minimal with the increase of  $h_2$ .

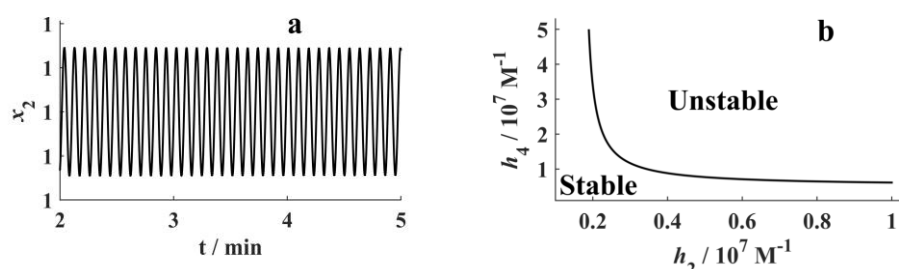


**Figure 1.** a) Numerical simulations of BL model in vicinity of Andronov-Hopf bifurcation; b) Bifurcation diagram which represent dependence of Andronov-Hopf bifurcation as function of the reciprocal steady-state concentration of HIO ( $h_2$ ) and I<sub>2</sub>O ( $h_4$ );  $M = \text{mol dm}^{-3}$

## CONCLUSION

Model of Bray-Liebafsky reaction was analyzed by using stoichiometric network analysis. It was shown that current rates  $j$  and reciprocal steady state concentrations  $h$  can be successfully used in finding location and tracing Andronov-Hopf bifurcation. Dependence of Andronov-Hopf bifurcation on the reciprocal steady-state concentrations of HIO and I<sub>2</sub>O was obtained which will facilitate further optimization of considered model.

## Acknowledgement

This work was supported by the Ministry of Education, Science and Technological Development of the Republic of Serbia (Grant no. 172015).

## REFERENCES

- [1] B. L. Clarke, *Cell Biochem. Biophys.* **1988**, *12* (1), 237–253.
- [2] W. C. Bray, *J. Am. Chem. Soc.* **1921**, *43* (6), 1262–1267.
- [3] Lj. Kolar-Anić, D. Misljenović, S. Anić, G. Nicolis, *React. Kinet. Catal. Lett.* **1995**, *54* (1), 35–41.
- [4] Lj. Kolar-Anić, Ž. Čupić, G. Schmitz, S. Anić, *Chem. Eng. Sci.* **2010**, *65* (12), 3718–3728.
- [5] S. R. Maćešić, Ž. D. Čupić, S. M. Blagojević, N. D. Pejić, S. R. Anić, Lj. Z. Kolar-Anić, *Open Chem. Cent. Eur. J. Chem.* **2015**, *13* (1), 591–599.
- [6] S. Maćešić, Ž. Čupić, Lj. Kolar-Anić, *React. Kinet. Mech. Catal.* **2016**, *118* (1), 39–55.

## ***E – Electrochemistry***



## AN ELECTROANALYTICAL DPV/BDDE METHOD FOR BRIMONIDINE DETERMINATION IN AQUEOUS HUMOR, SHORT- AND LONG-TERM STABILITY

V. Radulović<sup>1</sup>, M. Aleksić<sup>2</sup>, V. Kapetanović<sup>1</sup>, K. Karljiković-Rajić<sup>1</sup> and M. Jovanović<sup>3</sup>

*University of Belgrade, <sup>1</sup>Department of Analytical Chemistry, <sup>2</sup>Department of Physical Chemistry and Instrumental Methods, Faculty of Pharmacy, Vojvode Stepe 450, 11000 Belgrade, Serbia.*

*(valentina.radulovic@pharmacy.bg.ac.rs)*

*<sup>3</sup>University of Belgrade, Department of Ophthalmology, Faculty of Medicine, Dr Subotica 8, 11000 Belgrade, Serbia.*

### ABSTRACT

The differential pulse voltammetry (DPV) using boron doped diamond electrode (BDDE) was proposed for brimonidine determination in aqueous humor, based on oxidation peak. Linearity range was obtained within  $5.0 \times 10^{-6}$ - $5.0 \times 10^{-5}$  M of brimonidine. Limits of detection (LOD) and quantitation (LOQ) were  $1.94 \times 10^{-6}$  M and  $6.46 \times 10^{-6}$  M, respectively. Intra- and inter-day precision and accuracy were checked according to ICH regulations. The short-term stability study resulted in deviation of 1.86% for concentration of  $3.0 \times 10^{-5}$  M. Long-term stability study resulted in deviations of 1.63% and 3.56%, for  $3.0 \times 10^{-5}$  M and  $5.0 \times 10^{-5}$  M, respectively. Freeze/thaw stability study emphasized that sample may be frozen/thawed only once. The proposed method is marked with: simplicity of sample preparation, minimal consumption of organic solvent, short-time performance, good specificity and accuracy.

### INTRODUCTION

Brimonidine (BRIM; 5-Bromo-N-(4,5-dihydro-1H-imidazol-2-yl)-6-quinoxalinamine) is selective  $\alpha_2$ -adrenergic agonist for local use in therapy of glaucoma - progressive optical neuropathy. BRIM action is based on lowering production and stimulating outflow of aqueous humor from the eye. Different components of aqueous humor are: amino acids, proteins, organic/inorganic ions, carbohydrates, urea, glutathione, ascorbate, oxygen, carbon dioxide [1].

Brimonidine tartrate monograph is official in European Pharmacopoeia 9<sup>th</sup> [2]. BRIM concentration is significantly higher in aqueous humor than in vitreous body after topical application. Penetration of BRIM is enough for

neuroprotection in the eye. High Performance Liquid Chromatography–tandem Mass Spectrometry (HPLC-MS/MS) was employed for determination of BRIM in aqueous humor confirming direct relationship to the concentration of topically applied eye drops (0.1%, 0.15%) [3].

The aim of this work was development of electroanalytical method for BRIM determination in aqueous humor with simple sample preparation.

## EXPERIMENTAL

Potentiostat/galvanostat  $\mu$ AUTOLAB (Ecochemie, Utrecht, Netherlands) and interface IME 663 (Metrohm, Herisau, Switzerland), supported by GPES 4.9 program, were used. Working electrode was BDDE (Windsor Scientific Ltd.,  $d = 3$  mm), counter electrode was Pt and Ag|AgCl|3M KCl (Metrohm, Herisau, Switzerland) was a reference one. Combined electrode GK2401 (Radiometer, Copenhagen, Denmark) and pH meter (Radiometer PHM 220) were used for pH control of buffer solutions. Centrifuge (Hettich EBA 8S, Germany) was applied in sample preparation.

Chemicals were provided: brimonidine tartrate (Sigma-Aldrich, Germany); sodium dihydrogenphosphate monohydrate, disodium monohydrogenphosphate heptahydrate, boric and glacial acetic acid 100% (Merck, Germany); phosphoric acid 85% (Honeywell Speciality Chemicals Sellze, Germany); sodium hydroxide (Carlo Erba, Italy), methanol p.a. (Centrohem, Serbia), sulfuric acid (Fisher Chemicals, Great Britain). In all experiments bidistilled water was used.

Peak current *versus* pH was studied by DPV under the conditions: pulse amplitude 50 mV, pulse width 50 ms, scan rate 50 mV s<sup>-1</sup>, Britton-Robinson buffer (BR, pH 5.0–10.0) and 5.0×10<sup>-5</sup> M BRIM in cell. Optimal parameters were selected: supporting electrolyte NaH<sub>2</sub>PO<sub>4</sub>/Na<sub>2</sub>HPO<sub>4</sub>, pH 8.0; and previously quoted instrumental parameters. All experiments were done at room temperature (25 °C).

Manually polishing of BDDE with aqueous slurry of Al<sub>2</sub>O<sub>3</sub> (0.05  $\mu$ m) was done once at the beginning of working day. Electrochemical pre-treatment of BDDE was performed at potential of +1.2 V in 0.25 M H<sub>2</sub>SO<sub>4</sub> during 60 s, before each measurement. Solution, placed in electrochemical cell, was purged by N<sub>2</sub> for 15 minutes.

Unique pool of collected humane aqueous humor samples was thawed, poured into a tube and mixed with methanol, centrifuged and supernatant was filtered through a membrane filter (0.20  $\mu$ m).

## RESULTS AND DISCUSSION

Study of the current anodic peak intensity *versus* pH was performed by applying DPV and BDDE in universal BR buffer (pH 5.0-10.0). At pH  $\geq$

8.0, the higher intensities of more defined peak were observed and a linear dependence was expressed:  $E_p/V = 1.321 - 0.047 \times pH$  ( $R=0.991$ ). In accordance with physiological pH (7.2-7.4) and components of aqueous humor, determination of BRIM in aqueous humor was based on anodic peak at peak potential +0.95 V in phosphate buffer ( $\text{NaH}_2\text{PO}_4/\text{Na}_2\text{HPO}_4$ , pH 8.0).

The appropriate linear relationship between the current intensity and BRIM concentration was expressed by the equation:  $I_p = -0.388 + 0.854 \times 10^6 C$  ( $I_p/10^{-8}$  A,  $C/M$ ) ( $R=0.9924$ ), in the range  $5.0 \times 10^{-6}$ – $5.0 \times 10^{-5}$  M (Fig. 1.) Calculated from the calibration curve, LOD and LOQ were  $1.94 \times 10^{-6}$  M and  $6.46 \times 10^{-6}$  M, respectively. Precision and accuracy (Table 1.) showed the lowest *intra-day* precision for the lowest concentration ( $RSD=6.68\%$ ). *Inter-day* precision was checked during three consecutive days and all RSD values were within  $\pm 15\%$  recommended by ICH.

Deviations (%), calculated [4] by the equation:  $100 \times (C_x - C_0) / C_0$ , where  $C_x$  represented post storage concentration and  $C_0$  represented initial concentration, both measured in triplicate, expressed results of *short-term stability* study, using sample solution after recording voltammograms. The highest deviation was noticed for the lowest concentration and the lower deviations, 1.86 % and 6.18 %, were obtained for the higher concentrations ( $3.0 \times 10^{-5}$  M,  $5.0 \times 10^{-5}$  M). For examination of *long-term stability*, samples were kept frozen for 2 months, thawed and analysed. The obtained low values of deviations, 1.63% and 3.56%, indicated very slight changes of the sample solutions for the both examined concentrations,  $3.0 \times 10^{-5}$  M and  $5.0 \times 10^{-5}$  M. *Freeze and thaw stability study* was performed in three

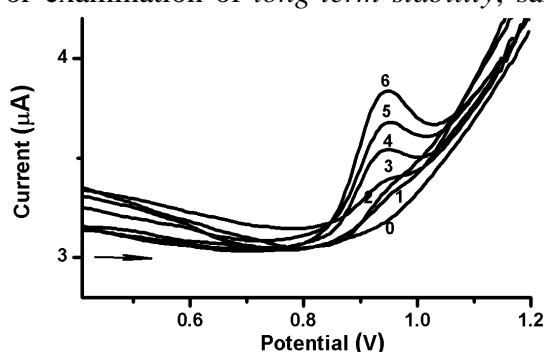


**Figure 1.** DP voltammograms of BRIM anodic peak: (1-6)  $5.0 \times 10^{-6}$  -  $5.0 \times 10^{-5}$  M in (0) aqueous humor pool blank (phosphate buffer pH 8.0).

cycles. Only after the first cycle for both examined concentrations of BRIM, the obtained recovery values (106.00% and 95.34%) were in accordance with ICH recommendations ( $\pm 15\%$ ). The results for the second and the third cycle exceeded regulations.

**Table 1.** Precision and accuracy results of proposed method for BRIM determination in aqueous humor.

Analyte	Method/ electrode	Amount added (M)	Amount found (M)	Precision RSD (%)	Recovery (%)	
<i>Intra-day</i>						
BRIM	DPV/	$1.50 \times 10^{-5}$	$1.42 \times 10^{-5}$	6.68	94.73	
		$3.00 \times 10^{-5}$	$3.18 \times 10^{-5}$	4.07	106.20	
		$5.00 \times 10^{-5}$	$4.36 \times 10^{-5}$	5.38	87.40	
	BDDE	<i>Inter-day</i>				
		$1.50 \times 10^{-5}$	$1.61 \times 10^{-5}$	8.65	107.33	
		$3.00 \times 10^{-5}$	$3.30 \times 10^{-5}$	11.83	110.00	
		$5.00 \times 10^{-5}$	$4.71 \times 10^{-5}$	10.09	94.12	

**CONCLUSION**

The proposed DPV/BDDE method for BRIM determination in aqueous humor showed good specificity with: minimal preparation of the sample, simplicity, time-effectiveness and satisfactory accuracy. The BDDE usage makes this method simple because no additional modification of electrode is needed, thus no electrode inactivation appears with time. Short-term stability study detected BRIM changes at the lowest examined concentration. Long-term stability study indicated sample solutions stability keeping frozen for two months, but the only once frozen and thawed sample kept enough stability.

**Acknowledgement**

This work was supported by the Project of the Ministry of Education, Science and Technological Development of the Republic of Serbia, No. 172033.

**REFERENCES**

- [1] M. Goel, R.G. Picciani, R.K. Lee, S.K. Bhattacharya, *The Open Ophthalmology Journal*, 2010, 4, 52-59.
- [2] European pharmacopoeia 9th ed., European Directorate for the Quality of Medicines (EDQM), Council of Europe, Strasbourg, France, 2017.
- [3] L.B. Cantor, D. WuDunn, Y. Catoira-Boyle, C.W. Yung, *J. Glaucoma*, 2008, 17, 529-534.
- [4] F.M. Kocak, O.O. Isiklar, A. Meral, *Biochem. Med. (Zagreb)*, 2015, 25, 57-63.

## THE RE-SYNTHESIS OF A CATHODE MATERIAL FROM SPENT LI-ION BATTERIES AND ITS EVALUATION IN AN AQUEOUS $\text{LiNO}_3$ SOLUTION

J. Senćanski<sup>1</sup>, M. Vujković<sup>2</sup>, D. Bajuk Bogdanović<sup>2</sup>, I. Stojković Simatović<sup>2</sup>, S. Uskoković-Marković<sup>3</sup> and S. Mentus<sup>2,4</sup>

<sup>1</sup>*University of Belgrade, Institute of General and Physical Chemistry, Studentski trg 12-15, 11000 Belgrade, Serbia. (jsencanski@iofh.bg.ac.rs)*

<sup>2</sup>*University of Belgrade, Faculty of Physical Chemistry, Studentski trg 12-15, 11000 Belgrade, Serbia.*

<sup>3</sup>*University of Belgrade, Faculty of Pharmacy, Vojvode Stepe 450, 11221 Belgrade, Serbia.*

<sup>4</sup>*Serbian Academy of Sciences and Arts, Knez Mihajlova 35, 11000 Belgrade, Serbia.*

### ABSTRACT

The recycling of Li-ion batteries is the subject of attention of many researchers, due to their rising impact on the environment. The study we report here demonstrates a solid state route of direct regeneration of the  $\text{Li}(\text{Co-Mn-Ni})\text{O}_2$  cathodic material from the spent Li-ion batteries. The chemical composition of the re-synthesized material was determined by Atomic Absorption Spectroscopy, while its structure and morphology was characterized by X-ray diffraction (XRD), Raman spectroscopy and Scanning Electron Microscopy (SEM). The capability of the resynthesized material to intercalate lithium ions in an aqueous solution was evidenced and evaluated by means of Cyclic voltammetry.

### INTRODUCTION

The rising use of Li-ion batteries in many portable electronic devices such as mobile phones, laptops and electronic vehicles causes the increase of their waste. This kind of waste contains many metals such as Li, Co, Ni, Mn Al and Cu having a harmful impact on the environment. In order to keep the environment protected, a cheap method to regenerate the cathode material from spent Li-ion batteries would be desirable[1]. Due to the fact that organic solvent used in commercial batteries is flammable and toxic, numerous studies were also devoted to the development of aqueous rechargeable batteries [2]. Following these trends, in this paper we propose a way to re-synthesize the cathode material from spent Li-ion batteries by means of a solid state reaction. The electrochemical behavior of re-

synthesized cathode material was checked in an aqueous solution of lithium salt.

### EXPERIMENTAL

The regeneration (re-synthesis) of the cathode material from spent Li-ion batteries type BL-5C produced by 3G Company was performed in several steps. First, cathode material was separated by its mechanical separation from the Al housing and then from its Al current collector. In order to estimate chemical formula of the cathode material, 0.2045g of it, after annealing at 700°C, was dissolved in 250 ml HNO<sub>3</sub> and 5ml 30% H<sub>2</sub>O<sub>2</sub>. To satisfy the molar ratio Li:ΣM=1:1, 0.1234g Li<sub>2</sub>CO<sub>3</sub> was added to the spent cathode material. After grinding in a mortar, the solid mixture was annealed at 700 °C to obtain crystalline material. The chemical composition of the re-synthesized cathode material was determined by Flame Atomic Absorption Spectrometry (GBC Sensa AA Dual A). The structure analysis was performed by X-Ray diffractometer, Rigaku Ultima IV (CuKα, λ=1.54178Å) while the morphological analysis was performed by scanning electron microscopy Model JSM-6610LV. The functionality of recycled material was examined in 6M aqueous solution of LiNO<sub>3</sub> by Cyclic Voltammetry (CV) using Gamry PCI4/300 Potentiostat/Galvanostat with three electrode system. The Pt electrode was a counter electrode and the saturated calomel electrode was a reference electrode. The Li(Co-Mn-Ni)O<sub>2</sub> working electrode was prepared according to the procedure described in ref [3].

### RESULTS AND DISCUSSION

The chemical composition of the re-synthesized sample was found to be LiNi<sub>0.15</sub>Mn<sub>0.77</sub>Co<sub>0.08</sub>O<sub>2</sub>. This composition is similar to LiMn<sub>0.712</sub>Ni<sub>0.208</sub>Co<sub>0.08</sub>O<sub>2</sub> (0.5 Li<sub>2</sub>MnO<sub>3</sub>·0.5 LiMn<sub>0.42</sub>Ni<sub>0.42</sub>Co<sub>0.16</sub>O<sub>2</sub>) obtained in ref [4].

The structural characterization of the re-synthesized material was studied by XRD and Raman spectroscopy. Compared to the XRD database, the diffraction peaks of the obtained materials, as shown in **Fig 1 a**, evidence clearly that expected layered structure is obtained. The separations of the reflections (006)/(102) and (108)/110, which evidence a hexagonal ordered structure, are registered. Nevertheless, the high value of (I<sub>006</sub>+I<sub>102</sub>)/I<sub>101</sub>=1.67 suggests a quite low degree of structural order. The presence of the monoclinic LiMn<sub>2</sub>O<sub>3</sub> phase, whose peaks are positioned at 19 ° i 21 ° (2θ) [5] (**Fig 1 a**), is hard to recognize in the XRD noise. However, Raman spectrum clearly shows that the re-synthesized material is a composite containing monoclinic LiMn<sub>2</sub>O<sub>3</sub> [4]. The peaks positioned at

high frequencies  $600\text{ cm}^{-1}$ ,  $551\text{ cm}^{-1}$ ,  $478\text{ cm}^{-1}$ ,  $429\text{ cm}^{-1}$  originate from M-O ( $M=\text{Mn, Ni i Co}$ ) vibrations, since the peaks positioned at low frequencies  $408\text{ cm}^{-1}$  and  $372\text{ cm}^{-1}$  originate from Li-O vibrations (**Fig 1 b**). The two main peaks positioned at  $479$  and  $599\text{ cm}^{-1}$  are assigned as  $E_g$  and  $A_{1g}$  active Raman modes of M-O vibrations in a layered  $\text{Li}(\text{Co-Mn-Ni})\text{O}_2$  oxide which possesses rhombohedral R-3m space group. The peak positioned at  $552\text{ cm}^{-1}$  originates from Mn-O which has  $C_{2/m}$  symmetry. This phase is added to the cathode material in order to improve its Coulomb capacity [4].

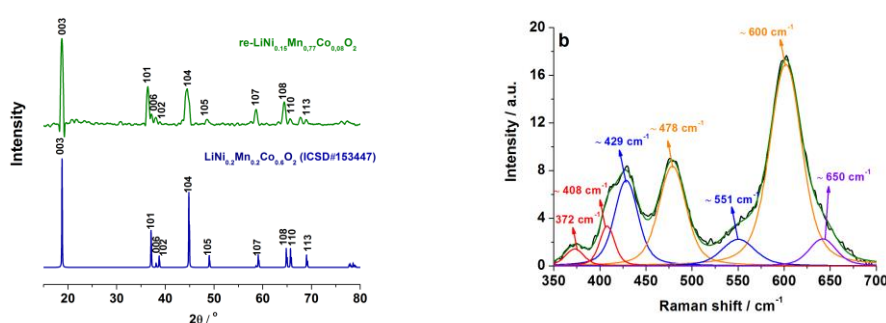


**Figure 1:** a) XRD and b) Raman spectrum of the re-synthesized material. SEM photograph (**Figure 2 a**) shows roughly uniform distribution of micrometric particles formed by solid state reaction in which mixing at molecular level is hardly achievable.

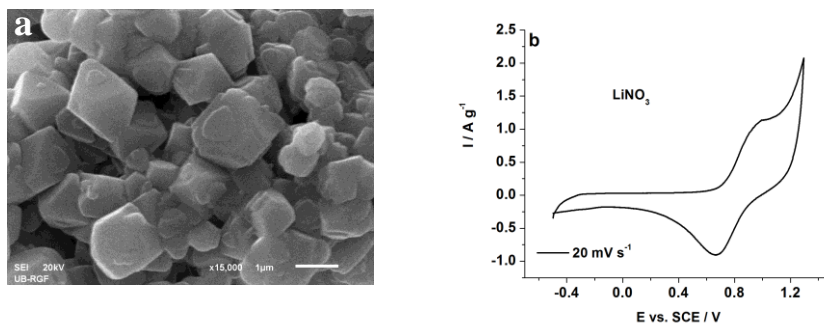


**Figure 2:** a) SEM photograph and b) CV of the re-synthesized cathode material in an aqueous  $\text{LiNO}_3$  solution

To examine the charge storage behavior of the re-synthesized cathode material in an aqueous  $\text{LiNO}_3$  solution, the cyclic voltammetry was performed. The cyclic voltammograms (**Fig 2 b**), measured at relatively high scan rate of  $20\text{ mVs}^{-1}$ , reveal the existence of anode and cathode peaks

positioned at 0.87 V and 0.7 V versus SCE, respectively. It shows the capability of the re-synthesized material to intercalate and de-intercalate  $\text{Li}^+$  ions from an aqueous solution. We suggest that this relatively low current response may be improved by better phase purity, reduced particle size and more electronically conducting additive.

## CONCLUSION

This work is addressed to recycle the cathode material from spent Li-ion batteries and to examine its structural, morphological and electrochemical properties. The layered structure was confirmed by XRD and Raman analysis, while uniform micron-sized particles were observed by SEM analysis. Raman spectroscopy revealed the presence of a monoclinic  $\text{Li}_2\text{MnO}_3$  phase as a synthesis by-product. The capability of the material to intercalate and de-intercalate  $\text{Li}^+$  ions in an aqueous solution of Li-salt was demonstrated by cyclic voltammetry. A relatively low current response was evidenced, however it may be improved on the ground of already existing knowledge.

## *Acknowledgement*

This work was supported by the Ministry of Sciences and Environmental Protection of Serbia Project III 45014, OI 172043 and III45006.

## REFERENCES

- [1] Zeng, X., Li, J. Singh, N., Crit. Rev. Env. Sci. Tec., 2014, 44, 1129-1165.
- [2] L. Liu, F. Tian, X. Wang, Z. Yang, Q. Chen, X. Wang, J. Solid State Electroctr, 2012, 16, 491–497.
- [3] M. Vujković, M. Mitrić, S. Mentus, J. Power Sources, 2015, 288, 176-186.
- [4] H. Yu, H. Kim, Y. Wang, P. He, D. Asakura, Y. Nakamura, H. Zhou, Phys. Chem. Chem. Phys., 2012, 14, 6584-6595.
- [5] J. Kim, O. Kim, C. Park, G. Lee, and D. Shin, J. Electrochem. Soc., 2015, 162, 1041-1045.

## ELECTROCHEMICAL BEHAVIOUR OF NICOTINE ADSORBED ON MONTMORILLONITE

T. Mudrinić, N. Jović-Jovičić, Z. Mojović, A. Milutinović-Nikolić,  
S. Marinović, M. Ajduković and P. Banković

*University of Belgrade, Institute of Chemistry, Technology and Metallurgy,  
Center for Catalysis and Chemical Engineering, Njegoševa 12,  
11000 Belgrade, Serbia (tihana@nanosys.ihtm.bg.ac.rs)*

### ABSTRACT

The montmorillonite (Mt) and acid modified montmorillonite (Mt<sub>A</sub>) were used as nicotine adsorbents. The optimal pH values for nicotine adsorption were 6 and 9 for Mt and Mt<sub>A</sub>, respectively. Mt and Mt<sub>A</sub>, previously saturated with nicotine via adsorption, at these characteristic pH values, were used as modifiers of carbon paste electrode. The cyclic voltammetry was performed at characteristic pH values (6 and 9) in Britton-Robinson buffer. The obtained cyclic voltammograms depended on both modifier and pH regime of the supporting electrolyte.

### INTRODUCTION

Nicotine can be found in surface and groundwater because of possible leaching of nicotine from tobacco industry waste. Monitoring of nicotine presence in water is a challenging task. Development of electrochemical sensors for nicotine could be regarded as promising solution. Such sensors are portable, fast and relatively inexpensive and do not require preparation of sample even the opaque ones. In this paper carbon paste electrode modified with montmorillonite was tested as first step in potential development of sensor that enables detection of nicotine and its differentiation from other analytes that might act as interferences.

### EXPERIMENTAL

The Wyoming, USA (Mt) with montmorillonite content of 90 – 100 % was obtained from Clay Mineral Society repository. Acid modified montmorillonite (Mt<sub>A</sub>) was prepared following the procedure [1]: 4.5M HCl, 2 h 90 °C, solid to liquid ratio 1:4.5. The rinsing until Cl<sup>-</sup> free was performed by dialysis.

The adsorption of nicotine ( $c=0.75 \text{ mmol dm}^{-3}$ ,  $V=50.00 \text{ cm}^3$ ) onto Mt and Mt<sub>A</sub> ( $m_{\text{ads}}=50 \text{ mg}$ ) was performed in a batch system at 25 °C in thermostated shaker (Memmert WNE 14 and SV 1422). Thermo Electron

Nicolet Evolution 500 UV-Vis was used for monitoring the nicotine concentration before and after adsorption ( $\lambda_{\max}=261$  nm). The materials with adsorbed nicotine were used as modifiers of carbon paste electrode. The electrode was prepared by hand mixing of clay, carbon black (Vulcan-XC 72R) and paraffin oil with mass ratio 10:1:4. The resulting paste was packed into the hollow electrode and used as working electrode. The reference electrode was Ag/AgCl in 3 M KCl, while a platinum rod served as a counter electrode. The cyclic voltammetry was performed using Autolab electrochemical workstation (Autolab PGSTAT302N, Metrohm-Autolab BV). The supporting electrolyte was 0.1 M Britton-Robinson buffer. pH meter (PHM240 MeterLab®) was used to control the solution pH.

## RESULTS AND DISCUSSION

The study of the influence of pH on the percent of the adsorbed nicotine onto Mt and Mt<sub>A</sub> (Fig. 1) was conducted using pH of initial nicotine solutions in the range from 2 to 12 [2]. The Mt as adsorbent showed the

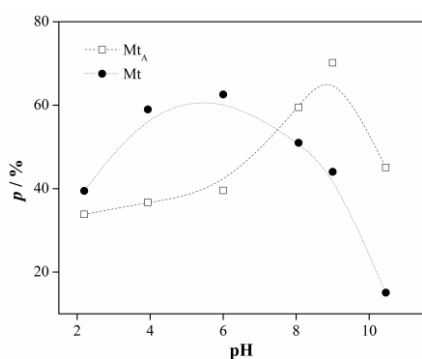


**Figure 1.** Percent of the adsorbed nicotine vs. pH.

highest efficiency at pH=6, while Mt<sub>A</sub> at pH=9. The adsorption of nicotine is governed by the form of nicotine molecule in solution and surface acidity of adsorbents. At different pH nicotine can be found as neutral molecule, mono- and di-protonated cations [3]. At pH<3 diprotonated form of nicotine is dominant. With the increase of pH, the presence of monoprotonated form of the nicotine increases. At pH=6 the molecular form of nicotine appears. With further

increase of pH, molecular form of nicotine becomes dominant. At pH≈9, solution contains approx. 90% of nicotine in the molecular form, while the rest is in monoprotonated form. Therefore, the most efficient adsorption onto Mt occurred at pH=6 with monoprotonated form of nicotine as the most dominant form. On the other hand at pH=9, where Mt<sub>A</sub> exhibited the best adsorption performance, molecular form of nicotine was mainly adsorbed.

Cyclovoltammograms (CV) were recorded on different pH values: the pH where adsorption was performed (Fig. 2a) and on opposite pH (Fig. 2b) i.e. if the adsorption was performed at pH=6 the CV was recorded at pH=9 and vice versa.

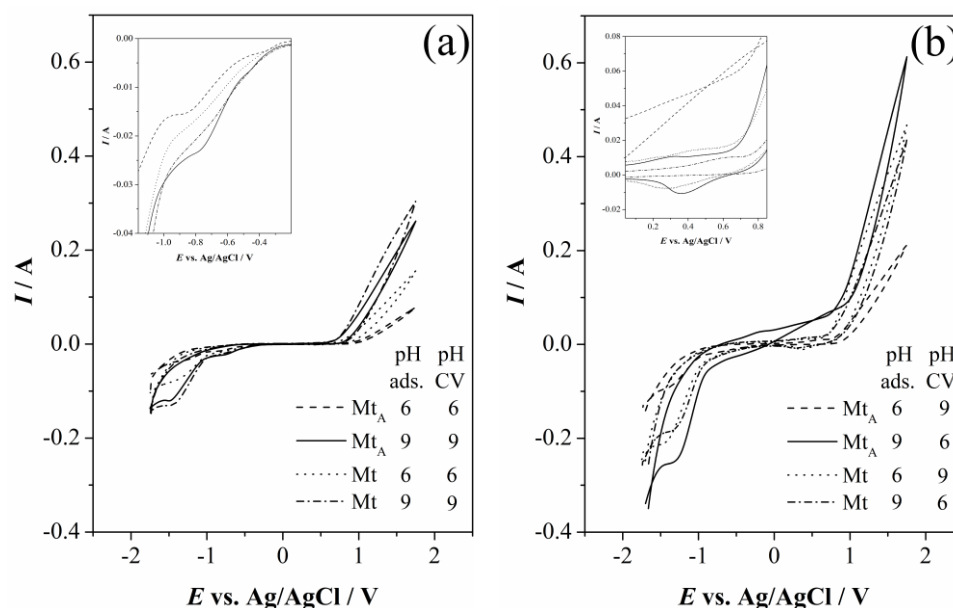


**Figure 2.** CV of nicotine adsorbed on Mt and Mt<sub>A</sub> in buffered solution. Adsorption and CV were performed: a) at same pH, b) at opposite pH

All CV exhibited increase of anodic current due to nicotine oxidation and cathodic peak due to nicotine reduction. These characteristic currents were lower for CV performed at pH where adsorption was performed in comparison to CV performed at opposite pH. CV recorded at pH where the adsorption was performed exhibited additional cathodic wave at lower potential than main cathodic peak (inserted graph in Fig. 2a). This peak was more expressed with carbon paste electrode modified with Mt<sub>A</sub>. CV recorded at the opposite pH exhibited additional pair of peaks at the foot of the anodic increase (inserted graph in Fig. 2b) due to nicotine oxidation. The peaks were best developed for CV recorded at pH=9 for electrode modified with Mt where nicotine was adsorbed at pH=6. CV recorded at pH=6 for electrode modified with Mt<sub>A</sub> where nicotine was adsorbed at pH=9 exhibited hysteresis.

Additional experiments are needed in order to clarify electrochemical behavior of nicotine particularly since literature data on this subject are deficient. Suffredini et al. [4] has suggested mechanism of nicotine electrooxidation that is not sufficient to elaborate the results obtained in this paper.

## CONCLUSION

The optimal pH values for nicotine adsorption on montmorillonite (Mt) and acid modified montmorillonite (Mt<sub>A</sub>) were 6 and 9, respectively. Mt and Mt<sub>A</sub> were saturated with nicotine by adsorption at pH 6 and 9. Materials prepared in this manner were used as modifiers of carbon paste electrode. The cyclic voltammetry was performed at same characteristic pH values in Britton-Robinson buffer. All CV exhibited increase of anodic current due to nicotine oxidation and cathodic peak due to nicotine reduction. These characteristic currents were lower for CV performed at pH where adsorption was performed in comparison to CV performed at opposite pH (meaning that if the adsorption was performed at pH=6 the CV was recorded at pH=9 and vice versa).

## Acknowledgement

This work was supported by the Ministry of Education, Science and Technological Development of the Republic of Serbia (III 45001).

## REFERENCES

- [1] Z. Vuković, A. Milutinović-Nikolić, Lj. Rožić, A. Rosić, Z. Nedić, D. Jovanović, *Clays and Clay Minerals*, 2006, 54, 697-702.
- [2] I. Ilić, N. Jović-Jovičić, P. Banković, Z. Mojović, D. Lončarević, I. Gržetić and A. Milutinović-Nikolić, *Science of Sintering*, 2018 *in Press*.
- [3] D. Hoffmann, I. Hoffmann, *Journal of Toxicology and Environmental Health*, 1997, 50, 307-364.
- [4] H. B. Suffredini, M. C. Santos, D. De Souza, L. Codognoto, P. Homem-de-Mello, K. M. Honório, A. B. F. da Silva, S. A. S. Machado, L. A. Avaca, *Analytical Letters*, 2005, 38, 1587–1599.

## THE ELECTROCHEMICAL BEHAVIOR OF PURPURIN IN AN AQUEOUS SOLUTION OF SODIUM NITRATE

J. Senćanski<sup>1</sup>, M. Vujković<sup>2</sup>, M. Pagnacco<sup>2</sup> and S. Mentus<sup>2,3</sup>

<sup>1</sup>*University of Belgrade, Institute of General and Physical Chemistry,  
Studentski Trg 12-15, 11000 Belgrade, Serbia. (jsencanski@iofh.bg.ac.rs)*

<sup>2</sup>*University of Belgrade, Faculty of Physical Chemistry, Studentski Trg 12-  
15, 11000 Belgrade, Serbia.*

<sup>3</sup>*Serbian Academy of Sciences and Arts, Knez Mihajlova 35, 11000  
Belgrade, Serbia*

### ABSTRACT

Purpurin – an organic colour obtained from the plant Maddre – was subjected to electrochemical characterization by cyclic voltammetry in an aqueous solution of NaNO<sub>3</sub>. Redox reactions corresponding to the insertion/deinsertion of Na<sup>+</sup> ions were evidenced. Carbonyl and hydroxyl groups present in purpurin molecules were found to be capable of bonding a substantial amount of sodium ions. Sodium storage capacity was found to amount to ~73 mAh g<sup>-1</sup>. However, such a high capacity was not kept on prolonged cycling. By means of UV/VIS spectroscopy, the dissolution of sodiated purpurin was found to be responsible for this capacity fade.

### INTRODUCTION

Li-ion batteries have become the main power source for many portable electronic devices, despite the fact that they contain hazardous metals such as Li, Co, Ni, and Mn as well as toxic and flammable electrolyte [1-3]. Recently, the replacement of them by more environmentally friendly batteries became realizable. In this regard, numerous studies have been performed to examine versatile organic materials (polyethylene glycol, self-polymerized dopamin, poly anthraquinonyl imide...), as environment friendly green cathodes for rechargeable Li-ions batteries [4]. Furthermore, sodium-ion batteries have been extensively studied as an alternative to lithium-ion batteries [3,5].

This work is focused to the examination of the organic compound purpurin in a Na-containing aqueous solution, as an attempt to develop a cathode material for sodium-aqueous rechargeable batteries. Purpurin is advantageous being completely natural product, obtained from the plant Maddre through an extraction process. To the best of the authors'

knowledge, there is no study that has been published so far reporting the electrochemical behavior of purpurin in a Na-containing aqueous solution.

### EXPERIMENTAL

After drying the plant material at room temperature (circa 20 degrees Celsius) for one week, it was ground into a uniform powder. The purpurin was then extracted by methanol and dissolved in 2 mol/L HCl, after which it was neutralized by a solution of NaOH and then again extracted by methanol. When the solvent evaporated, the solid residue was separated between chloroform and water. Thereafter, the solution in chloroform was extracted by 1 mol/L NaOH. In order to acidify the obtained solution, HCl was added. The obtained solution was extracted by chloroform. After melting at 260 °C, red needles of purpurin were obtained.

The Cyclic Voltammetry (CV) was carried out in a classical three-electrode cell using an aqueous solution of sodium nitrate (6M) as an electrolyte. The Pt foil was used as a counter electrode, while the potential was measured with respect to the saturated calomel electrode (SCE). The working electrode was made from the active material (purpurin), carbon black and a poly(vinylidene fluoride) binder in pyrrolidone (85:10:5). The suspension was pasted to an electronically conductive glassy carbon support. The CV measurements were carried out using Gamry PCI4/300 Potentiostat/Galvanostat.

The spectroscopic measurements were performed by Agilent 8453 spectrophotometer containing diode array detector in ultraviolet (UV) and visible (VIS) range. The UV/VIS spectra of aqueous electrolytic solutions of NaNO<sub>3</sub>, after the third electrochemical cycle were recorded.

### RESULTS AND DISCUSSION

The electrochemical behavior of purpurin was studied in an aqueous solution of NaNO<sub>3</sub> by means of cyclic voltammetry. The CVs measured over the initial 20 cycles at a scan rate of 20 mVs<sup>-1</sup> are shown in Fig.1 and Fig.2a. The main cathodic peak, positioned at -1.03V vs. SCE at the first cycle, corresponds to the insertion of the Na<sup>+</sup>-ions into the purpurin. Its high current response indicates that the significant amount of Na<sup>+</sup> ions is bonded during the first cathodic polarization. The bonding of sodium-ions to purpurin molecules is likely to occur through their exchange with protons in carbonyl and phenolic hydroxyl groups [6]. The initial sodium storage capacity was found to be substantial, amounting to ~73 mA h g<sup>-1</sup>. It can be said that the full capacity of material was not utilized since the negative potential had to be limited to -1.2 V vs SCE to avoid water reduction. However, the current response over the first anodic scan was significantly

reduced compared to the initial cathodic peak. The two anodic peaks, corresponding to the sodium deinsertion process, appeared at  $-0.71$  V and  $-0.2$  V (vs. SCE).

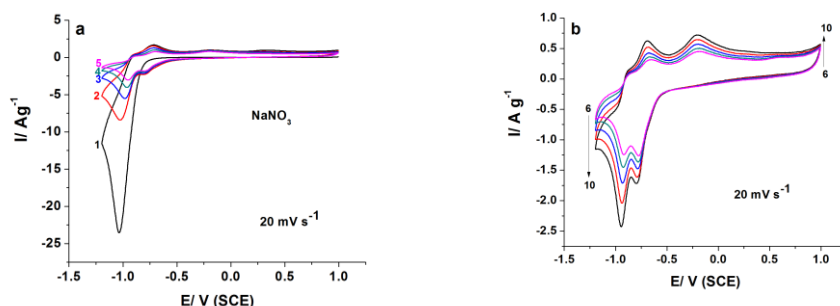


**Figure 1.** The CVs of purpurin measured in  $\text{NaNO}_3$  at a common scan rate of  $20 \text{ mV s}^{-1}$  over the initial five cycles (a) and the following five cycles (b).

It can be concluded that the sodiation of purpurin causes irreversible redox changes which was evidently accompanied by a change in the color of the electrolytic solution from colorless to orange.

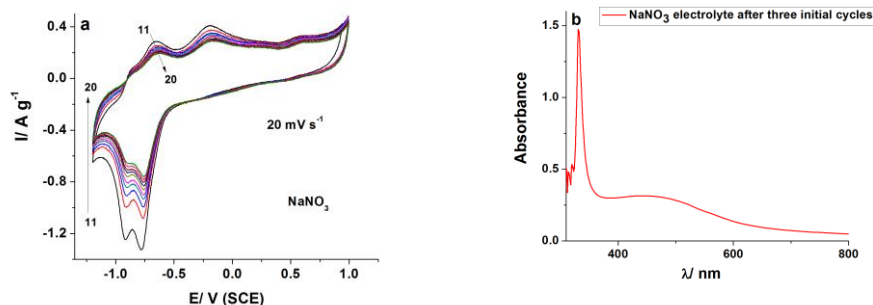


**Figure 2.** Cyclic voltammograms of a purpurin measured in an aqueous solution of  $\text{NaNO}_3$  at  $20 \text{ mV s}^{-1}$  11<sup>th</sup>-20<sup>th</sup> cycle, and b) UV/VIS absorption spectra of the electrolyte solution upon electrochemical experiments

The UV/VIS spectroscopy has shown that the sodiated form of purpurin becomes soluble in an aqueous electrolytic solution (Fig2b). The obtained sharp peak at  $\sim 290$  nm originated from purpurin, while wide peak at  $\sim 480$  nm originated from purpurin and/or the sodiated form of purpurin [7]. The sodiated form of purpurin is obviously responsible for the observed decrease in capacity during consecutive cycling. In other words, the redox behavior

of the sodiated purpurin, taking place in two-steps (Fig1b, Fig2a), is not sustainable over the successive cycling in  $\text{NaNO}_3$ . As a consequence, low coulombic capacities amounting to  $8 \text{ mA hg}^{-1}$  (cathodic scan) and  $7.5 \text{ mAh g}^{-1}$  (anodic scan) were measured after ten charging/discharging cycles.

## CONCLUSION

The electrochemical behavior of an organic material purpurin was examined in a sodium salt-containing aqueous solution. This compound was found to be capable of bound a large amount of sodium ions during the initial cathodic polarization at  $20 \text{ mVs}^{-1}$ , possessing a capacity of  $\sim 73 \text{ mA hg}^{-1}$ . However, the inserted sodium-ions cause irreversible redox changes which are followed by a change in the color of the electrolytic solution, from colorless (prior to cycling) to orange (after the first cycle). The sodiation of purpurin molecules, due to the solubility increase, results in a gradual electrode capacity loss throughout the consecutive cycling in an aqueous solution of  $\text{NaNO}_3$ .

## Acknowledgement

This work was supported by the Ministry of Science and Environmental Protection of Serbia Project III 45014 and 172015. Authors are also grateful to the prof. dr. Nedeljko Manojlović for preparing the purpurin for this investigation.

## REFERENCES

- [1] J. Xu, H.R. Thomas, R. W: Francis, K.R. Lum, J. Wang, B. Liang, J. Power Sources, 2008, **177**, 512-527.
- [2] M. S. Whittingham, Chem. Rev., 2004, **104**, 4271-4301.
- [3] J. Senćanski, D. Bajuk-Bogdanović, D. Majstorović, E. Tchernychova, J. Papan and M. Vujković, J. Power Sources, **342**, 2017, 690-703.
- [4] X. Yang, M. Zhou, and Y. Lei, Mater Today, **21**, 2017, 60-78.
- [5] M. Vujković, S Mentus, J. Power Sources, **247**, 2014, 184-188.
- [6] A.L.M. Reddy, S. Nagarajan, P. Chumyim, S.R. Gowda, P. Pradhan, S.R. Jadhav, M. Dubey, G. John, P.M. Ajayan, Sci. Rep. **960**, 2012, 1-5.
- [7] Z. Marković, N. Manojlović, S. Jeremić, Ž. Miroslav, Hem. Ind., **67**, 2013, 77-88.

## APPLICATION OF ELECTROCHEMICAL BIOSENSOR FOR INVESTIGATION OF ACRIDINE DERIVATIVES - DNA INTERACTION

J. Rugar<sup>1</sup>, M. Aleksić<sup>1</sup>, V. Dobričić<sup>2</sup>, O. Čudina<sup>2</sup>, J. Brborić<sup>2</sup> and S. Vladimirov<sup>2</sup>

*University of Belgrade, Faculty of Pharmacy,<sup>1</sup>Department of Physical Chemistry and Instrumental Methods ([marar@pharmacy.bg.ac.rs](mailto:marar@pharmacy.bg.ac.rs))*

*<sup>2</sup>Department of Pharmaceutical Chemistry, Vojvode Stepe 450, 11000 Belgrade, Serbia*

### ABSTRACT

The interaction between acridine derivatives and DNA was investigated using multilayer DNA modified glassy carbon electrode as electrochemical biosensor, applying square wave (SW) voltammetry. The decrease of DNA SW oxidation peak current is the evidence for the interaction, which is probably the result of the conformational changes in the DNA structure. Optimal conditions for most intense interaction with DNA were selected using 9Cl-A as a model compound. The most pronounced decrease in peak current was obtained at pH 4.5 with  $1 \times 10^{-4} \text{ molL}^{-1}$  9Cl-A after the 30 min of incubation. The study was extended to other acridine derivatives, indicating that the most intensive interaction with DNA occurs with 9PROPGABAA, and 9PAHA. These derivatives decrease DNA signal for additional 40-50% comparing to 9Cl-A, indicating very intense interaction with DNA what might suggest them as agents with potentially high antitumor activity.

### INTRODUCTION

Binding to DNA is important mechanism for many antitumor agents. Acridines are some of them, since they form complexes with DNA [1] what gives them possible chemotherapeutical role. Due to their numerous actions, acridines are also used as bactericidal, antiseptic and inhibitory agents.

DNA-based electrochemical biosensors consist of nucleic acid recognition layer that is immobilized over an electrochemical transducer [2] and therefore they may be successfully used for investigation and evaluation of DNA-drug interaction mechanisms [3]. The adsorbed nucleic acid at GCE surface undergoes charge-transfer reactions, producing signals due to the oxidation of deoxyguanosine (dG), and deoxyadenosine (dA), that can provide information about their concentration, changes in structure and

orientation upon interaction [4]. Decrease in oxidation peaks is proportional to intensity of interaction between DNA and antitumor agent.

To be able to use the biosensor, the electrochemical behavior of the acridine derivative was previously investigated [5], showing that 9Cl-A oxidation at GCE occurred as irreversible, pH depending process.

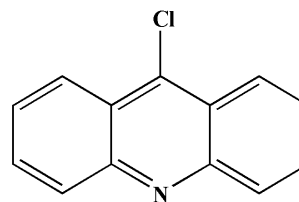


**Figure 1.** 9Cl-A structure

The aim of this work is to show the applicability of electrochemical biosensor and to investigate acridine derivatives: 9-chloroacridine (9Cl-A) (Fig.1.), propyl 4-(acridin-9-ylamino)butanoate (9PROPGABAA), ethyl 6-(acridin-9-ylamino)hexanoate (9ETAHA) and propyl 6-(acridin-9-ylamino)hexanoate (9PAHA) interaction with DNA immobilized on an electrode surface.

## EXPERIMENTAL

The voltammetric measurements were performed with  $\mu$ Autolab analyzer (EcoChemie, Utrecht, The Netherlands). Three-electrode system was employed with GCE working electrode, Ag/AgCl reference and Pt-auxiliary electrode. Before each experiment the GCE was manually polished using the aqueous slurry of  $\text{Al}_2\text{O}_3$  powder (particle size  $0.05\mu\text{m}$ ) on a smooth polishing pad, sonicated in bidistilled water and then in absolute ethanol. Calf thymus DNA, and 9Cl-A are produced by Sigma Aldrich, and other acridine derivatives are synthesized in our laboratory.

DNA biosensor was prepared by immobilization of double-stranded calf thymus DNA in multilayer at the GCE surface, by three times consecutively adding and drying (under nitrogen atmosphere) of small volumes of DNA solution ( $5\mu\text{L}$ , concentration  $73.95\mu\text{g mL}^{-1}$ ) at the GCE surface. The dsDNA-electrochemical biosensor was immersed and allowed to incubate in acridine derivative solutions of different concentration during different periods of time. The period of time when the interaction between DNA and acridine derivative is allowed to proceed is called incubation time ( $t_{\text{incubation}}$ ). After the incubation time, the biosensor was removed from the solution, washed with deionized water in order to remove the unbounded molecules and placed in the electrochemical cell containing only the supporting electrolyte, where the transduction was performed by SW voltammetry. The experimental parameters for SWV were: frequency 25 Hz and potential increment 1 mV, corresponding to an effective scan rate of  $26\text{ mVs}^{-1}$ , and the pulse amplitude of 5 mV.

## RESULTS AND DISCUSSION

The dsDNA oxidation studies were performed in the pH range from pH 4.5 to pH 7.0. Although the dsDNA oxidation peaks occurred at lower potentials at physiological pH (pH 6.9), in pH 4.5 the DNA oxidation peak currents were higher and better shaped and for this reason all experiments were carried out in pH 4.5, 0.1 M acetate buffer. SW voltammogram of dsDNA solution, pH 4.5, showed two peaks corresponding to the oxidation of deoxyguanosine (dG),  $E_p=1.1V$ , and deoxyadenosine (dA),  $E_p=1.3 V$ .

The interaction between dsDNA on the GCE surface with 9Cl-A was detected by comparing the changes in the purine base oxidation peak currents of dsDNA recorded after incubation with the results obtained using a control dsDNA-electrochemical biosensor without incubation. In order to confirm that the decrease of DNA voltammetric signals was due to the 9Cl-A-dsDNA interaction, a control dsDNA-electrochemical biosensor was also prepared according to described and held in buffer solution for time period what is the established as optimal incubation time.

SW voltammograms obtained with newly prepared dsDNA-electrochemical biosensors in buffer following described procedure for different concentrations:  $2.4 \times 10^{-4} \text{ molL}^{-1}$ ,  $1 \times 10^{-4} \text{ molL}^{-1}$  and  $5 \times 10^{-5} \text{ molL}^{-1}$  of 9Cl-A (Fig. 2.), during different incubation times of 10, 20 and 30 min were recorded. Since the oxidation peak of 9Cl-A overlapped with the oxidation of dG residues, making it difficult to clarify these two contributions, only change in dA peak is informative for discussion of investigated interaction.

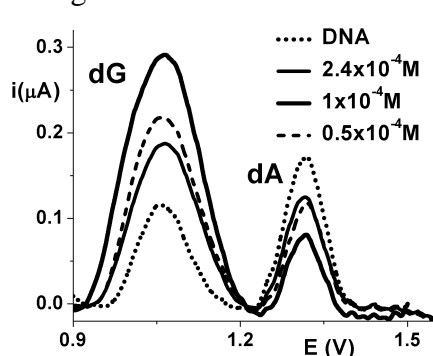


**Figure 2.** The effect of 9Cl-A concentration ( $t_{\text{incubation}} = 30 \text{ min}$ )

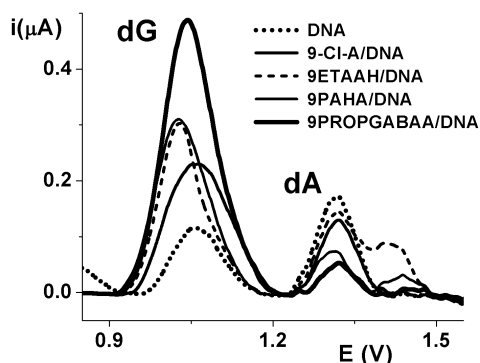


**Figure 3.** DNA–Acridine derivatives interaction with DNA

The experiment described above showed that structural modifications occurred in the dsDNA on the GCE surface upon interaction with 9Cl-A. It is evident that the most pronounced decrease in peak dA is observed for lower 9Cl-A concentrations which is possibly the result of forming rigid

structure with DNA layer, therefore the concentration of  $1 \times 10^{-4} \text{ molL}^{-1}$  was chosen for future work. The effect of incubation time was investigated analyzing the dependence  $i_{p(dA)} = f(t_{\text{incubation}})$ ; the most pronounced decrease of peak dA current occurs during first 10 min, and then dA peak current continues slowly to decrease until 30 minutes, therefore 30 min of incubation was selected for further work. Decrease of peak dA, together with slight shift of potential towards more positive value, indicates intercalation as the type of interaction. Under the selected conditions, the interactions of other acridine derivatives with DNA were investigated. According to results presented at Figure 3, 9PROPGABAA, and 9PAHA are showing very good results indicating very intense interaction with DNA what might suggest them as agents with potentially high antitumor activity.

### CONCLUSION

The interaction between 9Cl-A and DNA was investigated using multilayer DNA modified glassy carbon electrode as electrochemical biosensor. Decrease of dA DNA oxidation peak may be attributed to the aggregation of DNA strands and formation of more rigid structures due to the intercalation of 9Cl-A into DNA strands, what leads to the conformational changes in the DNA structure. The examined pH, incubation time and concentration effects showed that the most pronounced decrease in dA peak was obtained at pH 4.5 with  $1 \times 10^{-4} \text{ molL}^{-1}$  9-ClA after the 30 min of incubation. This study was extended to other acridine derivatives, indicating that the most intensive interaction with DNA occurs with 9PROPGABAA, and 9PAHA, indicating their possible chemotherapeutical role.

### Acknowledgement

This work was supported by the Ministry of Education, Science, and Technological Development of the Republic of Serbia, Grants no. 172033 and 172041.

### REFERENCES

- [1] A. Nasim, T. Brychcy, Mutation Research, 1979, **66**, 261-288
- [2] A. Erdem, Talanta, 2007, **74**, 318-325.
- [3] V. C. Diculescu, A. M. Chiorcea-Paquim, A. M. Oliveira-Brett, Trends in Analytical Chemistry, 2016, **79**, 23-36.
- [4] S. C. Oliveira, A. M. Oliveira-Brett, Comb. Chem. HighThroughput Screen. 2010, **13(7)**, 628-640.
- [5] J. Pantić, M. M. Aleksić, V. Dobričić, O. Čudina, J. Brborić, S. Vladimirov, 13<sup>th</sup> International Conference on Fundamental and Applied Aspects of Physical Chemistry, 2016, Proceedings 383-386.

## ELECTROCHEMICAL DNA BIOSENSOR MODIFIED WITH CARBONIZED POLYANILINE

J. Rupar, A. Janošević Ležaić, T. Ilić and M. Aleksić

*University of Belgrade, Department of Physical Chemistry and Instrumental Methods, Faculty of Pharmacy, Vojvode Stepe 450, 11000 Belgrade, Serbia  
(aleksandra.janosevic@pharmacy.bg.ac.rs)*

### ABSTRACT

DNA–electrochemical biosensor on glassy carbon electrode (GCE) was modified with carbonized polyaniline (Carb-PANI) in order to achieve more intense and reproducible biosensor signal. The multilayer Carb-PANI/DNA biosensor was prepared by successively covering the GCE surface with layers of Carb-PANI and DNA solution. Changes in square wave voltammometry (SW) oxidation peaks of deoxyguanosine (dG  $E_p=1.1V$ ) and deoxyadenosine (dA  $E_p=1.3V$ ) were observed due to the DNA-mediator interaction. When biosensor is formed, type and amount of conductive mediator were varied. Carbon based materials (Carb-PANI-HCl, Carb-PANI-SSA) were used as mediators. The increase of the peak current was observed when using three-layer Carb-PANI-HCl/DNA biosensor, where the percentage increase in dG peak current ( $I_p$ ) and surface ( $P$ ) is approximately 40%. It has been shown that morphology of the mediator has important role for interacting with DNA. Also, it was noticed that the increase in number of mediator layers increases the biosensor response.

### INTRODUCTION

DNA-electrochemical biosensor represent modified electrode with adsorbed DNA layer used to investigate changes in DNA structure, caused by damage or interaction with drugs and potential carcinogens [1]. The improvement of the conductivity characteristic may be achieved by modifying the surface of the electrode using conductive material as a mediator.

The nitrogen-containing carbon nanotubes (NCNT) have received growing attention in the recent years, because of their outstanding physicochemical properties and due to their versatile applicability as materials for energy conversion and storage (hydrogen storage, electrocatalysts for fuel cells, supercapacitors), analytical applications (gas sensors, electrochemical (bio)sensors), catalysis, nanoelectronics or adsorbents [2]. The carbonization of PANI nanotubes (PANI-NT) appears to be a promising route for the industrial-scale preparation of low-cost NCNT

without metal impurities, since various reliable and scalable template and template-free methods for the synthesis of PANI-NT were developed.

Carbonized polyanilines (Carb-PANI) could be good mediators if they increase the electrochemical signal of adenine/guanine oxidation in DNA. Changes in intensity and position of the voltammetric peaks are used to investigate the above mentioned changes and interactions.

## EXPERIMENTAL

In this work, the commercial DNA (Sigma-Aldrich, Deoxyribonucleic acid sodium salt from calf thymus) was used. Acetate buffer pH 4.6 was used as supporting electrolyte. The chemicals needed for the preparation of this buffer were p.a. degree of purity.

Carb-PANI-SSA and Carb-PANI-HCl were prepared by the procedure of Janošević et al. [3, 4].

$\mu$ Autolab analyzer with three-electrode system composed of GCE working electrode, Ag/AgCl reference and Pt-auxiliary electrode was used. Biosensor was prepared by successively covering the GCE surface with three layers of Carb-PANI and DNA solution (5  $\mu$ L, concentration 73.95  $\mu$ g mL<sup>-1</sup>). After placing each layer on the top of electrode surface, the electrode was dried under a flux of N<sub>2</sub>.

Afterwards, the biosensor was removed from the solution, washed with deionized water to remove the excess of unbounded material, placed in the electrochemical cell with supporting electrolyte, and SW voltammetry was performed. The experimental parameters for SWV were: frequency 25 Hz and potential increment 1 mV, corresponding to an effective scan rate of 26 mVs<sup>-1</sup>, and the pulse amplitude of 5 mV.

## RESULTS AND DISCUSSION

The SW voltammogram of 73.95  $\mu$ g mL<sup>-1</sup> dsDNA solution at pH 4.5, showed two peaks corresponding to the oxidation of deoxyguanosine (dG), E<sub>p</sub>=1.1V, and deoxyadenosine (dA), E<sub>p</sub>=1.3 V (Figure 1, curve 1). When modified biosensor is formed, type and amount of conductive mediator were varied. The increase of the dG and dA peak current was observed when using three-layer Carb-PANI-HCl/DNA biosensor, where the percentage increase in guanine peak current (I<sub>p</sub>) and surface (P) is approximately 40% (Table 1). Changes in SW-oxidation peaks of dG and dA, were observed due to the DNA-mediator interaction. In the region of the potentials of the characteristic DNA oxidation peaks, when the electrode was modified just with Carb-PANI-SSA and Carb-PANI-HCl, without DNA layer, there was no signal emanating from the applied material. When the modification of the electrode is carried out using the Carb-PANI-SSA, after the formation of the

biosensor, in the appropriate voltammogram, the peaks dG and dA can be seen, but the desired increase in their intensity is not noticed (Figure 1, curve 2).

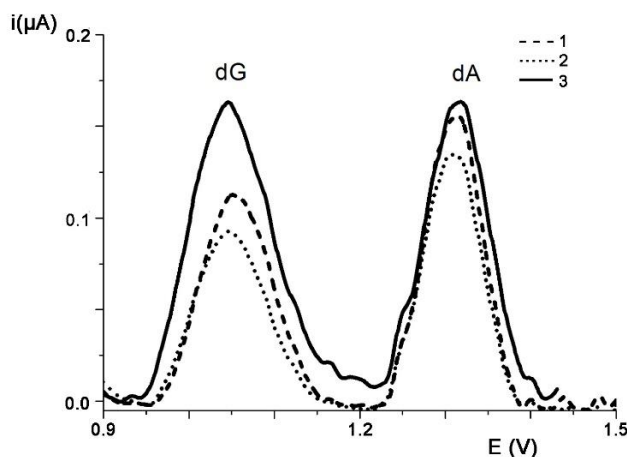


**Figure 1.** SW voltammograms obtained for: (---) DNA layer (•••) Carb-PANI-SSA/DNA and (—) Carb-PANI-HCl/DNA.

**Table 1.** The intensity of the peak current ( $I_p$ ) and the peak surface ( $P$ ) of dG and dA in voltammograms of three-layer Carb-PANI-HCl / DNA and DNA biosensors. Percentage increase in dG and dA peak current ( $I_p$ ) and surface ( $P$ ) in the Carb-PANI-HCl / DNA biosensor compared to the DNA biosensor.

DNK peak	E (V)	Carb-PANI-HCl/DNK biosensor		DNK biosensor		Percentage increase in peak current $\frac{I_{p1}}{I_{p0}} \times 100$ (%)	Percentage increase in peak surface $\frac{P_1}{P_0} \times 100$ (%)
		$I_{p1}$ ( $10^{-7}$ A)	$P_1$ ( $10^{-8}$ )	$I_{p0}$ ( $10^{-7}$ A)	$P_0$ ( $10^{-8}$ )		
dG	1.0	1.54	1.68	0.962	0.975	<b>37.5 %</b>	<b>42.0 %</b>
dA	1.3	1.59	1.43	1.48	1.26	6.9 %	11.9 %

Although the conductivity of Carb-PANI-HCl ( $0.44 \text{ S cm}^{-1}$ ) [4], is lower than the conductivity of Carb-PANI-SSA ( $0.83 \text{ S cm}^{-1}$ ) [3], the possible reason for the higher intensity of the DNK peaks in Carb-PANI-HCl/DNA biosensor SW voltammogram (Figure 1, curve 3) is the presence of long nanofibers in the morphology of Carb-PANI-HCl [4], which facilitate the

access and interaction with DNA chains, compared to nanorod/nanotubes observed in Carb-PANI-SSA morphology [3]

### CONCLUSION

It can be concluded that Carb-PANI materials can be used as potential mediators in DNA biosensors. It has been shown that morphology of the mediator has important role for interacting with DNA. Long nanofibers in Carb-PANI-HCl morphology are the most likely reason for the observed positive effect of this material on the enhanced current response of Carb-PANI-HCl / DNA biosensors. Also, it was noticed that the increase in a number of a mediator layers increases the biosensor response.

### *Acknowledgement*

This work was supported by the Ministry of Education, Science, and Technological Development of the Republic of Serbia, Grants no. 172033, 172041 and 172043.

### REFERENCES

- [1] Aleksić M., Kapetanović V., Acta Chim. Slov., 2014, **61**, 555–573
- [2] Ćirić-Marjanović G., Pašti I., Mentus S., *Prog. Mater. Sci.*, 2015, **69**, 61–182
- [3] Janosevic A., Pašti I., Gavrilov N., Mentus S., Krstic J., Mitric M., Travas-Sejdic J., Ćirić-Marjanovic G., *Microporous Mesoporous Mater.*, 2012, **152**, 50–57
- [4] Janosevic A., Bajuk-Bogdanovic D, Radoicic M, Mirsky V, Ćirić-Marjanovic G., *Synth. Met.*, 2016, **214**, 35–34

## ELECTRO-OXIDATION OF LANDFILL LEACHATE AFTER ELECTROCOAGULATION TREATMENT WITH ALUMINUM ELECTRODE

B.N. Malinovic, T. Djuricic and B. Mitric

*University of Banja Luka, Faculty of Technology, Stepe Stepanovica 73, 78000 Banja Luka, Bosnia and Herzegovina ([tijana.malinovic@tf.unibl.org](mailto:tijana.malinovic@tf.unibl.org))*

### ABSTRACT

In this paper has shown the results of combined electrocoagulation (EC) and electrooxidation (EO) treatment of landfill leachate, in which EO was applied as a post-treatment after the EC process. The applied current density in both processes was  $25 \text{ mA/cm}^2$  and the total treatment duration was 150 minutes. The results of purification of leachate were expressed through removal efficacy of chemical oxygen demand (COD), total nitrogen ( $N_{\text{tot}}$ ) and ammonia nitrogen ( $N\text{-NH}_3$ ). The highest achieved removal efficiencies was  $E_{\text{COD}} = 37.1\%$ ,  $E_{N_{\text{tot}}} = 48.1\%$  and  $E_{N\text{H}_3\text{-N}} = 90.9\%$ , respectively.

### INTRODUCTION

The landfill leachate is among the most problematic types of wastewater, from the point of view of toxicity, as well as in the selection of appropriate techniques for their purification. Research has also shown that each landfill is a separate system, and in this sense, composition and amount of leachate depends only on the characteristics of landfill [1].

In order to achieve an environmentally acceptable criterion for landfill leachate, acceptable values for their discharge must be achieved. Therefore, leachate must be collected and treated. Their composition must be controlled and must not pose a threat to the environment after purification.

Conventional treatments are not sufficient to achieve the required level of purification, which would eliminate the negative impact of leachate on the environment. In recent years considerable attention has been paid to electrochemical methods due to their efficiency and easy maintain. EC and EO has shown as promising electrochemical methods.

Cabeza *et al.* analyzed the applicability of the EO process with boron doped diamond electrode (BDD) to the landfill leachate, which characteristics are high ammonia nitrogen and COD as well as low biodegradability. Nearly complete removal of both contaminants was achieved for 6-8 hours of treatment, although the removal of ammonium nitrogen was slower than the removal of COD. The influence of the current

density of was also studied, and its impact is much greater in the removal of ammonia nitrogen than in the COD [2].

There is not much data available about the combined process of EC and EO. Only one group of researchers have processed this process. Norma *et al.* used a combination of EC/EO, and found that these techniques are cost-effective for purifying leachate from sanitary landfill [3].

Electrochemical treatment processes have been used for long time to remove not only particulate materials but also treat both COD and  $\text{NH}_3\text{-N}$  simultaneously and is capable of providing a high color removal [4].

In this paper has shown a part of results of case study for the Ramici regional landfill in Banja Luka, Bosnia and Herzegovina [5].

## EXPERIMENTAL

The experimental part of the research consist of treating landfill leachate by using EC and EO. The batch reactor for EC of 500 cm<sup>3</sup> capacity made from polypropylene with constant mixing (400 rpm) was used, combined with two electrodes of the same area surface. All the experiments were performed at an ambient temperature, with the leachate volume of 400 cm<sup>3</sup>. The total useful surface was 95.76 cm<sup>2</sup>, and the distance between electrodes 3 cm. As an electrode material for electrocoagulation was used aluminum (Al 99.5/ENAW-1050 A; max. 0.25% Si, max. 0.40% Fe, max. 0.05% Cu, max. 0.05% Mn, max. 0.05% Mg, max. 0.05% Ti, max. 0.07% Zn, min. 99.50% Al).

The anode material for the EO process was boron doped diamond - BDD (diamond coated with boron on a niobium substrate, Metachem, Germany; which is made in the form of a BDD grid - "mesh" type B). Useful surface was 30.4 cm<sup>2</sup>, and the cathode was made from copper (Cu-PHC/CW020A, EN 13601:2002; min. 99.95% Cu, 0.001-0.005% P, max. 0.005% Pb, max. 0.0005% Bi).

After each EC treatment leachate was collected and filtered, after which it was treated by EO. The samples of leachate before and after treatment were analyzed on the following parameters: COD, content of total nitrogen ( $\text{N}_{\text{tot}}$ ), content of ammonia nitrogen ( $\text{N-NH}_3$ ), in accordance with standard method [6]. The determination of total nitrogen was carried by the persulphate method in standard cuvettes (Lovibond 53 55 50, Germany). The determination of ammonia was done by salicinate method with standard cuvettes (Lovibond 53 56 50, Germany). COD was measured by the closed spectrophotometric method on COD Reactor (Hach, USA), colorimeter (COD CheckItDirect, Lovibond, Germany) by standard cuvette (Test Tube MR, Lovibond, Germany).

## RESULTS AND DISCUSSION

Results of the electrochemical treatment of landfill leachate are shown through removal efficiency,  $E$  (%), whose ratio could be described by following equation:

$$E = \frac{\gamma_i - \gamma_f}{\gamma_i} \times 100[\%] \quad (1)$$

where are  $\gamma_i$  and  $\gamma_f$  the initial and the final value of parameter which efficiency is determined.

The following figures shows the impact of electrolysis duration on removal efficiencies of total nitrogen (Figure 1), ammonia nitrogen (Figure 2) and COD reduction (Figure 3) during combined process.

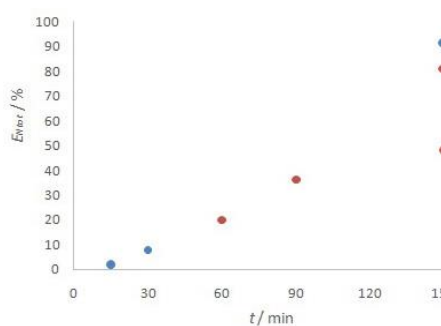


**Figure 1.** The impact of electrolysis time on  $N_{\text{tot}}$  removal efficiency ( $j=25 \text{ mA/cm}^2$ ,  $\gamma_{\text{NaCl}}=1 \text{ g/L}$ , stirring 400 rpm)

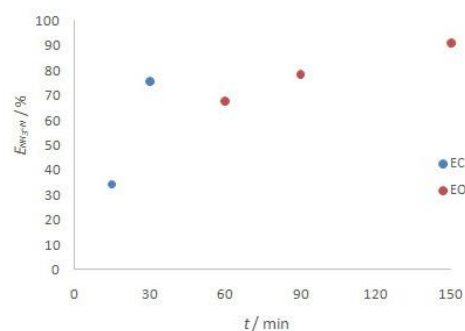


**Figure 2.** The impact of electrolysis time on  $\text{NH}_3\text{-N}$  removal efficiency ( $j=25 \text{ mA/cm}^2$ ,  $\gamma_{\text{NaCl}}=1 \text{ g/L}$ , stirring 400 rpm)

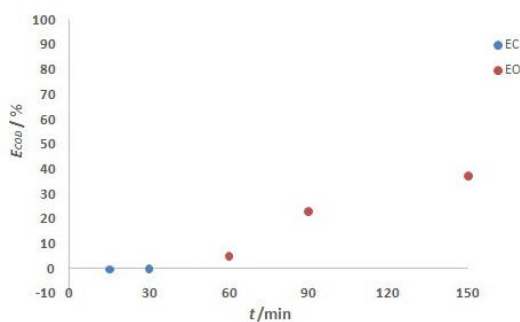


**Figure 3.** The impact of electrolysis time on COD removal efficiency ( $j=25 \text{ mA/cm}^2$ ,  $\gamma_{\text{NaCl}}=1 \text{ g/L}$ , stirring 400 rpm)

The samples were treated 30 minutes by EC, and after that 120 minutes more by EO, at a same current density of 25 mA/cm<sup>2</sup>. It can be seen that the EC did not achieve a decrease in COD, but there was a reduced amount of total nitrogen and a significant removal of ammonia. On the other hand, EO after EC proved to be a very efficient process. By prolonging the treatment time removal efficacy of all of examined parameters increases, and the highest removal efficiency was achieved for total nitrogen.

### CONCLUSION

By application of EO after EC process, it was noticed an increase in removal efficiency for all examined parameters. According to our results, it can be concluded that EC can be successfully applied as a pre-treatment to purify the leachate. In addition, it has been established that EO can be used as a post-treatment, and together with EC represents a good combination for purification of landfill leachate.

### *Acknowledgement*

This work was supported in part by the Ministry of Science and Technology of the Republic of Srpska under Project 19/6-020/961-19/15.

### REFERENCES

- [1] H. Ehring, H. Robinson, Landfilling: Leachate treatment in Solid Waste technology & Management, Volume 1 & 2 (ed. T.H. Christensen). Chichester, UK: John Wiley and Sons, Ltd., 2010.
- [2] A. Cabeza, A.M. Urtiaga, I. Ortiz. Electrochemical Treatment of Landfill Leachate Using a Boron-Doped Diamond Anode. *Industrial & Engineering Chemistry Research*, 2007, 1739-1446.
- [3] D. Norma, A. Fernandes, M.J. Pachecho, L. Ciriaco, A. Lopes. Electrocoagulation and Anodic Oxidation Intregated Process to Treat Leachate from Portuguese Sanitary Landfill. *Portugalia Electrochemica Acta*, 2012, 221-234.
- [4] Z.H. Musa, M.R. Othman, P. Abdullah, N. Nordin. Decoloriyation of landfill leachate using electrochemical technique, Sadguru Publications, 2013, 1-11.
- [5] B.N. Malinovic, M.G. Pavlovic, T. Djuricic, D. Bjelic, D. Neskovic Markic. Electrochemical treatmaent of leachate: case study for sanitary landfill "Ramici", Banja Luka in: XX international conference YuCorr, May 21-24, 2018, Tara Mountain, Serbia.
- [6] APHA. Standard Methods for the Examination of Water and Wastewater, New York: American public healt association, 1999.

## **Au-PANI SENSOR FOR DETECTION OF ARSENIC IN AQUEOUS MEDIA**

J. Milikić<sup>1</sup>, K. Radinović<sup>1</sup>, U. Stamenović<sup>2</sup>, V. Vodnik<sup>2</sup>, S.P. Ahrenkiel,<sup>3</sup>  
and B. Šljukić<sup>\*1</sup>

<sup>1</sup> Faculty of Physical Chemistry, University of Belgrade, Studentski trg 12-16, 11158 Belgrade, Serbia. (biljka@ffh.bg.ac.rs)

<sup>2</sup> Vinča Institute of Nuclear Sciences, University of Belgrade, P.O. Box 522, 11001 Belgrade, Serbia

<sup>3</sup> South Dakota School of Mines and Technology, 501 E. Saint Joseph St., Rapid City, SD 57701, USA

### **ABSTRACT**

The gold nanorods-polyaniline (Au-PANI) electrocatalyst was prepared by *in situ* method and characterized by SEM and TEM. Au-PANI was subsequently tested by cyclic voltammetry for potential application for arsenite (As(III)) detection in acidic media. Among different inorganic and organic pollutants, As is classified as one of the most dangerous elements in the environment. Au-PANI showed to be active for electroanalytical sensing of As(III) with a notably low limit of detection of As(III) of 0.213 ppb.

### **INTRODUCTION**

Environmental safety and human health protection are today's imperatives. Arsenic (As) is one of the most toxic elements in the environment, occurring in several oxidation states (-3, 0, +3 and +5), [1], with inorganic forms of arsenite (As(III)) and of arsenate (As(V)) being the most abundant in natural waters [2]. As(III) is a few dozen times (40 - 70) more toxic than As(V). The long-time intake of As(III) could lead to several health problems such as heart disease, cancer, mutagenic and genotoxic, dermal and respiratory changes [1,3]. In this work the gold nanorods-polyaniline (Au-PANI) composite was prepared and tested for sensing of As(III) by cyclic voltammetry (CV). Electrochemical methods are simpler and less expensive than other methods for As(III) detection such as X-ray fluorescence, atomic emission spectrometry and inductive coupled plasma mass spectrometry [1].

### **EXPERIMENTAL**

*In situ* chemical oxidative polymerization of aniline by Au<sup>3+</sup> ions at water/toluene interface was used as a method for Au-PANI nanocomposite preparation. This typical redox reaction, when gold nanorods and PANI

matrix are formed together, is described in detail in Ref. 4. Biphasic reaction mixture of  $\text{HAuCl}_4$  aqueous solution (10 ml, 50 mM) and aniline monomer in toluene (10 ml, 100 mM) was placed in the round bottom flask and left under vigorous stirring at  $25^\circ\text{C}$ . The formation of Au-PANI nanocomposite, in the water phase, was indicated by the change of its color, from colorless to dark green-olive. Besides, this coloration of the reaction mixture implied the formation of PANI in its doped, electroconductive form [4]. In post-synthetic treatment, after water phase decanting, and formed precipitate cleansing (with 5 mM  $\text{H}_2\text{SO}_4$ , lowering its pH below 2.5), drying, and pulverizing, dark green Au-PANI nanocomposite powder, with 28.9 wt % of Au, was obtained and characterized.

The catalytic ink was prepared by ultrasonically dispersing 5 mg of Au-PANI in 125  $\mu\text{L}$  2 % polyvinylidene difluoride solution in N-methyl 2-pyrrolidone during 30 min. 10  $\mu\text{L}$  of the catalytic ink was deposited onto a glassy carbon tip and left to dry at  $100^\circ\text{C}$  for 8 h. All electrochemical measurements were completed using Gamry PCI4/750 Potentiostat/Galvanostat in a one-compartment glass cell of 25 ml volume. The graphite rod was employed as a counter electrode and saturated calomel electrode (SCE) as a reference. Cyclic voltammograms (CVs) were recorded in 1 M  $\text{H}_2\text{SO}_4$  as supporting electrolyte in the potential range from 0 to 0.5 V at a scan rate of  $10\text{ mV s}^{-1}$ . Au-PANI electrode was held at the potential of the -0.4 V for 45 s before CV measurements. The limit of detection (LOD) was determined using the 3-sigma method [3,5].

## RESULTS AND DISCUSSION

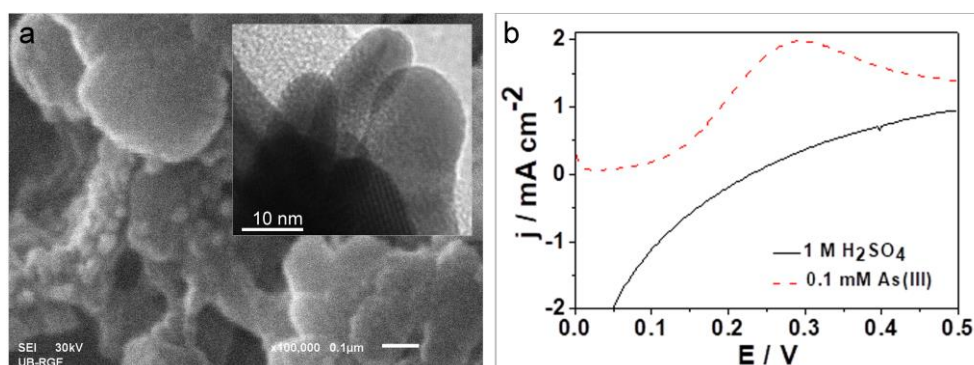


**Figure 1.** (a) Au-PANI SEM and TEM (Inset) images; (b) Anodic CVs scan of Au-PANI in 1 M  $\text{H}_2\text{SO}_4$  (—), and 1 M  $\text{H}_2\text{SO}_4$  + 0.1 mM  $\text{NaAsO}_2$  (---) at  $0.01\text{ V s}^{-1}$ .

High reactants concentrations ( $\geq 50\text{ mM}$ ) and highly acidic medium ( $\text{pH} < 2.5$ ) for the aniline polymerization process are the preconditions for

granular PANI morphology, as in the case of presented Au-PANI nanocomposite.

The induction period is shortened, and there is a formation of a great number of phenazine nucleates, that will randomly agglomerate into clusters. Further, these clusters grow into larger PANI granules that become adsorption sites for the remaining nucleates, and the growth of the new ones is initiated. PANI granules in Au-PANI nanocomposite are observed to be 60 - 400 nm in size (**Fig. 1a**). Together with the aniline polymerization by  $\text{Au}^{3+}$ , these ions are simultaneously reduced to Au nuclei that will grow to Au nanoparticles, mostly rod-shaped (**Fig. 1a, Inset**), stabilized by amine and benzene functional groups and incorporated into PANI matrix, or aggregated at the PANI surface.

The prepared Au-PANI electrode was used for As(III) detection in acidic media. **Fig. 1b** shows the anodic scan of CVs of Au-PANI electrode in 1 M  $\text{H}_2\text{SO}_4$  solution and in 1 M  $\text{H}_2\text{SO}_4$  + 0.1 mM  $\text{NaAsO}_2$ . CV recorded in 1 M  $\text{H}_2\text{SO}_4$  solution showed no peak. Contrary, CV in 1 M  $\text{H}_2\text{SO}_4$  + 0.1 mM  $\text{NaAsO}_2$  solution showed one well-defined anodic peak at potential of ca. 0.3 V corresponding to As oxidation [3].

**Table 1.** LOD of As (III) at Au-based electrodes

Electrodes	Electrolyte	LOD (ppb)	Ref.
Au-PANI	1 M $\text{H}_2\text{SO}_4$	0.213	This work
EG-AuNPs	1 M $\text{HNO}_3$	0.58	[6]
Au-PtNPs/GCE	0.5 M $\text{H}_2\text{SO}_4$	0.28	[7]
AuNPs-carbon films	0.1 M $\text{Na}_2\text{HPO}_4$	0.55	[2]
bare Au	0.1 M $\text{HAc-NaAc}$	44.4	[1]
$\text{Au}_{79}\text{Cu}_{71}$	0.1 M $\text{HAc-NaAc}$	12.8	[1]
$\text{Au}_{93}\text{Cu}_7$	0.1 M $\text{HAc-NaAc}$	3.43	[1]

Subsequently, the possibility of quantitative determination of As(III) by Au-PANI electrode was studied. For that reason, 10 additions of 5  $\mu\text{M}$   $\text{NaAsO}_2$  were made to 1 M  $\text{H}_2\text{SO}_4$  and the solution was slowly stirred by magnetic stirrer after each addition. A linear increase of peak current densities with the increase of As(III) concentrations was observed in the studied concentration range (not shown). The limit of detection (LOD) was calculated by 3-sigma method [3,5]. LOD of 6  $\mu\text{M}$ , i.e., 0.213 ppb was calculated, with this value being lower than values for different Au-based electrodes given in the literature reports ranging from 0.28 to 44.4 ppb (**Table 1**) [1,2]. Furthermore, the obtained LOD is well below the maximum limit allowed by WHO of 10  $\mu\text{g L}^{-1}$  (10 ppb), indicating that the Au-PANI

electrode can potentially be used for monitoring of the concentration of As(III) in water. It should be noted that further optimization of the electrode's performance for electroanalytical sensing of As(III) is possible by choosing more sensitive method than CV and optimizing its parameters.

## CONCLUSION

Au-PANI nanocomposite with granular morphology and incorporated gold nanorods was successfully synthesized via *in situ* chemical oxidative aniline polymerization by Au<sup>3+</sup> ions. The prepared Au-PANI was shown to be active for electroanalytical sensing of As(III) in acidic media as evident by a clear peak at ca. 0.3 V corresponding to As electrooxidation. Au-PANI electrode's high activity for As(III) detection was reflected in low LOD of As(III) of 0.213 ppb.

## Acknowledgement

Financial support for this study was granted by the Ministry of Education, Science and Technological Development of the Republic of Serbia (Projects no. 45020 and OI172043, as well as a PhD scholarship (K. Radinović).

## REFERENCES

- [1] M. Yang, Z. Guo, L.N. Li, Y.Y. Huang, J.H. Liu, Q. Zhou, X. Chen, X.J. Huang, *Sensors Actuators, B Chem.*, 2016, **231**, 70–78.
- [2] Z. Guo, M. Yang, X.-J. Huang, *Curr. Opin. Electrochem.*, 2017, **3**, 130–136.
- [3] R. Baron, B. Šljukić, C. Salter, A. Crossley, R.G. Compton, *Russ. J. Phys. Chem. A.*, 2017, **81**, 1443–1447.
- [4] U. Bogdanović, I. Pašti, G. Ćirić-Marjanović, M. Mitrić, S.P. Ahrenkiel, V. Vodnik, *ACS Appl. Mater. Interfaces.*, 2015, **7**, 28393–28403.
- [5] B. Šljukić, R. Baron, C. Salter, A. Crossley, R.G. Compton, *Anal. Chim. Acta*, 2007, **590**, 67–73.
- [6] J.P. Mafa, N. Mabuba, O.A. Arotiba, *Electroanalysis*, 2016, **28**, 1462–1469.
- [7] L. Bu, J. Liu, Q. Xie, S. Yao, *Electrochem. Commun.*, 2015, **59**, 28–31.

## APPLICATION OF MODIFIED HPMC ASSAY TO AROMATIC PLANTS ANTIOXIDANT ACTIVITY DETERMINATION

A. S. Ilić<sup>1</sup>, F. T. Pastor<sup>2</sup>, S. Ž Gorjanović<sup>3</sup>, M. Antić<sup>4</sup> and D. Ž Sužnjević<sup>3</sup>

<sup>1</sup>*Technical College of Applied Studies, Nemanjina 2, 12000  
Požarevac, Serbia*

<sup>2</sup>*University of Belgrade, Faculty of Chemistry, Studentski trg 12-16, 11000  
Belgrade, Serbia*

<sup>3</sup>*Institute of General and Physical Chemistry, P.O. Box 45, 11158  
Belgrade 118, Serbia*

<sup>4</sup>*Faculty of Agriculture, University of Belgrade, P.O. Box 14, 11080  
Belgrade, Serbia*

### ABSTRACT

A direct current (DC) polarographic assay based on the decrease of anodic current of HydroxoPerhydroxoMercury(II) Complex (HPMC) formation in Clark Lubs buffer (pH 9.8) in the presence of H<sub>2</sub>O<sub>2</sub> was modified by replacement of 50% of the electrolyte solution with ethanol. The modified assay was applied to determine antioxidant activity of the essential oils and extracts of *Lamiaceae* and *Apiaceae* species obtained by ultrasound-assisted maceration or Soxhlet extraction with 70 or 96 % ethanol.

### INTRODUCTION

A direct current polarographic assay based on the decrease of anodic limiting current of HydroxoPerhydroxoMercury(II) Complex [Hg(O<sub>2</sub>H)(OH)] (HPMC) upon addition of antioxidants (AOs) was developed and optimized by Sužnjević *et al.* [1,2]. The measurements were conducted in Clark Lubs (CL) buffer pH 9.8 as a working solution. The slope of the plot of percentage of HPMC anodic current decrease *vs* the volume of complex samples was used to express AO activity. The assay versatility was demonstrated by the application on a wide variety of complex samples, including extracts of medicinal herbs [3]. Recently, the assay was modified by introducing ethanol in CL buffer in order to extend its applicability on sample poorly soluble in water.

The aim of this work was to apply the modified assay to determine the AO activity of essential oils and extracts of members of *Lamiaceae* and *Apiaceae* families, widely used as food ingredients as well as home remedies in the treatment of different diseases, using modified HPMC

assay. Based on the obtained results, the AO activity of considered samples and the efficiency of extraction procedures applied (ultrasound-assisted maceration (UAM) and Soxhlet extraction (SE) with 70 and 96 % ethanol) was discussed.

## EXPERIMENTAL

The preparation of extracts and the essential oils Two extraction techniques, Soxhlet extraction (SE) and ultrasound-assisted maceration (UAM) were performed using 70 and 96% ethanol [4]. Essential oils were obtained by hydrodistillation for 2 h using a Clevenger type apparatus, according to the standard procedure [5].

The application of HPMC assay to the essential oils and extracts The current-potential (*i*-*E*) curves were recorded after each sample addition using the polarographic analyzer PAR (Princeton Applied Research), model 174A, equipped with X-Y recorder (Houston Omnigraphic 2000). A dropping mercury electrode (DME) with a programmed dropping time of 1 s as a working electrode, a saturated calomel electrode (SCE) as a reference and a Pt-foil as an auxiliary one were used.

A 100  $\mu\text{L}$  of 1.00 M  $\text{H}_2\text{O}_2$  was added into electrolytic cell with 19.9 mL of working solution (1:1 mixture of CL buffer pH 9.8 and 96 % EtOH). Essential oils (10 mg/mL) and extracts (1 mg/mL) were gradually added in aliquots of 100 or 200  $\mu\text{L}$  respectively into the working solution containing 5 mM of  $\text{H}_2\text{O}_2$ . After each addition *i*-*E* curves were recorded. The decrease of the initial anodic current of HPMC, observed upon each aliquot addition, was calculated and plotted vs the volume of the complex samples. The slope of dependence obtained (%/mL) was used to calculate the activity per mg of the extracted dry matter or mg of the essential oil.

## RESULTS AND DISCUSSION

### *The application of HPMC assay on essential oils and extracts of spices*

AO activity of essential oils and spices was measured by modified HPMC assay. The decrease of HPMC current intensity noticed upon samples addition is found to be linear. The polarograms obtained before and after the addition of six equal aliquots of 70 % ethanolic extract of 100  $\mu\text{L}$  of *Ocimum basilicum* L. and *Satureja montana* L., obtained by SE, are shown in Fig.1.

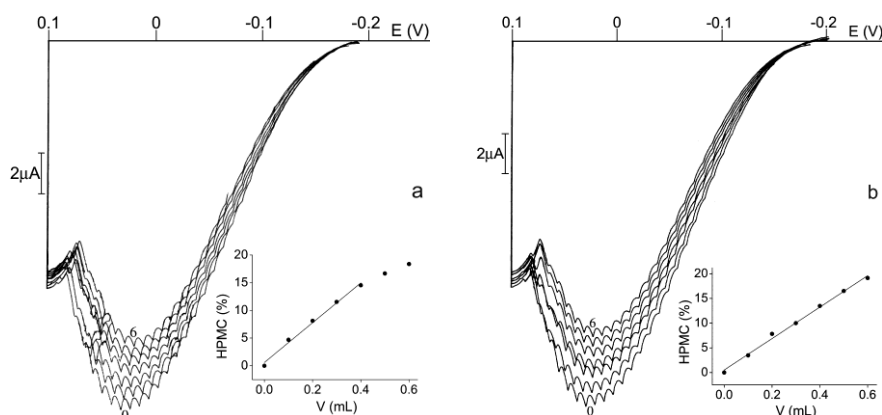


**Figure 1.** The anodic current of HPMC in 5.0 mM H<sub>2</sub>O<sub>2</sub> in 1:1 mixture of 96% ethanol and CL buffer (pH 9.8) before (0) and after the addition of six equal aliquots of 100  $\mu$ L of *O. basilicum* L. (A) and *S. montana* L. (B) extracts in 70 % ethanol, obtained by SE.

Antioxidant activity of all considered extract is shown in Table 1. The superior AO activity of the essential oils and extracts of *Lamiaceae* family members, basil and winter savory, in comparison to *Apiaceae* members was found to be in good agreement with literature data. Because of their chemical structure, volatile terpenoids are usually identified as the main compounds present in essential oils while phenolic compounds usually found in alcohol extracts.

**Table 1.** AO activity of plant extracts obtained by ultrasound-assisted maceration (UAM) and Soxhlet (SE) extraction with 70 and 96 % ethanol and essential oils determined by modified HPMC. The results are expressed in %/mg dry matter extracted or %/mg of the essential oil.

	Basil	Winter savory	Caraway	Anis
UAM <sub>70%</sub>	38.39 $\pm$ 2.62	35.27 $\pm$ 2.67	19.98 $\pm$ 0.91	13.71 $\pm$ 0.77
SE <sub>70%</sub>	35.90 $\pm$ 1.78	32.80 $\pm$ 1.24	18.56 $\pm$ 1.21	19.34 $\pm$ 0.50
UAM <sub>96%</sub>	25.74 $\pm$ 0.89	22.85 $\pm$ 0.52	14.55 $\pm$ 0.85	12.83 $\pm$ 0.70
SE <sub>96%</sub>	27.20 $\pm$ 1.79	20.30 $\pm$ 0.17	11.44 $\pm$ 0.41	9.24 $\pm$ 0.36
Essential oil	1.98 $\pm$ 0.07	1.74 $\pm$ 0.16	1.16 $\pm$ 0.07	1.24 $\pm$ 0.06

Remarkably higher AO activity of extract in comparison to oils is in accordance with their composition. Results presented in Table 1 also show that 70 % ethanol is more efficient solvent in both types of extraction.

### CONCLUSION

The results obtained enabled an insight into the efficiency of solvents used and also into the relationship between complex samples and individual compounds AO activity. Two orders of magnitude higher activity of flavonoids in comparison to terpenes is in accordance with the prominent difference in AO activity of extracts and essential oils.

### Acknowledgements

This work was supported by the Ministry of Education, Science and Technological Development, Republic of Serbia (Grant 43010).

### REFERENCES

- [1] Sužnjević et al, 2011. *Talanta* **85**: 1398–1403.
- [2] Sužnjević et al, 2015 *ElectrochimActa* **168**: 240–245.
- [3] Petrović et al, 2016. *Comb Chem High Throughput Screen* **19**: 58-65.
- [4] Alimpić et al, 2015. *Ind Crops Prod* **76**: 702-709.
- [5] Pharmacopoea Jugoslavica, Editio Quatra (*Ph. Jug.IV*) vol. 1, Federal Institute of Public Health, Belgrade, Yugoslavia, 1984.

## ELECTROCHEMICAL PERFORMANCE OF CARBONIZED COMPOSITE OF POLYANILINE WITH COLLAGEN

A. Rakić, J. Milikić, B. Šljukić, I. Pašti, and G. Ćirić-Marjanović

*University of Belgrade – Faculty of Physical Chemistry, Studentski trg 12-16, 11158 Belgrade, Serbia. (saska@ffh.bg.ac.rs)*

### ABSTRACT

Composite of polyaniline with collagen (PANI-Coll), synthesized in aqueous solution of aniline in the presence of hydrolyzed collagen using ammonium peroxydisulfate as an oxidant, was used as a precursor for the production of nitrogen-doped carbon material (c-PANI-Coll). Hollow c-PANI-Coll submicrospheres were observed with high electrical conductivity of  $2.00 \text{ S cm}^{-1}$ . The influence of collagen presence on the electrocatalytic performance of c-PANI-Coll towards the oxygen reduction reaction (ORR) was studied. c-PANI-Coll gave high ORR current densities at low overpotential.

### INTRODUCTION

Limited reserves of fossil fuels, their ecologically unacceptable exploitation, together with a growing need for more efficient and greener energy sources, direct researches towards the development of novel electrochemical energy sources [1].

Among different materials investigated for electrochemical energy storage and conversion devices (supercapacitors, batteries, fuel cells, water electrolyzers), nanoporous spheres of carbon materials have attracted special attention, since they are convenient for adsorption ( $\text{H}_2$  and  $\text{CH}_4$  gas storage) and catalysis (hydrogen evolution reaction, oxygen reduction reaction, ORR). The performance of carbon materials upon doping and/or functionalization has been reported to be improved with the best results being achieved with nitrogen-doped carbon materials. Dopants serve as active sites. Nanoporosity provides more active sites and shorter pathways for more efficient transport of reacting species and their products [2,3].

Polyaniline (PANI) proved to be superior for any energy-related task. Aniline polymerization is a simple, fast and cost-effective process in which the environmentally stable, naturally nitrogen-doped PANI material is produced. PANI on its own or in combination with other materials can adopt various required characteristics (including thermal stability, variable

conductivity, electrochemical activity, biocompatibility) by the adequate synthesis or/and post-synthetic treatment, which opens up countless possibilities for applications.

Upon carbonization, porosity and electrical conductivity of PANI are increased by one or two orders of magnitude and simultaneously as-synthesized morphological motifs remain preserved. Well defined, uniform PANI morphology motifs are being produced by a template-free method, or using soft or hard templates. Soft templates are convenient for preparation of hollow carbon precursors. Furthermore, PANI can be additionally doped. Recently, metal-free, nitrogen-enriched carbons including nanoribbon, nanofiber and hierarchical porous carbon materials, that manifest supreme electrochemical characteristics, have been synthesized starting from PANI precursor [2,4,5]. Biomass molecules (alginate, hydrolyzed collagen, chitosan) as renewable, eco-friendly, easily decomposable at elevated temperatures, together with being the source of heteroatoms, have attracted considerable attention. For instance, collagen is nitrogen (17%) and oxygen (25%) enriched material compared to PANI (12% of nitrogen and 20% oxygen) [6].

Within this study, a composite of PANI and hydrolyzed collagen (PANI-Coll) was prepared and subsequently carbonized yielding nitrogen-doped carbon material (c-PANI-Coll) that was tested as electrocatalyst for ORR.

## EXPERIMENTAL

PANI-Coll precursor was synthesized by mixing (1000 rpm) 0.2 M aniline and 0.2 M ammoniumpersulfate aqueous solutions in the presence of 10.0 g of collagen. As-synthesized PANI-Coll precursor was carbonized in a quartz reactor of Carbolite CTF 12/75/700 tube furnace. Heating rate of 10 °C min<sup>-1</sup> up to the temperature of 800 °C was regulated by Eurotherm 815P Prog/Controller.

Morphology of c-PANI-Coll was inspected with a transmission electron microscope (TEM) HITACHI H-8100 at an accelerating voltage of 200 kV. Electrical conductivity of c-PANI-Coll was measured using LCR-6100 High Precision LCR Meter.

Cyclic voltammetry (CV) measurements were performed using Gamry PCI4/300 potentiostat/galvanostat in a conventional three-electrode glass cell. Platinum foil (1 cm<sup>2</sup>) was employed as counter electrode and saturated calomel electrode (SCE) as reference electrode. Working electrode was rotating glassy carbon disc electrode (cross-section 0.196 cm<sup>2</sup>) fully covered with 10 µL of c-PANI-Coll catalytic ink (5 mg of c-PANI-Coll in 125 µL of polyvinyl difluoride in N, N-methyl pyrrolidone). CVs were recorded in 0.1 M KOH aqueous solution in the potential range from 0 to -0.8 V at scan rate

of  $0.01 \text{ V s}^{-1}$ . Electrolyte was saturated with high-purity nitrogen or with oxygen gas for the ORR study.

## RESULTS AND DISCUSSION

Morphology of c-PANI-Coll examined by TEM shows hollow submicrospheres within outer diameters in the 180–295 nm range and inner diameters in the 40–140 nm range, **Figure 1A**. Hydrolyzed collagen served as a template for the formation of PANI-Coll composite spheres. The collagen core, if existed, was decomposed during the carbonization, while high temperature–resistive PANI shell maintained the shape of the precursor material.

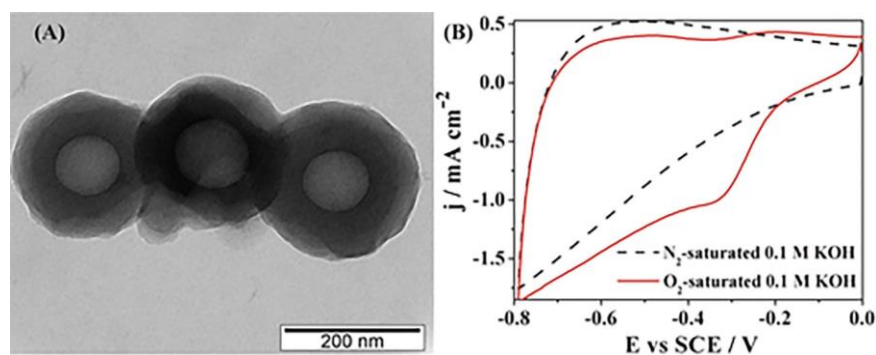


**Figure 1.** TEM image of c-PANI-Coll (A) with its CVs in 0.1 M KOH saturated with  $\text{N}_2$  (---) and with  $\text{O}_2$  (—).

The electrical conductivity of c-PANI-Coll was measured to have a high value of  $2.00 \text{ S cm}^{-1}$ . For comparison, electrical conductivity values ranging from  $0.32$  to  $0.85 \text{ S cm}^{-1}$  were previously reported for nitrogen-doped carbons synthesized by the carbonization of nanostructured PANI salt precursors: PANI 3,5-dinitrosalicylate (c-PANI-DNSA), PANI 5-sulfosalicylate (c-PANI-SSA), and PANI hydrogen sulfate (c-PANI) nanostructures [7].

Electrocatalytic activity of c-PANI-Coll towards ORR in alkaline media was subsequently investigated. CV of c-PANI-Coll in  $\text{N}_2$ -saturated 0.1 M KOH revealed no peaks, **Figure 1B**. Conversely, CV curves recorded in  $\text{O}_2$ -saturated 0.1 M KOH revealed a clear peak reaching current density of ca.  $1 \text{ mA cm}^{-2}$  at potential of ca.  $-0.3 \text{ V vs. SCE}$  corresponding to  $\text{O}_2$  reduction. ORR onset potential of ca.  $-0.18 \text{ V vs. SCE}$  was observed, being less negative than or comparable to that reported for ORR at c-PANI-DNSA ( $-0.22 \text{ V}$ ) and c-PANI ( $-0.18 \text{ V}$ ) [7], thus suggesting superior ORR activity of c-PANI-Coll. ORR Tafel slope at the electrode rotation rate of 1200 rpm

was evaluated to be  $-0.202 \text{ V dec}^{-1}$ . This value is comparable or higher than Tafel slope values reported for different carbon materials, such as ionic liquid-based carbon materials ( $-0.085 - -0.198 \text{ V dec}^{-1}$ ), nitrogen-doped mesoporous graphene framework ( $0.115 \text{ V dec}^{-1}$ ) and iron(II) phthalocyanine-based nitrogen doped carbon nanotube ( $0.087$  and  $0.171 \text{ V dec}^{-1}$ ) [8].

## CONCLUSION

Novel carbon material c-PANI-Coll possesses high electrical conductivity and electrocatalytic activity towards ORR (low onset potential, high  $\text{O}_2$  reduction current density) together with supercapacitor properties. The advantage over other PANI-based carbon materials is the simple, low-cost and eco-friendly polymerization of the precursor material using bulk, renewable and naturally occurring resource (hydrolyzed collagen) as a soft template for the formation of hollow submicrospheres.

## Acknowledgement

This work was supported by the Ministry for Science of the Republic of Serbia (Project no. OI 172043)

## REFERENCES

- [1] J. Quílez-Bermejo, C. González-Gaitán, E. Morallón, D. Cazorla-Amorós, *Carbon*, 2017, **119**, 62-71.
- [2] J. Liu, N.P. Wickramaratne, S.Z. Qiao, M. Jaroniec, *Nat. Mater.*, 2015, **14**, 763-774.
- [3] X. Li, X. Xiang, Y. Liu, D. Xiao, *Appl. Surf. Sci.*, 2018, **442**, 476-486.
- [4] Z. Ye, F. Wang, C. Jia, K. Mu, M. Yu, Y. Lv, Z. Shao, *Chem. Eng. J.*, 2017, **330**, 1166-1173.
- [5] I. Pašti, M. Milojević-Rakić, K. Junker, D. Bajuk-Bogdanović, P. Walde, G. Ćirić-Marjanović, *Electrochim. Acta* 2017, **258**, 834-841.
- [6] M. Rahman, K. Dey, F. Parvin, N. Sharmin, R.A. Khan, B. Sarker, S. Nahar, S. Ghoshal, M.A. Khan, M.M. Billah, H.U. Zaman, A.M.S. Chowdhury, *Int. J. Polym. Mater.* 2011, **60**, 1056-1069.
- [7] N. Gavrilov, I. A. Pašti, M. Mitrić, J. Travas-Sejdić, G. Ćirić-Marjanović, S. V. Mentus, *J. Power Sources* 2012, **220**, 306-316.
- [8] N. Zdolšek, A. Dimitrijević, M. Bendova, J. Krstić, R. P. Rocha, J. L. Figueiredo, D. Bajuk-Bogdanović, T. Trtić-Petrović, B. Šljukić, *ChemElectroChem* 2018, **5**, 1037-1046. and references therein

## MODELING OF THE PROCESS OF ELECTROCHEMICAL CORROSION OF STEEL REINFORCEMENT IN CONCRETE USING THE BATCH BIMETAL SENSOR. EVALUATION OF THE PROTECTIVE EFFECT OF DEEP PENETRATION HYDROPHOBIZATORS

D.S.Shevtsov, I.D. Zarcyn and E.S.Komarova

*Voronezh State University, Universitetskaya pl., 1, 394006, Voronezh,  
Russia ([shevtsov@chem.vsu.ru](mailto:shevtsov@chem.vsu.ru))*

### ABSTRACT

The possibility of using a bimetallic batch sensor for modeling the corrosion rate of reinforcement in concrete contaminated with chlorides is given. A test based on humidification / drying cycles to determine the effectiveness of secondary protection methods using a bimetallic batch sensor is introduced. The protective effect of a hydrophobisator grounded on isobutyltriethoxysilane under depassivation of reinforcement due to a high concentration of chloride ions is shown.

### INTRODUCTION

Corrosion of reinforced concrete is a complex physic-chemical process. To reveal the corrosion process at an early stage (reinforcement depassivation) and its deceleration or suppression is an important problem.

Hydrophobic processing is one of the ways to protect the secondary concrete under chloride corrosion. A wide range of different compositions makes it difficult to choose the most optimum solution for the customer and the executor. Rapid evaluation of the effectiveness of secondary protection reinforced concrete materials is an important scientific and technical task.

Various methods for assessing the quality of primary concrete protection are offered: accelerated chloride threshold level test [1], rapid macro cell test [2], chloride ion threshold test [3] etc.

Each of them has its advantages and disadvantages and, is often, not applicable for evaluating the effectiveness of secondary protection, especially in the case of high specific electrical resistance of concrete. It was suggested to use a bimetallic batch sensor. N.D. Tomashov applied a similar device for atmospheric corrosion modeling [4]. K. Tuutti used an analogue for modelling the corrosion of reinforcement in concrete [5].

## EXPERIMENTAL

The corrosion modeling was performed using a bimetallic batch sensor. The device is a set of steel (0.25 mm) and copper (0.10 mm) plates. The metals are separated by mica plates (0.20 mm). The plates are electrically interconnected. The plates were placed into epoxy resin to control the effective surface.

The sensor was placed into a fine concrete based on ordinary Portland cement with chloride, relative to the weight of cement: 0,00 (control); 0,10; 0,40; 1,00 and 3,25  $\text{mass}\%$ .

Measurement of the potential of free corrosion of the metal was performed using a voltmeter with high input resistance (10 M $\Omega$ ) [6]. The reference electrode was placed on the concrete surface, directly above the bimetallic batch sensor. The values are given relative to the copper-sulfate reference electrode. Specific electrical resistance of concrete on the surface was measured with Wenner sensor under direct current.

The hydrophobisator was applied to the concrete surface by spraying for two times. The consumption of the substance was 0.6 l/m<sup>2</sup> and was taken from the technical description.

The technique consisted of forced moisturizing cycles once per hour for 8 hours and cure at 100% relative humidity. Further, the samples were extracted and dried in the natural conditions of the laboratory.

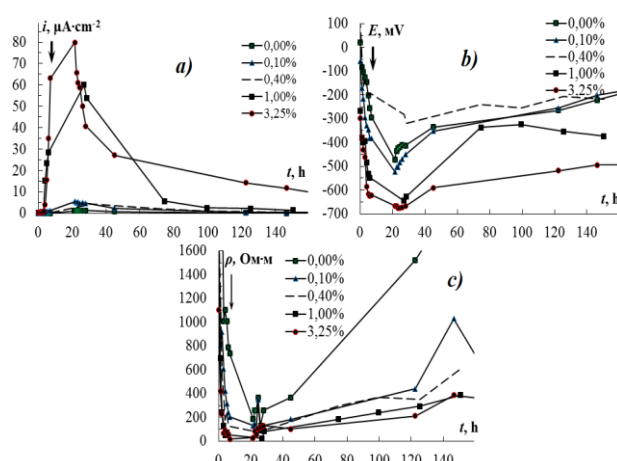


**Figure 1.** Dependence of  $i_{cor}$ (a),  $E_{cor}$ (b),  $\rho$ (c) on time during the cycles of wetting / drying for concrete with different chloride concentration,  $\text{mass}\%$ : 1 – 0.00; 2 – 0.10; 3 – 0.40; 4 – 1.00; 5 – 3.25. The vertical arrow indicates the humidification completion.

## RESULTS AND DISCUSSION

Initially, the bimetallic batch sensor was immersed in an aqueous extract of fine concrete to simulate pore liquid. Permanent state with current value of  $7.5 \pm 1.0 \mu\text{A}\cdot\text{cm}^{-2}$  in the solution without chlorides is achieved on the sensor.

With sodium chloride the current density ( $i_{cor}$ ) increases. The permanent state is not achieved during the experiment.

Three main stages of reinforced concrete lifecycle (Fig. 1) within the framework of the method of periodic structure wetting and drying have been established.

**I. Induction period** – the interval immediately after the beginning of the experiment. Concrete is saturated with water. Free corrosion potential ( $E_{cor}$ ) is shifted in the negative direction. The values of the potential of free corrosion more negative -350 mV correspond to the active corrosion of reinforcing steel under a layer of concrete [6]. The specific electrical resistance ( $\rho$ ) is also reduced. The value of  $i_{cor}$  is close to zero. The duration of the period depends on the chloride ions content and is from 3 to 7 hours.

**II. The period of intensive corrosion development** covers the end of moistening and the beginning of drying. The value of  $i_{cor}$  reaches the values of  $60 \mu\text{A}\cdot\text{cm}^{-2}$  and more by chloride content of more than  $1.00 \text{ mass}\%$ . This may correspond to a

significant corrosion rate (0.5-1.5 mm / year of steady destruction). The value of  $i_{cor}$  does not exceed  $\mu\text{A}\cdot\text{cm}^{-2}$  with the chloride content of  $0.40 \text{ mass}\%$  or less. The values of  $E_{cor}$  and  $\rho$  decrease and reach their minimum. The duration period is 1-2 days.

**III. The period of corrosion rate reduction** covers the completion of the drying period.  $i_{cor}$  monotonously decreases. Zero  $i_{cor}$

values are reached within 60-70 hours with low chloride content.  $i_{cor}$  does not reach zero during the experiment with high chloride content.

The effect of hydrophobisator based on izobutiltrietoksisilan (IBTES) on the suppressing of steel in concrete corrosion with different contents of

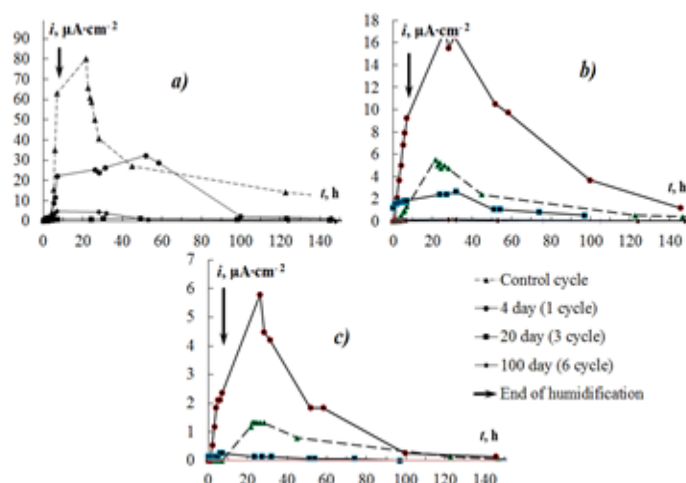


**Figure 2.** Dependence  $i_{cor}$  on time during the cycles of wetting / drying after hydrophobization for concrete with different chloride concentration,  $\text{mass}\%$ :  $a - 3.25$ ;  $b - 0.10$ ;  $c - 0.00$ . The vertical arrow indicates the completion of humidification.

chloride ions has been studied. The specific electrical resistance of all types of concrete has increased more than 10 times.  $i_{cor}$  is not fixed 2 weeks after the treatment with the chloride content of 0.00-0.40<sub>mass%</sub>.  $i_{cor}$  is reduced by more than 90% with the chloride content of 1.00<sub>mass%</sub> (Fig.2). An additional, no less than 5 times, treatment with a 3.0% solution of sodium chloride does not cause  $i_{cor}$  increase.

### CONCLUSION

The bimetallic package sensor can be used to evaluate the corrosion activity of the concrete environment in the presence of chlorides with respect to steel reinforcement without destroying the protective layer. Device can be used both in the laboratory and as an element of continuous monitoring of the reinforcement corrosion rate in real constructions.

A hydrophobisator based on IBTES effectively suppresses the corrosion process even in reinforced concrete with high concentration of chloride ions. The protective effect is probably based on the reduction of the amount of water in the capillary-pore structure of concrete. A significant increase in the electrical resistivity of concrete, in this case, is the result of a decrease in the amount of water.

### REFERENCES

- [1] D. Trejo, D.R. Miller, Determination of Chloride Corrosion Threshold for Metals Embedded in Cementitious Material, US Patent 6,646,427, 2003.
- [2] S.L. Martinez, D. Darwin, S.L. McCabe, C.E. Locke, *SL Report 90-4*, University of Kansas Center for Research, Lawrence, 1990.
- [3] ASTM G 109, Standard Test Method for Determining Effects of Chemical Admixtures on Corrosion of Embedded Steel Reinforcement in Concrete Exposed to Chloride Environments, 2013.
- [4] N.D. Tomashov, *Theory of Corrosion and Protection of Metals*, Moscow, 1960.
- [5] K. Tuutti, *Corrosion of Steel in Concrete*, Stockholm, 1982.
- [6] ASTM C 876-91, Standard Test Method for Half-Cell Potentials of Uncoated Reinforcing Steel in Concrete, 1999.

## SYNTHESIS, CHARACTERIZATION AND ELECTROCHEMICAL PROPERTIES OF $\text{Na}_{0.44}\text{MnO}_2$ IN $\text{NaNO}_3$ AND $\text{LiNO}_3$ AQUEOUS SOLUTION

A. Gezović<sup>1</sup>, M. Vujković<sup>1</sup>, D. Jugović<sup>2</sup>, I. Janković-Častvan<sup>3</sup>, I. Stojković Simatović<sup>1,\*</sup> and S. Mentus<sup>1,4</sup>

<sup>1</sup>University of Belgrade, Faculty of Physical Chemistry, Belgrade, Serbia.  
(ivana@ffh.bg.ac.rs)

<sup>2</sup>Institute of Technical Sciences of SASA, Belgrade, Serbia.

<sup>3</sup>University of Belgrade, Faculty of Technology and Metallurgy, Belgrade, Serbia

<sup>4</sup>Serbian Academy of Sciences and Arts, Belgrade, Serbia

### ABSTRACT

$\text{Na}_{0.44}\text{MnO}_2$  synthesized by glycine-nitrate method (GNM) was described in this paper and it was characterized by X-ray powder diffraction (XRD) and field-emission scanning electron microscopy (FE-SEM). Electrochemical performances of  $\text{Na}_{0.44}\text{MnO}_2$  were studied by cycling voltammetry (CV) at various scan rates in  $\text{NaNO}_3$  and  $\text{LiNO}_3$  aqueous solutions in order to compare the intercalation/deintercalation kinetics of  $\text{Li}^+$  and  $\text{Na}^+$  ions. The initial discharge capacity was found to be 27.1 and 27.44 in the aqueous solution of  $\text{NaNO}_3$  and  $\text{LiNO}_3$ , respectively, and after 30 cycles its values increased for 12% in both electrolytes.

### INTRODUCTION

The rechargeable batteries are seen as one of the most promising system for energy conversion and storage. Lithium-ion batteries (LIBs) are the most investigate type of rechargeable battery, due to its specific energy and specific power, high energy density storage, small weight and long life time [1]. In recent years, the development of the sodium-ion batteries (SIBs) has become more attractive, owing to the low cost and natural abundance of sodium, as well as the physicochemical similarity with lithium. The working principle of SIBs is identical to LIBs. One of the main problems of SIBs is the larger radius of Na-ion than of Li-ion, which could cause more difficult intercalation compared to Li-ion [2]. Until now investigated LIBs and SIBs use highly toxic and flammable organic solvents which have low ionic conductivity and high price. Aqueous LIBs and SIBs have a series of advantages: they do not contain flammable organic electrolytes, the ionic conductivities of the aqueous electrolyte is about two orders of magnitude higher than in nonaqueous electrolyte and the electrolyte salt and solvent are

cheaper. Manganese oxides, vanadium oxide or phosphates are used as electrode materials (cathodic and anodic) in both types of batteries. Li–Mn–O or Na–Mn–O systems with tunnel or layered crystal structures are the mostly used type of manganese oxides as electrode materials.  $\text{Na}_{0.44}\text{MnO}_2$  (NMO) have been synthesized by different methods such as hydrothermal process, thermo-chemical conversion process, polymer-pyrolysis process, molten salt technique, electrostatic spinning method, spray pyrolysis process and spray drying process [3]. In this work NMO was synthesized by glycine-nitrate method (GNM), which, according to the literature, has not been used for synthesis of this material so far.

### EXPERIMENTAL

$\text{NaNO}_3$  and  $\text{Mn}(\text{NO}_3)_2$  aqueous solutions were mixed in ratio corresponding to a stoichiometric ratio of Na/Mn in NMO. The glycine was added to the mixture with molar ratio of glycine-to-nitrate 1.2. The resulting precursor solution was placed in a glass beaker and heated in an oven until spontaneous ignition occurred. The obtained powder was heated in the air at  $900\text{ }^\circ\text{C}$  for 4 h.

The structure of synthesized powder was characterized by X-ray diffraction (XRD) and XRD pattern was recorded at Philips PW-1050 over a  $2\theta$  range  $10\text{--}70^\circ$  with a step of  $0.05^\circ$  and a counting time of 5 s. The morphology of the synthesized powder was analyzed by FE-SEM (TESCAN, MIRA 3 XMU) at 20 kV. The electrochemical behavior of NMO was investigated by cyclic voltammetry (CV) at various scan rates, in both  $\text{NaNO}_3$  and  $\text{LiNO}_3$  aqueous solutions using Gamry PCI4/300 Potentiostat/Galvanostat/ZR

A in three-electrode cell. A platinum foil was used as a counter electrode, saturated calomel electrode (SCE) was used as a reference electrode and the working electrode was made of NMO powder (85%), carbon black (10%) and polyvinylidene fluoride (5%) in N-methyl-2-pyrrolidone as solvent. The suspension was homogenized in an ultrasonic bath to form homogeneous slurry and afterwards transferred on

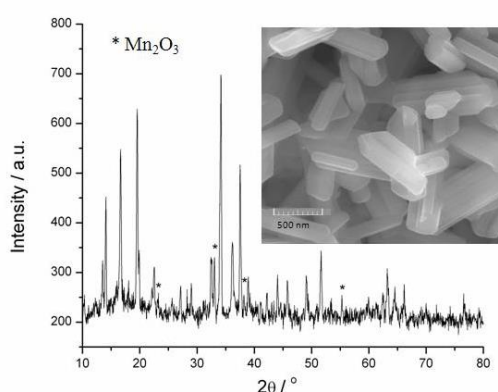


**Figure 1.** XRD pattern and FE-SEM image of  $\text{Na}_{0.44}\text{MnO}_2$ . The asterisk shows the positions of  $\text{Mn}_2\text{O}_3$  reflections.

glassy carbon rod and dried under vacuum 10-2 mbar at 140°C for 4h.

## RESULTS AND DISCUSSION

Fig. 1 shows the XRD pattern of the synthesized material. The sharp diffraction peaks indicated that the product was well-crystallized and was identified as orthorhombic structured of  $\text{Na}_{0.44}\text{MnO}_2$  with *Pbam* space group (JCPDS No.27-0750). A minor amount of impurities was detected and identified as  $\text{Mn}_2\text{O}_3$  (JCPDS No.41-1442) [3]. The FE-SEM images of NMO indicated that the powder consisted of uniform rod-like particles and the average width and length of particles were found to be ~80 nm and ~800 nm, respectively, Fig 1.

Cyclic voltammograms of NMO recorded in  $\text{NaNO}_3$  and  $\text{LiNO}_3$  aqueous solutions, by high polarization scan rates from 20 to 400  $\text{mV s}^{-1}$  within the voltage range -1.30 to 1.35 V vs. SCE, are shown on Fig. 2. For both solutions, the shape of CV's and peaks position were similar for all rates which means that process of intercalation/deintercalation of  $\text{Li}^+$  and  $\text{Na}^+$  are reversible and synthesized material can be used in lithium and sodium batteries. In  $\text{NaNO}_3$  electrolyte at a polarization rate of 20  $\text{mVs}^{-1}$ , NMO showed three anodic peaks at the potential 0.005, 0.723 and 1.168 V and two cathodic peaks at the potentials of 0.4 and - 0.32 V vs. SCE. In the case of  $\text{LiNO}_3$  as an electrolyte, the three anodic peaks were present at the potential 0.116, 0.649 and 1.206 V while two cathodic peaks were at the potential 0.729 and - 0.242 V vs. SCE.

The initial discharge capacity of NMO in  $\text{NaNO}_3$  and  $\text{LiNO}_3$  aqueous solution at the polarization rate of 20  $\text{mV s}^{-1}$  is 27.1 and 27.4  $\text{mAh g}^{-1}$  while

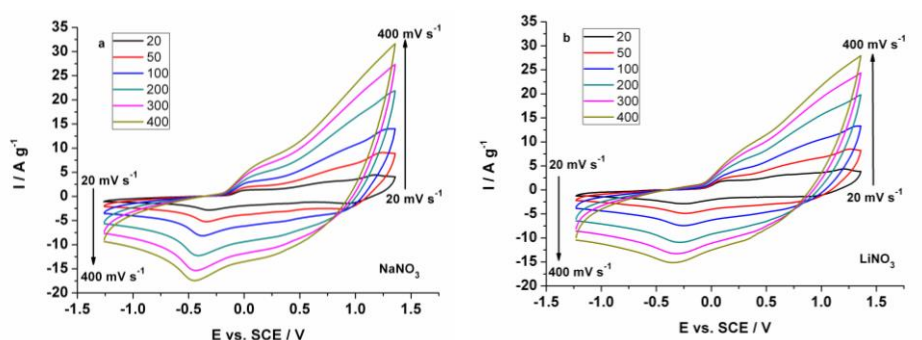


**Figure 2.** CV's of  $\text{Na}_{0.44}\text{MnO}_2$  in aqueous solution of a)  $\text{NaNO}_3$  and b)  $\text{LiNO}_3$  at scan rate of 20, 50, 100, 200, 300 and 400  $\text{mVs}^{-1}$ .

initial charge capacity is 30.6 and 30.5 mAh g<sup>-1</sup>, respectively. The discharge capacity of NMO in NaNO<sub>3</sub> and LiNO<sub>3</sub> electrolytes, after 30 cycles, at the same polarization rate, was increased to values 51.1 and 53.3 mAh g<sup>-1</sup>, while charge capacity was 50.8 and 53.9 mAh g<sup>-1</sup>, respectively. With the increase in polarization rates from 20 to 400 mVs<sup>-1</sup>, the discharge capacity decreases to 14.6 and 13.3 mAh g<sup>-1</sup>, and charge capacity decreases to 14.8 and 12.8 mAh g<sup>-1</sup>, in both NaNO<sub>3</sub> and LiNO<sub>3</sub>, respectively.

### CONCLUSION

In summary, Na<sub>0.44</sub>MnO<sub>2</sub> was successfully synthesized by glycine-nitrate method and the powder consisted of uniform rod-like particles. The intercalation/deintercalation of lithium and sodium ions in synthesized material were reversible in NaNO<sub>3</sub> and LiNO<sub>3</sub> aqueous electrolyte which indicated that Na<sub>0.44</sub>MnO<sub>2</sub> synthesized by glycine-nitrate method can be used as the positive material in lithium and sodium aqueous batteries.

### *Acknowledgement*

This work was supported by the Ministry of Sciences and Environmental Protection of Serbia (Project III 45014) and SANU (Electrocatalysis in the contemporary process of energy conversion).

### REFERENCES

- [1] E.C. Evarts, Nature Vol 526, pp 93-95, 2015.
- [2] A. M. Skundin, T. L. Kulova and A. B. Yaroslavtsev, Russian Journal of Electrochemistry Vol 54, pp. 131–174, 2018.
- [3] M. Vujković, B. Sljukić, I. Stojković-Simatović, M. Mitrić, C. Sequeira, S. Mentus, Electrochim. Acta Vol. 147, pp. 167, 2014.
- [4] X. Zhou, R. K. Guduru, P. Mohantya, J. Mater. Chem. A Vol 1, pp 2757-2761, 2013.

## APPLICATION OF A MODIFIED METHOD OF POLARIZATION RESISTANCE (MANSFELD METHOD) FOR CALCULATING THE RATE OF CORROSION OF REINFORCED STEEL IN CONCRETE

E.S. Komarova, D.S. Shevtsov and I.D. Zarcyn

*Voronezh State University, Universitetskaya pl., 1, 394006, Voronezh,  
Russia ([komarova.ekaterina2312@yandex.ru](mailto:komarova.ekaterina2312@yandex.ru))*

### ABSTRACT

The possibility of using the Mansfeld method for quantitatively determining the rate of corrosion of reinforced steel in concrete in the framework of the method of measuring the polarization resistance is shown experimentally. Compliance with qualitative and semi-quantitative non-destructive methods of corrosion monitoring of reinforcement in concrete has been established.

### INTRODUCTION

Steel in concrete is in a passive state. When aggressive ions penetrate to the surface of the reinforcement or as a result of carbonization, the passive state of the reinforcement is disrupted. The method of measuring polarization resistance ( $R_p$ ) is used to quantify the corrosion rate ( $i_{cor}$ ).

The expression for computation of the  $i_{cor}$  can be written as:  $i_{cor} = \frac{B}{R_p}$  (1).

The constant B is calculated from equation  $B = \frac{b_a b_c}{2.303 \cdot (b_a + b_c)}$  (2).

Measurement of linear polarization resistance (LPR) is the most common. Within the LPR method, the constant B is not directly determined, but 50 mV is assumed for the passive state and 25 mV for the active state.  $R_p$  is calculated as the ratio  $\Delta E/\Delta i$ . It is assumed that the linearity of the polarization curve is near  $E_{cor}$ . The total determination error can be 2-4 times relative to the real corrosion rate.

F. Mansfeld proposed a method of calculation, which was devoid of shortcomings of the LPR method [1]. The polarization curve near  $E_{cor}$  can

be analytically expressed as 
$$i = i_{cor} \left[ \exp\left(\frac{E - E_{cor}}{b_a/2.303}\right) - \exp\left(-\frac{E - E_{cor}}{b_c/2.303}\right) \right] \quad (3)$$

Substituting equation (1) taking into account (2) in equation (3), we can obtain the following equation:

$$2.3 \cdot R_p \cdot i = \frac{b_a b_c}{2.303 \cdot (b_a + b_c)} \cdot \left[ \exp\left(\frac{E - E_{cor}}{b_a / 2.303}\right) - \exp\left(-\frac{E - E_{cor}}{b_c / 2.303}\right) \right] \quad (4)$$

Then the graph at the coordinates  $(2.3 \cdot R_p \cdot i) - (E - E_{cor})$  is plotted (Fig.1). After this, using the computer program, this dependence is determined.

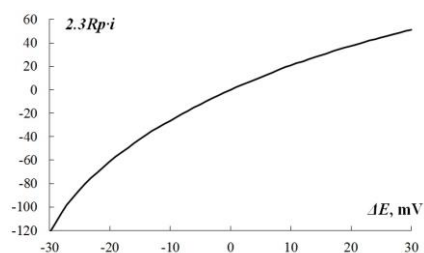


**Figure 1.** The graph at the coordinates  $(2.3 \cdot R_p \cdot i) - (E - E_{cor})$

The polarization curve is recorded in the interval  $\pm 30$  mV from  $E_{cor}$ . The activation of the metal due to external polarization does not occur with this formulation of the experiment.

The coefficients  $b_a$  and  $b_c$  (the Tafel slopes of the cathode and anodic half reactions) act as approximation parameters.  $R_p$  is calculated as the reciprocal of the derivative of the current density from the change in potential at the value  $E_{cor}$ . Thus, all the components of equation (1) are obtained within the framework of one experiment.

## EXPERIMENTAL

The experiments were carried out on steel grade 35GS according to GOST 5781-82 (analogue of steel BSt420S) in an aqueous extract of finely divided concrete and under a layer of concrete. The studies were carried out using a three electrode cell. The samples of concrete were made on the basis of ordinary Portland cement with different chloride content relative to the cement mass: 0.00; 0.40 and 1.00 wt%. Two reinforced bars and a bimetallic batch sensor were mounted in the concrete. The sensor was used as a comparison system [2-3]. Samples were held in a chamber with a constant relative humidity of 100%. Measurement of  $E_{cor}$  was made on the surface of concrete. The values of  $E_{cor}$  are given in relation to the copper-sulfate reference electrode. The specific electrical resistance of concrete was measured using a Wenner sensor. The current on the bimetallic package sensor was measured with a milliamperimeter with a fission rate of  $1 \mu\text{A}$ .

## RESULTS AND DISCUSSION

The growth of  $i_{cor}$  and the corrosion of steel in the aqueous extract of concrete was established only at chloride concentrations of  $1.00 \text{ mol/dm}^3$  (Table 1).

**Table 1.** Dependence of  $i_{cor}$  for steel in aqueous extract of concrete.

$C_{Cl^-}$ , mol/dm <sup>3</sup>	$i_{cor}$ , $\mu\text{A}/\text{cm}^2$
0.00	1.7±0.3
10 <sup>-3</sup>	1.3±0.3
10 <sup>-1</sup>	1.9±0.7
5·10 <sup>-1</sup>	1.8±0.3
1.00	2.6±0.6

A monotonic increase in the mass of concrete samples was established with an increase in the residence time in a chamber with a constant relative humidity of 100%. The mass of the sample tends to the limit value. Concretes with a high chloride content have a larger mass increase. This is due to the increase in hygroscopicity. The curves for samples without chlorides and with a content of 0.40 wt% are hardly distinguishable.

The specific electrical conductivity of concrete also increases with

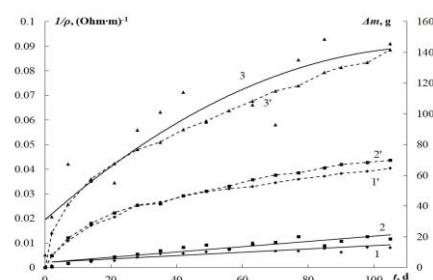


**Figure 2.** Dependence of specific electrical conductivity of concrete (1-3) and an increase in the mass of the samples relative to the initial value (1'-3') for samples of concrete with chloride content, mass%: 1, 1' - 0.00; 2, 2' - 0.40; 3, 3' - 1.00

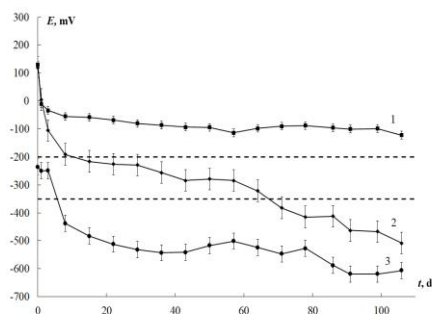


**Figure 3.** Dependence of  $E_{cor}$  for concrete samples with chloride content, mass%: 1 – 0.00; 2 - 0.40; 3 - 1.00. The area between the two dashed lines corresponds to undefined state

the active region is accompanied by the registration of the current on the bimetallic package sensor. Low corrosion rates of reinforcement for samples of concretes without chlorides and with an additive of 0.40 mass% (Fig. 4)

increase of the residence time in chamber with a constant relative humidity of 100% (Fig. 2).

It is shown that reinforced steel in concrete without chlorides is in a passive state; at a chloride content of 0.40% by weight is in an undefined state, after 70 days it passes into an active one; a rapid transition to the active corrosion zone is observed at 1.00 mass% in accordance with the criteria [4] (Fig. 3). The transition to

were experimentally recorded, almost linear growth of  $i_{cor}$  is observed with a chloride content of 1.00% by weight. Exceeding the value of  $i_{cor} > 1 \mu\text{A}/\text{cm}^2$  is observed after 20-30 days of soaking. In this case, there is active corrosion of the reinforcement in accordance with [5]. A correspondence has been established between the onset of active corrosion and the recording of current on a bimetallic package sensor (Fig. 4, dotted line).

Based on the calculations, the results of the  $E_{cor}$  measurement for samples with a chloride content of 0.40 mass% are refined. The condition of the valve is defined as passive.

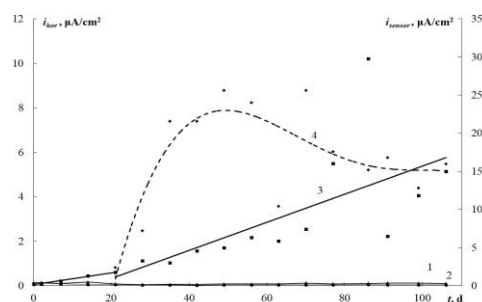


**Figure 4.** Dependence of  $i_{cor}$  for concrete samples with chloride content, mass%: 1 – 0.00; 2 - 0.40; 3 - 1.00 and the current density at the sensor,  $i_{sensor}$ , (4) of the time.

## CONCLUSION

The possibility of using the Mansfield method for calculating the rate of corrosion of reinforced steel in concrete under conditions of chloride activation is shown experimentally. A correspondence was established between the values obtained and the literature data, as well as the results of simultaneous measurements using qualitative methods for measuring the potential of free corrosion and resistivity and semi-quantitative measurements on a bimetallic package sensor.

## REFERENCES

- [1] F. Mansfeld, Advances in corrosion science and technology, 1976, **6**, 163-262.
- [2] K. Tuutti, Corrosion of Steel in Concrete, Stockholm, 1982.
- [3] I.D. Zarcyn, D.S. Shevtsov, Corrosion: materials and protection (Russia), 2018, **2**, 31-40.
- [4] B. Elsener, C. Andrade, C. Alonso, J. Gulikers et al, Material and Structures, 2003, **36**, 461-471.
- [5] C. Andrade, C. Alonso, J. Gulikers, R. Polder et al, Material and Structures, 2004, **37**, 623-643.

## MODIFICATION OF HPMC ASSAY FOR DETERMINATION OF ANTIOXIDANT ACTIVITY OF SAMPLES POORLY SOLUBLE IN WATER

F T. Pastor<sup>1</sup>, D. Ž. Sužnjević<sup>2</sup> and S. Ž. Gorjanović<sup>2</sup>

<sup>1</sup>University of Belgrade, Faculty of Chemistry, 11000 Belgrade, Serbia

<sup>2</sup>Institute of General and Physical Chemistry, 11158 Belgrade, Serbia

### ABSTRACT

The anodic current developed in an alkaline solution of H<sub>2</sub>O<sub>2</sub> at the potential of mercury oxidation was used to determine antioxidant activity of samples soluble in water applying direct current polarography. The aim of this work was to change the working solution by introducing optimal quantity of solvent such as ethanol, methanol, acetone and DMSO in Clark & Lubs (CL) buffer (pH 9.8). Ethanol was chosen as the most appropriate solvent. Modified HPMC assay procedure was applied on samples poorly soluble in water such as phenolics and terpenes present in spices.

### INTRODUCTION

Both direct current polarography (DCP) and differential pulse polarography (DPP) were applied to determine antioxidant (AO) activity [1-4]. Recently developed and optimized DCP assay for AO activity determination [1] was validated and widely used [4]. The assay is based on the decrease of anodic limiting current of [Hg(O<sub>2</sub>H)(OH)] (HydroxoPerhydroxoMercury(II) Complex-HPMC), formed in alkaline solution (CL buffer, pH 9.8) of H<sub>2</sub>O<sub>2</sub>, at potential of mercury oxidation, occurring upon AO addition. The aim of this work was to expand applicability of HPMC assay onto samples poorly soluble in water.

### EXPERIMENTAL

The current-potential (*i-E*) curves were recorded using the polarographic analyzer PAR (Princeton Applied Research), model 174A, equipped with X-Y recorder (Houston Omnigraphic 2000). A dropping mercury electrode (DME) with a programmed dropping time of 1 s as a working electrode, a saturated calomel electrode (SCE) as a reference and a Pt-foil as an auxiliary one were used. The intensity of HPMC anodic limiting current, i.e. the height of HPMC current peak, was plotted vs the concentration of H<sub>2</sub>O<sub>2</sub>.

**The influence of organic solvents on HPMC current formation** Aliquots of 1.00 M H<sub>2</sub>O<sub>2</sub> were added to 19.9 mL of working solutions prepared by

mixing 96 % ethanol, acetone, DMSO and methanol with Clark Lubb's (CL) buffer (pH 9.8) in the ratio 1:1.

Five aliquots of 2.00 mL of 96 % ethanol and 10  $\mu\text{L}$  of 1.00 M  $\text{H}_2\text{O}_2$  (to keep  $\text{H}_2\text{O}_2$  concentration constant) were added to 10 mL of 5.0 mmol/L solution of  $\text{H}_2\text{O}_2$  in 10 mL of CL buffer.

Five aliquots of 2.00 mL of CL buffer and 10  $\mu\text{L}$  of 1.00 M  $\text{H}_2\text{O}_2$  were added to 10 mL of 5.0 mmol/L solution of  $\text{H}_2\text{O}_2$  in 10 mL of 96 % ethanol.

The *i-E* curves were recorded. The intensity of each HPMC current recorded was plotted versus the volume of ethanol or CL buffer added.

**The application of HPMC assay to individual compounds** The aliquots of 25, 50 or 100  $\mu\text{L}$  of  $5 \times 10^{-3}$  M of individual phenolics and 100  $\mu\text{L}$  of  $1 \times 10^{-1}$  M of terpenoids were added gradually into the working solution containing 5 mM of  $\text{H}_2\text{O}_2$ . The phenolics and terpenoids were dissolved in 70 or 96% ethanol respectively. The *i-E* curves were recorded after each addition. The decrease of the initial anodic current of HPMC recorded upon each addition of investigated compounds was calculated and plotted versus their amount. The slope of dependence obtained (%/mol) was used as a criterion of AO activity of individual compounds.

## RESULTS AND DISCUSSION

The influence of four common solvents miscible with water (acetone, ethanol, methanol and DMSO), on the anodic current of HPMC formation in  $\text{H}_2\text{O}_2$  solution in Clark Lubs (CL) buffer (pH 9.8) was studied.

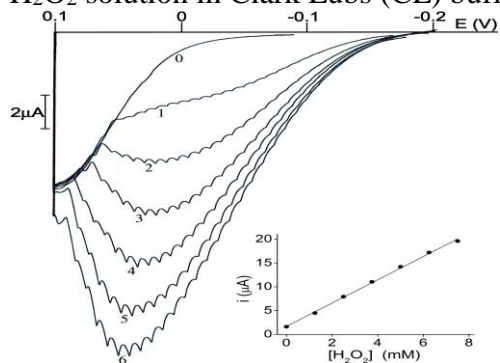


**Figure 1.** HPMC anodic current dependence on  $\text{H}_2\text{O}_2$  concentration in 1:1 mixture of CL buffer (pH 9.8) and 96 % ethanol: (0) 0, (1) 1.25, (2) 2.5, (3) 3.75, (4) 5.0, (5) 6.25 and (6) 7.5 mmol/L (insert: dependence of limiting anodic current  $i_1$  on  $\text{H}_2\text{O}_2$  concentration).

The dependence of HPMC limiting current intensity on  $\text{H}_2\text{O}_2$  concentration was followed in 1:1 mixture of CL buffer (pH 9.8) and solvents were chosen. In 1:1 mixture with 96 % ethanol very good linear dependence on  $\text{H}_2\text{O}_2$  concentration in the range 1.25-7.5 mmol/L shown in Fig.1 (insert), similar to the linearity reported in CL buffer without ethanol addition (1), is observed.

The HPMC current in mixtures containing constant concentration of peroxide but varying the ratio of ethanol and CL buffer was recorded. The dependence of anodic limiting current of HPMC recorded in 5.0 mmol/L solution of  $\text{H}_2\text{O}_2$  in CL buffer pH 9.8 before and after gradual addition of ethanol in portions of 2.0 mL until ratio 1:1 is reached as shown in Figure 2A. Almost constant intensity of HPMC current peak ( $i_1$ ) was obtained for ethanol content between 50 and 70%.

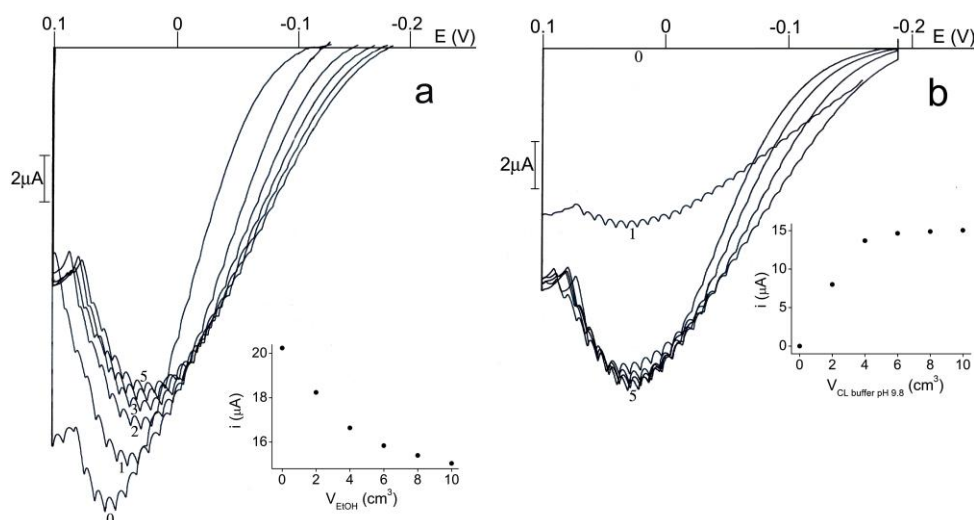


**Figure 2.** The dependence of HPMC anodic current intensity on the volume of ethanol added in 10 mL of 5.0 mmol/L  $\text{H}_2\text{O}_2$  in CL buffer (A) and on the volume of CL buffer added in 10 mL of 5.0 mmol/L  $\text{H}_2\text{O}_2$  in ethanol (B).

### The application of HPMC assay on individual compounds present in spices

Terpenes AO activity was found to be in good accordance with the results obtained by differential pulse polarography (DPP) in the working buffer containing 30 % of ethanol [3]. The AO activity of eugenol,  $\alpha$ -pinene, thymol, geraniol and D-limonene determined by DPP (68.25, 22.26, 18.68, 5.38, 5.23/mM) [2,3] was found in good correlation with obtained results ( $R^2 = 0.94$ ). Ratio between AO activity of eugenol, syringol and catechol was also found comparable with previously reported results [5]. As seen in Table 1, AO activity of terpenes is approximately two orders of magnitude lower than the activity of flavonoids. Such difference corresponds with chemical structure.

**Table 1.** Antioxidant activity of terpenes and phenolics determined by HPMC assay in 1:1 mixture of ethanol and CL buffer as a working solution.

Phenolics	HPMC (%/mol)	Terpenes	MC (%/mol)
Quercetin	$(38.50 \pm 3.00) \times 10^6$	<i>D-Carvone</i>	$(0.179 \pm 0.007) \times 10^6$
Rutin	$(23.92 \pm 0.41) \times 10^6$	<i>Linalool</i>	$(0.216 \pm 0.027) \times 10^6$
Chlorogenic acid	$(15.71 \pm 1.91) \times 10^6$	<i>p-Cymene</i>	$(0.112 \pm 0.006) \times 10^6$
Gallic acid	$(13.50 \pm 0.69) \times 10^6$	Camphor	$(0.149 \pm 0.004) \times 10^6$
Rosmarinic acid	$(23.12 \pm 0.60) \times 10^6$	Geraniol	$(0.159 \pm 0.004) \times 10^6$
Catechol	$(1.16 \pm 0.12) \times 10^6$	D-Limonene	$(0.130 \pm 0.016) \times 10^6$
Syringol	$(0.72 \pm 0.04) \times 10^6$	$\alpha$ -Pinene	$(0.250 \pm 0.020) \times 10^6$
Eugenol	$(0.50 \pm 0.02) \times 10^6$	<i>trans</i> -anethol	$(0.223 \pm 0.011) \times 10^6$
Thymol	$(0.14 \pm 0.01) \times 10^6$		

## CONCLUSION

The addition of ethanol to a working solution originally used in HPMC assay enabled its application to samples poorly soluble in water, such as terpenes or some flavonoids present in spices. Two orders of magnitude higher activity of flavonoids in comparison to terpenes corresponds with chemical structure.

## Acknowledgements

This work was supported by the Ministry of Education, Science and Technological Development, Republic of Serbia (Grant 43010).

## REFERENCES

- [1] Sužnjević et al, 2011. *Talanta* **85**: 1398–1403.
- [2] Palma et al, 2013. *J. Electrochem. Soc.* **160**: H213–H218.
- [3] Palma et al, 2014. *J. Agric Food Chem* **62**: 582–589.
- [4] Sužnjević et al, 2015. *Electrochim. Acta* **168**: 240–245.
- [5] Bortolomeazzi et al, 2007. *Food Chem.* **100**: 1481–1489.

*F–Biophysical Chemistry,  
EPR investigations of biosystems,  
Photochemistry,  
Radiation Chemistry*



## THE EFFECT OF THE MAGNETIC FIELD IN THE LIVING WORLD

D. Krstić<sup>1</sup>, N. Trifunović<sup>2</sup>, D. Zigar<sup>1</sup>, V. Marković<sup>3</sup> and Ž. Hederić<sup>4</sup>

<sup>1</sup> *University of Niš, Faculty of Occupational Safety,  
Čarnojevića 10a, 18000 Niš, Serbia. (dekikrs@gmail.com)*

<sup>2</sup> *Geoinstitut Beograd, Retired Geophysicst*

<sup>3</sup> *University of Niš, Faculty of Electronic engineering, Niš, Serbia*

<sup>4</sup> *University of Osijek, FERIT, Kneza Trpimira 2b, Osijek, Croatia*

### ABSTRACT

Scientific investigations of the biological effect of electromagnetic fields have taken the most of the consideration of the electrical component of the field. There are few studies that have analyzed the magnetic field and its effect on biological systems. The evolutionary development of a man went into the magnetic field, and the daily variation of the field is accompanied by the division of the cell. All this points to the significance of the natural magnetic field to the normal functioning of the human organism. In this paper are investigated the mechanisms of activity the magnetic field on materials which are an integral part of the human cell. Magnetic characterization of these materials is very important and therefore requires physical-chemical research of these compounds and magnetic typing of biological molecules, larger groups of biomolecules and organelles. The process of breathing oxygen exchange is explained by analyzing the magnetic properties of hemoglobin. Particularly, the forces on macromolecules in the non-homogeneous magnetic field of the cell were analyzed and given the macroscopic effects of continuous exposure of cells and organs to magnetic fields that are larger than the natural magnetic field of the earth. It was envisaged the connection of staying in reinforced magnetic fields with increasing the density of tissue and the induction of cancer. If there is a suitable magnetic field in the living space, a healthy area can be provided and the occurrence of certain diseases can be prevented.

### INTRODUCTION

The magnetic and gravitational field of the earth has influenced the development of all living organisms during evolution, and some species had developed instruments for the use of the magnetic field in the orientation in the environment. Contemporary research has increasingly confirmed that there is a magnetic field effect on other aspects of the living world. While

the gravitational field is constant, the magnetic field is poorly variable and it is the parameter of the environment that was ideal for a "fine" adjustment of life.

Urban space is most affected by electromagnetic pollution, with emphasis on changes in relation to the natural components of the electric and magnetic fields that superimpose with technically generated electromagnetic fields, forming new parameters of the environment in which a person resides. Insufficient knowledge of the influence about the action of electric and magnetic fields on biological processes in the normal functioning of a healthy organism define the guidelines for the investigation of potentially harmful effects of newly emerging fields (the development of technical communication systems, etc.).

The effects on the organism and its constituents depend of the strength of the electric and magnetic field in the biological matter. Also, it will depend on the incident field and the electromagnetic characteristics of the matter: dielectric constants, electrical conductivity, and magnetic susceptibility

Research has confirmed that the effects of magnetic fields on exposed organisms and their constituent parts depend on the intensity of field components present in the biological matter, that is, on the incidental field and electromagnetic characteristics of matter of the organism itself: dielectric constant, electrical conductivity and magnetic susceptibility. Particular emphasis should be placed on the connection of thermal effects in

On the other hand, studies of the influence of the magnetic field and the magnetic properties of the tissue have been completely ignored, assuming (wrongly) that the bulk of the biological tissue is of paramagnetic character, that the components of the magnetic field will not have a significant biological influence on the exposed tissue. In doing so, consideration was not given to the effect of the magnetic field on the microstructure of the cell and the cellular organelles, and their dominant influence on metabolism and the life of the cell.

#### **Physical phenomena of the action of the magnetic field on a matter**

The cause of magnetic field formation is the charge movement, and since there is a constant movement of charge in the atom, magnetism is the basic characteristic of matter and materials possess a certain amount of magnetic moments. It is explained by the orbital motion of the electron by its orbits and spin-like motion of the electron as well as rotary moving charges in the core.

Magnetic susceptibility  $\chi$ , quantitative measure of the extent to which a material may be magnetized in relation to a given applied magnetic field.

The magnetic susceptibility of a material is equal to the ratio of the magnetization  $M$  within the material to the applied magnetic field strength  $H$ ,  $\chi = M/H$ . This ratio, strictly speaking, is the volume susceptibility, because magnetization essentially involves a certain measure of magnetism (dipole moment) per unit volume. Materials that scatter the main field are called diamagnetic. Materials that concentrate the field are called paramagnetic, superparamagnetic, or ferromagnetic, depending on the magnitude of the effect.

Calcium salts (as found in cortical bone) are the most strongly diamagnetic substances in the human body. Nearly all biological tissues (muscle, fat, brain, liver, water) are also diamagnetic, but weakly so. Surprisingly, air is not susceptibility neutral but is slightly paramagnetic due to the presence of molecular oxygen.

It is important to point out that, force will be applied to the body in a non-homogeneous magnetic field, depending on the type of material, so that the field will tend to expel a diamagnetic object from that space (the force will be opposite from the direction of the magnetic field lines), and for the paramagnetic the ferromagnetic object of the force will be in the direction of the magnetic field.

### **Magnetic field and life**

The magnetic susceptibility of a substance which builds a human cell is responsible for the fine function of the human cell. Magnetic susceptibility at the molecular level and organelle level is significant for cell metabolism and the overall life of the cell.

The nature of the electrons within a sample determine the magnetic properties. The magnetic forces that are generated are mostly neutralized when two electrons become paired. Free unpaired electrons give rise to magnetic forces which are attracted to a magnetic field, and the strength of these attractive forces are in direct proportion to the number of free electrons. The presence of free electrons results in materials being classified as paramagnetic and the lack of them results in compounds being diamagnetic. Crystallinity, chemical reactions, oxidation states, and virtually anything that can alter the electronic configuration of a compound, may also change the magnetic properties.

**Magnetic susceptibility of organic molecules and parts of the organism****Table 1.** – Magnetic susceptibility of biological materials

Material	Volume Magnetic Susceptibility $\chi$ [ $\cdot 10^{-6}$ ]
Calcium carbonate	-13
Cortical bone	-11
Oxy-hemoglobin	-9.2
Water (& most tissues)	-9.0
Human tissues	-11 ÷ -7
Fat	-8.3
Whole blood	-7.4
Gadolinium in blood	+0.03
Hemoglobin molecules	+0.11
Methemoglobin	+0.12
Oxygen ( $O_2$ )	+0.37
Gadolinium in bladder	+13

**Table 2** - Mass magnetic susceptibility  $\chi_m$  [ $10^{-9} m^3 kg^{-1}$ ] of common ions,  $\chi = \chi_m \rho$ , [adopted by 14]

$H^+$	0	$Ba^{2+}$	2.9
$Na^+$	2.7	$Zn^{2+}$	1.9
$K^+$	4.2	$Al^{3+}$	0.9
$Cu^+$	2.4	$Ag^+$	2,8
$Ag^+$	2,8	$C^{4+}$	0,1
$NH_4^+$	8,0	$Mg^{2+}$	1,6
$Mg^{2+}$	1,6	$OH^-$	8,8
$Ca^{2+}$	2,5	$O_2^+$	9.4

The magnetic properties of the atoms and molecules originate from the magnetic moments of each individual electron and its motion around the nucleus and the spin movement as well as the motion of the positively charged nucleus around its axis. These magnetic moments are vector sizes and all of these magnetic moments in one molecule in accordance with the vector addition law generate the resulting magnetic moment of the molecule. In this way, a single magnetization vector representing a volume domain is obtained. Organic molecules are very often composed of a large number of atoms (hundreds or thousands of atoms) and represent complex spatial volumes in which electromagnetic forces dominate. In relation to the

volume domain occupied by one molecule of hydrogen, their volume domains are much larger, and the representation of them is one the magnetization vector cannot fully describe the forces that can occur on its individual parts in the electric and magnetic fields.

### **INTERACTION MECHANISMS BETWEEN MAGNETIC FIELDS AND BIOLOGIC SYSTEMS**

In order to correctly define the interaction mechanisms that affect biological systems exposed to electromagnetic fields, it is necessary to connect the electromagnetic nature of the biological substance (biological cells, molecules, atoms, ions) to the external electromagnetic field, and to classify the elemental physical phenomena of electromagnetism into measurable effects from the perspective of biomedical research.

The fundamental reaction of the force of the external electromagnetic field at a charge in motion is described by Lorentz force (Eq.1). Consequently in fluids occurs Hall Effect as separation of charge flow in the movement, which causes the appearance of transverse potential difference - magnetohydrodynamic (MHD) power generation (Eq.2). Magnetomechanical effects as next phenomenon to be described are associated with the polarization properties of the tissue (diamagnetic macromolecules) that cause the occurrence of the moment of rotation under the action of an external magnetic field.

For a long time, the component of the action of an external magnetic field on ferromagnetic and paramagnetic materials in biological tissue was neglected in the research. The development of microsystems and nano implants designed in modern medicine present increasingly probability of occurrence of the magnetic translation as the magnetomechanical force along the gradient direction (Eq.3).

The next level of observation should take into account time-varying magnetic fields, which can induce electrical currents in biological systems that can be evaluated by the Faraday law of induction (Eq.4). Finally, it is necessary to mention the effect of a magnetic field on a particle of magnetic or magnetizable material (such as a hemoglobin-bearing red blood cell) in a fluid that in medicine is investigated as a magnetophoresis. A similar effect to the retina or visual cortex is called Magnetophosphenes. The biological effects of the ELF magnetic field which consist of induction of visual sensations is essentially a change in the magnetic field that induces a current within the retina or visual cortex (resulting in the illusion of light).

The Lorentz force (external magnetic field  $\vec{B}$  and electric field  $E$ , the velocity  $\vec{v}$  of the charge  $q$ ), can be recognized as the effect of the interaction of magnetic fields with the cardiovascular system is the change in

electrocardiograms (ECG) as moving ionic charge carriers (electrolytes) in the blood.

$$\vec{F} = q\vec{E} + q(\vec{v} \times \vec{B}) \quad (1)$$

The Hall effect can be seen also in blood as result of Lorentz force that induces an electric potential given by:

$$\phi = v B d \sin \varphi \quad (2)$$

where  $v$  is the velocity,  $d$  is the diameter of the artery and  $\varphi$  is the angle between the direction of the blood flow and the magnetic field. For example, in a man with a blood flow rate of 0.6 m/s and an aortic diameter of 0.025 m, the expected induced potential is 15 mV/T [7].

Magnetomechanical effects of magnetic orientation of the diamagnetic macromolecules as effects happen at field strengths used in MR imaging systems. There are some interesting cases of orientations of living organisms that synthesizes magnetosome (specific organic chain structures) containing magnetite ( $\text{Fe}_3\text{O}_4$ ) crystals with a net permanent magnetic moment. To determine magnetic translation as the force on nanoscale implant in tissue must be calculated a magnetomechanical force in the gradient direction given by [15]:

$$F = V \cdot \frac{\mu}{\mu_0} \cdot B \cdot \frac{dB}{dx} \quad (3)$$

where  $V$  is the volume of the magnetic substance and  $\mu$  the magnetic susceptibility. In the case of sinusoidal fields with amplitude  $B_0$  and frequency  $f$  (Time-varying magnetic fields), the magnitude of the induced current density is given by:

$$J = \pi \cdot r \cdot f \cdot \sigma \cdot B_0, \quad (4)$$

where:  $r$  - radius of the induced currents loop,  $\sigma$  - electrical conductivity of the tissue. These currents are usually smaller than the nerve currents that connect our body with impulses.

### **MECHANISM OF MICRO ACTION OF MAGNETIC FIELD WITHIN A CELL**

All the previously mentioned effects clearly indicate the significance of the micromagnetic field effects on the functioning of the cell, which has so far been ignored. It was considered that the tissues have a high participation of water is mainly a paramagnetic substance on which the magnetic field has no significant effect. By examining the microcellular approach, the magnets of the characteristics of cell biomolecules or biological molecules, and the magnitude susceptibility of these molecules can explain the phenomena that classical medicine has not fully explained: breathing, cell division [12],

genesis of the cancer [9], autoimmune diseases [10], et cetera. Water is a good solvent and most of the compounds in the body underwater are subject to either a process of hydrolytic dissociation or hydrolysis resulting in ions that have altered magnetic properties, i.e. there is a change in the magnetic susceptibility in relation to the susceptibility of the compound from which they were derived. Generally, this change is aimed at generating paramagnetic that occur force on newly generated particles in the magnetic field.

For example, the compound that was a diamagnetic would be pushed out of the cell, that is, would act as a force from the nucleolus to the outside, and in the event that the paramagnet in the magnitude field of the nucleolus would be attracted to it.

There is little data on the magnetic properties, the magnetic susceptibility of biological substances, and even when there are data on pure compounds then magnetic susceptibility of ionic products of these substances and molecules in aqueous solution are not considered [5, 6].

Molecules are found in the magnetic field of the earth and the micromagnetic field of other molecules that surround them. Here we can speak of the effective micromagnetic field of larger groups of molecules which form biological entities as organelles or their parts. So we can talk about the magnetic field of the nucleus of the cell or the magnetic properties of the organelle, whereby this term implies an organelle acts as a magnetic dipole, an entity which generates a magnetic field in the space around it.

By the effect of this effective magnetic field on some domain of biological material (molecule or group of molecules) - the entity, there will be a change in the magnetic properties of that material-the entity if it is paramagnetic and ferromagnetic, and this phenomenon is called magnetization, which will have the magnetic properties changed. This effective external magnetic field acts on this entity and there occurs a force or torque that will lead to the startup of an entity in a fluid-viscous environment (such as intracellular or extracellular liquids). This activity will make it possible to bring the membrane closer and to enter or remove this entity from a space. More precisely, in the non-homogeneous magnetic field, the entities will be exposed to forces that will cause diamagnetic susceptibilities to be pushed out - remove from this space and paramagnetic and ferromagnetic substances into space. A simple mechanism it involves elementary knowledge of the physics of magnetism, but with interesting consequences for the processes in the cell.

The magnetic field in the cellular environment causes the following phenomena: magnetoseparation, the effect on the density of cellular fluids

by changing the intermolecular forces and changing the viscosity of the liquid.

### **Magnetoseparation**

Magnetic separation is a process in which magnetically susceptible material is extracted from a mixture using a magnetic force.

The need to separate unique cell types for use in therapeutics and diagnostics has been increasing dramatically over the past several years, not counting the current excitement concerning the isolation and use of human stem cells. The most popular methods to date for isolating desired cells have been fluorescence-activated cell scanning/sorting and magnetic cell separation [19].

There are methods for separating DNA from the cell material using magnetic fields, which shows that the nucleus and DNA are the places and the compound with the strongest magnetic characteristics. Using this physical phenomenon, it seems that the researcher has overlooked the fact that it must exist in the cell in a certain way. It is logical that magnetic separation is performed in the cell itself. If we accept that the nucleus is organelle with the highest magnetic properties, it will attract, ie, operate with a higher magnetic force on particles which have magnetic properties.

### **The effect on the density of cellular fluids by the change of intermolecular forces**

Increasing magnetic material properties in the presence of a magnetic field leads to an increase in the magnetic force of attraction, which is caused by a decrease in the molecular distance, resulting in an increase in the density of materials particular biological fluids, which for example leads to an increase in the density of body fluids or tissue density in a part of the space where there is an increased magnetic field. This will lead to a mild increase in tissue paramagnetism (a decrease in diamagnetism) which leads to an increased - accumulation in that part of the component space with paramagnetic molecules, leading in the end that individual tissues have higher magnetic characteristics than others. It called a viscous body magnetization (VBM),[9].

### **Changing the viscosity of the liquid**

The previous increase in the density of the liquid will be accompanied by a decrease in the viscosity - fluidity of body fluids, and in the blood vessels there will also be an additional decrease in viscosity due to the grouping of red blood cells rich in hemoglobin consisting of divalent iron which is ferromagnetic and which will be in the magnetized field additionally magnetized and lead to grouping of red blood cells, which will reduce the flow through the blood vessels [20].

## RESULTS AND DISCUSSION

### Clarification of biological phenomena in the light of the observation of the effect of magnetic fields on the human organism

#### *Proof that malignant cells are magnetized*

A new method of isolation from the blood of the cancer cell has been developed and in use [19]. It is based on the use of a magnetic field where blood flows across poles of a magnet, where cells are grouped and separated and sent to the lab for further testing. So it is clear that cancer cells are magnetized, i.e. have increased magnetic property, because they are formed in magnetic fields of greater intensity compared to the usual natural intensities of the earth magnetic field.

#### *The density of breast tissue and malignancies*

Breast tissue density in mammography that is equal to or greater than 75% is associated with an increased risk in relation to a mammographic finding without increased density [17, 18].

A good evidence that magnetic fields, increased intensity in relation to the natural magnetic field of the earth (anomalous magnet field - AMF), the cause of breast cancer is the density of the tissue (breast cell). After a prolonged stay at the AMF, the density of the tissue increases as a result of the production of VBM because the substances with paramagnetic characteristics are concentrated.

This feature can be used preventively until a para oncogene mutation has occurred in order to prevent cancer. The discovery of a higher breast density would require an intervention to remove a person from the AMF from the patient's living space and the onset of cancer would be prevented.

Measurement of breast tissue density should be used as an ancillary diagnostic tool at an early stage in the detection of malignant neoplasms of the breast, which is a much easier and cheaper procedure than looking for mutations of genes that are numerous and rarely the same.

#### *Breathing is contained by magnetic properties*

Breathing process is an exchange of  $O_2$  from the atmospheric air and  $CO_2$  from the blood. These gases exchange is done in alveoles and capillaries. Atmospheric air enters into alveoles (empty space) and capillaries (blood space) where the exchange of  $O_2$  and  $CO_2$  takes place.

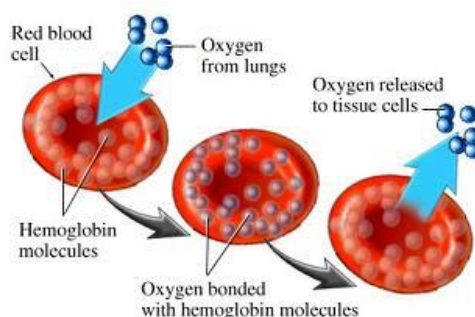


**Figure 1** - Oxygen exchange in erythrocyte

Dimension human cells are in average  $30\ \mu\text{m}$  another constituent of cells are capillaries  $30\ \mu\text{m}$ , erythrocyte  $7.8\ \mu\text{m}$ , phospholipid bilayer, and membrane pore  $4\text{-}10\text{nm}$ , molecule hemoglobin  $6.5\text{nm}$ , water molecule  $0.27\ \text{nm}$  and carbon atom  $0.34\text{nm}$ . Analyzing these dimensions, obviously, the red blood cell line cannot enter the cell, so that the molecule of hemoglobin does not penetrate the cell alone, because it would mean the destruction of the erythrocyte itself. How then is the process of oxygen exchange through hemoglobin?

The usual explanation for respiration is through diffusion and difference in the partial pressure of  $\text{O}_2$  and  $\text{CO}_2$  in the alveoli. Diffusion is a free moving of gas molecules from an area of higher concentration to the area of lower concentration, tending to equalize partial gas pressure, which is a tendency towards gas homogenization. Movements of molecules are random. Molecules collide and change their direction of movement.

Gyton [13] expresses a series of illogicalities in this way of explaining and practically disproves this hypothesis, but in the absence of other explanations, it is retained in medical education.  $\text{CO}_2$  makes molecular diffusion through respiration membranes are so rapid that the average partial pressure of  $\text{CO}_2$  ( $\text{PCO}_2$ ) in the blood of lung capillaries does not differ much from  $\text{PCO}_2$  in alveoles - the average difference is less than  $1\ \text{mmHg}$ -so that by today's methods such a small difference cannot be measured exactly [13].

The transfer of oxygen from the lungs to the tissues is carried out by loosely bonding between Fe in hemoglobin (Hgb) and oxygen  $\text{O}_2$ , thus creating an oxy-hemoglobin, unstable compound that can easily be broken down into Hgb and  $\text{O}_2$ . The magnetic properties of hemoglobin were described in 1936 by Pauling [16] and provided data on changes in the magnetic properties of oxy- and deoxy-hemoglobin. It is interesting that no one has hinted up the role of magnetic properties and the co-operation of these types of hemoglobin in the process of transmission and exchange of

oxygen between the red blood cell and the cell of the organism, except N. Trifunović [8].

Another fact is confirmed by the above. The worker in the caisson works in an atmosphere of increased pressure and the diver goes to the diving water and is exposed to increased pressures. It is known that the deeper the water the higher partial pressures become. For example, if the depth of water is 10 m pressure is 2 atmospheres, at the depth of 20 m pressure is 3 atmospheres etc. The partial pressure of  $O_2$  and Partial pressure of  $CO_2$  in the air under the water, also, gets higher, but the exchange of gases in diver's lungs is the same as on the surface.

The authors have arguments and are free to conclude that magnetic characteristics are the main factor in  $O_2$  and  $CO_2$  exchange. We suggest that this process is doing on next way:

- The red blood cell with hemoglobin in the oxidized state (oxy-hemoglobin) is transposed by a blood vessel system to a cell to be surrendered oxygen. This form of hemoglobin is a weak chemical bond between Fe in Hgb and oxygen  $O_2$ . This molecule is diamagnetic, although one end of it (the oxygen molecule has diamagnetic features). When approaching the cell, it is located in the non-homogeneous magnetic field of the cell, whereby the field is weakened by moving away from the center of the cell. It should be noted that the nucleus is the site with the strongest magnetic properties of the cell. This force will lead to the release of oxygen molecules. The molecule of the oxygen is a paramagnet and will be attracted to the nucleus, will pass through the pore of the cell and in the cytoplasm will allow oxidation and release of heat. Heat loss will drop its magnetic properties and lead to bonding with carbon and  $CO_2$  formation. Carbon dioxide is a paramagnet, and it will magnetically force out of the intracellular space.

- The red blood cell with hemoglobin in the form (deoxy-hemoglobin or methemoglobin) both paramagnetic go into the alveoli and the magnetic forces attract the molecule of the oxygen (paramagnet), and by binding it hemoglobin passes into oxy-hemoglobin. This is completely in accordance with the previously explained action of the particles in the magnetic field and formula 5. This completes the entire cycle of oxygen exchange, which is repeated cyclically in the same order.

$CO_2$  as a diamagnetic gets thrown out of cells, transports it into alveoli, from where through expirium it goes into the atmosphere.

## CONCLUSION

From all of the above, it is important to note that physical and chemical processes are the basis for the functioning of man. The basic forces in nature, both electric and magnetic, are constantly present in the functioning of the human body at the level of the cell. This paper points to the importance of understanding the magnetic characteristics of substances that build our body. From the point of view of the effect of magnetic forces, it is important to know the magnetic characteristics (properties) of cellular organelles, their parts to the constituent molecules themselves. The article deals with the explanation of the oxygen exchange process using the magnetic characteristics of hemoglobin and oxygen, the explanation of the role of the increased magnetic field in the formation of body viscous magnetization, the increase in the density of tissue and cancer. Knowing the action of the electric and magnetic fields on matter that builds the cell and its organelles will enable us to deepen the understanding of the process in the cell, which will ultimately lead to the elimination of problems in medicine and its development, while all other environmentalists will be provided with new knowledge as a technogenic development would not be at the expense of the nature and health of man.

## *Acknowledgment*

This work was partially supported by the Ministry for Science of the Republic of Serbia (III 43011 and III 43012).

## REFERENCES

- [1] Richard L. Liboff, A Biomagnetic Hypothesis, Biophysical Journal, Volume 5, Issue 6, November 1965, Pages 845-853.
- [2] De Ninno A, Pregolato M., Electromagnetic homeostasis and the role of low-amplitude electromagnetic fields on life organization, Electromagn Biol Med. 2017;36(2):115-122. doi: 10.1080/15368378.2016.1194293.
- [3] Liboff AR, Why are living things sensitive to weak magnetic fields?, Electromagn Biol Med. 2014 Sep; 33(3):241-5. doi: 10.3109/15368378.2013.809579.
- [4] Forms of Hemoglobin, On website „Questions and Answers in MRI“, Available on <http://mriquestions.com/types-of-hemoglobin.html>,
- [5] K. Frei & H. J. Bernstein, "Method for determining magnetic susceptibilities by NMR". J. Chem. Phys. 37 (8): 1891–1892. Bibcode:1962JChPh..37.1891F, 1962, doi:10.1063/1.1733393.
- [6] Marie Frenea-Robin, Noël Burais, François Buret, Naoufel Haddour, Laurent Nicolas, et al.. Electro magnetic characterization of biological

- cells. EHE'09: International Conference on Electromagnetic Fields, Health and Environment, Nov 2009, São Paulo, Brazil. 2009, bal-00435199.
- [7] P. Mansfield, P.G. Morris, *Biomagnetic effects*, (New York, Academic Press), Suppl. 2(1982) 247-252.
- [8] Trifunović N., Čizmić V., 2014 „Breathing Enable the Magnetic Properties of Erythrocytes (Hem Fe Oxygen, Cells and Carbon Dioxide“ *Journal of Health Science* 2 (2014) 270-283
- [9] Trifunović N, Čizmić V, 2015, „The Effect of Anomalous Magnetic Fields on Malignant Diseases“ *Open Access Library Journal* Vol2, No.4, April 2015 , DOI: 10.4236/oalib.1101459
- [10] Čizmić V, Trifunović N, 2016 „Cause of Autoimmune diseases Anomalous magnetic Fields“, *Journal of Pharmacy and Pharmacology* 4 (2016) 574-582.
- [11] Arthur Guyton, John Hall J, *Textbook of Medical Physiology*, Saunders Elsevier, 11th Edition, 2011.
- [12] Trifunovic N. Jevdic D. 2017. „Earth's magnetic field is factor that urges cell division. Reducing cell's magnetic characteristics occurs aging and death“. *World Journal of Pharmaceutical and life sciences (WJPLS)*, Available on <http://www.wjpls.org/download/article/12012017/1487054759.pdf>
- [13] John F. Schenck, The role of magnetic susceptibility in magnetic resonance imaging: MRI magnetic compatibility of the first and second kinds, *Medical Physics* 23, 815 (1996); doi: 10.1118/1.597854
- [14] J. M. D. Coey, *Magnetism and Magnetic Materials*, Cambridge University Press, 2009.
- [15] Zannella, S., Biological effects of magnetic fields, CAS - CERN Accelerator School: Measurement and Alignment of Accelerator and Detector Magnets, Anacapri, Italy, 11 - 17 Apr 1997, pp.375-386
- [16] Linus Pauling and Charles D. Coryell, The Magnetic Properties and Structure of Hemoglobin, Oxyhemoglobin and Carbonmonoxyhemoglobin, *Proc Natl Acad Sci USA*, 1936 Apr; 22(4): 210–216.
- [17] Ingrid Schreer, Dense breast tissue as an important risk factor for breast cancer and implications for early detection, *journal breast care (Bassel)*, 2009;4:89–92, April 24, 2009
- [18] McCormack VA, Santos S. I, Breast density and parenchymal patterns as markers of breast cancer risk: a meta-analysis, *Cancer Epidemiol Biomarkers Prev.* 2006 Jun; 15(6):1159-69.

- [19] Sim Siong Leong, Swee Pin Yeap, Jit Kang Lim, Working principle and application of magnetic separation for biomedical diagnostic at high- and low-field gradients, *Interface Focus*. 2016 Dec 6; 6(6): 20160048.
- [20] R.E Rosensweig, R.Kaiser, G.Miskolczy, Viscosity of magnetic fluid in a magnetic field, *Journal of Colloid and Interface Science*, Volume 29, Issue 4, April 1969, Pages 680-686.

## CEREBRAL ISCHEMIA AND HORMONE THERAPY AFFECT COMPONENTS OF PURINERGIC SIGNALLING

M. Zarić, I. Grković, N. Mitrović, I. Guševac Stojanović, J.  
Martinović and D. Drakulić

*University of Belgrade, VINČA Institute of Nuclear Sciences,  
Department of Molecular Biology and Endocrinology, Mike Petroviće Alasa  
12-14, 11001 Belgrade, Republic of Serbia. (drakulic@vin.bg.ac.rs)*

### ABSTRACT

Although ischemia/reperfusion (I/R) brain injury and steroid hormones effects are intensively investigated, their relationship with purinergic signaling components remains scarce. Thus, ecto-5'-nucleotidase (eN) activity was assessed by measuring rate of AMP hydrolysis in total membrane fractions of prefrontal cortex (PFC), hippocampus (HIP) and hypothalamus (HYP) in rat I/R model followed by a single dose of vehicle or dehydroepiandrosterone (DHEA). A significant post-ischemic eN activity increment was observed in all investigated brain regions, also after DHEA treatment in HYP, while in PFC and HIP of DHEA treated sham and I/R animals it was unaltered. Unchanged protein levels indicate that eN activity upregulation is governed by allosteric modulation of enzyme efficacy rather than *de novo* eN synthesis. Results imply that I/R and hormones could affect extracellular nucleoside levels and consequently control nucleoside-mediated cellular responses in regional specific manner.

### INTRODUCTION

The disturbance in oxygen and nutrient supply induced by sudden and transient (< 20 min) reduction of cerebral blood flow is cause of various pathophysiological events, like loss of ion pump homeostasis, intracellular Ca<sup>2+</sup> overload, excessive formation of free radicals that finally lead to brain hypoxia, cellular dysfunction and neuronal death. While initial restraint of blood supply pursued by later vascular restoration and associated reoxygenation is crucial for neuronal survival, it also exacerbates the tissue injury and induces additional brain damage, marked as "cerebral reperfusion injury". After cerebral ischemia/reperfusion (I/R) insult, the most prominent neuronal damage is observed in hippocampal CA1 neurons, cortical pyramidal neurons in layer III [1], as well as different hypothalamic cell types.

Various therapeutic strategies aim to protect brain from the deleterious ischemic effects by minimizing the activation of toxic pathways and increasing endogenous protective mechanisms. In recent years, several neuroprotectants are proposed, including circulating androgen precursor dehydroepiandrosterone (DHEA). Previous reports indicate that brain injury as well as hormonal therapy might provoke overall alterations in brain energy metabolism, resulting in modulation of ionic gradients and subsequent changes of membranes polarization. Within brain, these events might be interconnected with purinergic system. This complex signaling system is composed of three modulatory components: extracellular purine nucleotides, specific receptors and ectonucleotidases. Extracellular ATP acts *via* purinergic P2X and P2Y receptors and exhibits an important role in various cell functions, including maintenance of ionic gradients, protein and lipid synthesis, intracellular transport, neurotransmitter release and metabolism, as well as neuronal circuits modeling and control of synaptic plasticity. In extracellular environment, this short-lived molecule is rapidly metabolized to adenosine by members of ectonucleotidase family. The last and rate limiting step of extracellular ATP metabolism is catalyzed by ecto-5'-nucleotidase (eN) that hydrolyzes AMP to adenosine [2], [3]. Adenosine, a potent homeostatic regulator and also a neuromodulator at the synaptic level, has wide-ranging effects on neuronal and glial function in the brain *via* A1 and A2A receptors [4].

Since the association between brain injury, steroid hormone therapy and components of purinergic signaling is poorly understood, in the present study the rat I/R model and DHEA treatment were used to analyze extracellular AMP hydrolysis and eN expression in brain regions that might be affected by transient restriction of blood flow as well as hormone therapy.

## EXPERIMENTAL

Three-month-old male Wistar rats ( $n = 36$ , 350 – 400 g) were kept according to the compliance with European Communities Council Directive (2010/63/EU) for animal experiment, and the research procedures were approved by the Ethical Committee for the Use of Laboratory Animals of VINČA Institute of Nuclear Sciences, University of Belgrade, Republic of Serbia (Application No. 02/11). The animals were randomly divided into groups and 4 h following either sham or 15 min common carotid artery ligation, they were intraperitoneally injected either with vehicle (dimethyl sulfoxide, DMSO, 1.2 g/kg) or DHEA (dissolved in DMSO, 20 mg/kg). The rats from all experimental groups (control group – sham operated rats treated with DMSO, S + V; sham operated animals treated with DHEA,

S + D; I/R rats treated with DMSO, I/R + V; I/R animals treated with DHEA, I/R + D) were sacrificed 24 h postoperatively [1].

To examine the activity and protein expression of eN in prefrontal cortex (PFC), hippocampus (HIP) and hypothalamus (HYP), after decapitation and priority presented isolation of total membrane fractions [5], the samples were subjected to *in vitro* colorimetric assay for estimation of AMP hydrolysis under the conditions of initial velocity and substrate saturation, as well as immunoblot analysis using antibody against eN protein (anti-CD73 antibody, Cell Signaling Technology, Inc., Danvers, MA USA). Presented results were obtained from two independent isolations and all measurements were done in triplicate. Statistical significance was determined by two-way analysis of variance (two-way ANOVA) followed by Tukey's posthoc test using GraphPad Prism 6 Software. Data are presented as percents of the mean  $\pm$  SEM of control group. All results were considered significant at  $p < 0.05$  or less.

## RESULTS AND DISCUSSION

Our previous study shows that regional specific post-ischemic changes of pre- and postsynaptic markers of glutamatergic transmission (vGlu1 (vesicular glutamate transporter 1), PSD-95 (postsynaptic density protein 95), NR1 and NR2 subunits of NMDAR (N-methyl-D-Aspartate Receptor)) are accompanied with the signs of neuronal damage in the hippocampal CA1 area as well as histological changes in the layer III of PFC. In contrast, the expression of all investigated proteins and neuronal morphology are unaffected by DHEA *per se*, whereas DHEA treatment after I/R modulates investigated protein levels, pointing to reestablishment of NMDAR signaling [1]. Since the investigated proteins are essential for synaptogenesis and synapse maturation [3], their expression alterations might influence the molecular machinery vital for formation of new and disturbance of existing synapses, leading to synaptic rearrangements, remodeling of neuronal circuits and modulation of neuronal morphology.

Since synaptic rearrangements and signs of neuronal damage might be accompanied with alteration in ectonucleotidase activity and expression [3], the aim of current study was to analyze AMP hydrolysis rate and eN protein abundance in PFC, HIP and HYP under the influence of I/R and DHEA. In current experimental setup, the significant regional specific modulation of eN activities was observed using well defined eN enzyme assay, while Western blot analysis revealed the unchanged eN expression.

Regional changes in AMP hydrolysis after sham or I/R surgical procedure followed by a single dose of vehicle or DHEA were observed (**Figure 1.**), indicating that eN activity might be regional-specifically

influenced by both brain injury and hormonal therapy. The rates of AMP hydrolysis in PFC, HIP and HYP in control group were  $30.4 \pm 1.5$ ,  $76.3 \pm 1.8$ ,  $38.3 \pm 0.8$  nmol Pi/mg/min, respectively.

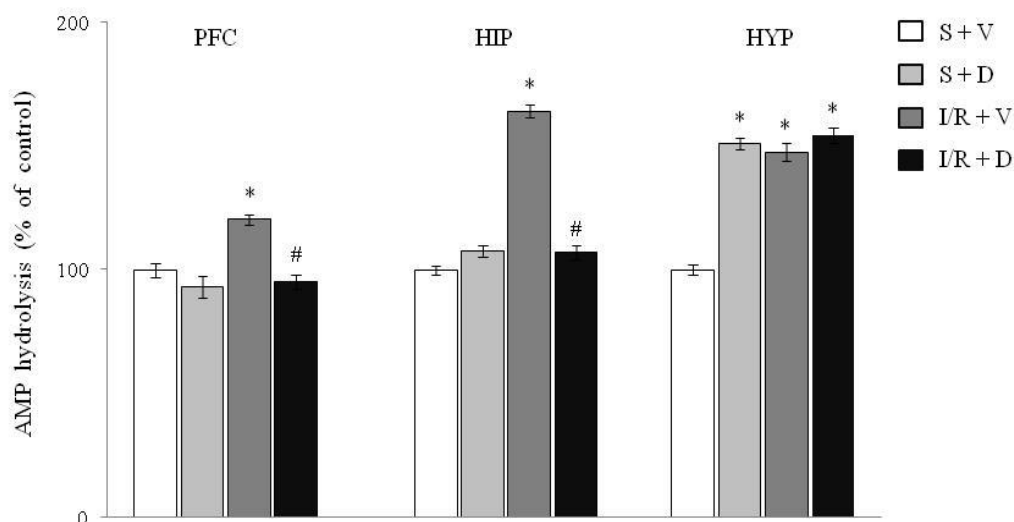


**Figure 1.** eN activity as a rate of AMP hydrolysis in total membrane fractions obtained from prefrontal cortex (PFC), hippocampus (HIP) and hypothalamus (HYP) of animals subjected either to sham or I/R surgical procedure followed by vehicle or DHEA treatment. Data are presented as the percent (%) of control AMP hydrolysis  $\pm$  SEM. Statistical analysis was performed using two-way ANOVA followed by Tukey's post-hoc test. \* $p < 0.05$  statistical significance compared to control group, # $p < 0.05$  statistical difference between I/R groups.

The observed alteration of AMP hydrolysis in pathological condition (I/R + V group) in all tested brain regions implies that eN is affected by disturbance of cerebral blood flow along with oxygen and nutrient supply. The literature emphasizes that brain injury and ensuing cell death provoke extensive release of ATP and other nucleotides into extracellular milieu [4], [6] which induce increment of intracellular  $Ca^{2+}$  both in neurons and glial cells by activation of specific receptors [4], [7]. The enhanced AMP hydrolysis may result in augmented production of adenosine in the extracellular space that influences the neuronal environment and glial cells function, as adenosine along with ATP and ADP affects synaptic transmission and neuronal excitability [8], [9]. Namely, adenosine *via* adenosine A1 and A2A receptors regulates the activity of cells by presynaptic inhibition or facilitation of neurotransmitter release or postsynaptic hyperpolarization or depolarization of neurons and/or

exhibiting nonsynaptic performance. For instance, it suppresses the release of glutamate by adenosine A1 receptors [4], [6] and as a consequence reduces its cytotoxic effects. Therefore, the observed increase of eN activity could create a tissue volume with upregulated ability of adenosine formation as an important compensatory mechanism to control a possible imbalance caused by I/R injury.

Under physiological conditions, DHEA induced the augmentation of AMP hydrolysis only in HYP, the brain region beyond blood brain barrier and the first brain area that is under direct influence of hormones. Moreover, in PFC and HIP, DHEA was inefficient in the modulation of AMP hydrolysis which could be correlated with unaffected levels of synaptic proteins and absence of morphological changes. Obtained results indicate that the upregulation of eN activity could be associated with biochemical and cellular events at the direct site of hormonal action, whereas unaltered eN activity in other tested brain regions could be a consequence of some general adaptive mechanism.

In PFC and HIP, DHEA treatment in I/R animals restored eN activity to control level, but had no effect on increased eN activity in HYP. Our results demonstrate that hormone-induced attenuation of I/R-promoted enhancement of eN activity is accompanied with the potential reestablishment of glutamatergic synapses in PFC and HIP, pointing to potential pharmacological effects of DHEA on components of purinergic and glutamatergic signaling.

Furthermore, the outcomes of brain injury and hormonal therapy on the eN expression in total membrane fractions obtained from PFC, HIP and HYP of animals subjected either to sham or I/R surgical procedure followed by vehicle or DHEA injections were determined by immunoblot analysis using eN-specific antibody. Although current study indicates significant region specific changes in the rate of AMP hydrolysis (**Figure 1.**), the pattern of protein expression was similar in all investigated brain regions (**Figure 2.**).

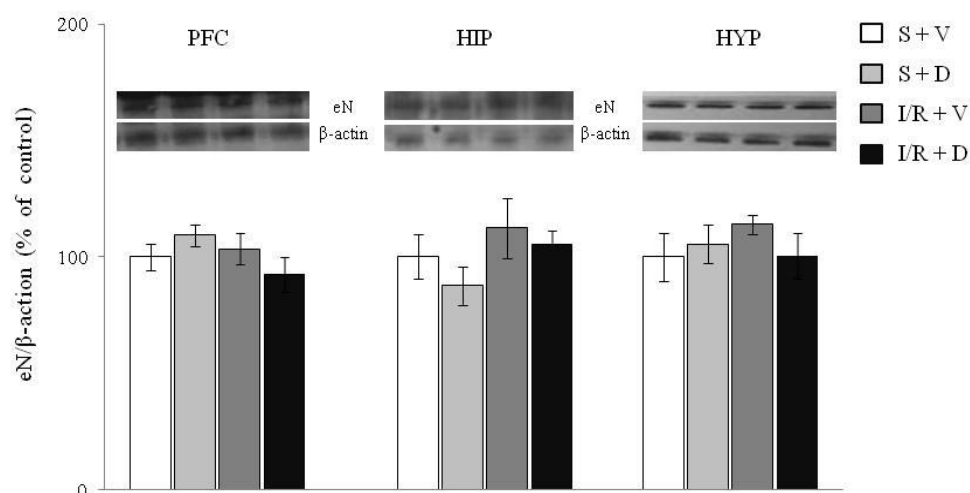


**Figure 2.** Representative immunoblots and eN protein abundances in total membrane fractions obtained from prefrontal cortex (PFC), hippocampus (HIP) and hypothalamus (HYP) of animals subjected either to sham or I/R surgical procedure followed by vehicle or DHEA treatment. Bars represent mean protein abundance/ $\beta$ -actin  $\pm$  SEM, whereas the values of the sham operated group treated with vehicle (S + V) are set as 100 %. Statistical analysis was performed using two-way ANOVA followed by Tukey's post-hoc test.

The unaltered protein levels might illustrate that eN activity upregulation is governed by allosteric modulation of enzyme catalytic efficacy rather than *de novo* eN protein synthesis. This assumption is confirmed by prior reports that point to nonessential association of the eN activity rate and enzyme protein levels [3], [10], [11], [12].

**Table 1.** Kinetic parameters

	$V_{\max}$ , $K_m$ and $V_{\max}/K_m$	
	Vehicle	Treatment
$V_{\max}$ (nmol Pi/mg/min)	$107.4 \pm 4$ .9	$103.5 \pm 6.7$
$K_m$ ( $\mu$ mol/l)	$47.7 \pm 4$ 6	$61.8 \pm 8.9$
$V_{\max}/K_m$	2.3	1.7

In our recent study the variations in the eN kinetic properties ( $V_{\max}$  and  $K_m$ , **Table 1.**) were tested in the presence of raising AMP concentrations (5 – 200  $\mu$ M). The Michaelis-Menten (**Figure 3A.**) and Eadie-Hofstee (**Figure 3B.**) reveal

that modulation of eN activity occurs due to changes of the enzyme affinity for substrate and consequent alteration of its catalytic efficiency [3].

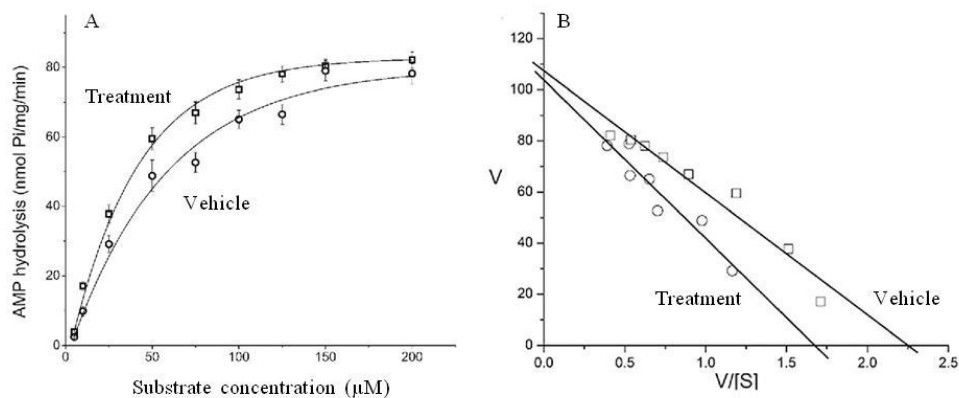


**Figure 3.** The eN kinetics plot. Kinetic representations of the eN properties. **(A)** Michaelis-Menten plot of velocity ( $V$ ) vs. AMP concentration ( $[S]$ ). Symbols specify mean activity (nmol Pi/mg/min)  $\pm$  SEM. **(B)** Linear semi-reciprocal Eadie-Hofstee plot of  $V$  vs.  $V/[S]$  from data presented at Michaelis-Menten plot.

## CONCLUSION

Presented results reveal that I/R injury upregulates eN activity in all tested brain regions, probably resulting in increased production of potent neuroprotector, adenosine. Moreover, DHEA alone and after I/R injury induces the regional-specific response and alteration in AMP hydrolysis. The similar pattern of protein expression was detected in all investigated brain regions, indicating that eN activity upregulation is governed by allosteric modulation of enzyme catalytic efficacy rather than *de novo* eN protein synthesis. Since the activity of eN depends on levels of its competitive suppressors in the extracellular milieu, ATP and ADP, which exhibit feed-forward inhibition towards eN [13], future studies are needed to determine ATP concentrations in the specific brain regions, as well as to define cell types and precise mechanisms involved in post-ischemic and hormonal control of nucleotide-mediated cellular responses.

## Acknowledgement

This work is supported by Ministry of Education, Science and Technological Development, Republic of Serbia (grants 173044 and 41014).

## REFERENCES

- [1] M. Zaric, D. Drakulic, I. Gusevac Stojanovic, N. Mitrovic, I. Grkovic, J. Martinovic, *Brain Res.*, 2018, **1688**, 73-80.

- [2] H. Zimmermann, M. Zebisch, N. Sträter, *Purinergic Signal.*, 2012, **8**, 37-502.
- [3] N. Mitrović, M. Zarić, D. Drakulić, J. Martinović, J. Sévigny, M. Stanojlović, N. Nedeljković, I. Grković, *J. Mol. Neurosci.*, 2017, **61**, 412-422.
- [4] F. Pedata, I. Dettori, E. Coppi, A. Melani, I. Fusco, R. A.M. Corradetti, Pugliese, *Neuropharmacology*, 2016, **104**, 105-30.
- [5] C.W. Cotman, D.A. Matthews, *Biochim. Biophys. Acta*, 1971, **249**, 380-394.
- [6] N. Nedeljkovic, I. Bjelobaba, S. Subasic, I. Lavrnja, S. Pekovic, D. Stojkov, A. Vjestica, Lj. Rakic, M Stojiljkovic, *Cell. Biol. Int.*, 2006, **30**, 541-546.
- [7] G. James, A.M. Butt. *Eur. J. Pharmacol.*, 2002, **447**, 247-60.
- [8] A.M. Sebastiao, J.A. Ribeiro. *Brain Res* 2015, 1621:102–113.
- [9] C.V. Gomes, M.P. Kaster, A.R. Tome, P.M. Agostinho, R.A. Cunha *Biochim. Biophys. Acta*, 2011, **1808**, 1380-1399.
- [10] I. Stanojević, I. Bjelobaba, N. Nedeljković, D. Drakulić, S. Petrović, M. Stojiljković, A. Horvat, *Int. J. Dev. Neurosci.*, 2011, **29**, 397-403.
- [11] D. Brisevac, I. Bjelobaba, A. Bajic, T. Clarner, M. Stojiljkovic, C. Beyer, P. Andjus, M. Kipp, N. Nedeljkovic. *Neurochem. Int.*, 2012, **61**, 681-8.
- [12] N. Mitrović, M. Zarić, D. Drakulić, J. Martinović, M. Stanojlović, J. Sévigny, A. Horvat, N. Nedeljković, I. Grković, *Neuroscience*, 2016, **324**, 286-296.
- [13] R.A. Cunha, *Neurochem. Int.*, 2001, **38**, 107-25.

## EFFECT OF POLYOXOMETALATES ON MEMBRANE ENZYMES

M. Čolović

*Department of Physical Chemistry, Vinča Institute of Nuclear Sciences,  
University of Belgrade, Serbia ([colovicm@vin.bg.ac.rs](mailto:colovicm@vin.bg.ac.rs))*

### ABSTRACT

12-tungstosilicic acid (WSiA) and decavanadate (V10) are polyoxometalate compounds (POMs) exhibiting biological activity. *In vitro* studies of the WSiA and V10 influence on synaptic plasma membrane (SPM) acetylcholinesterase (AChE) and Na,K-ATPase, showed that these POMs inhibit the enzyme activities in micromolar concentrations. As Na,K-ATPase and AChE are membrane associated enzymes, the inhibition of their activities can result from the membrane changes induced by the inhibitor binding. Thus, the effect of WSiA and V10 on the membrane structure was investigated by using Atomic Force Microscopy (AFM) technique. The obtained results demonstrated that the calculated average roughness values for WSiA and V10 treated SPM were significantly higher (about 6 and 1.5 times, respectively), compared to untreated SPM preparation. The obtained changes indicate that both investigated POMs bind to the plasma membranes, and consequently their approved strong inhibitory potencies toward the membrane bound enzymes might be assigned to the induced membrane modifications.

### INTRODUCTION

Polyoxometalates (POMs) are negatively charged inorganic compounds containing early transition metal ions in their highest oxidation state, surrounded by oxygen atoms [1]. These anionic complexes are relatively stable, some of them are even highly stable in aqueous solutions at physiological pH values [2]. Furthermore, POMs have been shown to exhibit biological activities *in vitro* as well as *in vivo*, including anticancer [3], antibacterial [4], antiviral [5], and antidiabetic [6] activities. However, their biological mechanisms of action at the molecular level are not well understood. Due to their anionic character and their high negative charge at physiologic pH values, POMs will hardly be able to penetrate cells [7]. Therefore, it has been speculated that POMs are likely to act extracellularly inhibiting several different enzyme families such as phosphatases, kinases, sulfotransferases, sialyltransferases, and ecto-nucleotidases, which are

mostly located on the plasma membrane and display extracellular binding sites [8].

Acetylcholinesterase (AChE) and Na,K-ATPase are membrane associated enzymes that catalyze key biochemical reactions. AChE (EC.3.1.1.7) is a membrane bound enzyme belonging to a group of serine hydrolases, and is involved in the termination of impulse transmission by rapid hydrolysis of the neurotransmitter acetylcholine in numerous cholinergic pathways in the central and peripheral nervous systems. The enzyme inactivation, induced by various inhibitors, leads to acetylcholine accumulation, hyperstimulation of nicotinic and muscarinic receptors, and disrupted neurotransmission [9]. Hence, AChE inhibitors, interacting with the enzyme as their primary target, are applied as relevant drugs and toxins. Reversible inhibitors mostly have therapeutic applications, while toxic effects are associated with irreversible AChE activity modulators. The inhibition of brain AChE is the major therapeutic target in the treatment of Alzheimer's disease associated with loss of cholinergic neurons in the brain and the decreased level of acetylcholine [10]. Na,K-ATPase is a heterodimeric transmembrane protein which regulates many cellular functions, including those associated with tumor cell growth. Published studies have suggested a role for Na,K-ATPase in regulation of cell growth and expression of particular subunits of Na,K-ATPase in some kinds of cancers. In addition, alterations in overall Na,K-ATPase activity and relative subunit abundance were observed in carcinoma cell lines obtained from a variety of tissues. Thus, Na,K-ATPase inhibitors could be considered as potential anti cancer therapeutics [11].

In this study the inhibitory influence of POM compounds, 12-tungstosilicic acid (WSiA) and decavanadate (V10) on synaptic plasma membrane (SPM) AChE and Na,K-ATPase activities is presented. As the activities of these membrane associated enzymes might be modified due to some membrane changes induced by the inhibitor binding, the effect of WSiA and V10 on the SPM structure was investigated by using Atomic Force Microscopy (AFM) technique as well.

## EXPERIMENTAL

### *Preparation of 12-tungstosilicic acid and decavanadate solutions*

WSiA ( $\text{H}_4\text{SiW}_{12}\text{O}_{40}$ ) was commercially available (Sigma Aldrich), and V10 ( $(\text{NH}_4)_6\text{V}_{10}\text{O}_{28}\cdot 5\text{H}_2\text{O}$ ) was synthesized [12, 13]. Stock solutions of WSiA and V10 ( $10^{-2}$  mol/L) were prepared daily, by solving the solid compounds in water shortly before use. Working solutions were prepared daily by diluting the stock solutions to desired concentrations. Preliminary studies

showed that the presence of WSiA (at  $5 \times 10^{-4}$  mol/L and lower concentrations) did not change pH of the medium assays.

#### ***Synaptic plasma membrane preparation***

SPM were isolated from the whole brain of 3-month-old male *Wistar albino* rats according to the method of Towle and Sze [14].

#### ***Na,K-ATPase assay***

The standard assay medium for investigation of Na,K-ATPase activity contained (in mmol/L): 50 Tris-HCl (pH 7.4), 100 NaCl, 20 KCl, 5 MgCl<sub>2</sub>, 2 ATP and 125 mg/L SPM proteins in a final volume of 200  $\mu$ L. Assay for SPM ecto-ATPase activity contained (in mmol/L): 50 Tris-HCl (pH 7.4), 5 MgCl<sub>2</sub>, 2 ATP and 125 mg/L SPM proteins. After preincubation for 10 min at 37°C in the absence (control) or in the presence of the investigated compounds, the reaction was initiated by addition of ATP and stopped after 10 min by adding 22  $\mu$ l ice cold of 3 mol/L HClO<sub>4</sub> and immediate cooling on ice. The released Pi liberated from the hydrolysis of ATP was determined by a modified spectrophotometric method [13, 15].

#### ***Acetylcholinesterase assay***

The AChE activity in the absence (control) and presence of the investigated compounds was determined by a slightly modified Ellman's method [16]. The experiments were performed by *in vitro* exposure of 20 $\mu$ L SPM preparation to the investigated POMs in 0.1 mol/L phosphate buffer pH 8.0 (final volume 0.650 mL). The standard medium assays were preincubated for 20 min at 37 °C in the absence or presence of the desired concentration of the POMs. Ten microliter acetylthiocholine iodide (0.075 mol/L) was used as the enzyme substrate in combination with 20  $\mu$ L DTNB (0.01 mol/L in 0.1 mol/L phosphate buffer pH 7.0) as a chromogenic reagent. The reaction was started by the addition of acetylthiocholine iodide (final concentration 0.001 mol/L), and allowed to proceed for 5 min at 37 °C until stopped by addition of 50  $\mu$ L SDS (10%). The released yellow product, 5-thio-2-nitrobenzoate was measured at 412 nm using Perkin Elmer Lambda 35 UV-VIS spectrophotometer (Shelton, USA). The AChE activity was expressed as the mean percentage of the enzyme activity relative to the corresponding control value. All experiments were performed in triplicate.

#### ***Atomic Force Microscopy experiments***

50  $\mu$ L of SPM preparation was mixed with 50  $\mu$ L of the investigated POM solution ( $1 \times 10^{-3}$  mol/L) (1:1), and then applied in drops onto a glass surface. The SPM preparation in combination with water (1:1) served as a control. The prepared samples dried overnight. AFM measurements were performed using a home-designed microscope [17] that can be operated under controlled environmental conditions. The AFM measurements were performed in air, at room temperature and constant 30% relative humidity.

The contact mode measurements were performed in the weak repulsive regime of constant force with a probe force below 1 nN from zero cantilever deflection. The high-resolution images have been collected at a scanning speed of 0.25–0.35 Hz.

## RESULTS AND DISCUSSION

### *The influence of decavanadate and 12-tungstosilicic acid on Na,K-ATPase activity*

The influence of V10 on SPM Na,K-ATPase activity was investigated by *in vitro* exposure to the enzyme in the concentration range from  $1 \times 10^{-10}$  to  $1 \times 10^{-3}$  mol/L [13]. The results showed that increasing concentrations of V10 induced the inhibition of the enzymatic activity in a concentration-dependent manner (Fig. 1). The dependence of the enzyme activity, expressed as a percentage of the control value (obtained without inhibitor), on inhibitor concentration fitted a sigmoidal function (Eq. (1), Fig. 1).

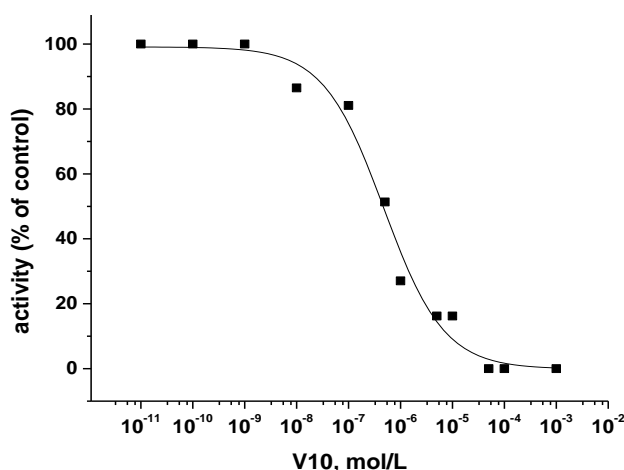


**Figure 1.** The concentration-dependent inhibition of SPM Na,K-ATPase by V10 [13].

The half-maximum inhibitory concentration ( $IC_{50}$ ) of the investigated compound was determined by sigmoidal fitting the experimental results.

$$y = \frac{A_1 - A_2}{1 + (x/x_0)^p} + A_2 \quad (1)$$

where  $x$  is  $c_{V10}$  (in mol/L),  $x_0$  is equal to  $IC_{50}$  value and  $y$  is activity (% of control).

IC<sub>50</sub> value of the enzyme activity was achieved at  $(4.74 \pm 1.15) \times 10^{-7}$  mol/L, and at the concentration of  $1 \times 10^{-5}$  mol/L V10 induced about 80% inhibition of Na,K-ATPase activity.

The results of inhibition study of WSiA also demonstrated concentration-dependent influence of increasing WSiA concentrations on SPM Na,K-ATPase activity, which fitted a sigmoidal function (Fig 2.) [15]. At WSiA concentration of  $(3.6 \pm 0.5) \times 10^{-6}$  mol/L, 50% of the control enzyme activity was obtained, suggesting the strong inhibitory potencies (in micromolar concentrations) of both investigated POMs.

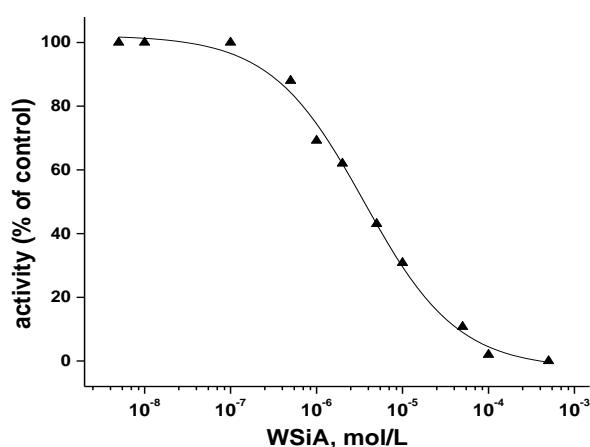


**Figure 2.** The concentration-dependent inhibition of SPM Na,K-ATPase by WSiA [15].

#### *The influence of decavanadate and 12-tungstosilicic acid on acetylcholinesterase activity*

The results of WSiA influence on SPM AChE showed that increasing WSiA concentrations induced the inhibition of the enzymatic activity in a concentration-dependent manner. The inhibition parameter, IC<sub>50</sub> value that is defined as the concentration of investigated compound with capability to inhibit 50% of the enzyme after given exposure time was achieved at  $6.2 \times 10^{-8}$  mol/L. The almost complete AChE inhibition was obtained even at WSiA concentrations higher than  $1 \times 10^{-6}$  mol/L, indicating a very strong sensitivity of AChE activity toward the investigated polyoxotungstate. On the contrary, the activity of AChE exposed to V10 concentration even of 1 mmol/L (and lower ones) was not changed.

***Effect of decavanadate and 12-tungstosilicic acid on synaptic plasma membrane roughness***

The image of the control SPM sample (without POM) obtained by AFM technique is presented in Fig. 3.

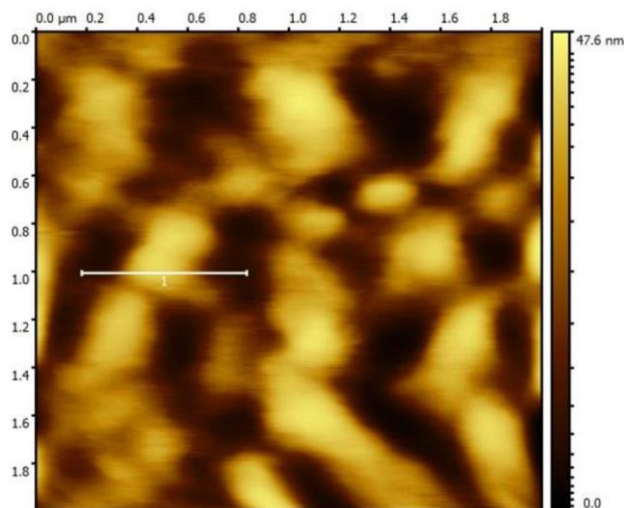


**Figure 3.** The image of the control SPM sample obtained by AFM technique.

The values of average roughness for the investigated POM (V10, WSiA)-SPM samples and control SPM were calculated and presented in Fig. 4. The obtained results demonstrate that the roughness value for the SPM after WSiA treatment significantly increased, more than 3 times, compared to the membrane roughness before the WSiA treatment (SPM alone). The presence of V10 also induced increase in the membrane roughness compared to the SPM control, but about 1.5 times.

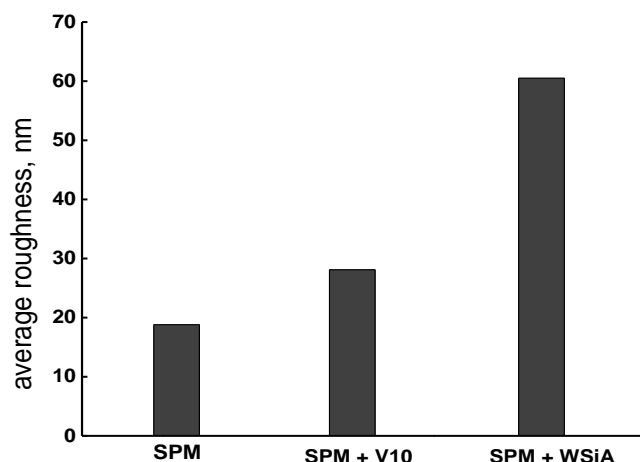


**Figure 4.** The calculated values of average roughness obtained for SPM before (SPM) and after V10 (SPM + V10), and WSiA (SPM + WSiA) treatment.

The obtained results indicate that both WSiA and V10 bind to the plasma membranes. Consequently, their previously approved strong inhibitory potencies ( $IC_{50}$  values in micromolar concentrations) toward the membrane bound enzymes (AChE and Na,K-ATPase) might be assigned to the induced membrane modifications.

## CONCLUSION

The studied polyoxometalates in this study, WSiA and V10, inhibit the activities of membrane associated enzymes, SPM AChE and Na,K-ATPase in micromolar concentrations. The results obtained by AFM technique demonstrate that both WSiA and V10 induce increase in average roughness values of SPM compared to the untreated SPM. Accordingly, it could be concluded that these compounds modify the plasma membrane structure, resulting in the affection of the membrane associated enzyme activities.

## Acknowledgement

This study was supported by the Ministry of Education, Science and Technological Development of the Republic of Serbia (Project No. 172023), and COST Action MP1302.

## REFERENCES

- [1] B. Hasenknopf, *Front. Biosci.*, 2005, **10**, 275–287.
- [2] G. Geisberger, S. Paulus, M. Carraro, M. Bonchio, G.R. Patzke, *Chem. Eur. J.*, 2011, **17**, 4619–4625.

- [3] X. Wang, J. Liu, J. Li, Y. Yang, J. Liu, B. Li, et al. *J. Inorg. Biochem.*, 2003, **94**, 279–284.
- [4] A. Seko, T. Yamase, K. Yamashita, *J. Inorg. Biochem.*, 2009, **103**, 1061–1066.
- [5] Y. Qi, Y. Xiang, J. Wang, Y. Qi, J. Li, J. Niu, et al. *Antiviral. Res.*, 2013, **100**, 392–398.
- [6] K. Nomiya, H. Torii, T. Hasegawa, Y. Nemoto, K. Nomura, K. Hashino, et al. *J. Inorg. Biochem.*, 2001, **86**, 657–667.
- [7] R. Prudent, V. Moucadet, B. Laudet, C. Barette, L. Lafanechere, B. Hasenknopf, et al. *Chem. Biol.*, 2008, **15**, 683–692.
- [8] S-Y. Lee, A. Fiene, W. Li, T. Hanck, K. Brylev, V. Fedorov, et al. *Biochem. Pharmacol.*, 2015, **93**, 171–181.
- [9] J. Bajgar, *Adv. Clin. Chem.*, 2004, **38**, 151–216.
- [10] M. Čolović, D. Krstić, T. Lazarević-Pašti, A. Bondžić, V. Vasić, 2013, **11**, 315–335.
- [11] V. Vasić, T. Momić, M. Petković, D. Krstić, *Sensors*, 2008, **8**, 8321–8360.
- [12] B. China, D. Dakternieks, A. Duthie, C.A. Ghilardi, P. Gili, A. Mederos, S. Midollini, A. Orlandini, *Inorg. Chim. Acta*, 2000, **298**, 172–177.
- [13] D. Krstić, M. Čolović, N. Bošnjaković-Pavlović, A. Spasojević-de Bire, V. Vasić, *Gen. Physiol. Biophys.*, 2009, **28**, 302–308.
- [14] A.C. Towle, P.Y. Sze, *J. Steroid Biochem.*, 1983, **18**, 135–143.
- [15] M.B. Čolović, D.V. Bajuk-Bogdanović, N.S. Avramović, I.D. Holclajtner-Antunović, N.S. Bošnjaković-Pavlović, V.M. Vasić, D.Z. Krstić, *Bioorgan. Med. Chem.*, 2011, **19**, 7063–7069.
- [16] G.L. Ellman, K.D. Courtney, V. Andreas, R.M. Featherstone, *Biochem. Pharmacol.*, 1961, **7**, 88–90.
- [17] A. Cricenti, R. Generosi, *Rev. Sci. Instrum.*, 1995, **66**, 2843–2847.

## AMINOXYL SPIN PROBES AS BLOOD BRAIN BARRIER INTEGRITY MARKERS – STILL A CHALLENGE AFTER 40 YEARS

A. Vesković<sup>1</sup>, A. Pavićević<sup>1</sup>, Đ. Nakarada<sup>1</sup>, B. Prokić<sup>2</sup>, M. Perović<sup>3</sup>, S. Kanazir<sup>3</sup>, M. Mojović<sup>1</sup> and A. Popović-Bijelić<sup>1</sup>

<sup>1</sup> EPR laboratory, University of Belgrade - Faculty of physical chemistry, Studentski trg 12-16, Belgrade, Serbia (ana@ffh.bg.ac.rs)

<sup>2</sup> University of Belgrade - Faculty of veterinary medicine, Bulevar oslobođenja 18, Belgrade, Serbia

<sup>3</sup> University of Belgrade - Institute for Biological Research "Siniša Stanković", Bulevar despota Stefana 142, Belgrade, Serbia

### ABSTRACT

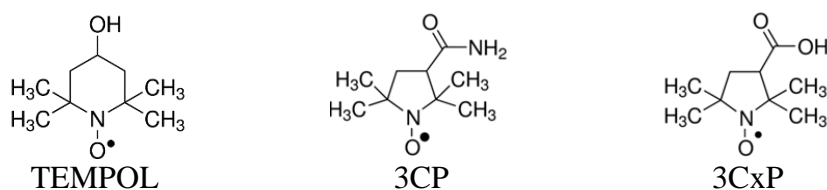
Aminoxyl radicals have been used extensively as EPR spin probes for the *in vivo* or *ex vivo* study of biosystems. Two piperidine-type probes, 3-carbamoyl-, and 3-carboxy- proxyl (3CP and 3CxP), have been proposed to be the most appropriate for the assessment of the blood brain barrier (BBB) integrity in experimental animal models for inflammatory and neurodegenerative disease, as it has been shown that they cannot pass BBB. In this study, we have re-evaluated their suitability in this respect, by recording EPR spectra of the brain tissues of healthy mice 20 min after the intravenous administration of the spin probes. The results indicate that both, 3CP and 3CxP (although to a smaller extent), can pass BBB, and that the permeability of BBB towards them is age-dependent and gender-independent. Furthermore, a 3D L-band EPR image shows that the spin probe is uniformly distributed in the brain tissue.

### INTRODUCTION

Aminoxyl radicals (nitroxides) are organic, usually heterocyclic molecules, with an unpaired electron localized on the NO group, sterically shielded by alkyl substituents. These stable spin probes are widely used in electron paramagnetic resonance (EPR) spectroscopy and imaging for the study of dynamic, structural, and functional properties of biological structures and biomolecules. Until now, a variety of spin probes have been synthesized and functionalized for their specific uses in EPR oximetry, pH measurements, tissue redox status estimation, spin labeling etc. In biological systems, the conversion of nitroxides to their EPR invisible forms, hydroxylamines or oxoammonium cations, is the result of their redox reactions with biological

compounds, enzymes or various oxidants, and occurs mainly within cells. Therefore, the potential of a spin probe to enter the cell, *i.e.* to pass the cell membrane, is an essential criterion for its particular application [1].

The pathogenesis of diabetes, cancer, and neurodegenerative diseases has been linked to the overproduction of reactive oxygen species (ROS), which results in oxidative stress. Specifically in neuroinflammation, and neurodegeneration, the altered redox status has been suggested to further lead to an impaired blood brain barrier (BBB) [2]. In quite a number of published papers, it has been suggested that specific nitroxides, which are cell membrane and/or BBB impermeable, may be used to evaluate the BBB integrity in ROS-related pathologies. The most often used nitroxides for *in vivo* investigations are derivatives of TEMPO (2,2,6,6-tetramethylpiperidine 1-oxyl), or PROXYL (2,2,5,5-tetramethylpyrrolodine 1-oxyl) radicals, Scheme 1.



**Scheme 1.** Structures of nitroxide free radicals TEMPOL, 3CP and 3CxP.

The slightly hydrophobic spin probe TEMPOL, is reduced quickly compared to the pyrrolidine-type (PROXYL) nitroxides, which can be explained by its piperidine ring structure, and the side groups that enable its great cell membrane permeability. The literature data shows that the hydrophilic 3-carbamoyl-PROXYL (3CP) is cell membrane permeable and BBB impermeable. On the other hand, 3-carboxy-PROXYL (3CxP), a hydrophilic and negatively charged molecule, due to its carboxylate substituent, is both, cell membrane and BBB impermeable (except by active anion transport) [3,4].

The aim of this study was to re-evaluate the applicability of PROXYL nitroxides, 3CP and 3CxP, for the assessment of the BBB integrity.

## EXPERIMENTAL

The EPR measurements were performed on Bruker E540 Elexsys II EPR spectrometer, on male and female, 4- and 9-month old, wild-type (WT) mice (3 per group). The animals were anesthetized and the spin probe (3CP or 3CxP) was injected in the tail vein. After 20 minutes, the animals were sacrificed and perfused. The brains were isolated and homogenates were prepared with physiological saline (1  $\mu$ l per mg of tissue) for *ex vivo* X-band

EPR experiments. EPR spectra were acquired immediately after brain isolation, and also after reoxidation with potassium ferricyanide. The experimental conditions were: microwave frequency 9.5 GHz, microwave power 10 mW, modulation amplitude 2 G, modulation frequency 100 kHz. The L-band *in vivo* 3D EPR image was taken on a 13-month-old female WT mouse using 3CP, with the following experimental conditions: microwave frequency 1.1 GHz, microwave power 3.6 mW, modulation amplitude 2 G, modulation frequency 30 kHz, gradient 20 G/cm.

## RESULTS AND DISCUSSION

The brain homogenates isolated from mice that had received 3CP and 3CxP intravenously, both displayed typical three-peak nitroxide EPR signals (an example for 3CxP is given in Figure 1). This implies that both spin probes had entered the brain tissue, contrary to the current literature data. The concentration of the spin probe per gram of brain tissue was determined from the intensity of the second peak in the EPR spectra recorded at nonsaturating microwave power levels and compared with 50  $\mu$ M 3CP or 3CxP, Table 1.

**Table 1.** The amount of 3CP and 3CxP per gram of brain tissue of 4- and 9-month-old female and male healthy mice, after 20 min of intravenous spin probe administration. The results are presented as mean  $\pm$  SD.

Mice		[ $\mu$ mol spin probe/g neural tissue]
	<i>3CP</i>	
Female 4 months		0.020 $\pm$ 0.005
Female 9 months		0.050 $\pm$ 0.015
	<i>3CxP</i>	
Female 9 months		0.030 $\pm$ 0.075
Male 9 months		0.030 $\pm$ 0.075

These results suggest that 3CP can pass BBB even in young healthy mice. More 3CP per gram of brain tissue of older mice can be attributed to age-related increase of BBB permeability. The experiments with 3CxP, which has been considered in literature as both, cell membrane, and BBB impermeable, were performed on 9-month-old female and male mice. The results show that 3CxP is also found in the brains of healthy mice, independent of the gender. By comparing the results for 3CP and 3CxP for 9-month-old females, it is observed that less 3CxP passes BBB of healthy mice, indicating that this spin probe is less BBB permeable than 3CP. To evaluate the spatial distribution of the spin probe in the brain, the *in vivo* 3D EPR image of a 13-month-old female mouse brain was recorded after intravenous 3CP administration,

Figure 2. It is clear that the spin probe is uniformly distributed throughout the brain tissue.

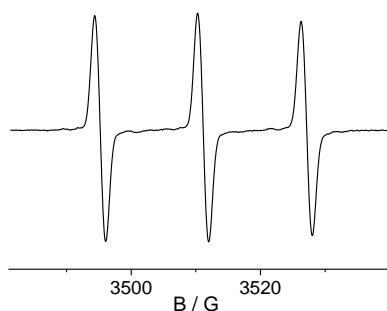


**Figure 1.** X-band EPR spectrum of 3CxP.

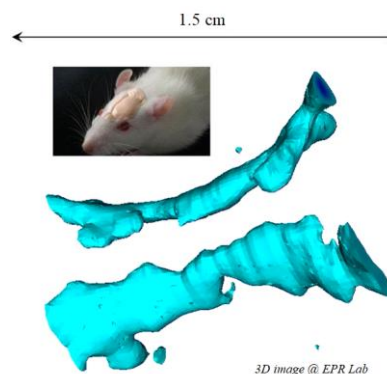


**Figure 2.** 3D L-band EPR image of a healthy 13-month-old female mouse brain after intravenous 3CP administration

## CONCLUSION

Two nitroxide spin probes, 3-carbamoyl-PROXYL (3CP), and 3-carboxy-PROXYL (3CxP) were detected by EPR in the brain tissue of healthy mice, 20 min after intravenous administration. The amount of the spin probe was found to be age-dependent, namely less probe entered the brains of younger mice, but not gender-dependent. Furthermore, BBB was less permeable for the anionic spin probe 3CxP. This suggests that these nitroxides may not be as suitable as proposed in literature for the assessment of the BBB impairment in inflammatory and neurodegenerative diseases. Future work is needed in the area of spin probe design and development, especially for the *in vivo* applications.

## Acknowledgement

This work was partially supported by the Ministry of Education, Science and Technological Development of the Republic of Serbia (Grants III41005 & 173056).

## REFERENCES

- [1] E. Bordignon, Encyclopedia of Magnetic Resonance, 2017, 6, 235-254.
- [2] M. Valko, *et al.* The International Journal of Biochemistry & Cell Biology, 2007, 39, 44-84.
- [3] Z. Zhelev, *et al.* Molecular BioSystems, 2012, 8, 2733-2740.
- [4] K. Matsumoto, *et al.* Magnetic Resonance in Medicine, 2016, 76(3), 935-945.

## ASSESSING CRISPR-Cas DESIGN PRINCIPLES BY BIOPHYSICAL MODELING

A. Rodić<sup>1</sup>, B. Blagojević<sup>2</sup>, M. R. Đorđević<sup>2</sup>, K. Severinov<sup>3,4</sup> and M. J. Đorđević<sup>1</sup>

<sup>1</sup> *University of Belgrade, Faculty of Biology, Studentski trg 16, 11000 Belgrade, Serbia. (andjela.rodic@bio.bg.ac.rs)*

<sup>2</sup> *Institute of Physics, University of Belgrade, Pregrevica 118, 11000 Belgrade, Serbia.*

<sup>3</sup> *Waksman Institute of Microbiology, Rutgers University, Frelinghuysen Road 190, 08854-8020 Piscataway, NJ, USA.*

<sup>4</sup> *Skolkovo Institute of Science and Technology, Nobelya Ulitsa 3, 121205 Moscow, Russia.*

### ABSTRACT

A number of biotechnological tools are based on the advanced bacterial immune system called CRISPR-Cas, but the activation dynamics of a native system in *E. coli* is poorly understood. Specifically, this system tends to stay silent even during infection by a bacteriophage, whose DNA is supposed to recognize and destroy, which hampers experimentally observing its activation dynamics. From previous research on CRISPR-Cas regulation, two distinctive regulatory features emerge: i) highly cooperative repression of both system promoters that can be abolished by some activators, and ii) fast non-specific degradation of a CRISPR transcript. To investigate the significance of these prominent system features, an artificial circuit design is proposed in which the unknown mechanism of system transcription induction is bypassed by putting *cas* genes under transcriptional control of another, well-explored bacterial immune system, restriction-modification system, with the same regulation principles.

### INTRODUCTION

Restriction-modification (R-M) systems encode a restriction enzyme which cuts specific DNA sequences, and a methyltransferase whose role is to methylate the same sequences in the host genome and protect them from cutting. CRISPR/Cas is a recently discovered, adaptive bacterial immune system in which Cas proteins are expressed from one promoter, while CRISPR array is transcribed from another one, into a long pre-crRNA. Cas6 protein cuts pre-crRNA into a large number of crRNAs (Fig. 1), which target Cas proteins to complementary foreign DNA to destroy it. Our group

previously modeled pre-crRNA processing upon Cas overexpression and the proposed model scheme is represented in Fig. 1a [1]. Regarding transcription regulation, qualitative similarities are noticed between CRISPR-Cas and the R-M system AhdI originally isolated from *Aeromonas hydrophila* (Fig. 1c): i) in AhdI, two dimers of control (C) protein bind with high cooperativity to the promoter governing transcription of the *c* gene itself and the restriction enzyme gene, and repress it, but binding of a second C dimer can be outcompeted by binding of RNA polymerase, ii) in CRISPR-Cas, very cooperative binding of H-NS proteins represses both promoters and can be abolished by binding of some activators, like LeuO, which also autoregulates transcription of its gene.

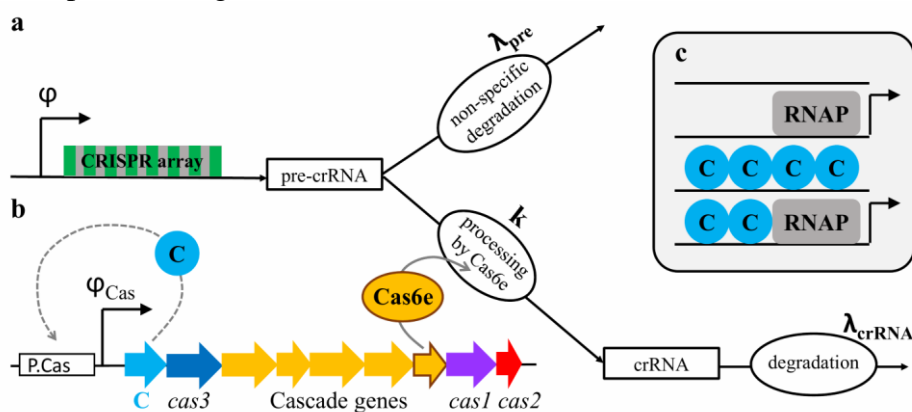


**Figure 1.** Schematical representation of the proposed setup for CRISPR-Cas activation. **a** Scheme of pre-crRNA processing into crRNA. Both pre-crRNA and crRNA can also be non-specifically degraded with denoted rate constants. **b** *cas* genes are put under control of the promoter from a R-M system (here named *P.Cas*), autoregulated by *C* protein. **c** Allowed configurations of *C* protein and RNA polymerase on the *P.Cas* promoter. Those transcriptionally active contain an arrow.

## EXPERIMENTAL

An artificial genetic circuit design was proposed and modeled in which *cas* genes are put under control of a promoter from the AhdI R-M system (Fig. 1b), which is autoregulated by binding of *C* dimers, as illustrated in Fig. 1c [2]. Transcription control of this promoter was previously studied in detail, both experimentally and by thermodynamic modeling [3]. CRISPR-Cas system is induced by introducing *cas* genes on a plasmid in a cell which already contains the CRISPR array. Three dynamical (sub)models are set and analyzed: i) the *baseline model*, in which crRNA production is induced by an abrupt increase of pre-crRNA processing rate  $k$  to its final value, ii) the

*constitutive model*, in which *cas* genes are constitutively expressed, and iii) the *cooperative model*, in which *cas* promoter is regulated by C proteins.

## RESULTS AND DISCUSSION

Amounts of crRNA at 20 min from the start of *cas* genes expression were predicted by all three of the constructed models, for different values of the pre-crRNA processing rate that are reached in equilibrium following system induction (Fig. 2). The state at 20 min post infection was tracked as the cell lysis happens at about this time, so a sufficient number of crRNAs to defend the cell has to be synthesized by that time. In contrast to the baseline and the constitutive models, the cooperative model exhibits more switch-like behavior, ensuring that leaks in *cas* promoter activity do not induce crRNA production, while that

crRNAs are rapidly produced once the system activation is needed, approaching the limit of infinitely fast production set by the baseline model. In all three models, saturation is reached at large enough  $k$  values, which can be relieved by simultaneous increase of CRISPR promoter activity.

The second prominent CRISPR-Cas regulatory feature - namely, fast non-specific degradation of pre-crRNA, is perturbed in the cooperative model (Fig. 3). Decreasing the pre-crRNA degradation rate  $\lambda_{pre}$  deforms the crRNA dynamics curve from the standard sigmoidal Hill shape, suggesting that this regulatory feature also contributes to the fast transition of the system from the OFF to the ON state, i.e. to its switch-like behavior. Moreover, this perturbation negatively affects the time delay of the beginning of the crRNA synthesis upon the start of system induction. This effect is more prominent at higher  $k_{eq}$  values (in Fig. 3,  $k_{eq}$  increases from the left to the right figure). Interestingly, it has been proposed that a delayed CRISPR-Cas activation may be required to enable *primed adaptation* - the acquisition of foreign DNA fragments similar to already possessed spacers, to be incorporated as new spacers in the CRISPR array, which serves to minimize infection by phages

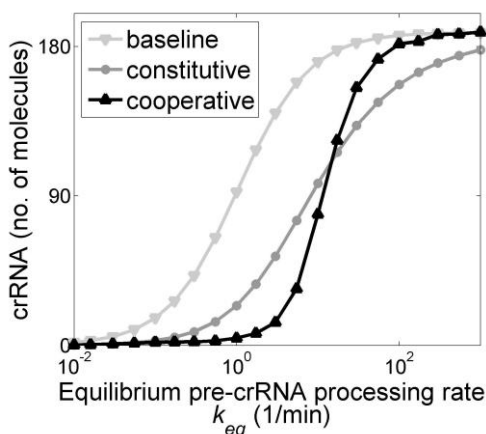


**Figure 2.** crRNA amounts 20min after introduction of the vector expressing *cas* genes, as a function of the maximal (equilibrium) value of the pre-crRNA processing rate  $k$  [2].

with mutated genome sequences, which would otherwise evade the interference.

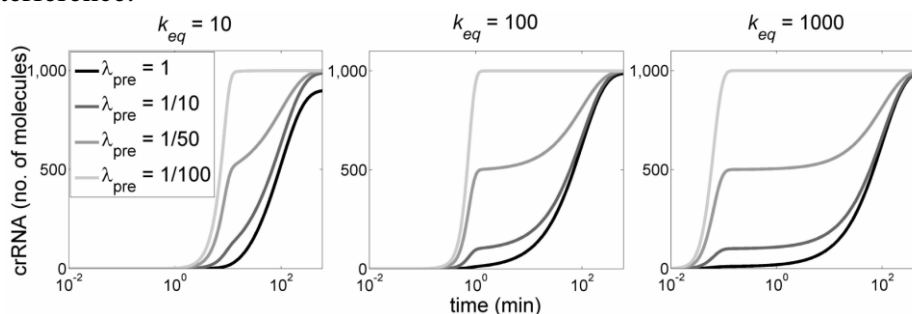


**Figure 3.** Perturbing the pre-crRNA degradation rate  $\lambda_{pre}$  in the cooperative model, at different values of the equilibrium pre-crRNA processing rate  $k_{eq}$  [2].

## CONCLUSION

Judging by the predicted CRISPR-Cas dynamic behavior, one may argue that its regulation - specifically, cooperative transcription regulation and fast non-specific substrate degradation - is optimized to achieve as fast as possible induction of the system, at higher pre-crRNA processing rates that are likely biologically relevant, with a time delayed system activation with respect to the signal onset. The proposed setup can be readily used to observe CRISPR-Cas activation dynamics experimentally *in vivo*. Also, the obtained model predictions from this artificial circuit can be compared to those of the full model taking into account the complex regulatory network that controls native CRISPR-Cas functioning.

## Acknowledgement

This work was funded by the Swiss National Science Foundation under SCOPES project number IZ73Z0\_152297, by Marie Curie International Reintegration Grant within the 7th European community Framework Program (PIRG08-GA-2010-276996) and by the Ministry of Education, Science and Technological Development of the Republic of Serbia under project number OI173052.

## REFERENCES

- [1] M. Djordjevic, M. Djordjevic, K. Severinov, *Biology direct*, 2012, 7, 24.
- [2] A. Rodic, B. Blagojevic, M. Djordjevic, K. Severinov, M. Djordjevic, *Frontiers in Microbiology*, 2017, 8, 2139.
- [3] E. Bogdanova, M. Djordjevic, I. Papanagioutou, T. Heyduk, G. Kneale, K. Severinov, *Nucleic acids research*, 2008, 36, 1429.

## INCLUDING POPULATION DYNAMICS EFFECTS IN MODELING REGULATION OF BACTERIAL RESTRICTION MODIFICATION SYSTEMS

S. Graovac<sup>1,2</sup>, A. Rodić<sup>2</sup> and M. J. Djordjević<sup>2</sup>

<sup>1</sup> *University of Belgrade, Faculty of Physics,  
Studentski trg 16, 11000 Belgrade, Serbia. (stefan.graovac@bio.bg.ac.rs)*

<sup>2</sup> *University of Belgrade, Faculty of Biology,  
Studentski trg 16, 11000 Belgrade, Serbia.*

### ABSTRACT

In vivo dynamics of protein expression in bacterial cells, depends not only on intracellular regulation, but also on the rates of cell and plasmid division that can change with time. These population effects can also significantly increase dimensionality of the parameter inference problem, as they effectively couple the dynamics of the proteins that otherwise do not regulate each other. We consider this problem on a relatively simple case of bacterial restriction-modification systems, where we exploit one of the first available measurements of in vivo expression of the restriction enzyme and the methyltransferase in these cells, which are under control of a control C protein. We find that including the dynamics effects of plasmid division is necessary to explain the experimental data, while neglecting them significantly distorts the predicted dynamics.

### INTRODUCTION

R-M gene expression regulation is completely encoded by plasmids and can spread through the bacterial population by horizontal genetic transfer. This implies that a single bacterial cell can have more than one plasmid within it. Here, we investigate influence of population dynamics on a model and on interpretation of experimental results.

One can model the transcription activity of the Esp1396I R-M system using thermodynamics and statistical physics. The transcription of the genes of this system is regulated by the control C protein by binding to the "C box". The genes are convergently oriented and the transcription is performed from two promoters – *P.CR* and *P.M*.

Transcription from *P.M* promotor is regulated by binding a RNA polymerase (RNAP) or dimer of C proteins to the MBS site, where in the first case we have a gene expression while in the second we have repression. Transcription from *P.CR* is regulated by the co-operative binding of C

proteins, where dimer of C protein is bound to the distal (left) binding site (DBS), which then recruits to the proximal (right) binding site (PBS) either RNA polymerase (RNAP) or another dimer of C protein forming tetramer of C proteins. As in the case of *P.M*, the binding of RNA polymerase leads to expression of the gene while the tetramer of C protein leads to repression. The situation in which only the dimer of C proteins are bound to the distant DBS binding site while the PBS is empty has not been taken into account due to the large co-operativity in the binding of dimer of C proteins, and no such situation has been observed in the experiment.

Now that we know all possible situations of C protein and RNAP binding to DNA, we can write the chemical equations of these reactions with the corresponding dissociation constants  $K_i$ . From this one can derive partition functions (statistical weights), which are allowed equilibrium configurations of the *P.CR* and *P.M* promoters.

It should be noted that the approximation of the rapid attainment of the equilibrium state is taken into account in the modeling, which is justified by the fact that the processes of association and dissociation between proteins and DNA or between two proteins are much faster compared to transcription, translation and degradation of protein molecules or RNA [1].

The most important assumption of thermodynamic modeling is that the transcriptional activity of the promoter can be approximated by the probability that the RNA polymerase binds to the promoter within the allowed equilibrium configurations [2]. Knowing this, we can model the transcriptional activities of the *P.CR* and *P.M* promoters:

$$\varphi_r(C) = \varphi_{bas\_r} \frac{1 + \frac{b}{a}[C]^2}{1 + \frac{b}{a+1}[C]^2 + \frac{c}{a+1}[C]^4} \quad (1)$$

$$\varphi_M(C) = \varphi_{bas\_M} \frac{1}{1 + K_M^2 [C]^2} \quad (2)$$

Here,  $a$ ,  $b$ ,  $c$  and  $K_M^2$  are parameters,  $\varphi_{bas\_r}$  and  $\varphi_{bas\_M}$  are basal transcriptional activities and  $[C]$  is the concentration of C protein. Parameters and basal transcriptional activities are determined through fitting model on experimental data.

Now that we have transcriptional promoter activities, we can build a dynamic model of the system that as a result gives us the dependence of the restriction endonuclease and methyltransferase concentration over time.

One can see in research of Morozova and her associates [3] that cell division rate slows down over time (approx. after 150 minutes). Naturally,

following this, one can expect that plasmid division rate will slow down over time in experiment as well.

One can then extend the dynamical model that our group previously developed [3], to fully include the population dynamics effects, in particular to include the dynamics of plasmid division ( $n_p(t)$ ). Full dynamical model is determined with the next set of differential equations:

$$\begin{aligned}
 1) \quad & \frac{dr}{dt} = n_p(t) \cdot \varphi_r(C) - \lambda_r \cdot r \\
 2) \quad & \frac{dC}{dt} = k_C \cdot r - \lambda_c \cdot C \\
 3) \quad & \frac{dR}{dt} = k_R \cdot r - \lambda_R \cdot R \\
 4) \quad & \frac{dm}{dt} = n_p(t) \cdot \varphi_m(C) - \lambda_m \cdot m \\
 5) \quad & \frac{dM}{dt} = k_M \cdot m - \lambda_M \cdot M
 \end{aligned} \tag{3}$$

In this model, we designate decay rates with  $\lambda$ , further  $k_C$ ,  $k_R$  and  $k_M$  are translational rates, transcripts are labelled with low-case letters while proteins are labelled with upper-case letters. Model is described by 17 parameters, where 3 parameters describe the plasmid dynamics - two for plasmid division rate, and one for transition time (the time when the division rate slows down). Later, we show that this is a minimal set of parameters, in the sense that not including them leads to a significantly worse agreement with the data.

## RESULTS AND DISCUSSION

It is important to observe that the first three equations do not depend on other two if the parameters for plasmid division rate are fixed, but with plasmid dynamics these equations become coupled. Computationally it is very hard

task to solve this system of equations in 17-dimensional parameter space. To resolve this, we developed a “mean field-like”

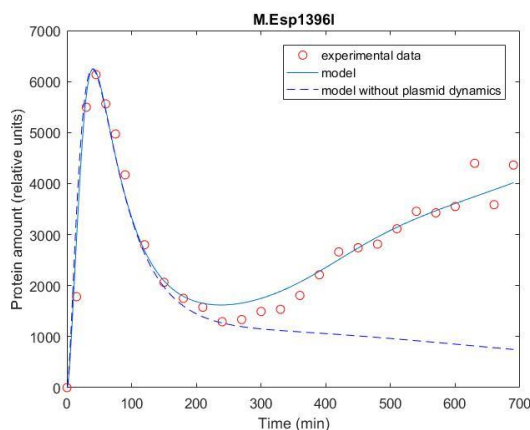


**Figure 1.** Full model of M dynamics with included plasmid dynamics and without it.

approach, which uses an iterative procedure, to decouple (in each step) R and M dynamics so that they can be solved independently (therefore drastically reducing dimensionality of the parameter space). In Figure 1, one can see solved differential equations for M dynamics (3). It is clear that model with plasmid dynamics is in good agreement with experimental results.

## CONCLUSION

A model with the population dynamics of the plasmids not only manages to quantitatively describe the model and fit appropriate to experimental data, but also qualitatively reproduces what is observed in the experiment:

- The number of plasmids per cell significantly increases in the experiment
- The transcription activity of the P.CR promoter is much lower compared to the transcriptional activity of the P.M promoter
- Model predicts that proteins are very stable which is in agreement with experiment observation
- In the model, one can see that the protein is more stable than the transcript, which is in good agreement with theoretical predictions

Consequently, while the population dynamics effects are often neglected, including them is necessary both to quantitatively explain experimental data, and not to qualitatively misinterpret experimental observations.

## *Acknowledgement*

This work was partially supported by the Ministry for Education, Science and Technological development of the Republic of Serbia by project 173052.

## REFERENCES

- [1] Phillips, R., et al. (2012). Physical biology of the cell, Garland Science.
- [2] Shea, M. A. and G. K. Ackers (1985). "The OR control system of bacteriophage lambda: A physical-chemical model for gene regulation." *Journal of molecular biology* **181**(2): 211-230.
- [3] Morozova, N., et al., Temporal dynamics of methyltransferase and restriction endonuclease accumulation in individual cells after introducing a restriction-modification system. *Nucleic acids research*, 2015. **44**(2): p. 790-800.

## DNA-SE I INHIBITORY PROPERTIES OF 4-THIAZOLIDINONE S-OXIDES: EXPERIMENTAL AND DOCKING STUDIES

Z. Džambaski<sup>1</sup>, A. Kolarević<sup>2</sup>, B.S. Ilić<sup>3</sup>, A. Rašović,<sup>1</sup> A. Šmelcerović<sup>2</sup> and B.P. Bondžić<sup>1,\*</sup>

<sup>1</sup>Center for Chemistry ICTM, University of Belgrade, P.O. Box 815, 11000 Belgrade, Serbia

<sup>2</sup>Department of Pharmacy, Faculty of Medicine, University of Niš, 18000 Niš, Serbia

<sup>3</sup>Department of Chemistry, Faculty of Medicine, University of Niš, 18000 Niš, Serbia

### ABSTRACT

Series of thiazolidinone S-oxides were synthesized and evaluated for inhibitory activity against bovine pancreatic deoxyribonuclease I (DNase I) *in vitro*. Three compounds inhibited DNase I with an IC<sub>50</sub> below 200 μM and showed to be more potent DNase I inhibitors than crystal violet (IC<sub>50</sub> = 365.90 ± 47.33 μM), used as positive control. Site Finder and Molecular docking defined the thiazolidinones interactions with the most important catalytic residues of DNase I.

### INTRODUCTION

According to several reports deoxyribonuclease I (DNase I) is considered one of the main nucleases involved in DNA degradation during apoptosis. Elevated levels of DNase I and excessive apoptosis have been observed in various pathological conditions, including AIDS, neurodegenerative disorders (Alzheimer's disease, Parkinson's disease, Huntington's disease, amyotrophic lateral sclerosis, cerebellar degeneration, retinitis pigmentosa, spinal muscular atrophy), graft-versus-host disease, ischemic injuries (myocardial infarction and stroke), idiopathic dilated cardiomyopathy, type 2 diabetes, cisplatin induced nephrotoxicity, acetaminophen induced hepatocellular necrosis. However, the number of known organic DNase I inhibitors, either natural or synthetic, is relatively small, and the discovery of novel organic DNase I inhibitors, especially those with potential therapeutic applications, would be of great interest.

Both natural and synthetic thiazolidinones represent compounds of great interest due to their broad range of biological activities, including antibacterial, antifungal, antitubercular, anticancer, analgesic, anti-

inflammatory, anticonvulsant, antidepressant, antiviral/anti-HIV, antidiabetic, antiarrhythmic, and trypanocidal (anti-epimastigote) activities. In order to find novel organic DNase I inhibitors, in the present study 4 synthesized thiazolidinone S-oxides, were evaluated for inhibitory activity against bovine pancreatic DNase I *in vitro*. Site Finder and Molecular docking are *in silico* drug design methods that were used to better understand the drug-target interactions.

## EXPERIMENTAL

Conformational search for ligand preparation was carried out by MOE LowModelMD method which performs molecular dynamic perturbations along with low frequency vibrational modes.

### Receptor preparation

The X-ray crystallographic structure of a complex between DNase I and the self-complementary octamer duplex d(GGTATACC)<sub>2</sub> (PDB code: 1DNK) was obtained from the Protein Data Bank. The errors of DNase I were corrected by the Structure Preparation process in MOE.

## RESULTS AND DISCUSSION

A series of thiazolidinones, was employed in DNase I inhibition assay. Among them, three compounds inhibited bovine pancreatic DNase I with IC<sub>50</sub> values below 200 μM, with compound **4** being the most potent (IC<sub>50</sub> = 115.96 ± 11.70 μM). These compounds showed higher DNase I inhibitory activity than crystal violet (IC<sub>50</sub> = 365.90 ± 47.33 μM), used as positive control (Table 1).

**Table 1.** Chemical structures and DNase I inhibition of 2-alkylidene-4-oxothiazolidine S-oxides **1-4**.

Compd.	R1	R2	R3	R3'	DNase I inhibition IC <sub>50</sub> ± SD (μM)
<b>1</b>	-Me	-CO <sub>2</sub> Et	-H	-H	141.53 ± 11.66
<b>2</b>	-Me	-Bz	-H	-H	> 200
<b>3</b>	-Me	-CONHPh	-H	-H	173.66 ± 17.86
<b>4</b>	-Me	-CONH(CH <sub>2</sub> ) <sub>2</sub> Ph	-H	-H	115.96 ± 11.70

The binding site residues in DNase I have been identified using the Site Finder implemented in the Molecular Operating Environment (MOE) software. The results from the analysis highlighted that amino acid residues like Asn 7, Arg 9, Glu 39, Tyr 76, Glu 78, Arg 111, His 134, Ala 136, Pro 137, Asp 168, Asn 170, Thr 203, Thr 205, Thr 207, Tyr 211, Asp 251 and His 252 constituted the binding pocket of the DNase I structure (Table S1). Our results are consistent with a recent study highlighting the conservation of the amino acids involved in the identified cation-binding sites across DNase I and DNase I-like protein.<sup>1</sup> It is worth mentioning that inhibitor-binding pocket, represented by a grey-red surface map, is within the region that interacts with DNA octamer  $d(\text{GGTATACC})_2$  (Fig. 1).

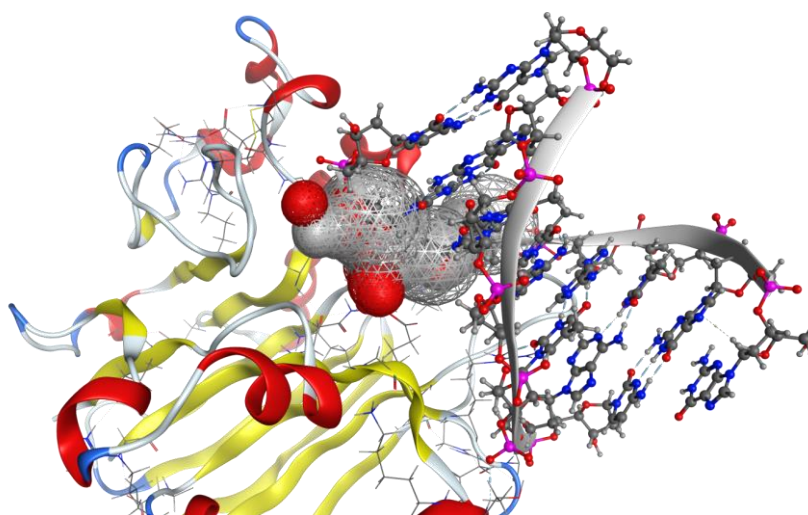


**Figure 1.** The top ranked DNase I binding site, represented by a grey-red surface map.

The intermolecular contacts between thiazolidinones and DNase I were analyzed using the ligand interaction diagram of MOE suite. It illustrates the existence of hydrogen bond, pi-H and H-pi interactions. Additionally, the bond distances, bond energy and binding free energy between the inhibitor and receptor atoms were also examined. Of note, the importance of Glu 39, His 134, Asp 168 and His 252 residues in the catalytic mechanism of DNase I has been already highlighted.<sup>1</sup> It was confirmed that catalytic residues His 134 and His 252 are a part of the ion binding site IV, which is implicated in the cleavage of scissile phosphate. Furthermore, several site-directed mutagenesis experiments on residues surrounding His 134 and His 252 demonstrated that single mutations of Glu 39 or Asp 168, resulted in very low

activities on DNA.<sup>2</sup> The effects of these mutations also confirmed the active role of Glu 39 and Asp 168 in the IV catalytic site. In addition, the importance of Ca<sup>2+</sup> coordination sites (site I and II) for the structural integrity and activity of DNase I is well known.<sup>1</sup>

### CONCLUSION

A series of thiazolidinones was employed in DNase I inhibition assay. These compounds showed higher DNase I inhibitory activity than crystal violet (IC<sub>50</sub> = 365.90 ± 47.33 μM), used as positive control. The interactions of thiazolidinones with the most important catalytic residues of DNase I, including H-acceptor interaction with residue His 134 and His 252 and/or H-donor interaction with residue Glu 39 and Asp 168, were shown. These observations could be potentially utilized to guide the rational design and optimization of novel thiazolidinone DNase I inhibitors.

### Acknowledgement

Support of this work by Ministry of Education, Science and Technological Development of the Republic of Serbia (Grants No. OI 172020 OI 172044, OI 171025 and TR 31060).

### REFERENCES

- [1] Guérout M, Picot D, Abi-Ghanem J, Hartmann B, Baaden M. How cations can assist DNase I in DNA binding and hydrolysis. *PLoS Comput. Biol.* 2010;6:e1001000
- [2] a) Jones SJ, Worrall AF, Connolly BA. Site-directed mutagenesis of the catalytic residues of bovine pancreatic deoxyribonuclease I. *J. Mol. Biol.* 1996;264:1154–1163; b) Pan CQ, Ulmer JS, Herzka A, Lazarus RA. Mutational analysis of human DNase I at the DNA binding interface: Implications for DNA recognition, catalysis, and metal ion dependence. *Protein Sci.* 1998;7:628–636

## TRANSPORT CAPABILITIES OF HUMAN SERUM ALBUMIN (HSA) FOR DICLOFENAC

A. Rakić<sup>1</sup>, D. Slavnić<sup>2</sup>, G. Janjić<sup>3</sup> and N. Vukelić<sup>1</sup>

<sup>1</sup> Faculty of Physical Chemistry, University of Belgrade, Studentski Trg 12-16, 11158 Belgrade, Serbia (saska@ffh.bg.ac.rs)

<sup>2</sup> Faculty of Technology and Metallurgy, University of Belgrade, Karnegijeva 4, 11120 Belgrade, Serbia

<sup>3</sup> Institute of Chemistry, Technology and Metallurgy Belgrade, University of Belgrade, Njegoševa 12, 11158 Belgrade, Serbia.

### ABSTRACT

Incredible transport capabilities of human serum albumin (HSA), not only found applications in medicine, pharmacy, life science, but also have promising possibilities for biosensor applications. Its power lays in specific structure and non-covalent binding properties. In our study we performed molecular docking calculations for non-steroid anti-inflammatory drug diclofenac (Dcf) and concurrent fatty acids (myristic (MA) and palmitic (PA) acid).

### INTRODUCTION

Human serum albumin (HSA), the most abundant protein in plasma, has 585 amino-acid residues in a polypeptide chain, divided into three structurally similar domains (I-III) (**Figure 1**). A domain contains grouped six  $\alpha$  helices in A sub-domain, while B sub-domain has four  $\alpha$  helices. HSA is a transport protein, present in high concentration in circulating blood of a human, which delivers different metabolites, nutrients, drugs and ions. [1]

Most of the fatty acids are bound to HSA in a blood stream, some of them are a constituent of lipoproteins, while a negligible quantity (<0.01%) circulates freely in plasma. Their primary function is to provide enough energy when blood glucose is low. Three high affinity fatty acid binding sites (FA2, FA4 and FA5) and four low affinity fatty acid binding sites (FA1, FA3, FA6 and FA7) are located in HSA protein (**Figure 1**). The highest affinity binding site is FA5. [2] The incredible transport capabilities include HSA among proteins with their biological electron transfer function, recently the most studied group of biological molecules. Upon doping with retinoate that contains conjugated double bonds, the electron transport function of HSA and consequently the solid-state electronic conductance is

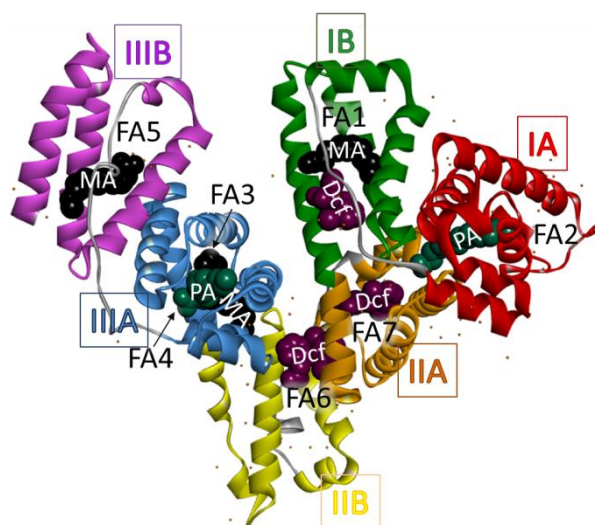


**Figure 1.** The crystal structure of HSA-PA-MA-Dcf complex (PDB ID: 4z69). HSA is coloured differently depending on the sub-domain: IA (red), IB (green), IIA (orange), IIB (yellow), IIIA (blue) and IIIB (pink). Ligands adopted solid ball representation: Dcf (violet), MA (black) and PA (green). FA1, FA2, FA3, FA4, FA5, FA6 and FA7 are binding sites for fatty acids. Water molecules are represented by dots.

increased by over two orders of magnitude. There is a great interest in using HSA as a biosensor being a part of biocompatible electronics. [3]

According to numerous useful functions and applications [4], the research of binding sites and binding affinities in HSA is of great importance. Our attention was drawn to the first non-steroidal anti-inflammatory drug diclofenac (Dcf) and its concurrent fatty acids. We performed molecular docking calculations to investigate non-covalent binding of Dcf, myristic acid (MA) and palmitic acid (PA). The results of the performed calculations

were compared with the experimentally obtained results from literature [1] and crystal structures from PDB.

## CALCULATIONS

3D structure of Dcf, MA and PA molecules (ligands) have been downloaded from Cambridge structural database (CSD) and optimized at B3LYP/6-31g\*\* level, while HSA was obtained from protein databank (PDB) with four-character unique PDB identifier (PDB ID) 4z69. First, molecular redocking confirmation of Dcf and PA substrates to receptor structure 4z69 was cleaned from Dcf, PA and water molecules. Afterwards, molecular docking calculations of Dcf, MA and PA molecules were performed on, beforehand, completely cleaned HSA (4z69) receptor from all substrates. Optimized structures of ligands and structure of protein were used for docking preparations in *AutoDockTools* software, while the docking study was done with *AutoDock* software [5].

## RESULTS AND DISCUSSION

Experimentally obtained complex of HSA protein with Dcf, MA and PA molecules by X-ray crystallography (PDB code 4z69) [1] is displayed in **Figure 1**. The data concerning the binding of Dcf, MA and PA obtained from X-ray crystallography or by molecular docking calculations are presented in **Table 1**.

After mixing 1.7 mM PA and 2.7 mM Dcf with 18.2 mg/mL HSA, three Dcf molecules were found in the long and narrow cavity of FA1 binding site (IB sub-domain), in the main (FA7) and side (FA6) chambers of the

**Table 1.** Comparison of binding positions in crystal structure of HSA-PA-MA-Dcf complex with theoretically obtained binding energies (kcal/mol) and conformational flexibility (number of clusters in parentheses).

Ligand (conc.)	IA (FA2)	IB	IIA	IIIA
<b>Crystal structure of of HSA-PA-MA-Dcf complex (4z69)</b>				
PA (1.7mM)	FA2			FA4
MA*		FA1		FA3
Dcf (2.7mM)		FA1↓	FA7 FA6	
<b>Ligand docking calculations to clean HSA</b>				
PA		-7.80 <sup>(26)</sup> FA1	-7.04 <sup>(5)</sup> FA6 -6.54 <sup>(7)</sup> FA6↓	-7.38 <sup>(26)</sup> FA4 -6.72 <sup>(19)</sup> FA3
MA		-7.28 <sup>(18)</sup> FA1	-6.17 <sup>(32)</sup> -6.05 <sup>(25)</sup> FA7 -6.32 <sup>(11)</sup> FA6	-6.59 <sup>(19)</sup> FA3
Dcf		-6.72 <sup>(61)</sup> FA1↓	-6.15 <sup>(45)</sup> FA7 -6.02 <sup>(14)</sup> FA6	-6.89 <sup>(12)</sup> FA4
<b>Ligand redocking calculations to HSA</b>				
PA	-6.93 <sup>(6)</sup>		-6.71 <sup>(51)</sup> FA7 -7.22 <sup>(7)</sup> FA6 -6.17 <sup>(10)</sup> FA6↓	-6.86 <sup>(5)</sup>
Dcf	-5.31 <sup>(1)</sup>	-5.13 <sup>(13)</sup> FA1↓	-5.93 <sup>(62)</sup> FA7 -6.18 <sup>(18)</sup> FA6	-7.09 <sup>(2)</sup> FA4

hydrophobic cavity in IIA sub-domain. Two PA molecules are bound to FA3 (IIIA sub-domain) and FA2 (IA sub-domain) binding sites, while MA was

found at FA5 (IIIB sub-domain) FA4 (IIIA sub-domain) and FA1 (IB sub-domain) binding sites. The clusters significant in numbers and with considerable high values of binding energies are of great interest for our studies. With the respect of binding energies and cluster number, the redocking of Dcf and PA was successful. Higher Dcf concentration and conformational freedoms were factors that provide an advantage over PA better binding energy values for Dcf to bind to FA6 and FA7 binding sites. The results of docking calculations of Dcf, MA and PA on completely clean HSA (without any ligands) clearly showed that according to binding energy values and conformational flexibility, the binding priority is given in the following order: firstly PA, following MA and lastly Dcf.

### CONCLUSION

According to the results obtained from the docking calculations, it is obvious that a number of Dcf binding sites in HSA strongly depend on the number of bonded fatty acids to HSA. Fatty acids and diclofenac bind competitively to certain binding sites. Since fatty acids have higher affinity, less abundance of fatty acids is preferable. Dcf competes with PA for FA4 and FA6 binding sites, but shares FA6 and FA7 binding sites with MA.

### *Acknowledgement*

This work was supported by the Ministry of Science of the Republic of Serbia (Project no. OI 172043 and 172023).

### REFERENCES

- [1] Y. Zhang, P. Lee, S. Liang, Z. Zhou, X. Wu, F. Yang, H. Liang, *Chem Biol. Drug. Des.*, 2015, **86**, 1178–1184.
- [2] B. Rizzuti, R. Bartucci, L. Sportelli, R. Guzzi, *Arch. Biochem. Biophys.*, 2015, **579**, 18-25.
- [3] N. Amdursky, I. Pecht, M. Sheves, and D. Cahen, *J. Am. Chem. Soc.* 2012, **134**, 18221–18224.
- [4] G. Fanali, A. di Masi, V. Trezza, M. Marino, M. Fasano, P. Ascenzi, *Mol. Aspects Med.*, 2012, **33**, 209–290.
- [5] O. Trott, A. J. Olson *J. Comput. Chem.*, 2010, **31**, 455-461.

## CYTOTOXIC ACTIVITY OF MACROCYCLIC Cu(II) BENZENE CARBOXYLATE COMPLEXES *IN VITRO*

S. Tanasković<sup>1</sup>, M. Antonijević-Nikolić<sup>2</sup>, J. Antić-Stanković<sup>1</sup> and B. Dražić<sup>1</sup>

<sup>1</sup> Faculty of Pharmacy, University of Belgrade, Vojvode Stepe 450, 11000 Belgrade, Serbia. (sladjana@pharmacy.bg.ac.rs)

<sup>2</sup> Higher Medical and Business-technological School of Applied Studies, Hajduk Veljkova 10, 15000 Šabac, Serbia,

### ABSTRACT

Cu(II) complexes with *N,N',N'',N'''*-tetrakis-(2-pyridylmethyl)-1,4,8,11-tetraazacyclotetradecane (tpmc) and bridged benzene carboxylate ligands, benzoic acid, phthalic acid (benzene-1,2-dicarboxylic acid), isophthalic acid (benzene-1,3-dicarboxylic acid) and terephthalic acid (benzene-1,4-dicarboxylic acid) were tested against tumor cell lines human cervix adenocarcinoma (HeLa) and human myelogenous leukemia (K562). The most cytotoxic compound is  $[\text{Cu}_4(\text{ipht})(\text{tpmc})_2](\text{ClO}_4)_6 \cdot \text{NaClO}_4 \cdot 2\text{CH}_3\text{CN}$ .

### INTRODUCTION

Advances in inorganic chemistry encourage synthesis of different metal complexes as anti-tumor drugs. Metal complexes have been used for treatment of various diseases [1].

Multi-carboxylic ligands with suitable spacers are good choices as building blocks in complex compounds, especially benzoic acid based ligands. The construction of these molecules depends largely on the nature of the dicarboxylato bridging and the blocking amine ligands as well as the availability of hydrogen bonding. The versatility of the bridging mono- and dicarboxylato ligands and metal ions results in the formation of different coordination bonding modes.

Previously we have described a series of copper(II) complexes with octaazamacrocycle *N,N',N'',N'''*-tetrakis-(2-pyridylmethyl)-1,4,8,11-tetraazacyclotetradecane and bridged mono- and dicarboxylic benzoic acid. The aim of this paper is to describe the results of their cytotoxic activities.

### EXPERIMENTAL

Four complexes  $[\text{Cu}_2(\text{C}_6\text{H}_5\text{COO})\text{tpmc}](\text{ClO}_4) \cdot \text{CH}_3\text{CN}$  (**1**),  $[\text{Cu}_2(\text{Hpht})\text{tpmc}]$

(ClO<sub>4</sub>)<sub>3</sub>·3H<sub>2</sub>O(2), [Cu<sub>4</sub>(ipht)(tpmc)<sub>2</sub>](ClO<sub>4</sub>)<sub>6</sub>·NaClO<sub>4</sub>·2CH<sub>3</sub>CN (3) and [Cu<sub>4</sub>(tpht)(tpmc)<sub>2</sub>](ClO<sub>4</sub>)<sub>6</sub>·5H<sub>2</sub>O (4) presented in Table I were prepared in solid state according to procedures described in the literature [2].

### **Materials and methods**

#### **Cell Culture**

HeLa (human adenocarcinoma) and K562 (chronic myelogenous leukemia cells) were maintained in an nutrient medium RPMI-1640 (Sigma-Aldrich) supplemented with 10% foetal bovine serum (Gibco, Grand Island, NY, USA), 2 mM L-glutamine, 100 U/ml penicillin, 100 mg/ml streptomycin and 50 μM 2-mercaptoethanol (all from Sigma-Aldrich). Cells were cultured in a humidified chamber (37°C, 5% CO<sub>2</sub>).

#### **Metabolic activity assay**

The metabolic activity of cells was assessed with tetrazolium MTS assay using CellTiter 96® Aqueous One Solution Cell Proliferation Assay (Promega, Madison, WI, USA) according to manufacturer's instructions. In brief HeLa and K562 cells were treated with different concentrations (200, 100, 50, 25 or 12.5 μM) of the compounds (1-4) or corresponding vehicle (control cells). Cells were than seeded in 96 well plates. After 45 h, 10 μL of MTS solution was added to each 100 μL of cell suspension. Following 3 h of incubation, the absorbance was measured at the Tecan Safire automated microplate reader (Tecan, Mannedorf /Zürich, Switzerland), at 492 nm.

To achieve cell survival, absorbance at 492 nm of a sample with cells grown in the presence of various concentrations of compounds tested was divided with absorbance of control sample (the absorbance of cells grown in nutrient medium only). Absorbance of blank was always subtracted from absorbance of a corresponding sample with cells. The data are presented as the average ± SD (standard deviation). IC<sub>50</sub> was defined as the concentration of the compound inhibiting cell survival by 50%, compared with a vehicle-treated control cells. All experimentally obtained IC<sub>50</sub> data were means of three measurements done in triplicate.

### **RESULTS AND DISCUSSION**

The cytotoxicity of complexes 1 - 4 was tested toward selected human cancer cell lines: cervix adenocarcinoma (HeLa) and human myelogenous leukemia (K562). The cytotoxic properties of target compounds are presented in Table 1. The data are presented as the average ± SD (standard deviation)

**Table 1.** Concentrations of compounds **1-4** and ligands that induced 50% decrease in cell survival (IC<sub>50</sub>).

	IC <sub>50</sub> ±SD (μM)	
	HeLa	K562
C <sub>6</sub> H <sub>5</sub> COONa	>200	>200
[Cu <sub>2</sub> (C <sub>6</sub> H <sub>5</sub> COO)tpmc](ClO <sub>4</sub> ) <sub>3</sub> ·CH <sub>3</sub> OH ( <b>1</b> )	82.57±12.36	42.78±9.87
KHpt	>200	>200
[Cu <sub>2</sub> (Hpt)tpmc](ClO <sub>4</sub> ) <sub>3</sub> ·3H <sub>2</sub> O ( <b>2</b> )	91.03±15.16	52.48±19.15
Na <sub>2</sub> ipht	>200	>200
[Cu <sub>4</sub> (ipht)(tpmc) <sub>2</sub> ](ClO <sub>4</sub> ) <sub>6</sub> ·NaClO <sub>4</sub> ·2H <sub>2</sub> O ( <b>3</b> )	24.80±0.88	9.47 ±1.74
Na <sub>2</sub> tpht	>200	>200
[Cu <sub>4</sub> (tpht)(tpmc) <sub>2</sub> ](ClO <sub>4</sub> ) <sub>6</sub> ·5H <sub>2</sub> O ( <b>4</b> )	71.27±3.48	31.62±7.56
Tpmc	>200	>200
NaClO <sub>4</sub>	>200	>200

All data are results from three independent experiments, each carried out in triplicate. The results are presented as mean IC<sub>50</sub> ± standard deviation (μM)

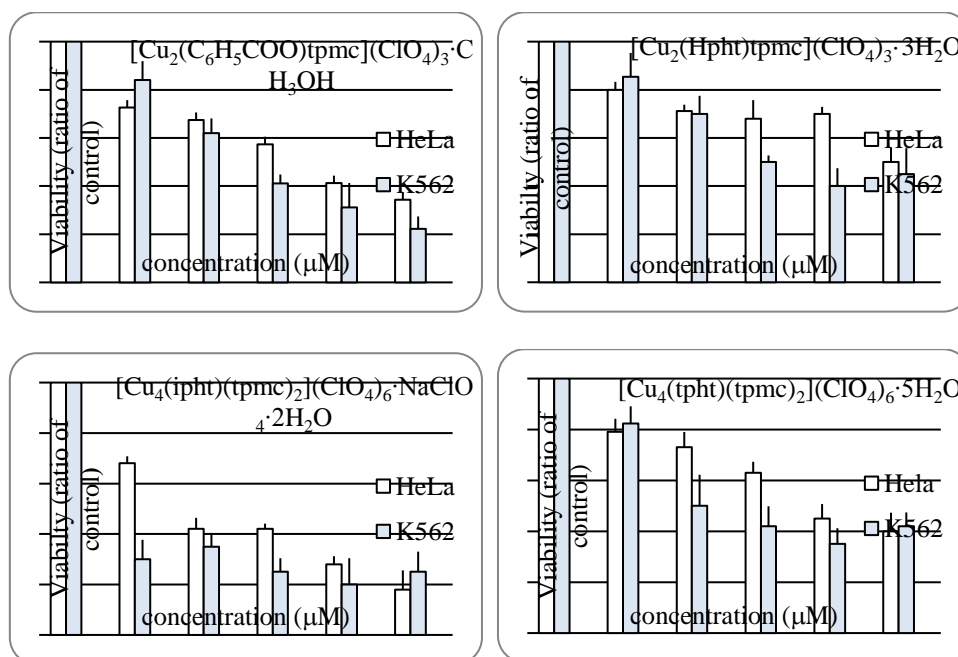


**Figure 1.** Cells were incubated with various concentrations of the test substances. After 48 hours of incubation, MTS reagent was added. Obtained data show the optical density of cell cultures. Each experiment was repeated three times and the results were presented as the mean value ± SD

by MTS test, after 48 h exposure to compounds. All four compounds have promoted significant decreases in the metabolic activity of the HeLa and K562 cells, which occurred in a dose-dependent fashion (Figure 1). Control groups, solvents, starting salts and ligands were inactive on the same conditions.

### CONCLUSION

The cytotoxicity of Four cationic octaazamacrocyclic Cu(II) complexes with bridged benzene mono/dicarboxylate ligands was tested with selected human cancer cell lines: cervix adenocarcinoma (HeLa) and human myelogenous leukemia (K562) *in vitro*. The results show that the tested complexes have considerable activity toward the evaluated cell lines in the concentration-dependent matter.

The most active compound is complex Cu(II) tpmc with isophthalic acid (benzene-1,3-dicarboxylic acid). Control groups, solvents, starting salts and ligands were inactive on the same conditions which means that antiproliferative activity derived from the complexes.

### Acknowledgement

This work was partially supported by the Ministry for Science of the Republic of Serbia (Grants no.172014 and 175011).

### REFERENCES

- [1] A. Shircliff, |K.Wilson, D. Cannon-Smith, D. Jones, Z. Zhang, Z. Chen, G. Yin, T. Prior, T. Hubin, J. Timothy. *Inorg. Chem. Comm.* 2015, 59, 71-75
- [2] G. Vučković, M. Antonijević, D. Poleti, J. Serb. Chem. Soc., 2002, 67(10), 677-684

## METHYLENE BLUE DEGRADATION BY IRRADIATION OF SOLUTION CONTAINING CARBON WASTE TIRE CHAR

Đ. Petrović, R. Vujasin, K. Kumrić, A. Devečerski, M. Omerašević, M. Mirković and Lj. Matović

*Vinča Institute of Nuclear Sciences, University of Belgrade, 11001  
Belgrade, Serbia. (kkumric@vinca.rs)*

### ABSTRACT

A new approach for degradation of methylene blue is presented in this work. It combines the use of carbon material, as an adsorbent matrix and low energy irradiation derived from the radioactive waste sources. The activated carbon-based material was prepared by pyrolysis of waste rubber granules. The  $\gamma$ -irradiations were conducted using  $^{192}\text{Ir}$ ,  $^{75}\text{Se}$  and  $^{60}\text{Co}$  radiographic sources. Based on the results obtained using UV–VIS spectrophotometry and FTIR analysis, one can conclude that this way of degradation is the promising method for treating dye molecules in the aquatic systems.

### INTRODUCTION

Dyes and pigments are used by many industries to color their products [1]. Presence of dye molecules, even at very low concentrations, is undesirable and may significantly affect photosynthetic activity in aquatic systems by reducing light penetration and thus eutrophication and perturbations in the aquatic life [2]. Therefore, a lot of efforts have been made to remove traces of paint from the wastewater.

The most common procedure involves the use of activated carbons as adsorbent due to their high adsorption capacities for organic compounds in wastewater treatments [3]. Because of their relatively high cost, efforts were made to utilize naturally occurring adsorbents to minimize costs [4]. Many materials have been used as adsorbents with purpose to replace activated carbon with less costly alternatives, and to use various waste products as adsorbents [5-10]. Processes that use ionizing radiation ( $\alpha$ ,  $\beta$  and  $\gamma$ ) for degradation of dyes are characterized as advanced oxidation processes which normally utilize a strong oxidizing species such as  $\bullet\text{OH}$  radicals which cause break down of the macromolecules [11].

In this study, we reported a new approach that combines the use of carbon material, as an adsorbent matrix, coupled with the low energy irradiation derived from the radioactive waste sources. Methylene blue (MB) was used

as an example of contaminant. An adsorbent made of waste tire carbon char was simultaneously coupled with the gamma irradiation to the dye solutions of methylene blue in order to study their synergistic effect on the degradation of the dye.

## EXPERIMENTAL

*Materials: Methylene blue (MB) (C<sub>16</sub>H<sub>18</sub>ClN<sub>3</sub>S) was purchased from Sigma-Aldrich, USA. Preparation of activated carbon:* Carbon-based material (CBM) investigated in this study was prepared by pyrolysis of waste rubber granules purchased from Eco-recycling (Novi Sad, Serbia). The waste rubber granules were firstly pyrolyzed and after that activated with KOH into a quartz tube furnace under an N<sub>2</sub> flow at heating rate up to 800 °C for 4 h. The resulting activated carbon-based powder (KF) was extensively washed with 0.5 M HCl solution and deionized water [12,13]. The activated carbon-based material was then dried in an oven at 110 °C for 24 h. *The  $\gamma$ -irradiations were conducted* using <sup>192</sup>Ir and <sup>75</sup>Se radiographic sources. Industrial sources <sup>60</sup>Co were used for  $\gamma$ -irradiations, too. The  $\gamma$ -irradiation doses were from 60 up to 180 Gy and the dose rate was 15 kGy/h. All irradiations were carried out in hot cells at the "Vinča" Institute of Nuclear Sciences. *Solution preparation and experimental set-up:* The experiments were performed by mixing 20 cm<sup>3</sup> of 0.1 mg·cm<sup>-3</sup> of MB and different amounts of carbon material in glass vials ranging from 5 to 25 mg. The prepared suspensions were placed in a hot cell and irradiated over the dose ranging from 0.1 to 60.0 Gy by different radioactive sources. Small-sized radioactive sources (5 x 2 mm) were placed at a distance of 6 cm from the vials. Then, the liquid phase was separated from the solid phase by filtration through a 0.2  $\mu$ m Millipore disc. *Experimental techniques used for studying dye degradation:* UV–VIS spectrophotometry was used for quantitative analysis of dye degradation measuring and characterization of material was carried out by FTIR analysis.

## RESULTS AND DISCUSSION

Absorption spectra of un-irradiated and irradiated MB solutions is shown in Figure 1. Lack of characteristic absorption bands on the spectra can indicate degradation of MB. Degradation is even more pronounced with the presence of carbon adsorption media. Significant difference in absorption of unirradiated and irradiated batches depended on the amount of sorbent as it can be seen in Figure 2.

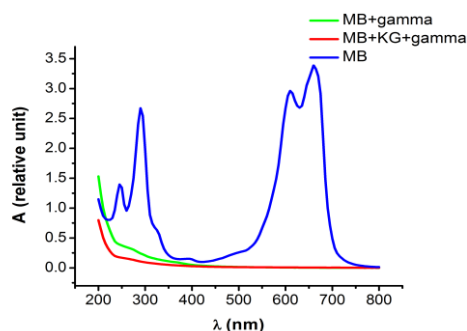


**Figure 1.** Absorption spectra of un-irradiated and irradiated material

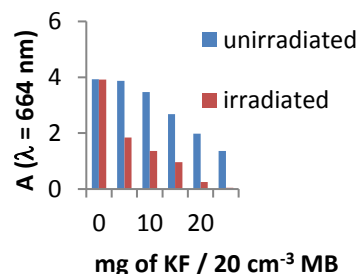


**Figure 2.** Absorption of un-irradiated and irradiated MB aqueous solutions with different amounts of sorbent

Irradiated solutions of MB with carbon-based material showed significantly greater decrease in absorption than the un-irradiated solutions with carbon-based material.

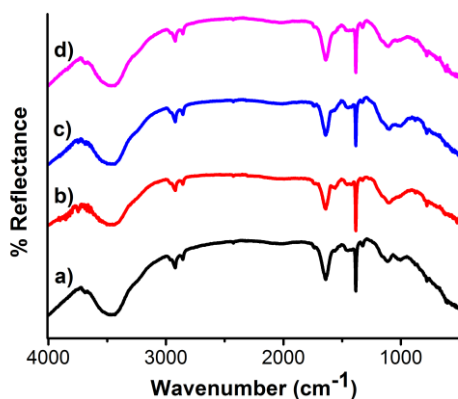


**Figure 3.** FTIR spectra of: a) prepared carbon matrix, b) MB adsorbed on carbon matrix, c) MB degraded in the presence of irradiation and carbon matrix, and d) carbon material irradiated in the aqueous solution

Numerous bands with maxima near 3450, 2920, 2850, 1640, 1380, 1100  $\text{cm}^{-1}$  confirm the presence of different functional groups on the surface of investigated carbon matrix (Figure 3). Comparing FTIR spectra of as prepared carbon matrix, as well as before and after the adsorption of MB and irradiation, it can be noticed that adsorption and/or irradiation didn't induced the formation of new groups on the surface of the samples; positions of

all bands in spectra remain unchanged except a slight shift and changes in the relative intensities of the bands at 1100  $\text{cm}^{-1}$  assigned to C-O stretching in phenolic groups (1000-1250  $\text{cm}^{-1}$  [14]).

## CONCLUSION

Irradiation of MB by high energy  $\gamma$  radiation caused degradation of dye in the presence of carbon based material. The amplitude of all absorption bands characteristic for MB disappeared completely.

## Acknowledgement

This research was supported by the Serbian Ministry of Education, Science and Technological Development under Grants III 45012 and III 45006.

## REFERENCES

- [1] D. Solpan, O. Guven, E Takacs L. Wojn arovits , K. Dajka, Radiation Physics and Chemistry 2003, 67, 531 – 534.
- [2] C. Guillard, H. Lachheb, A. Houas, M. Ksibi, E. Elaloui, J.M. Herrmann, Journal of Photochemistry and Photobiology A: Chemistry 2003, 158, 27–36.
- [3] A. Pearson, H. Zheng, K. Kalantar-zadeh, S. K. Bhargava, V Bansal, Langmuir 2012, 28, 14470–14475.
- [4] S. Markovic, V. Rajic, A. Stankovic, Lj. Veselinovic, J. Belosevic-Cavor, K. Batalovic, N. Abazovic, S. D. Skapin, D. Uskokovic, Solar Energy 2016, 127, 124–135.
- [5] N. Modirshahla, M.A. Behnajady, Dyes and Pigments 2006, 70, 54–59.
- [6] J. He, W. Ma, J. He, J. Zhao, J.C. Yu, Applied Catalysis B: Environmental, 2002, 39, 211–220.
- [7] S. Wang, Dyes and Pigments 2008, 76, 714–720.
- [8] J.H. Ramirez, C.A. Costa, L.M. Madeira, Catalysis Today 2005, 107–108 (2005) 68–76.
- [9] S. Meric, H. Selcuk, M. Gallo, V. Belgiorno, Desalination 2005, 173, 239–248.
- [10] J. Wu, T. Wang, Ozonation of aqueous azo dye in a semi-batch reactor, Water Research 2001, 35, 1093–1099.
- [11] M.A. Rauf, S. Salman Ashraf, Journal of Hazardous Materials 2009, 166, 6–16.
- [12] Lj. Matovic, A. Đukic, M. Omerasevic, K. Kumric, O. Roskopfova, A. Hamarova, P. Rajec, J Radioanal Nucl Chem, 2017, 314, 897–905.
- [13] Teng H, Lin YC, Hsu LY, J Air Waste Manag Assoc 2000, 50, 1940–1946.
- [14] H. Guedidi, L. Reinert, Y. Soneda, N. Bellakhal, L. Duclaux, Arab. J. Chem. 2017, 10, S3584-S3594.

## EPR AND THEORETICAL INVESTIGATION OF HYDROXYL RADICAL SCAVENGING OF SELECTED CATECHOLAMINES

A. Radović, D. Dimić, Đ. Nakarada and J. Dimitrić-Marković

*University of Belgrade, Faculty of Physical Chemistry,  
Studentski trg 12-16, 11000 Belgrade, Serbia. (ddimic@ffh.bg.ac.rs)*

### ABSTRACT

In the central nervous system (CNS) neurotransmitters and their metabolites act as the first line of defense against oxidative stress. Dopamine, epinephrine, norepinephrine, 3,4-dihydroxy-L-phenylalanine (L-DOPA), catechol as well as dopamine metabolites (3,4-dihydroxyphenylacetic acid (DOPAC), homovanilic acid (HVA) and 3-methoxytyramine (3-MT)) were investigated experimentally and theoretically for their ability to scavenge hydroxyl radical. Electron paramagnetic resonance (EPR) spectroscopy was used to determine the antiradical activity of investigated molecules, and density functional theory calculations were used to determine most probable reaction mechanism. The obtained results show that hydrogen atom transfer (HAT) mechanism is preferable. All investigated molecules can be classified as excellent antiradical scavengers, except for 3-MT and HVA.

### INTRODUCTION

Significant amounts of reactive oxygen species (ROS) are formed in the brain because more than 20% of the body's oxygen is used in the brain. When they are formed in the brain, they can cause lipid peroxidation and damage to biologically important molecules, such as DNA and proteins [1,2].

Due to the inability of natural and artificial antioxidants to pass the blood-brain barrier, the first line of defense, against oxidative stress, consists of molecules that are synthesized in the brain. These molecules include catecholamines – dopamine, epinephrine and norepinephrine, which function as hormones and neurotransmitters in the central nervous system (CNS). It is also considered that precursors and metabolites of these catecholamines, such as 3,4-dihydroxy-L-phenylalanine (L-DOPA), 3,4-dihydroxyphenylacetic acid (DOPAC), homovanilic acid (HVA) and 3-methoxytyramine (3-MT), have an important role in the antioxidative defense of CNS [2]. All the above-mentioned molecules, except 3-MT and HVA, contain catechol moiety, and therefore the catechol is investigated with those molecules.

The reaction between the hydroxyl radical and antioxidant molecules, which includes H-atom abstraction, can be described using three different mechanisms: hydrogen atom transfer (HAT), single electron transfer followed by the proton transfer (SET-PT) and sequential proton loss electron transfer (SPLET). Thermodynamic parameters which correspond to the above mentioned mechanisms are: the Bond Dissociation Energy (BDE) in the HAT mechanism, the Ionization Potential (IP) and the Proton Dissociation Enthalpy (PDE) in the SET-PT mechanism, the Proton Affinity (PA) and the Electron Transfer Enthalpy (ETE) in the SPLET mechanism [2]. These values can be calculated from the enthalpies of the respective species as shown in [2]

In this paper, the antiradical activity of catecholamines, their precursors and their metabolites, towards hydroxyl radical was determined. A theoretical approach was used to determine the most probable mechanism of reaction between hydroxyl radical and investigated molecules.

## EXPERIMENTAL/THEORETICAL METHODS

The ability of dopamine, epinephrine, norepinephrine, DOPAC, L-DOPA, 3-MT, HVA and catechol to scavenge  $\cdot\text{OH}$  radical was tested using Fenton reaction, as an “ $\cdot\text{OH}$  producing” system, with spin-trap DEPMPO [4]. EPR measurements were performed using a Bruker Elexsys E540 EPR spectrometer operating at X-band (9.85 GHz), at room temperature. Samples were drawn into gas-permeable Teflon tubes and recorded 60 min after the start of Fenton’s reaction. The blank samples were prepared under the same conditions as samples with investigated molecule and spectra were recorded after 2 mins. The ratio between areas under signal of sample and blank is presented as antiradical activity (AA).

The calculations were performed using Gaussian Program Package [3]. All geometries were optimized with the M06-2X functional, and the 6-

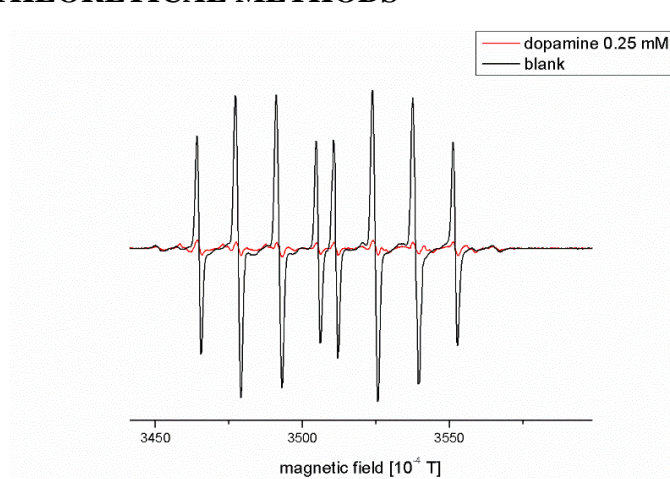


**Figure 1.** EPR spectra of sample with addition of dopamine,  $c=250 \mu\text{M}$

311++G(d,p) basis set. The solvent effects are accounted for by using the conductor-like polarizable continuum model (CPCM).

## RESULTS AND DISCUSSION

The hydroxyl radical forms the stable spin adduct with spin trap DEPMPO [4], and the resulting adduct signal is used to monitor AA.

It has been observed that the addition of dopamine (Fig 1.) and other investigated molecules leads to a significant decrease in the intensity of the peaks in the EPR spectra. This indicates that all investigated molecules have antiradical properties. By comparing AA (Table 1.), these molecules can be divided into two groups. The first group includes catechol and molecules that contain catechol moiety, while the second group consists of molecules that don't possess this structural element. Table 1 shows that molecules belonging to the

first group have a high AA (>95%), while the AA of the molecules from the second group is significantly lower (about 30%). These results indicate that the presence of the catechol moiety greatly improves the antiradical activity of the molecule.

The investigated molecules have a different number of

“active” sites that can be significant for AA. Those sites are OH groups attached to the benzene ring, COOH and NH<sub>2</sub> groups. Thermodynamic parameters for different mechanisms are shown in Table 2. The lower values represent the more probable reaction mechanism. The values of all thermodynamic parameters, related to NH<sub>2</sub> and COOH groups, are substantially higher than the parameters corresponding to OH groups, and from this, it can be concluded that AA of the investigated molecules primarily comes from OH groups attached to the benzene ring. It can also be seen that BDE values in all investigated molecules are significantly lower than IP and PA values. From this, it follows that the most probable mechanism of the reaction is HAT mechanism. By comparing the BDE values, it can be noticed that molecules with catechol moiety, have lower BDE values (about 15 kJ mol<sup>-1</sup>), in comparison with molecules without catechol moiety. This is due to the fact that in these molecules intramolecular hydrogen bonds can be formed, which additionally stabilizes the resulting radical of the investigated molecule.

**Table 1.** Antiradical activities of investigated molecules, c=250 μM

Molecule	Antiradical activity
Catechol	100.0 %
Dopamine	96.0 %
L-DOPA	99.1 %
DOPAC	98.6 %
Epinephrine	100.0 %
Norepinephrine	96.8 %
3-MT	71.3 %
HVA	65.8 %

**Table 2.** Thermodynamic parameters for investigated molecules (kJ mol<sup>-1</sup>)

Molecule	Site	HAT	SET-PT		SPLET	
		BDE	IP	PDE	PA	ETE
Catechol	OH	-156	107	-264	-105	-52
Dopamine	p-OH	-163	95	-258	-102	-60
L-DOPA	p-OH	-161	102	-263	-105	-56
DOPAC	p-OH	-159	104	-263	-107	-52
Epinephrine	p-OH	-162	99	-261	-110	-53
Norepinephrine	p-OH	-161	96	-257	-104	-57
3-MT	p-OH	-147	87	-234	-72	-74
HVA	p-OH	-142	97	-239	-77	-65

## CONCLUSION

In the reaction of investigated molecules and hydroxyl radical, it has been shown that all molecules are excellent antiradical scavengers, except for 3-MT and HVA. The theoretical considerations have also shown that investigated molecules are good antiradicals, except 3-MT and HVA. This can be explained by stabilization effects of the intramolecular hydrogen bond present in radicals of the corresponding molecules, which contain catechol moiety. From the theoretical calculations it was also concluded that the most likely mechanism of the reaction with the hydroxyl radical is HAT mechanism.

## Acknowledgement

This work was partially supported by the Ministry for Science of the Republic of Serbia (Grants no. 172040, 41005 and 172015).

## REFERENCES

- [1] T. Shimizu, Y. Nakanishi, M. Nakahara, N. Wada, Y. Moro-oka, T. Hirano, T. Konishi, S. Matsugo, *J. Clin. Biochem. Nutr.*, 2010, 47, 181-190.
- [2] D. Dimić, D. Milenković, J. Dimitrić Marković, Z. Marković, *Phys. Chem. Chem. Phys.*, 2017, 19, 12970.
- [3] M. J. Frisch, et al., *Gaussian 09*, revision D.01, Gaussian, Inc., Wallingford CT, 2009.
- [4] J. Dimitrić Marković, B. Pejin, D. Milenković, D. Amić, N. Begović, M. Mojović, Z. Marković, *Food Chemistry*, 2017, 218, 440-446.

## DNA-SE I INHIBITORY PROPERTIES OF NEW BENZOCYCLOBUTANE-2,5-DIONES EXPERIMENTAL AND DOCKING STUDIES

Z. Džambaski<sup>1</sup> A. Kolarević<sup>2</sup>, B. S. Ilić<sup>3</sup>, A. Rašović,<sup>1</sup> A. Šmelcerović<sup>1</sup> and  
B. P. Bondžić<sup>1,\*</sup>

<sup>1</sup>Center for Chemistry ICTM, University of Belgrade, P.O. Box 815, 11000  
Belgrade, Serbia

<sup>2</sup>Department of Pharmacy, Faculty of Medicine, University of Niš, 18000  
Niš, Serbia

<sup>3</sup>Department of Chemistry, Faculty of Medicine, University of Niš, 18000  
Niš, Serbia

### ABSTRACT

Eight new benzocyclobutane-2,5-diones (**1a-1h**) were synthesized using photocycloaddition of duroquinone with various phenylsubstituted ethylenes.<sup>1</sup> Reaction is performed in the presence of 18W CFL lamp. Inhibitory properties against bovine pancreatic deoxyribonuclease I (DNase I) of studied compounds were examined *in vitro*. In order to analyze potential binding sites for the studied compounds with DNase I, molecular docking study was performed. To the best of our knowledge, this is the first report on biological activity of benzocyclobutane-2,5-diones.

### INTRODUCTION

The derivatives of 1,4-benzoquinone are known to exhibit various biological activities, such as antibacterial, antitumor, antioxidant, anti-inflammatory, anticoagulant, activities, and also act as urease and monoamine oxidase inhibitors.<sup>2</sup> In the present study several new benzocyclobutane-2,5-diones were synthesized and their inhibitory properties against bovine pancreatic deoxyribonuclease I (DNase I) were examined *in vitro*. For the compounds that inhibited DNase I activity, the mode of DNase I inhibition was determined. Finally, *in silico* studies, including molecular docking were performed.

### EXPERIMENTAL

#### Inhibition of DNase I activity

DNase I inhibitory properties of the studied compounds **1a-1h** were evaluated according to the previously published procedure (Ilić et al., 2018).

To determine the mode of DNase I inhibition by compounds **1a** and **1b**, Lineweaver-Burk plot analysis was performed. This kinetic study was carried out in the absence and presence of the inhibitor with varying concentrations of DNA as the substrate.

*Receptor preparation and docking protocol*

As no crystal structure with co-crystallized inhibitor is available, and since enzyme inhibition was assayed on bovine DNase, the crystal structures of bovine DNase I with N-acetylglucosamine and a DNA (PDB code: 2DNJ) was taken as the starting point (Lahm and Suck, 1991).

## RESULTS AND DISCUSSION

### DNase I inhibition

In order to expand the number of known organic compounds able to inhibit DNase I, newly synthesized benzocyclobutane-2,5-diones **1a-1h** (Figure 1) were employed in evaluation of DNase I inhibition *in vitro*.

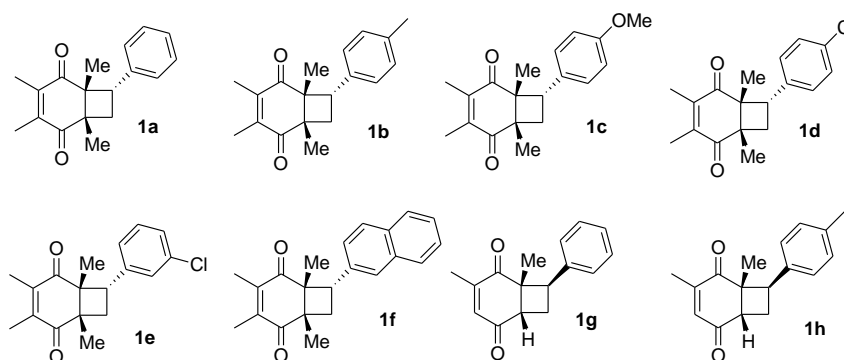


**Figure 1.** Studied compounds

Two out of eight studied compounds inhibited bovine pancreatic DNase I with  $IC_{50}$  values below 200  $\mu$ M. Compounds **1a** and **1b** inhibited DNase I activity with similar  $IC_{50}$  values of  $136.47 \pm 20.00 \mu$ M and  $135.58 \pm 25.47 \mu$ M, respectively. Crystal violet, used as positive control, exhibited weaker DNase I inhibition compared to compounds **1a** and **1b** ( $IC_{50} = 365.22 \pm 39.95 \mu$ M). Based on the obtained Lineweaver-Burk plots, compounds **1a** and **1b** inhibited bovine pancreatic DNase I in a non-competitive manner (Figure 2).

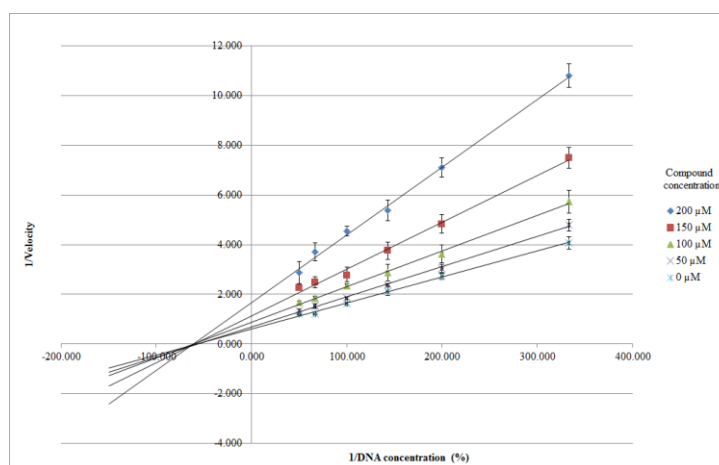


**Figure 2.** Lineweaver-Burk plots for the inhibition of DNase I by compound **1a** with DNA as substrate

The docking studies suggests that there might not be only one preferable binding site for small-molecule inhibitors, and that potency might be correlated with the ability of an inhibitor to bind to several, if not all suggested binding sites.

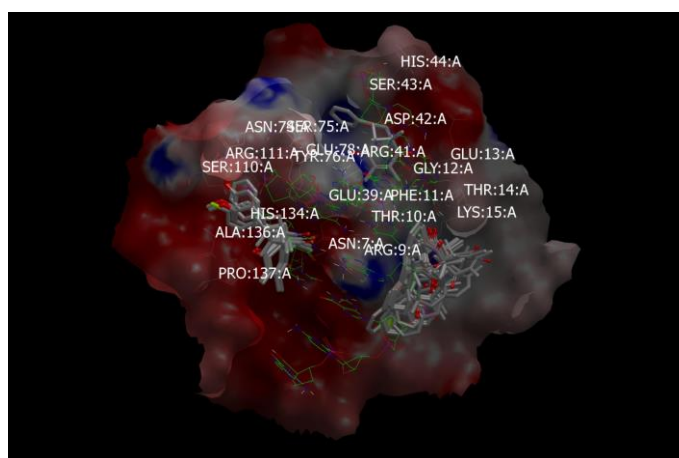


**Figure 3.** Result of docking studies into DNase I, 5 top-ranked poses for each compound is presented. Protein is presented as a surface with important amino acid residues in sticks, DNA fragment is rendered in sticks, and the docked molecule rendered as solid sticks coloured by atom type

This hypothesis might be reasoned by very large substrate-binding site of DNase I, which accommodates quite a large portion of a DNA double strand

and may indeed offer several binding sites for small molecules. This seems reasonable, as for an inhibitor to compete with the DNA double strand for the same binding site, binding of just one inhibitor molecule might be energetically too weak to compensate for dissociation of a DNA double strand (Figure 3).

### CONCLUSION

To summarize, we have synthesized a small series of new benzocyclobutane-2,5-diones **1a-1h**. Obtained compounds were tested on DNase I inhibitory activity. Compounds **1a** and **1b** inhibited bovine pancreatic DNase I in a non-competitive manner with IC<sub>50</sub> values below 200 μM. Docking studies revealed potential binding sites.

### *Acknowledgement*

Support of this work by Ministry of Education, Science and Technological Development of the Republic of Serbia (Grants No. OI 172020 OI 172044, OI 171025 and TR 31060).

### REFERENCES

- [1] Maruyama, K. and Osuka, A. (1988) Recent advances in the photochemistry of quinones, in *The Quinonoid Compounds: Volume 1* (1988) (eds S. Patai and Z. Rappoport), John Wiley & Sons, Inc., Chichester, UK. Chapter 13, pp 759–878.
- [2] (a) Batra, M., Kriplani, P., Batra, C., & Ojha, K. G. (2006). An efficient synthesis and biological activity of substituted *p*-benzoquinones. *Bioorganic and Medicinal Chemistry*, 14(24), 8519–8526. (b) Mostert, S., Petzer, A., & Petzer, J. P. (2017). The evaluation of 1,4-benzoquinones as inhibitors of human monoamine oxidase. *European Journal of Medicinal Chemistry*, 135, 196–203.

## SPIN-LABELING EPR SPECTROSCOPY AS A USEFUL TOOL FOR THE INVESTIGATION OF BIOPHYSICAL PROPERTIES OF BLOOD CELL MEMBRANES AND SERUM ALBUMIN

A. Pavićević<sup>1</sup>, A. Vesković<sup>1</sup>, M. Lakočević<sup>2</sup>, A. Popović-Bijelić<sup>1</sup> and M. Mojović<sup>1</sup>

<sup>1</sup> *University of Belgrade, Faculty of Physical Chemistry, Studentski trg 12-16, 11000 Belgrade, Serbia. (aleks.pavicevic@ffh.bg.ac.rs)*

<sup>2</sup> *Clinical Centre of Serbia, Clinic of Endocrinology, Diabetes and Metabolic Diseases, Dr Subotića 13, 11000 Belgrade, Serbia*

### ABSTRACT

Spin-labeling electron paramagnetic resonance (EPR) spectroscopy, applied to particular blood components, i.e. human serum albumin, erythrocytes or peripheral blood mononuclear cells (PBMCs), can successfully be used as a diagnostic tool for metabolic and metabolic-like disorders. In this paper, we show that spin-labeling of erythrocytes membranes can successfully be used to monitor the effectiveness of the enzyme replacement therapy (ERT) of patients suffering from Gaucher disease (GD) and that spin-labeling of serum albumin, improved with new selection of spin-labels, can be used for diagnosis of various malignancies.

### INTRODUCTION

A plethora of physicochemical techniques have been developed to study biomolecules and bimolecular assemblies. One of these techniques implies the implementation of the stable paramagnetic compounds into these macromolecular systems, which are further detected using the EPR spectroscopy. These paramagnetic species are called spin probes (SPs) if they bind to the system under investigation in a non-covalent manner, or spin labels (SLs) if they form covalent bonds with the biomacromolecule. SPs and SLs are organic compounds which have the unpaired electron usually located on a nitrogen atom of the aminoxyl group (Figure 1). SPs typically used to examine membrane properties are aminoxyl derivatives of different kinds of lipids, primarily fatty acids or phospholipids. These compounds contain aminoxyl group (mainly doxyl group) bounded to different carbon atoms of the hydrophobic chain, thereby allowing the assessment of the membrane properties at different depths of the lipid bilayer. Spin-labeled fatty acids can also be used to monitor conformational changes and the binding capacity of

the proteins which are able to bind lipids with relatively high-affinity (e.g. human serum albumin, HSA).

However, more commonly used approach involves the covalent attachment of the site-specific SLs to the free sulfhydryl or amino groups on the protein [1].

The principle of the EPR/SP/SL technique relies on the sensitivity of the SPs' and SLs' EPR spectra to the molecular environment: polarity, proticity, motional restrictions, etc. Thus, measurement of certain EPR spectral parameters such as parallel hyperfine splitting ( $2A_{\parallel}$ ) and order parameter ( $S$ ) provide information about changes in the protein and membrane structure [1]. Taking all

of the aforementioned in consideration, EPR/SP/SL technique has a great diagnostic potential, as it may be applied to study alterations in proteins and membranes induced by certain pathologies.

In this work, we show that this approach, when applied to erythrocytes blood cell membranes, can successfully be used for the diagnosis of GD, and the follow-up of the ERT treatment effectiveness. GD [2] is a most common inherited lysosomal storage disorder caused by mutations in a *GBA1* gene. These mutations may result in a deficient activity of the  $\beta$ -glucocerebrosidase, a lysosomal enzyme responsible for the degradation of the glucosylceramide (GlcCer) to glucose and ceramide. Consequently, GlcCer accumulates inside monocytes and macrophages, leading to the alterations of the membrane properties, which are reflected in the EPR spectra through the statistically significant changes of the  $2A_{\parallel}$  and  $S$ , the parameter used as a measure of membrane ordering.

On the other hand, in malignancy-related pathologies, small peptide fragments and other metabolites are released into the blood where they bind to HSA modifying its binding capacity. Therefore, HSA from the blood plasma/serum of the patients suffering from various types of cancers and other diseases show altered binding of spin-labels [3]. These changes are commonly shown using spin-label 16-doxy stearic acid (16-DS) through

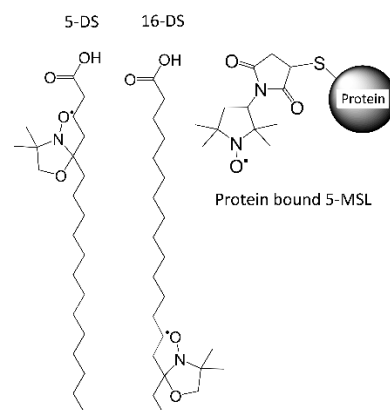


**Figure 1.** Chemical structures of 5- and 16-doxy stearic acid (5-DS and 16-DS) and 3-maleimido proxyl (5-MSL) covalently bound to sulfhydryl group of protein.

different contributions of EPR spectral components (unbound, strongly and weakly bound [3]).

### EXPERIMENTAL

As in the general spin labeling/probing procedure, small amount of the SL/SP (in this case 5-doxyl stearic acid, 5-DS) dissolved in some organic solvent (due to their low water-solubility) is added to the bottom of the test tube, and the solvent is left to evaporate. Afterwards, the cell suspension (or the protein) solution is added to this tube, and the mixture is gently vortexed. In order to examine erythrocyte membranes, blood samples were collected from healthy controls (HC) and GD patients (one therapy-naive (TN) group and two groups receiving plant based ERT at two different doses) by venipuncture, into the tubes containing sodium citrate as an anticoagulant. Blood samples were centrifuged 10 min at 700 x g, and the supernatant (plasma) was discarded. Saline solution was added to wash erythrocytes, and the sample was centrifuged 10 min at 700 x g. This procedure was repeated three times. The final sample containing the labeled erythrocytes was transferred to the resonator cavity of the EPR spectrometer (X-band Bruker Elexsys II E540) and the EPR spectra were acquired.

### RESULTS AND DISCUSSION

The typical EPR spectrum of the freely rotating aminoxyl molecules in solution is characterized by three sharp lines of the almost equal intensities (Figure 2a, left). However, when these compounds are incorporated into the cell membranes, or proteins, their motional freedom is restricted, which results in the asymmetrically broadened anisotropic EPR spectra (Figure 2a, right).

The results obtained by probing erythrocyte membranes with 5-DS (Fig. 2b) indicate that parameters  $2A_{\parallel}$  and  $S$  can be used to successfully distinguish between TN patients and HC, as well as between patients receiving ERT (both doses) and TN patients. The values of  $2A_{\parallel}$  and  $S$  calculated for erythrocytes were analyzed using one-way ANOVA with Bonferroni correction. Thus, we propose that the EPR/spin labeling of blood cell membranes and statistical analysis of  $2A_{\parallel}$  and  $S$  values can be used as an efficient assay for Gaucher disease.

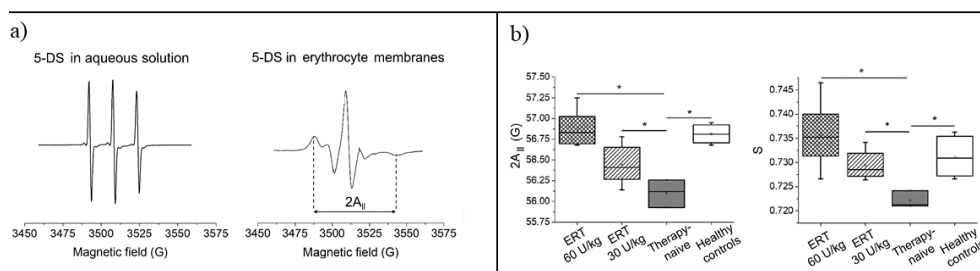


**Figure 2.** a) Typical EPR spectra of 5-DS in an aqueous solution (left) and erythrocyte membranes (right); b) Box charts showing the distribution of the  $2A_{||}$ , and  $S$  values in GD patients (TN and those receiving two different doses of ERT) and healthy controls. Asterisk denotes  $p < 0.05$ .

Furthermore, in our recent studies (data not shown) we have demonstrated that, besides 16-DS, other SPs and SLs, like 5-DS and 3-maleimido proxyl (5-MSL) which binds to free cysteine residues, are also sensitive to the presence of other ligands, and the structural changes in serum albumin [4,5]. Thus, we suggest that 5-DS and 5-MSL may be valuable allies for diagnosis of various malignant diseases.

## CONCLUSION

Based on the results obtained for the EPR/spin-labeling/spin-probing of different blood cell membranes and albumin from blood plasma/serum of patients suffering from various pathologies, we suggest that this technique has the great potential for the diagnostic purposes.

## Acknowledgement

This study was supported by the Ministry of Education and Science of the Republic of Serbia (Grant #41005).

## REFERENCES

- [1] L.J. Berliner, Spin Labeling: Theory and Applications, 1976, Academic Press, New York, USA.
- [2] A. Pavićević et al., Biol. Chem. 2018, 399, 447-452.
- [3] A. Gurachevsky et al., Clin. Chem. Lab. Med. 2008, 46, 1203-1210.
- [4] A. Pavićević et al., Eur. Biophys. J. 2017, 46, 773-787.
- [5] A. Pavićević et al., J. Phys. Chem. B, 2014, 118, 10898-10905.

## APPLICATION OF MALDI-TOF/TOF MASS SPECTROMETRY IN DIFFERENTIATION OF YEASTS

S.M. Mitić<sup>1</sup>, Ž. Mitić<sup>2</sup>, B. Danilović<sup>1</sup>, S. Živanović<sup>2</sup>, S. Stojanović<sup>2</sup>,  
S. Najman<sup>2</sup> and D. Savić<sup>1</sup>

<sup>1</sup>*Faculty of Technology, University of Niš, RS-16000 Leskovac, Serbia  
([sanja.novakovic6@gmail.com](mailto:sanja.novakovic6@gmail.com))*

<sup>2</sup>*Faculty of Medicine, University of Niš, RS-18000 Niš, Serbia*

### ABSTRACT

Whole cells of 5 yeast strains belonging to 3 genera (*Candida albicans* ATCC 2091, *Saccharomyces cerevisiae* ATCC: 2601, 9763 and ME, and *Rhodotorula glutinis*) grown in the different media were analyzed by using matrix assisted laser desorption/ionization-time of flight mass spectrometry (MALDI-TOF MS). The numerical data of scans were subjected to Hierarchical Cluster Analysis (HCA) in order to differentiate the species. The results showed that MALDI-TOF/TOF MS can be a useful technique for differentiation of three genera regardless of media used for their growth.

### INTRODUCTION

Yeasts have wide ranging fundamental and industrial importance in scientific disciplines, food, medicine and agriculture [1]. The rapid identification of yeast species has importance in developing economic losses in the food industry [2] and the appropriate treatment [3]. MALDI-TOF MS method is applicable for macromolecule analysis such as proteins, DNA, peptides, carbohydrates, natural or fragmented biomolecules, such as viruses, bacteria, molds and yeasts [4]. MALDI-TOF MS for identification microbial species using proteomic analysis is popular as an alternative to chromatographic and even DNA-dependent methods. This technique is based upon the detection of microbial proteins in a mass range of 2–20 kDa by the time-of-flight (TOF) mass analyzer in which the velocity of the ion depends on the mass-to-charge ratio ( $m/z$ ) [5]. In order to differentiate and even identify the microorganism, the spectral data are subjected to statistical analysis, applying HCA. The aim of this work is to use statistical techniques on data obtained from MALDI-TOF/TOF MS as a simple and fast method that will make easier differentiation of yeasts.

### EXPERIMENTAL

**Materials.** Five different yeasts strain of three genera were used for testing. *Rhodotorula glutinis* strain was previously isolated from piller deep frozen

apple dices produced in cold storage Jugprom (Leskovac, Serbia) and identified by VITEK 2 Systems Version: 07.01. (Faculty of Technology, Novi Sad, Serbia), *Saccharomyces cerevisia* was represented with 3 strains ATCC: 2601, 9763 and selection yeast strain Maurivin Elegance (ME, Aromatica, Serbia) and *Candida* with one *C. albicans* strain ATCC 2091. Prior to scanning, all strains were cultivated on two solid media during 48 h at 25 °C each in triplicate [6]: Sabouraud Maltose Agar (SMA, Lab a Neogen Company, UK) with the addition of chloramphenicol 50 mg/L (HiMedia, India) and gentamycin 50 mg/L (Galenika AD, Serbia) and on Dichloran Rose Bengal Chloramphenicol agar (DRBC, HiMedia, India).

**MALDI-TOF/TOF MS.** The method was consisted of the fast formic acid extraction [6]. A thin layer of a colony was transferred directly to the 384-well polished steel target plate and allowed to air-dry. Then, 1  $\mu$ L of 70% formic acid (FA, Carlo Erba, France) was applied to the sample spot and after a short drying period, the spot was covered by 1  $\mu$ L of a daily prepared solution of  $\alpha$ -cyano-4-hydroxycinnamic acid (CHCA, Bruker Daltonics, Germany). MALDI-TOF/TOF MS measurements were performed on an Autoflex speed instrument (Bruker Daltonics, Germany) operating in linear positive mode in the  $m/z$  range of 2–20 kDa. A solid-state, Nd:YAG 535 nm SmartBeam laser, with a frequency of 1000 Hz was used for ionization. Typically, the spectra were collected by accumulating 3000 laser shots from 6 different spots. The spectra were acquired using the FlexControl software (Bruker Daltonics, Germany).

**Statistical analyses.** HCA was processing by the MicrobeMS software, version 0.80 (Robert-Koch-Institute, Germany) with prerequisites and spectra pre-processing described by the manufacturer, using allowed mass tolerance of 800 ppm, Ward's as clustering method and correlation as a distance method.

## RESULTS AND DISCUSSION

The MALDI-TOF/TOF mass spectra of yeasts grown on SMA medium, obtained by using CHCA as a matrix, are shown in Fig. 1. MALDI-TOF/TOF MS on Fig. 1., contain some prominent peaks in the 3000–8000 Da range, such as at  $m/z$  3801, 6372, 6396, 6509, 6779, 7217, 7250, 7290, 7331 and 7355 for *C. albicans*; 3678, 6382, 6412, 6449, 6830, 7432, 7743, 7936, 7974 and 8014 for *R. glutinis*; and 3578, 3647, 3812, 6326, 6496, 6521, 6849, 6876, 6908 and 7311 for *S. cerevisiae*. Very similar MALDI-TOF MS of *C. albicans*, as shown in Fig. 1.a., have already shown by Panda et al. [5].

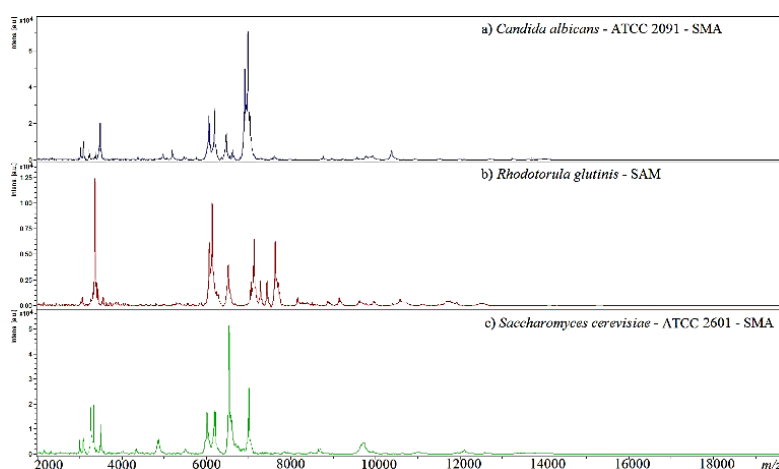


**Figure 1.** The MALDI-TOF/TOF mass spectra of yeast strains grown on SMA: a) *Candida albicans*, b) *Rhodotorula glutinis* and c) *Saccharomyces cerevisiae*.

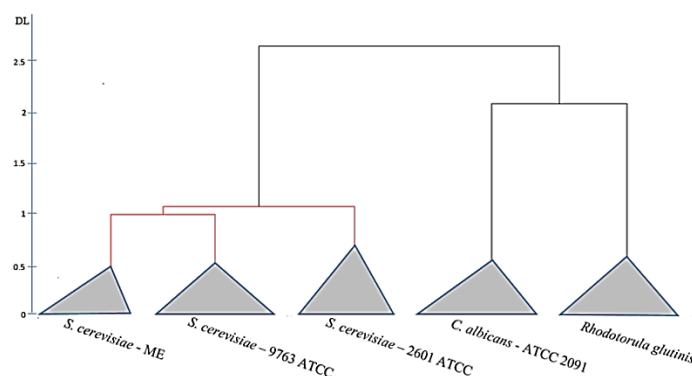


**Figure 2.** Dendrogram of Cluster analysis MALDI-TOF/TOF MS of yeast strains grown on SMA and DHRB.

The MS spectra of investigated yeast strains were subjected to HCA in order to estimate the potential of MALDI-TOF/TOF MS regarding to differentiate strains. The statistical analysis clearly separates the spectra of 5 used strains regardless of the media the yeast were grown on (Fig 2.). The level of differentiation between *R. glutinis* and *C. albicans* seems to be approximately 2 units, while all three *S. cerevisiae* strains are clearly separated on a distance level of 1 unit.

## CONCLUSION

The results of this study are confirmed the great potential of MALDI-TOF/TOF MS in differentiation and identification of microorganisms, especially yeasts. MALDI-TOF/TOF MS is a useful technique for differentiation of three genera (*C. albicans*, *R. glutinis* and *S. cerevisiae*) regardless of media used for their growth. HCA results show satisfactory levels of differentiation between three genera were used in this work.

## Acknowledgement

This work was partially supported by the Faculty of Medicine, University of Niš, Republic of Serbia (Grant no. **11-14629-4/16**) and the Ministry for Science of the Republic of Serbia (Grant no. **III41017**)

## REFERENCES

- [1] C.P. Kurtzman, J.W. Fell, T. Boekhout, *The Yeasts*, a taxonomic study, Elsevier, London, 2011.
- [2] R. Quintilla, A. Kolecka, S. Casaregola, H.M. Daniel, J. Houbraken, M. Kostrzewa, T. Boekhout, M. Groenewald, *International Journal of Food Microbiology*, 2018, 266, 109-118.
- [3] J. Qian, J.E. Cutler, R.B. Cole, Y. Cai, *Analytical and Bioanalytical Chemistry*, 2008, 392, 439-449.
- [4] C.H. Wick, *Identifying Microbes by Mass Spectrometry Proteomics*, CRC Press, Boca Raton, 2014.
- [5] A. Panda, A.K. Ghosh, B.R. Mirdha, I. Bijay, S. Paul, J.C. Samantaray, A. Srinivasan, S. Khalil, N. Rastogi, Y. Dabas, *Journal of Microbiological Methods*, 2015, 109, 93-105.
- [6] C. Cassagne, A.L. Cella, P. Suchon, A.C. Normand, S. Ranque, R. Piarroux, *Medical Mycology*, 2013, 51, 371-377.

## DEVELOPMENT OF BIOACTIVE Ag/CS-PVA HYDROGEL MEMBRANE CONTAINING CHITOSAN NANOPARTICLES BY IONIZING RADIATION

J. Krstić<sup>1</sup>, A. Radosavljević<sup>1</sup>, J. Spasojević<sup>1</sup>, D. Jovanović<sup>2</sup>,  
Z. Rakočević<sup>1</sup>, S. Popović<sup>3</sup> and Z. Kačarević-Popović<sup>1</sup>

<sup>1</sup> Vinca Institute of Nuclear Sciences, University of Belgrade, 11001  
Belgrade, Serbia. (jelenak@vinca.rs)

<sup>2</sup>Institute of Microbiology, Military Medical Academy, 11000 Belgrade,  
Serbia.

<sup>3</sup>Clinic for Endocrinology, Diabetes, and Metabolic Diseases, Faculty of  
Medicine, University of Belgrade, 11000 Belgrade, Serbia.

### ABSTRACT

This research aims to develop novel hydrogel nanocomposites based on silver and chitosan nanoparticles incorporated into poly(vinyl alcohol) cross-linked matrix (Ag/CS-PVA), using  $\gamma$ -irradiation technology. Radiation-chemical modification of polymer/metal constituents down to nanoparticle form and also their integration enabled the fine adjustment of their predefined inherent properties, for biomedical applications. Porous morphology of hydrogel nanocomposites, capable to absorb and retain large amounts of biological fluids over a long period of time, together with improved physico-chemical properties, such as biocompatibility, antibacterial activity, mechanical stability, are the major breakthrough of radiolytic method for synthesis of innovative materials for biomedical applications.

### INTRODUCTION

Radiation nanotechnology open up new strategy to manipulate with advanced functional materials containing noble metals, natural and synthetic polymers at nanometer scale, in order to obtain hybrid 3D-hydrophilic environment for biomedical applications [1]. The polymer blends for biomedical applications are commonly defined as systems whose primary role is to connect with biological tissues in order to improve their basic function or to replace tissue or organs. Today, the biodegradable hydrogel membranes were intensively produced for the medical market due to their improved biocompatible properties. In the last few decades, the need for polysaccharide modification has intensified, especially for biomedical purposes, because polysaccharides are biological polymers that can be obtained from several natural sources such as microbiological, animal and plant sources. For the synthesis of hydrogels

for the treatment of wounds, it is extremely important to achieve the biodegradability, biocompatibility and antibacterial efficacy as much as possible without the use of chemical and toxic agents [2-4].

The aim of this study is to synthesize and design specific properties of Ag/CS-PVA hydrogel nanocomposites using the radiation-chemical "bottom up" method that would enable the production of membranes for wound treatment applications. In this sense, it is important to optimize the parameters of  $\gamma$ -irradiation for the radiation-chemical synthesis of the hydrogel nanocomposites, to examine their antibacterial potential, the role of CS in nanoparticle form, and also investigate the synergistic effect of Ag and CS NPs.

## EXPERIMENTAL

All chemicals for synthesis were purchased from commercial sources and used without further purification. Poly (vinyl alcohol) (PVA) ( $M_w$  72 kDa; DH min. 99%), silver nitrate ( $\text{AgNO}_3$ ) and 2-propanol ( $(\text{CH}_3)_2\text{CHOH}$ ) were supplied from Merck (Germany). Chitosan (CS) ( $M_w$  95 kDa; DD (75-85) %;  $\eta$  (20-300) cP) were from Sigma-Aldrich (USA). Acetic acid ( $\text{CH}_3\text{COOH}$ ) is the product of Zorka Pharma, Serbia. Argon (Ar) with high purity (99.5%) is the product of Messer Tehnogas, Serbia. Milli-Q Water System with 4 ion exchange columns ( $18.0 \text{ M}\Omega\text{-cm}$  at  $25 \text{ }^\circ\text{C}$ ) was used for water purification. 8 wt% PVA solution was prepared under magnetic stirring at  $90 \text{ }^\circ\text{C}$ . 5 wt% CS solution was prepared in 1M  $\text{CH}_3\text{COOH}$ , under magnetic stirring at  $25 \text{ }^\circ\text{C}$ . CS solution was exposed to  $^{60}\text{Co}$   $\gamma$ -radiation (100 kGy; 20 kGy/h) due to decreasing its molar mass down to 22 kDa and obtaining CS nanoparticles. After neutralization with 1 M NaOH, pH was corrected to 7. Supernatant was dialyzed using semipermeable membrane (3.5 kDa) over a seven day period, due to remove residual acetic acid. *In situ* synthesis of hydrogel nanocomposites by  $\gamma$ -irradiation was performed by exposing  $\text{AgNO}_3/\text{PVA}/\text{CS}$  solutions with different compositions (table 1) up to 200 kGy and 280 kGy (12.2 kGy/h). Ag/PVA control sample was also synthesized under the same conditions by exposing  $\text{AgNO}_3/\text{PVA}$  solution to the absorbed dose of 200 kGy (12.2 kGy/h). Characterization of obtained hydrogel nanocomposites was performed by Atomic Force Microscopy (AFM NanoScience Instruments), Thermo Mechanical Analysis (TMA Q400 EM, TA Instruments) and Test of Antibacterial Activity against *E. coli* (ATTC 25922) and *S. aureus* (ATTC 25923).

## RESULTS AND DISCUSSION

*Morphological properties.* CS nanoparticles size distribution obtained by AFM (figure 1), showed that most of the polymer chains have degraded, through breaking the glycoside bonds, with average chain length around 100 nm. Low molecular CS derivatives with particles size below 100 nm, formed as products of Maillard reaction were obtained in lower yield.

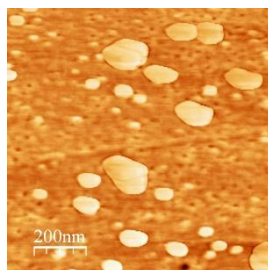


**Figure 1.** Particle size distribution of CS nanoparticles obtained by AFM.

*Mechanical properties.* The highest values of Young's module elasticity and compressive modulus (figure 2), as indicators of the capability of membrane to store energy during deformation, shows the greatest extent (around 20 kPa) for hydrogel nanocomposite S2, and its resistance in response to an applied force.

**Table 1.** Hydrogel nanocomposites synthesized by  $\gamma$ -irradiation.

Samples	Composition of mixture	Absorbed dose (kGy)
S1	8mM AgNO <sub>3</sub> /8wt% PVA	200
S2	8mM AgNO <sub>3</sub> /8wt% PVA/2wt% CS	200
S3	8mM AgNO <sub>3</sub> /8wt% PVA/2wt% CS	280
S4	8mM AgNO <sub>3</sub> /8wt% PVA/4wt% CS	280

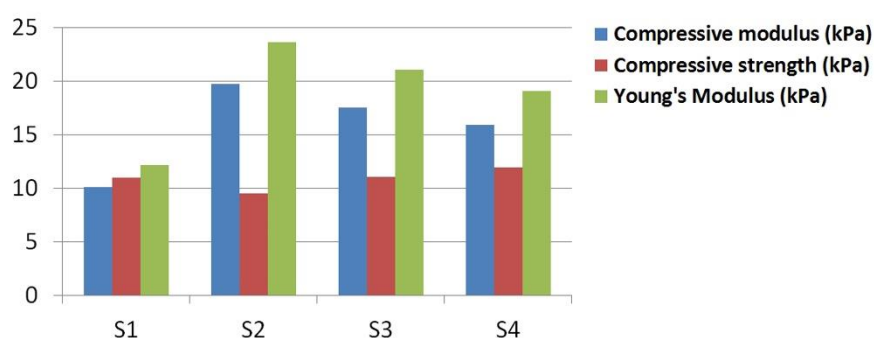


**Figure 2.** Compressive modulus, compressive strength and Young's modulus of hydrogel nanocomposites obtained by  $\gamma$ -irradiation.

*Antibacterial activity.* Zone of inhibition for disc diameter 12 mm (S4) against *E. coli* was around 22 mm, while a slightly higher inhibition zone appears against *S. aureus* bacteria (around 31 mm) (figure 3). The zones of inhibition are far greater than those obtained for the systems that contain the same Ag concentration and do not contain CS (not shown here).

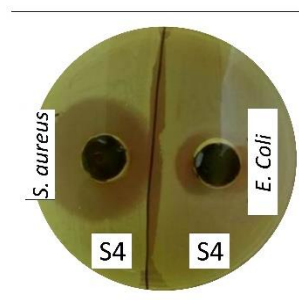


**Figure 3.** Antibacterial activity of S4 against *E. Coli* and *S. Aureus*.

## CONCLUSION

Ag/CS-PVA hydrogel nanocomposites synthesized by *in situ*  $\gamma$ -irradiation technology have significant biomechanical availability ensured by adequate material design, innovative combination components and simple synthesis procedure, applied during this research. Radiation degradability of CS under  $\gamma$ -radiation, together with the attachment of low-molecular-weight products, were used to modulate its structure and solubility under physiological conditions in order to improve mechanical performance of synthesized hydrogel nanocomposites and enhance its antibacterial potential.

## Acknowledgement

This work is financed by the MESTD, III 45005, and by IAEA, CRP: F22051, 16733.

## REFERENCES

- [1] M. I. Baker, S. P. Walsh, Z. Schwartz, B. D. Boyan, J. Biomed. Mater. Res. B: Appl. Biomater. 100 (2012) 1451-1457.
- [2] B. Gullón, M. I. Montenegro, A. I. Ruiz-Matute, A. Cardelle-Cobas, N. Corzo, M. E. Pintado, Carbohydr. Polym. 137 (2016) 382-389.
- [3] W. Pasanphan, P. Rimdusit, S. Choofong, T. Piroonpan, S. Nilsuwankosit, Rad. Phys. Chem. 79 (2010) 1095-1102.
- [4] N. M. Huang, S. Radiman, H.N. Lim, P. S. Khiew, W. S. Chiu, K. H. Lee, A. Syahida, R. Hashim, C. H. Chia, Chem. Eng. J. 155 (2009) 499-507.

## INFLUENCE OF THE LOW FREQUENCY RANGES OF MAGNETIC FIELD ON *SACCHAROMYCES CEREVISIAE* RESPIRATION

I. N. Bubanja<sup>1</sup>, B. Lončarević<sup>2</sup>, M. Lješević<sup>2</sup>, V. Beškoski<sup>3</sup>, G. Gojgić-Cvijović<sup>2</sup>, Z. Velikić<sup>4</sup> and D. Stanisavljev<sup>1</sup>

<sup>1</sup>*Faculty of Physical Chemistry, University of Belgrade, Studentski trg 12-16, Belgrade, Serbia ([itana.bubanja@ffh.bg.ac.rs](mailto:itana.bubanja@ffh.bg.ac.rs))*

<sup>2</sup>*Department of Chemistry, Institute of Chemistry, Technology and Metallurgy, University of Belgrade, Njegoševa 12, Belgrade, Serbia*

<sup>3</sup>*Department of Biochemistry, Faculty of Chemistry, University of Belgrade, Studentski trg 12-15, Belgrade, Serbia*

<sup>4</sup>*Institute of Physics, University of Belgrade, Pregrevica 118, Zemun, Serbia*

### ABSTRACT

In this paper influence of the low frequency magnetic field on *Saccharomyces cerevisiae* respiration was examined. Influence of four low frequency magnetic field ranges was examined: 10-200 Hz, 200-300 Hz, 300-650 Hz and 650-1000 Hz. All analyzed frequency ranges gave the same influence on the yeast cells respiration.

### INTRODUCTION

Over the years, due to the fast technological development, our environment has become more and more influenced by man-made low frequency electromagnetic fields (EMFs). Therefore it is not surprising that this increasing exposure of the population in everyday life to EMFs has earned such a wide public interest. Recently, effects of electric fields (EFs), magnetic fields (MFs) or EMFs on different microbes have become a very popular topic since the mentioned physical fields could potentially act as a stress factors and thus affect the survival of the microbial cells as well as their metabolism and behavior [1]. The influence of static (0 Hz) and 50 Hz magnetic fields on growth of the *Saccharomyces cerevisiae* (by the measurements of solution optical density at 600 nm) was already examined by many authors [2,3]. In this study the influence of different low frequency ranges of the magnetic fields (up to 1 kHz) were examined on the yeast cells respiration. To the best of our knowledge, this is the first time that the influence of magnetic fields is examined on yeast cells by using Micro-Oxymax® respirometer and constant frequency scan regime in the given ranges.

## EXPERIMENTAL

All experiments were performed, in two specially designed glass bottles. Both bottles contained 3 mL of yeast suspension. One bottle was a control sample while the other one was set up inside of the spiral Cu-coil where the low frequency magnetic fields were generated. In order to avoid undesirable temperature increase of the yeast sample because of the heating effect of the coil, sample bottle was set up in a glass water recirculation jacket and all together wrapped in Cu-coil. Control vessel was connected in line with working vessel to minimize possible temperature differences between samples. Arbitrary function generator (Gw Instek AFG-2105, Good Will Instrument Co., Ltd, Taiwan) was used to set up a desired frequency range and a scan interval during which frequencies from set up range are continuously changed from lowest to highest. In this paper we examined influence of four different low frequency ranges: 100-200 Hz, 200-300 Hz, 300-650 Hz and 650-1000 Hz. In all experiments the scan interval was 100 s and total time of exposure was 24 h. In order to achieve the maximal effective current of 2,00 A trough the coil a signal amplifier was used. Maximal effective current of 2,00 A corresponds to magnetic induction of 33 mT. Before every experiment, oscilloscope was used to adjust maximal current. Respiration activity of *Saccharomyces cerevisiae* was measured by a twelve-channel Micro-Oxymax® respirometer (Columbus Instruments, USA). Cell respiration was measured every 20 min during 24 h. Cumulative O<sub>2</sub> consumption and cumulative CO<sub>2</sub> production (in mL) were determined. Experimental setup is shown in Figure 1.

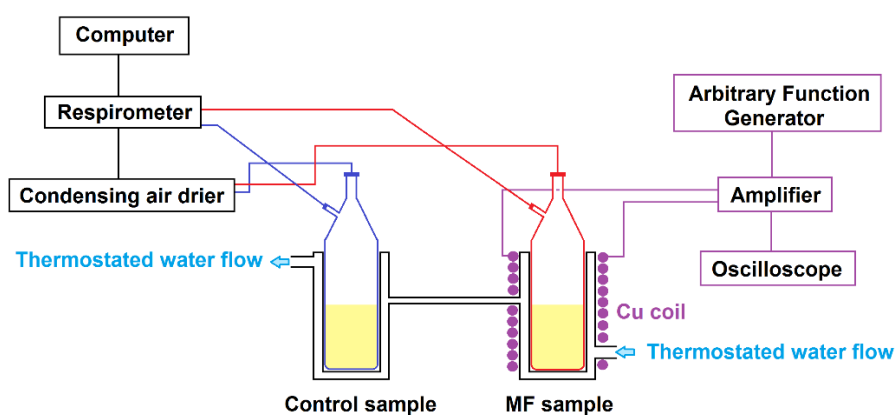


**Figure 1.** Experimental setup.

## RESULTS AND DISCUSSION

Like it was mentioned in Experimental part of this work influence of four low frequency ranges (100-200 Hz, 200-300 Hz, 300-650 Hz and 650-1000 Hz) on yeast respiration were examined.

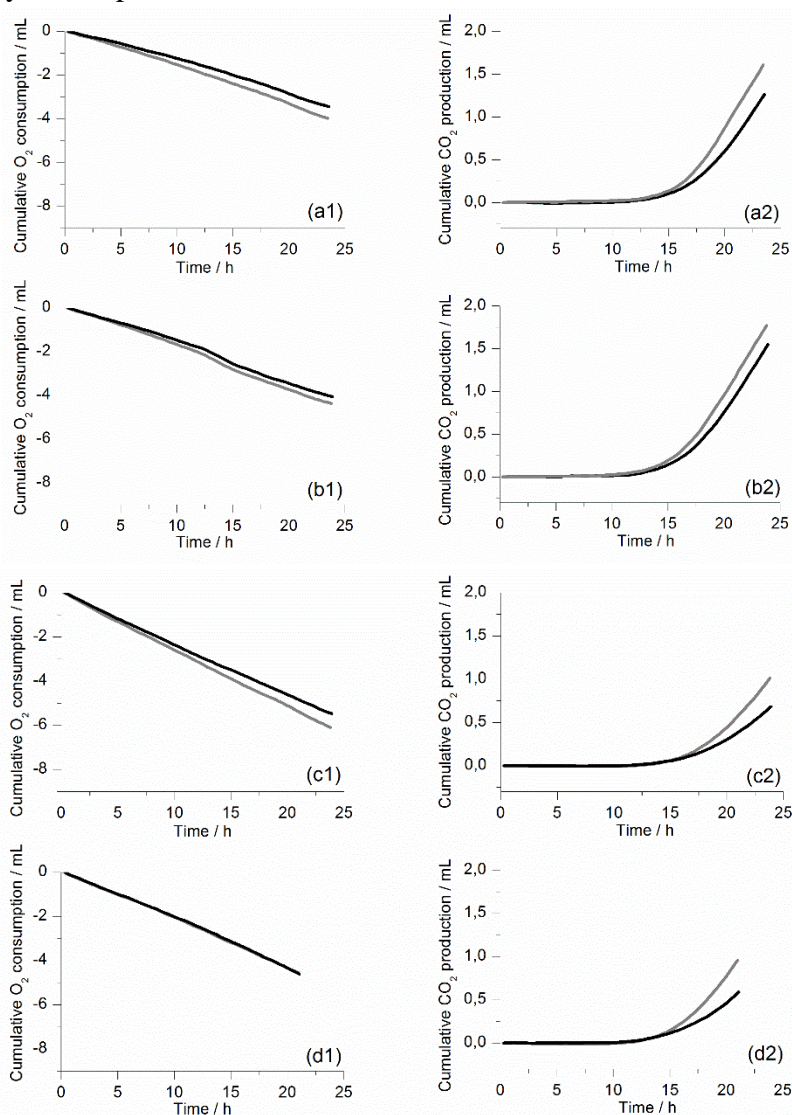


**Figure 2.** Experimentally obtained cumulative O<sub>2</sub> consumption in mL (a1, b1, c1, d1) and cumulative CO<sub>2</sub> production in mL (a2, b2, c2, d2) over 24 h of exposure, for different frequency ranges (100-200 Hz (a1, a2), 200-300 Hz (b1, b2), 300-650 Hz (c1, c2) and 650-1000 Hz (d1, d2)). Gray curve represents changes in control sample and black curve changes of the O<sub>2</sub> and CO<sub>2</sub> in magnetic field sample.

Cumulative O<sub>2</sub> consumption and cumulative CO<sub>2</sub> production were followed in control and magnetic field samples during 24h. Figure 2. shows cumulative O<sub>2</sub> consumption and cumulative CO<sub>2</sub> production in control and magnetic field samples over 24 h obtained for analyzed frequency ranges. Cumulative O<sub>2</sub> consumption is negative because oxygen at the beginning of the experiment (of 21% in air) is taken as reference (0 mL). As it can be seen from Figure 2, up to 15th hour the differences in cumulative CO<sub>2</sub> production between control and magnetic field sample at all investigated frequency ranges are negligible. After 15th hour those differences begin to grow and are the biggest at the end of exposure. Cumulative CO<sub>2</sub> production in magnetic field sample was lower in comparison to control sample for all frequency ranges. Cumulative O<sub>2</sub> consumption, for frequency ranges from 100-200 Hz, 200-300 Hz, 300-650 Hz, in magnetic field sample was lower in comparison to control sample but for 650-1000 Hz range difference is negligible.

## CONCLUSION

All experiments showed lower cumulative O<sub>2</sub> consumption and lower cumulative CO<sub>2</sub> production in magnetic field which confirms magnetic effects. Considering mentioned lower consumption/production of gases, this influence is probably due to deceleration of yeast metabolism or cell division, which should be further investigated and confirmed by statistical tests. It is challenging task to design magnetic treatment to produce desired metabolic changes without using chemical reagents. Obtained results are preliminary and further investigations are necessary to verify proposed hypothesis.

## Acknowledgement

This research was financially supported by the Ministry of Education, Science and Technological Development of Republic of Serbia, through Projects No. OI 172015 and III 43004.

## REFERENCES

- [1] W. Fan, Z. Huang, B. Fan, *Microbial Pathogenesis* 2018, **115**, 117–122.
- [2] M. J. Ruiz-Gomez, M. I. Prieto-Barcia, E. Ristori-Bogajo, M. Martinez-Morillo, *Bioelectrochemistry* 2004, **64**, 151–155.
- [3] J. Novák, L. Strašák, L. Fojt, I. Slaninová, V. Vetterl, *Bioelectrochemistry*, 2007, **70**, 115–121.

## INFLUENCE OF 12-TUNGSTOSILICIC ACID AND 12-TUNGSTOPHOSPHORIC ACID ON THE ACTIVITY AND SECONDARY STRUCTURE OF ACETYLCHOLINESTERASE

A. Bondžić<sup>1</sup>, T. Parac Vogt<sup>2</sup>, A. Vujačić Nikezić<sup>1</sup>, D. Krstić<sup>3</sup> and M. Čolović<sup>1</sup>

<sup>1</sup> *Department of Physical Chemistry, Vinča Institute of Nuclear Sciences, University of Belgrade, P.O. Box 522, 11000 Belgrade, Serbia (aleksandrab@vin.bg.ac.rs)*

<sup>2</sup> *Department of Chemistry, KU Leuven, Celestijnenlaan 200F, Leuven, Belgium*

<sup>3</sup> *Institute of Medical Chemistry, Faculty of Medicine, University of Belgrade, Višegradska 26, 11000, Belgrade, Serbia.*

### ABSTRACT

Inhibition of acetylcholinesterase (AChE) is presented as a promising strategy in the treatment of Alzheimer disease providing inspiration for new discoveries and investigations less toxic and more effective potential anti Alzheimer drugs. In this paper, it demonstrated that the activity of acetylcholinesterase can be effectively inhibited by polyoxometalates (POMs), 12-tungstosilicic acid (WSiA) and 12-tungstophosphoric acid (WPA) without significant changes on the secondary structure of this enzyme. The obtained values of partition coefficient implicated on smooth pass of these POMs trough cell membrane and satisfied necessary criteria for the drugs used in the treatment of the central nervous system disease. Based on these obtained results it is possible to conclude that POM could represent new generation of potential anti Alzheimer drugs.

### INTRODUCTION

Acetylcholinesterase (AChE) is a key enzyme of cholinergic brain synapses and neuromuscular junctions which the major biological role is the termination of impulse transmission by rapid hydrolysis of the cationic neurotransmitter acetylcholine. Besides that, AChE affects cell proliferation, differentiation and responses to various insults, including stress [1]. In medicine, AChE inhibitors are currently used in the therapy of Alzheimer's disease. Polyoxometalates (POMs) are inorganic cluster compounds that possess a number of pharmacological properties such as antibacterial, antiviral and anticancer activities. However, their molecular mechanism of

action is still unknown. The numerous literature data relate their biological activity with the inhibition of enzymes. For example, their antiviral properties are closely associated with inactivation of reverse transcriptases [2] while the activity of the POM decavanadate against leishmania may be due to the inhibition of phosphoglycerate mutase and various phosphatases [3]. In order to confirm possible role of POMs in the treatment of Alzheimer disease we were investigating their influence on the activity and secondary structure of acetylcholinesterase, target enzyme in the treatment of this common neurological disease.

## EXPERIMENTAL

*Chemicals.* Acetylcholinesterase, acetylthiocholine iodide (AChI), 5,5'-dithio-bis(2-nitrobenzoic acid) (DTNB), sodium dodecyl sulfate (SDS), WSiA and WPA were purchased from Sigma-Aldrich (Germany). The other medium assay chemicals, were obtained from Merck (Germany).

*AChE assay.* AChE activity was determined in 0.1 M phosphate buffer pH 8, containing 20  $\mu$ l 2U/ml commercial enzyme and 70  $\mu$ l desired inhibitor concentrations in the final volume of 650  $\mu$ l, using Ellman's procedure [4] and expressed as the mean percentage of enzyme activity relative to the corresponding control value (REA).

### *Measurement of the partition coefficient*

The partition coefficient of the selected POMs was measured using "shake-flask" method, in two phase system composed of n-octanol and deionised water [5]. The absorbance of POMs in the aqueous phase was measured spectrophotometrically at 263 nm for WSiA and at 257 nm for WPA, and used for the determination of the concentration of POMs left in the aqueous phase.

*Fluorescence measurements* were performed using a Fluorolog-3 model FL3-221 spectrofluorimeter (HORIBA Jobin- Yvon) in front face mode. Excitation and emission monochromators were of double grating design, with a dispersion of 2.1 nm mm<sup>-1</sup> (1200 grooves per mm), blazed at 295 nm for excitation and 315 – 420 nm for emission. A xenon lamp provided excitation and a Horiba TBX-04 PMT detector was used for the emission measurements in a right angle configuration using a 1 cm path cuvette.

*Circular Dichroism spectra* were recorded using a Jasco 1500 spectrophotopolarimeter equipped with a Peltier thermostatic system under constant nitrogen flux at 25 °C, with a 0.1 cm quartz cuvette in the range of 190 – 260 nm. The CD spectrum of each sample was recorded three times at a scan rate of 10 nm min<sup>-1</sup>. For the base line, a solution which contain 0.1M phosphate buffer, pH = 8 was used.

## RESULTS AND DISCUSSION

In order to gather information about the influence of selected POMs on AChE activity, the commercially available enzyme was exposed to increasing concentrations of POMs, in the range from  $1 \times 10^{-9}$  to  $1 \times 10^{-4}$  M. Sigmoid-shaped inhibition curves were obtained in both cases (**Fig. 1**). Inhibitory

parameters, half-maximum inhibitory concentration values ( $IC_{50}$ ) and Hill coefficient ( $n$ ) were obtained using Hill analysis of inhibition curves (**Inset, Fig. 1**) and presented in the **Table 1**.

The obtained  $IC_{50}$  values for the selected POMs complexes suggest a powerful inhibition of AChE activity, which is in the submicromolar range. The values of Hill coefficient  $n \sim 1$  indicate no cooperative binding of inhibitor to the enzyme and one binding site of POMs. The obtained values of partition coefficient (**Table 1**) implicated on smooth pass of these POMs through cell membrane and satisfied necessary criteria for the drugs used in the treatment of the central nervous system disease.

**Table 1.** Parameters of AChE inhibition induced by selected POMs and their log P values.

POM	log P	Hill analysis	
		$IC_{50}$ , M	$n$
WSiA	-0.47	$(7,23 \pm 0,02) \times 10^{-8}$	$0,93 \pm 0,09$
WPA	-0.29	$(1,23 \pm 0,01) \times 10^{-6}$	$1,23 \pm 0,17$

Fluorescence and CD spectroscopy studies performed on these systems pointed out that the inhibition of AChE activity with selected POMs does not related with the changes in the secondary structure of this enzyme (**Fig. 2a and 2b**). In our experiments commercial AChE in phosphate buffer (pH 8) has its characteristic emission peak at 443 nm under excitation at 295 nm and characteristic negative maximum at 208 nm in the CD spectrum. After incubation with POMs at the range of concentrations  $1 \times 10^{-7} - 1 \times 10^{-6}$  for

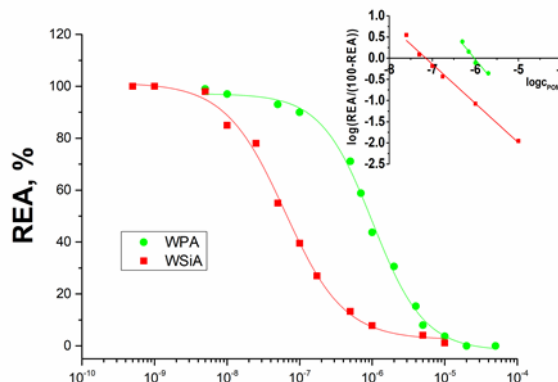
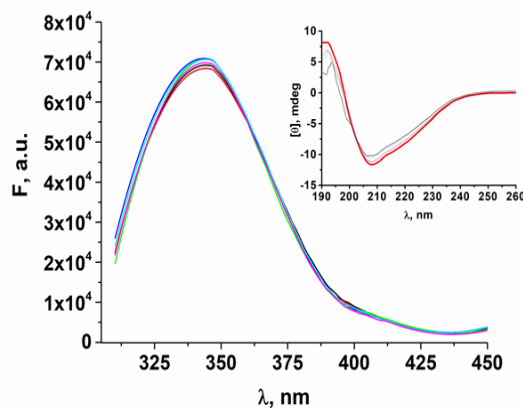


**Figure 1.** Inhibition of AChE induced by selected POMs. Inset: Hill analysis of inhibition curves.

15 min, the peak of AChE in fluorescence and CD spectra showed no shift, which indicated that AChE retained its natural secondary structure.

### CONCLUSION

Investigated POMs present potent inhibitors of AChE activity with  $IC_{50}$  values in the submicromolar range of concentrations, and their inhibitory potency is not related to changes in the secondary structure of this enzyme. The log P values satisfied necessary criteria for smooth pass through cell membrane and criteria for the drugs used in the treatment of the central nervous system disease. Based on these obtained results, the conclusion can be made that POMs could represent new generation of potential anti Alzheimer drugs.



### Acknowledgement

This work was supported by the Ministry for Science of the Republic of Serbia (Grants no. 172023) and COST action CM 1203.

### REFERENCES

- [1] I. Venekei, L. Szilagyi, L. Graf, W.J. Rutter, FEBS Lett., 1996, 383, 133-138.
- [2] D. A. Judd, J. H. Nettles, N. Nevins, J. P. Snyder, D. C. Liotta, J. Tang, J. Ermolieff, R. F. Schinazi, C. L. Hill, J. Am. Chem. Soc., 2001, 123, 886-897.
- [3] T. L. Turner, V. H. Nguyen, C. C. McLauchlan, Z. Dymon, B. M. Dorsey, J. D. Hooker, M. A. Jones, J. Inorg. Biochem., 2012, 108, 96-104.
- [4] G. L. Ellman, K. D. Courtney, V. Andreas, R. M. Featherstone, Biochem. Pharmacol., 1961, 7, 88-90.
- [5] C. D. Klein, G. F. Tabeteh, A. V. Laguna, U. Holzgrabe, K. Mohr, Eur. J. Pharm. Sci., 2001, 14, 167-175.

## EFFECT OF POLYOXOMETALATES ON SYNAPTIC PLASMA MEMBRANE STRUCTURE

M. Čolović<sup>1</sup>, D. Krstić<sup>2</sup>, M. Luce<sup>3</sup> and A. Cricenti<sup>3</sup>

<sup>1</sup> Department of Physical Chemistry, Vinča Institute of Nuclear Sciences, University of Belgrade, Serbia ([colovicm@vin.bg.ac.rs](mailto:colovicm@vin.bg.ac.rs))

<sup>2</sup> Institute of Medical Chemistry, Faculty of Medicine, University of Belgrade, Serbia

<sup>3</sup> Istituto di Struttura della Materia, Consiglio Nazionale delle Ricerche, Roma, Italy

### ABSTRACT

12-tungstosilicic acid (SiW12) and decavanadate (V10) are polyoxometalate compounds (POMs) exhibiting biological activity. *In vitro* studies of the influence SiW12 and V10 on synaptic plasma membrane (SPM) acetylcholinesterase (AChE) and Na,K-ATPase, respectively, showed that these POMs inhibit the enzyme activities in submicromolar concentrations. As Na,K-ATPase and AChE are membrane associated enzymes, the inhibition of their activities can result from the membrane changes induced by the inhibitor binding. Thus, the effect of SiW12 and V10 on the membrane structure was investigated by using Atomic Force Microscopy (AFM) technique. The obtained results demonstrated that the calculated average roughness values for SiW12 and V10 treated SPM were significantly higher (about 6 and 1.5 times, respectively), compared to untreated SPM preparation. The obtained changes indicate that both investigated POMs bind to the plasma membranes, and consequently their approved strong inhibitory potencies toward the membrane bound enzymes might be assigned to the induced membrane modifications.

### INTRODUCTION

Decavanadate (V10) and 12-tungstosilicic acid (SiW12) are polyoxometalates (POMs), negatively charged inorganic compounds containing early transition metal ions in their highest oxidation state, surrounded by oxygen atoms [1]. POMs have been shown to exhibit biological activities *in vitro* as well as *in vivo* [2-5]. However, their biological mechanisms of action at the molecular level are not well understood [6]. It has been speculated that POMs are likely to act extracellularly inhibiting several different enzyme families mostly located on the plasma membrane and display extracellular binding sites [7].

The results of inhibitory influence of V10 and SiW12 on synaptic plasma membrane (SPM) acetylcholinesterase (AChE) and Na,K-ATPase showed that V10 induces 50% decrease in Na,K-ATPase activity at concentration of  $5 \times 10^{-7}$  mol/L ( $IC_{50}$ ) [8], while  $IC_{50}$  value of  $6.2 \times 10^{-8}$  mol/L SiW12 for AChE was obtained. However, the structural and conformational modifications of these membrane enzymes in the presence of the tested polyoxometalates, which are expected to influence the activity, were not clarified. Furthermore, the activities of Na,K-ATPase as a transmembrane enzyme and AChE as a membrane bound enzyme might be modified due to some membrane changes induced by the inhibitor binding. Therefore, the aim of this study is to investigate the influence of SiW12 and V10 on the SPM structure by using Atomic Force Microscopy (AFM) technique.

### EXPERIMENTAL

SiW12 ( $H_4SiW_{12}O_{40}$ ) was commercially available (Sigma Aldrich), and V10 ( $(NH_4)_6V_{10}O_{28} \cdot 5H_2O$ ) was synthesized [8, 9]. Stock solutions of SiW12 and V10 (0.01 mol/L) were prepared daily, by solving the solid compounds in water shortly before use. Working solutions (0.001 mol/L) were prepared daily by diluting the stock solutions. SPM were isolated from the whole brain of 3-month-old male *Wistar albino* rats according to the method of Towle and Sze [10]. Preliminary studies showed that the presence of  $5 \times 10^{-4}$  mol/L SiW12 did not change pH of the SPM preparation (7.4). 50  $\mu$ L of SPM preparation was mixed with 50  $\mu$ L of 0.001 mol/L investigated POM solution (1:1), and then applied in drops onto a glass surface. The SPM preparation in combination with water (1:1) served as a control. The prepared samples dried overnight. AFM measurements were performed using a home-designed microscope [11] that can be operated under controlled environmental conditions. The AFM measurements were performed in air, at room temperature and constant 30% relative humidity. The contact mode measurements were performed in the weak repulsive regime of constant force with a probe force below 1 nN from zero cantilever deflection. The high-resolution images have been collected at a scanning speed of 0.25–0.35 Hz.

### RESULTS AND DISCUSSION

The image of the control SPM sample (without POM) obtained by AFM technique is presented in Fig. 1.

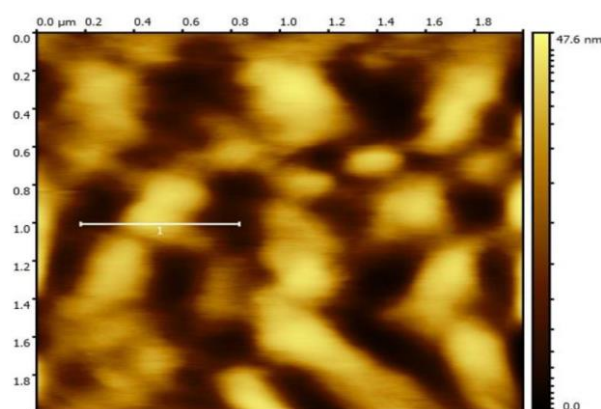


*Figure 1. The image of the control SPM sample obtained by AFM technique.*

The values of average roughness for the investigated POM (V10, SiW12)-SPM samples and control SPM were calculated and presented in Fig. 2. The obtained results demonstrate that the roughness value for the SPMs after SiW12 treatment significantly increased, more than 3 times, compared to the membrane roughness before the SiW12 treatment (SPM alone). The presence of V10 also induced increase in the membrane roughness compared to the SPM control, but about 1.5 times.

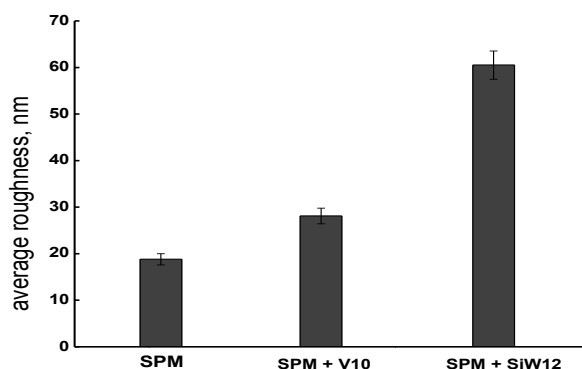


**Figure 2.** The calculated values of average roughness obtained for SPMs before (SPM) and after V10 (SPM + V10), and SiW12 (SPM + SiW12), treatment.

The obtained results indicate that both SiW12 and V10 bind to the plasma membranes. Consequently, their previously approved strong inhibitory potencies ( $IC_{50}$  values in submicromolar concentrations) toward the

membrane bound enzymes (AChE and Na,K-ATPase) might be assigned to the induced membrane modifications.

### CONCLUSION

The investigated polyoxometalates in this study, SiW12 and V10, inhibit the activities of membrane associated enzymes, SPM AChE and Na,K-ATPase in submicromolar concentrations, respectively. The results obtained by AFM technique demonstrate that both SiW12 and V10 induce increase in average roughness values of SPM compared to untreated SPM. Accordingly, it could be concluded that these compounds modify the plasma membrane structure, resulting in the affection of the membrane associated enzyme activities.

### *Acknowledgement*

This study was supported by the Ministry of Education, Science and Technological Development of the Republic of Serbia (Project No. 172023), and COST Action MP1302.

### REFERENCES

- [1] B. Hasenknopf, *Front. Biosci.*, 2005, **10**, 275–287.
- [2] X. Wang, J. Liu, J. Li, Y. Yang, J. Liu, B. Li, et al. *J. Inorg. Biochem.*, 2003, **94**, 279–284.
- [3] A. Seko, T. Yamase, K. Yamashita, *J. Inorg. Biochem.*, 2009, **103**, 1061–1066.
- [4] Y. Qi, Y. Xiang, J. Wang, Y. Qi, J. Li, J. Niu, et al. *Antiviral. Res.*, 2013, **100**, 392–398.
- [5] M. Aureliano, D.C. Crans, *J. Inorg. Biochem.*, 2009, **103**, 536–546.
- [6] R. Prudent, V. Moucadel, B. Laudet, C. Barette, L. Lafanechere, B. Hasenknopf, et al. *Chem. Biol.*, 2008, **15**, 683–692.
- [7] S-Y. Lee, A. Fiene, W. Li, T. Hanck, K. Brylev, V. Fedorov, et al. *Biochem. Pharmacol.*, 2015, **93**, 171–181.
- [8] D. Krstić, M. Čolović, N. Bošnjaković-Pavlović, A. Spasojević-de Bire, V. Vasić, *Gen. Physiol. Biophys.*, 2009, **28**, 302–308.
- [9] B. Chinea, D. Dakternieks, A. Duthie, C.A. Ghilardi, P. Gili, A. Mederos, S. Midollini, A. Orlandini, *Inorg. Chim. Acta*, 2000, **298**, 172–177.
- [10] A.C. Towle, P.Y. Sze, *J. Steroid Biochem.*, 1983, **18**, 135–143.
- [11] A. Cricenti, R. Generosi, *Rev. Sci. Instrum.*, 1995, **66**, 2843–2847.

## OXIDATIVE STRESS RESPONSES OF 12-TUNGSTOSILICIC AND 12-TUNGSTOPHOSPHORIC ACID

M. Čolović<sup>1</sup>, A. Bondžić<sup>1</sup>, A. Vujačić Nikezić<sup>1</sup> and D. Krstić<sup>2</sup>

<sup>1</sup> *Department of Physical Chemistry, Vinča Institute of Nuclear Sciences, University of Belgrade, Serbia*

<sup>2</sup> *Institute of Medical Chemistry, Faculty of Medicine, University of Belgrade, Serbia ([daniijela.krstic@med.bg.ac.rs](mailto:daniijela.krstic@med.bg.ac.rs))*

### ABSTRACT

*In vitro* oxidative stress responses of two Keggin-type polyoxotungstates, 12-tungstosilicic (WSiA) and 12-tungstophosphoric acid (WPA), were investigated using rat synaptosomes as a model system. WSiA induced concentration-dependent increase in catalase activity, up to about 6 times compared to the control activity in untreated synaptosomes, and glutathione peroxidase was not significantly affected after WSiA treatment. On the contrary, WPA treatment resulted in the increase of glutathione peroxidase activity, while synaptosomal catalase was even reduced related to the control, at all investigated WPA concentrations. Both investigated polyoxotungstates did not significantly change malondialdehyde content in synaptosomal preparations. It could accordingly be concluded that WSiA and WPA probably induce reactive oxygen species generation, resulting in the activation of the antioxidant defense enzymes. However, these polyoxotungstates are not strong prooxidants being able to cause oxidative stress, and consequently synaptosomal membrane lipid damage.

### INTRODUCTION

12-tungstosilicic acid,  $H_4SiW_{12}O_{40}$  (WSiA) and 12-tungstophosphoric acid,  $H_3PW_{12}O_{40}$  (WPA) are Keggin structure polyoxotungstates belonging to a family of polyoxometalates (POMs). These compounds are polyanionic oligomeric aggregates with a high density of negative charge, which contain transition metal ions held together by oxygen bridges [1]. They were synthesized in order to be applied in catalysis, separations, analysis, and as electron-dense imaging agents [2]. Additionally, *in vitro* and *in vivo* studies indicate that some of these complexes exhibit biological activity [3].

The results of our previous *in vitro* study [4] demonstrated that WSiA and WPA affect the activities of  $Na^+/K^+$ -ATPase and E-NTPDase in micromolar concentrations, key enzymes in cancer cell migration and purinergic signaling

[5]. However, the main limitation for polyoxometalate application in biomedicine is their approved toxic action [6]. Taking into account this fact, the purpose of this study is to test oxidative stress responses of various doses of WPA and WSiA by determining antioxidant enzyme activities, catalase (CAT) and glutathione peroxidase (GPx), and lipid peroxidation in rat brain synaptosomes.

## EXPERIMENTAL

WSiA and WPA are commercially available (Sigma-Aldrich, Germany). Synaptosomes were isolated from the whole brains of *Wistar albino* rats [7]. Aliquots of synaptosomal preparations were incubated at 37 °C for 2 h in water bath in the absence (control) and presence of desired concentrations of WSiA and WPA, and then used for biochemical analysis.

Catalase activity was measured by the H<sub>2</sub>O<sub>2</sub> degradation assay [8]. GPx activity was measured in a coupled enzyme method by measuring the decrease of NADPH at 340 nm [9]. The level of lipid peroxidation was estimated as the concentration of thiobarbituric acid reactive product MDA by using the method of Aruoma et al. [10].

## RESULTS AND DISCUSSION

The influence of exposure toward increasing concentrations (within the range 10<sup>-6</sup>–10<sup>-3</sup> mol/L) of WSiA and WPA on the specific activity of synaptosomal antioxidant enzymes, CAT and GPx is presented in Figure 1(a and b). The obtained results show that WSiA significantly increased synaptosomal CAT in a dose-dependent manner. The lowest investigated WSiA concentration (1 × 10<sup>-6</sup> mol/L) induced about 4 times higher specific CAT activity compared to the control value (specific CAT activity in the untreated synaptosomes), while the highest WSiA concentration resulted in more than 6 times increase. On the contrary, WPA caused a noticeable decrease in CAT activity at all investigated concentrations (Fig. 1a), indicating the enzyme inhibition induced by WPA. Unlike CAT, synaptosomal GPx activity was not significantly affected by WSiA compared to the control (Fig. 1b). However, WPA induced significantly increase in GPx activity. It can be observed (Fig. 1b) that the lowest investigated WPA concentration (1 × 10<sup>-6</sup> mol/L) caused the maximal increase (about 2 times in comparison with the control value). On the other hand, the GPx activity obtained in the presence of 1 × 10<sup>-3</sup> mol/L WPA was almost equal to the control value, suggesting the potential inhibition of GPx at high WPA concentrations. The obtained increase in CAT and GPx activities (Fig. 1) could be assigned to the production of reactive oxygen species (ROS) in the presence of WSiA and WPA, respectively.

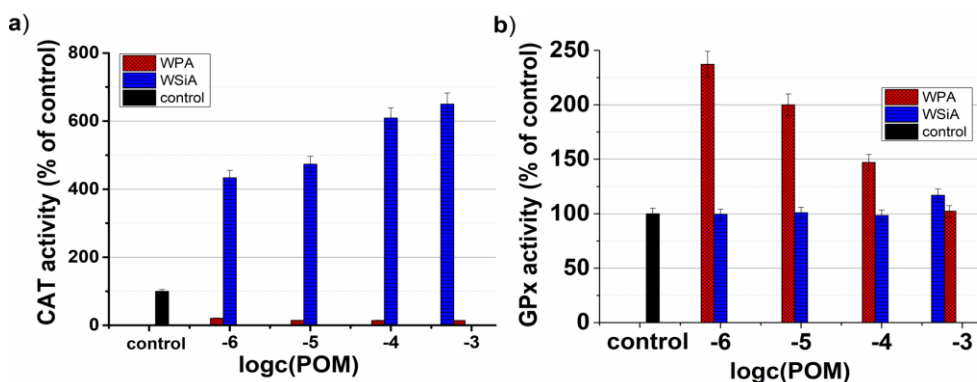


**Figure 1.** CAT (a) and GPx (b) activities in rat brain synaptosomes obtained in the absence (control) and presence of different WPA and WSiA concentrations. The specific enzyme activities are expressed as a percentage of the control value (100%). Values are mean  $\pm$  SD.

The effect of synaptosomal exposure toward WPA and WSiA (within the range  $10^{-6}$ – $10^{-3}$  mol/L) on the level of MDA, as a marker of synaptosomal lipid peroxidation, is shown in Fig. 2. It can be seen that all investigated concentrations of both WPA and WSiA do not induce significant changes in MDA level related to the control value (untreated synaptosomes). The similar values of synaptosomal MDA obtained in both absence and presence of the investigated compounds indicate that these polyoxotungstates do not induce lipid peroxidation. Actually, the induced WSiA/WPA increase in CAT and GPx activities (Fig. 1) suggests that the activation of these antioxidant enzymes prevents oxidative stress, and consequently synaptosomal membrane damage.

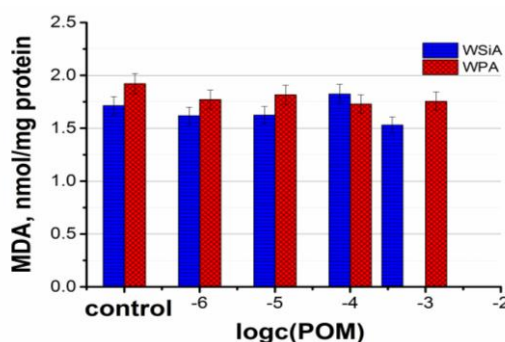


**Figure 2.** MDA contents in rat brain synaptosomes obtained in the absence (control) and presence of different WPA and WSiA concentrations. Values are mean  $\pm$  SD.

## CONCLUSION

The studied polyoxotungstates in this study, WSiA and WPA, induce the activation of the antioxidant enzymes, CAT and GPx respectively, but do not significantly affect MDA level in rat synaptosomes, the marker of oxidative stress and membrane lipid peroxidation. Accordingly, it could be concluded that both WSiA and WPA cannot be considered as strong prooxidants capable to induce oxidative stress and membrane damage.

## Acknowledgement

This study was supported by the Ministry of Education, Science and Technological Development of the Republic of Serbia (Project No. 172023).

## REFERENCES

- [1] B. Hasenknopf, *Front. Biosci.*, 2005, **10**, 275–287.
- [2] M.T. Pope, A. Muller, *Polyoxometalate Chemistry*; Kluwer: Dordrecht-Boston-London, 2001.
- [3] Y. Qi, Y. Xiang, J. Wang, Y. Qi, et al. *Antiviral Res.*, 2013, **100**, 392–398.
- [4] M.B. Čolović, D.V. Bajuk-Bogdanović, N.S. Avramović, I.D. Holclajtner-Antunović, et al. *Bioorgan. Med. Chem.*, 2011, **19**, 7063–7069.
- [5] I. Matsuoka, S. Ohkubo, *J. Pharmacol. Sci.*, 2004, **94**, 95–99.
- [6] M.B. Čolović, B. Medić, M. Četković, T. Kravić Stevović, M. Stojanović, W. Ayass, et al. *Toxicol. Appl. Pharm.*, 2017, **333**, 68–75.
- [7] A.C. Towle, P.Y. Sze, *J. Steroid Biochem.*, 1983, **18**, 135–143.
- [8] E. Beutler, *A Manual of Biochemical Methods*; Grune and Startton: New York, 1984.
- [9] W.B. Jakoby, *Enzymatic Basis of Detoxication*; Academic Press: New York, 1980.
- [10] O.I. Aruoma, B. Halliwell, M.J. Laughton, G.J. Quinlan, J.M.C. Gutteridge, *Biochem. J.*, 1989, **258**, 617–620.

## INFLUENCE OF MAGNIFICATION ON SCATTERED DOSE LEVEL AROUND PATIENT IN INTERVENTIONAL RADIOLOGY

D. Arandić<sup>1</sup>, P. Božović<sup>2</sup>, J. Stanković Petrović<sup>2</sup>, Đ. Lazarević<sup>1</sup>, S. Čeklić<sup>1</sup>, O. Ciraj-Bjelac<sup>2</sup> and V. Antić<sup>3</sup>

<sup>1</sup>*University of Belgrade, Institute of General and Physical Chemistry,  
Studentski trg 12/V, 11000 Belgrade, Serbia.  
(danijela.arandjic@gmail.com)*

<sup>2</sup>*University of Belgrade, Vinca Institute of Nuclear Sciences,  
Mike Alasa 12-14, Belgrade, Serbia*

<sup>3</sup>*Clinical centre of Serbia,  
Pasterova 2, Belgrade, Serbia.*

### ABSTRACT

In this work the influence of magnification level on scattered radiation around patient in interventional radiology was investigated. Measurements were performed on x-ray unit dedicated to interventional procedures with a flat panel detector. The results show that scatter level decreases as magnification increases due to the fact that DAP values decreases as well.

### INTRODUCTION

Radiation dose to medical staff in interventional radiology can be very high [1, 2, 3] especially in cardiology procedures. Interventional cardiologists receive the highest radiation doses among all professionally exposed personnel in medicine [4, 5, 6]. Furthermore, the number of interventional procedures has rapidly increased in a last 20 years [7].

Radiation field around interventional x-ray unit is composed of scattered radiation that comes from the patient and the leakage radiation from the x-ray housing. Scattered radiation level around the patient depends on the tube to image detector geometry [8], patient characteristics [8, 9] and the dose to the patient in terms of specific dosimetry quantity, dose area product (DAP) [10].

The new generation of interventional x-ray units has the ability for image magnification that is expressed as size of the field of view (FOV). By decreasing FOV the image is being magnified. According to investigations of other authors [10] the magnification affects the entrance surface dose (ESD) on patient by significantly increasing its value. The level of scattered radiation in an x-ray room increase with the increased ESD value [11] and therefore the assumption that magnification increases the scatter level seems to be in

place. However, during the routine measurements of ambiental dose equivalent rate it was observed that scatter level is decreased by magnification. This means that DAP value should be taken into account during the analyses since the ESD influence the scatter through the DAP. In this work, the influence of magnification on scatter level around patient and the DAP value was investigated.

### EXPERIMENTAL

Investigation was carried out on C-arm interventional x-ray unit, Siemens Axiom Artis dFC/dFA (Erlangen, Germany) with flat panel image detector. Measurements were performed on phantom positioned in isocenter of C-arm (with 120 cm focus to detector distance) using the automatic exposure control (AEC) and protocols that are available on the unit. Phantom was made of PMMA plates with dimensions of 25cmx25cmx1cm and 20 cm total thickness. Measurements were performed in fluoro and cine mode using different number of pulses (7.5, 15, 30 imp/s) and FOVs (25, 20, 16).

The scatter radiation level was measured in terms of ambiental dose equivalent rate  $H^*(10)$  expressed in  $\mu\text{Sv/h}$  at 100 cm from the isocenter in controlled area using ionization chamber Victoreen 451P (Fluke, SAD). The values in  $\mu\text{Sv/h}$  were recorded at 60 cm under the patient table, 60 cm over the patient table (measured from the isocenter) and 170 cm over the patient table (measured from the floor). DAP values were obtained using the display on the console of x-ray unit. A priori to measurements DAP meter was calibrated.

### RESULTS AND DISCUSSION

Results are presented in Figures 1a – d. Scattered radiation level increases with higher pulse rate and it is much higher in cine than in fluoro mode. Ambiental dose equivalent rates are higher at the 60 cm under the patient table compared with other two positions. This confirms that tube under the table geometry is more suitable for medical staff from radiation protection point of view. All three figures (1a, b, c) show the scattered radiation level decreases with increased magnification (decreased FOV) regardless of pulse rate.

DAP values increase with the pulse rate and it is higher in cine mode (Figure 1d) because of increased ESD. With lower FOV, DAP values are decreased because field size is also decreased. Since ESD increases with magnification [10] DAP must be decreased because of significantly smaller field size. Vano et al. [8] made a conclusion that magnification decreases field size while increasing ESD and therefore DAP remains the same. However, in their investigation measurements were performed for just one FOV size.

Therefore, results presented in this paper and discussion made is more valuable.

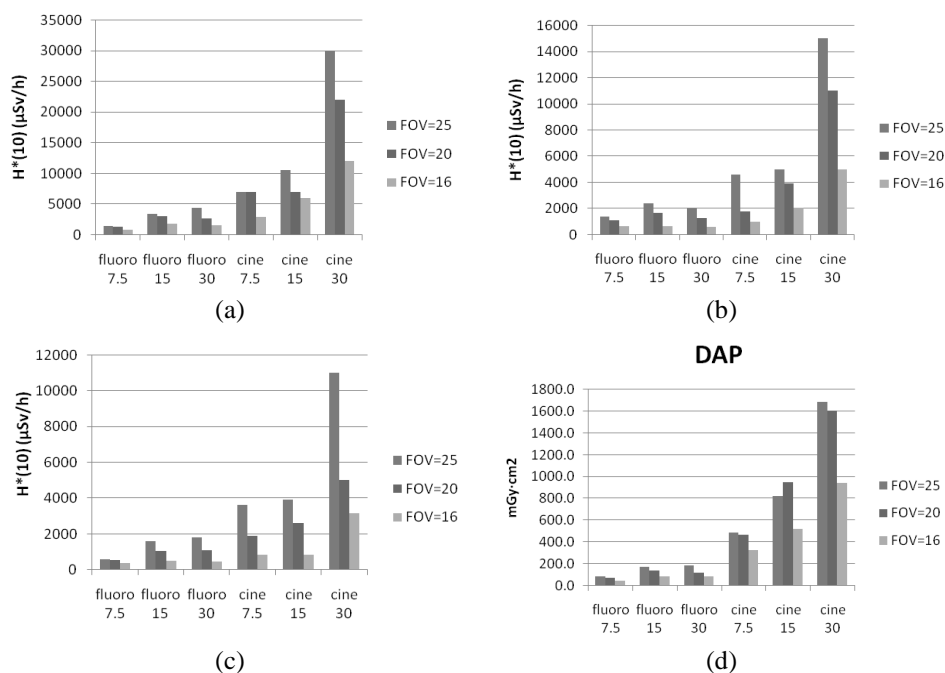


**Figure 1.** Influence of magnification on scatter level around the patient and DAP: (a) at the 60 cm under the patient table, (b) at the 60 cm over the patient table, (c) at the 170 cm from the floor and (d) DAP value.

**CONCLUSION**

Radiation dose to medical staff in interventional radiology can be very high. Radiation field around interventional x-ray unit comes from scattered and the leakage radiation. Scattered radiation level around the patient depends on different factors. In this work influence of magnification on scattered radiation level was investigated. It was found that DAP value and the scatter level are lower with increased magnification.

Risk for stochastic effects on patient are estimated based on DAP value while for deterministic effects ESD is more representative quantity. Therefore, the magnification option on modern interventional x-ray units has to be used carefully since the indicators for patient dose and dose to the medical staff are different. The rule “By decreasing dose to the patient the dose to medical staff is also decreased” cannot be applied in this case.

**Acknowledgement**

This work was partially supported by the Ministry for Science of the Republic of Serbia (Grants no. ON171028, III43009 and ON171007).

**REFERENCES**

- [1] E. Vano, L. Gonzalez, F. Beneytez and F. Moreno. Lens injuries induced by occupational exposure in nonoptimized interventional radiology laboratories. *Br. J. Radiol.* 71 (1998) 728–733.
- [2] J.R. Williams. The interdependence of staff and patient doses in interventional radiology. *Br. J. Radiol.* 70 (1997) 498–503.
- [3] M. Zuguchi, K. Chida, M. Taura, Y. Inaba, Ebata and S. Yamada. Usefulness of non-lead aprons in radiation protection for physicians performing interventional procedures. *Radiat. Prot. Dosim.* 131 (2008) 531–534.
- [4] A.J. Camm, J. Reid, M. Raphael, P. Wilde, R. Boyle, M. Clarke, S. Qureshi, M. Rothman and A. Shaw. Radiation hazards to the cardiologist: a report of a subcommittee of the British Cardiac Society. *Br. Heart. J.* 70 (1993) 489–496.
- [5] E. Vano, L. Gonzalez, E. Guibelalde, J.M. Fernandez and J.L. Ten. Radiation exposure to medical staff in interventional and cardiac radiology. *Br. J. Radiol.* 71 (1998) 954–960.
- [6] E. Vano, L. Gonzalez, J.M. Fernandez, F. Alfonso and C. Macaya. Occupational radiation doses in interventional cardiology: a 15-year follow-up. *Br. J. Radiol.* 79 (2006) 383–388.
- [7] M. Bhargavan. Trends in the utilization of medical procedures that use ionizing radiation. *Health Phys* 95 (2008) 612–627.
- [8] E. Vano, L. Gonzalez, J. M. Fernandez, Z. J. Haskal. Eye Lens Exposure to Radiation in Interventional Suites: Caution Is Warranted. *Radiology* 248 (2008) 945 - 953
- [9] E. Vano, C. Ubeda, F. Leyton, P. Miranda, L. Gonzalez. Staff Radiation Doses in Interventional Cardiology: Correlation With Patient Exposure. *Pediatr Cardiol* 30 (2009) 409–413.
- [10] V. Tsapaki, S. Kottou, N. Kollaros, P. Dafnomili, Z. Kyriakidis, V. Neofotistou, Dose performance evaluation of a charge coupled device and flat-panel digital fluoroscopy system recently installed in an interventional cardiology laboratory. *Radiation Protection Dosimetry.* 111(2004) 297–304.
- [11] K. Chida, Y. Morishima, Y. Inaba, M. Taura, A. Ebata, K. Takeda, H. Shimura, M. Zuguchi. Physician-received scatter radiation with angiography systems used for interventional radiology: comparison among many x-ray systems. *Radiation Protection Dosimetry* (2011) 1–6.

## EPR DETERMINATION OF ANTIOXIDATIVE ACTIVITY OF WATER-INSOLUBLE COMPOUNDS TOWARDS BIOLOGICALLY RELEVANT RADICALS – EXAMPLE OF AVAROL

Đ. Nakarada<sup>1</sup>, A. Pavićević<sup>1</sup>, A. Vesković<sup>1</sup>, B. Pejin<sup>2</sup>, A. Popović -  
Bijelić<sup>1</sup> and M. Mojović<sup>1</sup>

<sup>1</sup> *University of Belgrade, Faculty of Physical Chemistry,  
Studentski trg 12-16, 11000 Belgrade, Serbia. ([milos@ffh.bg.ac.rs](mailto:milos@ffh.bg.ac.rs))*

<sup>2</sup> *Department of Life Sciences, Institute for Multidisciplinary Research, IMSI,  
University of Belgrade, Kneza Višeslava 1, 11030 Belgrade, Serbia*

### ABSTRACT

Determination of the antioxidant activity of water-insoluble compounds is highly limited by the fact that *ex vivo* generation of biologically relevant free radical species is usually performed using water as a solvent. In this study, we present a novel approach to surpass this problem, by incorporating a highly potent, but water-insoluble antioxidant avarol, as a model molecule, into the liposome bilayer. Our results show that this unique method could successfully be applied for measuring the antioxidative activity of water-insoluble compounds towards biologically relevant radicals in an aqueous surrounding, showing the remarkable radical scavenging potential of avarol.

### INTRODUCTION

Antioxidants are very important bioactive compounds due to many health benefits they provide. Their varying effectiveness can be ascribed to the difference in their molecular structure. Many of antioxidant molecules are insoluble, or have low solubility in water, and hence, their antioxidative activity towards biologically relevant radicals is difficult to study. Compared to UV-Vis spectrometry, or electrochemical measurements, which are routinely used for studying antioxidative activities of different compounds towards free radicals, electron paramagnetic resonance (EPR) spectroscopy provides much higher sensitivity and reproducibility. EPR does not depend on the optical characteristics of substances, and is the only experimental technique capable of direct radical detection. However, a significant problem is the fact, that biologically relevant free radicals, like  $\cdot\text{OH}$ ,  $\cdot\text{O}_2^-$ , and  $\text{NO}\cdot$ , have to be generated using water as a solvent. Other organic solvents, like methanol/ethanol, could generate carbon-based radicals as artifact during their interaction with reactive oxygen species, which seriously brings into

question the usability of the obtained results. One of the ways to overcome this problem is to incorporate water-insoluble molecules inside of the lipid structures like liposomes, which are, due to their polarity, able to carry these molecules through the water medium in a more facilitated way.

Avarol is a sesquiterpenoid hydroquinone isolated from marine sponge *Dysidea avara*, together with a minor amount of avarone, its oxidized form. Avarol and its derivatives are among the most important marine metabolites because they show a wide spectrum of rather interesting biological activities and low toxicity. Some of these activities include antiviral, antifungal, antipsoriatic, antibacterial, antitumor, antimitotic, antioxidative, and to some extent, analgesic activity. Moreover, avarol can cross the blood-brain barrier, which makes it a prospective compound for the treatment of neurodegenerative disorders. However, one major downside of avarol is the fact that it is not soluble in water. Hence, alternative ways should be developed in order to administer this molecule more efficiently.

Herein, using avarol as a model molecule, we present a novel way of studying antioxidant activity of water-insoluble substances using EPR, by previously incorporating them into 1,2-dipalmitoyl-sn-glycero-3-phosphocholine (DPPC) liposomes.

## EXPERIMENTAL

Multilamellar liposomes were prepared from avarol (10%) and DPPC (90%) by the modified thin-film method [1]. This was done by dissolving avarol and DPPC in the mixture of chloroform and methanol (4:1 v/v) in a rotary flask. Solvent was slowly evaporated at room temperature using rotary vacuum evaporator. The remaining thin film was hydrated with 2 ml of 18 MΩ water in increments of 250 μl, each followed by 3 min of vigorous vortexing and 3 min of ultrasounding using ultrasound ice bath. Suspension was further sonicated for 20 minutes using ultrasound ice bath. In order to obtain the uniform size of liposomes, the suspension was extruded through 100 nm membrane. Finally, liposomes were concentrated to the volume of 250 μl using vacuum concentrator. The final concentration of avarol in liposomes suspension was 4 mM.

EPR spin-trapping technique was employed in order to trap short-lived free radical species generated directly in the liposome suspension, and to measure the kinetics of their interaction with liposomes.

In order to study the interaction of hydroxyl radical with avarol containing liposomes, the intensity of hydroxyl spin-adduct EPR signal was measured. 26 μl of the liposome suspension was mixed together with 2 μl of 5 mM H<sub>2</sub>O<sub>2</sub> and 1 μl of 100 mM 5-(diethoxyphosphoryl)-5-methyl-1-pyrroline-N-oxide (DEPMPO). After the addition of 1 μl of 5 mM FeSO<sub>4</sub>, the mixture was

transferred into 1 mm diameter teflon tubes, and EPR spectra were recorded [2].

The interaction of superoxide radicals with avarol containing liposomes was studied by measuring the intensity of the superoxide spin-adduct EPR signal using riboflavine/light as the generator system [3]. In 2 ml centrifuge tube, 18.5  $\mu$ l of the liposome suspension was mixed with 5  $\mu$ l of 24 mM diethylenetriaminepentaacetic acid (DTPA) and 1  $\mu$ l of 100 mM DEPMPO. After the addition of 7.5  $\mu$ l of 3 mM riboflavin, the sample was irradiated by 30 W UV light for 30 s, prior to transferring the mixture into 1 mm diameter teflon tube and recording the EPR spectra.

All EPR spectra were recorded under the following parameters: center field 3500 G, microwave power 10 mW, microwave frequency 9.85 GHz, modulation frequency 100 kHz, modulation amplitude 1 G.

## RESULTS AND DISCUSSION

The decrease of the intensities of both, DEPMPO/OH and DEPMPO/OOH, adduct EPR signals were measured for 30 min after their generation in the suspension of avarol liposomes (Figure 1). The reduction of the EPR signal was calculated using the formula:

$$\Delta h = \frac{h_i - h_{30}}{h_i} \times 100 (\%)$$

where  $h_i$  and  $h_{30}$  refer to the intensities of the control adduct signal (DPPC liposomes without avarol) and the signal after 30 min (avarol-containing liposomes). The calculated percentage of the EPR signal reduction was 91.1% for DEPMPO/OH, and 85.6% for DEPMPO/OOH adduct. These results indicate that avarol liposomes have rather strong antioxidant capacity towards  $\cdot$ OH and  $\cdot$ O<sub>2</sub><sup>-</sup> radicals. To confirm that these results arise only from avarol, and not from DPPC, control experiments were performed using 100 % DPPC liposomes (prepared using the same procedure previously described). These experiments showed no adduct signal reduction (data not shown) other than its modest decay caused by the expected half-life of the spin-adducts. Altogether, the results presented in this paper strongly indicate that avarol has significant antioxidant potential, which is not affected by the DPPC liposomes in which it was incorporated. Furthermore, this novel approach for measuring the antioxidative activity of water-insoluble molecules towards biologically relevant radicals could successfully be applied to a vast number of other biologically active compounds.

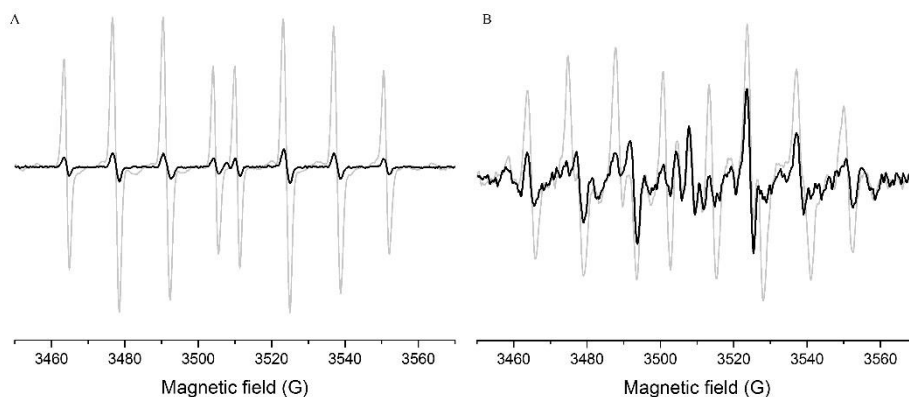


**Figure 1.** EPR spectra of DEPMPO/OH adduct (A) and DEPMPO/OOH adduct (B) recorded in the control sample (gray) and 30 min (black) after their generation in the suspension of avarol-containing liposomes.

## CONCLUSION

Liposomes are important nanostructures that can be used in order to study antioxidant activity of water-insoluble molecules. Herein, the method of incorporating a biologically active compound into liposomes was applied for avarol, assessing its antioxidative activity towards hydroxyl and superoxide radicals. Avarol-containing liposomes reduced the intensity of DEPMPO/OH and DEPMPO/OOH adduct EPR signal by 91.1% and 85.6% respectively, showing its extraordinary antioxidant potential. The proposed novel experimental method could successfully be applied for a vast number of other biologically active, but water-insoluble, compounds.

## Acknowledgement

This work was partially supported by the Ministry of Education, Science and Technological Development of the Republic of Serbia (Grant no. III41005).

## REFERENCES

- [1] V. Weissig, *Liposomes: Methods and Protocols*, Vol. 1: Pharmaceutical Nanocarriers, Humana Press, Mumbai, 2010.
- [2] M. Mojović, M. Vuletić, G. Bačić, Detection of Oxygen-Centered Radicals Using EPR Spin-Trap DEPMPO: The Effect of Oxygen, *Ann. N. Y. Acad. Sci.*, 2006, (1048), 471 – 475.
- [3] V. Roubaud, S. Sankarapandi, P. Kuppusamy, P. Tordo, J. Zweier, The spin-trapping of superoxide and hydroxyl free radicals with DMPO (5,5-dimethylpyrroline-N-oxide): more about iron, *Free Radic. Res. Commun.*, 1993, 19 (1), 79 – 87.

## NON-INVASIVE CHARACTERIZATION OF AFLATOXIN-STRESSED WHEAT SEEDS USING 2D EPR IMAGING AND EEM FLUORESCENCE SPECTROSCOPY

D. Bartolić, M. Stanković, V. Maksimović, D. Mutavdžić and K. Radotić

*Institute for Multidisciplinary Research, University of Belgrade, Kneza Višeslava 1, 11030 Belgrade, Serbia. ([dragana.bartolic@yahoo.com](mailto:dragana.bartolic@yahoo.com))*

### ABSTRACT

In this work, two non-invasive and independent methods for the characterization of aflatoxin-stressed wheat seeds were applied. Aflatoxins (AFs) are secondary toxic fungi metabolites, which exhibit hazardous effects on plants (phytotoxic), as well as on humans and animals. First, for 2D EPR imaging, we used 3-CP spin probe for the estimation of changes in the redox state of the aflatoxin-stressed seed. On the other side, an excitation-emission fluorescence approach was used to evaluate the spectral profiles of the key biological molecules. We determined their areas and the ratio of the two emission peaks at 355 nm (Ex 290) and 430 nm (Ex 350), corresponding to protein and phenol emission, respectively. Our results showed that the ratio of the two peaks (p/f) decreased in the presence of AFs. Both methods revealed to be useful for the rapid, non-invasive assessment of the seeds' stress state induced by AFs.

### INTRODUCTION

Aflatoxins are mycotoxins, which are toxic secondary metabolites produced by fungi that colonize crops and are commonly found as contaminants in cereal food. Chemically, they are difuranocoumarin derivatives produced in a polyketide pathway; among the known aflatoxins, Aflatoxin B1 (AFB1) is the most toxic, mutagenic and carcinogenic [1, 2]. It has been shown that AFB1 can be harmful to both consumer health and plants (phytotoxic effects) [2]. Several analytical methods have been employed to analyze aflatoxins in agricultural food crops and feed [1]. Non-invasive methods, such as EPR imaging and fluorescence spectroscopy provide useful information about normal and physiological as well as pathophysiological processes of the biological systems [3, 4, 5]. These methods were used to analyze AFB1 contaminated wheat seeds. The changes in redox state of the stressed seeds comparing with unstressed ones were correlated with the structural changes observed by fluorescence spectroscopy.

## EXPERIMENTAL

Wheat (*Triticum aestivum* L.) seeds, contaminated - and uncontaminated with aflatoxin B1 (AFB1), were used in this study. EPR experiments were carried out with a Bruker ELEXSYSII spectrometer, operating in the X-band frequency domain (9.8 GHz). The following conditions were set for the measurement: Sweep width, 284.85 G; microwave power, 10.02 mW. All measurements were performed at ambient temperature. 2D imaging was done in the YX plane with respect to the main fields; the magnetic field gradient was 30 G/cm. We used 3-carbamoyl-2, 2, 5, 5-tetramethyl-1-pyrrolidonyl-N-oxyl (3-carbamoyl PROXYL or 3-CP) as spin probe. The seeds were imbibed one hour before the start of the measurement. The program software The Bruker Xepr, was used to process the EPR data. Also, we study the fluorescence characteristics of seed samples via their excitation-emission matrix (EEM) spectrum. The samples' fluorescence spectra were recorded using an F13-221 P spectrofluorimeter (Jobin Yvon, Horiba, France), equipped with a 450 W Xe lamp and a photomultiplier tube. The emission spectra ranging from 300 to 600 nm were recorded with an excitation wavelength ranging from 280 to 350 nm. Integration time was 0.1 s. A spectral bandwidth of 2 nm was for both the excitation and emission slits.

## RESULTS AND DISCUSSION

Figure 1 (A) shows the 2D image of the unstressed (-AFB1) and AFB1-stressed (+AFB1) wheat seeds. The seeds were positioned in a quartz capillary, one above another, as shown in Figure 1 A. The EPR imaging was applied for the mapping of redox state of the seeds through detection and localization of the 3-CP spin probe. The levels of 3-CP redox-sensitive spin active probe and the rate at which it is reduced, depends partly on the tissue redox status [4]. We observed the higher signal intensity of the 3-CP spin probe in the unstressed seed compared with AFB1-stressed seeds (Figure 3 A). The 2D images demonstrated that the spin probe appears to be concentrated in a particular region of the seed coat.

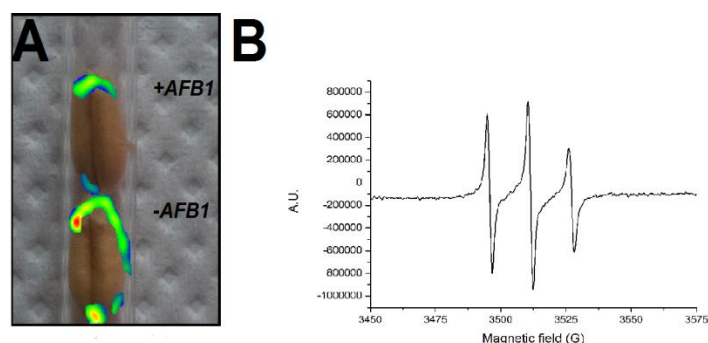


**Figure 1.** 2D EPR imaging of clearance of the 3-CP spin probe in aflatoxin stressed (+ AFB1) and unstressed (-AFB1) seeds (**A**); and typical EPR spectrum of 3-carbamoyl-PROXYL spin probe in seeds (**B**).

EEM fluorescence spectroscopy was employed to analyze the unstressed (A) and AFB1-stressed (B) seeds of wheat. In Figure 2, the representative contour maps are depicted. The comparison of the contour maps shows that both samples have fluorescence peaks which are characteristic for the protein and phenol regions, located at 355 nm (Ex 290 nm) and 430 nm (Ex 350 nm), respectively. The areas of the analyzed peaks were determined using the equation shown in (3).

$$\Phi_i = \int_{\lambda_{em}} I(\lambda_{em}) d\lambda_{em} \quad (3)$$

$\Phi_i$ —Area of  $i$ -th excitation;  $I(\lambda_{em})$  - Intensity at emission wavelength at  $\lambda_{em}$ ;  $\lambda_{em}$  - Emission wavelength.

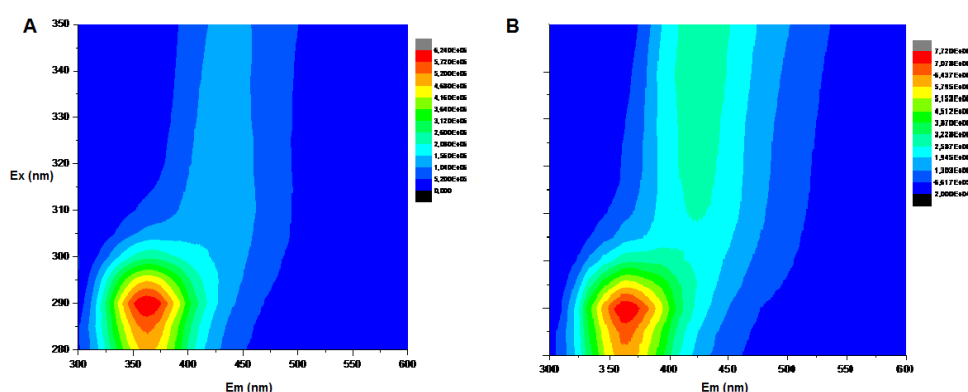


**Figure 2.** The representative EEMs of (A) unstressed (-AFB1) and (B) AFB1stressed (+AFB1) seeds

The fluorescence areas and ratios of the analyzed peaks are shown in Table 1. The results showed that the areas of the protein peaks were similar, whereas

the areas of the phenol peaks differed. The ratio of the AFB1-stressed seeds was about half of the ratio of the unstressed seed. In the phenol region of the spectrum, aflatoxins exhibit natural fluorescence. It has been proposed that the decrease in the ratio is due to an increase in the concentration of the fluorescence component(s).

**Table 1.** The fluorescence areas and their ratio for the aflatoxin-unstressed (-AFB1) and AFB1-stressed seeds.

Samples	Fluorescence Area (A.U.)		
	Em 355nm (Ex 290)	Em 430 nm (Ex 350)	<b>Ratio p/f</b>
(-AFB1)	85,05	20,814	<b>4,09</b>
(+AFB1)	82,36	47,64	<b>1,73</b>

## CONCLUSION

2D EPR imaging was successfully applied for the redox characterization of aflatoxin-stressed seeds. The spin probe appears to be concentrated mostly in a particular region of the seed coat. To our understanding, the aflatoxin contamination leads to a change in the seeds' redox status, providing important information about its impact on seed metabolism. Also, the investigation of the EEM fluorescence and peak area ratios can contribute to a better understanding of fluorescence species in aflatoxin-stressed seeds.

## Acknowledgements

This work was supported by the grants 173017, III41005 and 173040 from the Ministry of Education, Science and Technological Development of the Republic of Serbia.

## REFERENCES

- [1] A.P. Wacco, D. Wendi, P.C. Vuzi, J.F. Hawumba, *J. Appl. Chem.*, 2014, **43**: 1-15.
- [2] A.A. Ismaiel, J. Papenbrock, *Agriculture*, 2015, **5**:492-537.
- [3] G. Bačić, T. Walczak, F. Demsar, H.M. Swartz, *Magnet. Reson. Med.*, 1988, **8**:209-219.
- [4] G. Bačić, A. Pavićević, F. Peyrot, *Redox Biol.*, 2016, **8**: 226-2.
- [5] P. Milovanovic, D. Hrnčić, K. Radotić, *Life Sci.*, 2017, **191**: 9-16.

## INFRA RED SPECTROSCOPIC ANALYSIS OF MAIZE INBRED LINE GRAINS: IDENTIFICATION OF BIOMOLECULAR UNSTABLE STATES AND THEIR CHARACTERIZATION

Č. N. Radenović<sup>1,2</sup>, G. V. Maksimov<sup>3</sup>, O. Slatinska<sup>3</sup>, F. Protopopov<sup>3</sup>, N. Delić<sup>1</sup>, Z. Čamdžija<sup>1</sup>, J. Pavlov<sup>1</sup>, M. Sečanski<sup>1</sup>, M. D. Pavlović<sup>4</sup> and M. V. Beljanski<sup>4</sup>

<sup>1</sup>*Maize Research Institute, Zemun Polje, Belgrade, Serbia*

<sup>2</sup>*University of Belgrade, Faculty for Physical Chemistry, Belgrade, Serbia*

<sup>3</sup>*M.V. Lomonosov Moscow State University, Faculty of Biology, Moscow, Russia*

<sup>4</sup>*Institute of General and Physical Chemistry, BioLab, Belgrade, Serbia  
(mbel@matf.bg.ac.rs)*

### ABSTRACT

Characteristics of Fourier Transform Infrared (FTIR) spectra of three maize inbred lines grains: ZPPL 186, ZPPL 225 and M1-3-3 Sdms, in absorption range between 2925 to 400  $\text{cm}^{-1}$  are described. They are connected to various molecular movements (oscillations, vibrations, rotations, translations, etc) in biomolecules and correspond to different functional groups such as: alkanes, nitriles, alkynes, aldehydes, ketones, carboxylic acids, nitro- compounds, aromatic rings, etc. Using FTIR spectroscopy measurements is possible, to analyzed maize inbred lines chemical content and to get information about their unstable (excited), conformational and functional characteristics.

### INTRODUCTION

In our previous papers [1], [2], we reported on structural changes of carotenoid molecules of various maize inbred line. We revealed that their structural characteristics may be used as molecular markers for estimation of their agronomic values. Recently, we reported on Infrared spectra characteristics, of most prominent spectral bands, of maize inbred lines grain [3]. Here are presented results on Fourier Transform Infrared (FTIR) spectroscopy analysis of three maize inbred lines (ZPPL 186, ZPPL 225 and M1-3-3 Sdms) with special attention at weak and variable intensity spectral bands.

### EXPERIMENTAL

The investigation was performed on three new maize inbred lines: ZPPL 186, ZPPL 225 and M1-3-3 Sdms, developed at the Maize Research Institute

Zemun Polje. Morphological and agronomic traits of the inbreds were studied in the research fields and described in detail in [3]. Three to five FTIR spectroscopy measurements were acquired, per one maize inbred line, in transmission mode, in the 4,000 - 400  $\text{cm}^{-1}$  region with a 4  $\text{cm}^{-1}$  resolution, (IR Prestige Shimadzu Corp., Japan). There were no significant difference between recorded IR spectra. The grain samples were prepared immediately before measurements, using the KBr disk technique [4].

## RESULTS AND DISCUSSION

Characteristics of Infrared spectra of grain of maize inbred lines: ZPPL 186, ZPPL 225 and M1-3-3 Sdms reveals numerous absorption features, more than 40 in 4,000 - 400  $\text{cm}^{-1}$  region. Prominent absorption bands were described elsewhere [3]. Here we analyzed less prominent, previously in literature, not described features. In absorption range between 2925 to 400  $\text{cm}^{-1}$  there are numerous absorption bands in all of three inbred lines. However, they significantly differ by kinetical parameters and may be, generally, classified into three clusters: (i) 950 - 400  $\text{cm}^{-1}$  with similar absorption features, (ii) 1600 - 1200  $\text{cm}^{-1}$  with slightly different features and (iii) there are, also, some characteristics absorption features in the range 2800 - 1680  $\text{cm}^{-1}$ . We hypothesized that spectral bands of low intensity and various kinetics parameters represent unstable (excited) state of biological system [5]. They are apparent and characteristic for certain functional groups as revealed in **Table 1**. Unstable (excited) states of biological system

**Table 1.** Absorption bands in FTIR spectra in grains of three maize inbred lines (Abbreviations: s – strong, w – weak, v – variable, intensity of spectral bands)

Maize inbred lines			Assignment of the major IR absorption bands of functional groups in biological macromolecules	Assignment of the IR absorption bands of functional groups in small organic molecules
ZPPL 186	ZPPL 225	M1-3-3 Sdms		
2925 s	2925 s	2925 s	2925, CH <sub>2</sub> asymmetric stretch; lipids, proteins	
			2873 $\text{cm}^{-1}$ , CH <sub>3</sub> symmetric stretch; lipids, proteins	2850-2970 s, C-H, alkanes
2850m	2850m	2850m	2854, CH <sub>2</sub> symmetric stretch; lipids, proteins	2500-2700 b, O-H, hydrogen-bonded carboxylic acids
2375/ 2340w		2375/ 2340 /2300 w	2370, 2340 $\text{cm}^{-1}$ , CO <sub>2</sub> bend	2210-2280 s, C≡N, nitriles 2100-2260 v, C≡C, alkynes

1740m	1740m	1740m	1735, Ester C=O stretch; lipids	
<b>1650 s</b>	<b>1650 s</b>	<b>1650 s</b>	1655, Amide I (protein C=O stretch), $\alpha$ -helices 1636, Amide I (protein C=O stretch), $\beta$ -sheet	1690-1760, C=O, aldehydes, ketones, karboxylic acids, esters 1650, H-OH stretching, water 1610-1680 v, C=C, alkenes
1550m	1550m	1550m	1545, Amide II (protein N-H bending and C-N stretching)	1500-1600 v, C=C, aromatic rings 1500-1570 s, NO <sub>2</sub> , nitro compounds
1515m	1515 m	1515 m	1590-1595, 1510, C=C in plane aromatic vibrations, lignin 1515, Tyrosine ring breathing vibration (C-C/C=C stretching)	
1465 m	<b>1465 m</b>	1465 m	1467, CH <sub>2</sub> bending; lipids, protein	1340-1470 s, C-H, alkanes
1425w	<b>1420 (1300-1500 b)</b>	1425 w	1420, glucan <sup>d</sup>	1300-1370 s, NO <sub>2</sub> , nitro compounds
	<b>1400 (1300-1500 b)</b>		1400, COO symmetric stretching; proteins, fatty acids	
1380/1340 w	<b>1380/1350w (1300-1500 b)</b>	1380/1350w	1380, CH <sub>3</sub> bending; lipids, proteins	
			1280, Amide III of collagen	1180-1360 s, C-N, amines, amides
1246/1225 w	1246w	1246w	1246, cellulose	1050—1300 s, C-O alcohols, ethers, carboxylic acids, esters
		1225w	1220–1240, PO <sub>2</sub> asymmetric stretch; nucleic acids, lipids Amide III of collagen	
			1204 Amide III of collagen	
<b>1160 s</b> 1080 m <b>1000 s</b>	<b>1160 s</b> 1080 m <b>1000 s</b>	<b>1160 s</b> 1080m <b>1000 s</b>	1000–1200, C=O stretching; carbohydrates	
930 m 850 m 780 m 720 m 580 m 520 m	930 m 850 m 780 m 720 m 670 w 615/580m 520 m	930 m 850 m 780 m 720 m 580 m 520 m	1080, PO <sub>2</sub> symmetric stretch; nucleic acids, lipids 750-950, a and b conformers of pyranoid and furanoid ring vibrations of mono- and polysaccharides	675-995 s, C-H, alkenes 670-990 s, C-H, aromatic rings

(molecules, functional group, ion) are connected to various molecular movements (oscillations, vibrations, rotations, translations, etc) in

biomolecules. As revealed in **Table 1**, less prominent absorption bands are connected to, for example: CH<sub>2</sub> symmetric stretch in lipids and proteins (2854 cm<sup>-1</sup>), Amide II (protein N-H bending and C-N stretching at 1545 cm<sup>-1</sup>), PO<sub>2</sub> symmetric stretch characteristic for nucleic acids and lipids (1080 cm<sup>-1</sup>), etc.

## CONCLUSION

Using FTIR spectroscopy measurements it is possible, not only, to analyse maize inbred lines chemical content, but also, to get information about their unstable (excited), conformational and functional characteristics.

## *Acknowledgement*

This work was partially supported by The Maize Research Institute, Zemun Polje, Belgrade and The Ministry of Education, Science and Technological Development of The Republic of Serbia (Projects no. TR 31055 and 172015).

## REFERENCES

- [1] Č. N. Radenović, M. Jeremić, G. V. Maksimov, M. N. Mišović, B. V. Trifunović, *Journal of Scientific Agricultural Research*, 1994, 55, 291-296.
- [2] Č. N. Radenović, M. Jeremić, G. V. Maksimov, M. N. Mišović, D. Selaković, *Proceedings for Natural Sciences, Matica Srpska, Novi Sad*, 1998, 95, 41-50.
- [3] Č. N. Radenović, G. V. Maksimov, D. M. Grozdinskiy, *Fiziologija rastenii i genetika (ru.)*, 2015, 47, 15-24.
- [4] Č. N. Radenović, G. V. Maksimov, E. V. Tytyaev, V. V. Shutova, N. Delić, Y. Čamdžija, Y. O. Pavlov, Ž. Jovanović, *Agricultural Biology*, 2016, 51, 645-653.
- [5] O. R. Klyos, G. V. Maksimov, Č. N. Radenović, *Biofizika ritmičeskogo vozbuđenija*, MGU, Moskva, 1-206, 1993.

## ORIENTATION OF CELL WALL POLYMERS IN THE *Arabidopsis thaliana* STEM

J. Simonović Radosavljević<sup>1</sup>, J. Stevanić<sup>2</sup>, D. Đikanović<sup>1</sup>, L. Salmén<sup>2</sup> and  
K. Radotić<sup>1</sup>

<sup>1</sup> Institute for multidisciplinary research, University of Belgrade, Kneza  
Višeslava 1, 11000 Belgrade, Serbia. (jasna@imsi.rs)

<sup>2</sup> RISE/Innventia AB, Drottning Kristinas väg 61, SE-114 86 Stockholm,  
Sweden.

### ABSTRACT

Mechanical and physical properties of plant fibres are dependent on the orientation of constituent polymers (cellulose, hemicellulose, lignin). Fourier transform infrared (FTIR) microscopy was used to examine the orientation of the main plant polymers in transversal and longitudinal direction of the isolated cell wall of the *Arabidopsis thaliana* stem. The polarised FTIR measurements indicated that xylan and glucomannan have parallel orientation with regard to the orientation of cellulose, as well as lignin.

### INTRODUCTION

Plant cell wall (CW) can be considered as a nano-composite in which cellulose, lignin and hemicelluloses are interconnected in a specific manner. It is well recognised that the cell wall development and expansion and deposition implies an anisotropic arrangement of the cell wall components [1]. Structural organisation of the cell wall and related polymers is important for both mechanical properties of plants and chemical reactions occurring in the wall space, especially in the response to stress. Understanding the arrangement and anisotropy of the polymers in cell wall is important for understanding the mechanical properties of plant, which has implications in plant response to stress. By using imaging FT-IR microscopy, run in transmission mode and at different polarisation modes (from 0° to 90°), it is possible to follow the chemical variability and the orientation of cell wall polymers [2]. The orientation of cellulose, hemicellulose (xylan and glucomannan) and lignin, as essential components of the plants, were analysed by FTIR with regard to the sample axis.

### EXPERIMENTAL

The purified isolated cell wall material was obtained from *Arabidopsis thaliana* stem by methanol extraction and subsequent purification using a

series of solvents (phosphate buffer, 1% Triton X-100, 1M sodium chloride, distilled water, methanol, acetone) [3]. FTIR microscopy measurements were carried out using a Spectrum Spotlight 400 FTIR Imaging System (Perkin Elmer Inc, Shelton, CT, USA). Spectral resolution:  $8\text{ cm}^{-1}$ ; spectral range: from  $1800\text{ cm}^{-1}$  to  $720\text{ cm}^{-1}$ . Polarisation: the incident IR radiation was polarised by a gold wire grid polariser from  $0^\circ$  to  $90^\circ$  polarisation in relation to the fibre orientation with intervals of  $5^\circ$ . The sample was mounted on the sample stage as parallel as possible to the orientation of the  $0^\circ$  polarisation. The IR spectra were processed by the software Spotlight 1.5.1, HyperView 3.2 and Spectrum 6.2.0 (Perkin Elmer Inc., Shelton, CT, USA) [2].

## RESULTS AND DISCUSSION

From the in-depth study of polymer orientation, three areas from the sample were selected. The transmission spectra recorded at  $0^\circ$  and  $90^\circ$  polarisation modes were processed using a ratio function to produce an orientation spectrum ( $R = A_{0^\circ} - A_{90^\circ}$ ), where R is the anisotropy spectra, indicating the orientation of components,  $A_{0^\circ}$  is the absorbance spectra recorded at  $0^\circ$  and  $A_{90^\circ}$  is the absorbance spectra recorded at  $90^\circ$ . Spectral signals related to absorptions from cellulose, xylan, glucomannan and lignin in the wavenumber range between  $1800\text{ cm}^{-1}$  and  $720\text{ cm}^{-1}$  can be identified. Figure 1 (left) shows average absorbance spectra at  $0^\circ$  and  $90^\circ$  polarization angle and Figure 1 (right) shows the average orientation spectra for the *Arabidopsis thaliana* stem cell wall. In Figure 1 (right), the positive signals indicate that their corresponding functional groups are arranged in a more parallel orientation to the fibre axis, and the negative signals indicate that their corresponding functional groups are arranged in a perpendicular orientation to the fibre axis.

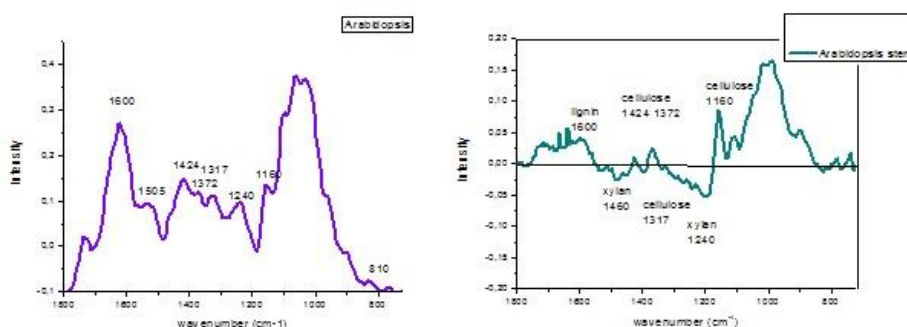


**Figure 1.** Average absorbance spectra of *Arabidopsis thaliana* stem cell wall (left); The average orientation spectra of *Arabidopsis thaliana* stem cell wall (right).

The relative absorbance spectra are presented (Figure 2) as specific absorption peaks ( $RA = (I_p - I_{min}) / (I_{max} - I_{min})$ ) where RA is relative absorbance,  $I_p$  is intensity of the absorbed IR radiation at a given angle of the polarisation, P,  $I_{max}$  is maximal intensity observed for a given vibration and  $I_{min}$  is minimal intensity observed for a given vibration. These relative absorbance values were presented in relation to the angle of the incident IR polarisation (from  $0^\circ$  to  $90^\circ$ ).

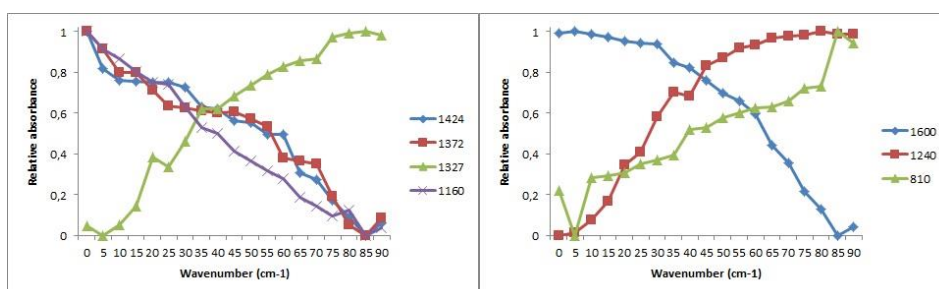


**Figure 2.** The relative absorbance of IR specific absorption wavenumbers plotted against the polarisation angle for the cellulose (left) and xylan, glucomannan and lignin (right) for *Arabidopsis thaliana* stem.

It is evident (Fig. 2) that the three cellulose peaks ( $1160\text{ cm}^{-1}$ ,  $1370\text{ cm}^{-1}$  and  $1424\text{ cm}^{-1}$ ) [3-5] had high absorption levels at low polarisation angles, which is a consequence of a more parallel orientation of the corresponding groups to the CW longitudinal axis. The fourth cellulose peak (the perpendicular signal at  $1317\text{ cm}^{-1}$ ) had the greatest intensity at a high polarisation angle, due to the perpendicular orientation of the corresponding group (Fig. 2). For the xylan, the characteristic band signal ( $1240\text{ cm}^{-1}$ ) [4-6] increased with an increase in the polarisation angle. Due to the parallel orientation of these side groups in xylan, an orientation parallel to the longitudinal CW axis is indicated (Fig. 3). A glucomannan absorbance vibration, indicating the orientation of glucomannan, was observed at  $810\text{ cm}^{-1}$  (equatorially aligned hydrogen on the  $C_2$  atom in the mannose residue) [4, 6]. The peak was negative (Fig. 3.). This group is oriented orthogonally to the glucomannan backbone, which is the reason why it may be concluded that glucomannan is also oriented in parallel to the CW longitudinal axis. For the lignin, the characteristic band signal ( $1600\text{ cm}^{-1}$ ) [4-6] decreased with an increase in the polarisation angle (Fig. 3), indicating that lignin is organised in parallel with the longitudinal CW axis.

## CONCLUSIONS

It has been demonstrated here that xylan and glucomannan are oriented in parallel to the cellulose and more or less parallel to the axis of a cell wall, in isolated CW fragments from *Arabidopsis thaliana* stem. There was also a clear indication of lignin being oriented in parallel to the longitudinal CW axis. This indicates that both lignin and hemicelluloses enhance the main role of cellulose in elastic/stiffness property of CW. It is believed that this structuring of the lignin in the S<sub>2</sub> layer of the cell wall might be the result of the spatial constraints within the cell wall, as occurring due to the previously deposited cellulose/hemicellulose organization of a strongly oriented assembly.

## Acknowledgement

This work was supported by Ministry of Education and Science of Republic Serbia (Project #173017, 45012) and COST Action FP0802.

## REFERENCES

- [1] L. Salmén, *Comptes Rendus Biologies*, 2004, 327: 873-880
- [2] J. S. Stevanic, L. Salmén, *Holzforschung*, 2009, **63**, 497-503.
- [3] M. Chen et al., *Phytochem. Anal.*, 2000, **11**, 153-159.
- [4] R. H. Marchessault, *Pure Appl. Chem.*, 1962, **5**, 107-129.
- [5] R. H. Marchessault, C. Y. Liang, *J. Polym. Sci.*, 1962, **59**, 357-378.
- [6] M. Åkerholm et al., *Carbohydr. Res.*, 2004, **339**, 569-578.

## LACK OF DEHYDROEPIANDROSTERONE TREATMENT EFFICIENCY IN RAT MODEL OF TRANSIENT ISCHEMIC ATTACK?

M. Zarić<sup>1</sup>, D. Drakulić<sup>1</sup>, M. Dragić<sup>1,2</sup>, I. Guševac Stojanović<sup>1</sup>, N. Mitrović<sup>1</sup>,  
I. Grković<sup>1</sup> and J. Martinović<sup>1</sup>

<sup>1</sup>*Department of Molecular Biology and Endocrinology, Vinča Institute of nuclear sciences, University of Belgrade, Mike Petrovića Alasa 12-14, 11351 Belgrade, Republic of Serbia (marinazaric@vin.bg.ac.rs)*

<sup>2</sup>*Department for General Physiology and Biophysics, Faculty of Biology, University of Belgrade, Studentski trg 3, 11001 Belgrade, Republic of Serbia*

### ABSTRACT

Numerous agents used for cerebral ischemia treatment proved inefficient in clinical trials. While effects of postischemic dehydroepiandrosterone (DHEA) treatment remain scarce, there is no data on largely understudied condition such as transient ischemic attack. Current study evaluated infarction presence, neuronal morphology and pro- and anti- apoptotic protein ratio (Bax/Bcl2) in hippocampus (HIP), region most vulnerable to ischemic damage. Four hours after sham operation or 15 min common carotid arteries occlusion (I/R), male Wistar rats were treated with a single dose of vehicle or DHEA. Results showed absence of infarction following I/R with morphological changes in CA1 area and tendency of mitochondrial Bax/Bcl2 increment. DHEA *per se* did not affect investigated parameters but postischemic treatment instigated Bax/Bcl2 augmentation accompanied with altered morphology of CA1 neurons. Data suggest DHEA therapeutic ineffectiveness in I/R-induced changes and potential neurotoxicity.

### INTRODUCTION

Transient ischemic attack (TIA) represents a brief episode of neurological dysfunction due to vascular cause, with no detectable infarction [1]. Although in the past TIA was considered as nonthreatening condition, nowadays it is recognized as heralds of forthcoming ischemic stroke. TIA may be associated with cognitive decline or brain atrophy, suggesting it likely leads to some degree of permanent brain injury that is beyond the detection limits [1, 2]. Decades of stroke research have revealed numerous potentially neuroprotective therapeutics, but all of them failed due to serious side effects

or lack of medical efficiency. Furthermore, research focusing on potential treatment for TIA patients is lacking.

Naturally present in human body, circulating androgen precursor dehydroepiandrosterone (DHEA) has become one of the therapeutic candidates showing rather conflicting effects from neuroprotective to neurotoxic [3]. Furthermore, there are no data focusing on DHEA effects on ischemic conditions like TIA. Therefore, 15 min common carotid artery occlusion with 24 h reperfusion time (I/R) performed to induce TIA was validated by 2,3,5-triphenyltetrazolium chloride (TTC) staining. Afterwards, potential I/R effects alongside 4h postoperative DHEA treatment were evaluated by assessment of neuronal morphology. Moreover to determine potential cell susceptibility to apoptosis, the ratio of pro- (Bcl-2-associated X protein, Bax) and anti- apoptotic (B-cell lymphoma 2, Bcl-2) protein level was also investigated in hippocampus (HIP), the brain region most vulnerable to ischemic damage.

## EXPERIMENTAL

All experimental procedures were performed on three-months-old male Wistar rats and approved by the Ethics Committee for the Use of Laboratory Animals of Vinča Institute of Nuclear Sciences. Twenty four hours after previously described surgical procedure and treatment [4], brains were removed on ice and: a) coronal slices were stained with 1% TTC solution to evaluate the presence of potential infarct core (n=20, 5 *per* group); b) prepared for routine histological hematoxylin- eosin (H&E) staining for the purpose of neuronal morphology assessment (n=16, 4 *per* group); c) homogenized for hippocampal cytosolic and mitochondrial fractions preparation used for Bax to Bcl2 protein ratio evaluation by Western blot. Two-way ANOVA and Tukey's post hoc test were performed for statistical analysis using GraphPad Prism 6 Software. The results were presented as percents of the mean  $\pm$  SEM of the control sham operated group. All results were considered significant at  $p < 0.05$  (n=16, 4 *per* group).

## RESULTS AND DISCUSSION

TTC staining revealed no infarct core either in HIP (Figure 1A) or in other brain regions (data not shown) in any of experimental groups. Lack of infraction in presented experimental conditions fulfills one of the main criteria for validity of TIA model [1, 2] thus representing a valuable novel finding. Regular neuronal morphology through HIP with no signs of histopathological changes in untreated or treated sham operated animals was observed. However, aberrant neuronal morphology was detected in both I/R groups exclusively in CA1 area while other hippocampal areas were

unaffected (Figure 1A) which is in accordance with our previously published data [4].

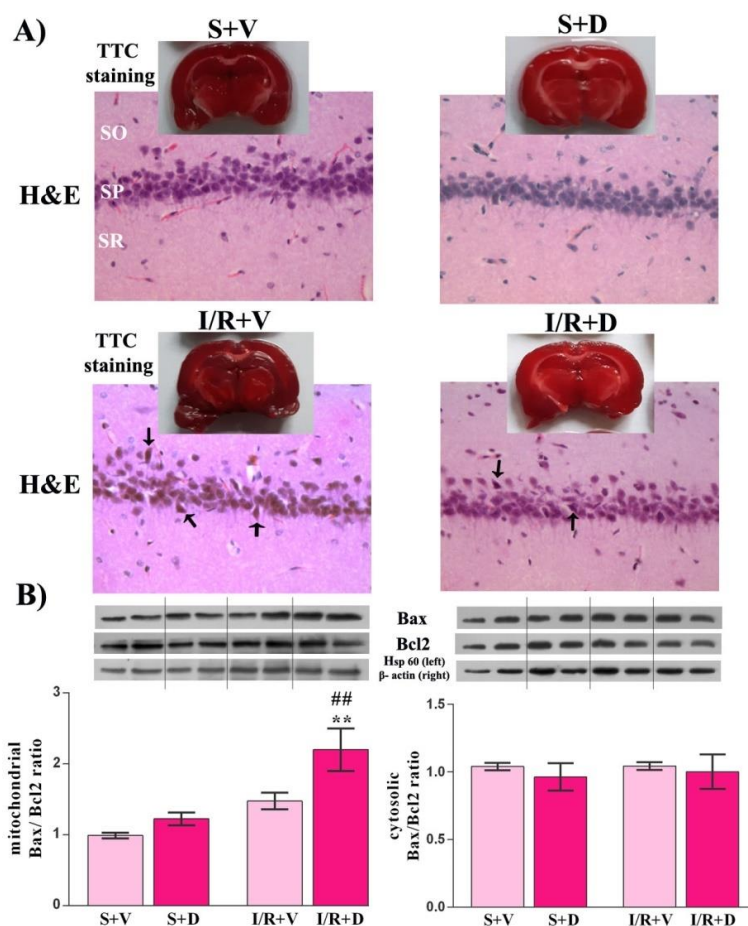


**Figure 1.** A) TTC and H&E staining of hippocampal CA1 area; Arrows indicate neurons showing aberrant morphology. S+V - sham operated group injected with DMSO, S+D - sham operated group injected with DHEA, I/R+V - I/R group injected with DMSO; I/R+D - I/R group injected with DHEA, SO-*stratum oriens*, SP-*stratum pyramidale*; SR-*stratum radiatum*. Scale bar = 50  $\mu$ m. B) Bax to Bcl2 protein ratio in mitochondrial (left) and cytosolic fraction (right) of HIP. Hsp 60 and  $\beta$ -actin were used as a loading controls in mitochondrial and cytosolic fraction, respectively. Data are expressed as mean  $\pm$  SEM. Symbols indicate significant differences between respective group and S+V (\*\*  $p < 0.01$ ) and S+D (##  $p < 0.01$ ).

Two-way ANOVA revealed significant main effects of I/R ( $F_{1, 12} = 17.04$ ,  $p < 0.01$ ) and treatment ( $F_{1, 12} = 7.356$ ,  $p < 0.05$ ) on mitochondrial Bax/Bcl2 protein ratio but showed no effect of two factors in cytosolic fraction. Although Bax/Bcl2 ratio increment was observed in I/R untreated group, post hoc test showed its significant augmentation only in I/R operated DHEA group compared to control ( $p < 0.01$ ) and sham operated DHEA group ( $p < 0.01$ ) suggesting a potential ineffectiveness of DHEA following I/R (Figure 1B).

### CONCLUSION

Under physiological conditions DHEA had no effect at histological level and mitochondrial and cytosolic Bax/Bcl2 ratio, while in ischemic milieu it increased mitochondrial Bax/Bcl2 ratio and pointed to therapeutic ineffectiveness on morphological alternations observed after 24h and even potential neurotoxicity. Further research is needed to elucidate DHEA effects more precisely in ischemic conditions, especially TIA.

This study points to potential detrimental postischemic changes, visible on molecular but not at macroscopical level, supporting the relevance of TIA in clinical practice.

### *Acknowledgement*

Supported by the Ministry of Education, Science and Technological Development, Republic of Serbia, grants 173044 and 41014.

### REFERENCES

- [1] Durukan Tolvanen A, Tatlisumak E, Pedrono E, Abo-Ramadan U, Tatlisumak T. TIA model is attainable in Wistar rats by intraluminal occlusion of the MCA for 10min or shorter. *Brain research*. 2017;1663:166-73.
- [2] Pedrono E, Durukan A, Strbian D, Marinkovic I, Shekhar S, Pitkonen M, et al. An optimized mouse model for transient ischemic attack. *Journal of neuropathology and experimental neurology*. 2010;69(2):188-95.
- [3] Maninger N, Wolkowitz OM, Reus VI, Epel ES, Mellon SH. Neurobiological and neuropsychiatric effects of dehydroepiandrosterone (DHEA) and DHEA sulfate (DHEAS). *Frontiers in neuroendocrinology*. 2009;30(1):65-91.
- [4] Zaric M, Drakulic D, Stojanovic IG, Mitrovic N, Grkovic I, Martinovic J. Regional-specific effects of cerebral ischemia/reperfusion and dehydroepiandrosterone on synaptic NMDAR/PSD-95 complex in male Wistar rats. *Brain research*. 2018;1688:73-80.

## ESTROGEN RECEPTORS MODULATE ECTONUCLEOTIDASES ACTIVITY IN HIPPOCAMPAL SYNAPSES OF MALE RATS

N. Mitrović<sup>1</sup>, M. Dragić<sup>1,2</sup>, M. Zarić<sup>1</sup>, D. Drakulić<sup>1</sup>, I. Guševac Stojanović<sup>1</sup>, J. Martinović<sup>1</sup> and I. Grković<sup>1</sup>

<sup>1</sup>*Department of Molecular Biology and Endocrinology, Vinča Institute of nuclear sciences, University of Belgrade, Mike Petrovića Alasa 12-14, 11351 Belgrade, Republic of Serbia (natasa@vin.bg.ac.rs)*

<sup>2</sup>*Department for General Physiology and Biophysics, Faculty of Biology, University of Belgrade, Studentski trg 3, 11001 Belgrade, Republic of Serbia*

### ABSTRACT

17 $\beta$ -estradiol (E2) provokes remodeling of hippocampal synapses by interacting with several molecular and cellular processes. Literature highlights the specific roles of ectonucleotidases and their coordinated actions in E2-mediated spine remodeling and maintenance in male as well as in female rodents. Since the data for males are scarce current study aimed to explore the effects of E2 and the contribution of each estradiol receptor subtype (ER $\alpha$ / $\beta$ ) to modulation of ectonucleotidases activities in the hippocampal synapses of male rats. Obtained results demonstrate that E2 attenuates adenine nucleotide hydrolysis by ecto-nucleoside triphosphate diphosphohydrolase (NTPDase)/ecto-5'-nucleotidase (eN) enzyme chain. E2, by acting at ER $\beta$  decreases the activity of NTPDases, while both classic and non-classic receptors activation is necessary for eN activity modulation. In summary, all examined ectonucleotidases are differently regulated by estradiol receptors suggesting that each enzyme may specifically contribute to hippocampal physiology.

### INTRODUCTION

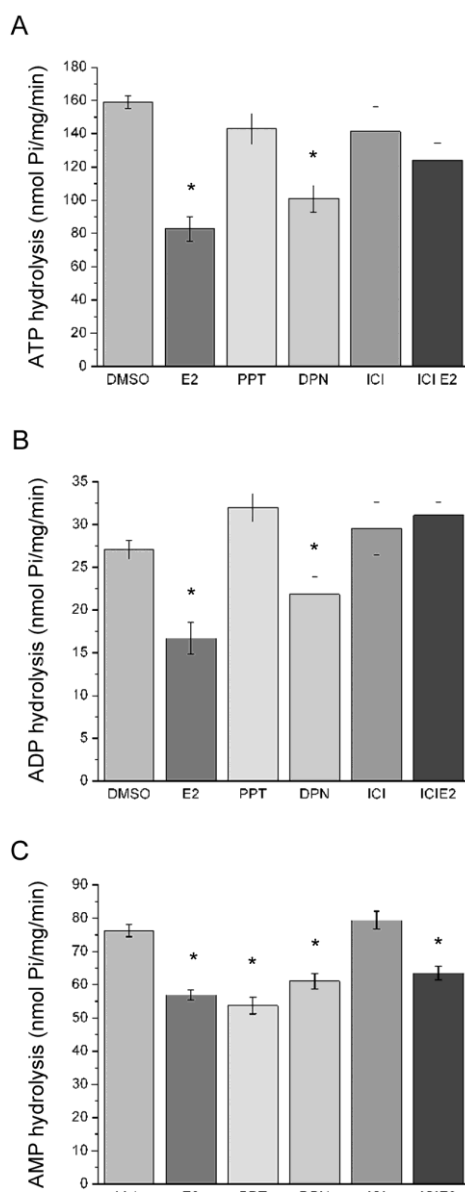
By binding to estrogen receptors (ER/ $\beta$ ), 17 $\beta$ -estradiol (E2), rapidly affects hippocampal morphology, plasticity and memory in male as well as in female rodents [1]. However, the interaction with other metabolic processes, such as extracellular adenine nucleotides metabolism, are currently scarce. Extracellular adenine nucleotides act as a versatile autocrine/paracrine signaling molecules in the central nervous system (CNS) which are tightly controlled by ectonucleotidase enzyme chain. The first step in the sequential hydrolysis of extracellular ATP is catalyzed by members of ecto-nucleoside

triphosphate diphosphohydrolase (NTPDase) family. The last and the rate-limiting step of the extracellular ATP metabolism is catalyzed by ecto-5'-nucleotidase (eN), which hydrolyzes AMP to adenosine [2]. Since our previous evaluation supports the idea of specific roles of different ectonucleotidases and their coordinated actions in E2-mediated spine remodeling and maintenance [3,4], the aim of current study was to get closer insight in the E2-induced decrease in NTPDase/eN enzyme chain activity in the hippocampal synaptic compartment of male rats and to identify estradiol receptors responsible for the observed effects.

### EXPERIMENTAL

Three-month old, gonadally intact male Wistar rats (300 – 350 g) were kept according to the standards of Ethical Committee for the use of laboratory animals of Vinča Institute of nuclear sciences, University of Belgrade, Republic of Serbia, and divided into six groups (6 – 9 rats/group): (1) DMSO group, received an injection of (dimethyl sulfoxide; DMSO) (1 ml/kg) used as a solvent and it was used as a control group; (2) E2 group, injected with 17 $\beta$ -estradiol 3-benzoate (33.3  $\mu$ g/kg); (3) PPT group, received an injection of a selective ER $\alpha$  agonist PPT (2.5 mg/kg); (4) DPN group, injected with selective ER $\beta$  agonist DPN (2.5 mg/kg); (5) ICI group, treated with a non-selective ER antagonist, ICI 182.780 (2 mg/kg); (6) ICIE2 group, subjected to an injection of ICI 182.780, 2 h prior to E2 administration (2 mg/kg + 33.3  $\mu$ g/kg). Animals were treated *s.c.* and sacrificed 24 h later. Hippocampal synaptosomes are isolated as previously described [3].

Rates of ATP/ADP and AMP hydrolysis reflecting NTPDase, eN activities, respectively, were determined spectrophotometrically based on liberated inorganic phosphate [3]. The reaction medium used to assay ATP and ADP hydrolysis contained 5.0 mM KCl, 1.5 mM CaCl<sub>2</sub>, 0.1 mM EDTA, 10 mM glucose, 225 mM sucrose, and 45 mM TRIS–HCl buffer, pH 8.0, in a final volume of 200  $\mu$ l. AMP hydrolysis was assayed in the reaction medium containing 1 mM MgCl<sub>2</sub>, 50 mM Tris-HCl buffer, pH 7.4 in a final volume of 200  $\mu$ l [3]. Synaptosomal proteins (10  $\mu$ g protein) were added to the reaction mixture and preincubated for 10 min at 37 °C. The reaction was initiated by addition of 150  $\mu$ M ATP/ADP or AMP in a final concentration and stopped after 15 min for ATP/ADP or 30 min for AMP by addition of 22  $\mu$ l 3 M perchloric acid (PCA). Test tubes were chilled on ice and assayed for liberated inorganic phosphate (Pi). Incubation times and protein concentrations were chosen in order to ensure the linearity of the reactions. Controls with the addition of sample after PCA were used to correct non-enzymatic hydrolysis of the substrates.



## RESULTS AND DISCUSSION

E2 induced significant decrease in ATP ( $82.7 \pm 1.2$  nmol Pi/mg/min,  $p < 0.05$ ; **Fig. 1A**) and ADP ( $18.0 \pm 1.6$  nmol Pi/mg/min,  $p < 0.05$ ; **Fig. 1B**) and AMP ( $56.3 \pm 1.6$  nmol Pi/mg/min; **Fig. 1C**), hydrolysis compared to respective DMSO ( $162.1 \pm 5.5$  nmol Pi/mg/min for ATP and  $29.1 \pm 1.2$  nmol Pi/mg/min for ADP and  $76.3 \pm 1.8$  for AMP). As shown in **Fig.1** only DPN had the ability to mimic E2 effect and induce decrease of both ATP ( $72.5 \pm 13.01$  nmol Pi/mg/min) and ADP ( $19.84 \pm 1.23$  nmol Pi/mg/min) hydrolysis indicating that ER $\beta$  rather than ER $\alpha$  might be involved in E2-induced decrease in NTPDase activity.

**Figure 1.** Effects of E2 and ERs on (A) ATP, (B) ADP and (C) AMP hydrolysis. Bars represent mean activity (nmol Pi/mg/min)  $\pm$  SEM. \* $p < 0.05$  or less, indicates significant difference compared to control DMSO group.

Both, PPT and DPN, effectively reduced the rate of AMP hydrolysis ( $53.69 \pm 2.48$  nmol Pi/mg/min and  $61.03 \pm 2.35$  nmol Pi/mg/min, respectively,  $p < 0.001$ ) compared to control ( $76.3 \pm 1.8$  nmol Pi/mg/min), indicating that both ER subtypes are mediating the reduction of eN activity. However, the modest decrement was also observed after the ICIE2 treatment ( $63.49 \pm 2.08$  nmol Pi/mg/min;  $p < 0.05$ ) compared to DMSO control. Since the presence of ICI 182.780 failed to block the effect of E2, obtained results

may imply that besides activation of ER $\alpha/\beta$ , E2 action may be also mediated by activation of nonclassical ER subtypes.

### CONCLUSION

According to obtained results E2 probably through activation of ER $\beta$  decreases the activity of NTPDase enzymes. In contrast E2-mediated modulation of eN activity may not be completely explained by its actions on classical ERs and alternative receptors may be involved. The diverse effects of ER $\alpha$  and ER $\beta$  activation on ectonucleotidases indicate that each receptor might have divergent contributions to neuronal physiology, synaptic plasticity and hippocampal dependent behavior in male rats.

### *Acknowledgement*

This work was supported by the Ministry of Education, Science and Technological development of the Republic of Serbia (grants 173044 and 41014).

### REFERENCES

- [1] K.M. Frick, J. Kim, J.J. Tuscher, A.M. Fortress, *Learning & memory*, 2015, 22, 472-493
- [2] H. Zimmermann, M. Zebisch, N. Strater, *Purinergic signalling*, 2012, 8, 437-502.
- [3] N. Mitrovic, M. Zaric, D. Drakulic, J. Martinovic, M. Stanojlovic, J. Sevigny, A. Horvat, N. Nedeljkovic, I. Grkovic, *Neuroscience*, 2016, 324, 286-296.
- [4] N. Mitrovic, M. Zaric, D. Drakulic, J. Martinovic, J. Sevigny, M. Stanojlovic, N. Nedeljkovic, I. Grkovic, *Journal of molecular neuroscience*, 2017, 61, 412-422.

## ANALYSIS OF AMINO ACID DISTANCES IN PROTEIN CHAINS

M. Maljković<sup>1</sup>, M. Beljanski<sup>2</sup> and N. Mitić<sup>1</sup>

<sup>1</sup>*Department of Computer Science, Faculty of Mathematics, University of Belgrade, P.O.B. 550, Studentski trg 16, 11001 Belgrade, Serbia*

*(mirjana@matf.bg.ac.rs)*

<sup>2</sup>*Bio-lab, Institute of General and Physical Chemistry, P.O.B. 45, Studentski trg 12/V, 11001 Belgrade, Serbia*

### ABSTRACT

Interactions of amino acids within protein chains were analyzed based on geometric distances between every two amino acids in the same chain. For each pair of amino acids in a chain, three types of distances were calculated: a distance between C $\alpha$  atoms of amino acids, a minimal and a maximal distance without taking into account hydrogen atoms. Using different criteria based on distance threshold and properties of proteins and amino acids, different groups of amino acid distances were analyzed. For each pair of amino acids in each analyzed group, descriptive statistics were calculated. The obtained results can be viewed at <http://bioinfo.matf.bg.ac.rs/aadis/statistics.html>.

### INTRODUCTION

The packing of the protein chain into its 3D structure is determined by the interactions of its amino acids. One approach to the analysis of interactions between amino acids refers to geometric distances between the pairs of amino acids in proteins. An early result has been published by Singh and Thornton in *Atlas of Protein Side-Chain Interactions* in 1992 [1] where they analysed all possible pairwise interactions between the 20 side-chains for 533 protein chains. Based on the printed atlas, Laskowski made the Web Atlas, an online accessible database of side-chain/side-chain interactions in proteins[2].

The objective of this paper is to obtain an updated statistical analysis of geometric distances between every two amino acids. In the research, pairwise distances between 20 amino acids in protein chains were statistically analyzed. In the analysis, distance threshold and properties of proteins and amino acids were taken into account.

## MATERIALS AND METHODS

The data of proteins, used in the dataset, were downloaded from the Protein Data Bank (PDB) database [3]. The dataset was filtered by PDBselect [4] to eliminate proteins with mutual sequence similarity larger than 25%. 3D structures of all proteins in the dataset were revealed by X-ray crystallography with the resolution up to 3Å and R-factor up to 0.3. The dataset contained 940 polypeptide chains of 933 proteins. To each amino acid in chains was assigned a secondary structure using DSSP [5]. Using protein structural classification (SCOP) database [6], a class was assigned to each protein in the dataset.

Atomic coordinates of proteins described in the PDB database were used to calculate three different types of distances between every pair of amino acids in the same chain. Using Euclidean metric, the following distances were calculated: distances between C $\alpha$  atoms of amino acids, denoted  $d_{C\alpha}$ , minimal distances without taking into account hydrogen atoms (atoms with element symbol H in PDB files), denoted  $d_{\min}$ , and maximal distances without taking into account hydrogen atoms, denoted  $d_{\max}$ .

For each distance type and each pair of amino acids in used protein chains, the following data were extracted: PDB identifier of a protein, SCOP class of a protein, chain identifier, the first amino acid in a pair, secondary structure type of the first amino acid in a pair, the second amino acid in a pair, secondary structure type of the second amino acid in a pair, distance type and distance.

## RESULTS AND DISCUSSION

The calculated amino acid distances were divided into groups for analysis. Criteria that were used for the definition of groups were: type of distances, distance threshold in angstrom unit (3Å, 5Å and 8Å), intra-secondary or inter-secondary structure pairs, types of secondary structures of amino acids and SCOP class of proteins.

For every two amino acids in each obtained group of distances were calculated the following descriptive statistics: number of pairs, average distance, minimal distance, maximal distance, the standard deviation of distances, 5th, 10th, 25th, 50th, 75th and 90th percentiles of distances and lower outer bound for outliers. Statistical data for pairs of amino acids in a group for analysis were presented in the form of 20x20 tables. In Table 1 are shown average distances (in Å) for amino acid pairs from one of the obtained groups.

**Table 1.** Average distances for pairs of amino acids from the group with all minimal distances calculated without taking into account hydrogen atoms; amino acid pairs are from all proteins and from different secondary structures; the first amino acid in pairs belongs to  $\alpha$ -helix (H) secondary structure and the second amino acid in pairs belongs to extended strand (E) secondary structure.

	ARG	LYS	ASP	GLU	ASN	GLN	HIS	PRO	TYR	TRP	SER	THR	GLY	ALA	MET	CYS	PHE	LEU	VAL	ILE
ARG	21	21.9	20.8	21	20.3	21.1	19.9	21.7	19.9	19.1	20.6	20.7	20.6	19.8	19	19.5	18.9	19.2	19.7	19
LYS	22.2	22.5	21.5	22.2	21.3	21.5	20.6	22.9	20.5	19.4	20.9	21.7	21.3	20.7	19.9	19.9	19.5	20.1	20.7	19.8
ASP	21.5	22.2	21.9	22.5	20.9	21.3	20.8	23.4	20.6	19.7	21.6	21.8	21.3	20.7	20.2	20	19.6	20	20.5	20
GLU	21.5	22.3	21.6	22.2	21.1	21.5	20.8	22.8	20.8	19.6	21.1	21.5	21.4	20.7	19.8	20	19.7	20	20.6	19.9
ASN	21.3	22.3	21.5	21.8	21	21.8	20.6	22.6	20.2	19.5	21.3	21.4	20.9	20.1	19.7	20.1	19.4	19.9	20.2	19.8
GLN	22	22.7	21.8	22.7	21.4	22	21	23.2	20.7	19.9	21.7	21.9	21.2	20.5	19.5	19.4	19.8	20.4	20.5	19.6
HIS	20.9	21.9	20.1	21.4	20.3	20.9	19.8	22.2	19.9	18.6	20.1	21	20.1	19.2	18.5	19.2	18.7	19.2	19.9	19.1
PRO	21.7	22.3	21.5	21.3	20.8	21.9	20.1	22.7	20.4	19.1	20.8	21.4	20.7	20	19.5	19.1	19.2	19.7	20.2	19.5
TYR	19.1	20.4	18.8	19.9	18.9	19	18.5	20.3	18.5	17.6	19	19.6	18.8	18.2	17.4	17.4	17.5	17.9	18.3	17.9
TRP	19.2	20.2	18.8	19.4	17.7	17.6	17.6	20.3	17.3	16.3	18.5	19.4	18.5	17.8	16.4	17.3	16.5	17.2	18.1	17.1
SER	20.6	21.1	20.9	20.9	20.1	21	19.8	22	19.7	19.3	20.5	20.6	20	19.3	18.6	19.2	18.6	19	19.5	18.8
THR	21	21.7	20.6	21.1	20.2	20.7	19.9	21.7	20	19.2	20.3	20.8	20.6	19.4	18.3	19	18.6	19.1	19.4	18.8
GLY	21.3	21.5	20.6	21.8	19.8	20.8	19.5	22	19.8	18.7	20	20.6	20	19.2	18.5	18.3	18.6	18.8	19.7	18.5
ALA	21.1	21.3	20.6	21.1	20.5	20.8	19.6	22	20	18.7	20.2	20.7	20.3	19.5	19	19.4	18.6	19.1	19.5	18.8
MET	20	20.7	19.4	20.3	18.5	20	18	21.4	18.6	16.9	19.5	19.5	18.6	18.3	16.9	17.3	17.6	18	18.4	17.7
CYS	20.2	19.8	18.9	19.9	17.3	18.9	18.1	20.3	18.2	17.1	17.9	18.7	17.7	17.3	16.6	15.8	16.7	17.2	17.9	17.1
PHE	18.9	19.6	18.3	19.1	18	18.5	17.7	19.7	17.5	16.9	17.9	18.7	18.5	17.2	16.3	16.6	16	16.6	17.4	16.8
LEU	19.6	20	19.4	20	18.8	19.4	18.5	20.5	18.5	17.7	19.1	19.4	19.1	18	17.7	17.9	17.2	17.4	18	17.3
VAL	19.9	20.2	19.6	20.7	19.4	19.7	19.1	20.7	19.2	17.5	19.4	19.9	19.5	18.5	17.9	18.7	17.5	18	18.4	17.9
ILE	19.1	20.1	19.1	19.7	18.7	19.1	18.4	20.6	18.3	16.9	19	19.4	18.6	17.9	17.2	17.4	16.7	17.3	17.9	17.2

Obtained descriptive statistics of distances could be used for analyzing distances of amino acids with specific characteristics using the different criteria. For example, by analyzing groups of distances of amino acid pairs from different secondary structures, from all proteins and without distance threshold, it could be noticed that the calculated value for Cys-Cys pair is the minimum of calculated values for all amino acid pairs or is at most 1.4Å higher than the minimal value in the group. In Table 2 is shown the comparison of Cys-Cys pair with other amino acid pairs. This is consistent with the fact that disulfide bonds influence on the stabilization of protein structure and on the link between amino acids from different segments of a sequence [7].

All results of calculated statistics are presented on the website Amino Acid Distances (AADIS) and could be found at the <http://bioinfo.matf.bg.ac.rs/aadis/statistics.html>.

## CONCLUSION

The obtained data can contribute to the identification and better understanding of previously not observed unique interactions between amino acids in order to better predict the protein structure and function.

**Table 2.** Comparison of Cys-Cys pair with other amino acid pairs.

Descriptive statistic	Method: $d_{C\alpha}$ Minimum value for all pairs	Method: $d_{C\alpha}$ Value for Cys-Cys pair	Method: $d_{\min}$ Minimum value for all pairs	Method: $d_{\min}$ Value for Cys-Cys pair	Method: $d_{\max}$ Minimum value for all pairs	Method: $d_{\max}$ Value for Cys-Cys pair
5th percentile	5.4	5.4	2.04	2.04	8.19	8.19
10th percentile	6.13	6.13	3.43	3.43	9.11	9.11
25th percentile	11.44	11.44	8.51	8.51	14.14	14.14
50th percentile	17.92	17.92	15.1	15.1	20.71	20.71
average distance	19.3	19.3	16.47	16.47	22.13	22.13
75th percentile	25.06	25.06	22.31	22.31	28.01	28.01
90th percentile	34.02	34.02	29.98	30.98	36.64	36.64
lower outer bound for outliers	45.49	45.49	41.58	43.01	48.81	48.81

**Acknowledgement**

This work was supported by the Serbian Ministry of Education, Science and Technological Development (projects III44006 and 174021).

**REFERENCES**

- [1] J. Singh, J. M. Thornton. Atlas of Protein Side-Chain Interactions. IRL Press: Oxford. 1992. Vols I and II.
- [2] R. A. Laskowski, J. M. Thornton. Atlas of Side-chain Interactions. <http://www.biochem.ucl.ac.uk/bsm/sidechains/>
- [3] H. M. Berman, J. Westbrook, Z. Feng, G. Gilliland, T. N. Bhat, H. Weissig, I. N. Shindyalov, P. E. Bourne. The Protein Data Bank. *Nucleic Acids Res.* 2000; 28:235–242.
- [4] S. Griep, U. Hobohm. PDBselect 1992-2009 and PDBfilter-select. *Nucleic Acids Res.* 2010;38:D318-319.
- [5] W. Kabsch, C. Sander. Dictionary of protein secondary structure: pattern recognition of hydrogen-bonded and geometrical features. *Biopolymers.* 1983;22:2577-2637.
- [6] A. G. Murzin, S. E. Brenner, T. Hubbard, C. Chothia. SCOP: a structural classification of proteins database for the investigation of sequences and structures. *J Mol Biol.* 1995;247:536-540.
- [7] A. Aitken, M. Learmonth. Quantification and location of disulfide bonds in proteins. *Methods Mol Biol.* 1997;64:317–328.

## THE EFFECT OF SOME MIXED TETRAOXANES ON GERMINATION AND ANTIOXIDANTS IN MAIZE SEEDLINGS

V. Dragičević<sup>1</sup>, D. Opsenica<sup>2</sup>, J. Mesarović<sup>1</sup>, M. Brankov<sup>1</sup>, M. Simić, N. Kravić<sup>1</sup> and D. Milojković-Opsenica<sup>3</sup>

<sup>1</sup> Maize Research Institute "Zemun Polje", Slobodana Bajića 1, 1185 Zemun Polje – Belgrade, Serbia. (vdragicevic@mrizp.rs)

<sup>2</sup> University of Belgrade, Institute for Chemistry, Technology and Metallurgy, Njegoseva 12, 11000 Belgrade, Serbia.

<sup>3</sup> University of Belgrade, Faculty of Chemistry, Studentski trg 16, 11000 Belgrade, Serbia.

### ABSTRACT

Application of natural or synthetic substances could increase maize vigor. In this study we examined the influence of four mixed tetraoxanes on germination and seedlings growth of maize inbred line with low germination ability. Tetraoxanes expressed positive influence on germination rate and maize seedlings growth through increased DPPH-scavenging activity, improve water and antioxidative status by increase of phytic acid and phenoles concentration.

### INTRODUCTION

Germination is one of the most sensitive phases in growth of agricultural plants, where optimal conditions in temperature and water accessibility are required. Seedlings are particularly sensitive to environmental stressors, especially when maize lines are considered. They tend to germinate and grow slower, have poorer adaptability to stress and seeds could lose germination ability relative fast. Application of natural or synthetic substances could increase maize vigor, particularly of seeds with poor viability. It is proven that some stimulators positively affect growth, water absorption and antioxidative response of plants [1-4]. The aim of experiment was to examine the influence of four mixed tetraoxanes on germination and early growth (seven-day old seedlings) of maize inbred line with low germination ability (<50%).

### EXPERIMENTAL

Seeds of maize line with lower germination ability (about 40%) were soaked into distilled water (control) and mixed tetraoxanes solution ( $10^{-6}$  M; T1-T4).

The seeds were germinated under controlled laboratory conditions on filter paper (BP, 20⇔30°C, ISTA Rules [5]). After 7 days, germination rate was determined and length of roots and shoots were measured. After drying at 60°C roots and shoots fresh and dry weight were determined. Free energy ( $\Delta G$ ) of free water was calculated using sorption isotherm [6]:

$$\Delta G = -RT \ln(a_w)$$

From root and shoot samples DPPH reduction capacity was determined by the method of Abe [7], phytic acid (Pphy), phenoles (Phen) and soluble thiolic groups (PSH) were determined from the same extract [8-10]. Results are present with standard deviation (SD) and the dependences between examined parameters were obtained by correlation (Pearson's coefficients).

## RESULTS AND DISCUSSION

It was observed that all applied treatments induced increasing in germination rate (Figure 1), but the highest impact expressed T1 and T2, with increase for 11.3% correspond to control. From this point, dual role of peroxide (toxic and signalling) was surpassed [1], indicating greater safety with tetraoxanes usage.

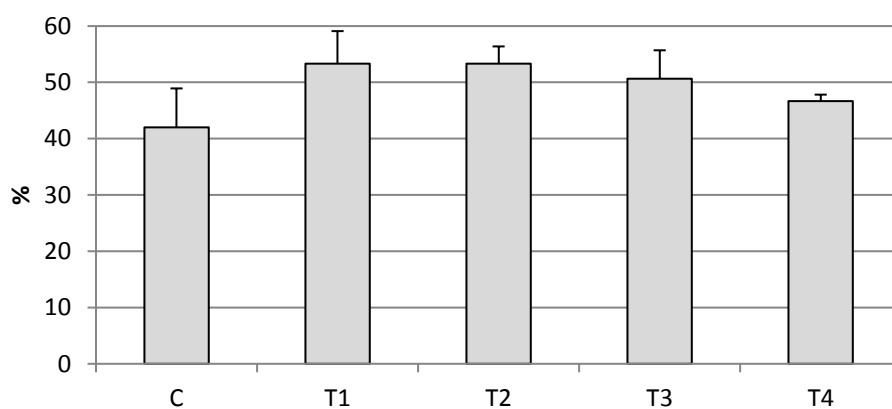


**Figure 1.** The influence of mixed tetraoxanes (T1-T4) and control (C) on germination rate

It was shown that maize seedlings react variously to applied treatments. Root and shoot length were increased by all treatments. For root the highest length increase was with T2 and T4 treatments and with T4 for shoot. High impact on the antioxidant parameters (DPPH, Pphy, Pphe and PSH) was observed in the root after treatment with all compounds, in comparison to control, indicating potentially increased stress tolerance [3]. Treatments with

T1 and T4 resulted with the highest values for DPPH, which is also tied with the highest values in Phen and lowest values in Pphy, indicating crucial Phen role as protective compounds against oxidative stress [2,9]. In addition, although treatments with T2 and T3 results with smallest change in DPPH, Phen and PSH, they exhibited the highest increase of Pphy, which had at the same time the highest variability among antioxidants. It is also important to underline that increase of DPPH-scavenging activity was positive connected to increase of phenolics and negative with increase of phytic acid, outlining them as a main antioxidants on the root level [2,4]. On the shoot level, treatment with T4 showed the highest impact on length, Pphy and Phen values. While the increase of shoot length coincidence with the highest Phen value, it is reversely related with Pphy.

**Table 1.** The influence of mixed tetraoxanes (T1-T4) on root and shoot length, free energy of free water ( $\Delta G$ ), DPPH-scavenging activity, phytic acid (Pphy), phenolics (Phen) and soluble thiol groups (PSH)

	Length (cm)	$\Delta G$ (J mol <sup>-1</sup> )	DPPH (%)	Pphy (mg P g <sup>-1</sup> )	Phen ( $\mu\text{g g}^{-1}$ )	PSH (nmol g <sup>-1</sup> )
Root						
C#	8.86	0.21	71.90	0.62	208.18	125.38
T1	11.26	0.20	95.59	0.30	421.70	122.99
T2	13.37	0.21	75.56	2.43	220.63	67.08
T3	11.58	0.21	78.89	1.49	202.84	78.26
T4	13.12	0.24	99.58	0.63	330.06	78.26
Mean	11.64±1.81	0.21±0.01	84.31±12.45	1.09±0.87	276.68±96.39	94.40±27.59
Shoot						
C	4.84	0.22	90.85	1.48	572.05	214.83
T1	7.33	0.22	94.14	1.58	492.87	239.58
T2	7.33	0.20	99.25	1.93	548.92	190.07
T3	6.20	0.21	75.14	1.30	653.90	224.41
T4	8.16	0.22	99.20	0.69	701.05	223.61
Mean	6.77±1.29	0.21±0.01	91.72±9.93	1.40±0.46	593.76±83.35	218.50±18.22
C# Control, distilled water.						

## CONCLUSION

Applied mixed tetraoxanes expressed various effects on maize germination and seedlings growth. Generally positive influence on germination rate and maize seedlings growth was achieved, through increase in DPPH-scavenging

activity, improve of water and antioxidative status by increasing of phytic acid and phenolics concentration.

### ***Acknowledgement***

This work was supported by the Ministry for Science of the Republic of Serbia (Grants no. ON 172008 and TR 31037) and innovative grant No 391-00-16/2017-16/7.

### **REFERENCES**

- [1] Ł. Wojtyła, K. Lechowska, S. Kubala, M. Garnczarska, *Front Plant Sci.*, 2016, 7, 66.
- [2] Z.A. Salama, A.A. Gaafar, M.M. El Fouly, *Agricult. Sci.*, 2015, 6, 397-405.
- [3] N. Kaur, A. Kumar, K. Kaur, A.K. Gupta, I. Singh *Ind. J. Biochem. Biophys.*, 2014, 51, 407-415.
- [4] E. Graf, J.W. Eaton, *Free Radic. Biol. Med.*, 1990, 8, 61-9.
- [5] ISTA, 2015. *International Rules for Seed Testing 2015*. International Seed Testing Association, Bassersdorf, Switzerland.
- [6] W.Q. Sun, in: *Desiccation and Survival in Plants: Drying Without Dying*, Black M. & Pritchard H. W. (Ed.), CABI Publishing, New York, USA, 2002, 47-91.
- [7] N. Abe, T. Murata, A. Hirota, *Biosci. Biotechnol. Biochem.* 1998, 62, 661-666.
- [8] V. Dragičević, S. Sredojević, V. Perić, A. Nišavić, M. Srebrić, *Acta Period. Technol.* 2011, 42, 11-21.
- [9] A. Simić, S. Sredojević, M. Todorović, L. Đukanović, Č. Radenović, *Seed Sci. Technol.*, 2004, 32, 213-218.
- [10] L.J. de Kok, P.J.L. de Kan, G. Tanczos, J.C. Kupier, *Physiol. Plant.*, 1981, 53, 435-438.
- [11] H.-F. Fan, L. Ding, C.-X. Du, X.Wu, *Bot. Stud.*, 2014, 55, 46.

CIP - Каталогизација у публикацији - Народна библиотека Србије, Београд

544(082)

621.35(082)

577.3(082)

543.42(082)

INTERNATIONAL Conference on Fundamental and Applied Aspects of Physical Chemistry (14 ; 2018 ; Beograd)

Physical Chemistry 2018 : proceedings. Vol. 1 / 14th International

Conference on Fundamental and Applied Aspects of Physical Chemistry,

September 24-28, 2018, Belgrade ; [editors Željko Čupić and Slobodan Anić].

- Belgrade : Society of Physical Chemists of Serbia, 2016 (Belgrade :

Jovan). - VI, 550 str. : ilustr. ; 24 cm

Tiraž 200. - Bibliografija uz svaki rad.

ISBN 978-86-82475-36-1

1. Society of Physical Chemists of Serbia (Beograd)

a) Физичка хемија - Зборници b) Електрохемијско инжењерство - Зборници

c) Биофизичка хемија - Зборници d) Спектроскопија - Зборници

COBISS.SR-ID 267528204